NUREG/CR-1602

Strength and Stiffness of Tensioned Reinforced Concrete Panels Subjected to Membrane Shear, Two-Way Reinforcing

Manuscript Completed: March 1980
Date Published: July 1980

Prepared by
P. C. Perdikaris, R. N. White, P. Gergely

Department of Structural Engineering
Cornell University
Ithaca, NY 14853

Prepared for
Division of Reactor Safety Research
Office of Nuclear Regulatory Research
U.S. Nuclear Regulatory Commission
Washington, D.C. 20555
NRC FIN No. B5688

U. S. Nuclear Regulatory Commission

Previous Reports in Concrete Structure Research Series

Analysis of Shear Transfer in Reinforced Concrete with Application to Containment Wall Specimens, P. Leombruni, O. Buyukozturk, J. J. Connor, Massachusetts Institute of Technology, NUREG/CR-1085, October 1979.

Safety Analysis of Nuclear Concrete Containment Structures, P. Petrina, R. Sexsmith, R. N. White, Cornell University, NUREG/CR-1097, December 1979.

Shear Transfer in Large Scale Reinforced Concrete Containment Elements Report No. 1, R. G. Oesterle, H. G. Russell, Construction Technology Laboratories, Portland Cement Association, NUREG/CR-1374, April 1980.

ABSTRACT

The transfer of shear stresses along pre-existing cracks by means of the interface shear transfer (aggregate interlock) and dowel action mechanisms is of major importance in the response of reinforced concrete structures.

The main objective of this report is to present and discuss experimental results on the effects of combined fully reversing cyclic membrane shear, and biaxial tension loading, on the degradation of the shear rigidity and strength of precracked reinforced concrete flat specimens. Only two-way orthogonal reinforcement is considered in the present study.

The specimen configuration and loading scheme employed were chosen to best simulate the membrane stress state in the wall of a reinforced concrete nuclear containment vessel subjected to the combined loading of an accidental internal pressurization plus membrane shear due to seismic forces. The specimens were 4 ft. square and 6 inches thick orthogonally reinforced with 3/4 inch diameter bars. Sixteen specimens were tested; test parameters included the level of biaxial tension, the peak shear stress level and the loading history (monotonic and cyclic shear). The effect on each of these on the shear stiffness, cracking patterns and ultimate strength were investigated.

Engineering models are proposed with predictive equations for the effective shear modulus G_{cr} for cracked reinforced concrete and for the ultimate strength under membrane shear and simultaneous biaxial tension. It was found that at shear stresses less than about 100 psi the shear resistance is provided by the combined mechanisms of interface shear transfer and dowel action along the orthogonal cracks. For shear stresses above 100 psi which produce extensive diagonal cracking, the prevailing shear transfer mechanism is that of diagonal tension and compressive strut action in the concrete. The measured effective shear modulus values in the cracked specimens are less than 10% of that for uncracked concrete. The effect of cycling caused a 15 to 20% reduction in shear capacity relative to the monotonically loaded specimens. The experimental results on ultimate strength are considered to be very conservative since they are based on the total cross-sectional area of the specimen and failure occurred at a diagonal crack.

The initial extensional (axial) stiffness in both reinforcing directions in four axial tests on identical flat specimens with No. 4 and No. 6 bars is determined so that estimates of the initial crack width at the orthogonal cracks can be calculated.

Finally, design implications for the allowable membrane shear in nuclear containment vessels and tentative design recommendations are given.

This improved understanding of the shear transfer phenomenon in cracked two-way reinforced concrete panels should result in the reduction or even the elimination of the additional diagonal steel normally used to help resist seismic membrane shear. Also, these research results will lead to a more rational dynamic analysis of cracked reinforced concrete containment structures.

TABLE OF CONTENTS

LIST OF FIGURES

LIST OF TABLES

FOREWORD

U. S. Nuclear Regulatory Commission has established a research program on reinforced concrete related to licensing of containments and other safety related Category I structures. Participants of this program are: Construction Technology Laboratories, a Division of the Portland Cement Association (PCA); Cornell University; and Massachusetts Institute of Technology (MIT). The Portland Cement Association and Cornell University contribute to this program with experimental testing of structural elements. The Portland Cement Association is testing large-scale elements. Cornell University is testing intermediate size elements. Massachusetts Institute of Technology contributes with analytical interpretation, primarily for PCA's test program.

This report is the first of a series of several reports to be issued on the Cornell University research. It treats reinforced concrete wall elements with two-way orthogonal reinforcement subjected to combined biaxial tension and membrane shear.

U. S. Nuclear Regulatory Commission

CHAPTER 1

INTRODUCTION

1.1 Motivation and Purpose

The present research was motivated from design considerations for reinforced concrete containment structures. A major design problem in the construction of nuclear containment vessels, offshore structures or other similar thick-walled cylindrical reinforced concrete structures is to efficiently proportion the materials of concrete and steel to carry the heavy seismic forces across already existing cracks.

In the case of reinforced concrete nuclear containment vessels (RCCV's) the wall would be cracked in the hoop and meridional direction during the internal pressurization acceptance test. This would result in vertical and horizontal cracks that separate the cylindrical wall into blocks of uncracked concrete held together by the reinforcing bars. Thus, the induced seismic shear forces have to be transferred to the base of the structure across the existing horizontal and vertical cracks by the shear transfer mechanisms. These include interface shear transfer along the rough crack interfaces, dowel action of the reinforcing bars, and tensile forces in the bars that are inclined to the crack plane.

An actual pattern of horizontal and vertical cracks in the wall of a nuclear containment vessel during the internal pressurization acceptance tests is shown in Fig. 1.1. To best simulate the stress conditions in the shaded region of the wall in Fig. 1.2, a square flat reinforced concrete

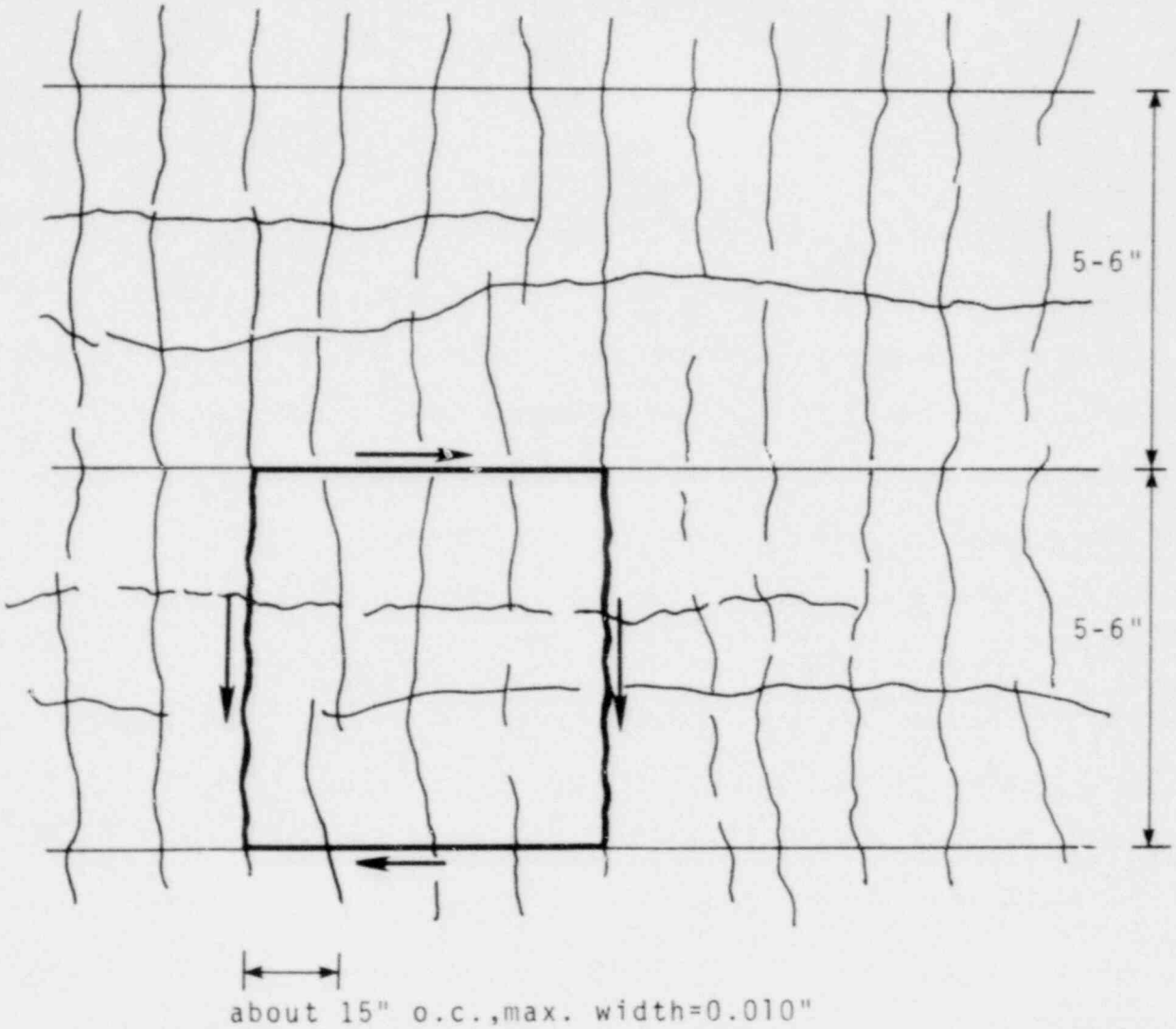

Fig. 1.1 Crack pattern in containment wall (horizontal cracks at each construction joint,plus one or two smaller cracks between joints).

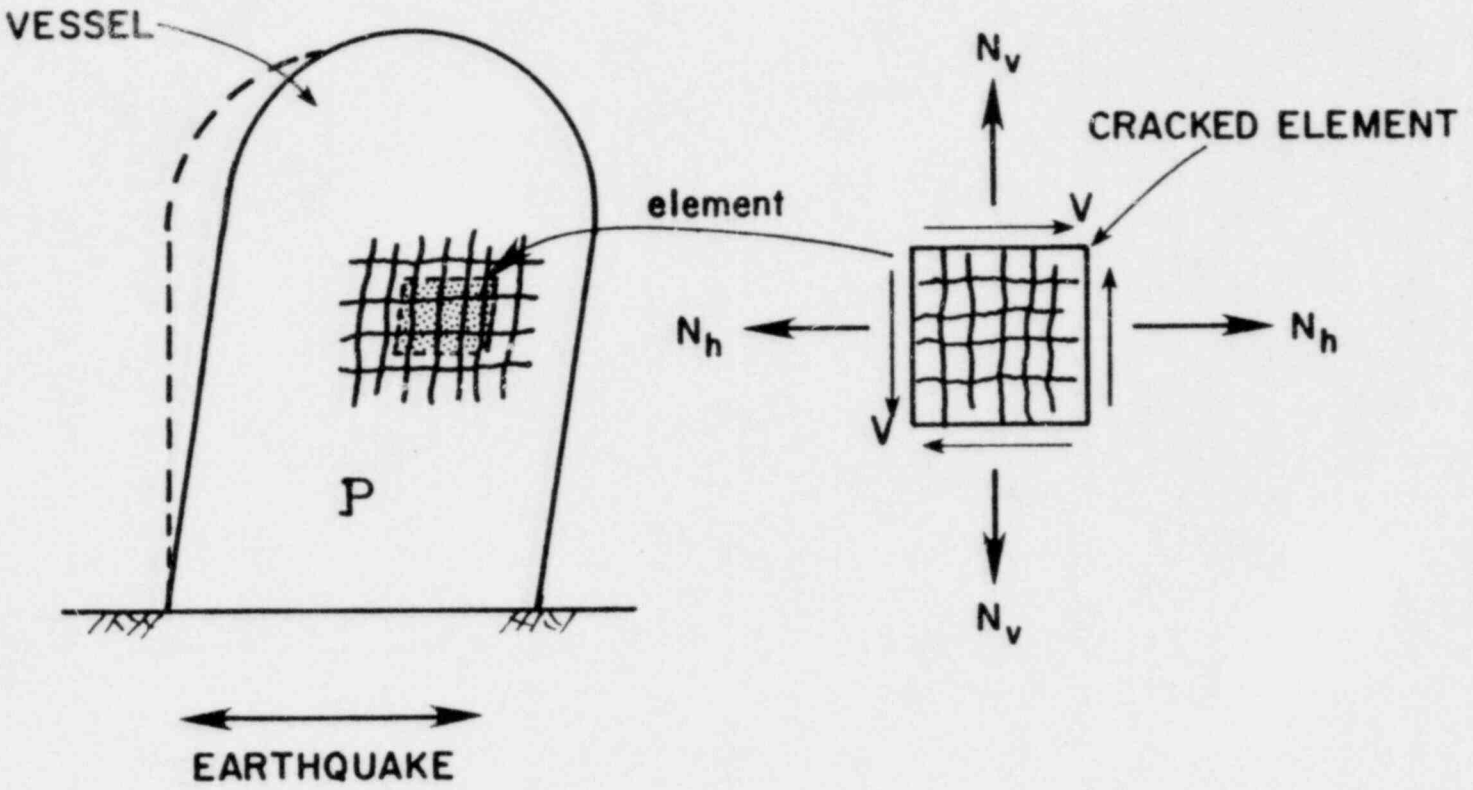

Fig. 1.2. Nuclear containment vessel under combined internal pressurization (p) and seismic forces.

specimen was utilized in the present investigation. In a containment structure there is also a 1/4 to 1/2 inch thick steel plate liner anchored on the wall to guarantee a leak tight structure even if cracking occurs in the concrete. This steel liner was not included in this work.

The required biaxial tension in the orthogonal reinforcement and shear forces in the concrete were applied to the specimen through specially designed tensioning and shear loading devices. The actual dynamic membrane shear stresses were simulated in these tests by fully reversing cyclic shear stresses statically applied to the specimen.

1.2 Objective

The major objective of this report is to determine the stiffness and strength of precracked reinforced concrete panels subjected to combined biaxial tension and fully reversing cyclic membrane shear loads. Parameters such as the shear stress level, the biaxial tension level, and the number of cycles are studied and their effect on the overall hysteretic behavior of the structure is determined.

The mechanisms involved in the shear transfer stiffness degradation are defined and an engineering model is proposed with predictive expressions for: (a) the effective shear modulus after cracking, and (b) the ultimate shear capacity. The expression for the shear modulus of cracked concrete panels under a biaxial state of stress will help to more accurately define the shear stiffness of a cracked element for implementation into a nonlinear finite element analysis of reinforced concrete structures. The prediction formulae for the ultimate strength will contribute to a better understanding of the failure mechanisms taking place and provide

more realistic design recommendations for large reinforced concrete structures, such as secondary nuclear containment vessels. The deformation behavior under cyclic reversing shear will have significant influence on the dynamic response and on the amounts of deformations that the steel liner plate in the containment experiences during combined biaxial tension and cyclic shear. In addition, this research will lead to a better understanding of important factors needed in a more rational dynamic analysis, such as damping, hysteretic behavior, and nonlinear response inherent in the shear transfer phenomenon.

Four-way reinforcing schemes with diagonals in both directions are often used in the construction of reinforced concrete nuclear containments where seismic membrane shear forces are high. It is therefore important to investigate whether the additional diagonal bars positioned at ±45 degrees to the horizontal are actually needed. The wall is already heavily congested with the orthogonal bars and other secondary reinforcement and it becomes costly to fabricate and place the additional diagonal steel (designed to carry the membrane shear forces). In addition, it is very difficult to attain high quality concrete due to the excessive steel congestion. A two-way orthogonal reinforcement scheme was utilized in the present experimental work in order to establish the fact that the orthogonal steel in the containment can mobilize considerable shear stiffness and strength. A better understanding of the shear transfer phenomenon in cracked concrete panels with two-way reinforcing patterns could lead to a substantial reduction of the amount of additional diagonal steel, and even eliminate it in some cases.

1.3 Outline

In Chapter 2 the results of an extensive experimental program conducted on flat concrete specimens subjected to simultaneous biaxial tension and simulated seismic membrane shearing forces are presented. The specimens are 6 inches thick and orthogonally reinforced with two layers of reinforcement in one direction and one layer in the other. They are cracked by tensioning the reinforcement to about 36 ksi. The tension level is held at a constant value (0, $0.3f_y$, $0.6f_y$ or $0.9f_y$) while fully reversing shear stresses are applied. The normal cyclic shear loading regime begins at a shear stress of ±125 psi for 10 cycles and then increases in increments of 50 psi, with 10 cycles of reversing shear at each load level. Increments of shear are added until failure results. Identical specimens are also subjected to combined tension and monotonic shear to failure. These results establish a basic interaction curve for biaxial tension plus shear and are used to assess the decrease in stiffness and strength produced by cyclic shear loading. Finally, the experimental results from the biaxial tests are compared with uniaxial tests on block specimens.

An expression estimating the effective extensional stiffness parallel to the orthogonal directions of the reinforcing bars is given in Chapter 3. Results on axial tests performed on four specimens with No.4 and No.6 rebars (0.5 in. and 0.75 in. or 13 mm and 19 mm diameter) are also presented. Based on measurements of total elongations on the concrete surface, the concrete tension stiffening effect is determined and its influence in estimating an effective steel modulus in tension is pointed out. A statistical analysis is performed to determine the average crack spacing

of the orthogonal cracks that formed after tensioning the bars in both directions. In addition, a literature review on axial tests with a single crack, and formulae for predicting the crack spacing and steel strain are included in this chapter. Finally, a comparison is made between the predicted values of the extensional stiffness given by the proposed expression and those measured in uniaxial tests or biaxial tests with larger size bars.

Chapter 4 is concerned with the development of an engineering model for prediction of shear stiffness and strength in the presence of biaxial tension. In the beginning of the chapter an extensive literature review is given regarding the interface shear transfer (IST) and dowel action (DA) mechanisms at a single crack and the determination of an effective shear modulus for cracked reinforced concrete panels. Also presented, is a review of previous analytical studies on planar reinforced concrete members and various expressions predicting the ultimate strength of block specimens with a single crack. An expression for the effective shear rigidity of concrete panels under biaxial tension and shear is proposed by generalizing the relation of shear stiffness along a single crack to bidirectional cracking normal to the orthogonal reinforcement. The effect of diagonal cracking on the shear modulus is also identified as the shear transfer sliding mode is gradually replaced by a diagonal tension-compression strut mode. The predicted shear rigidity values are compared with the experimental findings and values predicted by other relations in the literature (Duchon, Collins). Finally, the failure mode of the specimens tested is identified and equilibrium studies are performed to determine the shear transfer mechanisms active as failure is approached in biaxially tensioned reinforced concrete.

Tentative recommendations and implications regarding the design of nuclear secondary reinforced concrete containment vessels are given in Chapter 5.

Chapter 6 includes a summary of the conclusions drawn from the present research on the shear transfer phenomenon and a discussion with comments on additional future work needed to better understand this rather complex type of structural behavior.

CHAPTER 2

EXPERIMENTAL PROGRAM

2.1 Outline

Previous experimental investigations (see Section 4.2) have dealt with the subject of shear transfer along a preformed crack in reinforced concrete, but they focused on the case of combined uniaxial tension and shear acting at the crack. Effects of parameters such as cracking in two directions and applied biaxial tension on the shear transfer behavior were ignored. However, the wall of a reinforced concrete containment structure, cracked in both the hoop and the meridional directions and subjected to seismic shear forces, is in a state of biaxial stress (neglecting the variation of stresses through its thickness). Data on the stiffness and strength of such a section is definitely needed to better evaluate the shear transfer phenomenon and to improve design methodology.

This chapter describes the experimental program conducted to study the combined mechanisms of interface shear transfer (aggregate interlock) and dowel action in precracked reinforced concrete wall sections subjected to membrane biaxial tension and fully reversing cyclic shear. The specimen employed is described in detail in Section 2.2. This type of specimen was chosen to model the behavior of a cracked segment of a secondary nuclear containment vessel under internal pressurization and seismic forces. In addition, the size of the specimen was small enough so that it could be handled easier than a larger-scale specimen, which would have

resulted in an unreasonably high expense. During this experimental study a large range of variables could be investigated faster and more efficiently by utilizing the thinner specimens. This is the first specimen configuration reported in the literature that adequately represents the complex phenomenon of shear transfer at a crack interface in specimens subjected to simultaneous biaxial tension and in-plane shear.

Although it would be ideal to apply dynamic shear loads to the specimen, the shear loads were applied in a static manner, either monotonically or cyclically in predetermined increments. The formation of the shear planes was accomplished by tensioning the embedded reinforcing bars to about 36 ksi (248 MPa) in both the x and y directions (see Fig. 2.1a). Then the tension was held constant at a prescribed value for each specimen and the shear stresses were superimposed to create the desired stress conditions.

One of the major difficulties met during the design of the specimen and the reaction frame was how to apply the shear loads without interfering with the orthogonal cracking produced by biaxial tension, and at the same time creating in the central region of the specimen a reasonably uniform distribution of shear stresses. In fact, the shear loads were applied as equal tensile and compressive loads at the thickened corners of the specimen and in the direction of the diagonals (see Fig. 2.1b). Thus, the total shear force on each of the four edges of the specimen was transferred to the cross section as the sum of two equal projections of the diagonal tensile and compressive loads on a direction parallel to that side. A linear finite element analysis was employed to determine the elastic distribution of shear stresses in the specimen on the planes through the origin of the

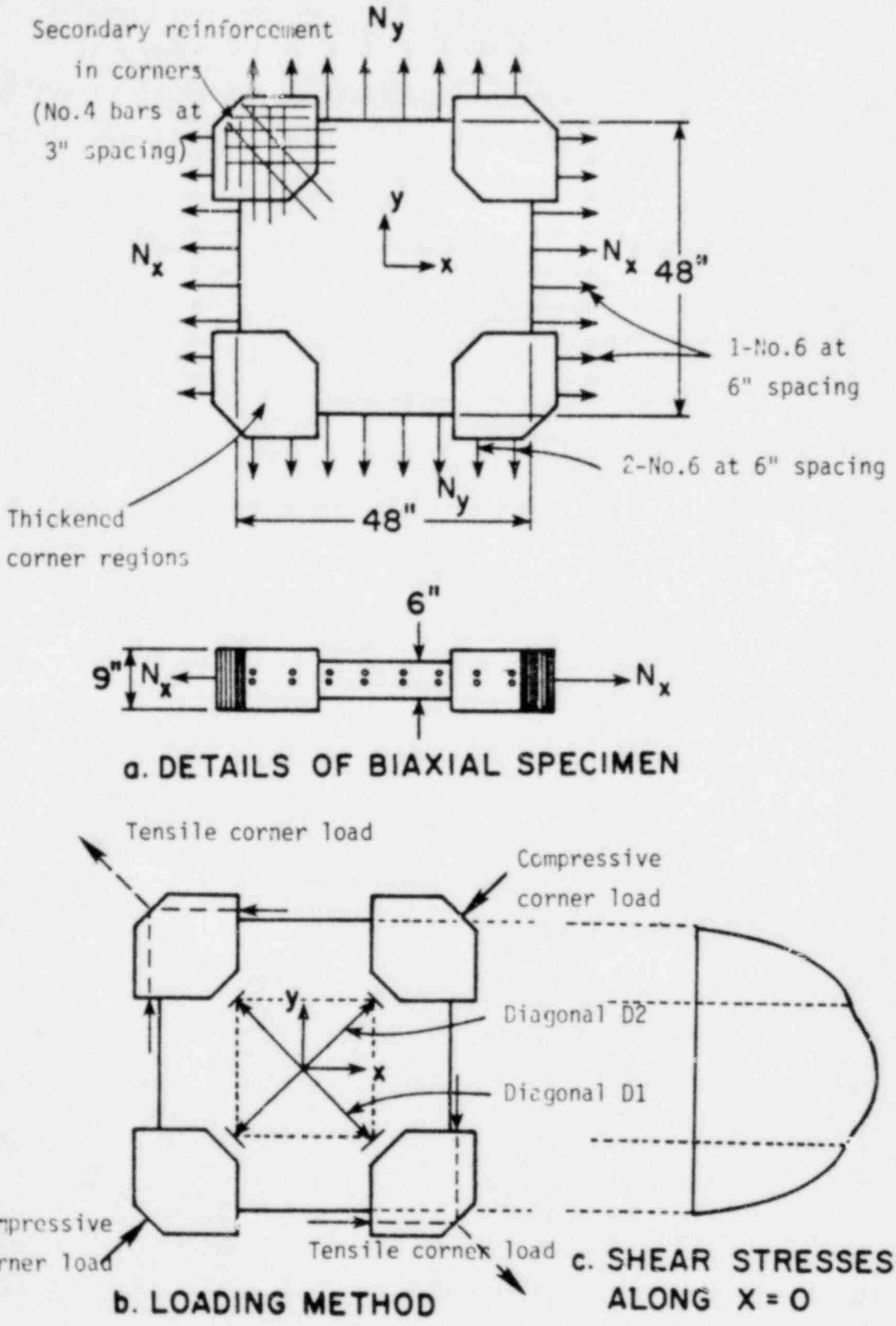

Fig. 2.1. Geometry and loading of biaxial specimen.

x-y coordinate system and parallel to the direction of the bars, as shown in Fig. 2.1c. Although this analysis is valid only prior to cracking, it can be seen that a reasonably uniform distribution of shear stresses exists at the central portion of the specimen, which is the region of interest.

Variables studied during the course of the experiments included applied tension in the bars, shear stress level, cyclic load history, and type of loading (monotonic or cyclic). Sixteen specimens were tested at different preselected tension stress levels, between 0 and $0.9f_y$, in the reinforcement. The reinforcement ratio was kept constant for all specimens (0.0122 in one direction and 0.0244 in the other direction). In all, twelve specimens were subjected to fully reversing shear (Series A,B,C) and four specimens to monotonic shear loading up to failure (Series M), to study the effect of cycling on the degradation of stiffness and strength. More details on the load history for each test and the loading procedures followed are given in Section 2.5.

Extensive measurements were performed at the central 2 ft. square region of the specimen, including crack slips and crack width changes along the orthogonal cracks, shear distortion of the panel, and extensional deformations in both directions parallel to the bars. The instrumentation procedure and description of the devices used to measure the deformations mentioned above are explained in detail in Section 2.4. All experimental work was conducted in the George Winter Structural Research Laboratory at Cornell University.

In Section 2.6, the experimental results are discussed in terms of cracking patterns observed, shear stress-displacement response, and ultimate strength attained for each specimen. The general behavior and

observations are also summarized for each group of tests. Finally, comparisons and conclusions are drawn in Section 2.7.

2.2 Description of Specimen - Materials

The specimen employed in the present experimental program is a 4 ft. (1.22 m) square reinforced concrete flat slab, 6 inches (152 mm) thick. It is reinforced with one layer of No.6 (0.75 in. or 19 mm diameter) bars at 6 inches (152 mm) spacing in the (x) direction (ρ_x = 0.0122) and with two layers of No.6 bars at 6 inches (152 mm) spacing in the orthogonal (y) direction (ρ_y = 0.0244). The layers in each direction were centered in the thickness of the slab to avoid eccentricity effects. All details of the specimen geometry are defined in Fig. 2.1a. The specimen provides a shearing area of 288 in^2.

The concrete mix consisted of Type III high early strength Portland cement, sand with a maximum size of 0.125 inches (3 mm), and locally available crushed gravel aggregate with a maximum size of 1.5 inches (38 mm). The above aggregate consisted of one part of N.Y. #1 type with a gradation of 3/8 to 1/2 inches (10 to 13 mm) and five parts of N.Y. #2 type aggregate with a gradation of 5/8 to 1 1/2 inches (16 to 38 mm). A representative gradation of the sand and the two types of aggregate used is shown in Table 2A. The average nominal compressive strength was about 3800 psi (26 MPa) with a specified slump of 3 to 3.5 inches (76 to 89 mm). Compressive strength, modulus of elasticity and ultimate strain in the concrete were determined from standard compressive tests on 6 x 12 inch (152 x 305 mm) cylinders. Compressive strengths of concrete in all specimens are

Table 2.A. Gradation of crushed gravel aggregates and course sand.

Sieve Size	Sand	N.Y. #1 Gravel	N.Y. #2 Gravel
1 1/2"			100
1"			99
3/4"		100	87
1/2"		98	7
3/8"	100	70	1
#4	99	2	
#8	90	1	
#16	65		
#30	25		
#50	9		
#100	2		
#200	1		
	(Percent Finer by Weight)		

contained in Table 2B. A representative stress-strain curve obtained from a 6 x 12 inch cylinder loaded in a very stiff MTS testing machine with an average strain rate of 0.01 in/in per minute, is shown in Fig. 2.2.

The reinforcement used was Grade 60 with an average yield strength of about 61 ksi (421 MPa). Four coupons 8 inches (203 mm) long were instrumented with electrical resistance strain gages and loaded to failure. The measured stress-strain relationship for the No.6 deformed bars is given in Fig. 2.3. The reinforcing bars used for all specimens have a nominal diameter of 0.75 inches (19 mm) and a cross-sectional area of 0.44 in^2 (125 mm^2).

The four corners of the specimen were made 3 inches (76 mm) thicker than the central portion, so that the reversing shear loads could be applied. Secondary reinforcement of No.4 (0.5 in. or 13 mm diameter) Grade 40 deformed bars in the form of prefabricated mesh (as shown in Fig. 2.1a),

Table 2.B. Cylinder compressive strength of concrete (f_c').

Specimen No.	Sample Compressive Strength (psi)		Average Compressive Strength (psi)	Specimen No.	Sample Compressive Strength (psi)		Average Compressive Strength (psi)
.0(A)	2688	3148	2980	.6(A)	3000	3200	3100
	3077	3006			3100		
.0(B)	3077	3431	3400	.6(B)	3350	3150	3300
	3714	3395			3400	3300	
.0(C)	3926	3890	3930	.6(C)	3608	3696	3790
	3890	4032			3890	3961	
.0(M)	3077	3042	3160	.6(M)	3600	3254	3700
	3148	3360			3855	4103	
.3(A)	3360	3254	3500	.9(A)	3466	3501	3580
	3678	3706			3714	3523	
.3(B)	3873	3890	3900	.9(B)	3183	3961	3650
	3926				3554	3890	
.3(C)	3590	3537	3620	.9(C)	3310	3537	3380
	3643	3714			3183	3480	
.3(M)	4545	4463	4600	.9(M)	3325	3908	3620
	4598	4775					

was placed in the corners (top and bottom) to ensure a better transfer of the corner loads to the thinner section of the slab. This additional reinforcement was needed to effectively anchor the corners to the flat portion of the specimen and diminish the undesirable cracking due to stress concentration effects at that area.

The concrete mix was prepared on site by a local concrete contractor according to the specified proportions and requirements, and was placed into two reusable forms fabricated from plastic-coated plywood. All plywood pieces were carefully oiled before casting to ease the process of

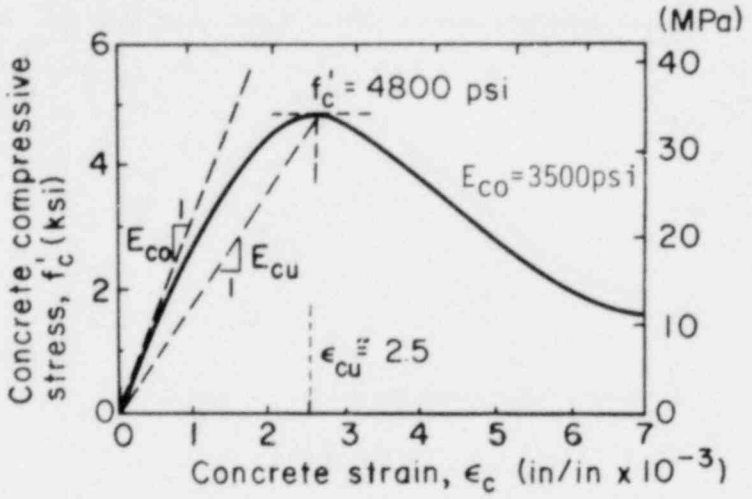

Fig. 2.2. Stress-strain curve for concrete in compression with f'_c=4800 psi (6x12 inch cylinder).

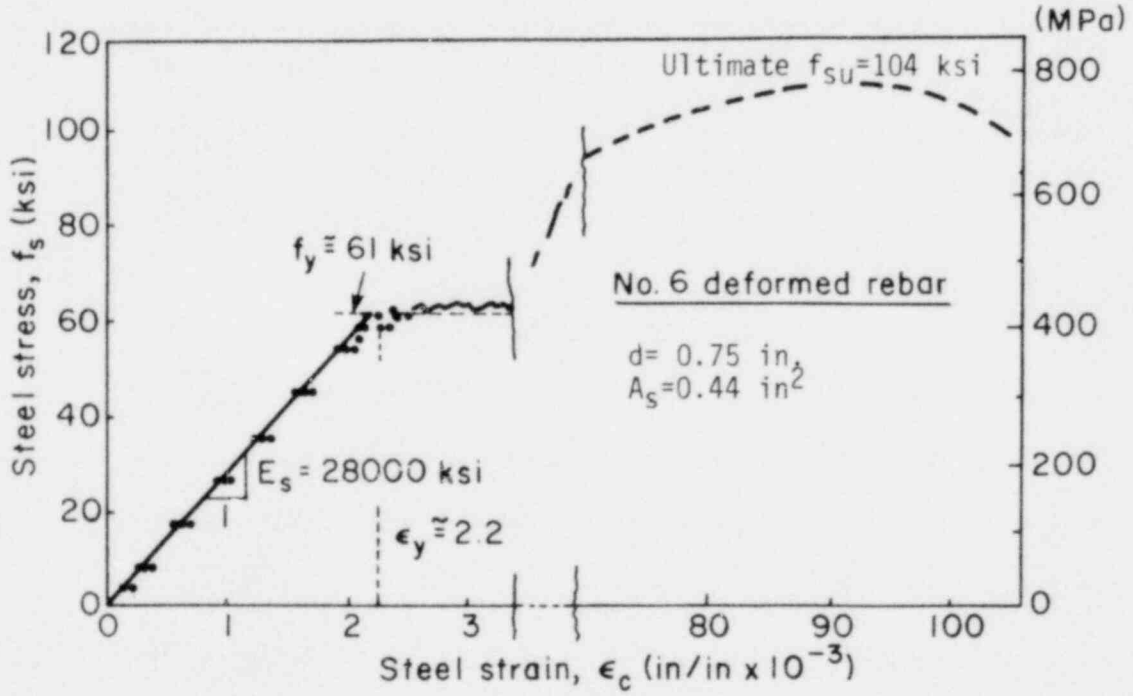

Fig. 2.3. Stress-strain curve for No.6 rebar (four 8 inch long coupons were tested).

dismantling the forms and thus prolong their life. The form with the reinforcement in place is shown in Fig. 2.4. The side panels of the forms were constructed in two half pieces and at the level of the joint in both directions holes were drilled in the plywood to hold the main reinforcement bars. Steel plates with threaded inserts were fastened on the form itself so that after removing the forms, special steel fixtures could be attached on the specimen to aid in transferring the shear-inducing compressive and tensile corner loads (see Fig. 2.5). Four threaded inserts were also embedded in concrete, one at each corner, to be used for lifting the specimen from the casting position to the testing frame with a large crane.

The concrete mix was compacted by a hand vibrator, especially at the corners of the specimen where the steel congestion made casting more difficult. The specimens were left in the forms for at least 7 days after casting. They were covered with wet burlap immediately after casting and were periodically moistened to lessen shrinkage cracking. The curing process took at least 14 days after casting, at which time at least 4 cylinders were tested to determine the compressive strength of concrete.

2.3 Experimental Setup and Loading Scheme

The biaxial tensile load was applied in the embedded No.6 bars with hydraulic rams that reacted against structural steel frames around the specimen. The reversing loads were transmitted to the slab by alternately pushing and pulling on the corners through two large hydraulic rams connected to a prestressed concrete reaction frame.

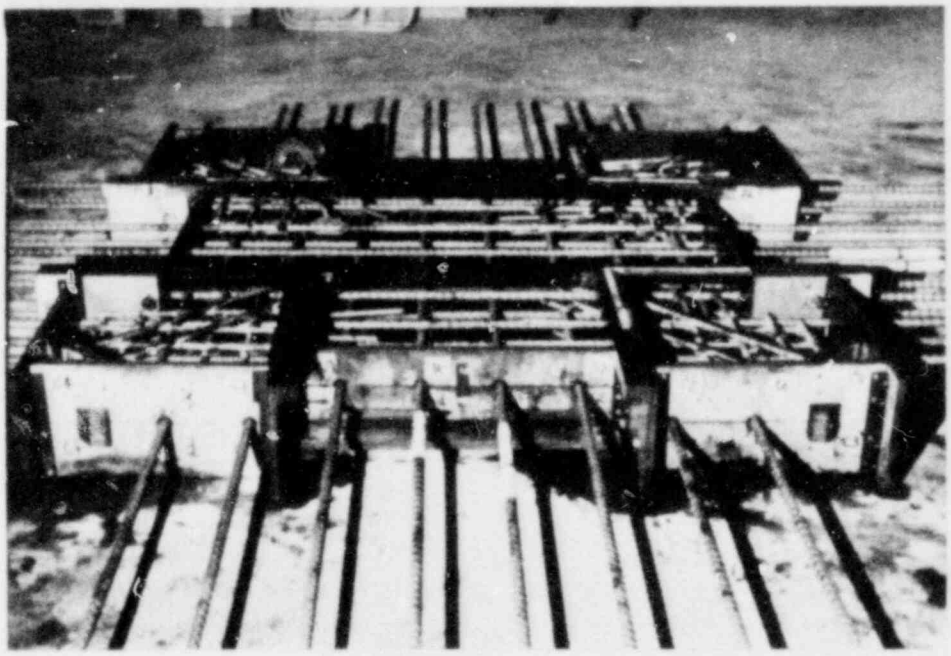

Fig. 2.4. Form and reinforcing bars for the biaxial specimen.

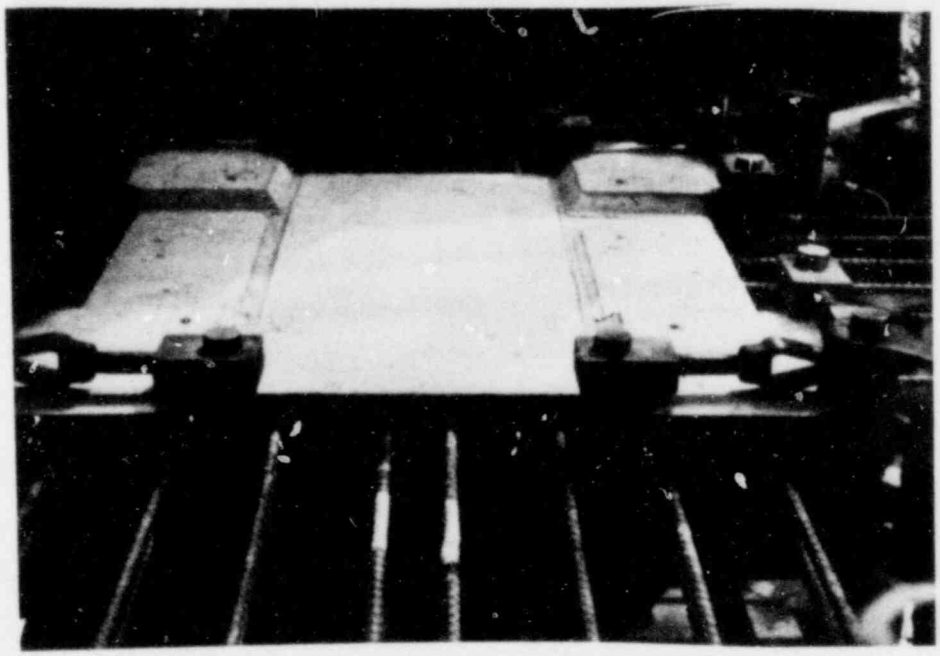

Fig. 2.5. Corner fixtures for applying the shear load.

The reaction system for the bar tensile loads consisted of 8 individual frames (4 frames in each direction), each fabricated of two horizontal heavy-walled steel pipes with vertical rectangular steel tubular end sections (see Figs. 2.6a, 2.6b). The tensile loads were applied by four 30 ton capacity single-acting center hole hydraulic jacks (Enerpac RCH-302) in the single layer and four 60 ton capacity jacks (Enerpac RCH-603) in the double layer, powered by two independent hand pumps. The load from the jacks was transmitted to the bars reacting against a tubular section-nut assembly welded to the ends of the bars. All jacks were held by pipes welded on the end tubular sections, which were also resting on steel I-beams. The I-beams could move freely in the horizontal direction on ball-bearing plates. Each hydraulic ram was capable of tensioning two bars in the single layer and four bars in the double layer up to the yield strength of the steel.

A large prestressed concrete frame employed to react to the shear corner loads was preferred over a steel frame of equal capacity, since the former was both stiffer and less expensive. It consisted of two inverted post-tensioned frames at right angles to each other as shown in Fig. 2.7. High strength steel rods were used to post-tension the beams and vertical cantilevers in the concrete frame. The two 200 ton capacity heavy duty solid plunger hydraulic rams used to apply the shear loads were of the double-acting type with a 13 inch (330 mm) stroke capacity (Enerpac RR-20013). They were powered by two independent electric pumps. Also, two large tubular section load cells were used on the opposite corners of the specimen to monitor the applied shear loads.

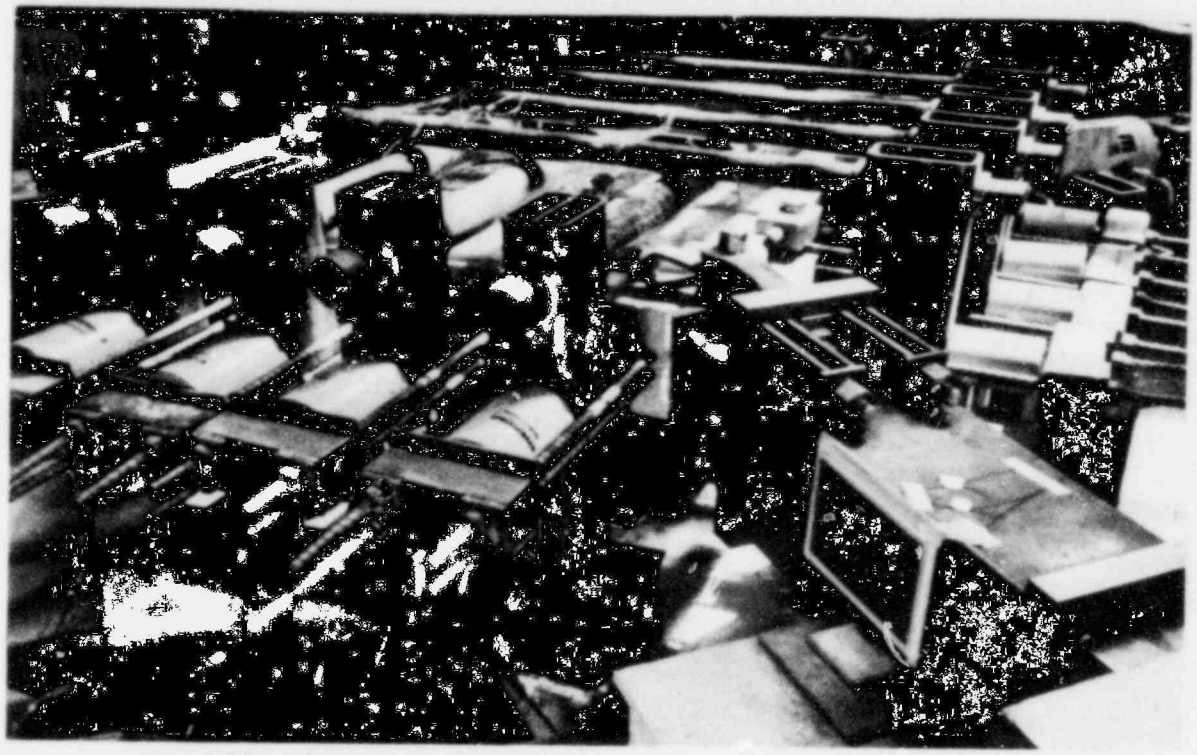

a. Side view.

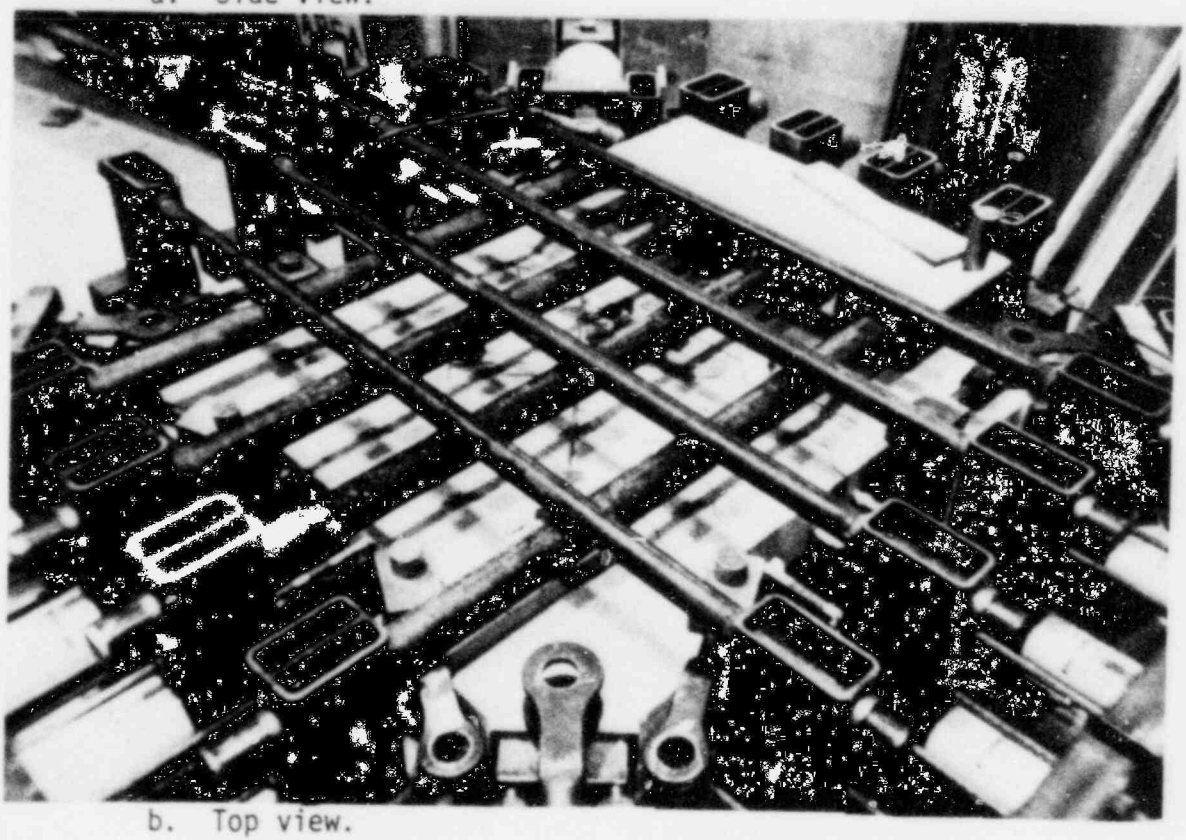

b. Top view.

Fig. 2.6. Tensioning reaction frame.

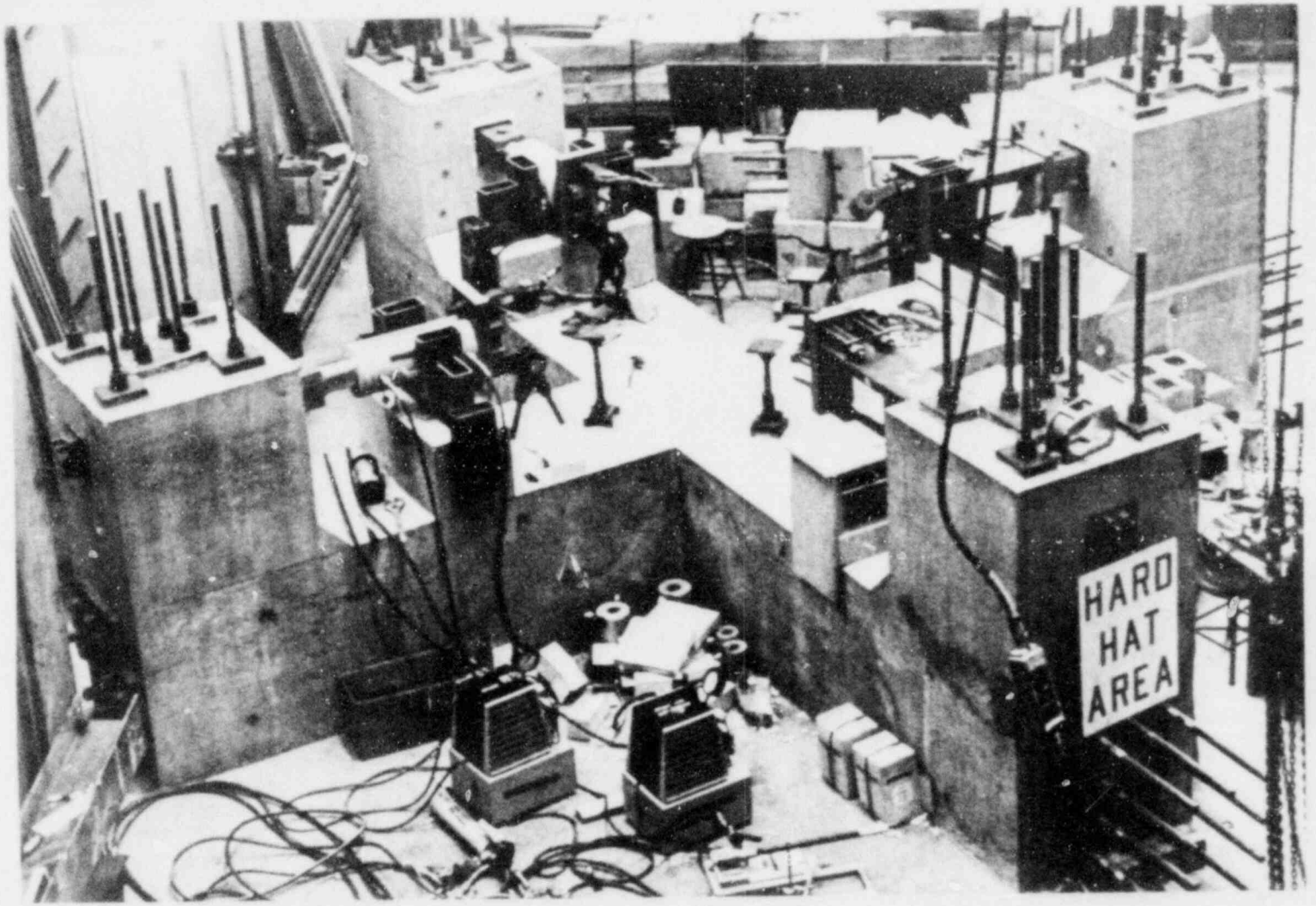

Fig. 2.7. Prestressed concrete reaction frame.

Both hydraulic rams and tubular sections were connected with hinge-type steel linkages to the columns of the concrete reaction frame to permit free rotations while the specimen was deforming. A linkage system existed also between the corners of the specimen and the rams or the load cells. The latter linkage was designed to transmit either compressive (high strength steel bearing plates with a male and a female pin connection) and tensile corner loads (high strength steel pins and heavy clevises) and at the same time allow free horizontal movement of the slab. The above rather massive connection fittings and linkages at the corners of the specimen are shown in Fig. 2.8. Peak shear stresses of about 550 psi (3.8 MPa) may be generated in the specimen with the hydraulic rams pressurized at a load of 112 kips (498 kN), which is the maximum tension capacity of the rams.

After the specimen was placed in the test frame it was leveled to a precise position with the aid of four vertical mechanical supporting jacks permanently fastened to the concrete beams of the frame. Between the specimen and the jacks specially designed ball-bearing plates were placed in order to achieve free horizontal movement during the test (see Fig. 2.9). Then, the external pipe and tubular steel frames for stressing the bars at the prescribed level of tension were positioned around the specimen in both directions. The major advantage of this experimental setup is that the bar stressing systems are independent in the two directions of the bars, and both are completely independent of the shear loading system. Thus, undesired restraints and interaction are avoided. Considering the extreme difficulties present in the load application system, the reaction frames and the tensioning devices and linkages, the system functioned very well. It is the first successful experimental setup for application of fully

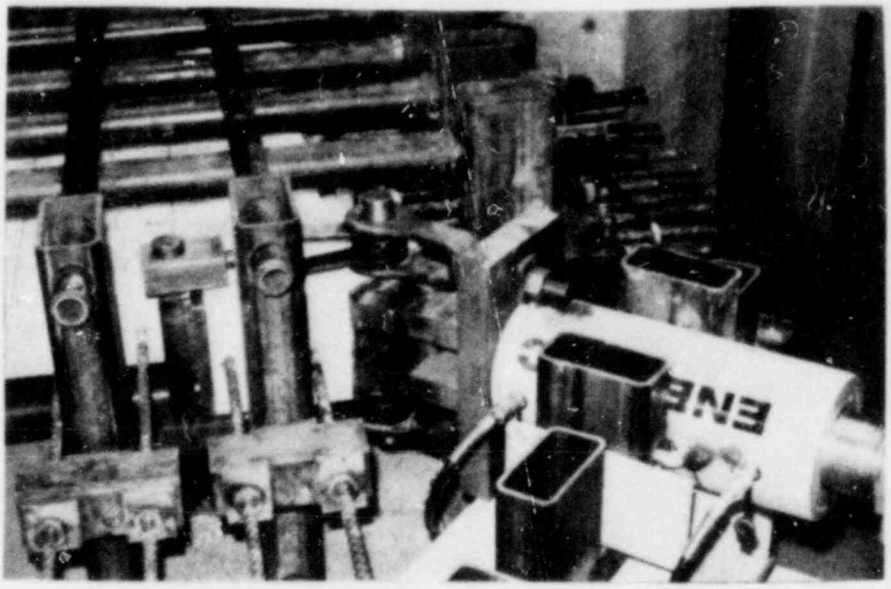

a. Corner linkage system for tension load.

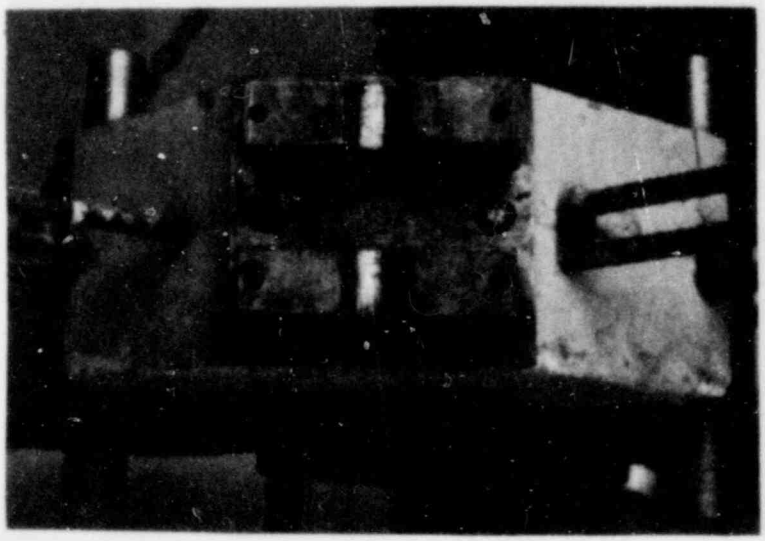

b. Bearing plate for compression load.

Fig. 2.8. Corner fittings and linkages.

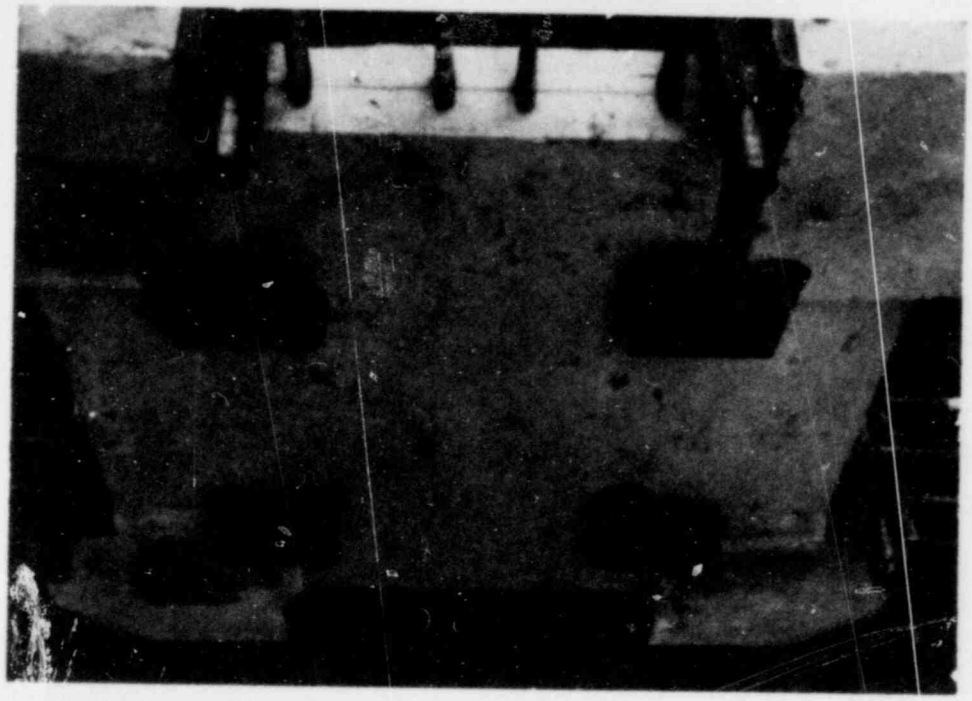

a. Bottom side of specimen with bearing plates.

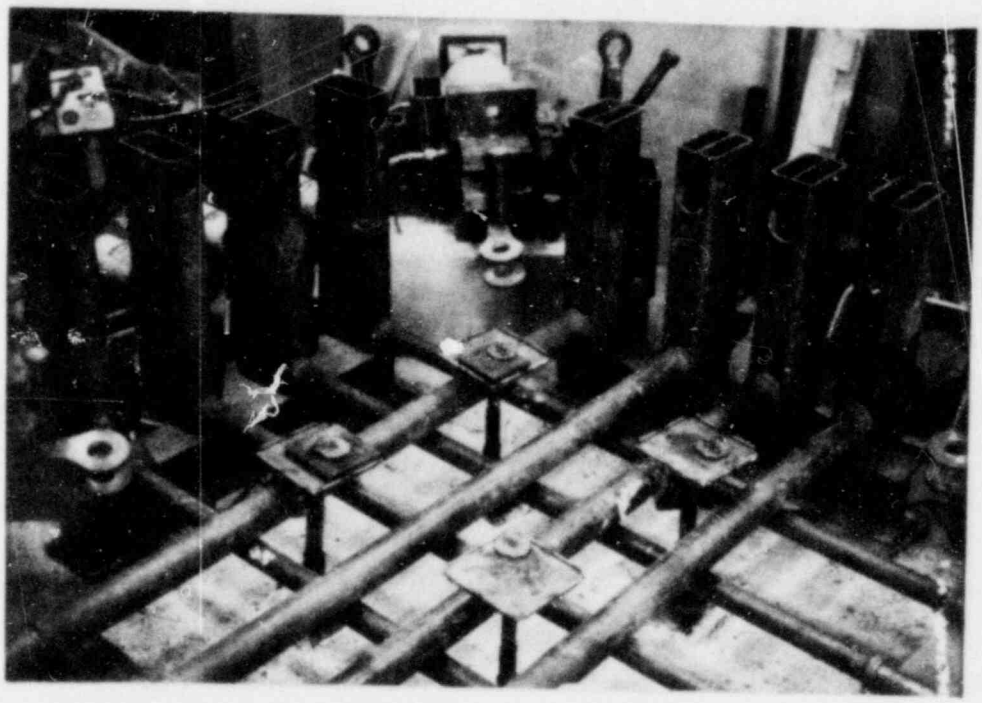

b. Vertical jacks with ball-bearings.

Fig. 2.9. Vertical supporting system.

independent biaxial tension and reversing shear stress to reinforced concrete specimens.

After the specimen was cracked in both directions, a 6 inch (152 mm) square grid was drawn with a felt-tipped pen on the concrete surface and the orthogonal cracks were marked. Then, the dial gages and/or the displacement transducers (DCDT's) were mounted on the top of the specimen at the appropriate positions (see Section 2.4 for details on the instrumentation procedure). The shear loads were then applied according to the load history of each specimen (see Section 2.5) and the additional diagonal cracking was recorded at preselected peak shear stress levels. An overall view of the specimen in the testing frame is given in Fig. 2.10.

2.4 Instrumentation - Measurements

In the central 2 ft. (610 mm) square region of the slab specimen three different types of deformations were measured during the tests: the crack width changes perpendicular to the crack planes, the crack slips parallel to the crack, and the compressive and tensile diagonal deformations. The crack slip and crack width measurements were conducted for only one selected major orthogonal crack in each direction. Therefore, these measurements are influenced by local effects and are not representative of the entire panel. The shear distortion, on the other hand, was measured over a larger gage length of 34 inches (864 mm) and included several orthogonal cracks in both directions. This integration of deformations over several cracks provides realistic deformational patterns characteristic of the overall behavior of the specimen. Both dial gages and

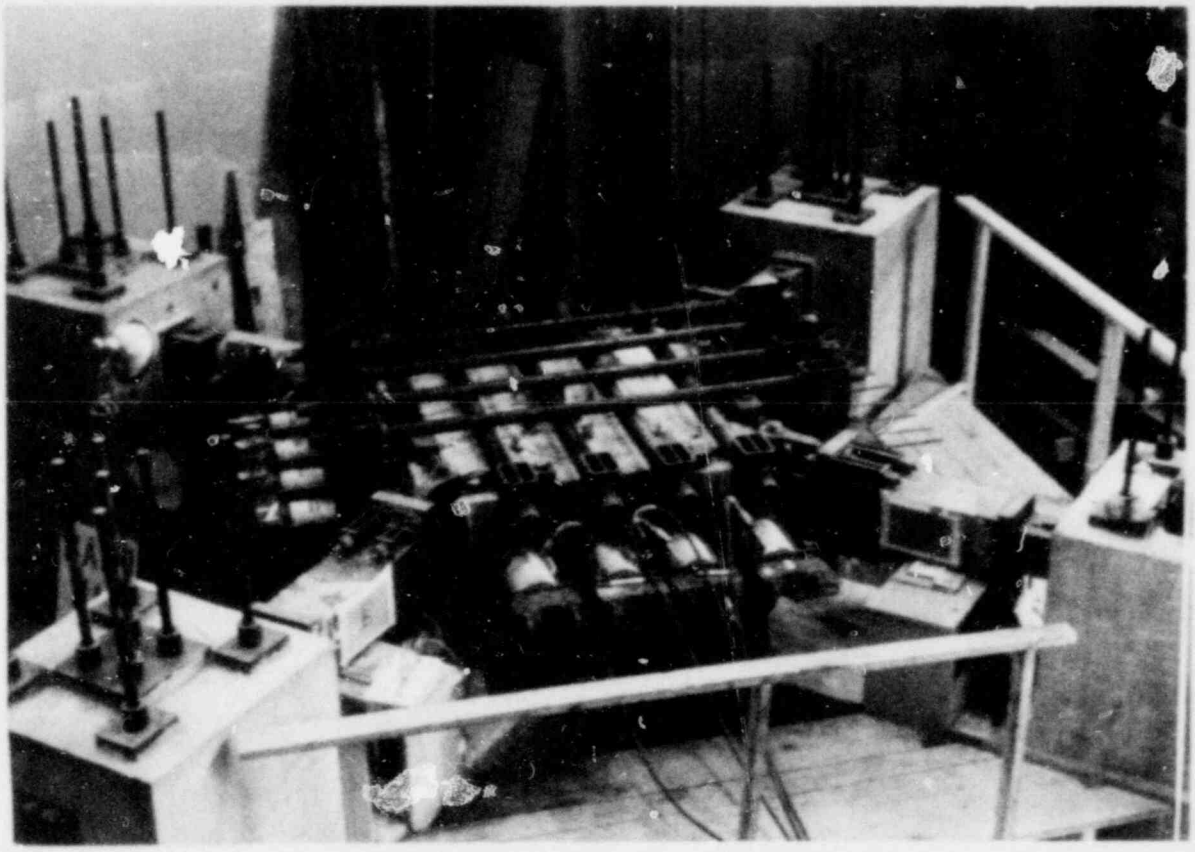

Fig. 2.10. General view of experimental setup and specimen during testing.

linear displacement transducers were used to measure deformations. Dial gages were used for the first four experiments and transducers for the remainder of the tests as a new data acquisition system was obtained. However, occasionally dial gages were used together with transducers for verification purposes.

A general view of the instrumentation is shown in Fig. 2.11a, and a close-up photograph of the instrumentation is shown in Fig. 2.11b. The crack slip (S1, S2) and the crack width gages (C1, C2) were mounted parallel and perpendicular to a major orthogonal crack, respectively, in both the direction of the single layer (x) and the double layer of bars (y). The diagonal deformations (D1, D2) were measured with the use of special brackets and a thin bar along the diagonals to span the moving and the rigid part of the gage (see Fig. 2.12). The dial gages employed had a least reading of either 0.0001 or 0.001 inches (0.0025 or 0.025 mm). The displacement transducers made by Hewlett Packard were of two kinds: four DCDT's with displacement range of ±0.5 inches (±12.7 mm) and two with a range of ±1.0 inch (±25.4 mm) were used. Both were excited by a DC power supply at 6 volts and had a guaranteed linearity error of less than 0.5% of the full scale.

For selected specimens the axial elongation in both x and y directions was measured with dial gages of a least reading of 0.0001 inches (0.0025 mm). More details are given in Section 3.3, dealing with the extensional axial stiffness of the specimen. The test specimens were also instrumented to measure the applied shear loads and the tension in the reinforcement. The load cells employed to measure the shear corner loads were prepared and installed using four 1 inch (25.4 mm) long wire SR-4 electrical strain

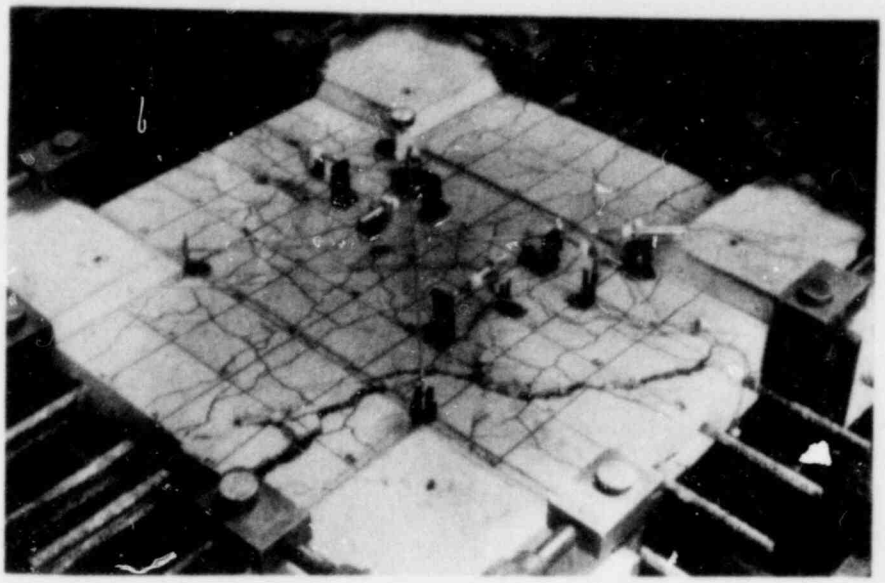

a. General view.

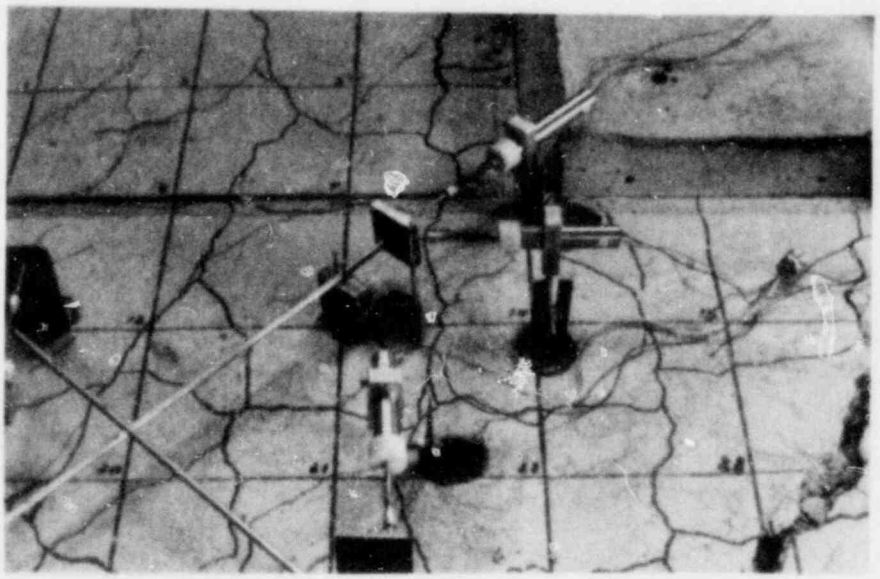

b. Close up view.

Fig. 2.11. Instrumented specimen during testing.

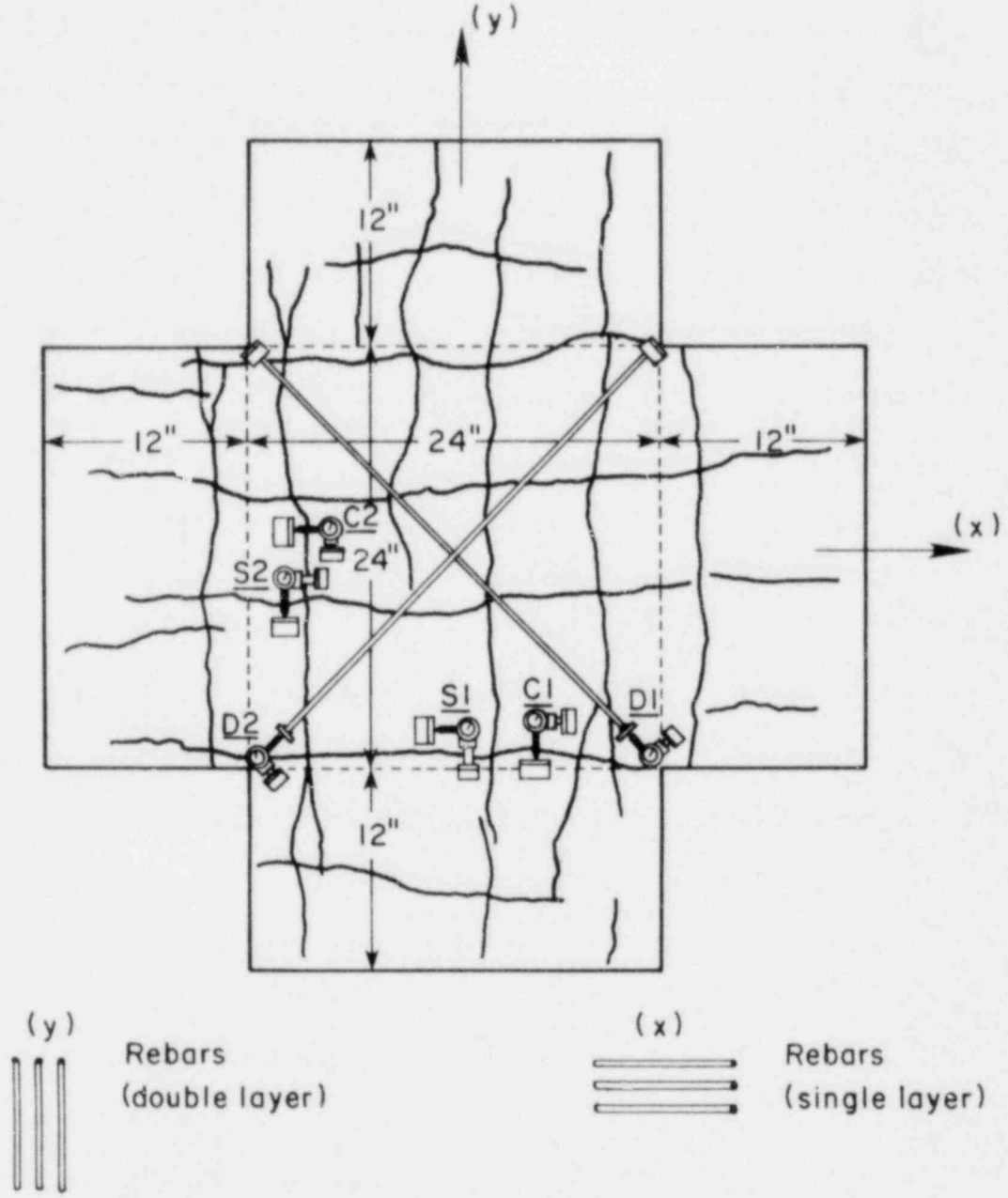

Fig. 2.12. Sketch of the 2 ft. square central region with a typical layout of gages.

gages, connected in a full bridge configuration. The measured axial strain according to the calibration was about 7 micro-strains per 1 kip (4.5 kN) of axial load, which produces a shear stress of 5 psi (0.034 MPa). Also, wire electrical strain gages were used to monitor the bar strains. Two strain gages were cemented on diametrically opposite sides of selected bars in each direction outside the specimen. The axial load was also checked in an approximate fashion with pressure gages mounted on the hand pumps that powered the hydraulic rams of the tensioning frames.

The average shear distortion γ of the central part of the specimen was obtained by taking the average of the tensile (Δt) and compressive (Δc) diagonal deformations measured, through the use of the relation

$$\gamma = c\ \Delta d, \text{ with } \Delta d = \frac{|\Delta t| + |\Delta c|}{2} \qquad (2.1)$$

where $c = 589.2 \times 10^{-4}$ (see Section 2.6 for derivation of the above Eqn. 2.1). Based on Eqn. 2.1, an expression for the effective shear modulus G_{cr} during cracking can be derived to describe the overall shear deformations of the 2 ft. square portion of the concrete panel. More details on the evaluation of an effective shear modulus are given later in Section 2.6.1c.

For the cyclically loaded specimens all deformations were recorded incrementally only for the 1st, 2nd and 10th cycle at each shear stress level (see Section 2.5), during loading and unloading in both directions. During the remaining cycles (3rd to 9th) the specimen was loaded to the peak positive and negative shear stress ($0 \rightarrow + v_{max} \rightarrow 0 \rightarrow - v_{max} \rightarrow 0 \rightarrow \ldots 0$) and deformations were measured at these peak levels only. On

the other hand, the monotonically loaded specimens were subjected to incremental shear loading and measurements were recorded at 25 psi (0.17 MPa) increments.

Readings from each displacement transducer used in this program were recorded by the 3052A Hewlett Packard Digital Data Acquisition system interfaced with an HP-9825A calculator, and an HP-9871A fast impact printer. The raw data was stored on tape cassetts for subsequent analysis and plotting by an HP-9862A X-Y plotter. After each load stage all specimens were inspected visually for additional diagonal cracking and any evidence of splitting cracks. Cracking patterns were marked on the specimen and recorded. Photographs were also taken during the test and at failure.

2.5 Test Procedure - Test Series - Load History

Each specimen was initially precracked by tensioning the orthogonal reinforcing bars at a stress of about $0.6f_y$ or 36 ksi (248 MPa) in the x and y direction. The crack openings in the y direction were smaller than in the x direction, since the amount of steel in the y direction was double of that in the x direction. More details on the actual measurements of the axial stiffness are presented in Section 3.3. Then the tensile load in the bars was released and set at a prescribed value corresponding to the desired biaxial tension. Four different tension levels of 0, $0.3f_y$, $0.6f_y$, and $0.9f_y$ were considered to study the effect of biaxial tension. This tension load was kept constant throughout each test.

The dial gages and/or the displacement transducers (DCDT's) were cemented on the concrete surface and all the electrical wiring was

completed and verified. The specimen was leveled relative to the corner loading devices and shear stresses were produced along the shear planes of the orthogonal cracks. Positive shear loading was defined as tension on diagonal D1 and equal compression on diagonal D2 . This was also the shear loading direction employed for the specimens subjected to monotonic shear. For the case of fully reversing shear the direction of the corner loads was reversed and reloading was commenced in the opposite direction after releasing the load to zero. The loading history of all tests is explained later in this section.

Sixteen flat specimens with constant reinforcement ratio of $\rho_x = 0.0122$ and $\rho_y = 0.0244$ in the x and y direction, respectively, were tested in this program under combined biaxial tension and cyclic or monotonic shear to study the major components of shear transfer, that is interface shear transfer and dowel action. A summary of the testing program is given in Table 2.C. The specimens were arranged in four groups of four specimens each. The same value of biaxial tension was applied to the specimens of each group.

In each group two duplicate specimens (labeled A and B) were subjected to cyclic shear stress starting at ±125 psi (0.86 MPa). Ten cycles at this shear stress level were then applied. The shear stress was increased in 50 psi (0.34 MPa) increments (±175 [illegible]1 MPa), ±225 (1.55 MPa), etc.) with 10 fully reversing cycles at each shear stress level until failure occurred (see Fig. 2.13). Failure load is defined here as the maximum possible shear stress that could be sustained by the specimen. A third specimen (labeled C) was cycled with the initial shear stress starting at the average failure shear stress for specimens A and B. Finally, a fourth

Table 2.C. Testing program.

Specimen No.	Rebar Tension	Load History
.0(A)	No Tension	Cyclic
.0(B)		Cyclic
.0(C)		Cyclic
.0(M)		Monotonic
.3(A)	$0.3f_y$	Cyclic
.3(B)		Cyclic
.3(C)		Cyclic
.3(M)		Monotonic
.6(A)	$0.6f_y$	Cyclic
.6(B)		Cyclic
.6(C)		Cyclic
.6(M)		Monotonic
.9(A)	$0.9f_y$	Cyclic
.9(B)		Cyclic
.9(C)		Cyclic
.9(M)		Monotonic

Notes:

Steel: Grade 60
$\rho_x = 0.0122$ (single layer)
$\rho_y = 0.0244$ (double layer)

Concrete: $f_c' \approx 3800$ psi

specimen (labeled M) was subjected to monotonically increasing shear stress in 25 psi (0.17 MPa) increments up to failure, so that the effects of cyclic shear load history on the shear strength and stiffness could be assessed.

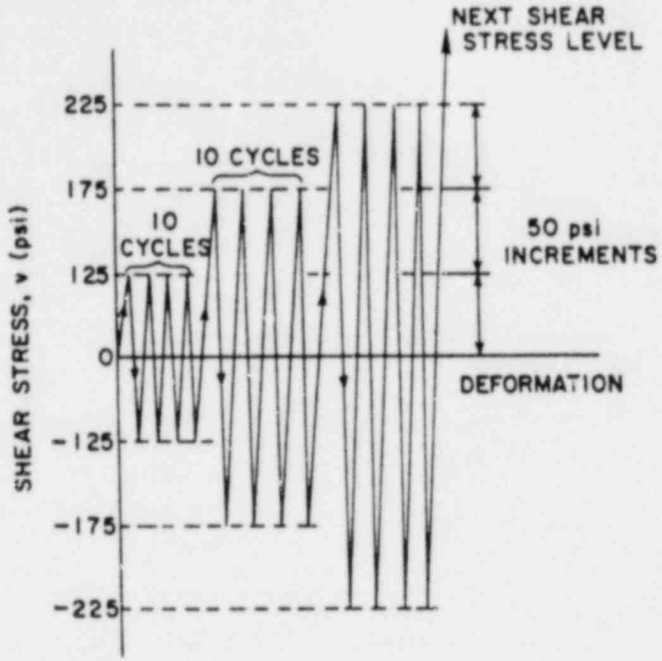

Fig. 2.13. Stress history under cyclic shear (specimen Series A and B).

The designation of specimens in Table 2.C indicates the bar tension ratio level of the tension in the bar to the yield strength of steel f_y and in parenthesis the type of shear stress load history. For example, a designation number .3(M) means that the specimen was subjected to a monotonic shear loading at a constant biaxial tension in the reinforcement bars of $0.3f_y$.

2.6 Description of Experimental Results

2.6.1 Monotonically loaded specimens (Series M)

All four biaxial tests described below were performed under a monotonic shear loading up to failure in 25 psi (0.17 MPa) increments. Specimens .0(M), .3(M), .6(M) and .9(M) were tensioned to 0, $0.3f_y$, $0.6f_y$ and $0.9f_y$, respectively, in each rebar in the single and the double layer.

a) Cracking patterns

In all four specimens tension was applied up to $0.6f_y$ level in order to precrack them in the two orthogonal directions parallel to the rebars. More details on the procedure followed during tensioning are given in Section 3.3. First cracking occurred between 15 ksi ($0.25f_y$) and 25 ksi ($0.4f_y$) tension in each reinforcement bar, with the cracking perpendicular to the double layer occurring at a lower bar tension level than the cracking in the orthogonal direction, as expected. The orthogonal cracking in each specimen at the specified tension level is more or less similar, with an average crack spacing of about 7.0 and 6.0 in. (178 and 152 mm) in the x and y direction, respectively. The tension cracking patterns are not much different since all primary orthogonal cracks formed at the same initial tension level of $0.6f_y$ in all specimens. The cracking pattern for each specimen is shown in Figs. 2.14a(1) to 2.14d(1), on a 6 inch wide square grid that was used to record each crack during tensioning.

Diagonal cracking was initiated at approximately 45 degrees to the reinforcing bars when the shear stresses at the cracks were in the range of 75 to 125 psi (0.52 to 0.86 MPa) level. The lower values of shear stress

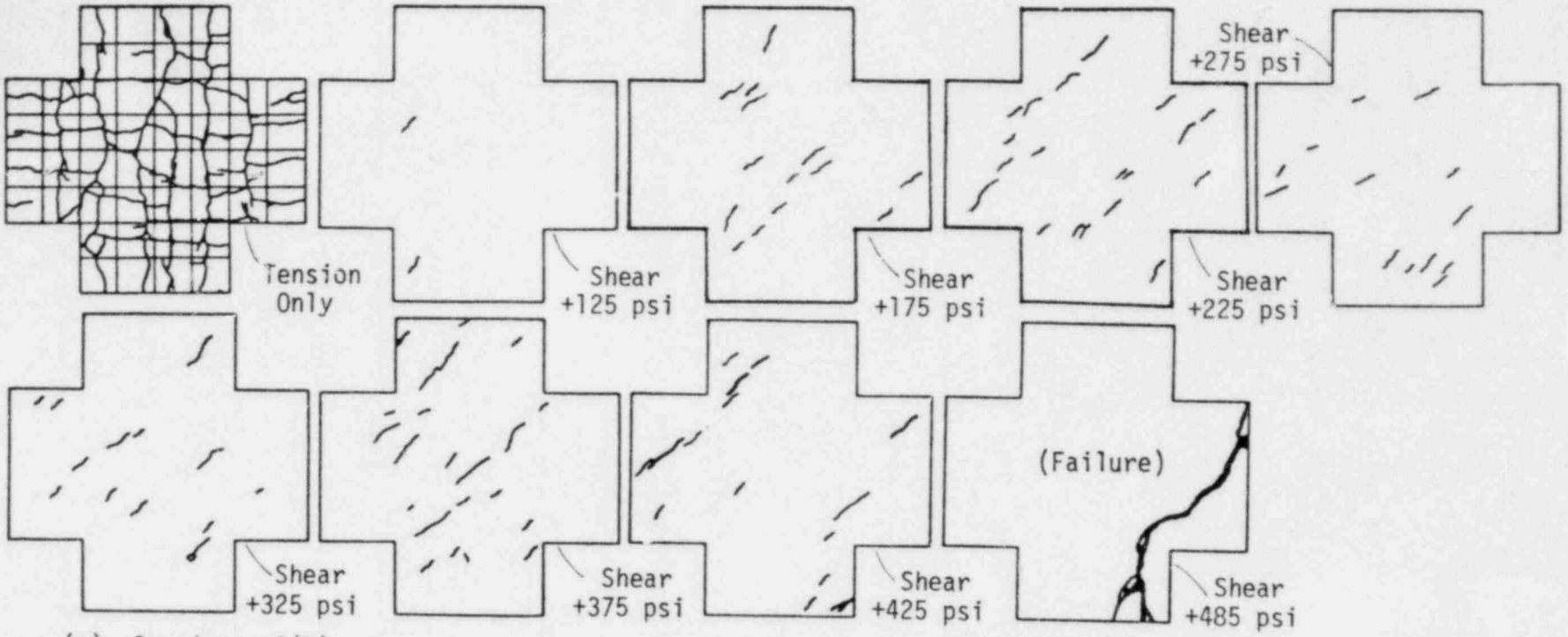

(a) Specimen .9(M)

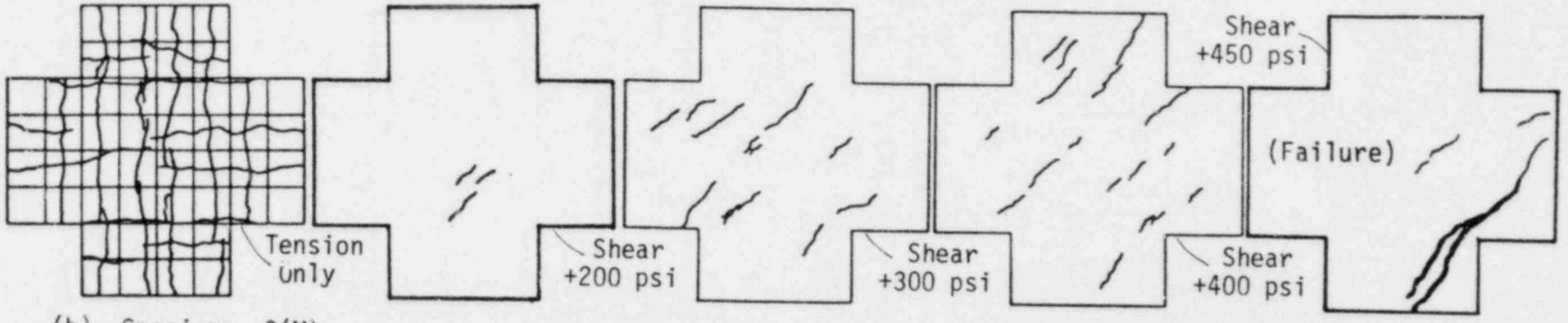

(b) Specimen .3(M)

Fig. 2.14. Cracking patterns for monotonic shear (diagonal cracking shown is the additional cracking at each specified shear stress level).

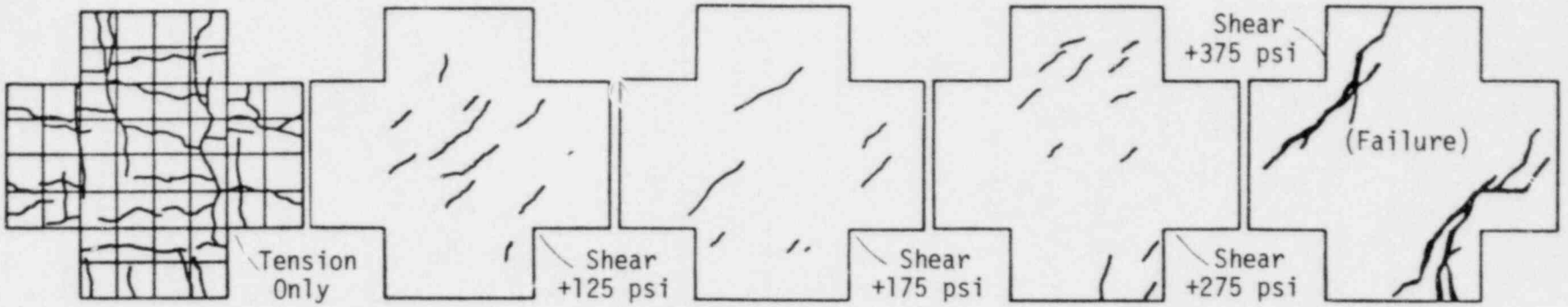

(c) Specimen .6(M).

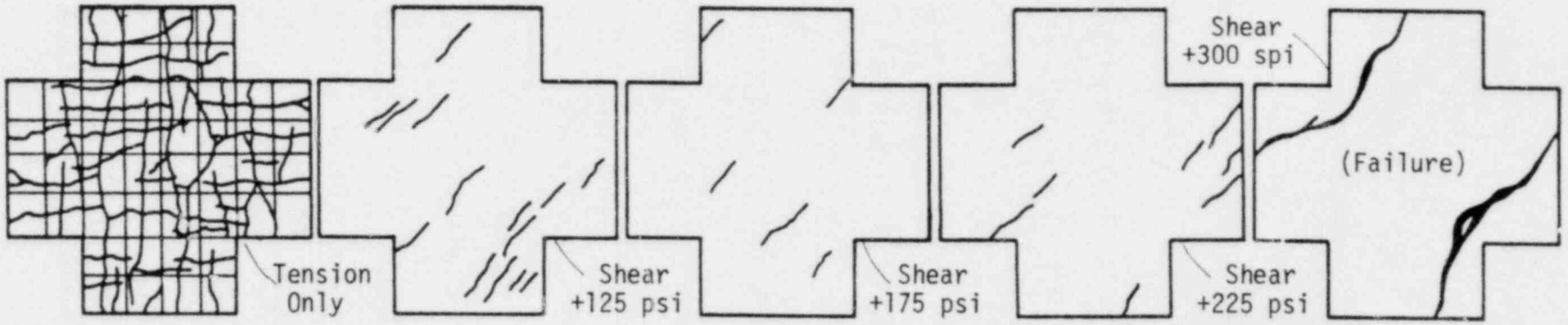

(d) Specimen .9(M).

Fig. 2.14. (Continued)

at first cracking correspond to the higher tensioned specimens. It is apparent that since the orthogonal cracking was dictated more or less from the spacing of the transverse rebars and the tension cracks formed in the vicinity of the reinforcement, the bond transfer capability of each bar would be impaired. Thus, little difference is expected in the shear stress level that would cause the first diagonal crack for the various tension levels. A more rational approach is undertaken in Chapter 3 to explain the possible reason for the relatively low diagonal cracking shear stress level. The additional diagonal cracks at preselected shear stress levels are shown in Figs. 2.14a to 2.14d (2, 3, 4, etc.). The diagonal cracking at failure is also included. All monotonically loaded specimens after testing are shown in Figs. 2.15a(4) to 2.15d(4).

b) Shear stress versus displacement response

For each specimen a set of two orthogonal cracks was chosen for the positioning of the dial gages and/or displacement transducers to measure the crack slip and crack widths during the loading history of the experiments. The crack width and slip were denoted by C1, S1 and C2, S2 at an orthogonal crack parallel to the x (1) and y (2) direction, respectively.

In general, the crack slip and/or width variations versus the applied shear stress were inconsistent and erratic. This unfortunately was unavoidable because of the inherent random character of cracking. Each tension crack did not always extend completely across the entire width of the specimen. Therefore, having also in mind the irregularity of the crack interface, the shear slip and crack width measured at one point of the

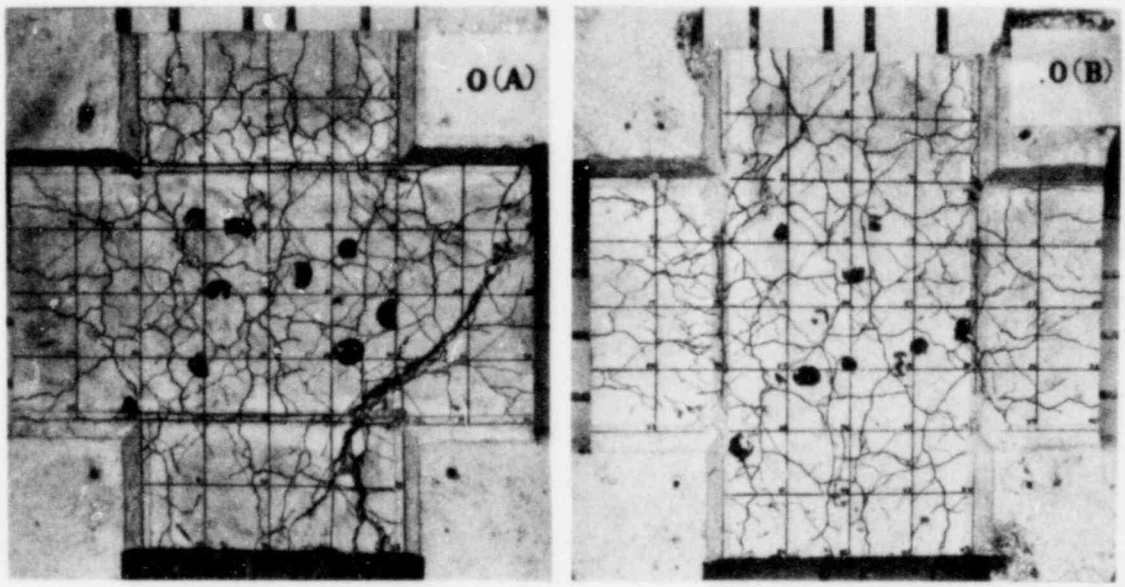

(1) (2)

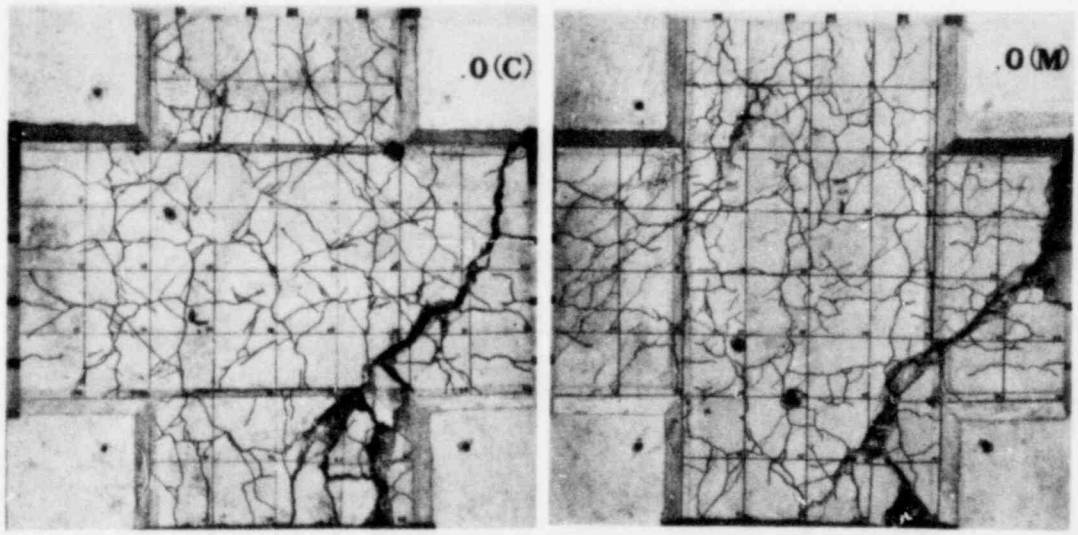

(3) (4)

a) Biaxial bar tension = 0

Fig. 2.15. Biaxial specimens after failure under monotonic shear (M) or cyclic shear (A,B,C) at selected bar tension levels.

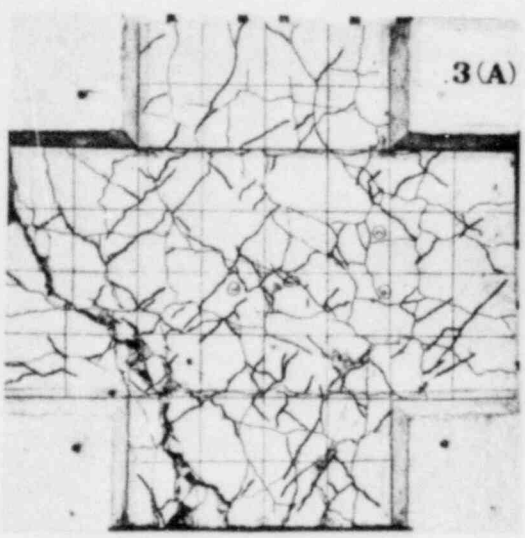

(1)

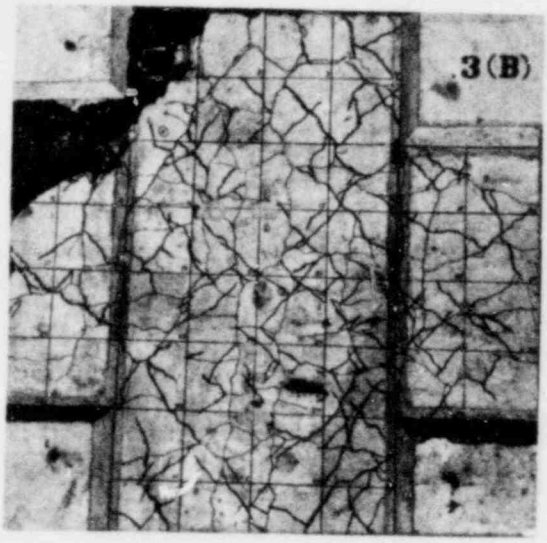

(2)

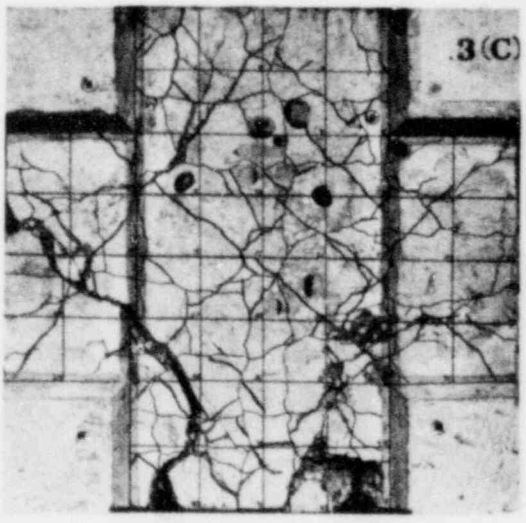

(3)

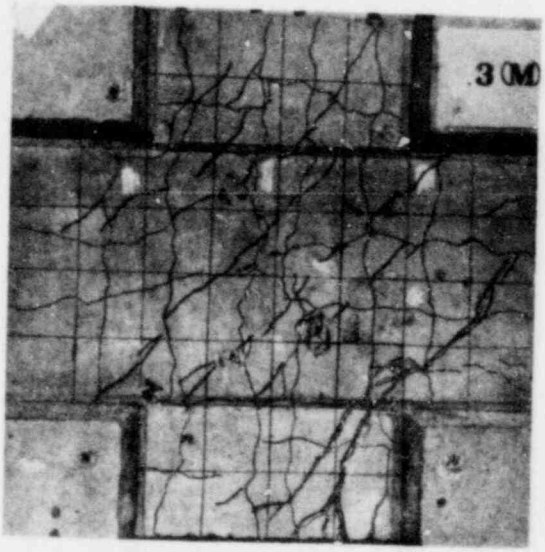

(4)

b) Biaxial bar tension = $0.3f_y$

Fig. 2.15. (Continued)

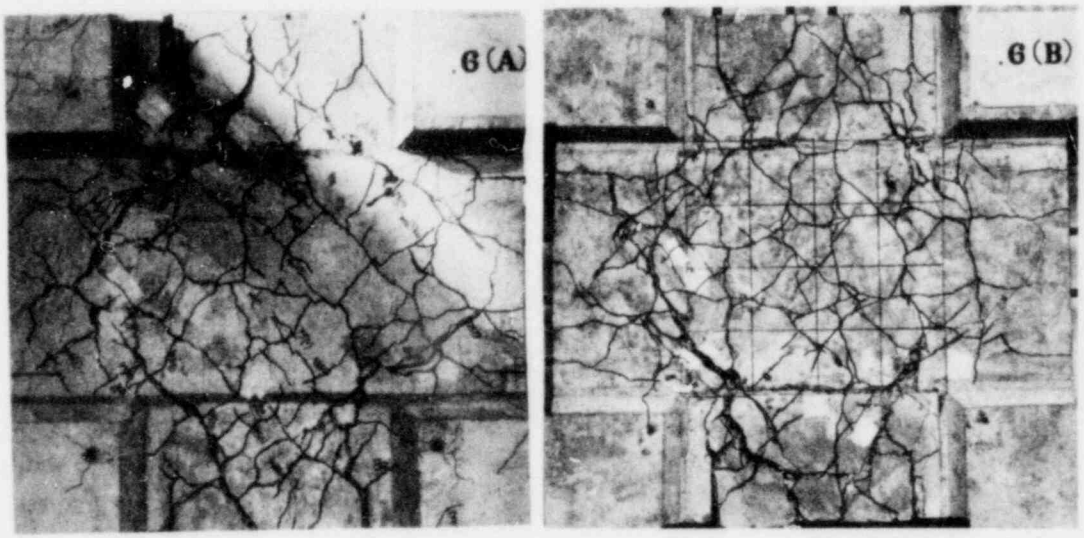

(1) (2)

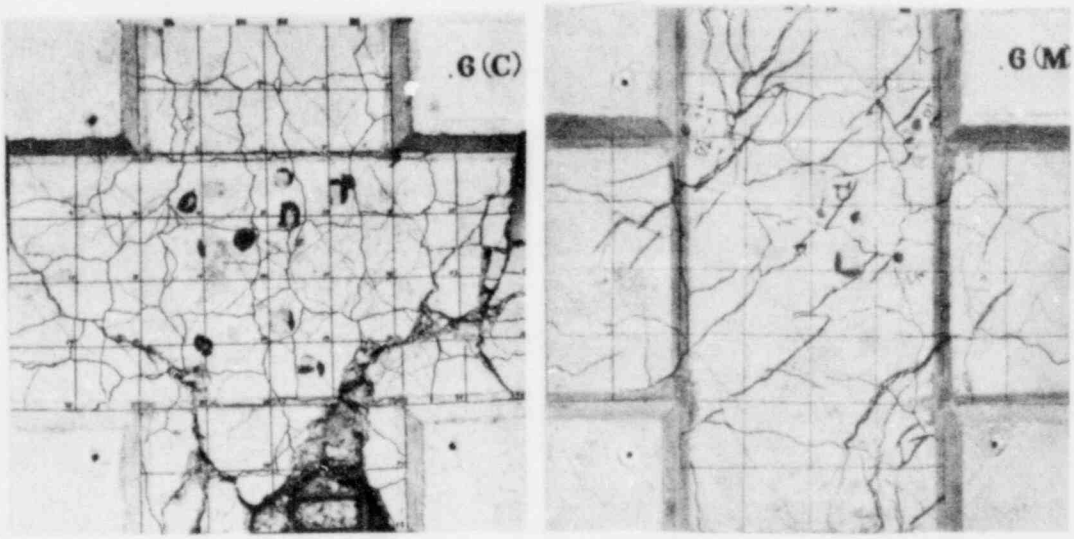

(3) (4)

c) Biaxial bar tension = $0.6f_y$

Fig. 2.15. (Continued)

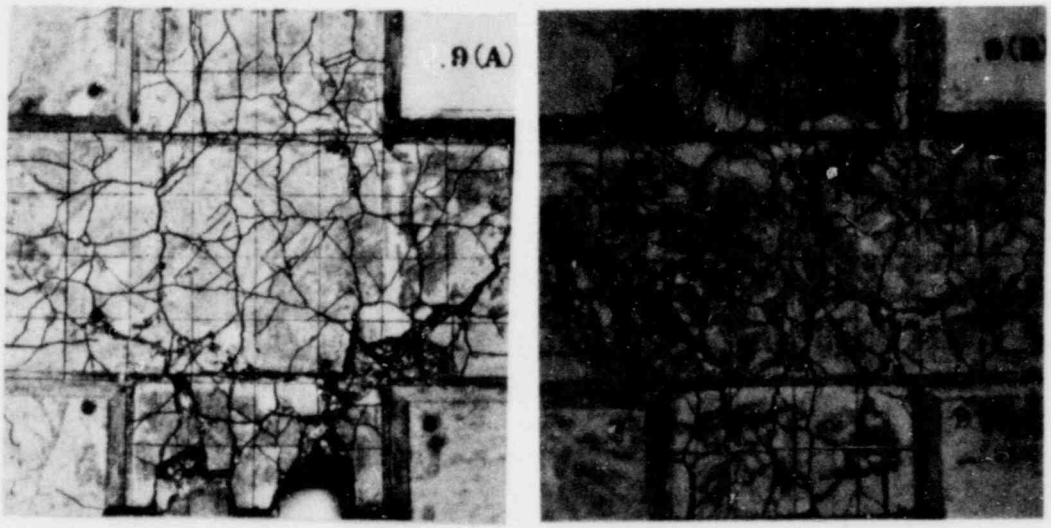

(1) (2)

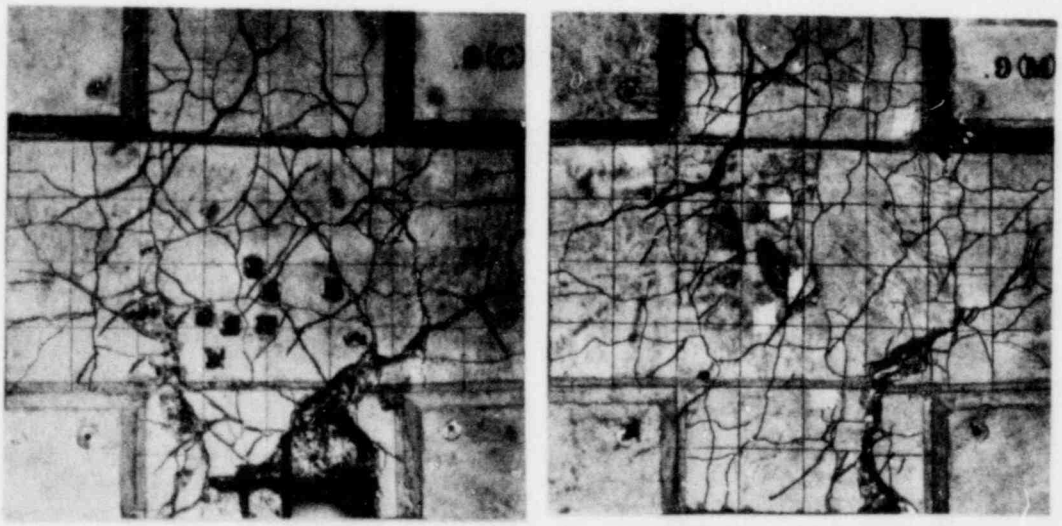

(3) (4)

d) Biaxial bar tension = $0.9f_y$

Fig. 2.15. (Continued)

crack will in general contain some scatter. Nevertheless, the crack slips and widths measurements provide a good qualitative picture of the behavior of the specimens during the application of the monotonic shear loading.

The recorded changes in both the slips and crack openings for all four monotonically loaded specimens are shown in Fig. 2.16(a,b,c,d). The changes in crack width are the variations of the initially preset values for the corresponding tension level in the reinforcement before the shear loading is applied.

The general trend shows that as the constant applied tension increases from specimen .0(M) to .9(M) and the average initial crack width present at the orthogonal cracks assumes larger values, the resistance offered by the asperities at the crack interface to slip decreases. This causes larger relative movement of the crack surfaces. The above can be seen in Fig. 2.16 comparing the slips S1 and S2 for each specimen.

c) Effective shear modulus

As mentioned in Section 2.4, the average distortion of the middle 2 ft. square region of the specimen was measured by recording the total compressive (Δc) and tensile (Δt) deformation at the two diagonals D1 and D2, as shown in Fig. 2.17. Distortion was calculated by taking the average of Δt and Δc. An effective shear modulus for cracked concrete, G_{cr}, was then evaluated using the expression

$$G_{cr} = \frac{v}{\gamma} = \frac{v\alpha}{\Delta d\sqrt{2}} \qquad (2.2)$$

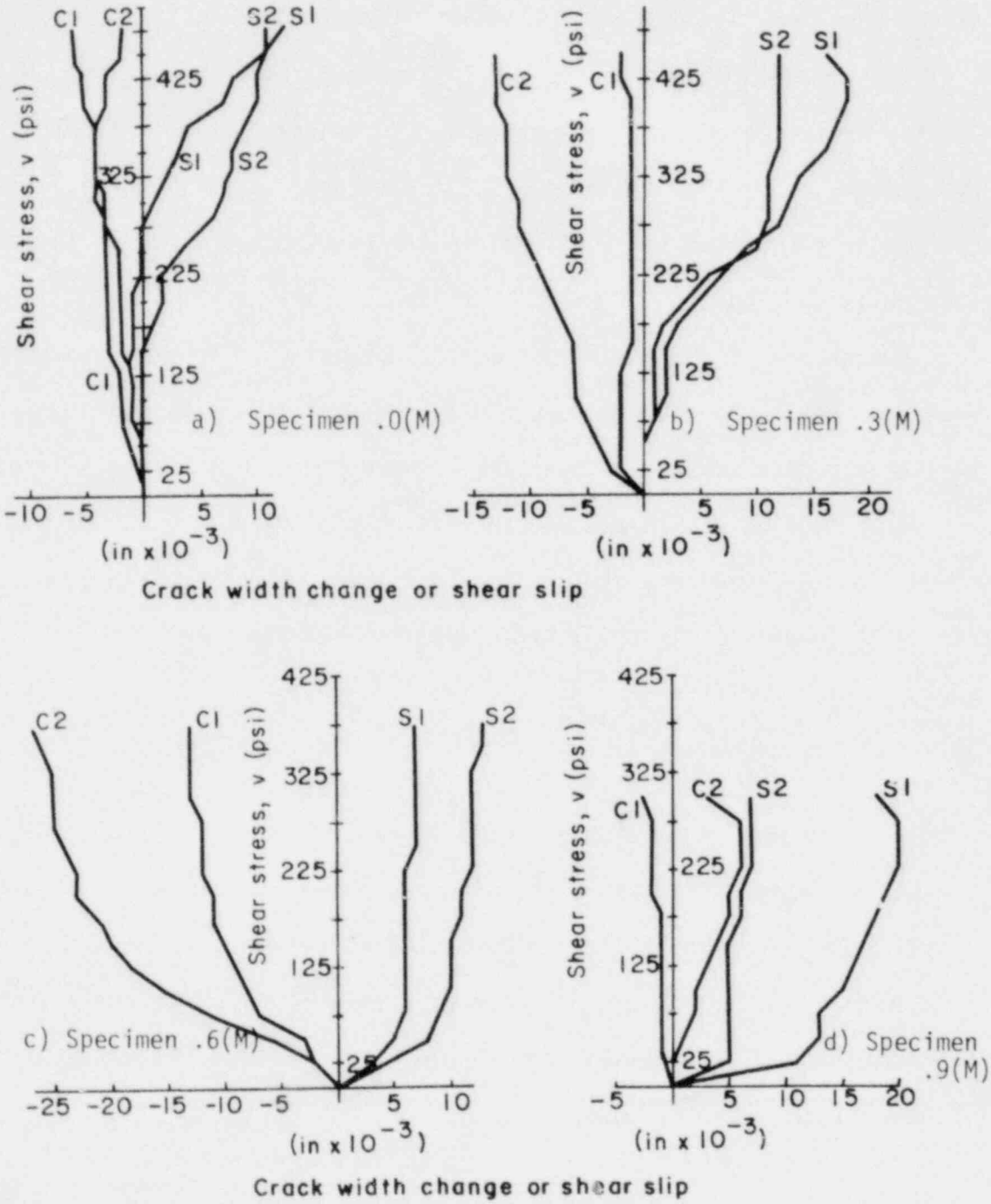

Fig. 2.16. Shear stress versus crack width changes and crack slip for specimens under monotonic shear.

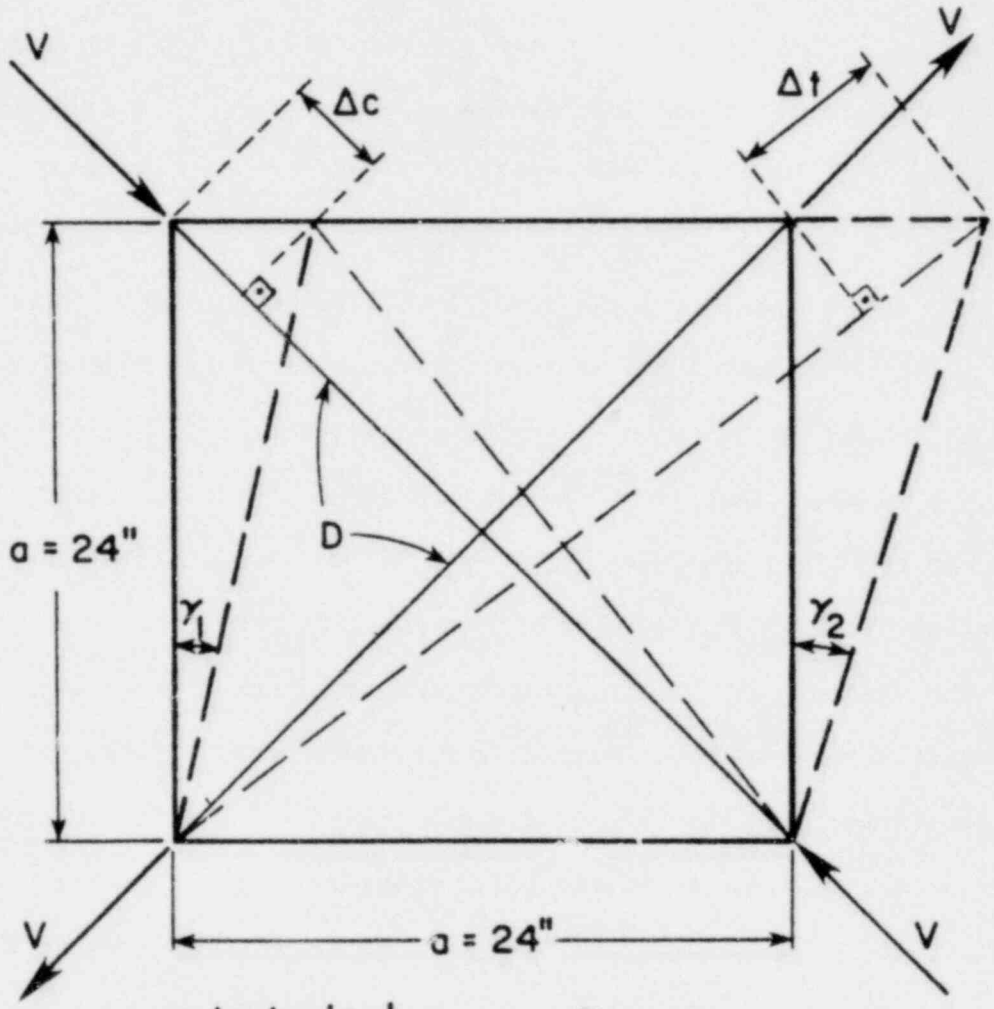

$$\Delta_d = \frac{|\Delta_t| + |\Delta_c|}{2} \; ; \; G_o = \frac{E_c}{2\,(1+\nu)}$$

$$\gamma = \frac{\gamma_1+\gamma_2}{2} = \frac{\Delta_d\sqrt{2}}{a} = 589.2\,\Delta_d \times 10^{-4}$$

$$\bar{G} = \frac{v}{\gamma} = \frac{va}{\Delta_d\sqrt{2}} \; ; \; \frac{\bar{G}}{G_o} = \frac{va\,(1+\nu)\sqrt{2}}{\Delta_d\,E_c}$$

Fig. 2.17. Shear deformations and effective shear modulus G_{cr}.

where v is the applied nominal shear stress in psi, α is the dimension of the instrumented square region (24 in. or 610 mm) and Δd is the average total diagonal deformation, also in inches.

This effective shear modulus accounts for the deformation at the orthogonal cracks (crack slip and crack width), the effect of diagonal cracking, and the shear deformation in the uncracked concrete blocks. Of course, fully developed and equally spaced cracks are assumed in the above expression for G_{cr}. This relation for G_{cr} can be input in a nonlinear finite element analysis as a variable in the material stiffness matrix.

The variation of the average shear strain of the central portion of each specimen loaded under a monotonically increasing shear is plotted in Fig. 2.18 as a function of the applied shear stress v. Especially for higher tensioned specimens (.6(M) and .9(M)) a relatively low shear stiffness exists for shear stresses up to about 25 psi (0.17 MPa). This shift of the shear stress-strain curve to the right could be attributed to the so-called "free slip." That is, a finite relative slip is required at the crack to mobilize the interface shear transfer mechanism, because an initial crack opening is present after tensioning. This explains the distinct change in stiffness at higher shear stresses as the crack surfaces come into contact. The above stiffness increase does not occur in specimen .0(M), which with very small initial crack widths mobilizes the interface shear transfer much faster. In addition to the above explanation of "free slip," another reason that could have contributed to the observed soft response is shrinkage cracking that was observed before testing.

Above 25 psi (0.17 MPa) the response is approximately linear. There is a definite decrease in shear stiffness and increase in shear

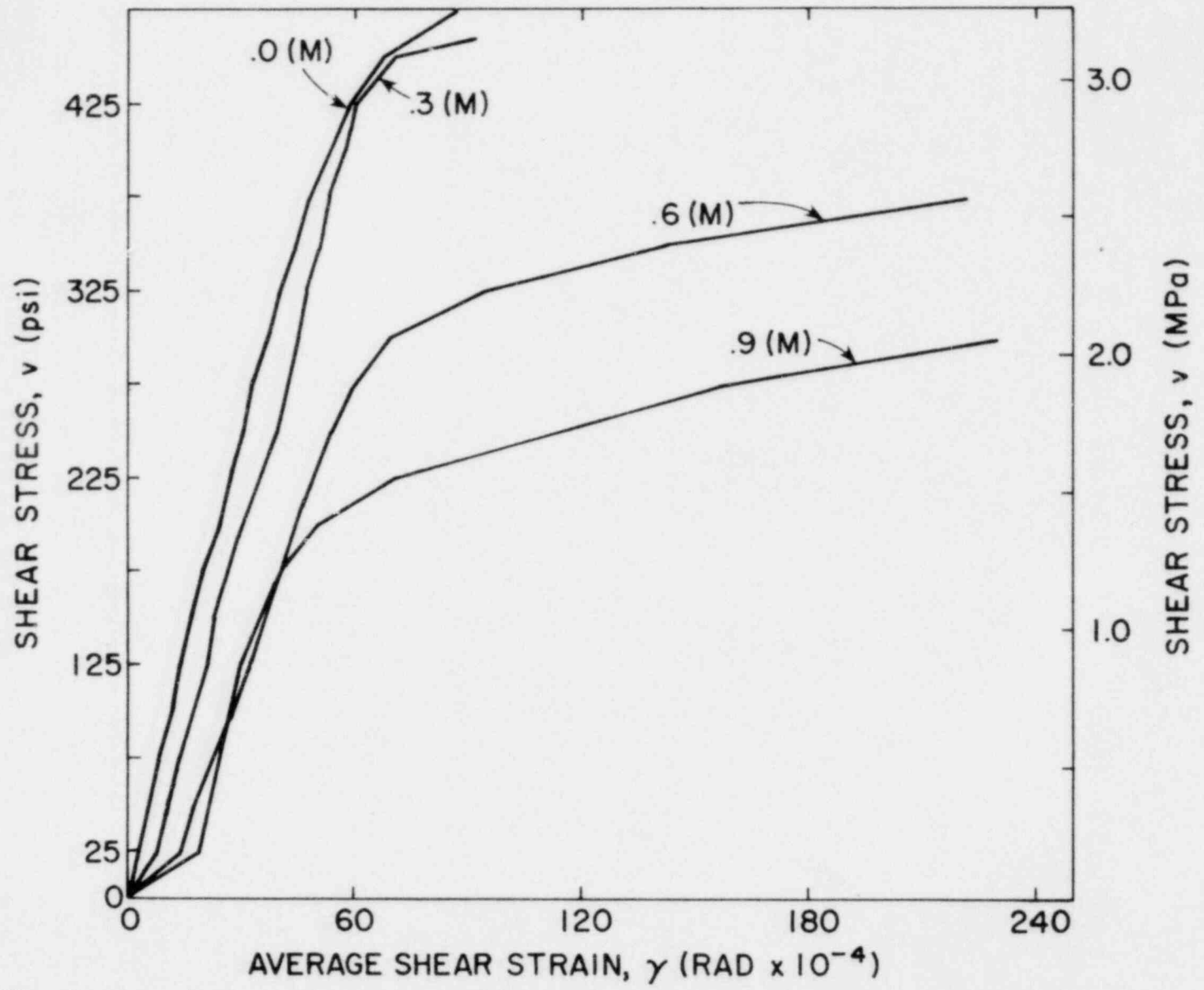

Fig. 2.18. Average shear strain versus applied shear stress for monotonic shear.

deformations as the tension level in the reinforcing bars increases from 0 to a maximum value of $0.9f_y$. More details on the actual measured values of the shear stiffness are presented in the discussion of the experimental results in Section 2.7. The above decrease in shear stiffness corresponds mainly to the secant stiffness, which reflects the total shear deformation induced at any shear stress level. The local tangent stiffness, on the other hand, which is the slope of the curve, remains nearly constant for all biaxial tension levels. Specimens .0(M) and .3(M), at least for shear stresses up to about 175 psi (1.21 MPa), exhibited similar tangent and secant shear stiffness.

The complete recorded data for the average diagonal deformation Δd and the corresponding equivalent average distortion values γ at each shear stress level for the specimens subjected to monotonic shear are tabulated in Table 2.D.

d) Ultimate strength

Failure in the specimens resulted from yielding in the steel crossing a diagonal crack near a corner loaded in tension (see Figs. 2.15a(4) to 2.15d(4) for cracking at failure). The peak shear stresses at failure v_u at each biaxial tension level for the monotonically loaded specimens are shown in Table 2.E.

The peak shear stresses transferred to the specimens at failure decreased with increased applied tension from a value of 485 psi (3.35 MPa) for specimen .0(M) to 300 psi (2.07 MPa) for specimen .9(M). At $0.3f_y$ tension the ultimate strength was 450 psi (3.10 MPa) and at $0.6f_y$

Table 2.D. Average diagonal deformations for specimens under monotonic shear.

Shear Stress (psi)	.0(M) Δd (in)	.0(M) γ*	.3(M) Δd (in)	.3(M) γ*	.6(M) Δd (in)	.6(M) γ*	.9(M) Δd (in)	.9(M) γ*
0	0	0	0	0	0	0	0	0
25	0.005	3	0.013	8	0.024	14	0.032	19
50	0.010	6	0.019	11	0.030	18	0.037	22
75	0.014	8	0.023	14	0.038	22	0.041	24
100	0.020	12	0.029	17	0.048	28	0.046	27
125	0.024	14	0.036	21	0.055	32	0.051	30
150	0.029	17	0.039	23	0.062	37	0.059	35
175	0.034	20	0.045	27	0.069	41	0.068	40
200	0.042	25	0.052	31	0.076	45	0.086	51
225	0.046	27	0.060	35	0.084	49	0.120	71
250	0.052	31	0.067	39	0.092	54	0.192	113
275	0.056	33	0.072	42	0.102	60	0.268	158
300	0.063	37	0.077	45	0.118	70	0.391	230
325	0.068	40	0.081	48	0.160	94	-	-
350	0.076	45	0.087	51	0.242	143	-	-
375	0.082	48	0.091	54	0.378	223	-	-
400	0.091	54	0.098	58	-	-	-	-
425	0.100	59	0.103	61	-	-	-	-
450	0.116	68	0.121	71	-	-	-	-
460	0.138	81	0.156	92	-	-	-	-
475	0.149	88	-	-	-	-	-	-

*(rad. x 10^{-4}).

Table 2.E. Ultimate strength for monotonic shear (specimen Series M).

Specimen No.	$\frac{f_s}{f_y}$	v_u (psi)
.0(M)	0	485
.3(M)	0.3	450
.6(M)	0.6	375
.9(M)	0.9	300

decreased to 375 psi (2.59 MPa). A linear representation of the ultimate strength as a function of the applied biaxial tension provides a very good fit to the data available (see Fig. 2.19).

Interaction curves for the ultimate strength versus the applied biaxial tension stress level in each rebar are given in Figs. 2.19a and 2.19b. The shear stress parameter $v_u/\sqrt{f_c'}$, which is used in Fig. 2.19b to include the effect of the variation in the compressive strength of concrete, or the ultimate shear stress v_u, are plotted in terms of the dimensionless tensile stress parameter f_s/f_y. A linear regression analysis with a correlation coefficient of about 0.97 gives the following straight lines

$$v_u = (8.5 - 4.0\ f_s/f_y)\ \sqrt{f_c'} \quad \text{(psi)} \tag{2.3a}$$

or

$$v_u = 510\text{-}220\ f_s/f_y \quad \text{(psi)} \tag{2.3b}$$

where v_u is the ultimate strength in psi, f_s is the applied tensile stress per rebar, f_y is the yield strength of steel, and f_c' is the compressive cylinder strength of concrete in psi.

2.6.2 Cyclically loaded specimens (Series A,B,C)

All twelve specimens in Series A, B and C were loaded under shear according to the loading history described in Section 2.5. The only exception was specimen .9(A), in which cycling began at a lower shear stress level than 125 psi (0.86 MPa), because it was the first specimen tested at $0.9f_y$ tension and the shear stress failure level was incorrectly expected

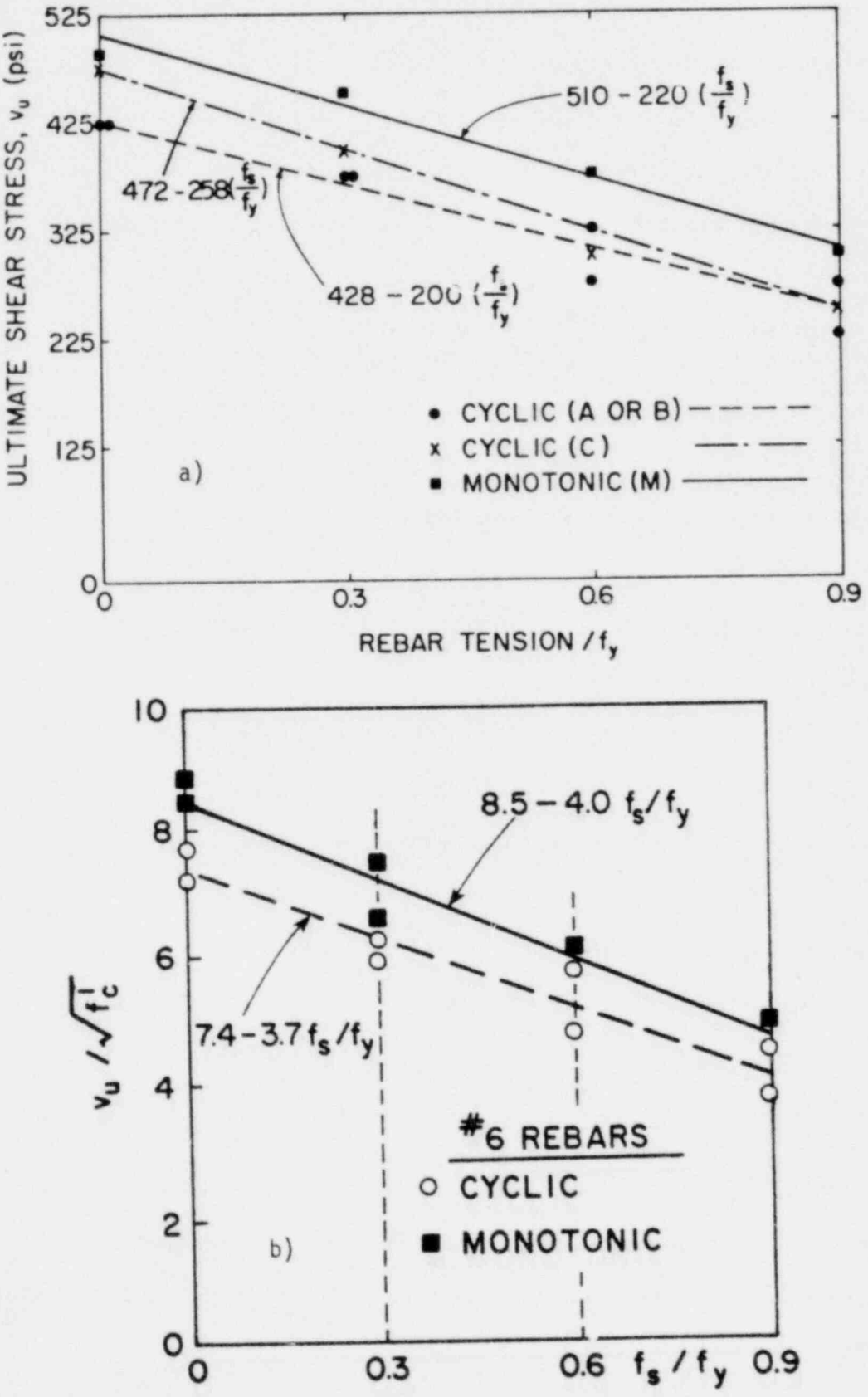

Fig. 2.19. Ultimate strength of biaxial specimens as a function of bar tension.

to be in the range of 100 psi to 125 psi (0.69 to 0.86 MPa). The actual loading history followed for this specimen was 10 cycles at each of ±25, ±50, ±75, ±100 and ±125 psi peak shear stress levels. Above 125 psi the loading procedure was identical with the rest of the specimens.

a) Cracking patterns

The orthogonal cracking was similar to that observed for the monotonically loaded specimens since the tensioning procedure was the same. The cracking patterns due to bar tension and the additional inclined cracking produced by the shear stress are shown in Figs. 2.20 to 2.23 for all twelve specimens. Again here the diagonal cracking first occurred at a shear stress of 125 psi or lower.

The main difference observed between cyclic and monotonic shear loadings was the much more severe diagonal cracking that occurred after fully reversing cycles of shear were applied to the specimen. The important influence of cyclic loading in causing extensive diagonal cracking, and as a result, in lowering the capacity of concrete to withstand shear stresses, is therefore evident.

b) Shear stress versus displacement response

In all specimens the crack width variation and shear slip were measured as the shear stress increased (loading) or decreased (unloading) incrementally within the limits of the specified peak shear (positive or negative).

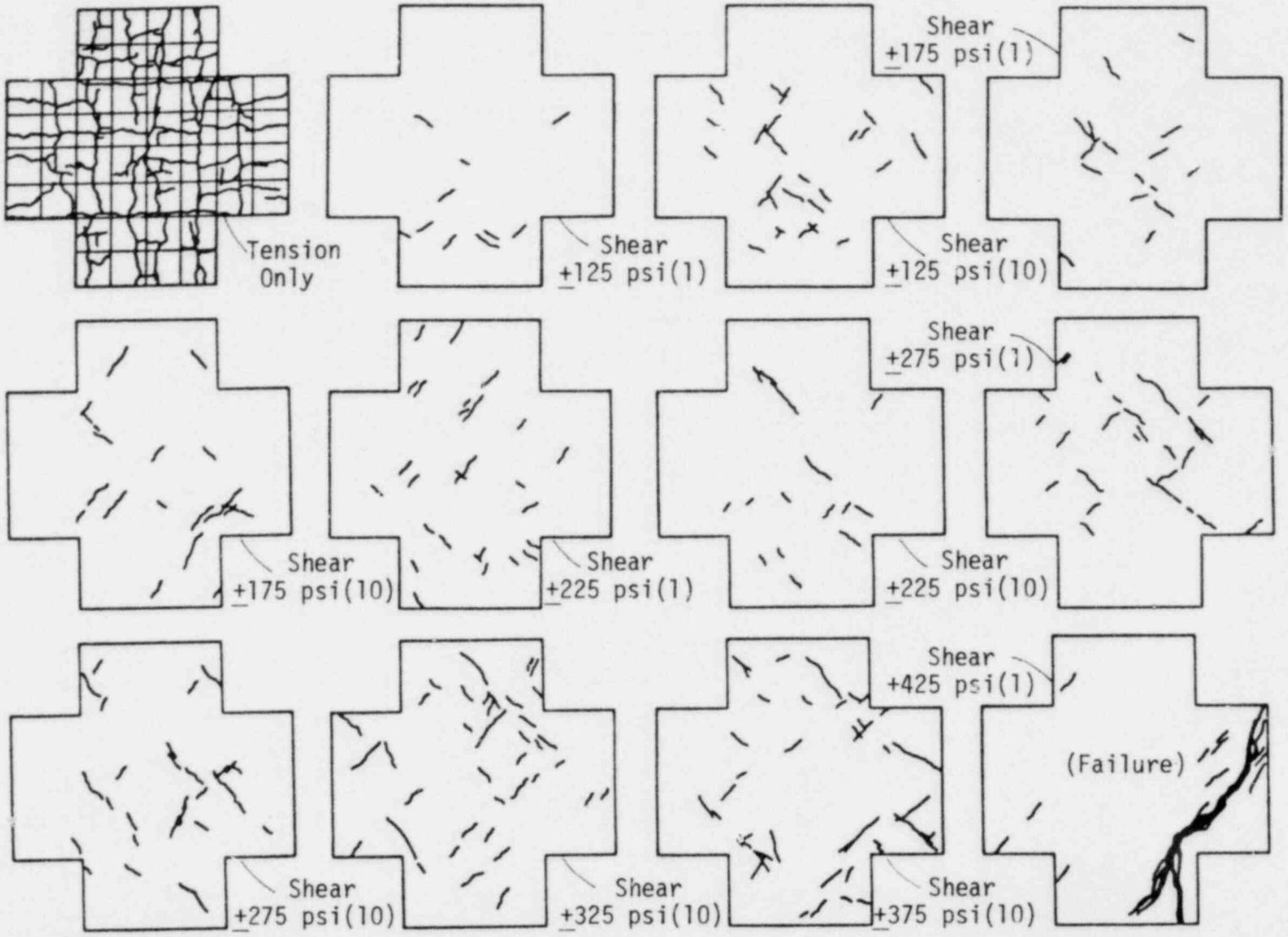

a) Specimen .0(A)

Fig. 2.20. Cracking patterns for cyclic shear and zero biaxial tension (diagonal cracking shown is the additional cracking at each specified shear stress level; load cycle No. in parentheses).

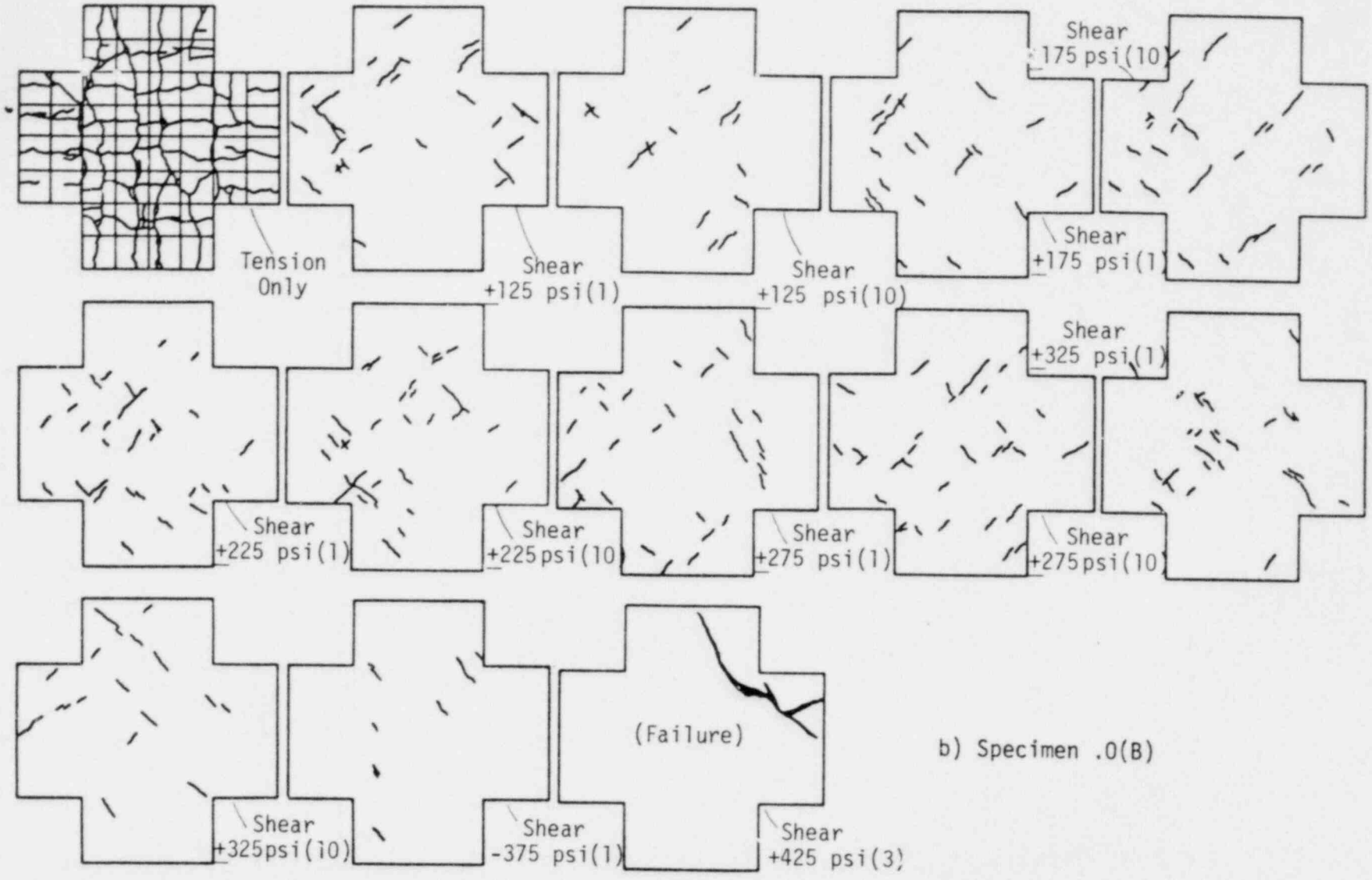

b) Specimen .0(B)

Fig. 2.20. (Continued)

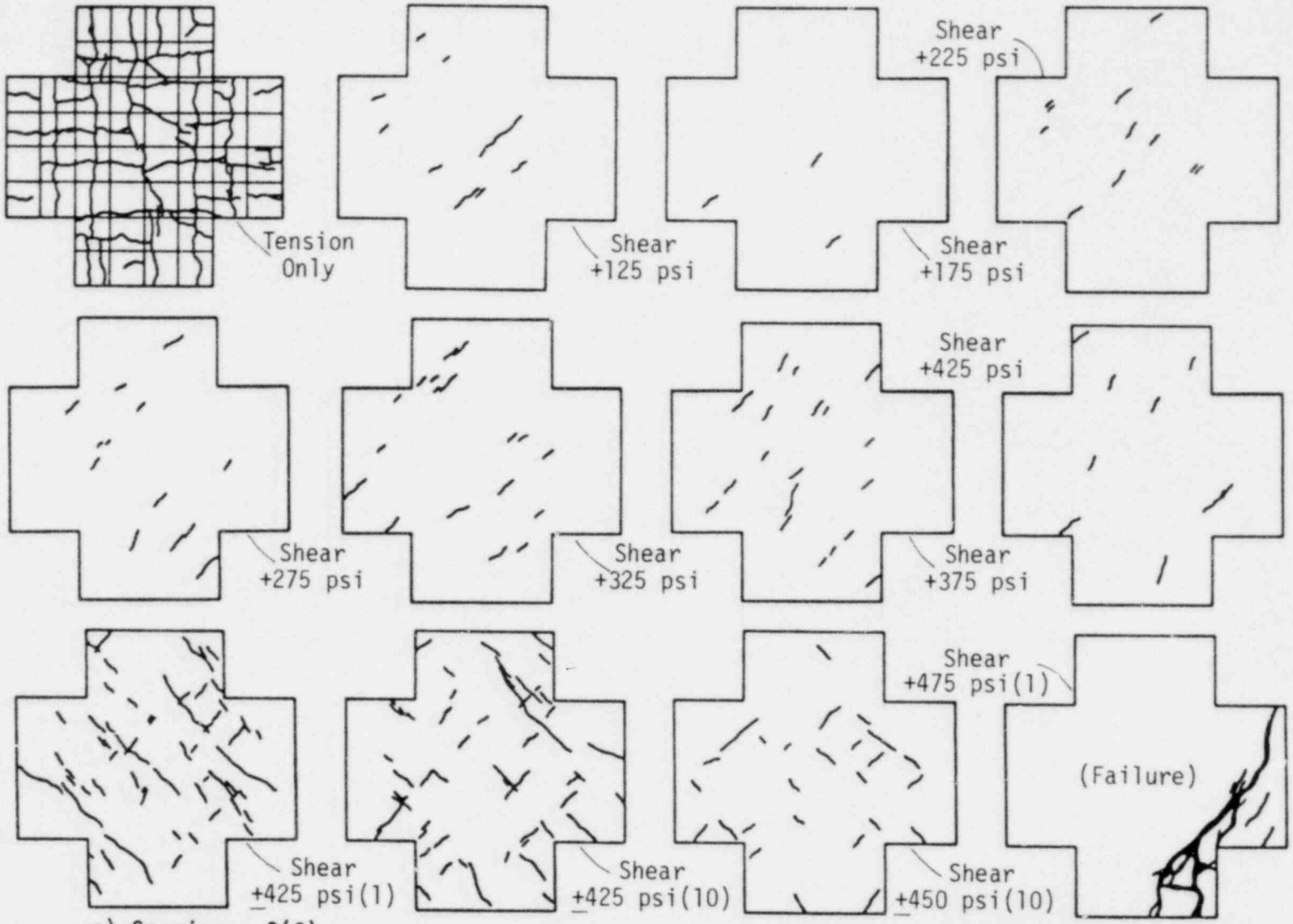

c) Specimen .0(C)

Fig. 2.20. (Continued)

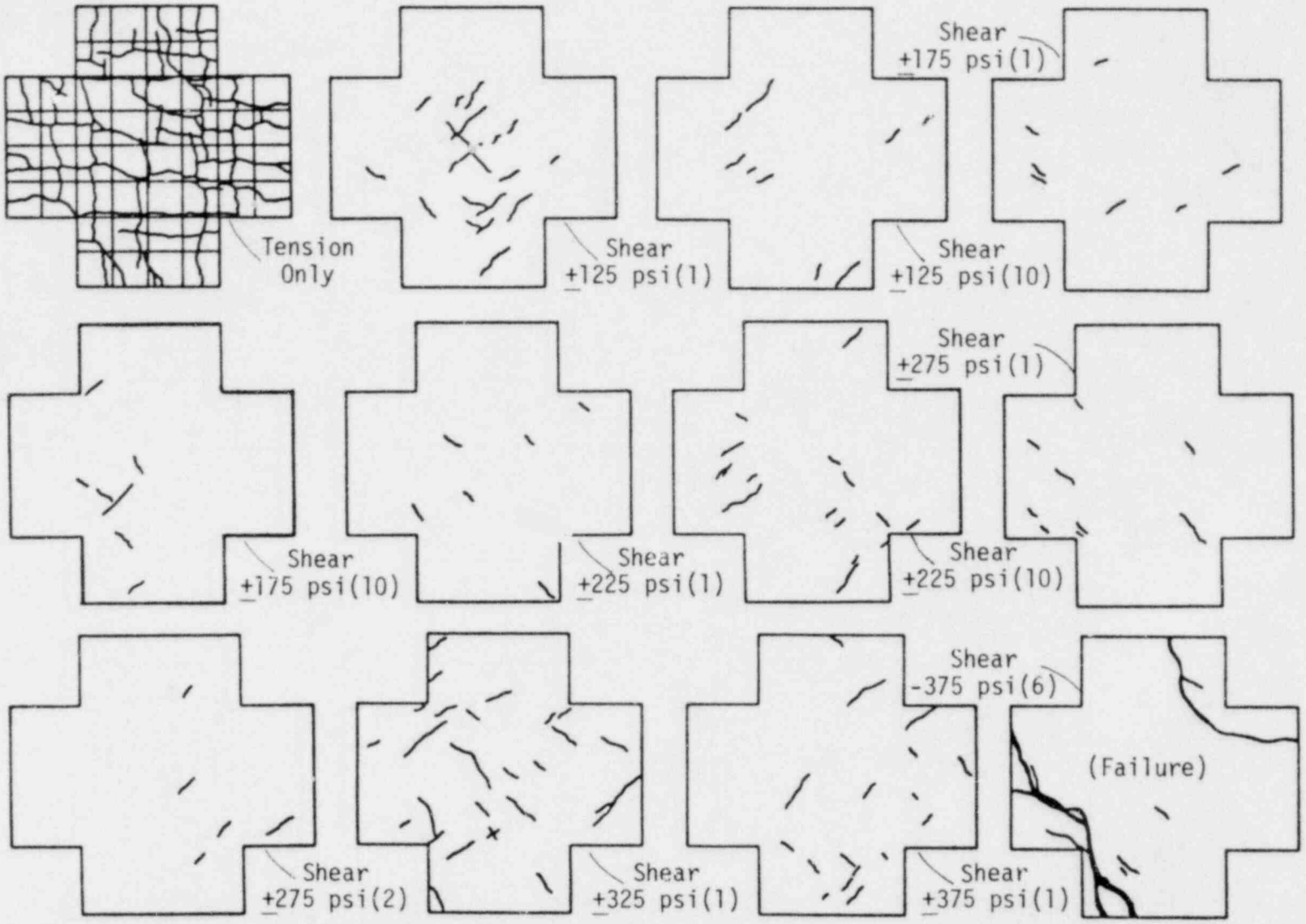

a) Specimen .3(A)

Fig. 2.21. Cracking patterns for cyclic shear and $0.3f_y$ biaxial tension (diagonal cracking shown is the additional cracking at each specified shear stress level; load cycle No. in parentheses).

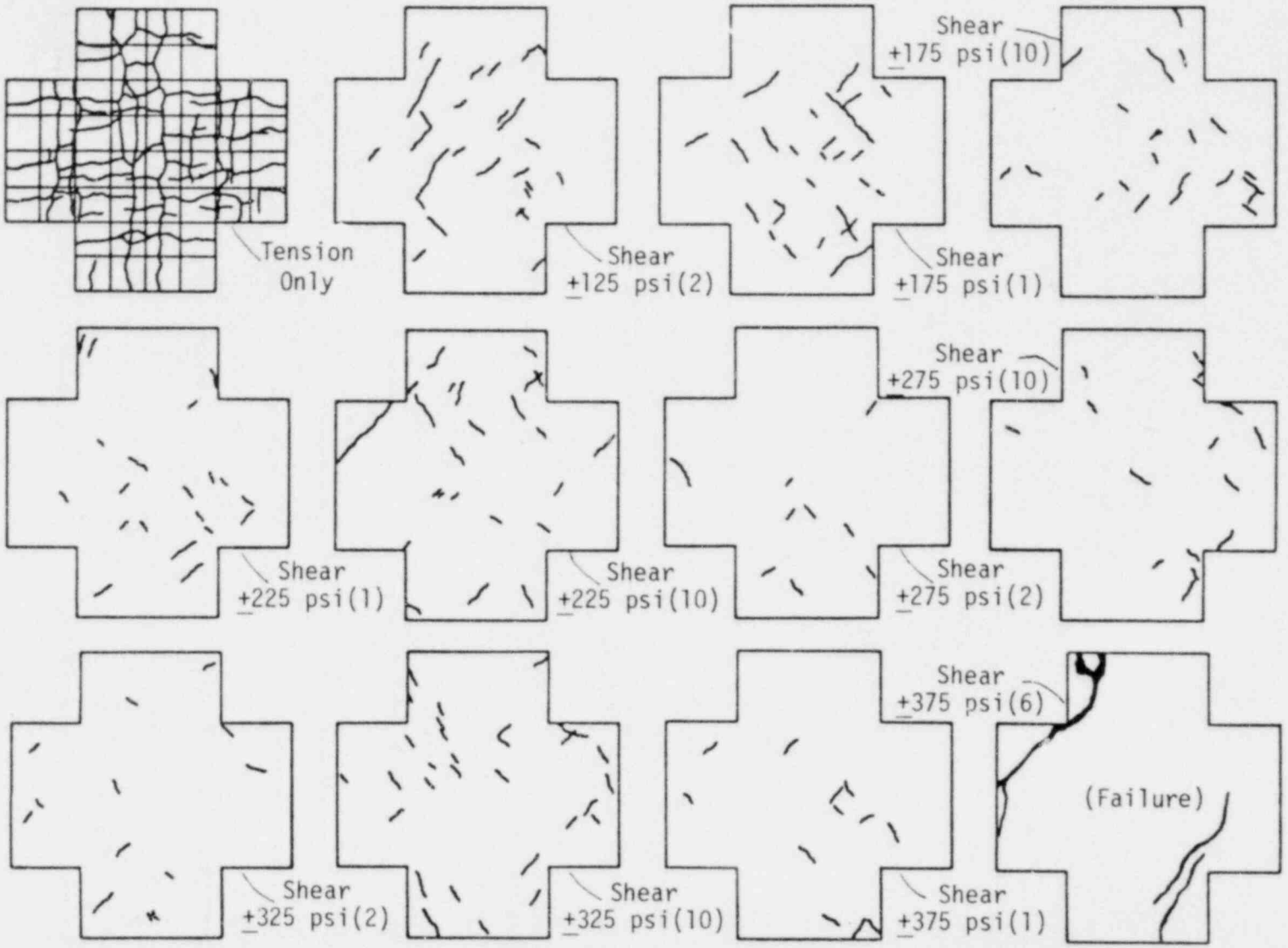

b) Specimen .3(B)

Fig. 2.21. (Continued)

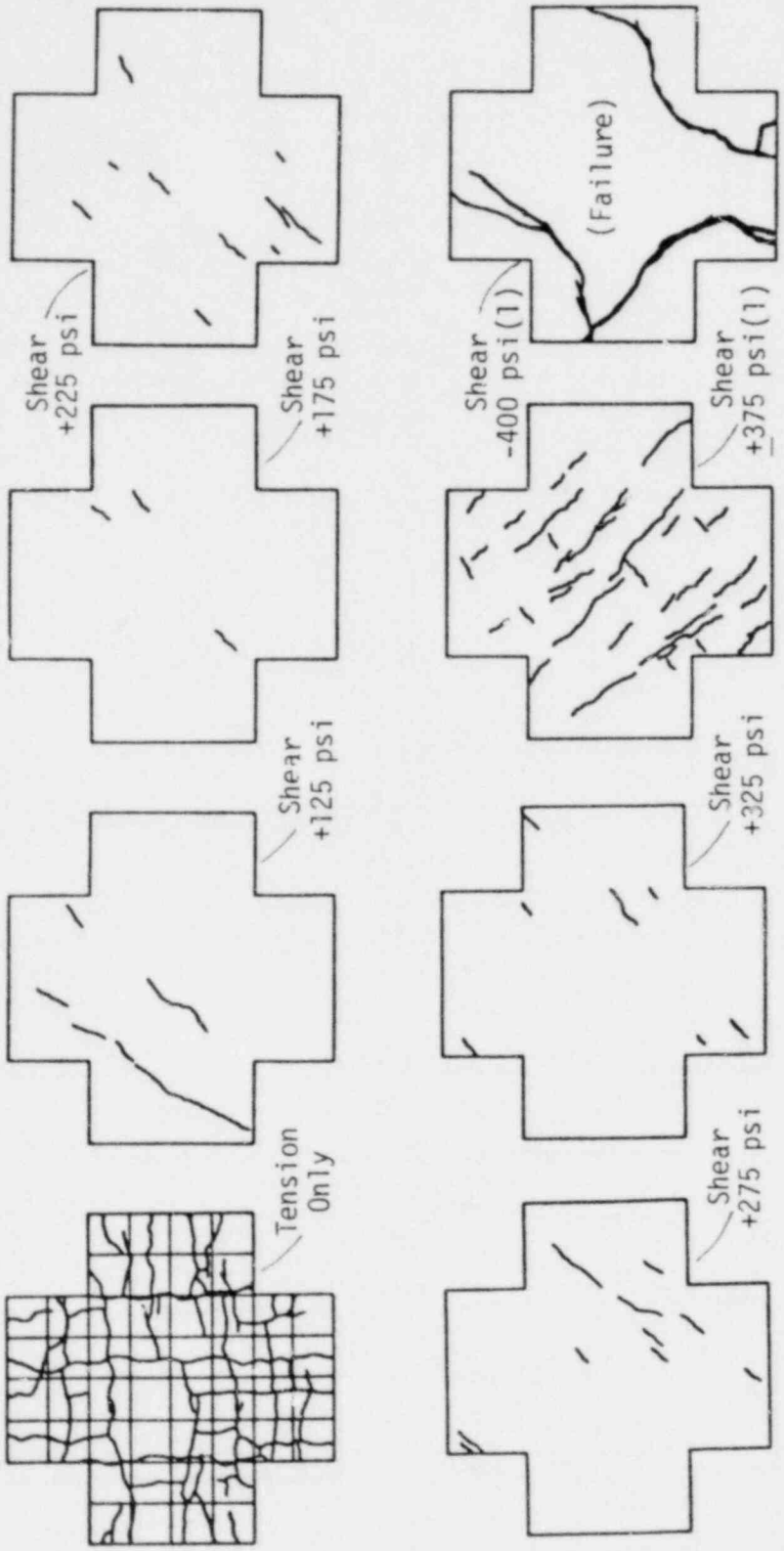

c) Specimen .3(C)

Fig. 2.21. (Continued)

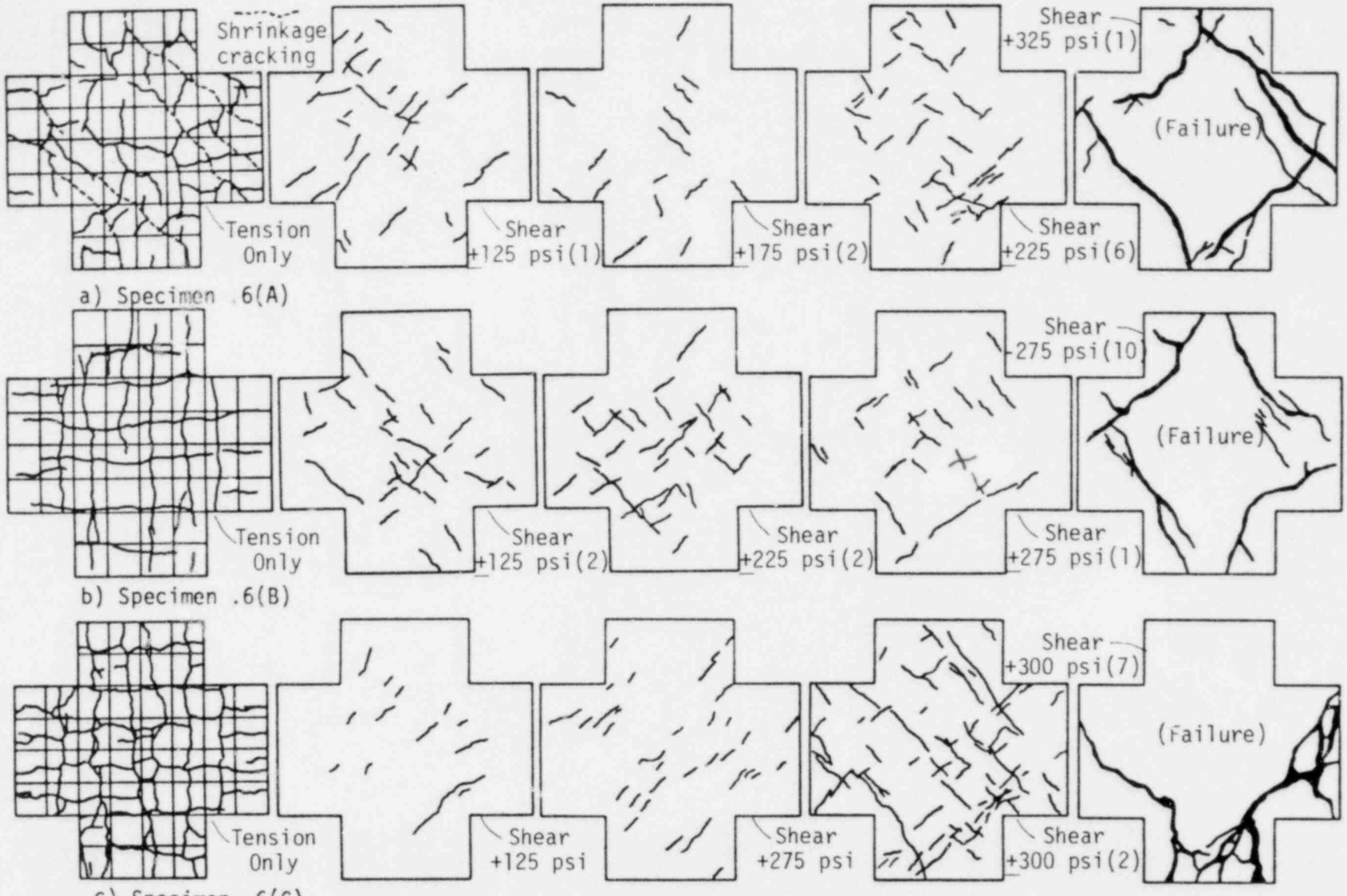

Fig. 2.22. Cracking patterns for cyclic shear and $0.6f_y$ biaxial tension (diagonal cracking shown is the additional cracking at each specified shear stress level; load cycle No. in parentheses).

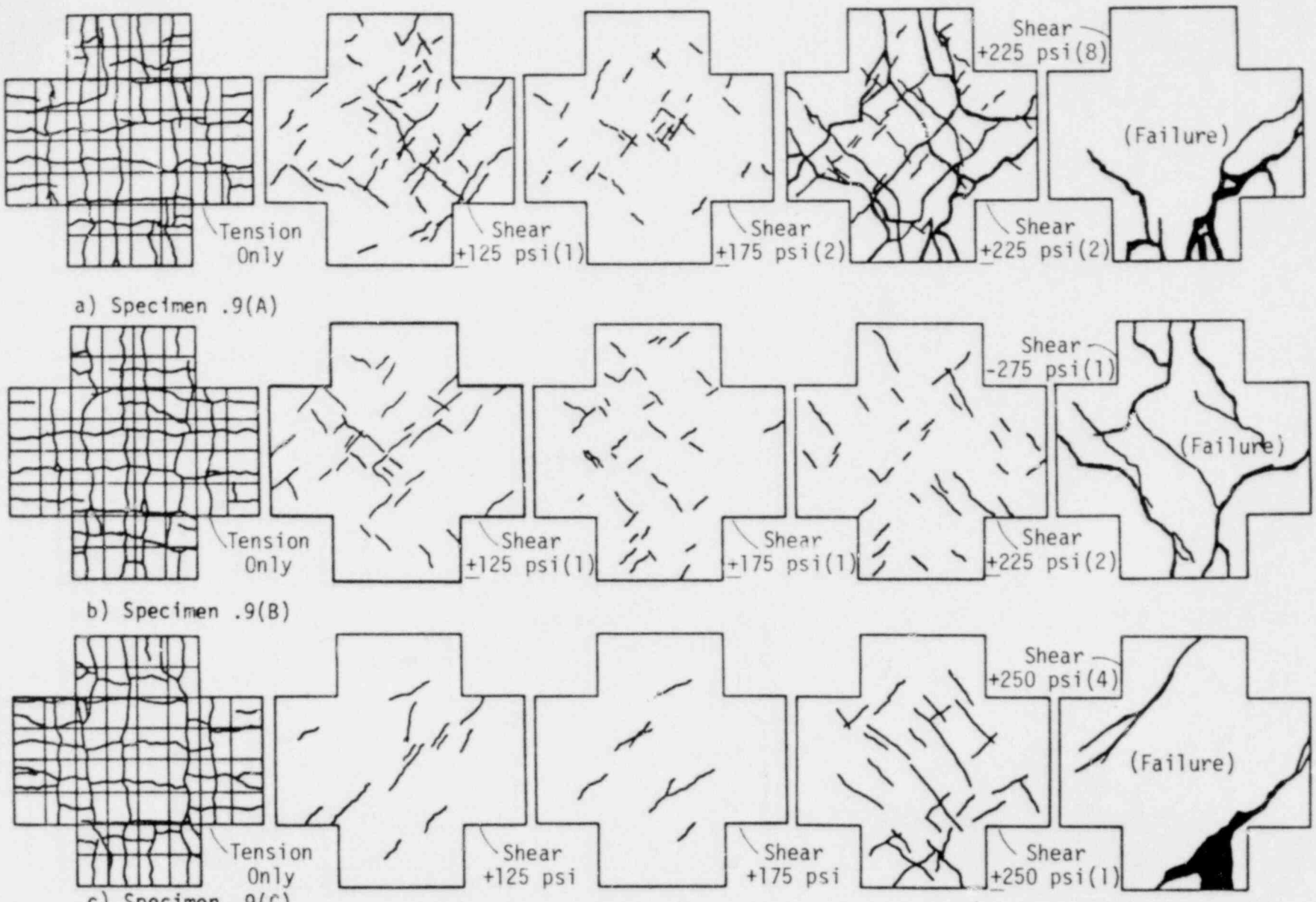

Fig. 2.23. Cracking patterns for cyclic shear and $0.9f_y$ biaxial tension (diagonal cracking shown is the additional cracking at each specified shear stress level; load cycle No. in parentheses).

As the shear deformations measured at the selected two orthogonal cracks were also erratic in the Series A, B and C specimens, it was very difficult if not impossible to base any quantitative conclusions on these results. However, selected graphs of the response will be presented in this section. These give qualitative insight into the effect of cycling, peak shear stress level, biaxial tension level and direction of crack on the crack opening or closing and the relative slip of the crack surfaces.

In Fig. 2.24 (a,b,c) the variation of the slip S1 at the tension crack parallel to the single bars is plotted versus the applied shear stress at

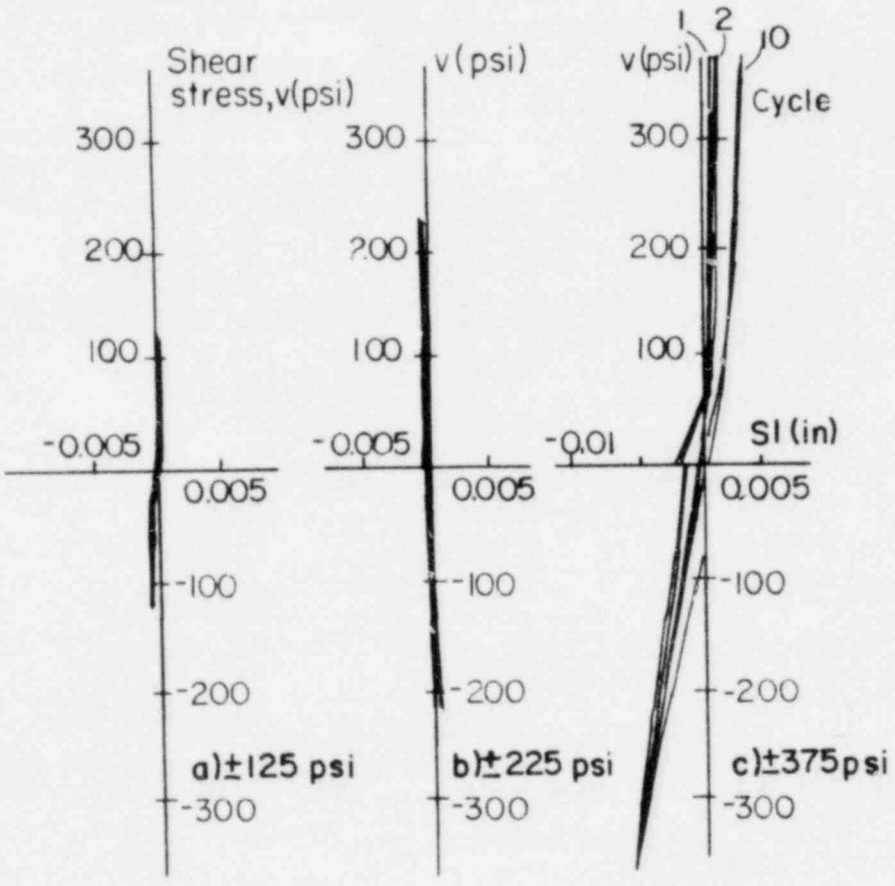

Fig. 2.24. Crack slip S1 versus applied cyclic shear (specimen .0(A)).

the 1st, 2nd and 10th cycle at three preselected stress levels of (a) ±125 psi, (b) ±225 psi, and (c) ±375 psi for specimen .0(A). The influence of cycling in increasing the slip values is insignificant for this case. About 0.005 in. (0.13 mm) average maximum slip was measured at the crack at the relatively high stress level of ±375 psi (2.59 MPa). For lower shear stresses very little slip took place.

The corresponding values for the crack width C1 are given in Fig. 2.25 (a,b,c,d) at three selected stress levels (±125, ±225, ±325 and ±375 psi). The values of crack width shown are the changes from the initial

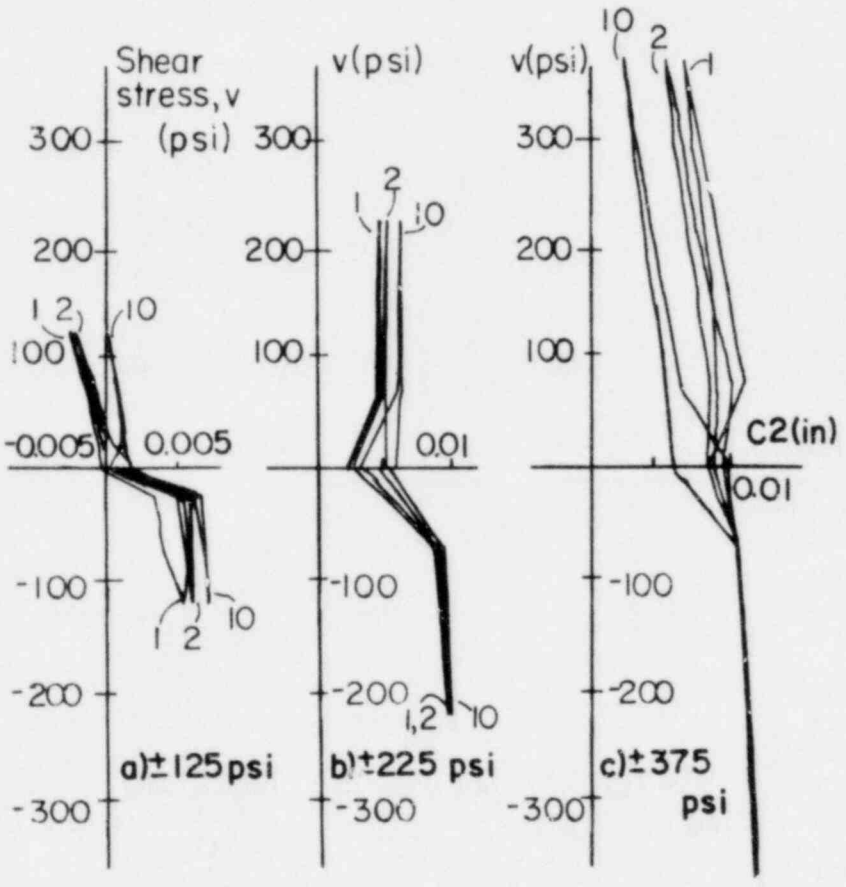

Fig. 2.25. Crack width changes C2 versus applied cyclic shear (specimen .0(A)).

crack width value at the beginning of the test; a negative value means closing of the crack. An increase in either the peak shear stress or the number of cycles results in further closing of the crack in both positive and negative direction of loading. This is a very important point, since it shows that at a shear stress higher than a certain level of about 125 psi (0.86 MPa) the shear transfer mechanism through sliding, which requires increase in the crack width, does not control any more and another mechanism becomes dominant. The latter is believed to be the diagonal tension-compression strut mechanism. The compressive stress in the concrete could cause the [illegible] of the orthogonal cracks with subsequent opening of the newly developed inclined cracks.

The absolute variation of crack width in the crack parallel to the double bars (C2 - see Fig. 2.26(a,b,c)) seems to be similar to that of C1. However, crack width C2 increases at intermediate stress levels but shows some decrease as failure is approached. Although there is the possibility that the above observation does not reflect the true overall behavior, it does bring up the argument that some interaction of the two shear transfer mechanisms, mentioned in the previous paragraph, takes place. Since some sliding has to occur in the beginning and crack width C1 decreases, crack width C2 must increase to permit the required slip that does not occur in the other direction. Fig. 2.27 shows exactly that. The increase in slip S2 is much larger than S1. Of course, for much larger initial crack widths the response could be different as it will be seen below. Specimen .3(A) shows approximately the same behavior as .0(A), although increasing residual slips are present at zero shear stress, especially for shear slip S2. The changes in the quantities C1, C2, S1 and S2 for specimen .3(A) are

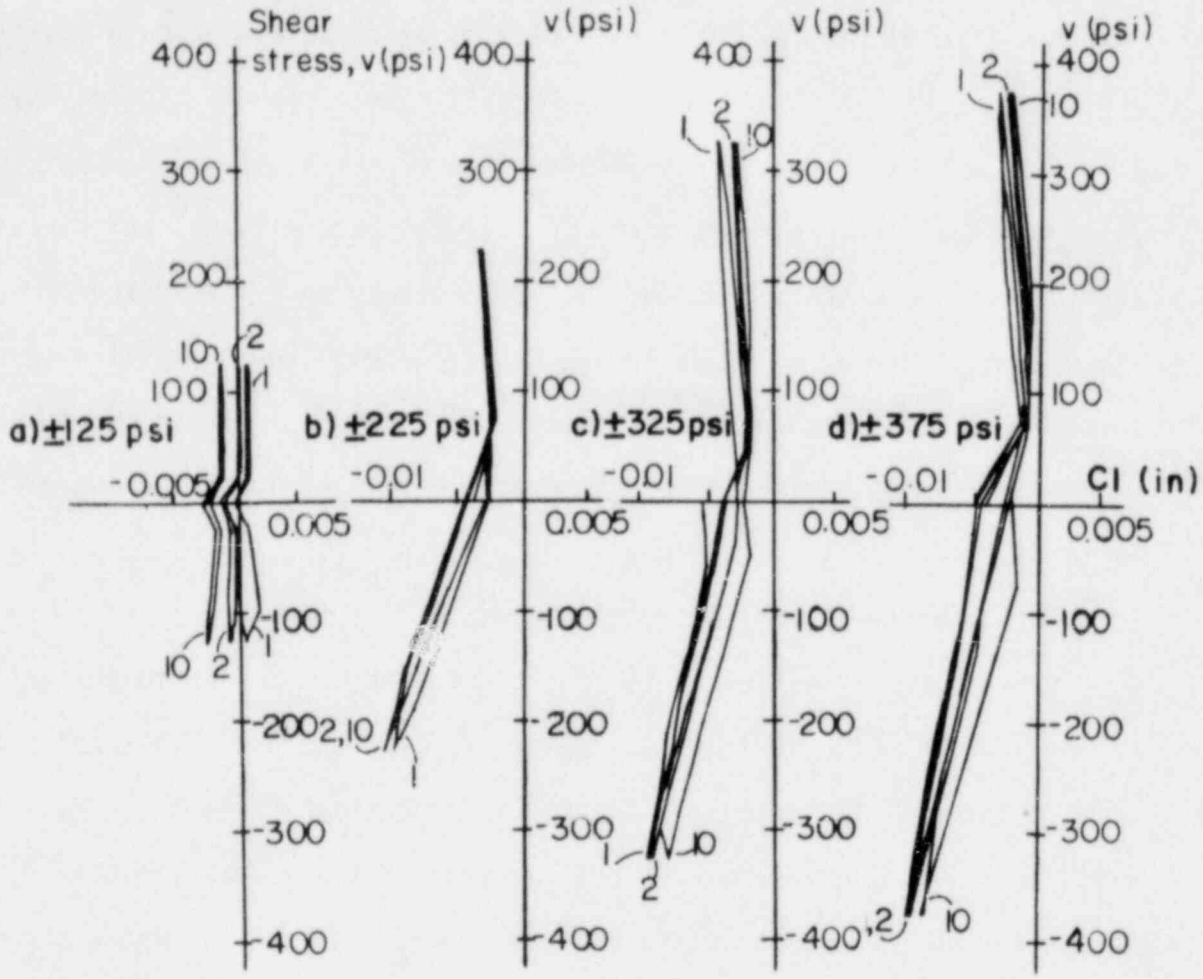

Fig. 2.26. Crack width changes C1 versus applied cyclic shear (specimen .0(A)).

given with the corresponding stress-displacement diagrams in Figs. 2.28 to 2.31, respectively.

The results of specimen .3(C) are presented in Fig. 2.32(a,b,c,d). During the initial monotonic loading up to +375 psi (2.59 MPa) both crack widths increased. Upon subsequent cycling, crack width C1 remained more or less constant in the positive loading direction and decreased in the

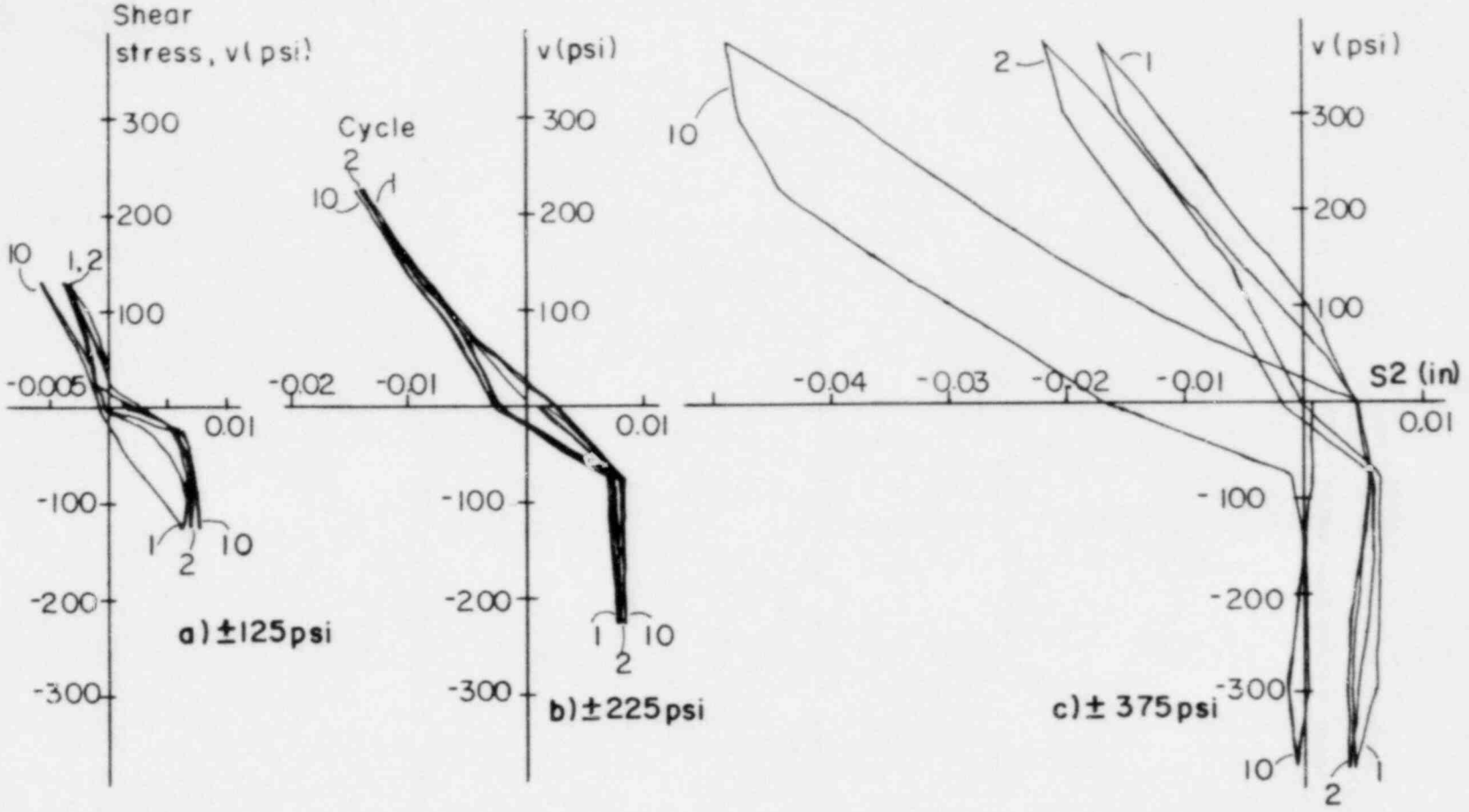

Fig. 2.27. Crack slip S2 versus applied cyclic shear (specimen .0(A))

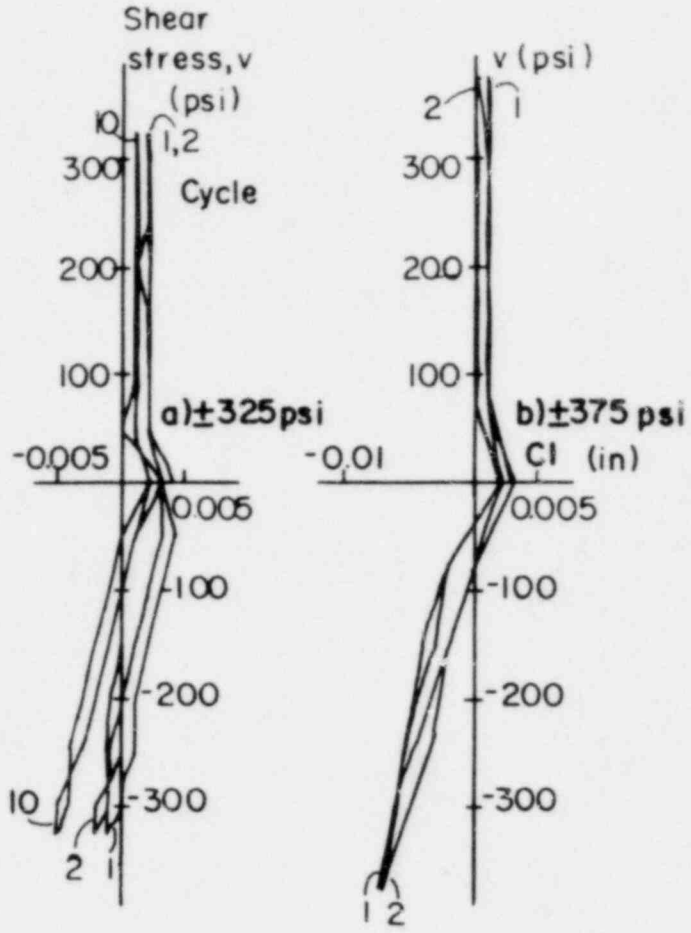

Fig. 2.28. Crack width changes C1 versus applied cyclic shear (specimen .3(A)

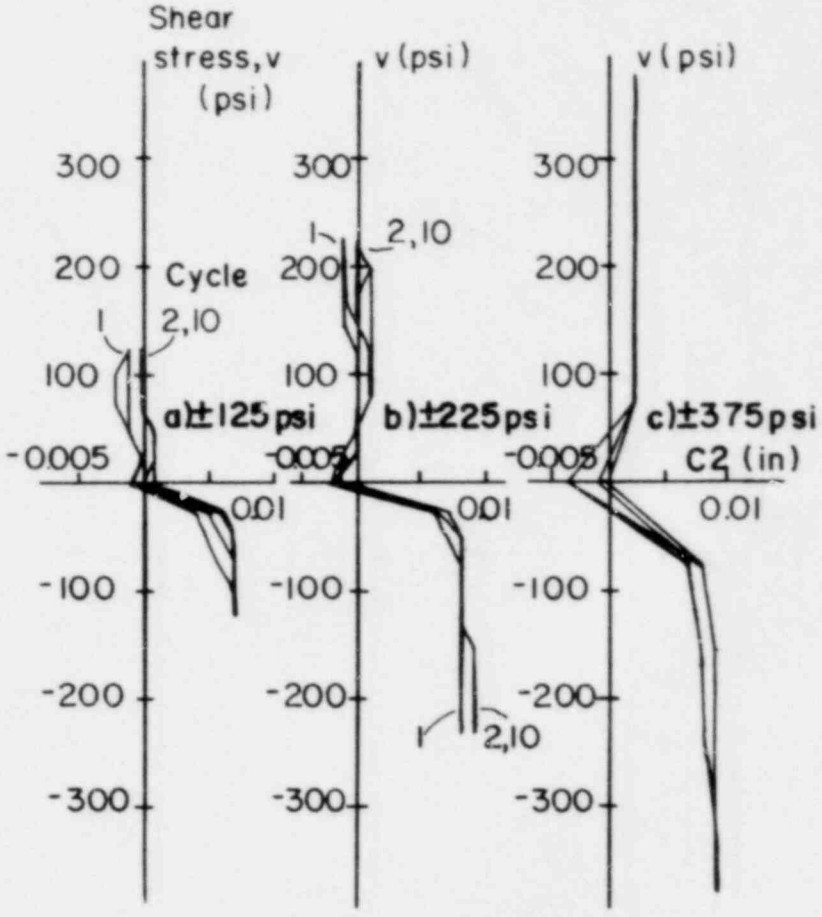

Fig. 2.29. Crack width changes C2 versus applied cyclic shear (specimen .3(A)).

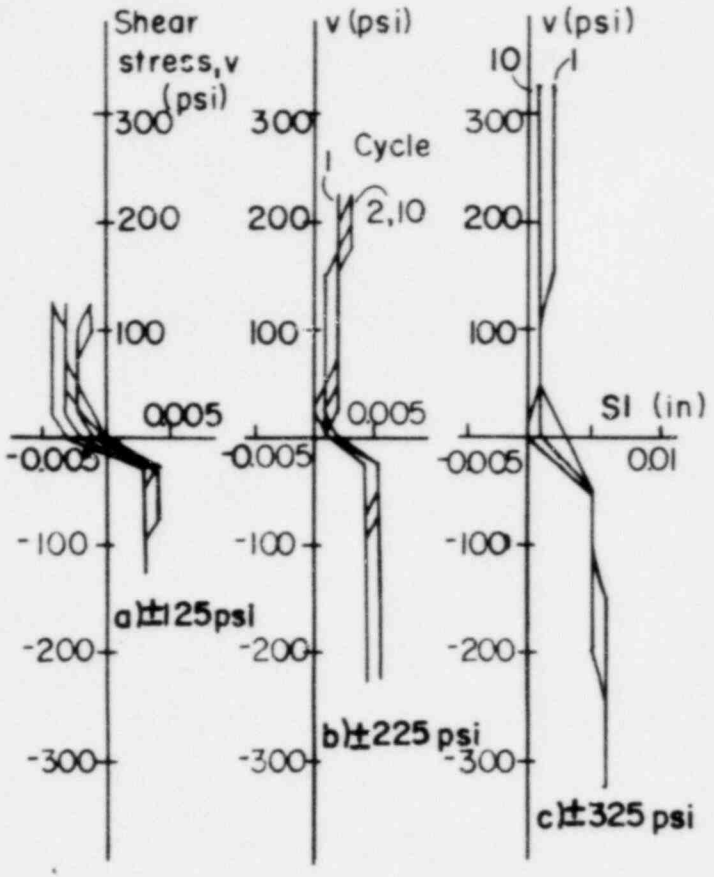

Fig. 2.30. Crack slip S1 versus applied cyclic shear (specimen .3(A)).

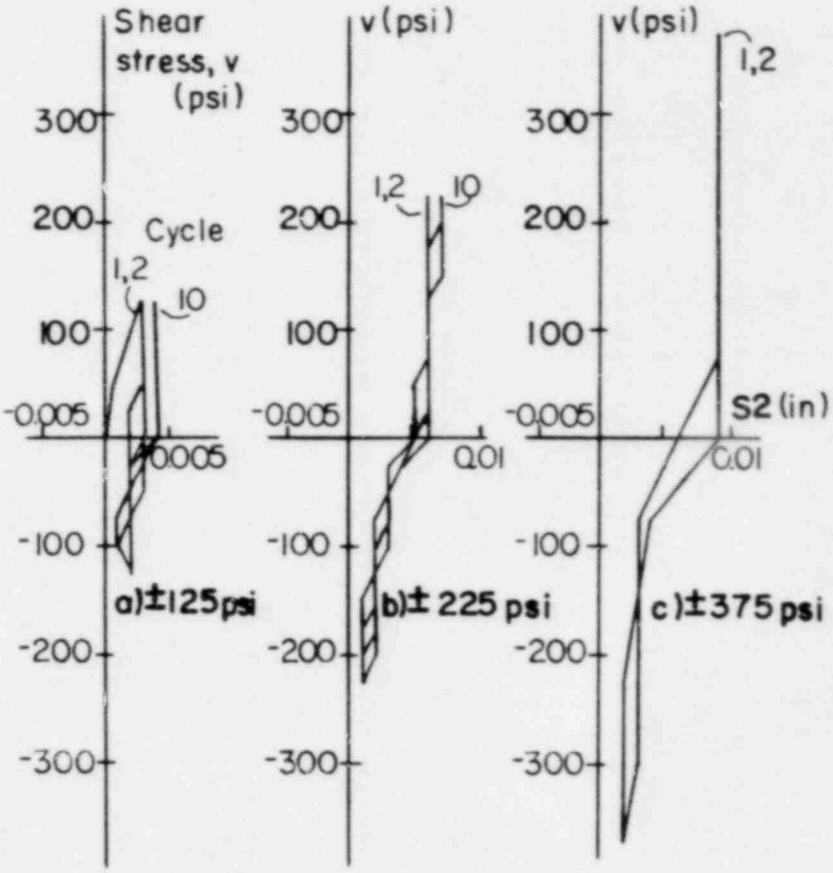

Fig. 2.31. Crack slip S2 versus applied cyclic shear (specimen .3(A)).

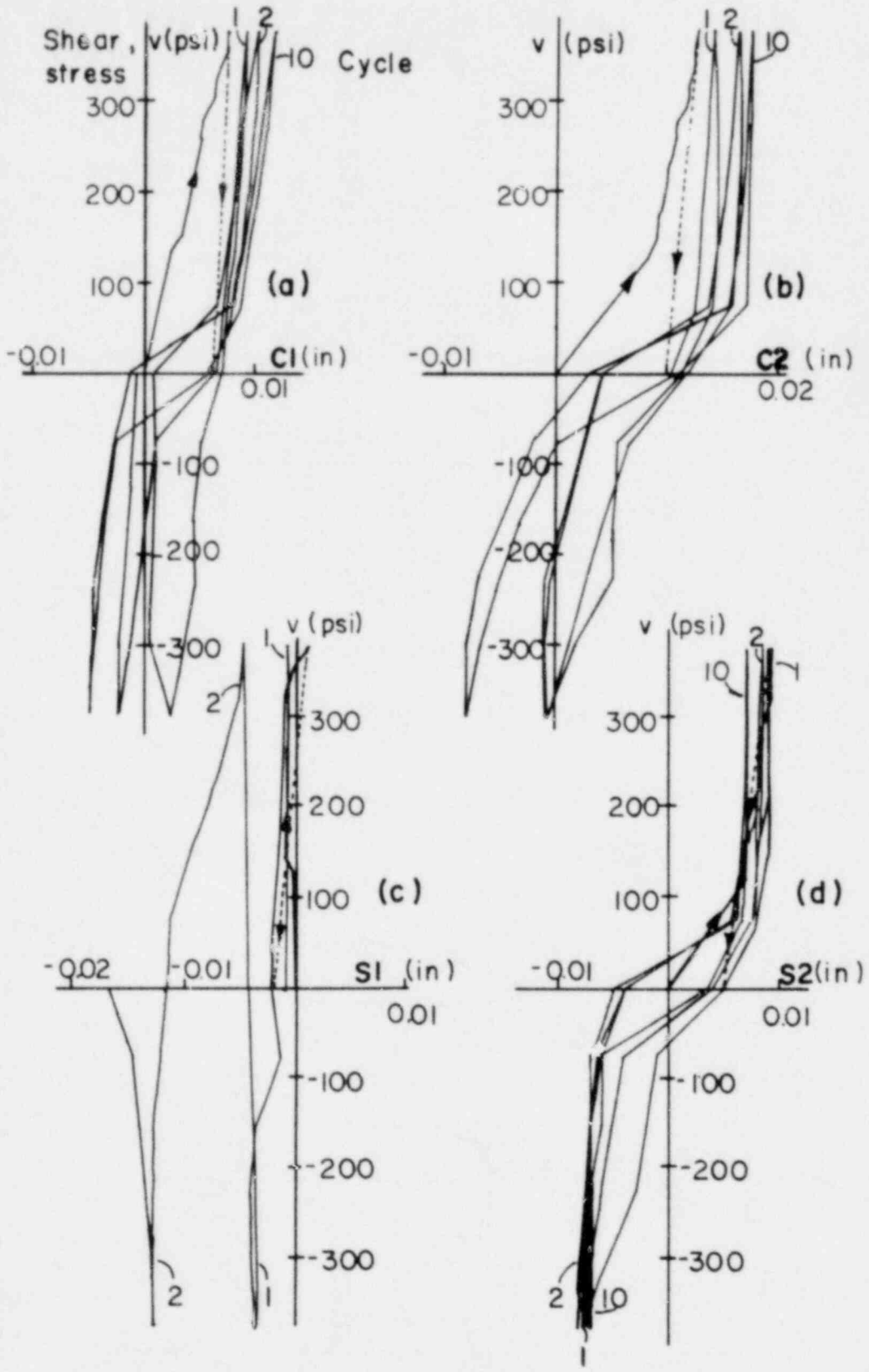

Fig. 2.32. Crack width changes C1, C2 and crack slip S1, S2 versus applied cyclic shear (specimen .0(C)).

negative direction (see Fig. 2.32a). Crack width C2 exhibited larger deformations in the same loading directions (see Fig. 2.32b).

In specimen .6(A), crack width C1 assumed smaller values during loading and increased to about the initial value upon unloading (see Fig. 2.33). No data is available for C2 due to a malfunction of the measuring device. Crack slips S1 and S2 were distinctly larger than those in the previous mentioned cases of lower applied tension (0 to $0.3f_y$) and reached the average maximum values of 0.025 and 0.014 in. (0.64 and 0.36 mm), respectively, during the 1st cycle at a peak shear stress of ±275 psi (1.90 MPa). These values for S1 and S2 increased to 0.028 and 0.017 in. (0.71 and 0.43 mm), respectively, after 10 cycles of reversing loading at the same maximum shear (see Figs. 2.34 and 2.35).

The duplicate specimen .6(B) experienced much less sliding along the crack parallel to the single bars (S1) (see Fig. 2.36). Specimen .6(A) could be inherently softer in its response since excessive shrinkage cracking was observed prior to the test, while specimen .6(B) had no visible initial distress. As also noticed in specimen .3(A), the curve for S2 kept shifting to the left with no relative difference in slip between the positive and negative shear stress (see Fig. 2.37). This shows a preference of the crack slipping to occur mainly in one direction causing continuously increasing residual slip relative to the beginning of the test. Thus, although locally the crack surfaces still keep sliding in both directions under reversing shear load, a permanent shear distortion is present in one direction, which probably shows less ability to transfer shear stresses in that direction.

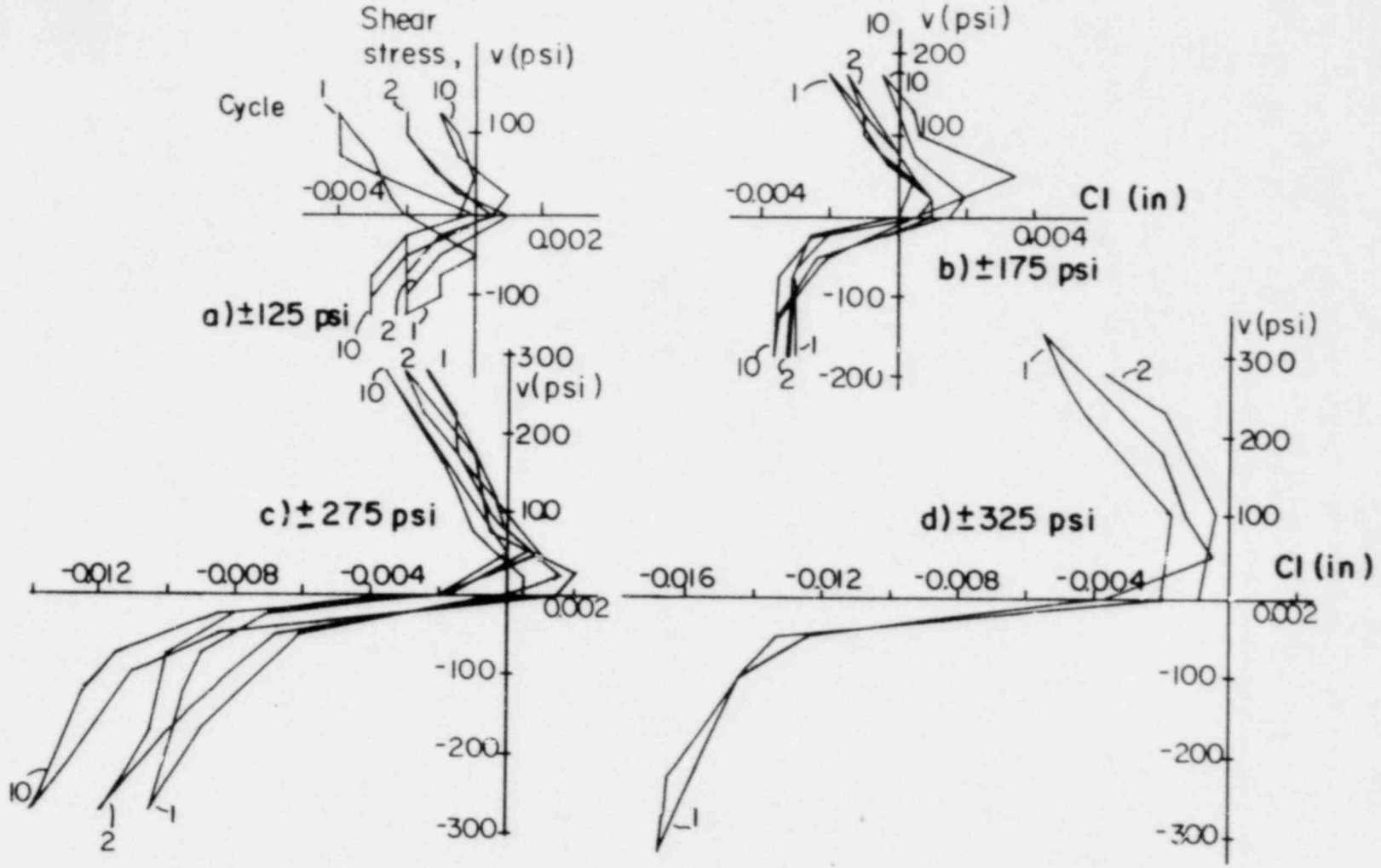

Fig. 2.33. Crack width changes Cl versus applied cyclic shear (specimen .6(A)).

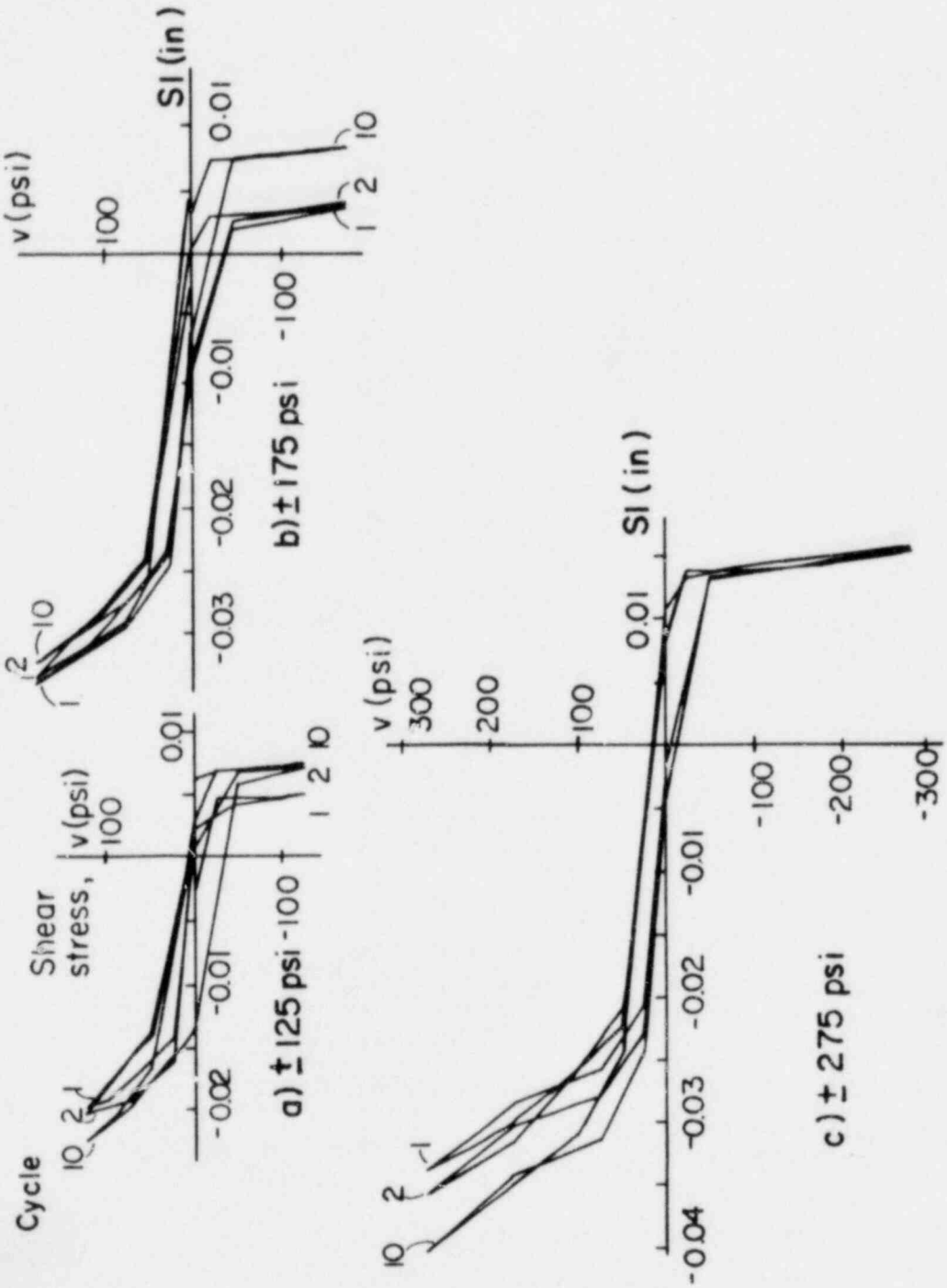

Fig. 2.34. Crack slip Sl versus applied cyclic shear (specimen .6(A)).

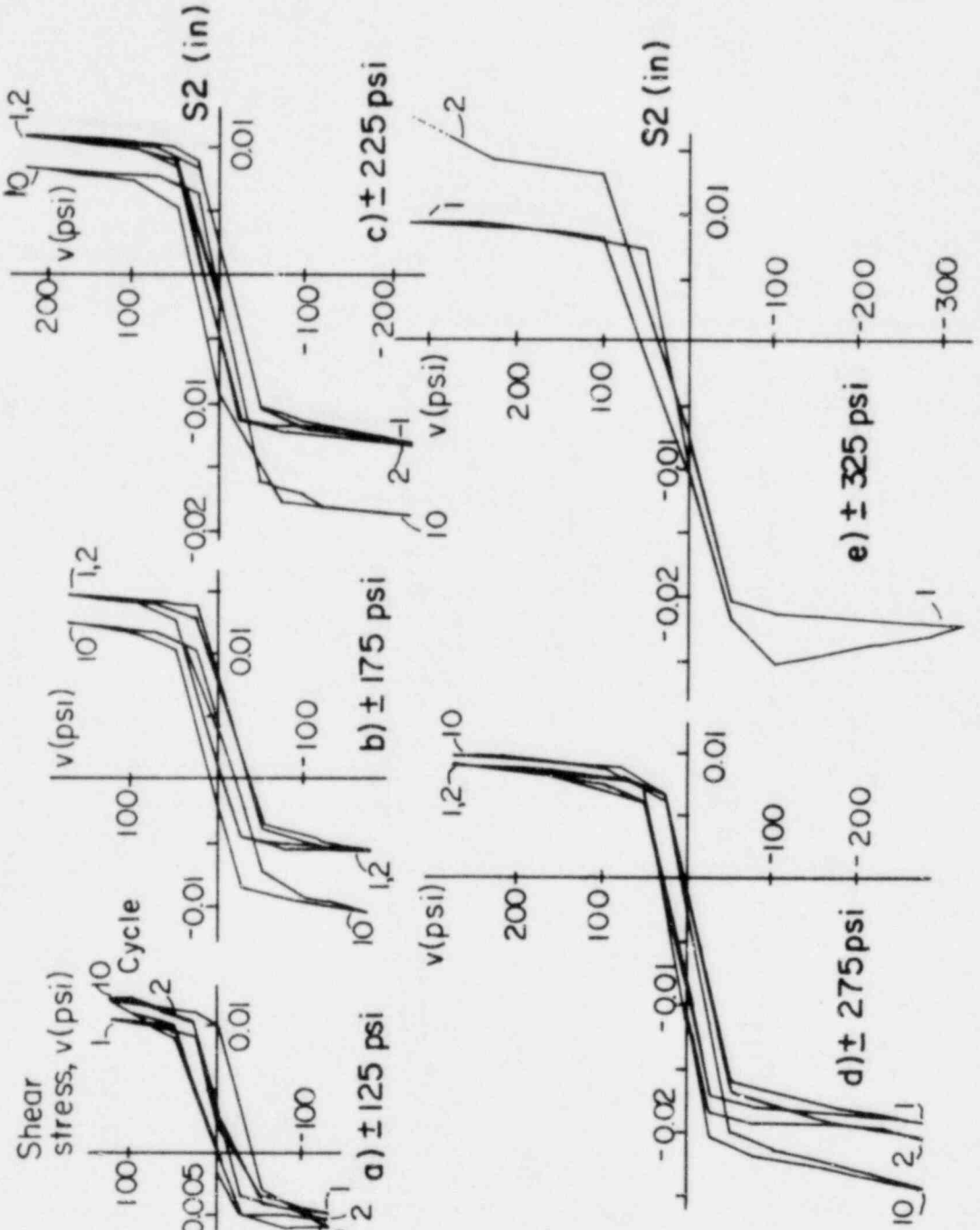

Fig. 2.35. Crack slip S2 versus applied cyclic shear (specimen .6(A)).

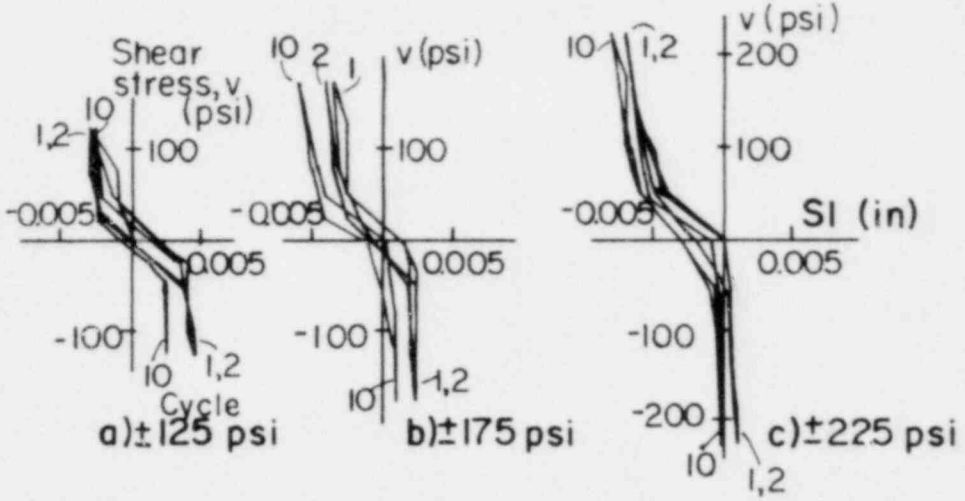

Fig. 2.36. Crack slip S1 versus applied cyclic shear (specimen .6(B)).

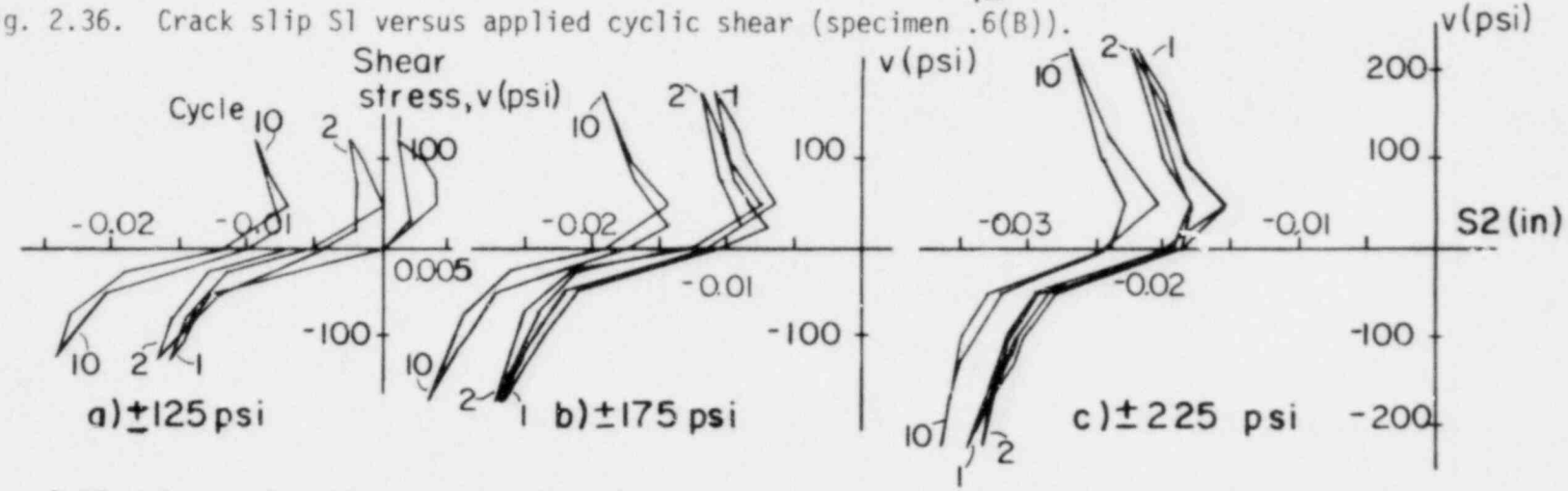

Fig. 2.37. Crack slip S2 versus applied cyclic shear (specimen .6(B)).

The companion specimen of .3(C), .6(C), as shown in Fig. 2.38 (a,b, c,d), showed closing of cracks C1 and C2 at least for low and intermediate shear stress levels, as the shear stress was increased up to +300 psi. At that high shear stress slip values (S1, S2) were more sensitive to cycling.

The deformation along the chosen single cracks in the duplicate specimens .9(A) and .9(B) are given in Figs. 2.39 to 2.42 and Figs. 2.43 to 2.46, respectively. Similar behavior was noticed in both specimens for the shear slip S1. Intense cycling of specimen .9(A) at peak shear stresses lower than 125 psi did not seem to have any effect whatsoever (see Figs. 2.41(a,b) and 2.45a). Crack width values C1 and C2 showed consistent decreases up to about ±225 psi in specimen .9(A) (Figs. 2.39 and 2.40). At that shear stress level and higher, the width of the crack started increasing erratically. Due to the high applied tension of $0.9f_y$, cracking was very severe and therefore spalling of concrete occurred on the surface, especially around the main diagonal crack at failure. This could have resulted in sliding of the steel base of the dial gage relative to the concrete surface, in which case measurements would be unreliable.

All maximum values for C1, S1, C2 and S2 of the cyclically loaded specimens at the 1st, 2nd and 10th cycle at selected shear stress levels are given in Table A.1 (Appendix A).

c) Effective shear modulus

The measured hysteretic response of the specimens in Series A, B and C is presented in Figs. 2.47 to 2.58 in the form of shear deformation versus shear load loops, at the 1st and 10th loading cycle. Two ways are

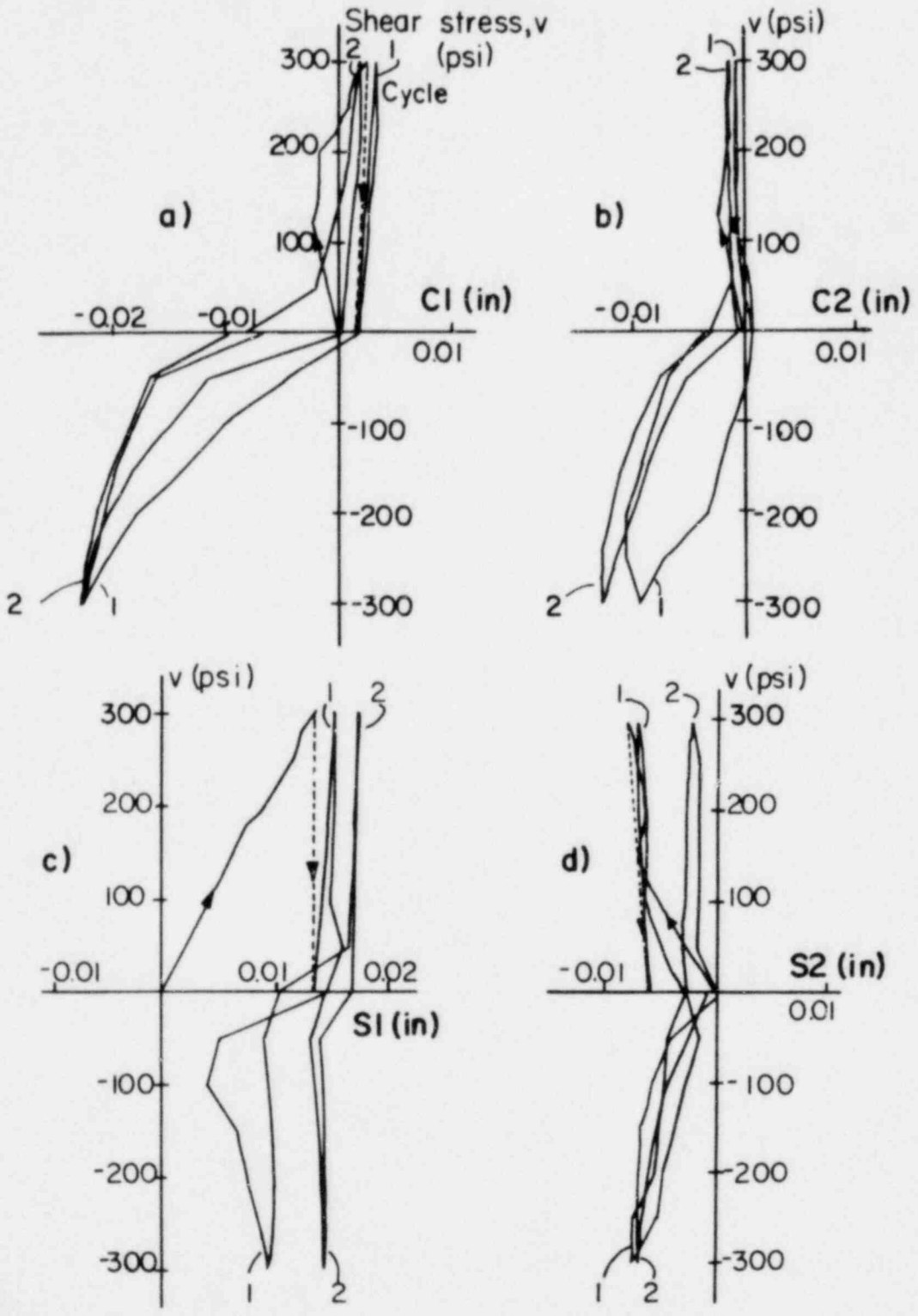

Fig. 2.38. Crack width changes C1, C2 and crack slip S1, S2 versus applied cyclic shear (specimen .6(C)).

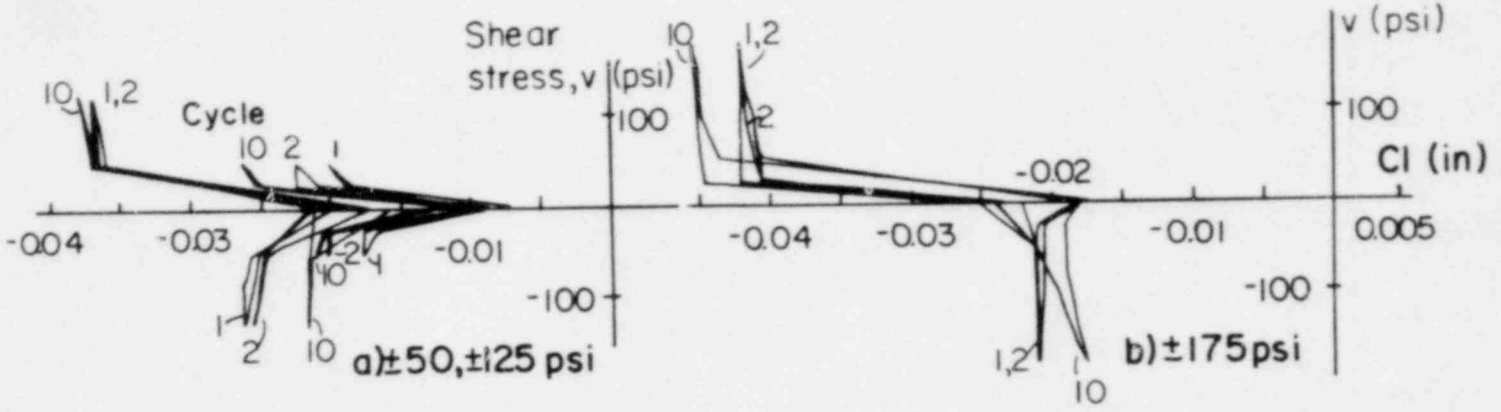

Fig. 2.39. Crack width changes C1 versus applied cyclic shear (specimen .9(A)).

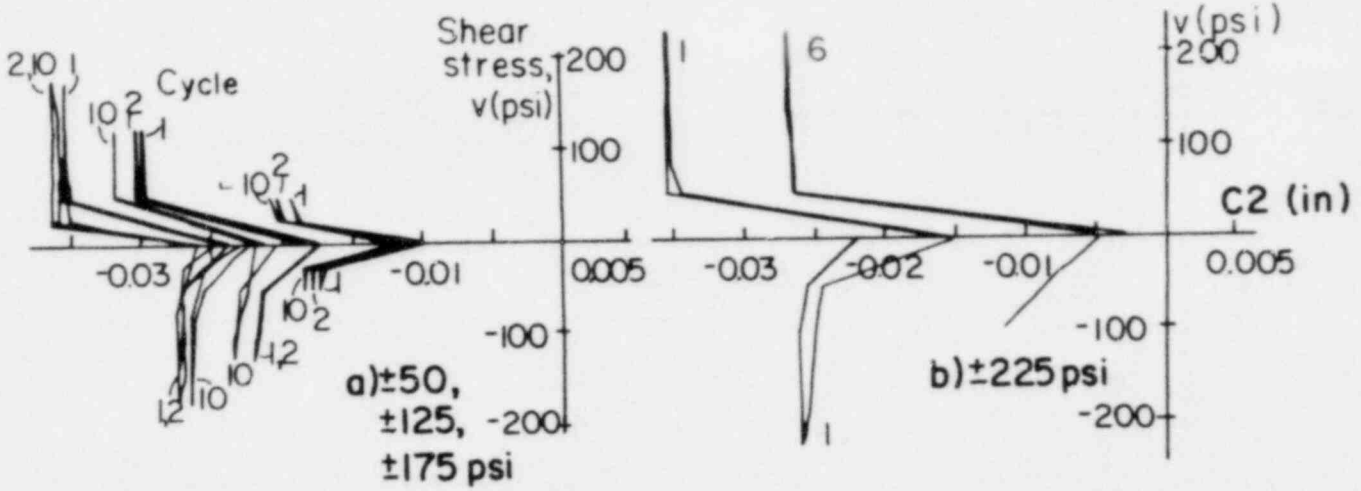

Fig. 2.40. Crack width changes C2 versus applied cyclic shear (specimen .9(A)).

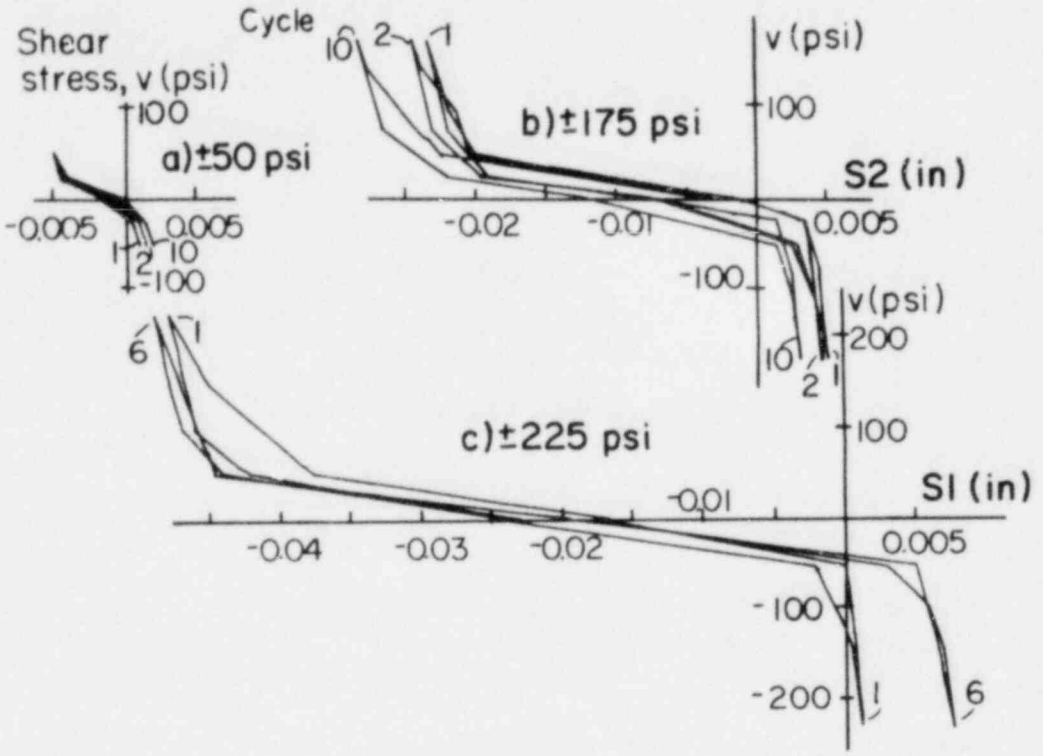

Fig. 2.41. Crack slip S1 versus applied cyclic shear (specimen .9(A)).

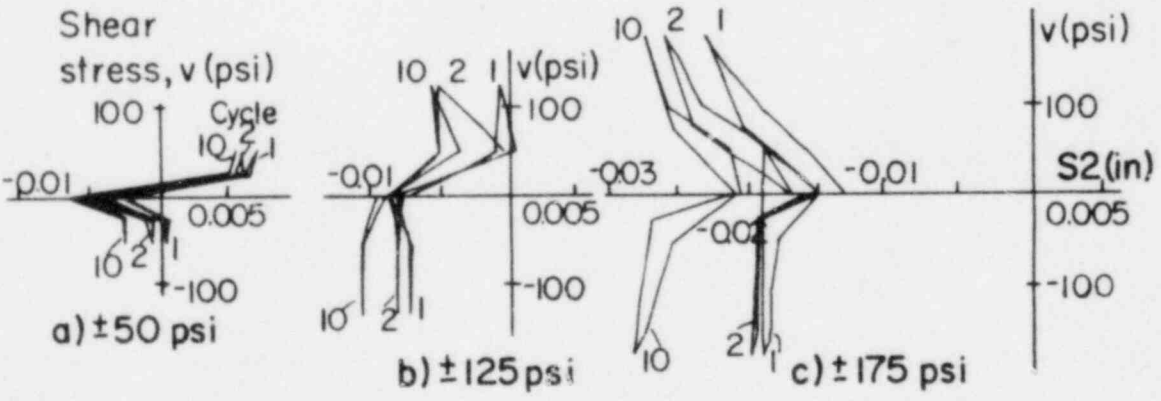

Fig. 2.42. Crack slip S2 versus applied cyclic shear (specimen .9(A)).

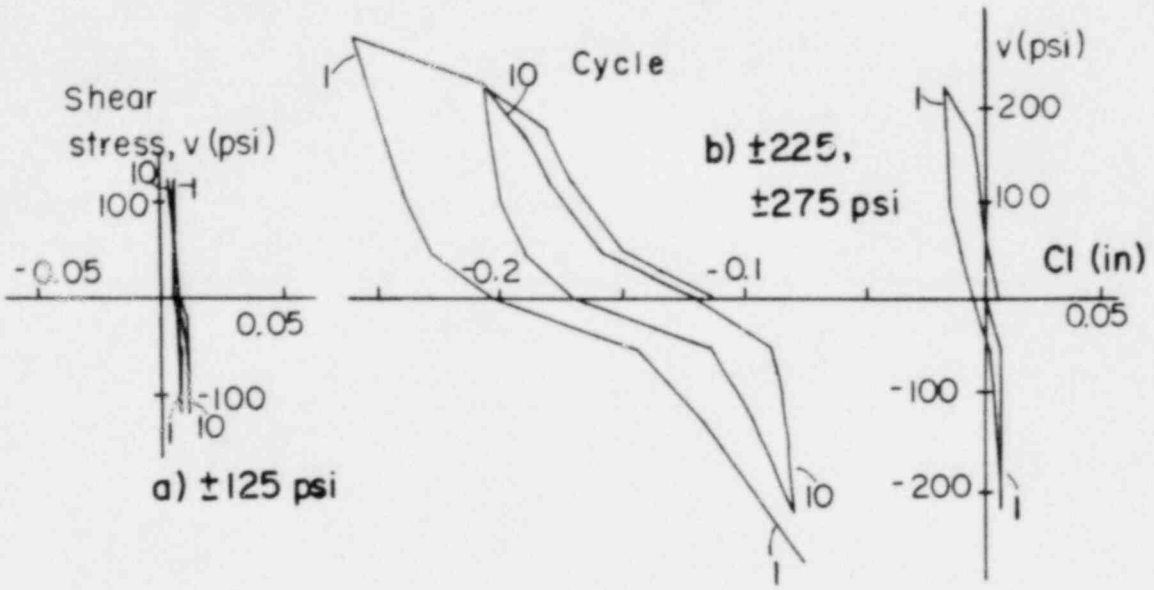

Fig. 2.43. Crack width changes C1 versus applied cyclic shear (specimen .9(B)).

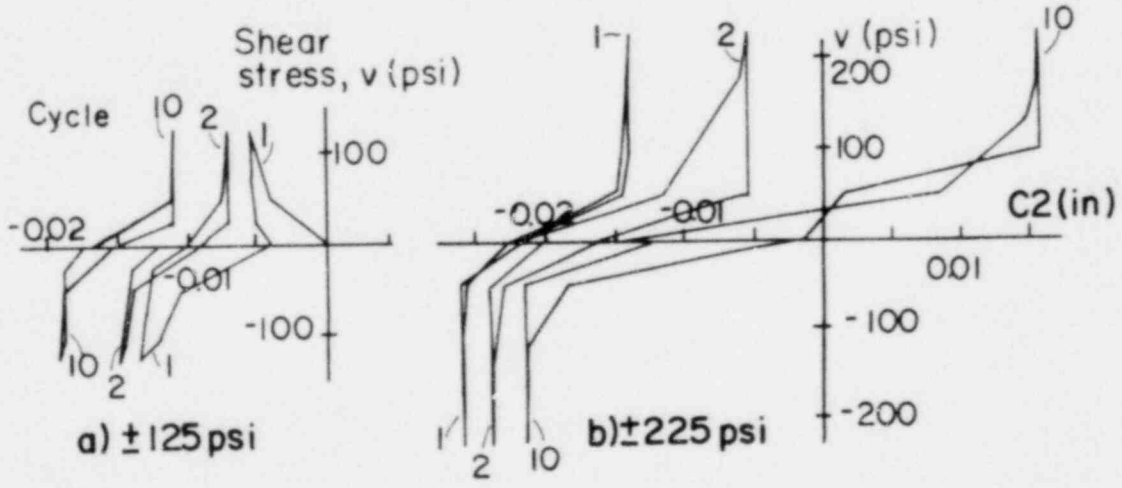

Fig. 2.44. Crack width changes C2 versus applied cyclic shear (specimen .9(B)).

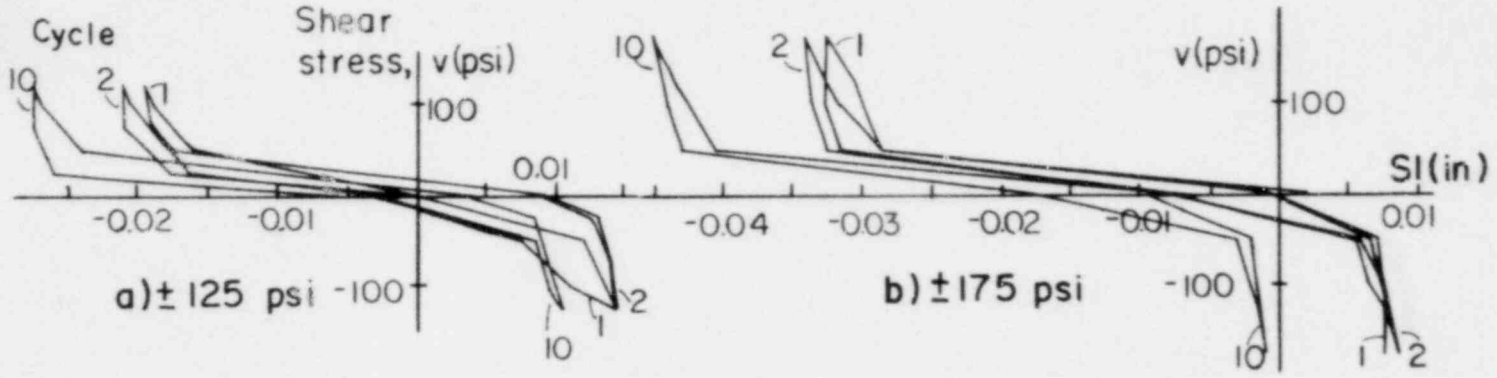

Fig. 2.45. Crack slip S1 versus applied cyclic shear (specimen .9(B)).

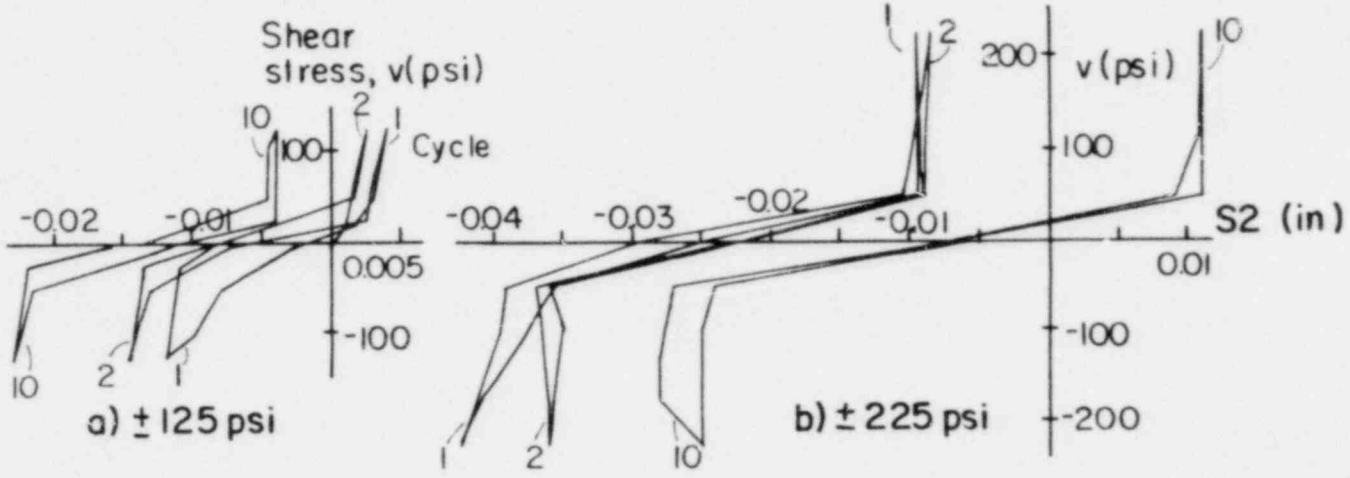

Fig. 2.46. Crack slip S2 versus applied cyclic shear (specimen .9(B)).

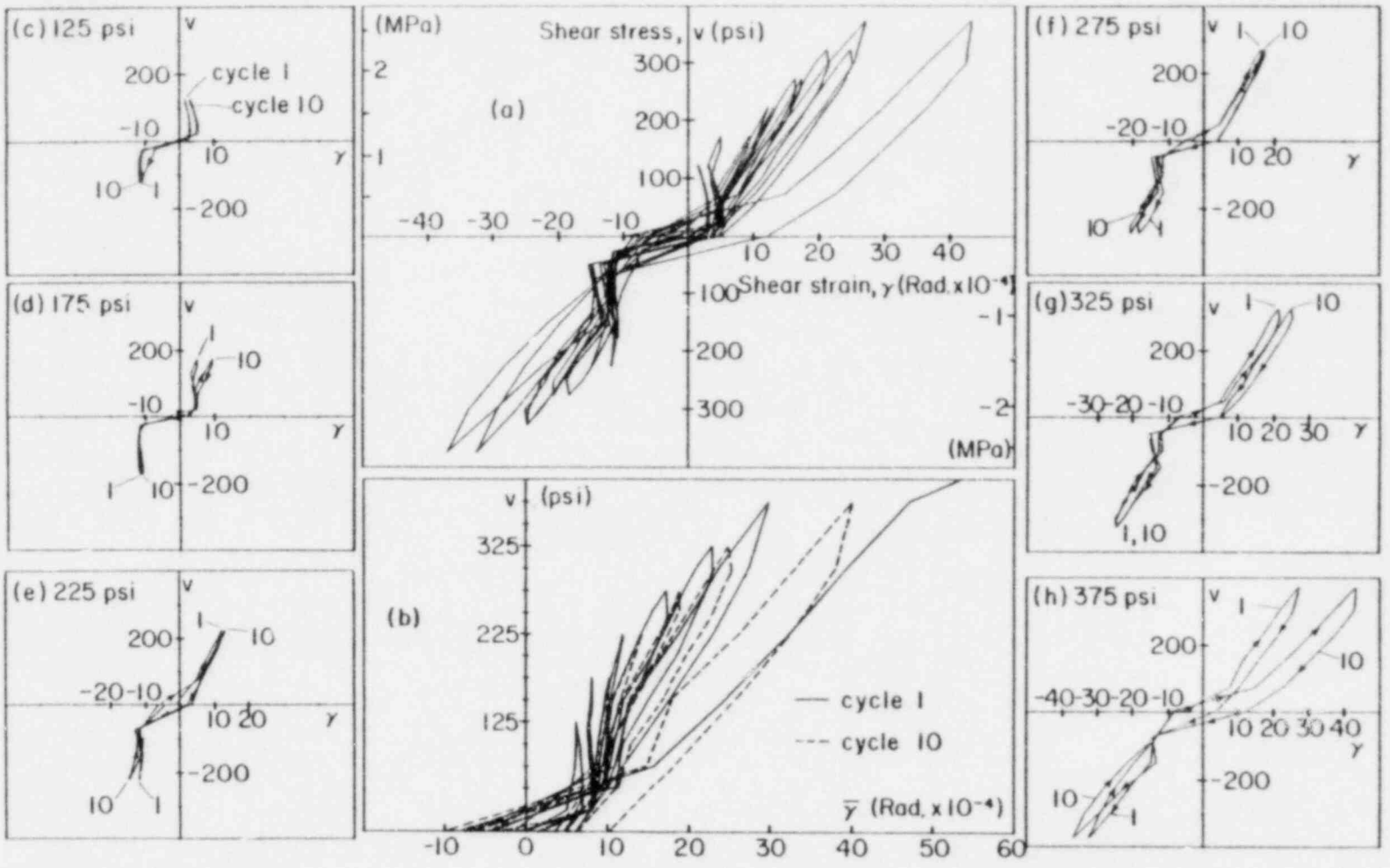

Fig. 2.47. Shear stress-strain hysteresis loops (specimen .0(A)).

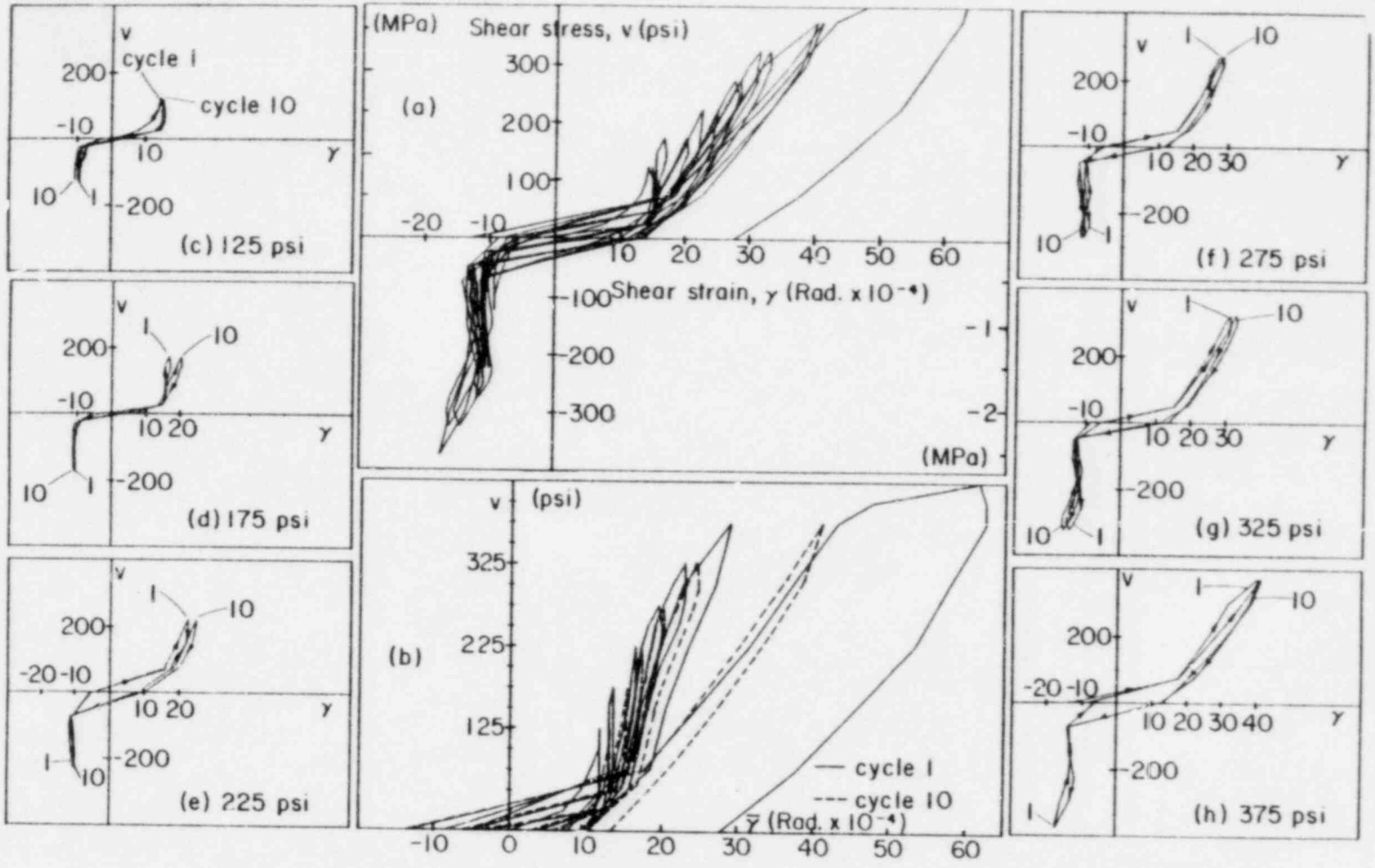

Fig. 2.48. Shear stress-strain hysteresis loops (specimen .0(B)).

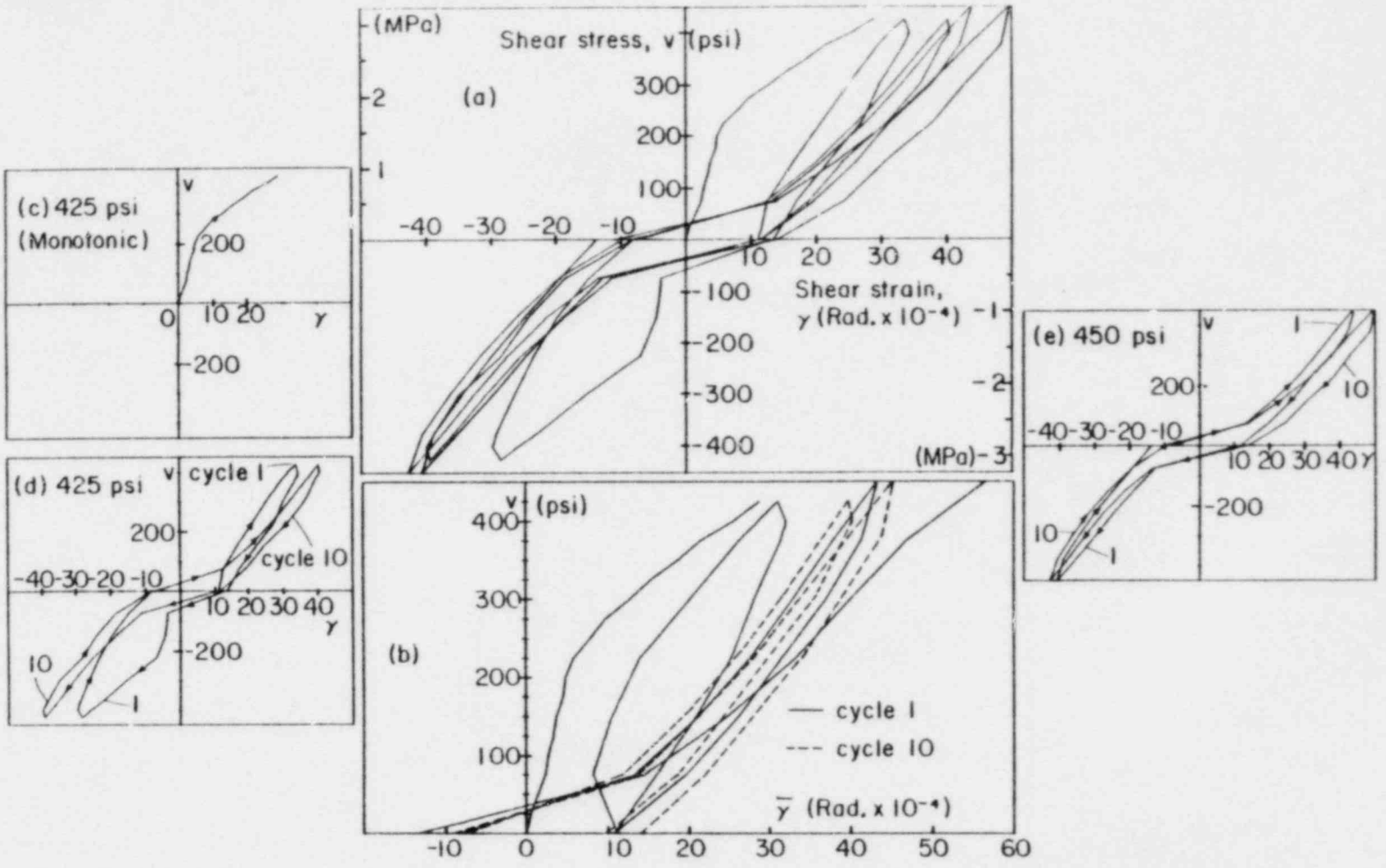

2.49. Shear stress-strain hysteresis loops (specimen .0(C)).

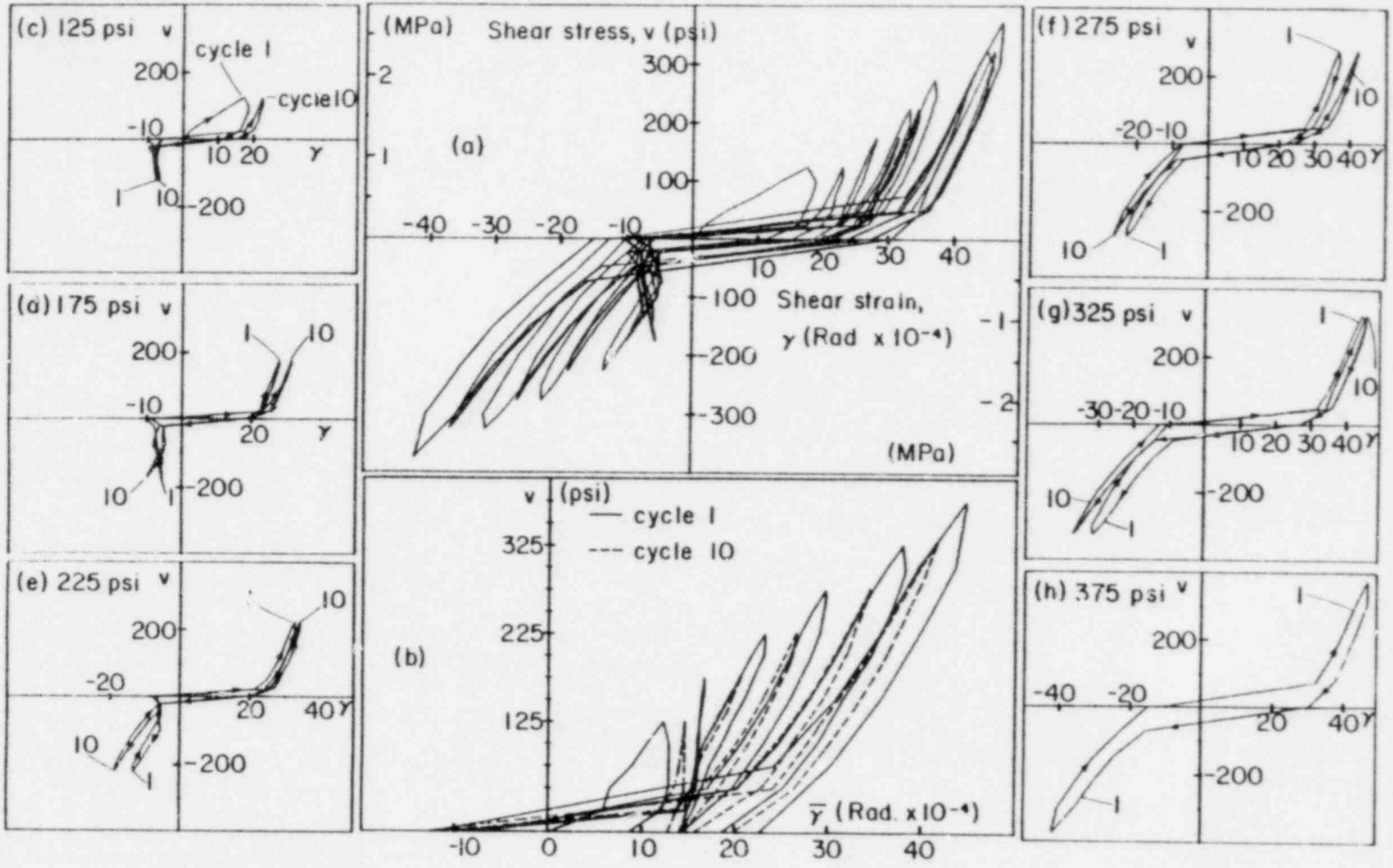

2.50. Shear stress-strain hysteresis loops (specimen .3(A)).

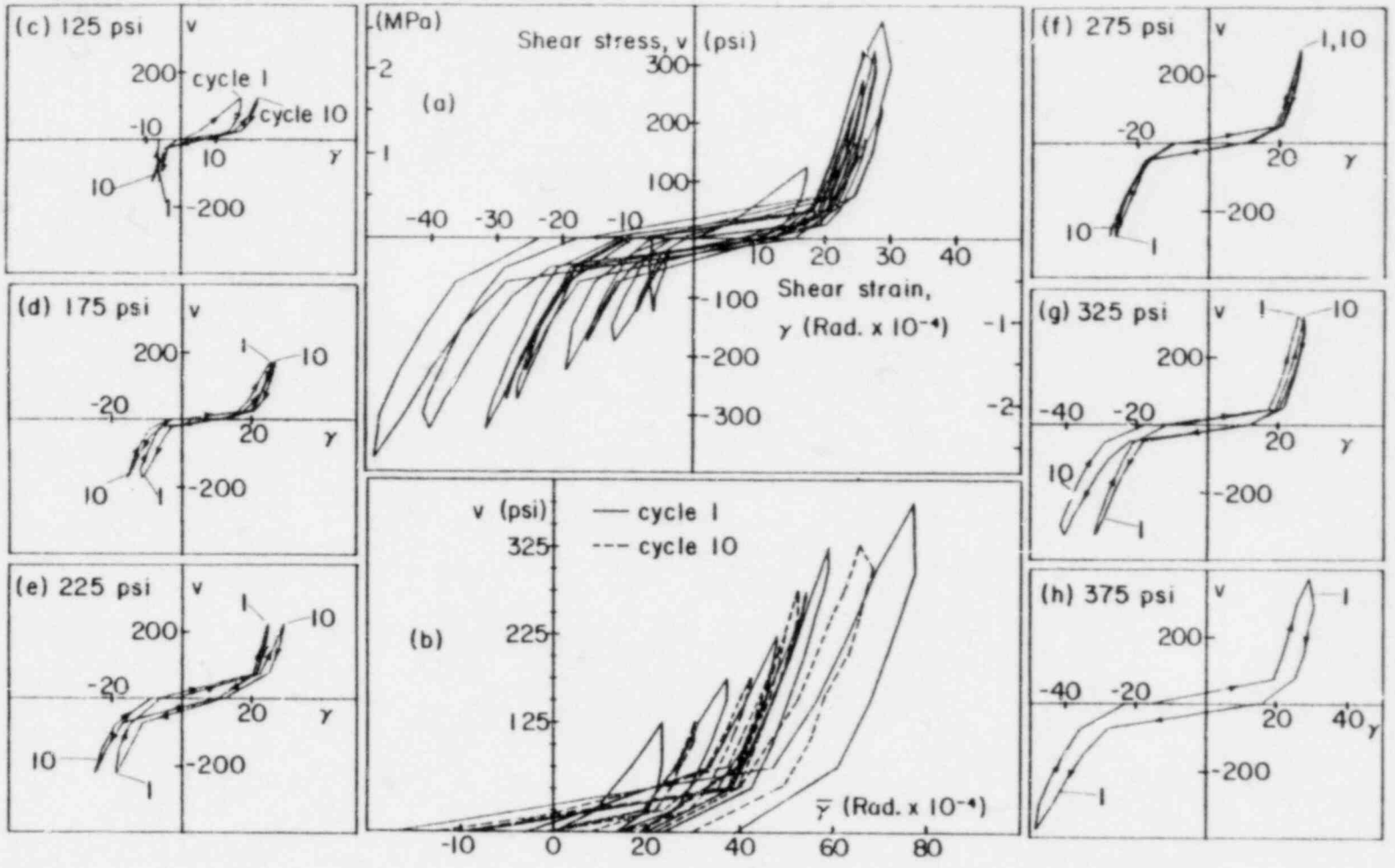

Fig. 2.51. Shear stress-strain hysteresis loops (specimen .3(B)).

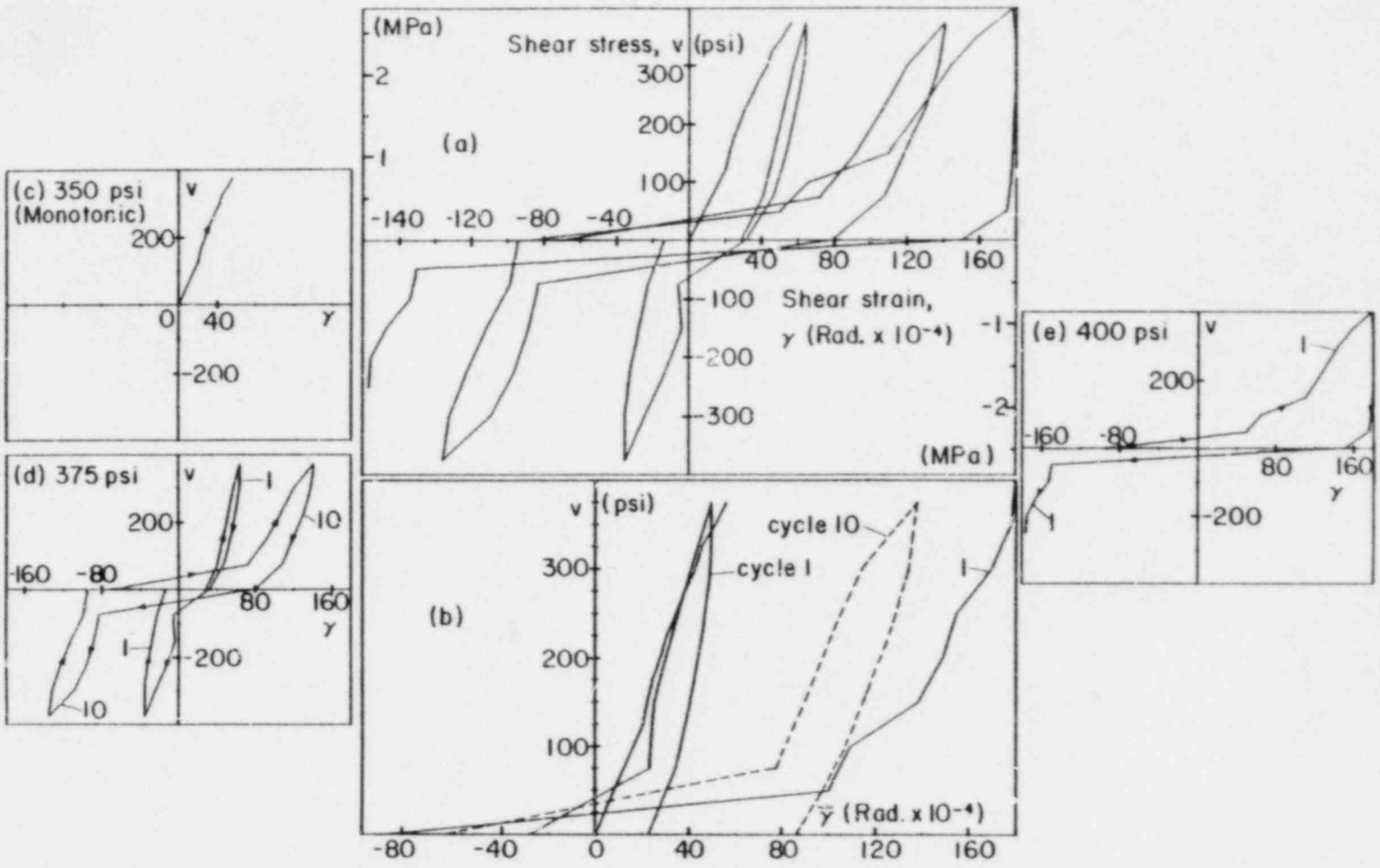

Fig. 2.52. Shear stress-strain hysteresis loops (specimen .3(C)).

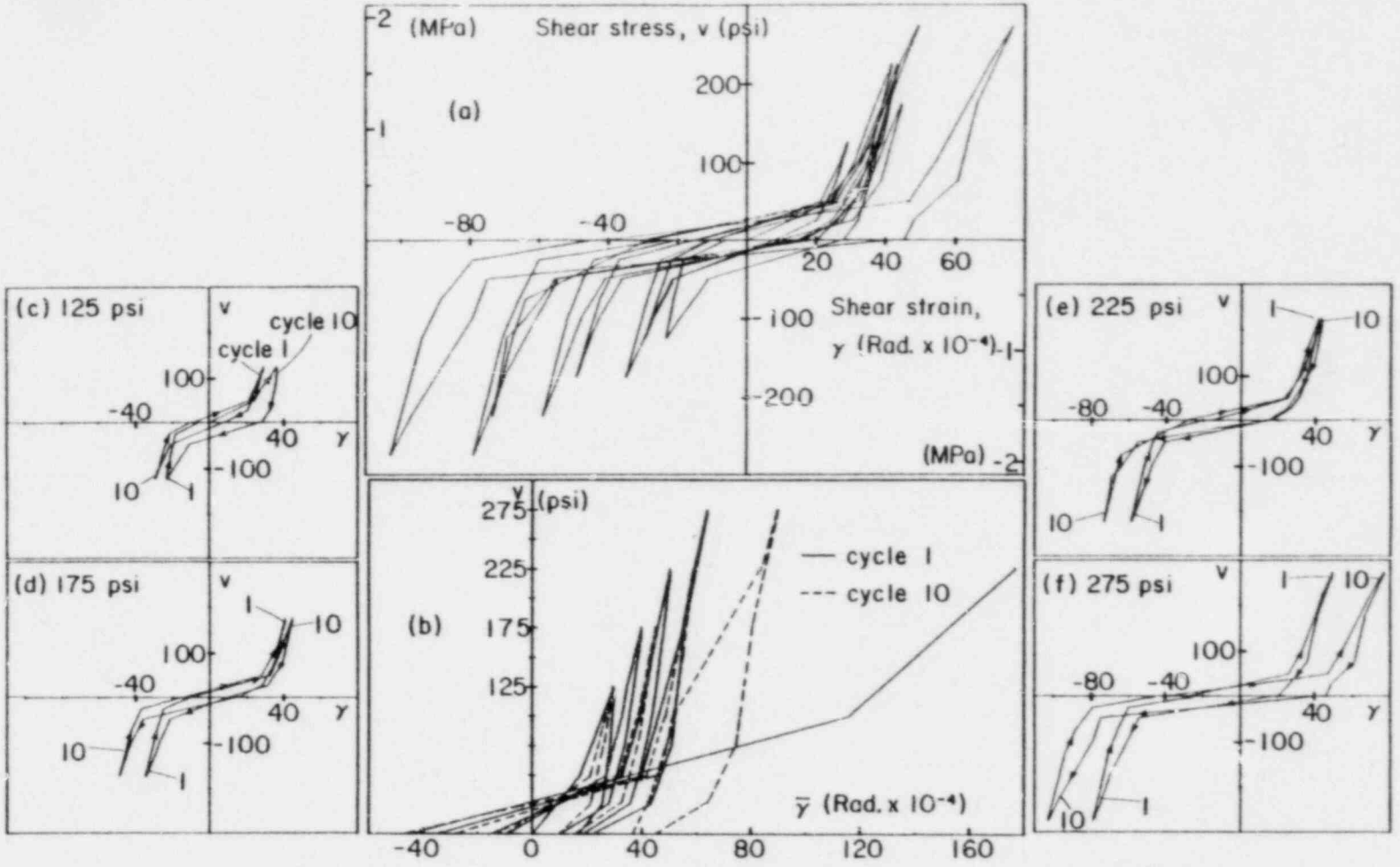

Fig. 2.53. Shear stress-strain hysteresis loops (specimen .6(A)).

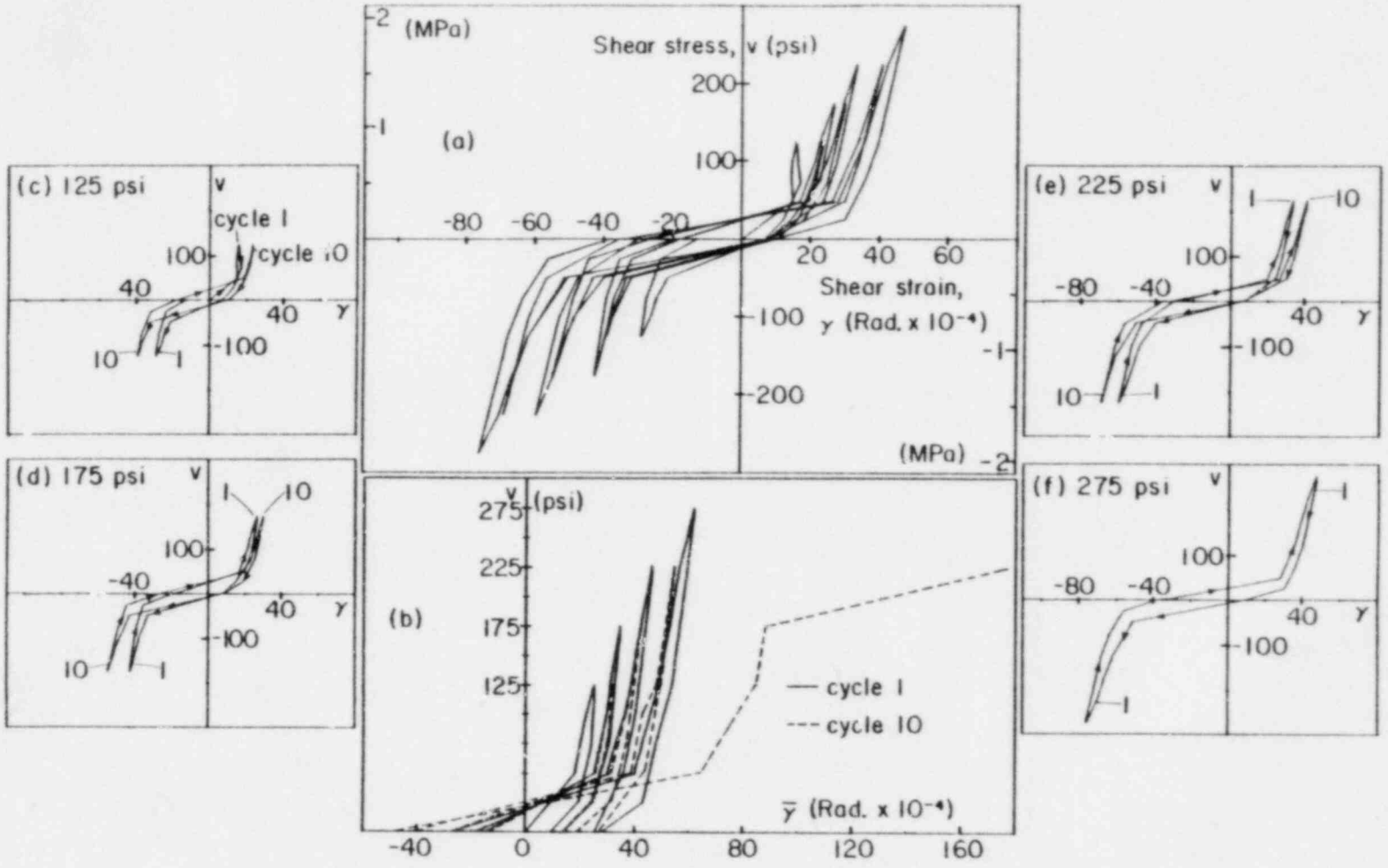

Fig. 2.54. Shear stress-strain hysteresis loops (specimen .6(B)).

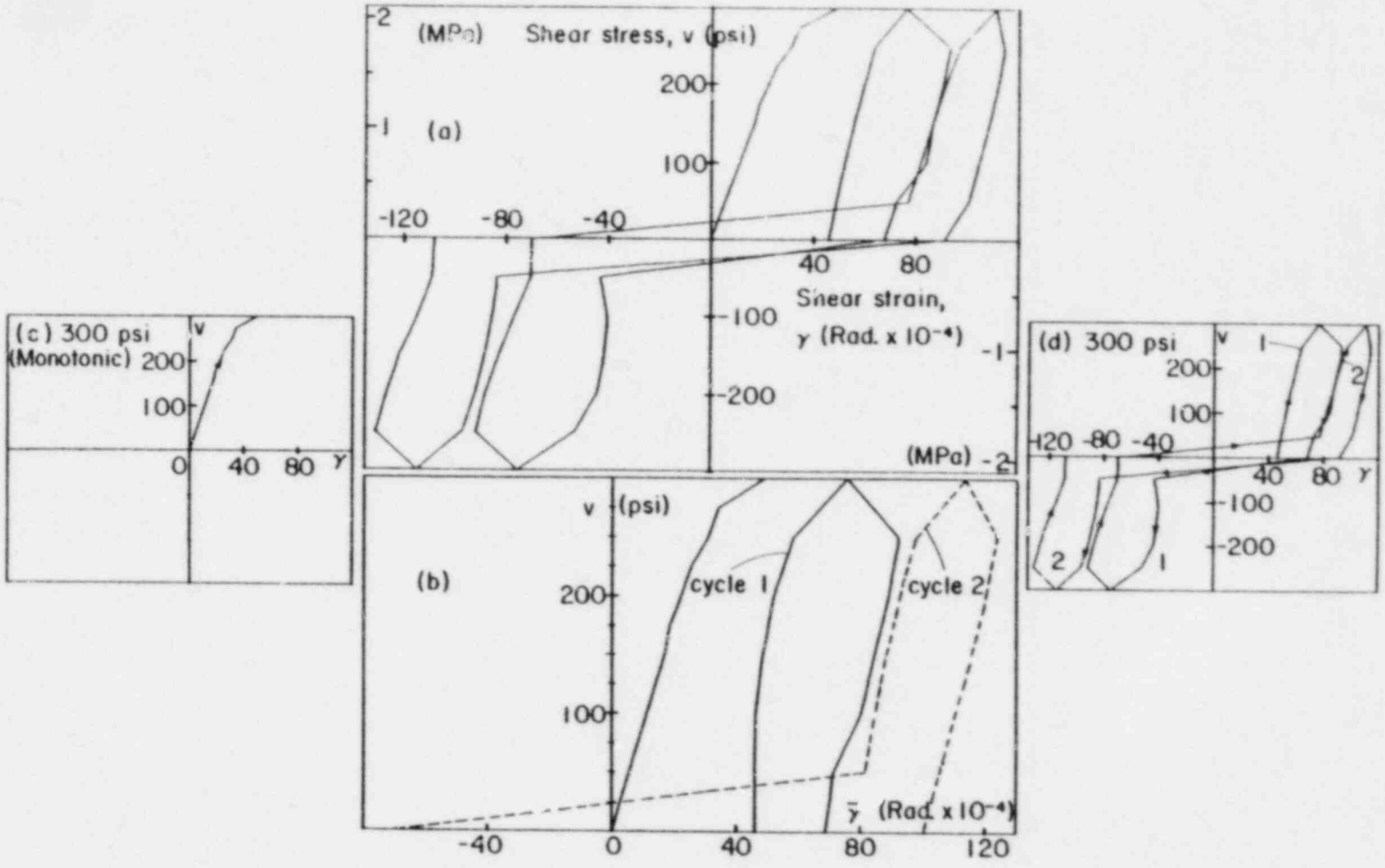

Fig. 2.55. Shear stress-strain hysteresis loops (specimen .6(C)).

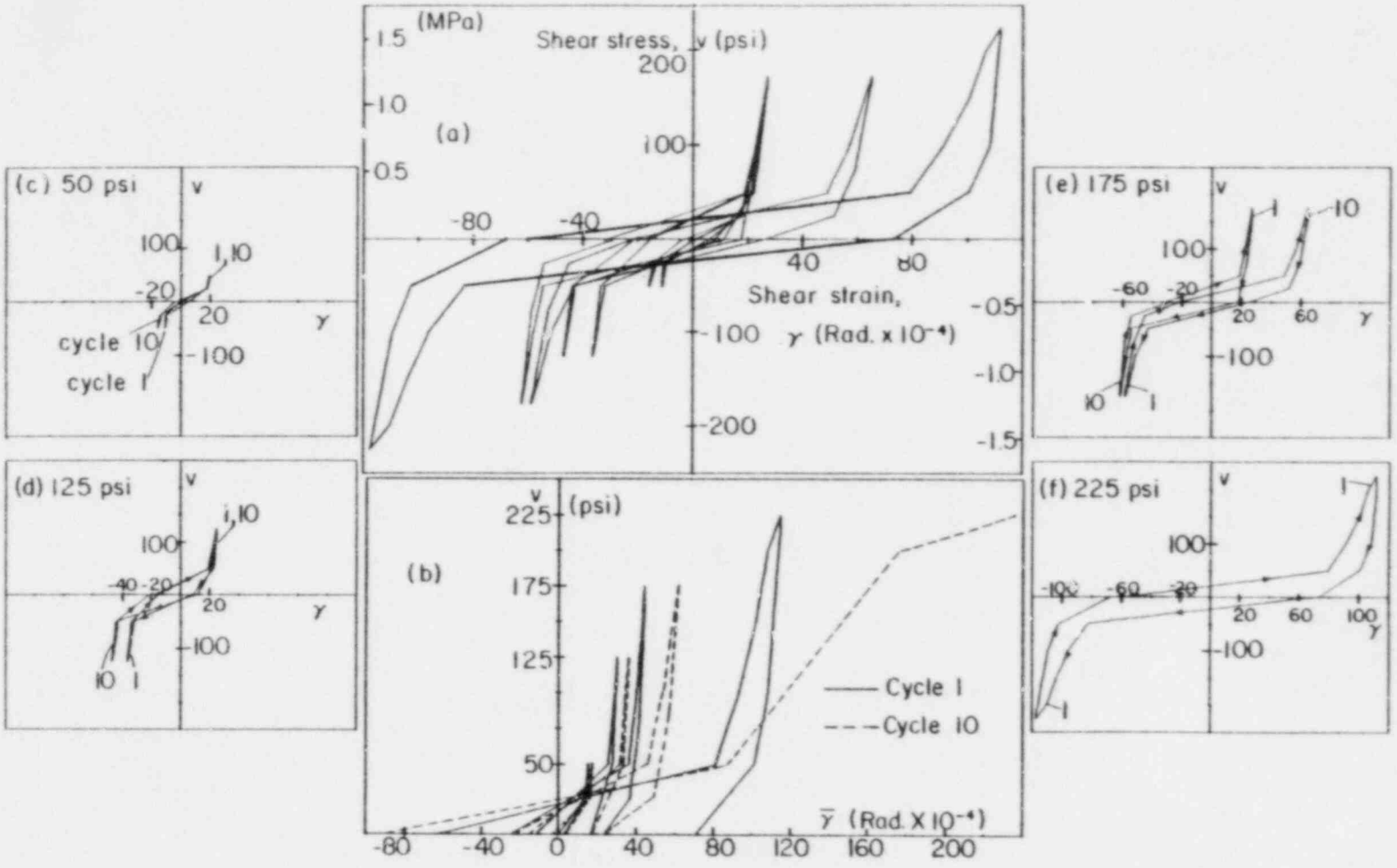

Fig. 2.56. Shear stress-strain hysteresis loops (specimen .9(A)).

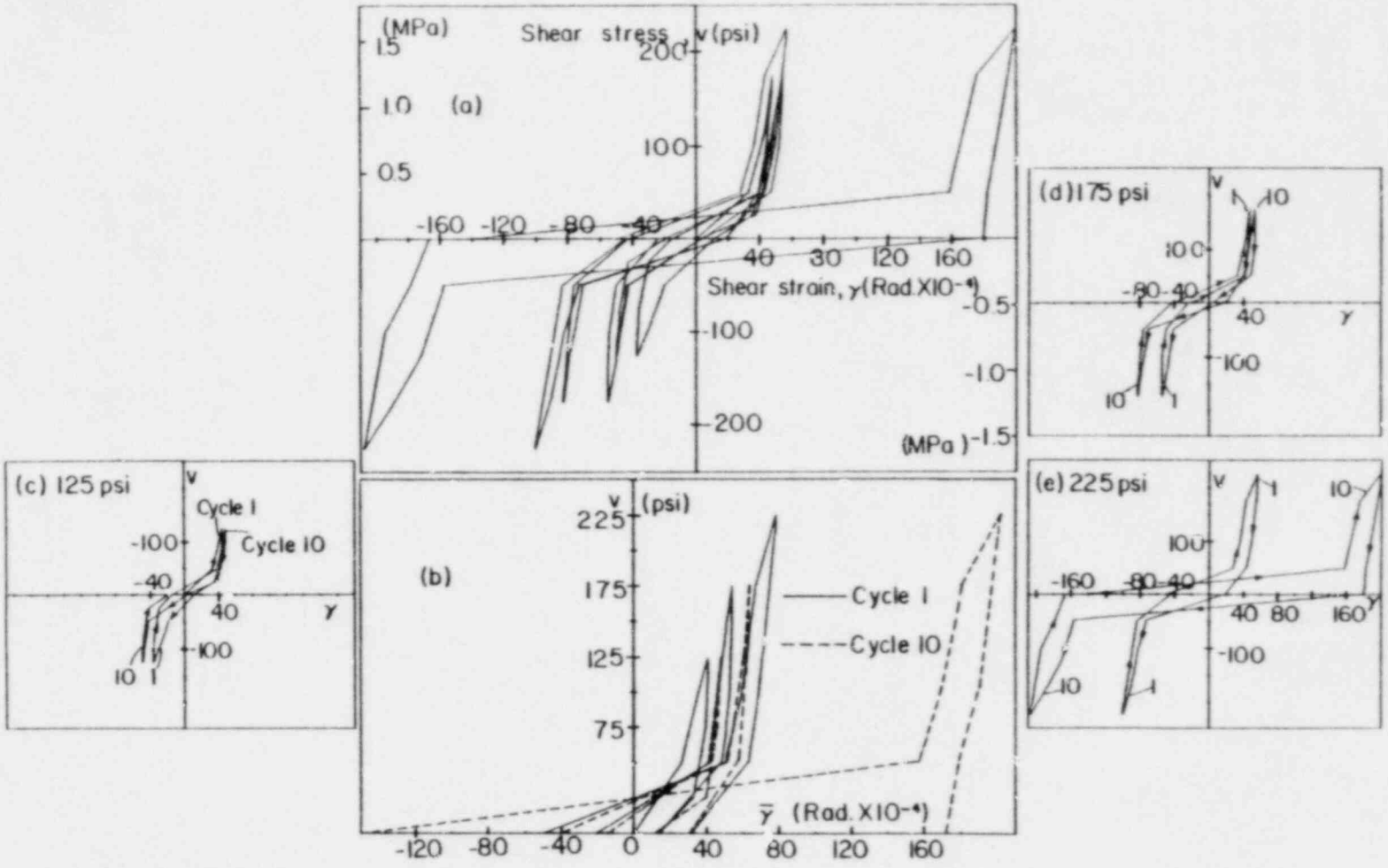

Fig. 2.57. Shear stress-strain hysteresis loops (specimen .9(B)).

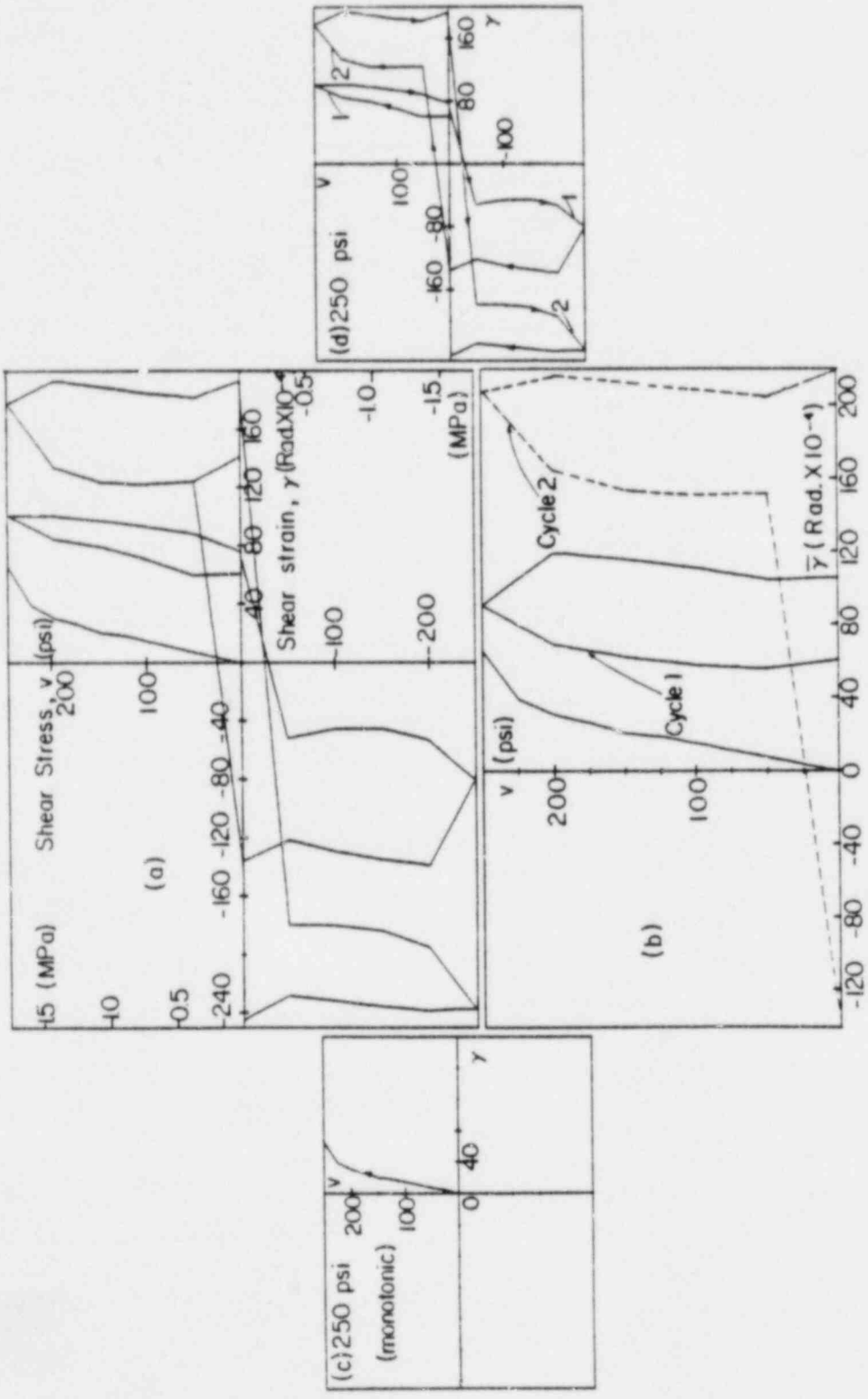

Fig. 2.58. Shear stress-strain hysteresis loops (specimen .9'C)).

used to illustrate the above behavior. The actual changes in shear strain γ versus the applied shear stress v in both positive and negative directions at all selected peak stress levels (1st and 10th cycle) are given in part (a) of each figure. In part (b) only the positive portions of the hysteresis loops are shown in terms of the calculated average shear strain $\bar{\gamma}$ in the positive and negative loading directions. The 1st cycle is indicated by solid lines and the 10th cycle by dashed lines. For further clarity the loops at each peak shear stress level (±125 psi, ±175 psi, etc.) are drawn separately in parts (c), (d) etc. These figures show the effects of axial tension, cycling and shear on the overall shear stiffness. The response changes drastically upon unloading or loading in the opposite direction, exhibiting hysteretic properties. Significant values of residual distortion were recorded at zero shear stress. For a peak shear stress of ±175 psi, average permanent distortions of about 0.0003, 0.0015, 0.0020 and 0.0020 radians were measured at zero external load after 10 cycles of fully reversing shear in specimens .0(A), .3(A), .6(A), and .9(A), respectively.

Duplicate specimens .0(B), .3(B), .6(B) and .9(B) experienced similar residual deformations. For the same Series A specimens and peak shear of ±175 psi the maximum average diagonal deformations measured at the central 2 ft. square region had values of 0.014, 0.028, 0.068 and 0.076 inches (0.36, 0.71, 1.73 and 1.93 mm) at the end of the 1st cycle and 0.017, 0.035 0.077 and 0.106 inches (0.43, 0.89, 1.96 and 2.69 mm) at the end of the 10th cycle at biaxial tension levels of 0, $0.3f_y$, $0.6f_y$ and $0.9f_y$, respectively. These values correspond to effective secant shear modulus G_{cr} values of 0.140, 0.070, 0.029 and 0.026 times the uncracked shear modulus

of concrete G_o (=1500 ksi or 10350 MPa) at the 1st cycle and 0.120, 0.060, 0.026 and 0.019 G_o at the 10th cycle. Increase of biaxial tension from 0 to $0.9f_y$ caused about 79% loss in shear stiffness at the 1st load cycle. Reversed loading of 10 cycles resulted in approximately 12 to 27% further stiffness degradation relative to the 1st load cycle at 0 to $0.9f_y$ axial tension, respectively. The average shear deformations ($\overline{\Delta}d$ in inches and $\overline{\gamma}$ in radians) together with the calculated shear modulus G_{cr} in terms of the ratio G_{cr}/G_o at each prespecified applied peak shear stress for the cyclically loaded specimens in Series A and B are given in Table 2.F (only cycles 1 and 10 are shown). Very similar response is observed for the above duplicate specimen Series A and B at each biaxial tension level (see also Figs. 2.47 to 2.57).

Specimens in Series C, cycled at higher peak shear loads, revealed a more severe degrading influence of the number of cycles. Relatively wide hysteresis loops with large permanent deformations, as shown in Fig. 2.49 for .0(C), Fig. 2.53 for .3(C), Fig. 2.55 for .6(C) and Fig. 2.58 for .9(C), demonstrate the above observation. Thus, the influence of the value of the maximum shear stress applied during cycling is enhanced as this value approaches the ultimate strength v_u under monotonic loading. In this group, .9(C) gave unreliable results due to a malfunction of the instrumentation setup at the beginning of the test.

One characteristic of the shear stress-strain curves for all cyclically loaded specimens is the very low stiffness observed at shear stresses less than about 50 psi (0.34 MPa). For higher values of shear stress a hardening effect was evidenced with a sudden increase in stiffness, as the concrete surfaces along each crack come into bearing contact and the

Table 2.F. Average diagonal deformation $\overline{\Delta d}$ and effective secant cracked shear modulus G_{cr} for the cyclically loaded specimens in Series A and B (cycle 1 and 10).

Peak Shear Stress v(psi)	.0(A) Cycle 1 $\overline{\Delta d}$ (1)	$\overline{\gamma}$ (2)	$\frac{G_{cr}}{G_o}$ (3)	.0(A) Cycle 10 $\overline{\Delta d}$	$\overline{\gamma}$	$\frac{G_{cr}}{G_o}$	.0(B) Cycle 1 $\overline{\Delta d}$	$\overline{\gamma}$	$\frac{G_{cr}}{G_o}$	.0(B) Cycle 10 $\overline{\Delta d}$	$\overline{\gamma}$	$\frac{G_{cr}}{G_o}$
BIAXIAL TENSION: $f_s = 0$												
±125	0.011	6.2	0.13	0.012	7.2	0.12	0.020	11.8	0.07	0.022	12.7	0.07
±175	0.014	8.2	0.14	0.017	10.0	0.12	0.023	13.7	0.08	0.026	15.5	0.08
±225	0.020	12.0	0.12	0.024	13.6	0.11	0.028	16.5	0.09	0.030	17.4	0.09
±275	0.029	17.4	0.10	0.032	19.0	0.10	0.033	19.5	0.09	0.034	20.2	0.09
±325	0.039	23.0	0.09	0.042	24.8	0.09	0.039	22.9	0.10	0.042	24.5	0.09
±375	0.051	29.8	0.08	0.068	40.2	0.06	0.049	28.8	0.09	-	-	-
BIAXIAL TENSION: $f_s = 0.3f_y$												
v(psi)	.3(A)						.3(B)					
±125	0.022	12.4	0.07	0.025	14.7	0.06	0.020	11.6	0.07	0.026	15.2	0.05
±175	0.028	16.8	0.07	0.035	20.7	0.06	0.032	18.8	0.06	0.036	21.2	0.06
±225	0.040	23.2	0.06	0.046	26.6	0.06	0.041	24.2	0.06	0.042	24.9	0.06
±275	0.051	29.8	0.06	0.058	34.4	0.05	0.046	27.2	0.07	0.044	26.3	0.07
±325	0.064	38.0	0.06	0.070	41.4	0.05	0.050	29.6	0.07	0.056	33.0	0.07
±375	0.076	44.6	0.06	-	-	-	0.066	38.7	0.06	-	-	-
BIAXIAL TENSION: $f_s = 0.6f_y$												
v(psi)	.6(A)						.6(B)					
±125	0.051	29.9	0.03	0.050	29.3	0.03	0.038	22.6	0.04	0.054	31.5	0.03
±175	0.068	39.8	0.03	0.077	45.2	0.03	0.059	34.8	0.03	0.072	42.6	0.03
±225	0.086	50.4	0.03	0.100	58.4	0.03	0.079	46.6	0.03	0.094	55.0	0.03
±275	0.109	64.3	0.03	0.153	89.9	0.02	0.104	61.8	0.03	-	-	-
BIAXIAL TENSION: $f_s = 0.9f_y$												
v(psi)	.9(A)						.9(B)					
±125	0.052	30.8	0.03	0.061	35.9	0.02	0.070	41.2	0.02	0.084	49.5	0.02
±175	0.076	44.8	0.03	0.106	62.2	0.02	0.093	55.0	0.02	0.112	65.8	0.02
±225	0.195	114.7	0.01	-	-	-	0.134	79.1	0.02	0.345	203.6	0.01

(Continued)

Table 2.F. (Continued)

Notes:

(1) $\overline{\Delta d}$ = average peak diagonal deformation in the positive and negative shear loading direction (in).

(2) $\overline{\gamma}$ = average peak shear distortion in the positive and negative shear loading direction (rad. x 10^{-4}).

(3) $\frac{G_{cr}}{G_o}$ = ratio of the effective shear modulus of cracked concrete to that of uncracked concrete (G_o = 1500 ksi).

interface shear transfer mechanism is mobilized. A diagonal tension-compression strut type of shear transfer mechanism gradually develops as diagonal cracks form at an angle of about 45 degrees to the x direction. Further discussion on the behavior and the effect of combined inplane biaxial tension and cyclic shear to the shear stiffness of reinforced concrete panels is given in Section 2.7.

All maximum values for the average diagonal deformation Δd of the cyclically loaded specimens at the 1st, 2nd, and 10th cycle at selected maximum shear stress levels are given in Table A.1 (Appendix A).

d) Ultimate strength

The failure loads for all cyclically loaded specimens are given in Table 2.G. Failure in these specimens also occurred near a corner due to yielding of the steel (see Figs. 2.14a (1,2,3) to 2.14d (1,2,3) for crack patterns at failure).

Specimens .0(A) and .0(B) reached an ultimate strength of 425 psi (2.93 MPa). This is 60 psi less than the 485 psi carried by the companion specimen .0(M, subjected to monotonic shear. Specimen .0(C) failed at an intermediate shear stress of 475 psi (3.28 MPa) during the 1st cycle.

Table 2.G. Ultimate strength for cyclic shear (specimen Series A, B and C).

Specimen No.	$\frac{f_s}{f_y}$	v_u (psi)
.0(A)		425
.0(B)	0	425
.0(C)		475
.3(A)		375
.3(B)	0.3	375
.3(C)		400
.6(A)		325
.6(B)	0.6	275
.6(C)		300
.9(A)		225
.9(B)	0.9	275
.9(C)		250

By increasing the biaxial tension to $0.3f_y$ in specimens .3(A) and .3(B), the ultimate strength decreased to a value of 375 psi (2.59 MPa) in the 4th and 6th cycle, respectively. Specimen .3(C) withstood a shear stress of 400 psi (2.76 MPa) and failed in the 1st cycle.

Specimens .6(A) and .6(B) failed at 325 and 275 psi (2.59 and 1.90 MPa) shear stress in the 1st and 10th cycle, respectively. The relatively large discrepancy of 50 psi is at least partially due to the loading procedure followed, since a 50 psi increment in peak shear stress after every 10 cycles was set for all tests. Thus, in specimen .6(A) the shear stress was raised from 275 psi to 325 psi. The average value of 300 psi (2.07 MPa) is a good estimate of the shear capacity at the $0.6f_y$ biaxial tension level. That level of shear stress was the shear capacity for specimen .6(C) that occurred at the 4th cycle.

Specimens .9(A) and .9(B) withstood an applied shear stress of 225 psi (1.55 MPa) at the 8th cycle and 275 psi (1.90 MPa) at the 1st cycle. Again here the average value of 250 psi (1.72 MPa) was assumed as the ultimate strength of the previous specimens. Failure in specimen .9(C) occurred at 250 psi shear, after 4 cycles of loading.

The ultimate shear stress v_u and the shear stress parameter $v_u/\sqrt{f_c'}$ for specimens under cyclic shear (Series A and B) are plotted versus the applied tension stress ratio f_s/f_y in Figs. 2.19a and 2.19b, respectively. The linear best-fit curve of the data is given by the following expressions

$$v_u = (7.4 - 3.7\ f_s/f_y)\sqrt{f_c'} \qquad \text{(psi)} \qquad (2.4a)$$

or

$$v_u = 428 - 200\ f_s/f_y \qquad \text{(psi)} \qquad (2.4b)$$

where v_u, f_s, f_y and f_c' are in psi. A correlation coefficient of 0.96 was obtained for the above Eqn. 2.4 showing that the assumption of linear variation of the ultimate strength with the changing biaxial tension is valid.

The data from specimens in Series C are also plotted in Fig. 2.19a. The best-fit straight line is

$$v_u = 472 - 258\ f_s/f_y \qquad \text{(psi)} \qquad (2.5)$$

This line is located between the other two lines (Eqns. 2.3 and 2.4) for cyclic and monotonic shear and closer to the former one for applied tension higher than $0.6f_y$, as expected.

2.7 Discussion of Experimental Results

The general response and the observations related to the crack formation, the shear stiffness and the ultimate strength of the precracked reinforced concrete flat slabs subjected to combined biaxial tension and shear are presented and discussed in this section.

2.7.1 Cracking patterns

All specimens were initially cracked by applying a tensile stress of $0.6f_y$ (36 ksi) in the two-way reinforcement. The specimens exhibited similar orthogonal cracking approximately perpendicular to each set of transverse reinforcing bars. No additional major tensile cracking was observed above the $0.6f_y$ tension level.

In general, the primary orthogonal cracks normal to the double layer were more closely spaced and with smaller surface crack openings than those normal to the single layer direction, resulting in more cracks in the former case. These primary cracks extended through the thickness of the specimen, but they did not always extend across the entire 48 inch width.

Horizontal and vertical splitting cracks were also visible on the surface of the sides of the slab between most of the rebars in the single and the double layer, respectively, at the tensile stress of $0.6f_y$, as shown in Fig. 2.59(a,b). At higher tensile loads there was a tendency to have some horizontal splitting cracks also forming on the sides normal to the double bars connecting the already existing vertical splitting cracks (see Fig. 2.59b). It is not known how far these splitting cracks

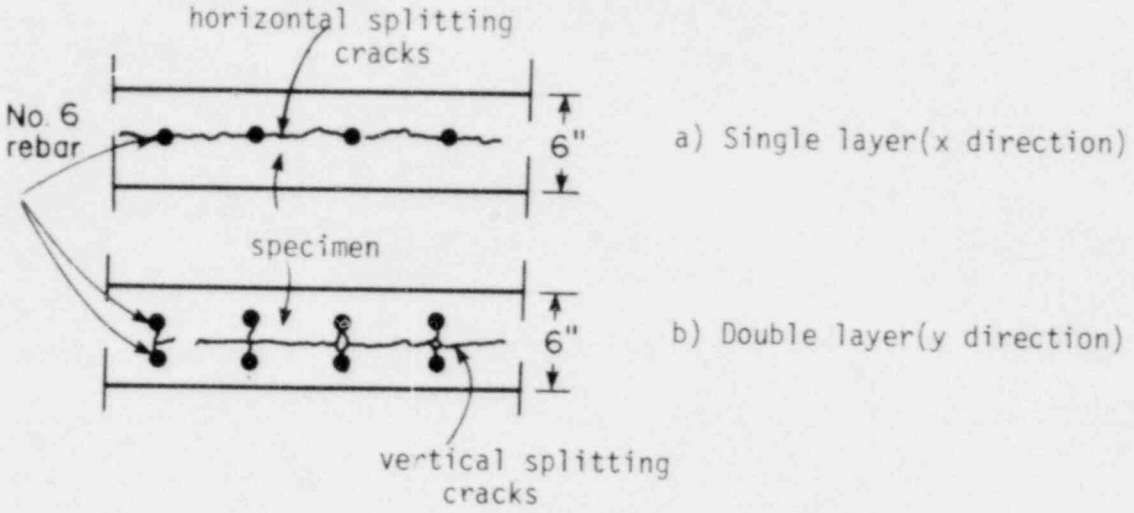

Fig. 2.59. Splitting cracks due to biaxial tension (part of the specimen is shown.

penetrated through the specimen. Under the subsequent shear loading (especially the cyclic loading) propagation of these cracks probably occurred inside the specimen due to the dowel and bond forces, thus causing further deterioration and loss of the overall shear stiffness. At that stage, essentially complete horizontal splitting was observed on the surface of all four sides of the 6 inch thick central portion of the specimen. However, in the tests described, these splitting cracks did not seem to be the primary cause of failure. Splitting cracks in the single layer of rebars in specimens subjected to various biaxial tension levels are shown in Fig. 2.60(a,b,c,d).

Upon shear loading, diagonal cracking inclined at about 45 degrees to the reinforcement formed in the central region of the specimens at shear stresses as low as 75 psi (0.52 MPa), as mentioned in Section 2.6. A discussion concerning the diagonal cracking initiation based on experimental

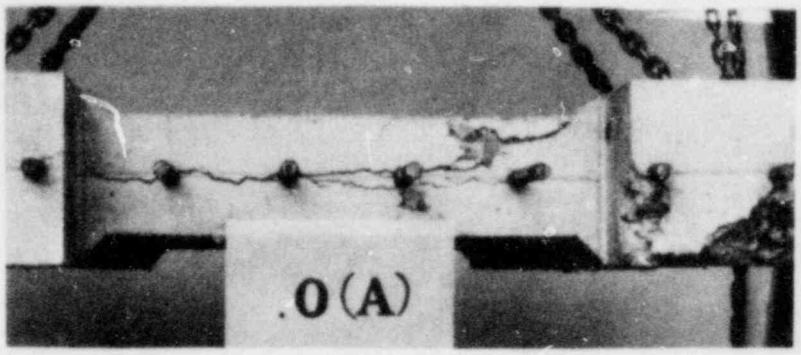

(a)

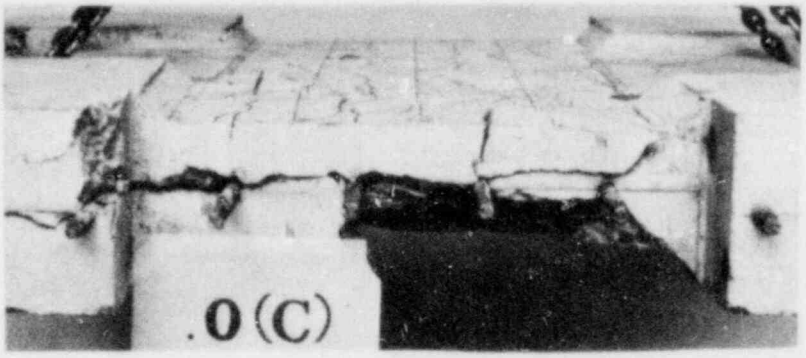

(b)

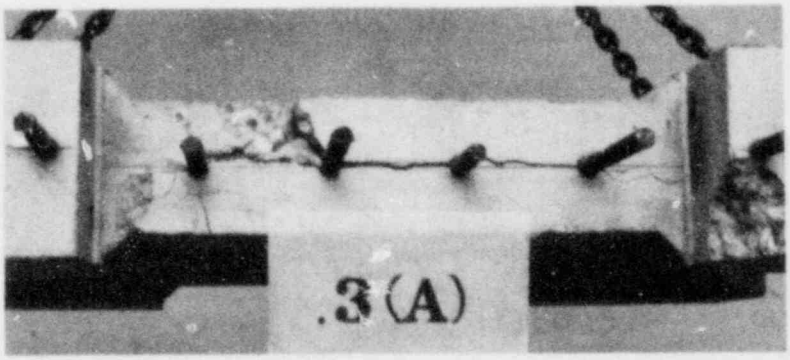

(c)

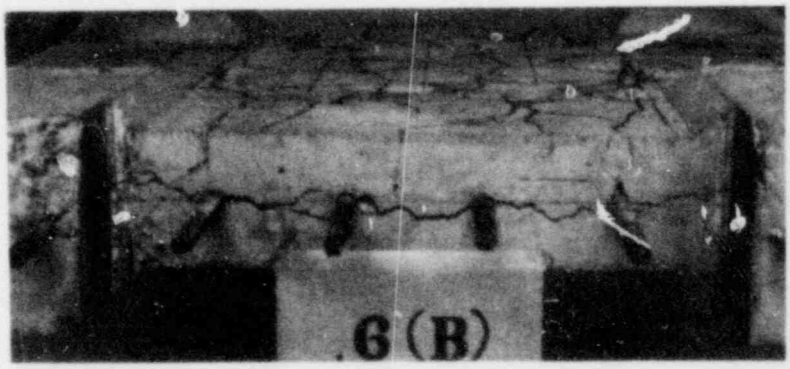

(d)

Fig. 60. Splitting cracks on the side of the specimens.

and analytical evidence is given in Section 4.3.2a (see Fig. 4.53). The main reason for these low shear stress levels at first diagonal cracking is believed to be the effect of bond stresses transferred from the steel to the blocks of concrete between the orthogonal cracks. These forces caused additional shear stresses due to bond that were superimposed on the existing shear stresses due to the externally applied shear loads, and together with the presence of internal cracking at the steel-concrete interface, resulted in the aforementioned diagonal cracking. The fact that the first diagonal cracks formed near an intersection of the orthogonal bars supports the above argument.

Shear cycling was found to produce significant additional diagonal cracking at the same peak shear stress. A portion of the cracked specimen subjected to a shear stress v (only the positive direction is shown) and a tensile stress σ_s in the bars is shown in Fig. 2.61. The orthogonal cracks approximately follow the reinforcing bars. The diagonal cracks will most probably form near the corners of the uncracked regions of concrete between the bars at the 1st load cycle, as shown in Fig. 2.61. Redistribution of stresses will take place during the later cycles of shear due to diagonal cracking. As the tensile principal stresses in the concrete σ_1 increase at stiffer regions of concrete farther from the primary orthogonal cracks and between the initially formed diagonal cracks, the tensile strength of concrete f_t' can be reached again and new diagonal cracks can form (see Fig. 2.61). Similar behavior is expected when the shear is applied in the opposite direction (negative) with diagonal cracks forming nearly at right angles to those shown in the above figure. Also, reversing cycling tends to further close the orthogonal cracks (see Figs.

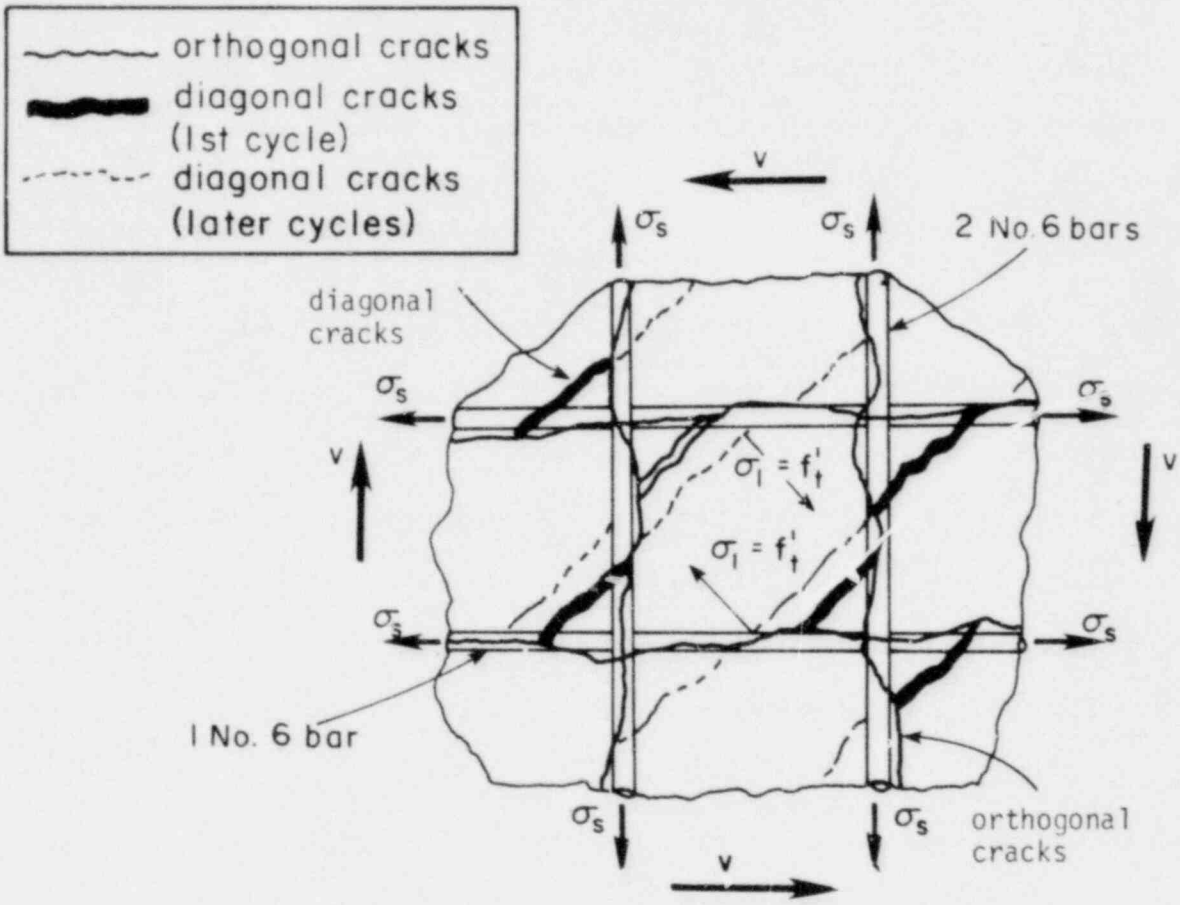

Fig. 2.61. Diagonal cracking during cycling.

2.26 and 2.33), particularly for shear stresses higher than 125 psi. This can improve the bond at the interface between the steel and the concrete. As a result, the principal tensile stresses in the concrete σ_1 at the immediate vicinity of the bars will also increase. Therefore, it appears that cycling will cause more extensive diagonal cracking than that under monotonic shear at the same peak shear level.

The extensive diagonal cracking due to cycling resulted in further loss of the integrity of concrete as compared to monotonically loaded specimens. As the shear load approached the ultimate level, the inclination

angle of the major diagonal cracks to the x direction increased with decreasing applied tension, remaining at about the same original 45 degree value at a tension of $0.9f_y$ in the rebars.

2.7.2 Shear stiffness

a) Monotonic shear

For the monotonically loaded specimens (Series M) a decrease in secant stiffness and an increase in shear deformations was observed as the tension in the steel increased from 0 to the maximum value of $0.9f_y$. As shown in Fig. 2.18, for shear stresses up to 25 psi (0.17 MPa) a very low shear stiffness was observed.

For comparison, the normalized secant and tangent shear modulus G_{cr} in terms of the shear modulus for uncracked concrete G_o (given in Table 2.H) is plotted versus the shear stress level for all specimens under monotonic shear in Fig. 2.62. Shear stiffness (G_{cr}/G_o) values of 0.056, 0.021, 0.012 and 0.009 were calculated in specimens .0(M), .3(M), .6(M) and .9(M), respectively, at a shear of 25 psi. The degrading incluence of increasing applied tension is evident although it appears to be less significant for tension levels of $0.6f_y$ and higher.

However, the most important finding is that the effective shear modulus G_{cr} is less than 10% of that for uncracked concrete (G_o). For shear stresses higher than 25 psi, there was a distinct increase in the tangent shear stiffness for applied tension ranging from $0.3f_y$ to $0.9f_y$ with the interface shear transfer becoming active as the crack surfaces came into contact. The latter increase, however, does not result in raising the

Table 2.H. Test results of ultimate strength values.

(1) Specimen No.	(2) Applied Rebar Tension	Ultimate Strength v_u(psi)	(3) $\frac{v_u}{\sqrt{f_c'}}$	(4) $\rho f_y - \sigma_N$ (psi)	(5) Failure at Cycle
.0(A)	No Tension	+425	7.8	744	1st
.0(B)		+425	7.3	744	3rd
.0(C)		+475	7.6	744	1st
.0(M)		+485	8.7	744	-
.3(A)	$0.3f_y$	-375	6.3	521	4th
.3(B)		+375	6.0	521	6th
.3(C)		-400	6.6	521	1st
.3(M)		+450	6.6	521	-
.6(A)	$0.6f_y$	+325	5.8	298	1st
.6(B)		-275	4.8	298	10th
.6(C)		+300	4.9	298	7th
.6(M)		+375	6.2	298	-
.9(A)	$0.9f_y$	+225	3.8	75	8th
.9(B)		-275	4.6	75	1st
.9(C)		+250	4.3	75	4th
.9(M)		+300	5.0	75	-

(1) (A) or (B): CYCLIC (10 cycles at each shear stress level; start at 125 psi and continue at 50 psi increments).

(C) : CYCLIC (monotonic loading up to the average failure load of (A) and (B); if no failure occurs continue cycling).

(M) : MONOTONIC (monotonic loading up to failure).

(2) Rebar tension of 0, $0.3f_y$, $0.6f_y$ and $0.9f_y$ is the same in both directions (x and y).

(3) f_c' = average cylinder compressive strength of concrete.

(4) ρ = 0.0122 (weak direction) is used; σ_N = normal tension.

(5) Cycle number is within a group of 10 cycles at the indicated stress level.

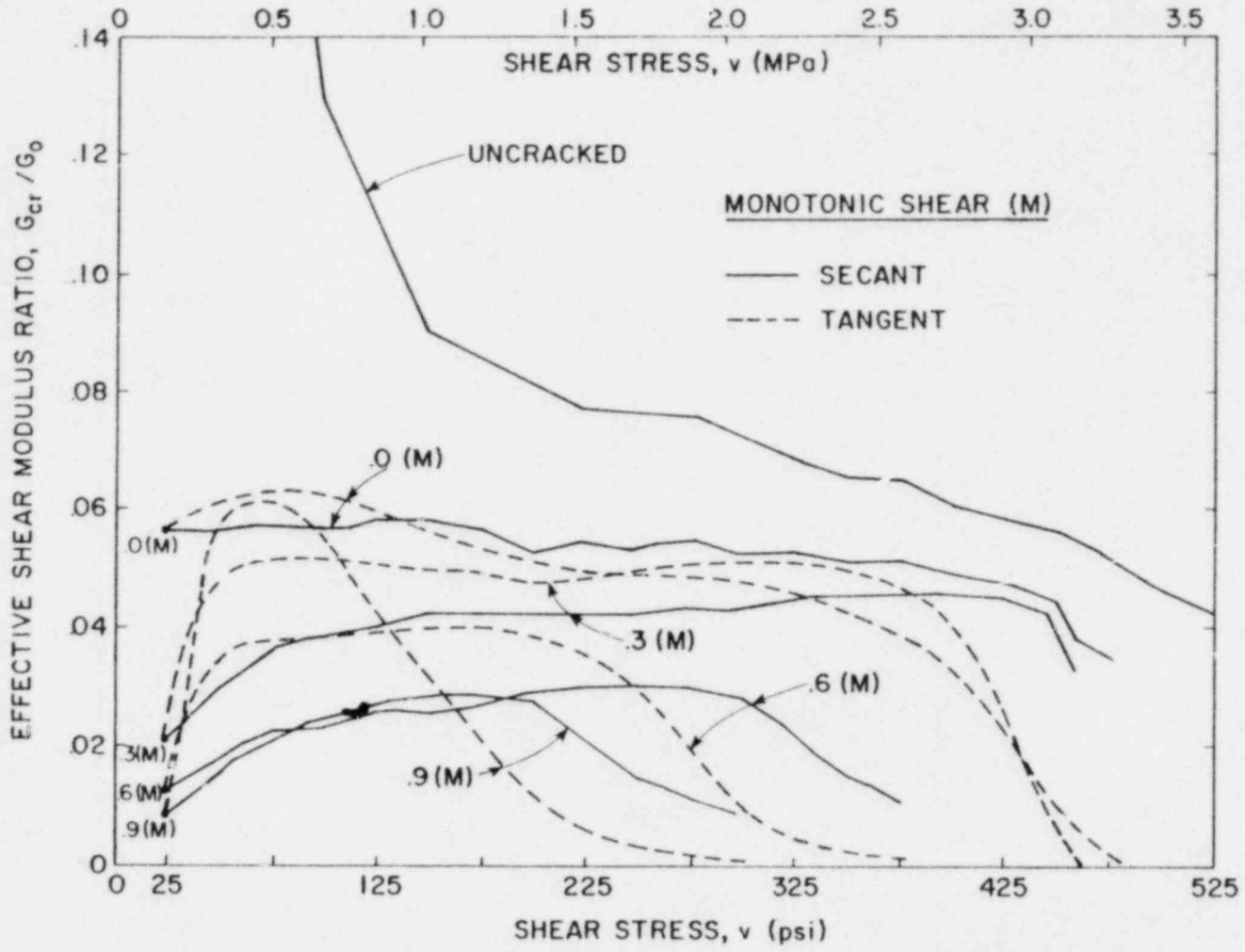

Fig. 2.62. Effective shear modulus G_{cr} versus the applied monotonic shear stress v.

shear modulus G_{cr} above the 0.10 G_o value. For shear stresses between 50 and 125 psi, the effective tangent shear modulus G_{cr} was approximately equal to values ranging from 4 to 6% of G_o for all biaxial tension levels.

To find a more representative value for the shear stiffness under monotonic shear, the data from the shear stress-shear distortion curves for specimens in Series A, B and C at the 1st positive cycle are plotted together with the data from Series M. The combined test results for monotonic shear are shown in Fig. 2.63 (a,b,c,d) for each biaxial tension level. Due to the scatter of the data, the average values of the gross shear distortion at the corresponding shear stress is calculated and shown as full dots in the above figures. Straight lines were fit through these average data points for shear stresses between 25 psi and a stress level up to which an approximately linear response still held for each tension level. These results are summarized in Fig. 2.64. The average values of the effective tangent shear modulus determined for shear stresses higher than 25 psi are tabulated below:

Biaxial Tension	G_{cr}, psi (MPa)	G_{cr}/G_o
0	102000 (704)	0.068
$0.3f_y$	70400 (486)	0.047
$0.6f_y$	83100 (574)	0.055
$0.9f_y$	73700 (508)	0.049

Thus, contrary to the findings at shear stresses less than 25 psi, the response at higher shear stresses is not strongly sensitive to the level of biaxial tension. This shows that the initial crack width does not play a

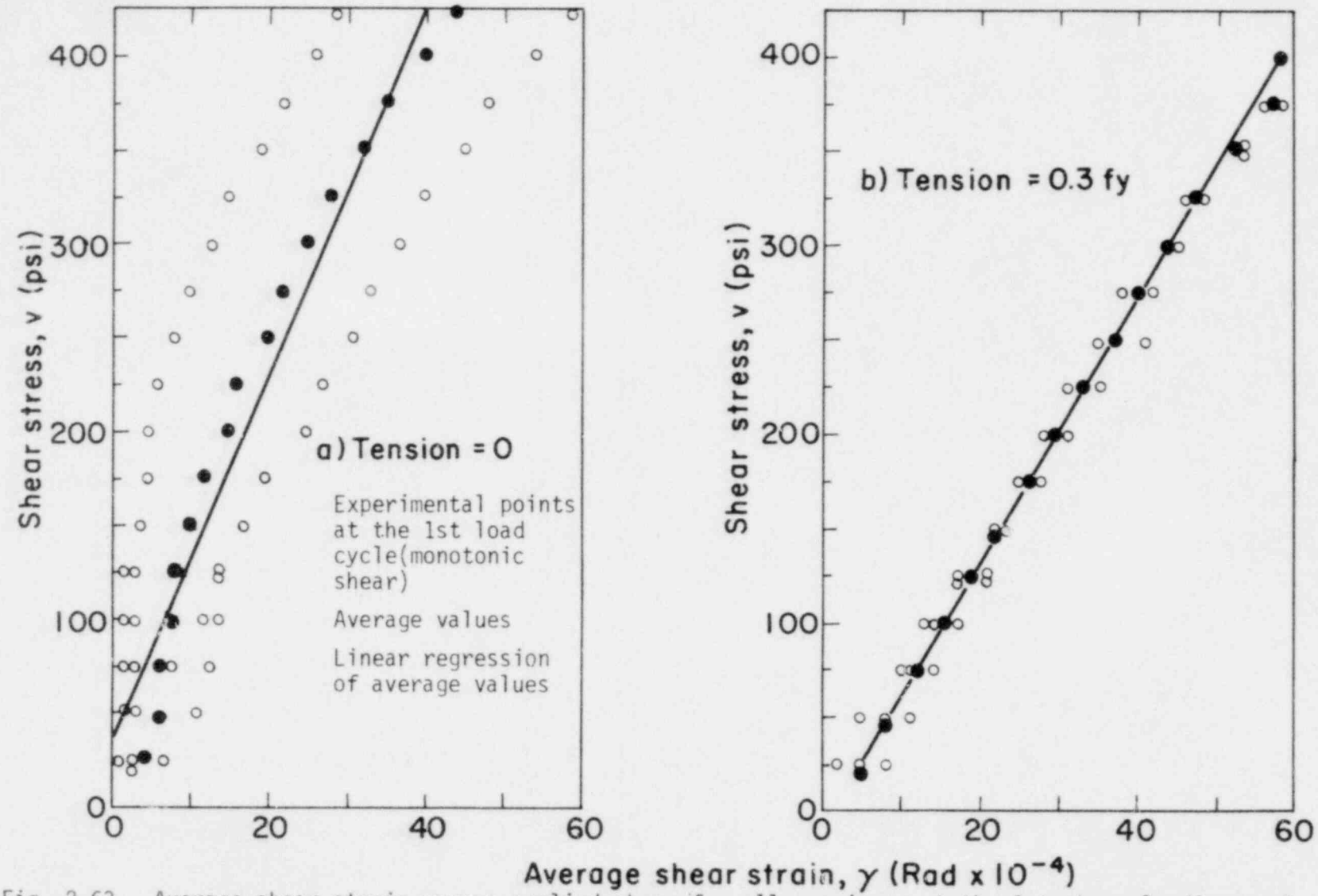

Fig. 2.63. Average shear strain versus applied shear for all specimens at the 1st shear loading cycle.

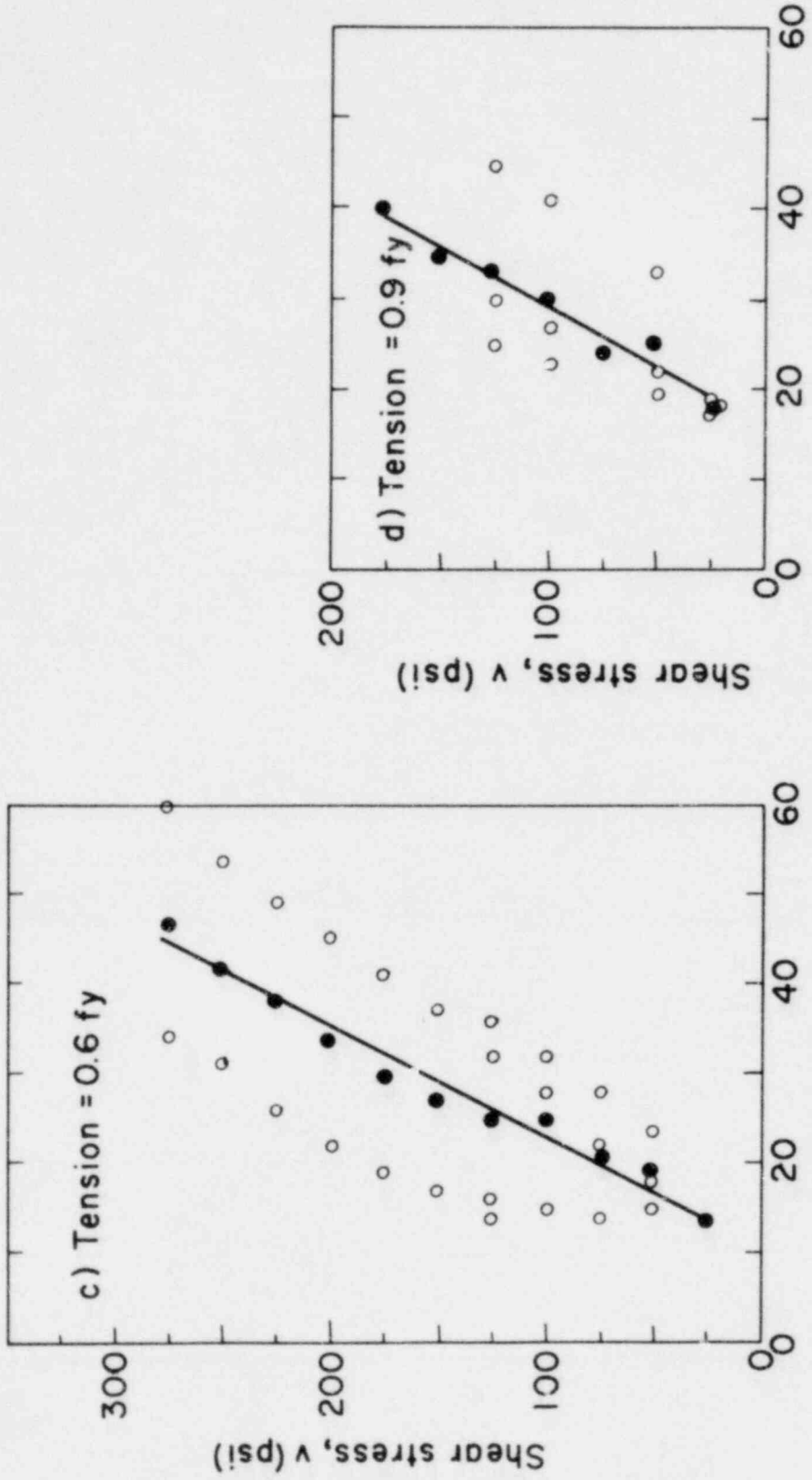

Fig. 2.63. (Continued)

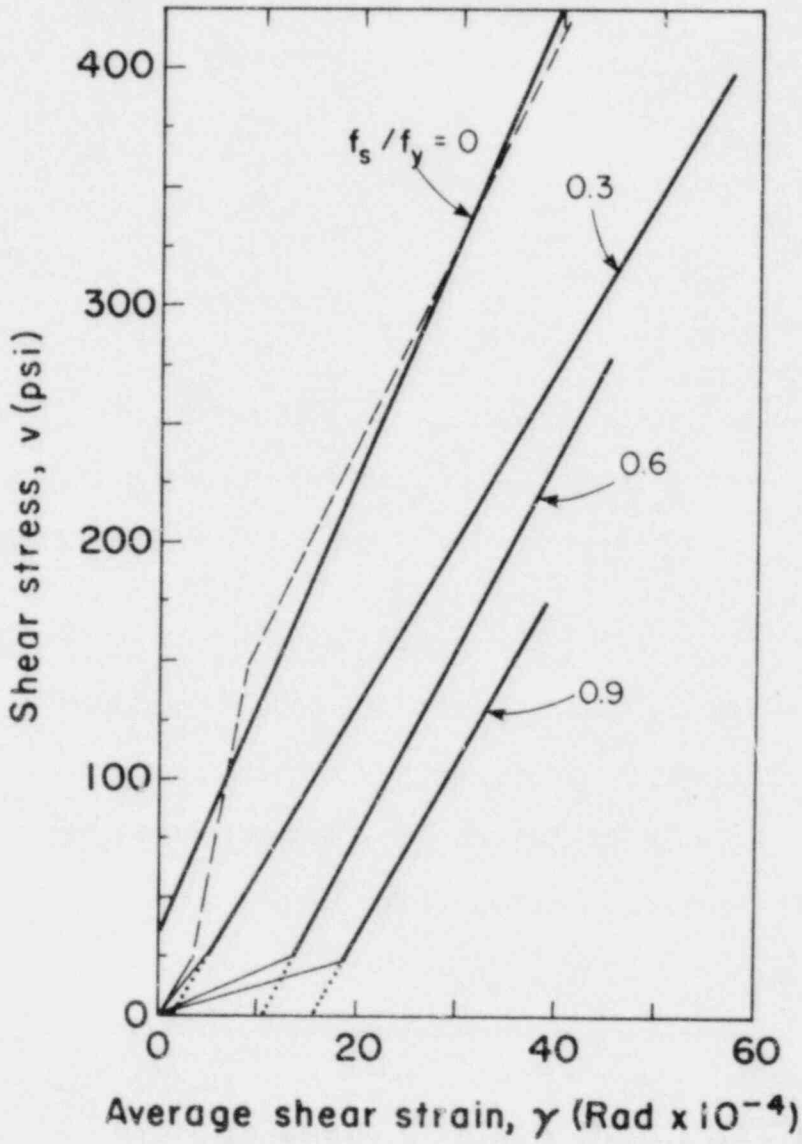

Fig. 2.64. Linear regression curves of the experimental shear stress-shear strain response in the 1st load cycle at selected biaxial tension levels.

significant role in the resulting effective tangent shear modulus, at least for monotonically applied shear higher than 25 psi. On the other hand, the effective secant shear modulus (reflecting the total deformational behavior of the specimen) is decreasing with increasing applied biaxial tension due to the increasing initial shift of the shear stress-shear strain curve at low shear stresses.

b) Cyclic shear

Three distinct stages of behavior may be identified for the hysteresis loops (after several load cycles) for the specimens loaded under fully reversing cyclic shear (Series A, B and C), as shown in Figs. 2.47 to 2.58:

1) Stage I (low stiffness; shear stress less than 50 psi):

Due to the residual crack openings upon unloading, relatively large shear deformations were required to mobilize the shear transfer mechanism at these low shear stresses after several load reversals. This initial softness in shear stiffness appeared to increase with cycling because the residual slips at zero shear stress increased with increasing number of cycles and peak shear stress (see Figs. 2.47 to 2.58). As more concrete crushed around the bar at the crack and the unbonded length of the bar increased with cycling, gains in shear slip and crack width were expected. Consequently, with increasing number of cycles, dowel action became the most important mechanism with the interface shear transfer becoming less active because of the progressive deterioration of the concrete surfaces at the cracks. As the dowel forces increased with cycling they caused additional damage to the bond transfer mechanism because of local crushing

around the bars. As a result, the unbonded length of the bars was increased. With the concrete providing less resistance, the dowel action mechanism became less effective in transferring stresses, and the specimen became more flexible in shear.

Since dowel action was the major shear transfer mechanism at shear stresses less than 50 psi, the total shear tranferred at the cracks would be almost entirely carried by shear forces in the bars. In the weaker reinforcing direction (single layer) of the specimens with ρ_x = 0.0122 a shear stress of 50 psi would cause a shear stress equal to 4.1 ksi per bar. This shear stress is far lower than the shear stress of about 35 ksi ($=f_y/\sqrt{3}$), that is expected to cause yielding in the No.6 bars. Thus, the dowel action mechanism is capable of fully resisting these low shear stresses.

2) Stage II (high stiffness; shear stress higher than 50 psi):

At shear stresses higher than 50 psi a dramatic increase in the tangent shear stiffness occurred because the interface shear transfer mechanism was mobilized as the shear slip resulted in contact of the asperities of both sides of the crack interfaces. This shear stiffness increase was particularly evident for very small initial crack widths, that is, for low applied biaxial tension. At this stage, as the shear stresses increased, the diagonal tension-compression strut mechanism started predominating (at about 100 psi) over a slipping type mechanism. This caused opening of the diagonal cracks normal to the tensile direction, and some closing of the orthogonal cracks due to the compressive stresses in the concrete. The diagonal tension-compression mode is described in Chapter 4 (Section 4.3.2a).

With an increasing number of load cycles and higher peak shear stress the interface shear transfer became less effective, resulting in degradation of the stiffness and a cumulative gain in shear deformations. However, for specimens with bar tension as high as $0.9f_y$, which produced large crack openings, dowel action was the major shear transfer mechanism. A 300 psi shear stress would produce a shear stress of about 25 ksi in each bar of the single layer. This high shear stress plus bending stresses and high tension of $0.9f_y$ could possibly cause yielding in the bars. Part of the dowel shear could be induced by kinking in the bars, as described in Section 4.4.

3) Stage III (unloading from peak shear stress):

Unloading led to some reduction in deformations, but appreciable residual deformations could remain at zero shear stress because of the interlocking of the asperities along the crack surfaces and the wedging action of concrete at the surface of the reinforcement. The tangent shear stiffness remained nearly the same as in the loading Stage II.

Regarding the effective shear modulus at shear stresses less than 50 psi (Stage I), a value of about $0.05G_o$ was calculated in the case of zero tension during shearing in the initial load cycles. This value decreased to $0.02G_o$ due to the combined effects of cycling and increasing of the peak shear stress. Although a three-line segment idealization of the hysteresis loops would be more accurate for the positive and negative portion of the curve, a simple bilinear representation is chosen, shown in Fig. 2.65(a,b,c,d) for each specified biaxial tension applied in the No.6 rebars. The stiffer loading portion of the curves in Fig. 2.65a showed a

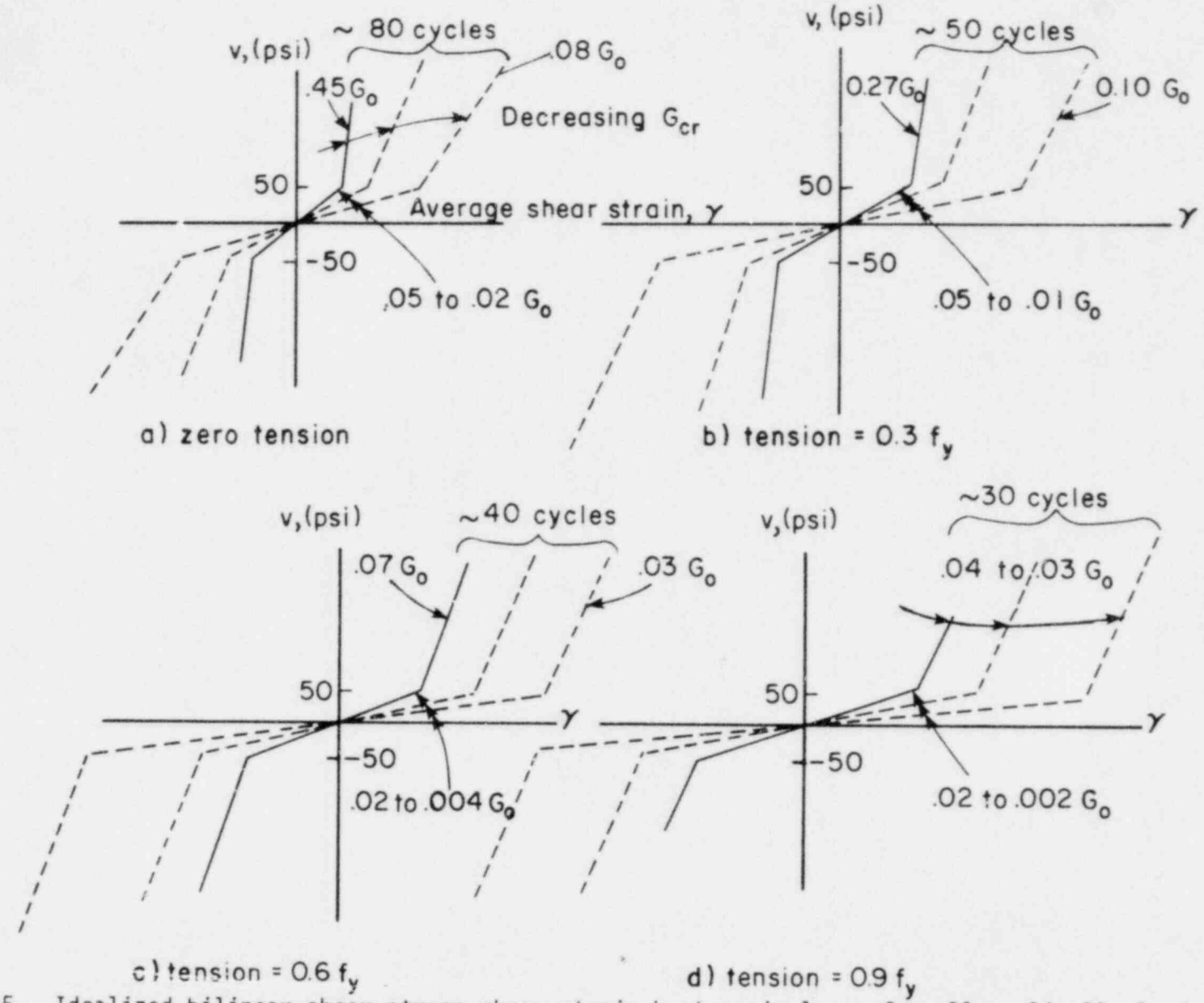

Fig. 2.65. Idealized bilinear shear stress-shear strain hysteresis loops for all cyclically loaded specimens(Series A,B) and effective tangent shear modulus G_{cr} (G_o=1500 ksi).

drastic decrease in the tangent stiffness from about 45% that of uncracked concrete to about 10% as failure was approached after some 80 cycles at selected shear stress levels with zero tension in the bars.

With a $0.9f_y$ applied tension (see Fig. 2.65d) an extremely low initial shear stiffness of about 2% of G_o was measured at shear stresses less than 50 psi. In later cycles this shear rigidity assumed values of less than 1% of G_o. Above the 50 psi shear level the stiffer portion of the response resulted in a tangent shear modulus of about 0.03 to 0.04 G_o. The increase in shear deformations, particularly near failure, was apparent at this high applied biaxial tension level, which produced large crack widths and caused severe degradation of the bond mechanism. The specimens subjected to $0.6f_y$ biaxial tension showed similar behavior to those at $0.9f_y$ (see Fig. 2.65c). In the case of $0.3f_y$ tension (see Fig. 2.65b), the effective tangent shear modulus decreased due to cycling and increasing peak shear stress from 0.05 to 0.01 G_o and 0.27 to 0.10 G_o at low and high shear stresses, respectively.

In general, the shear stiffness degraded with increasing number of fully reversing shear loading cycles causing an increase in shear deformations. The percentage increase of the peak average diagonal deformation $\bar{\Delta}d^{(n)}$ in the specimens at cycle n (relative to the deformation at cycle 1 $\bar{\Delta}d^{(1)}$) as a function of the applied peak shear stress v, is given for different biaxial tension levels in Fig. 2.66(a,b,c,d). After 10 load cycles, at lower shear stress levels for the low tension levels of 0 and $0.3f_y$, there is an increase in deformation of 15 to 20% (see Fig. 2.66(a,b)). At shear stresses higher than 225 psi (1.55 MPa) the increase is about 10%. The increase in deformations, relative to cycle 1 values, at the end of the 2nd cycle at each peak shear stress level is practically constant at

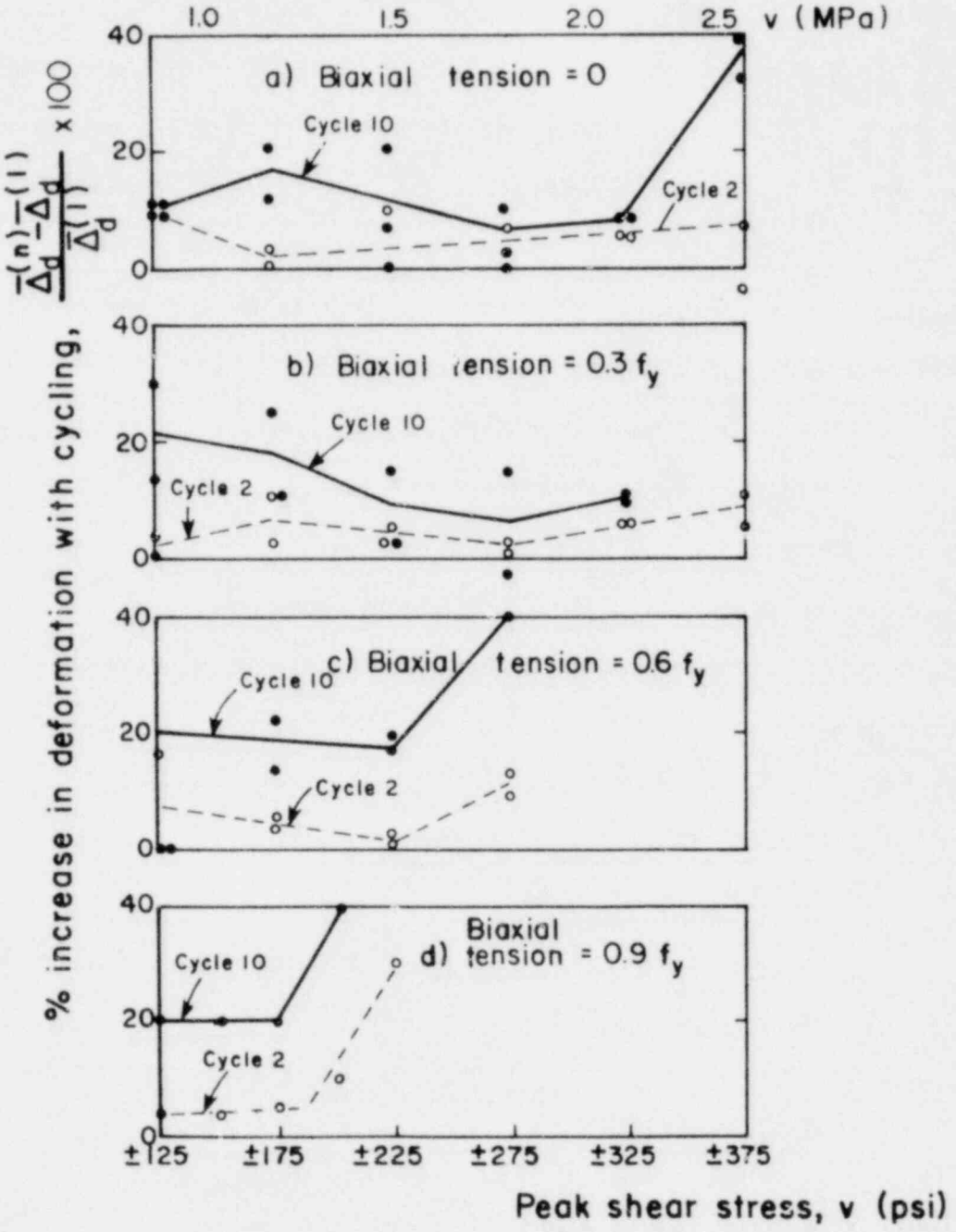

Fig. 2.66. Percent increase in peak average diagonal deformation $\bar{\Delta}d$ after n cycles versus the applied peak shear stress v in specimen Series A and B (No.6 bars).

5%. On the other hand, biaxial tensions of $0.6f_y$ and $0.9f_y$ result in a nearly constant 5% and 20% increase in shear deformations after 2 and 10 cycles of shear load, respectively. As failure is approached, cycling results in higher increases in deformations at all biaxial tension levels. It appears that, independently of the biaxial tension level, reversing cycling at increasing peak shear stress has the same degrading influence regarding the integrity of the specimens after only 2 cycles of shear loading. At a biaxial tension level of 0 or $0.3f_y$, as the number of shear loading cycles is increased to 10, the effect of cycling decreases as the applied peak shear stress increases.

Since the change in shear deformations versus the applied shear stress, shear load cycling, and biaxial tension level is a measure of the effective secant shear modulus G_{cr}, the following average values of G_{cr} at the end of 10 cycles of reversing shear at a particular peak value can be calculated:

$$G_{cr}^{(10)}(\text{secant}) = \frac{G_{cr}^{(1)}}{1.20} = 0.83\, G_{cr}^{(1)}, \text{ for } \frac{f_s}{f_y} \leq 0.6 \text{ and } v < 225 \text{ psi}$$

$$\text{or } \frac{f_s}{f_y} = 0.9 \text{ and } v < 175 \text{ psi} \qquad (2.6a)$$

and

$$G_{cr}^{(10)}(\text{secant}) = \frac{G_{cr}^{(1)}}{1.10} = 0.42\, G_{cr}^{(1)}, \text{ for } \frac{f_s}{f_y} \leq 0.3 \text{ and}$$

$$225 \leq v \leq 325 \text{ psi} \qquad (2.6b)$$

where $G_{cr}^{(i)}$ is the average secant shear modulus at peak shear during the

1st cycle. The secant shear modulus values at selected shear stress levels are given in Table 2.I for all cyclically loaded specimens.

The percentage increase of peak average shear deformations at the 1st cycle of each shear stress level, $\overline{\Delta d}^{(v)}$ (normalized by the peak deformation $\overline{\Delta d}^{(125)}$ at 125 psi shear), in terms of the dimensionless ratio of applied shear stress v to the ultimate strength v_u for all specimens in Series A and B, is given in Fig. 2.67. For ratios of v/v_u less than 0.9, it is possible to have as much as 250% gain in peak shear deformations relative to the maximum deformation at 125 psi shear stress. The amount of the total cumulative gain in deformations, that is the total decrease of the secant shear modulus, increases with decreasing applied tension in the bars and increasing shear stress ratio v/v_u. For v/v_u larger than 0.9, which means that yielding in the bars is imminent, large increases are present creating an extremely soft system, especially for high biaxial tension.

Finally, the shear stress-shear strain curves obtained in the present biaxial tests for monotonic shear are compared with those for cyclic reversing shear in Figs. 2.68(a,b,c,d) at bar tensions ranging from 0 to $0.9f_y$. For the specimens under cyclic shear only the positive portions of the average shear distortion versus shear load curves are shown for selected cycles of loading. In these figures the envelope curve connecting the peaks at the 1st cycle at all shear stress levels is also drawn in dots. It can be said that for all bar tensions and intermediate shear stress levels the curves for monotonic shear are approximately parallel to that envelope. For high tensions of $0.6f_y$ or $0.9f_y$, the monotonic curves follow very closely the path of that envelope (see Figs. 2.68c and 2.68d). However,

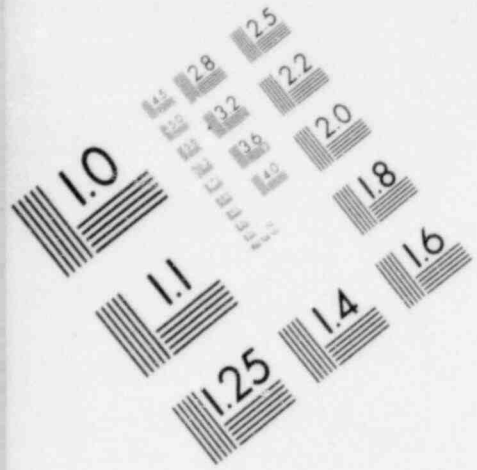

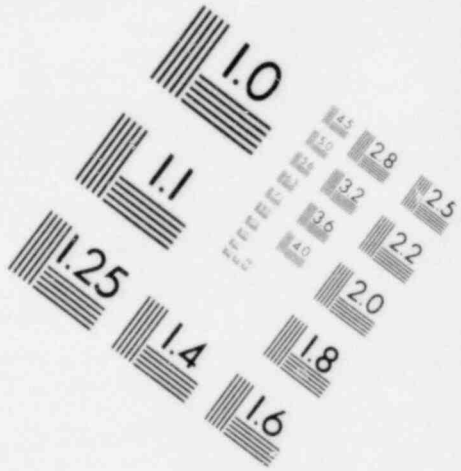

IMAGE EVALUATION TEST TARGET (MT-3)

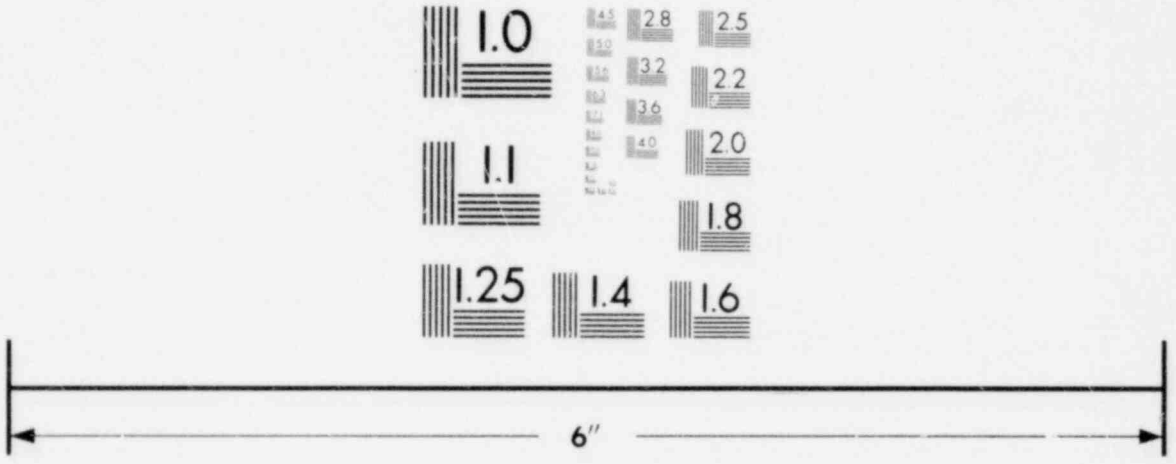

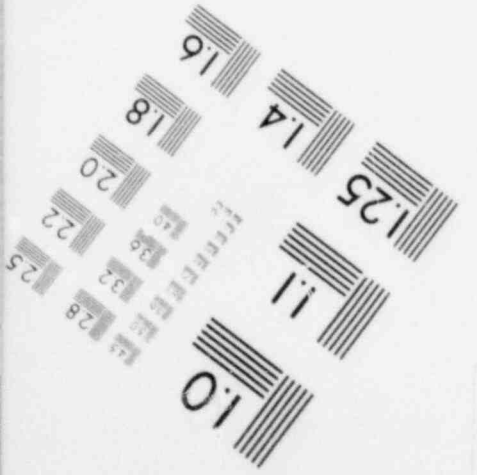

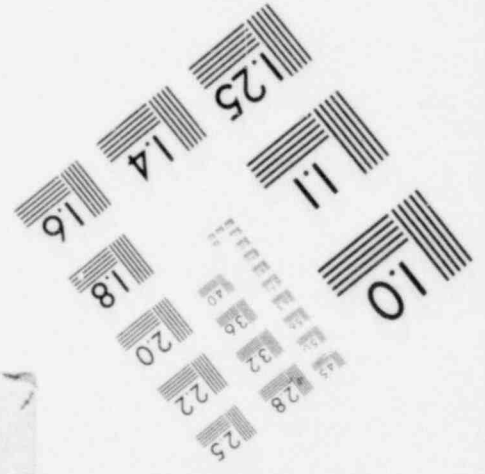

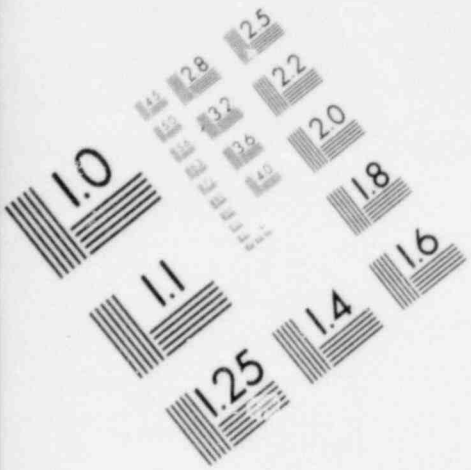

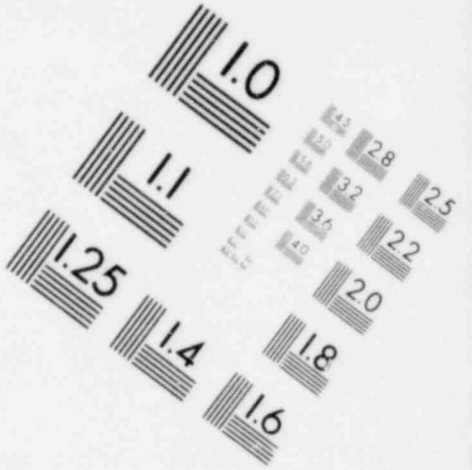

IMAGE EVALUATION TEST TARGET (MT-3)

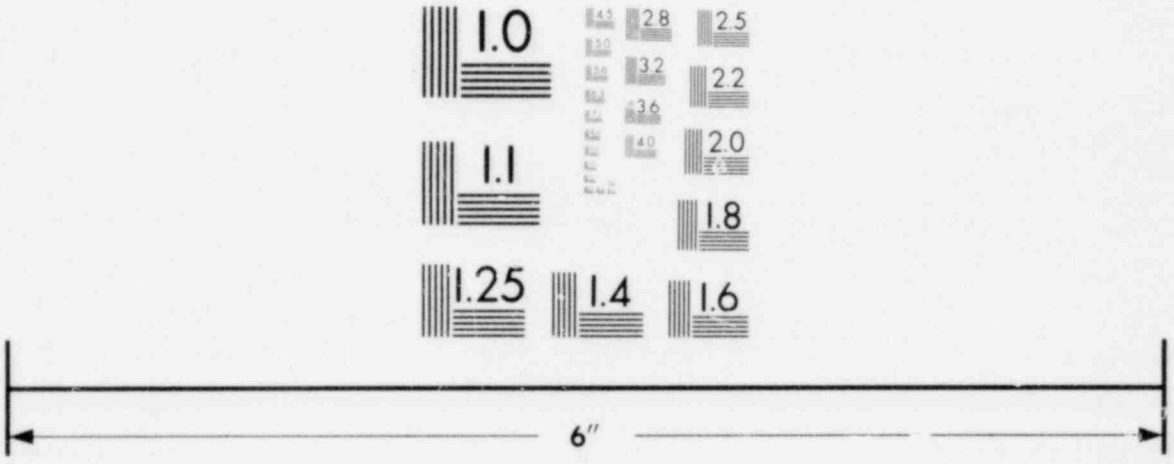

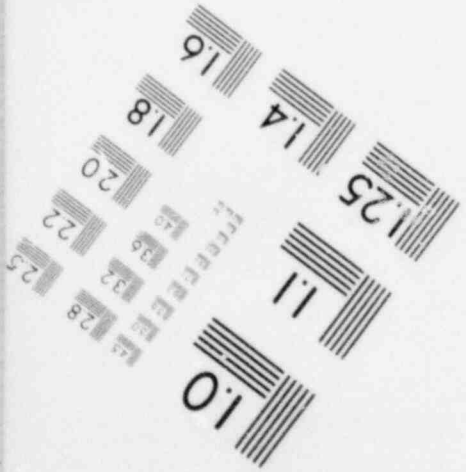

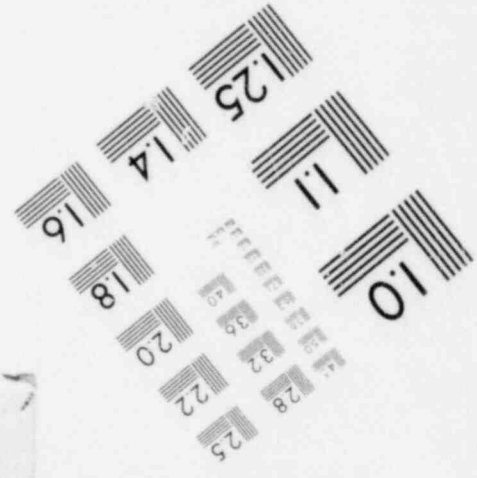

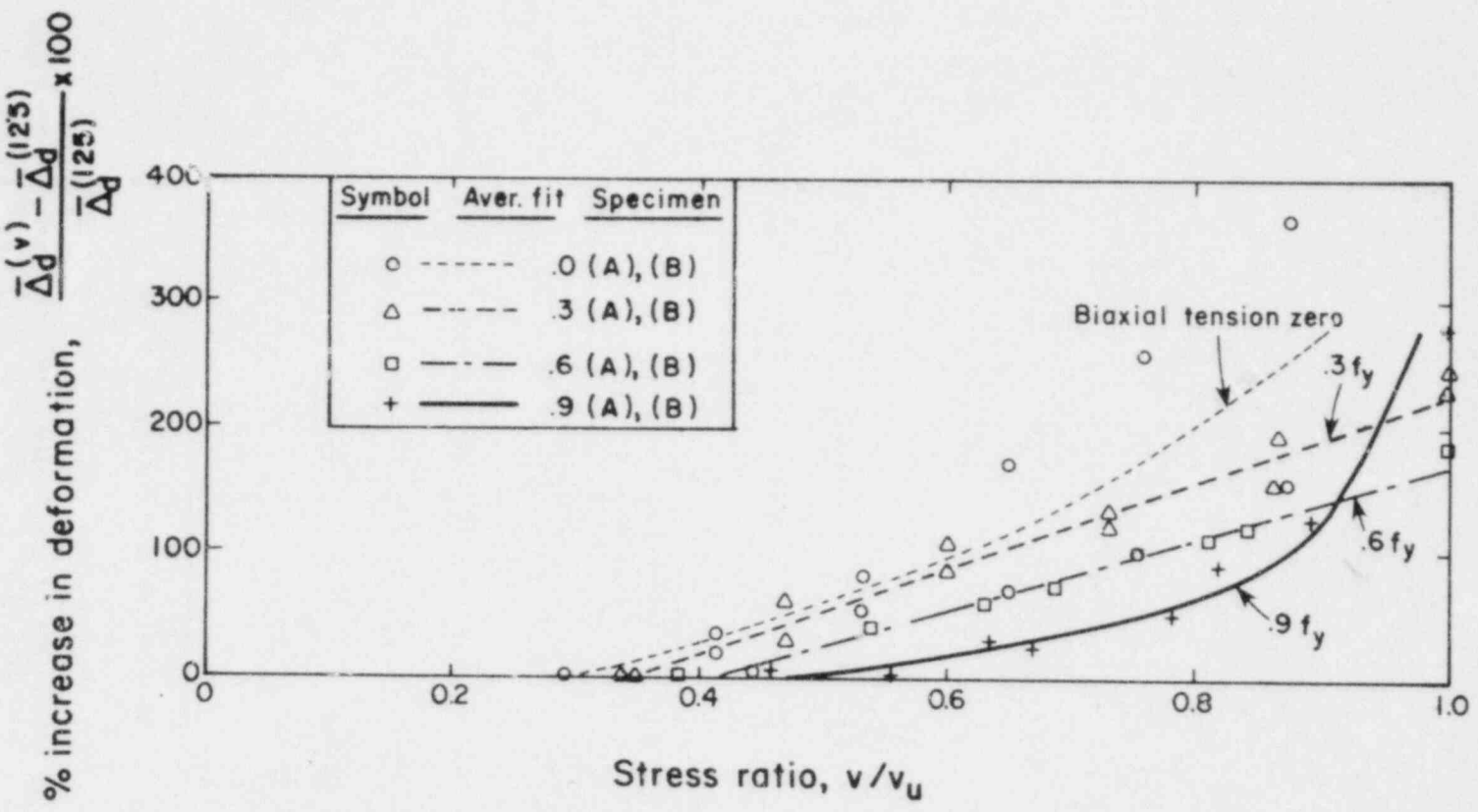

Fig. 2.67. Normalized % increase of peak average diagonal deformation $\bar{\Delta}d$ at the 1st cycle of each stress level versus the ratio of the applied peak shear stress v to the ultimate strength v_u in specimen Series A and B (No.6 bars).

Table 2.I. Effective secant and tangent shear modulus G_{cr} in terms of G_o for monotonic shear.

Shear Stress v(psi)	Specimen .0(M) $\frac{G_{cr}}{G_o}$ (sec)	Specimen .0(M) $\frac{G_{cr}}{G_o}$ (tan)	Specimen .3(M) $\frac{G_{cr}}{G_o}$ (sec)	Specimen .3(M) $\frac{G_{cr}}{G_o}$ (tan)	Specimen .6(M) $\frac{G_{cr}}{G_o}$ (sec)	Specimen .6(M) $\frac{G_{cr}}{G_o}$ (tan)	Specimen .9(M) $\frac{G_{cr}}{G_o}$ (sec)	Specimen .9(M) $\frac{G_{cr}}{G_o}$ (tan)
0	0	0	0	0	0	0	0	0
25	0.056	0.056	0.021	0.021	0.012	0.012	0.009	0.009
50	0.056	0.067	0.030	0.056	0.018	0.042	0.015	0.067
75	0.062	0.056	0.036	0.056	0.023	0.033	0.021	0.067
100	0.056	0.056	0.039	0.048	0.024	0.033	0.025	0.056
125	0.059	0.067	0.040	0.056	0.026	0.037	0.028	0.042
150	0.059	0.056	0.043	0.056	0.027	0.037	0.029	0.033
175	0.058	0.042	0.043	0.042	0.028	0.042	0.029	0.021
200	0.053	0.048	0.043	0.042	0.030	0.042	0.026	0.011
225	0.056	0.056	0.043	0.042	0.031	0.037	0.021	0.005
250	0.054	0.056	0.043	0.048	0.031	0.030	0.015	0.004
275	0.056	0.056	0.044	0.056	0.031	0.021	0.012	0.003
300	0.054	0.048	0.044	0.056	0.029	0.010	0.009	~0
325	0.054	0.042	0.045	0.056	0.023	0.005	-	-
350	0.052	0.042	0.046	0.056	0.016	0.003	-	-
375	0.052	0.037	0.046	0.048	0.011	~0	-	-
400	0.049	0.030	0.046	0.048	-	-	-	-
425	0.048	0.024	0.046	0.026	-	-	-	-
450	0.044	0.011	0.042	0.008	-	-	-	-
460	0.038	0.008	0.033	~0	-	-	-	-
475	0.036	~0	-	-	-	-	-	-

for low bar tensions of 0 and $0.3f_y$, the monotonically loaded specimens .0(M) and .3(M), as shown in Figs. 2.68a and 2.68b, experience larger peak shear deformations at the same shear stress. The monotonic loading portion of the shear stress-shear strain curve at the 1st cycle for specimen .0(C) is also plotted in Fig. 2.68a. This much steeper curve falls to the left of the envelope of .0(A) indicating an apparent scatter for monotonic shear tension and a high sensitivity at low shear stresses. The low shear stiffness at very low shear stresses in specimens .0(M) and .3(M) shift the whole curve towards larger deformation resulting in lower secant shear

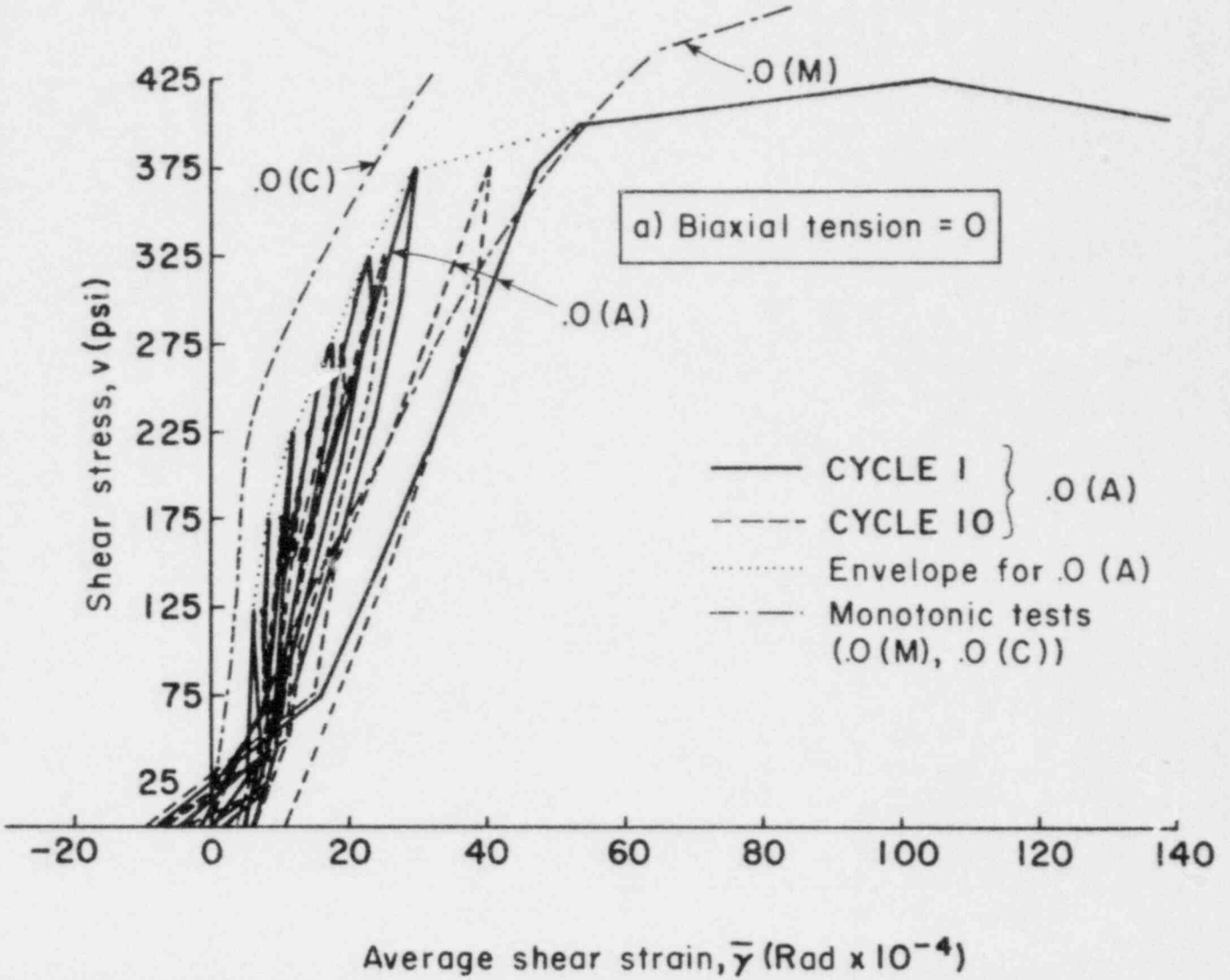

Fig. 2.68. Comparison of the shear stress-shear strain curves for the biaxial specimens under monotonic and cyclic shear.

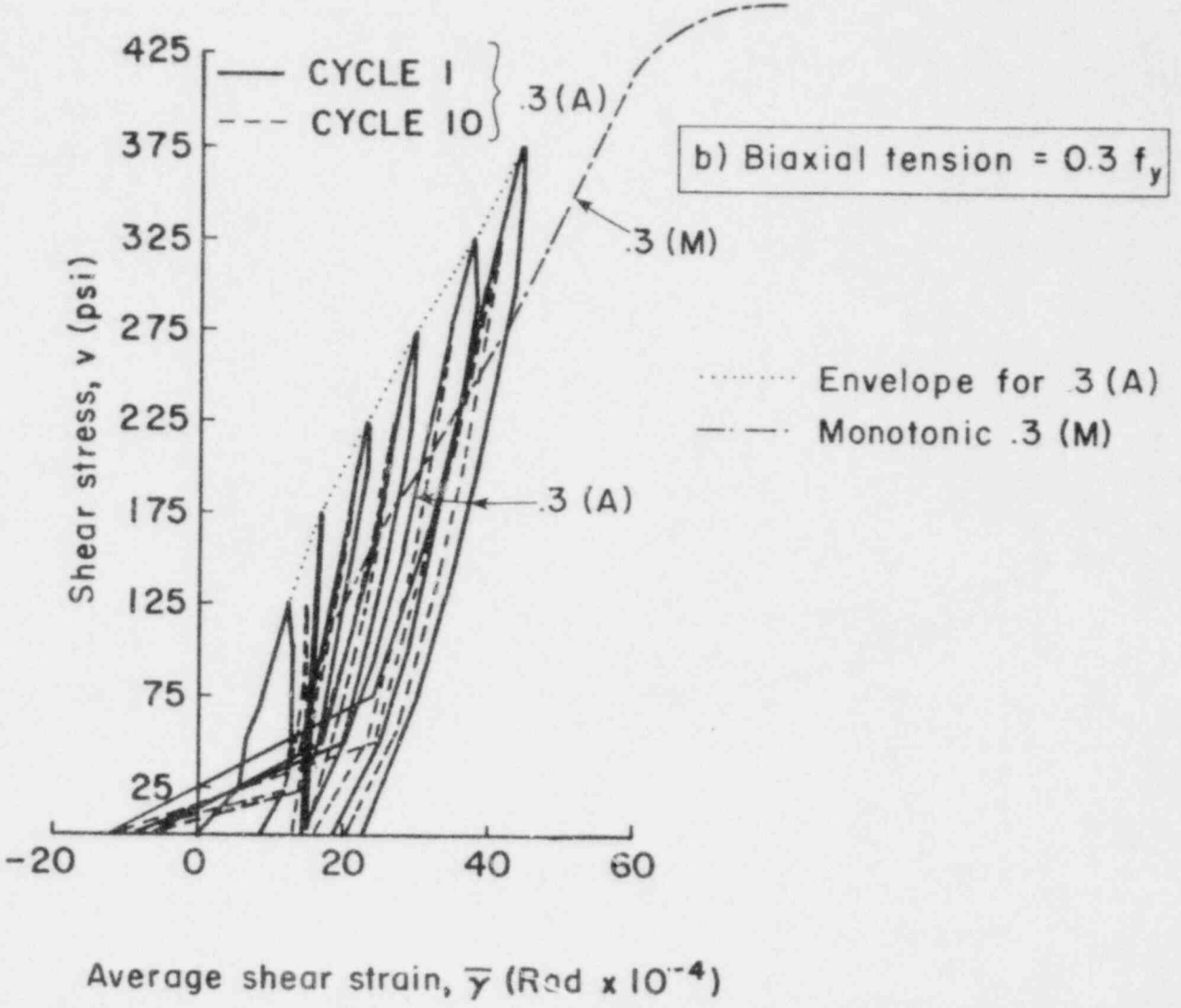

Fig. 2.68. (Continued)

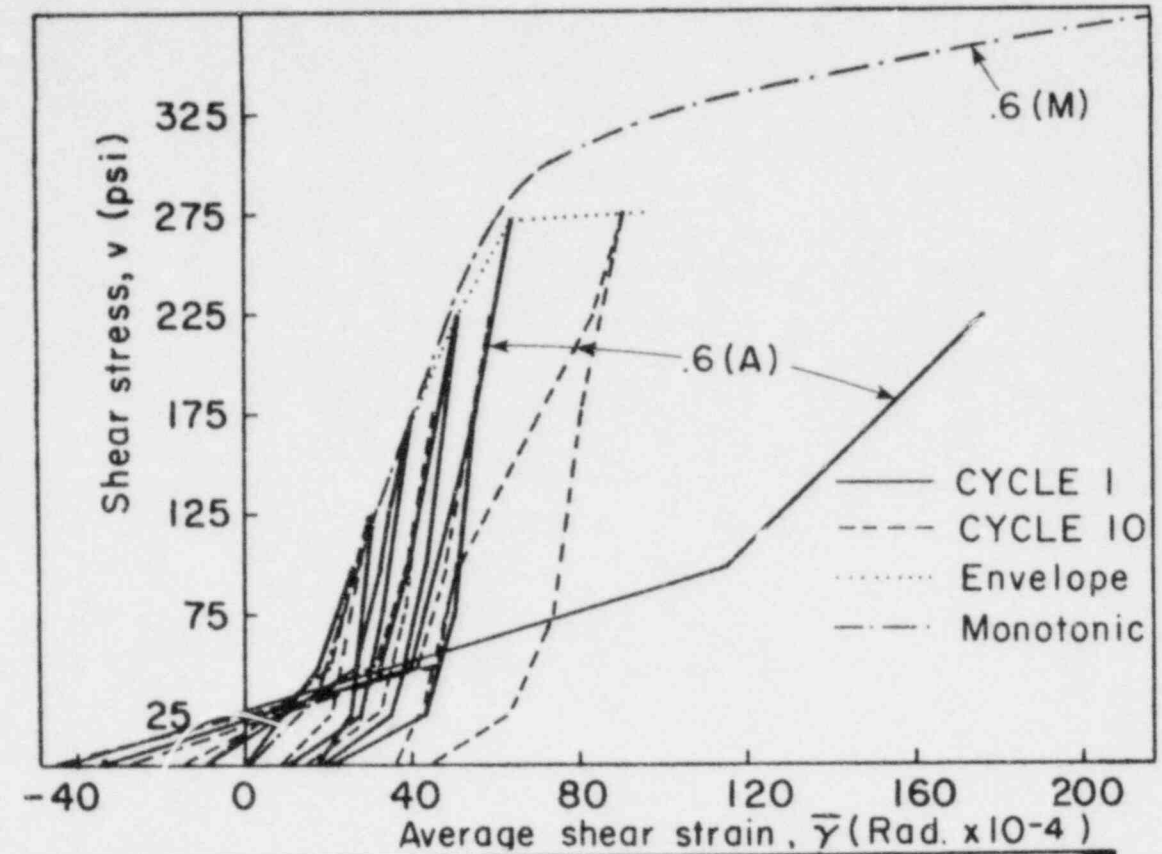

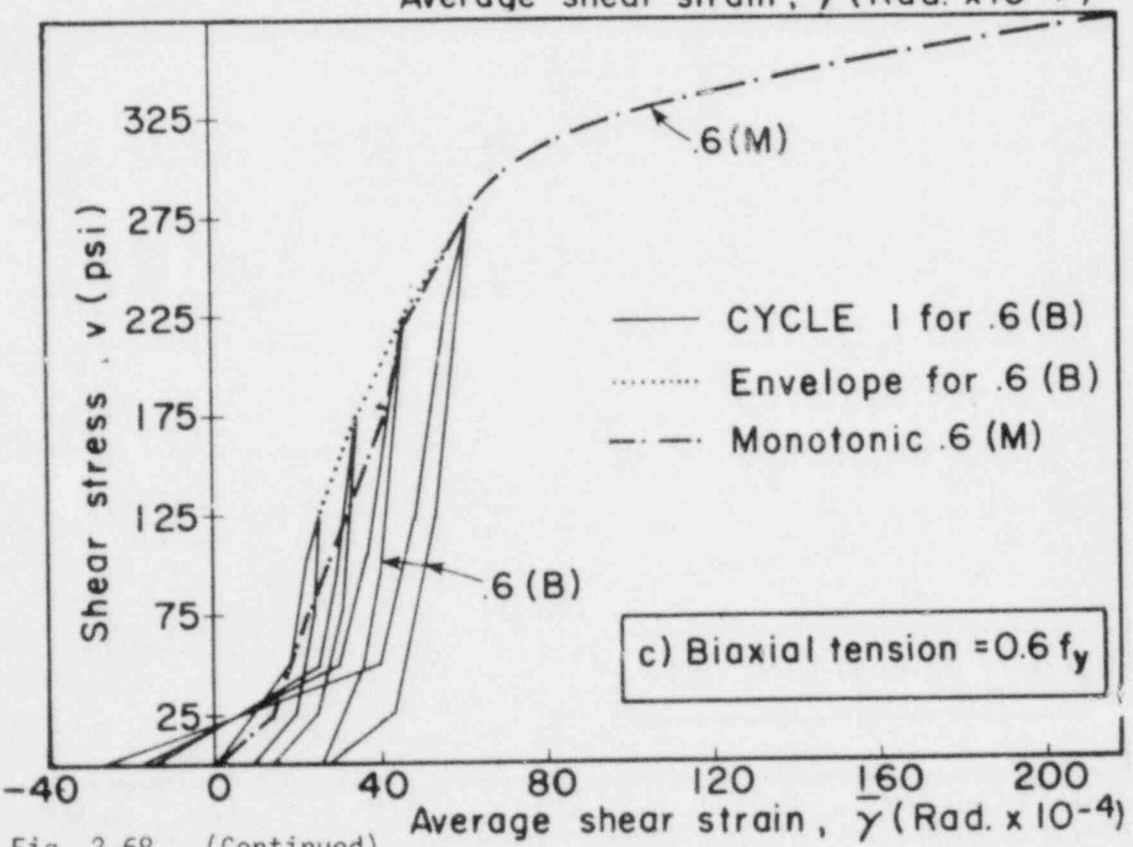

Fig. 2.68. (Continued)

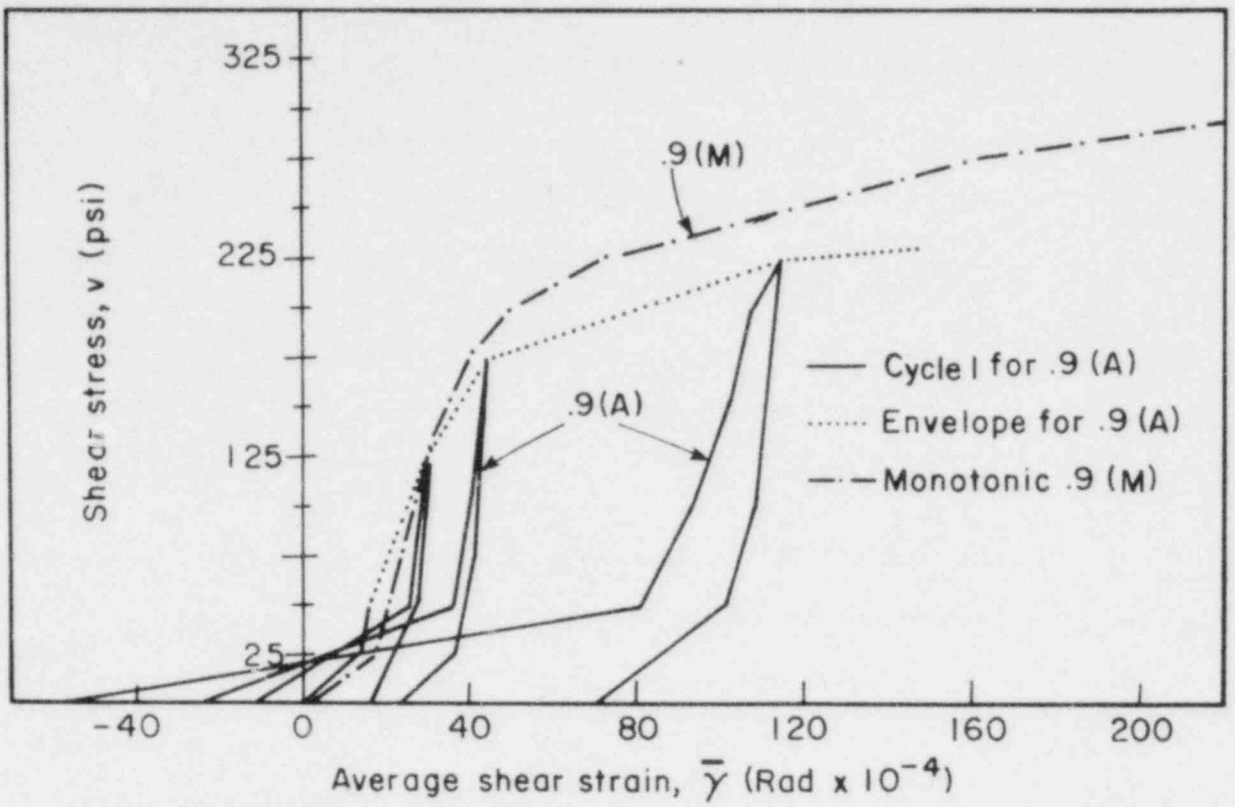

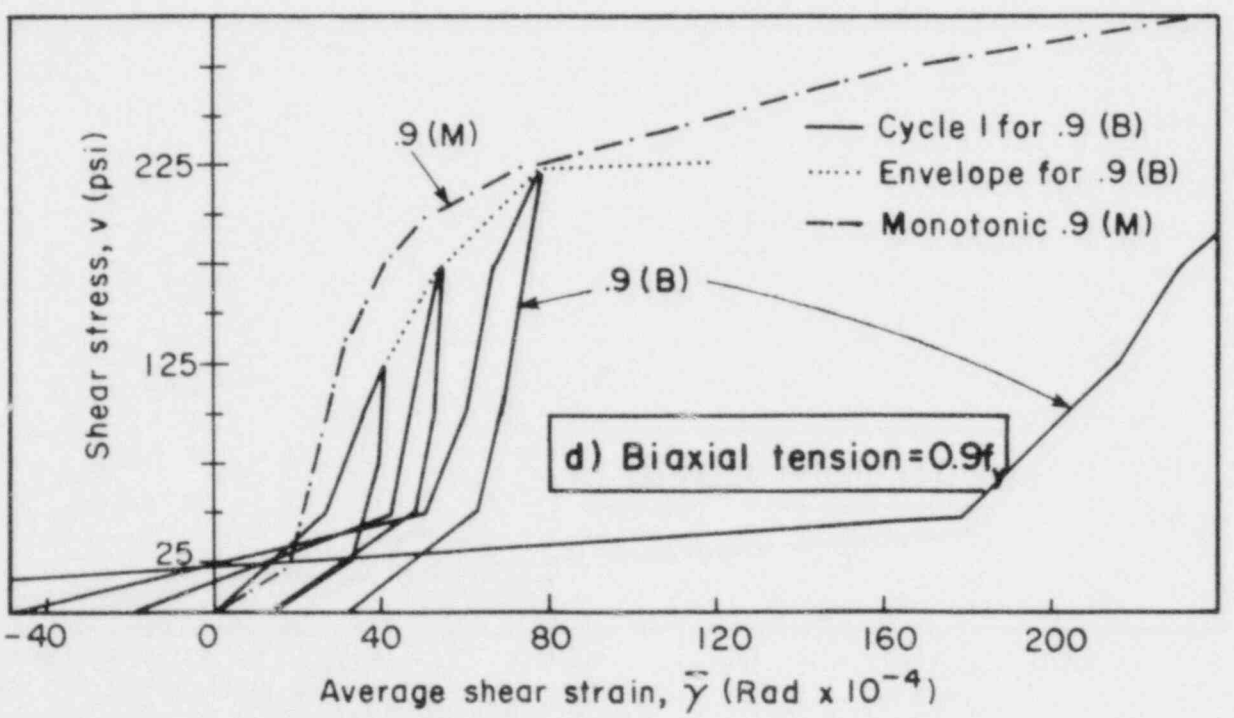

Fig. 2.68. (Continued)

stiffness values than would be predicted by the envelope curves of the reversing loading-unloading hysteresis loops. The major cause of this, as mentioned before, is believed to be the shrinkage cracking. The local tangent shear stiffness in specimens .0(M) and .3(M) does not seem to be affected by the above factor and compares favorably with that of the envelope curves.

2.7.3 Ultimate strength

It is evident from the test results that shear capacity was always governed by yielding of the reinforcement in the region near a corner. The diagonal tension-compression strut system resulted in increasing crack openings at the diagonal cracks, which caused higher bar tensions and eventually yielding of the steel. It is emphasized that this response led to an opening-type mode of failure at a diagonal crack and not to a sliding shear-type mode along an orthogonal crack. According to the free body equilibrium analyses at failure (see Section 4.4) and assuming yielding in the bars in both reinforcing directions, appreciable dowel forces are computed in each bar in the double and the single layer of No.6 bars, respectively. Kinking of the bars at the failure crack is also probable as failure is approached.

The initially cracked specimens with zero tension in the reinforcement during the application of shear carried a shear stress of about $8.5\sqrt{f_c'}$ and $7.4\sqrt{f_c'}$ for monotonic and cyclic shear, respectively. As applied biaxial tension is increased to $0.9f_y$, the shear strength decreases to about $5\sqrt{f_c'}$ and $4\sqrt{f_c'}$ for monotonic and cyclic shear loading, respectively.

Strength is decreased by some 15% by the action of cyclic loading, as compared to the monotonically loaded specimen strengths (see Fig. 2.19b). The ultimate strength values measured in all specimens are given in Table 2.H. It is believed that the lower ultimate strength values measured under cyclic shear compared to those under monotonic shear are mainly due to the lower expected dowel strength of the No.6 reinforcing bars subjected to cyclic shear loading. Reversing cycling causes progressive damage of the concrete around the bars near the failure crack which results in smaller dowel forces at failure.

These same results are plotted in Fig. 2.69 in terms of the steel stress parameter $(\rho f_y - \sigma_N)$. In this parameter, ρ is the steel ratio in the more lightly reinforced direction, and σ_N is the applied normal tension stress in the same direction.

The mean ultimate strength values in the present experimental study for specimens with No.6 rebars are given by the following linear regression expressions with a correlation coefficient of 0.97:

Monotonic shear $v_u = [4.5 + 0.005(\rho f_y - \sigma_N)] \sqrt{f_c'}$ (psi) (2.7a)

and

Cyclic shear: $v_u = [3.8 + 0.005(\rho f_y - \sigma_N)] \sqrt{f_c'}$ (psi) (2.7b)

providing the relationships $\rho f_y = 744$ psi ($\rho = 0.0122$, $f_y = 61$ ksi) and $75 \leq (\rho f_y - \sigma_N) \leq 744$ psi are satisfied, and f_y, σ_N, f_c' are in psi. Ultimate strength increases with increasing steel ratio ρ or with decreasing axial tension. An approximately 50% variation in strength is observed in the present results with applied biaxial tension ranging from 0 to $0.9f_y$.

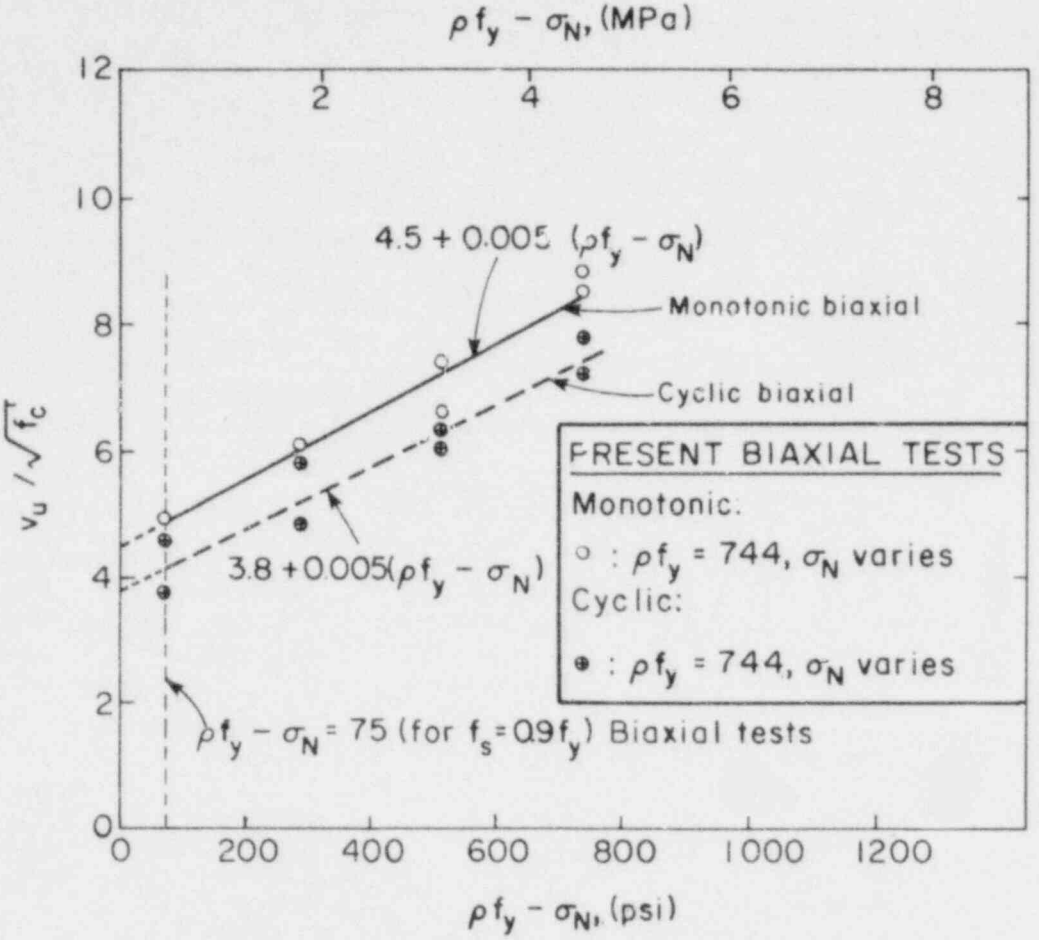

Fig. 2.69. Ultimate strength of the biaxial specimens versus the stress parameter (ρf_y-σ_N) under monotonic and cyclic shear.

The maximum shear stress values v given by Eqns. 2.7a and 2.7b are conservative when applied to a containment vessel because the failure type mode observed in the specimens cannot occur in a cylindrical shell, in which the region modeled by the specimens will be restrained by the rest of the structure. This aspect and the influence of the way the shear load was applied on the specimen to simulate a pure shear stress condition are discussed in Section 4.4.

CHAPTER 3

EXTENSIONAL STIFFNESS

3.1 Introduction

The main objective of this chapter is to present an estimate for the effective extensional (axial) stiffness K_N of the biaxially tensioned specimens. As previously mentioned in Chapter 2, all specimens reported here were initially cracked by tensioning each bar in both orthogonal directions (x and y) to about 36 ksi (248 MPa).

The principal tensile concrete strains induced by tensioning the bars in both directions were parallel to the orthogonal reinforcement. Twice as much steel was present in the double layer (direction y) as in the single layer in the orthogonal direction (x). Thus, the concrete surrounding the reinforcement in the former direction would be expected to experience more uniformly distributed strains than in the latter direction but of about the same maximum value. Experimental evidence, presented later in this chapter, showed that cracking in the concrete in the direction normal to the (y) direction (double layer) was initiated at a lower tensile stress in the bars than in the orthogonal direction.

If the bars were simultaneously tensioned in both (x) and (y) directions to the specified tension level, the direction of the initial cracking normal to the principal maximum strain direction would tend to be random because the applied principal strains in both directions were roughly equal. The Mohr's circle for strain would therefore collapse to a point.

In addition, the already existing sources of anisotropic behavior, such as shrinkage cracking, could easily lead to a different maximum principal strain direction. However, although the specimen could crack in any direction (not only normal to the reinforcing bars), the cracks will tend to follow the reinforcing bars because bars act as crack initiators.

To minimize the formation of inclined cracks, the bars in both directions were not tensioned simultaneously. Instead, the bars in one direction were first tensioned up to 36 ksi to induce cracks approximately normal to the stressed steel and then, after the tension in these bars was released, the bars in the orthogonal direction were stressed to 36 ksi to produce another set of parallel cracks normal to the first set. Finally, the bars in both directions were tensioned together up to 36 ksi and then the tension level was held constant at a preselected value of 0, $0.3f_y$, $0.6f_y$ or $0.9f_y$. The above procedure was followed to achieve an orthogonal cracking pattern more representative of the horizontal and vertical cracks observed during internal pressurization tests of reinforced nuclear containment vessels.

There is neither data or any analysis available in the literature on the subject of the axial stiffness in biaxially tensioned reinforced concrete elements. Considering the complex boundary conditions existing in a segment of a cracked containment wall subjected to a biaxial tensile loading, the following procedure was adopted. A simple relation for the extensional stiffness was obtained using the total external axial elongation measurements in the specimens during the application of the tensile loads in the reinforcing bars in both orthogonal directions. The existing average steel strains ε_{sm} within the gage length under consideration were

expressed as a function of the applied tensile stress f_s, the reinforcement ratio ρ and the Young's modulus E_s of the steel.

It is important to note that earlier experimental studies on the shear transfer across single cracks (Refs. 61, 70, 97, 117 and 126) dealt with prespecified constant initial crack widths or with constant axial restraining stiffness provided through external or embedded steel bars. The present study on shear transfer used two-way embedded reinforcement. Due to bond deterioration and splitting, slip could occur between steel and concrete, thus affecting the crack opening and shear-induced slip along the orthogonal cracks. This axial stiffness degradation depended on the tension level, the applied shear stress and the number of load cycles. There is no experimental data from the present research on the variation of the extensional stiffness during the application of combined biaxial tension and shear. Thus, a constant extensional stiffness is assumed for both the monotonically and cyclically loaded specimens, as determined by the tension tests described in this chapter.

From the relation between the applied axial tension in the bars and the total elongation in the surrounding concrete, an average effective extensional stiffness K_N is determined in both the x and y directions, parallel to the reinforcing steel. This stiffness (related to the local axial restraint stiffness of the embedded reinforcement at a single crack) plays a significant role in the ability of the cracked reinforced concrete panels to effectively transfer the applied shear forces across the cracks. The importance of K_N is demonstrated by the shear-friction theory, according to which the larger the compressive forces normal to the crack surfaces, the larger is the contribution of the interface shear transfer to the shear

transfer across the cracks. It is true, however, that in order to create sufficiently high compressive forces, equally high axial stiffness (provided by the reinforcement) is required normal to the cracks.

Since the extensional stiffness is interrelated with the crack openings during tensioning, the main parameters influencing the latter need identification. These parameters are the mean steel strain ε_{sm}, which includes the contribution of concrete to the axial stiffness (tension stiffening effect), and the crack spacing (mainly a function of concrete cover, bar size and concrete tensile strength) of the orthogonal cracks after a stabilized condition is achieved.

3.2 Literature Survey

The literature review on the subject of extensional stiffness and cracking deformations is divided into two sections. First a review is presented in Section 3.2.1 on the experimental results for axial restraint stiffness obtained from block specimens under uniaxial tension. Then, a number of proposed formulae for the calculation of the mean strain in the embedded reinforcement and the crack spacing, as well as different approaches used in estimating the tension stiffening effect of concrete, are given in Section 3.2.2.

3.2. Extensional (restraint) stiffness from uniaxial tests

In tests performed at Cornell University the effect of axial restraint stiffness has been studied on block concrete specimens with a predefined single shear crack. White and Holley (Ref. 126), and Laible (Ref. 70)

used external unbonded rods, while Jimenez et al. (Ref. 61) used embedded reinforcing bars crossing the single crack. Eleiott (Ref. 33 and 127) employed both embedded bars and external unbonded rods to study: (a) interface shear transfer alone, (b) dowel action alone, and (c) interface shear transfer and dowel action combined.

Laible and White and Holley performed studies on the effect of the restraining axial stiffness on the shear displacement of a single crack with a specified initial crack width c_{wm}^{o}. In their experiments the stiffness normal to the crack was provided by unbonded external rods bolted at the top and bottom of the specimen to reaction steel beams (see Fig. 4.7).

White and Holley concluded that an increase in restraint stiffness would result in smaller shear displacements and larger shear stiffness during either cyclic or monotonic shear loading, even for relatively large initial crack widths of 0.030 in. Direct comparisons were not possible since the specimens with the higher axial restraint stiffness (larger external steel rods) were cycled at a higher shear stress level than the specimens with the lower axial restraint stiffness.

Laible found that the reduction in the shear and normal displacements caused by an increase in axial stiffness was affected by cycling and the level of axial stiffness. The shear resistance in the bearing mode of the interface shear transfer at very small crack widths was highly dependent on the local roughness at the crack interface and on the value of c_{wm}^{o}, and was less dependent on the axial stiffness normal to the crack. This meant that the increase in crack width and bar forces with increasing shear load was not as large as in the frictional mode of behavior. In the latter case, the interface shear transfer stiffness was highly affected

by the axial restraint. The axial stiffness values (1780 k/in with four 1.0 inch (25 mm) diameter external bars, 3420 k/in with four 1.375 inch (34 mm) diameter external bars, and 5130 k/in or 7640 k/in with six 1.375 inch external bars) used in Laible's tests were lower than those in actual reinforced concrete vessels with embedded bars and the slips observed did not seem to be influenced at the high value of 7640 k/in.

In Table 3.A the ratio of the total restraining force to a fixed applied shear force of about 180 psi is given for different initial crack

Table 3.A. Restraining bar forces developed at a fixed shear force with decreasing average initial crack width according to Laible.

Series	Average initial crack width (c_{wm})	Ratio of total restraining force to applied shear force		
		Cycle 1	Cycle 15	% Increase
A	0.03 in. (0.76 mm)	30 to 40%	40 to 65%	33 to 62%
C	0.02 in. (0.51 mm)	30 to 40%	40 to 55%	33 to 38%
D	0.01 in. (0.25 mm)	10 to 20%	20 to 35%	100 to 75%

widths for specimens with axial stiffness equal to 3420 k/in. A decrease in the restraint forces with decreasing initial crack width is evident. It was observed that the total restraining force required to transfer a specific shear stress did not exceed 65% of the shear load, at least for the initial loading cycles. For initial crack widths of about 0.010 in. the axial restraining force could be as low as 10% of the shear force during the 1st cycle. The axial stiffness was less effective in decreasing the shear deformations in the initial loading cycles and axial stiffness

values larger than 3000 k/in (or 10 ksi/in for a 300 in^2 shearing area). For values larger than 10 ksi/in the axial stiffness was more effective in controlling shear deformations at subsequent cycles. As shown in Fig. 3.1, there was a critical level of K_N (normalized to the corresponding shearing area of concrete) above which an increase in restraint stiffness did not decrease shear displacements. Slips comparable to Loeber's results (discussed later in this section) were obtained for infinite axial restraint.

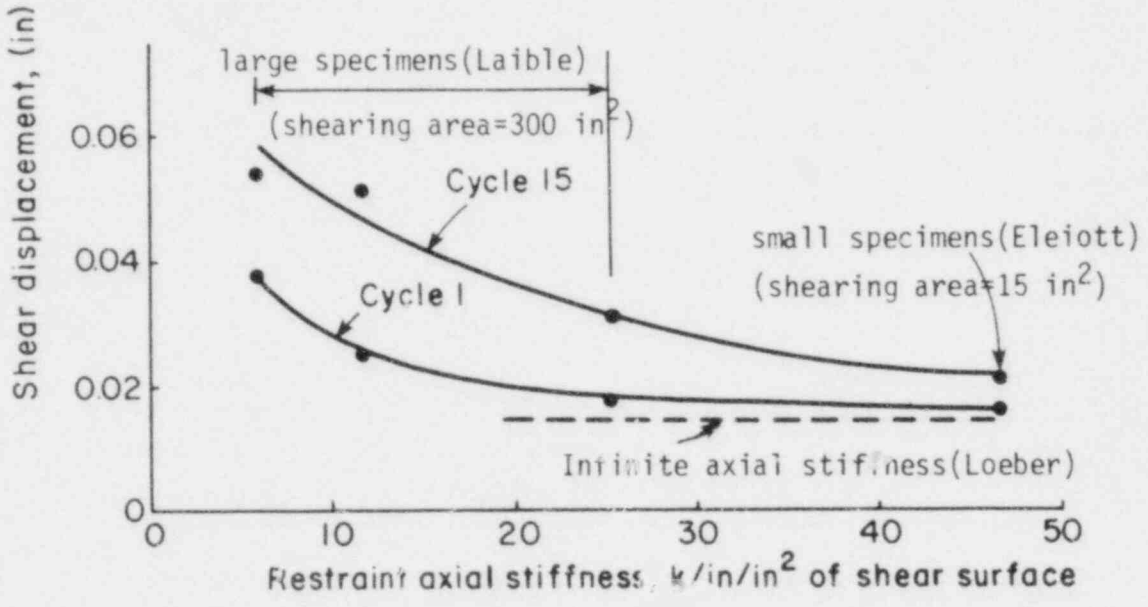

Fig. 3.1. Shear slip vs. restraint system stiffness (for initial crack width of 0.030 in.).

Eleiott (Refs. 33 and 127) using smaller scale specimens than Laible (one No.4 embedded reinforcing bar crossing a shearing area of 15 in^2

(see Fig. 4.20)), measured the increase of the bar stresses and the change in the extensional stiffness K_N under the combined action of the interface shear transfer and dowel mechanisms. He also performed two tests with external steel rods providing a restraint stiffness of about 700 k/in (47 k/in/in^2 of shearing area) to study the interface shear transfer mechanism alone. In the tests with the embedded bar the restraint stiffness depended on the bond developed between the steel and the surrounding concrete. However, no internal strain gages were placed on the bars at the vicinity of the crack plane to measure the change in the bar tension, because of their interference with bond. Instead, the corresponding change in the bar stress was indirectly estimated by multiplying the initially calculated axial stiffness by the increase in the crack width between zero and peak axial load (see Fig. 3.2).

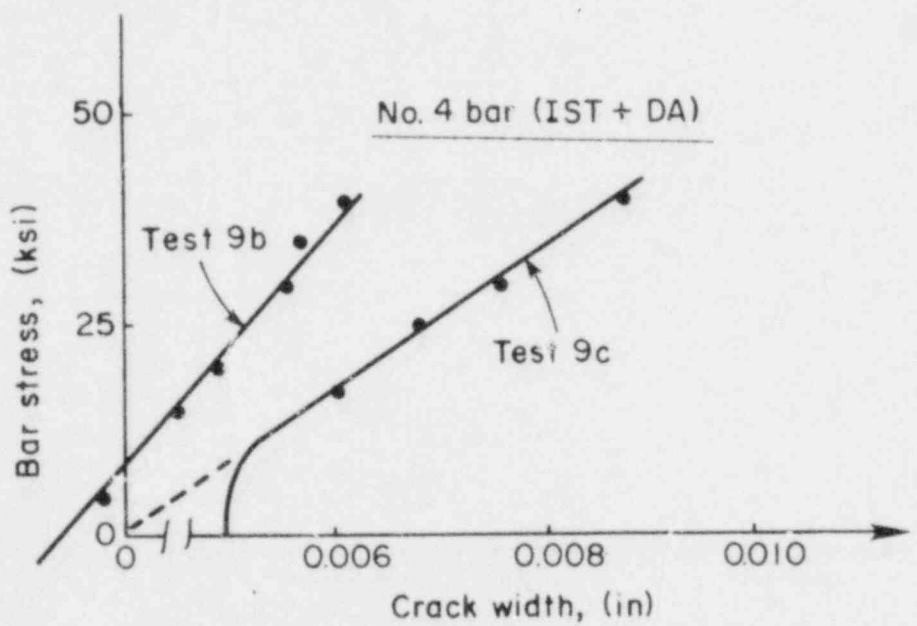

Fig. 3.2. Crack width variations, tests 9b and 9c(Eleiott).

Axial steel stresses of 25 and 50 ksi and peak shear stresses of ±150, ±250 and ±400 psi (1.04, 1.72 and 2.76 MPa) were applied to the specimen with the No.4 reinforcing bar. Due to cyclic shear loading, crushing of concrete around the bar lowered the bond transfer and decreased the extensional stiffness of the embedded bar (ρ = 0.0133). Results from two tests (9 and 10) with an initial crack width of 0.030 in. are presented in Table 3.B. Average increases in the bar stress of about 8% for an

Table 3.B. Eleiott's test results for combined interface shear transfer and dowel action with a single No.4 embedded rebar (average initial crack width of 0.030 in.).

(1) Test No.	(2) f_s (ksi)	(3) Peak Shear Stress v(psi)	(4) K_N (ksi/in)	(5) Δf_s (%)	(6) No. of Cycles
9	25	±150	-	8%	10
9a	50	±150	111 to 373	8 to 28%	15
9b	50	±250	111 to 213	12 to 20%	10
9c	50	±400	111 to 191	30 to 55%	10
10	50	±150	100 to 130	20 to 0%	10
10a	50	±250	78 to 186	24 to 19%	10
10b	50	±400	107 to 167	30 to 32%	8

Notes:

(4) The two values of K_N correspond to the left and right crack plane at the two ends of the specimen.

(5) Δf_s = then average % increase in bar stresses after a certain number of cycles.

(2) f_s = initially applied axial stress per bar.

applied steel stress of 25 ksi (10 cycles) and 8 to 55% for a steel stress of 50 ksi (loading history is shown in col. 6 of Table 3.B) were measured in these two tests.

Eleiott's experimental results regarding the effect of axial stiffness and cycling on the amount of shear slip in the tests studying the interface shear transfer mode (with external restraint steel rods) are included in Fig. 3.1 for comparison with Laible's and Loeber's results. Direct comparison with Laible's data cannot be done, since the effective extensional stiffness in Laible's larger specimens was 83% higher than that in Eleiott's small specimens. However, the size of the shearing area does not appear to influence appreciably the test results.

Paulay and Loeber (Ref. 97) and Taylor (Ref. 117) also studied indirectly the effect of axial stiffness provided by the reinforcing steel. They conducted tests where either the ratio of the shear slip to crack opening was fixed at the beginning of the test, or the normal forces required to maintain a constant initial crack width were measured during the test. The relation between the measured normal stress and the applied shear stress given by Loeber is shown in Figs. 3.3a and 3.3b. The size and shape of the aggregate and the initial crack width did not affect the magnitude of the normal force required. Generally, for low ratios of normal to shear displacement, Loeber found that the change of normal restraining force was appreciable only as failure was approached. However, for larger crack width openings, significant changes in the applied normal force occurred at lower shear stress levels. No extensional stiffness expression was developed by Loeber or Taylor.

Jimenez et al. (Ref. 61) established the following linear relation for the average total axial restraint stiffness as a function of the reinforcement ratio ρ at the shear crack (see Fig. 3.4)

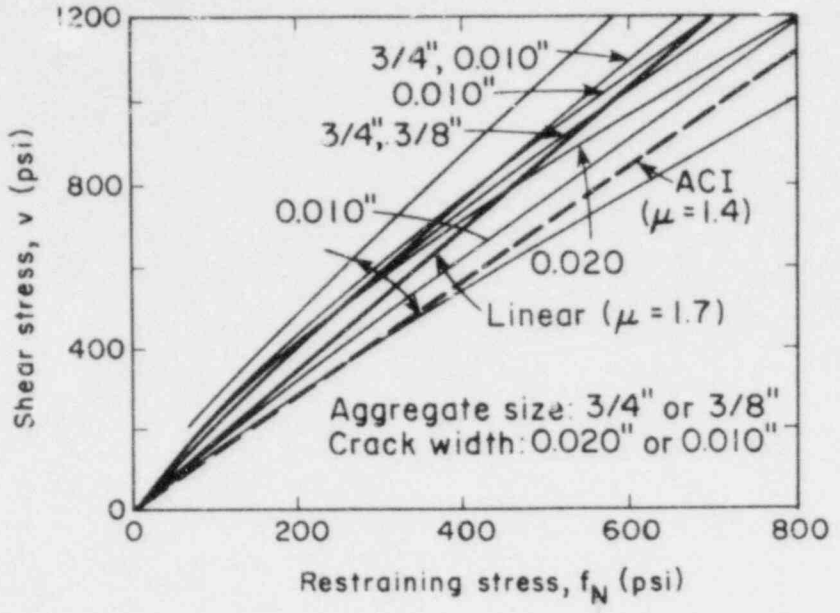

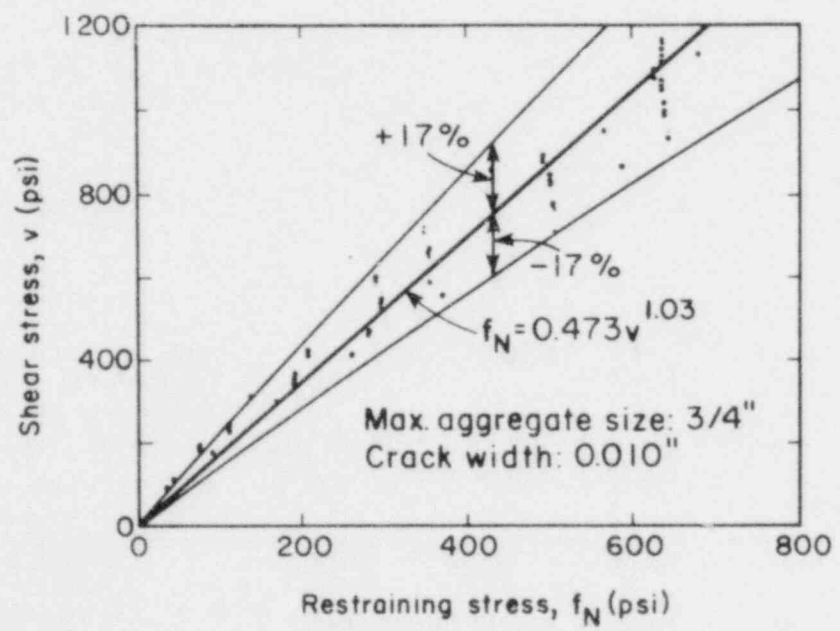

Fig. 3.3. Normal restraining stress f_N versus applied shear stress from Loeber's results (Ref. 97).

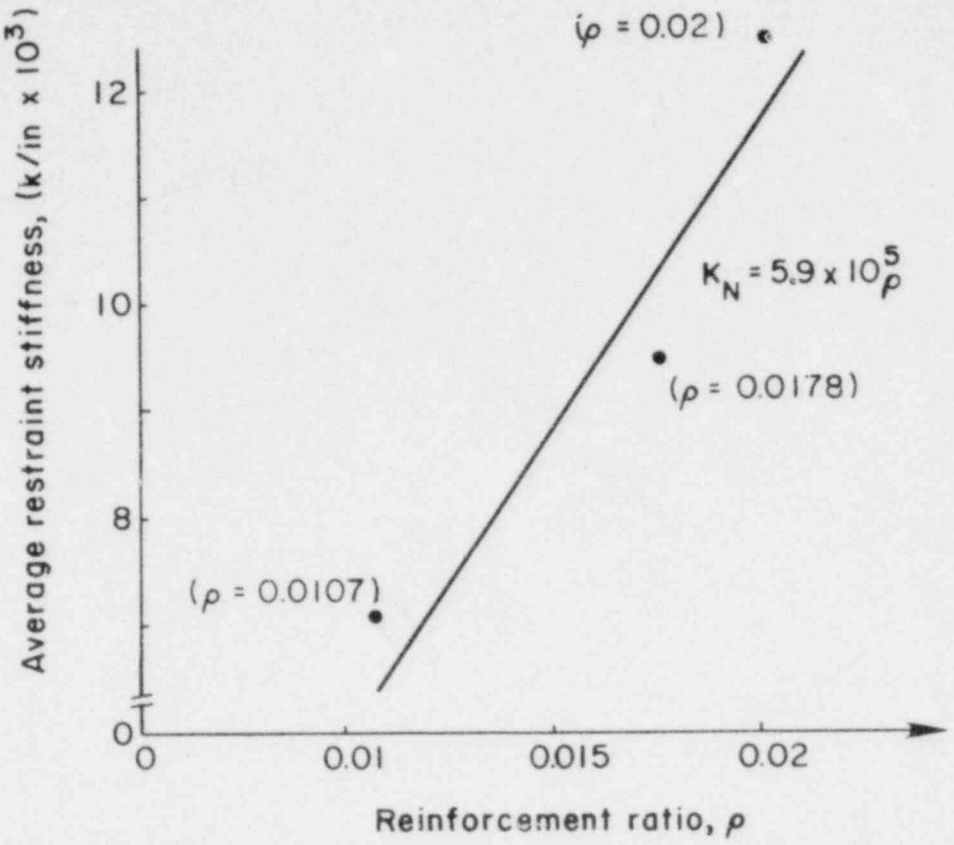

Fig. 3.4. Total axial restraining stiffness vs. reinforcement ratio determined from test Series C and D (Jimenez et al.,Ref. 61).

$$K_N = 590000\rho \quad (k/in) \tag{3.1a}$$

or

$$K_N = 590000\rho/225 = 2620\rho \quad (k/in) \tag{3.1b}$$

per in^2 of shear surface area normalized to the total shearing surface of 225 in^2. The specimens had a shearing area of 225 in^2 and ρ values from 0.0107 to 0.020.

According to Eqn. 3.1b for a single bar of diameter d the extensional stiffness is given by the following relation

$$K_N \text{ (per bar)} = 2060\ d^2 \qquad \text{(k/in)} \tag{3.2}$$

The axial restraint stiffness values measured by Jimenez et al. (see Figs. 3.5 and 3.6) in all specimens are summarized in Table 3.C. The stiffness values measured in the test series (D) (for studying dowel action

Table 3.C. Axial restraint stiffness values measured by Jimenez et al. (Ref. 61).

Specimen No.	ρ	K_N (k/in) (total)	K_N (k/in) (per bar)
C4 - 7A (4-No.7)	0.0107	7000	1750 (1-No.7)
C4 - 9A (4-No.9)	0.0178	9600	2400 (1-No.9)
C4 - 9B (4-No.9)	0.0178	9600	2400 (1-No.9)
C2 - 14B (2-No.14)	0.020	14800	7400 (1-No.14)
C2 - 14C (2-No.14)	0.020	13200	6600 (1-No.14)
D4 - 9A (4-No.9)	0.0178	10400	2600 (1-No.9)
D4 - 9C (4-No.9)	0.0178	7800	1950 (1-No.9)
D2 - 14B (2-No.14)	0.020	11600	5800 (1-No.14)

only), are shown in Fig. 3.5. The variation of the bar tension versus the crack width changes is linear in all cases. The deterioration of the bond mechanism under cycling and increasing axial tension in the bars was more severe in the specimens designed to provide only dowel resistance (Series D). For combined interface shear transfer and dowel action (Series C) the smaller deformations at the shear crack lowered the rate of bond damage resulting in higher values of axial stiffness (see Fig. 3.6).

Fardis and Buyukozturk (Ref. 35) gave a nonlinear expression for the extensional stiffness of a single bar in terms of the crack width c_w (inches) as,

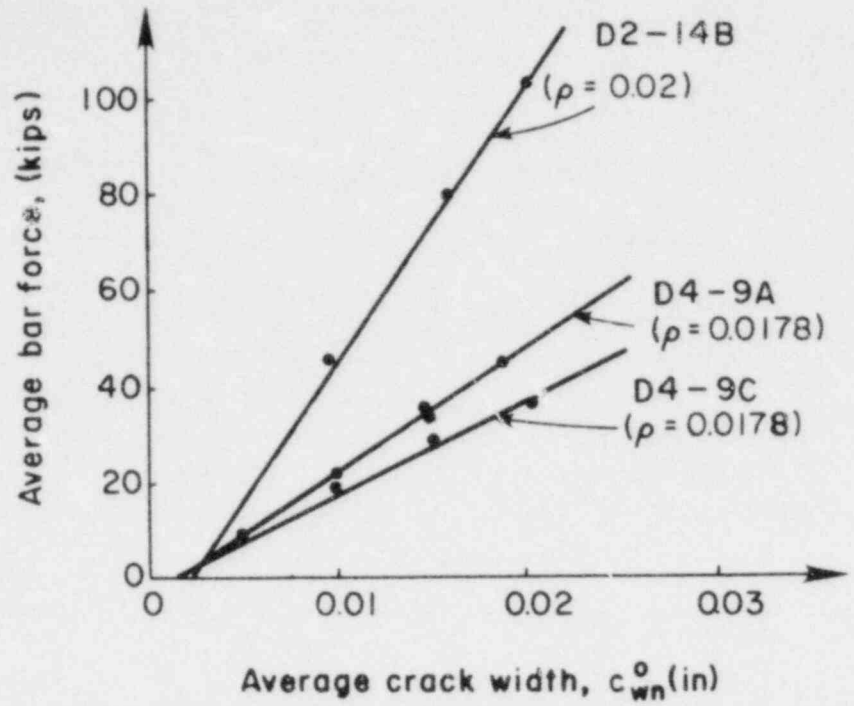

Fig. 3.5. Axial restraint stiffness curves for test Series D (Ref. 61).

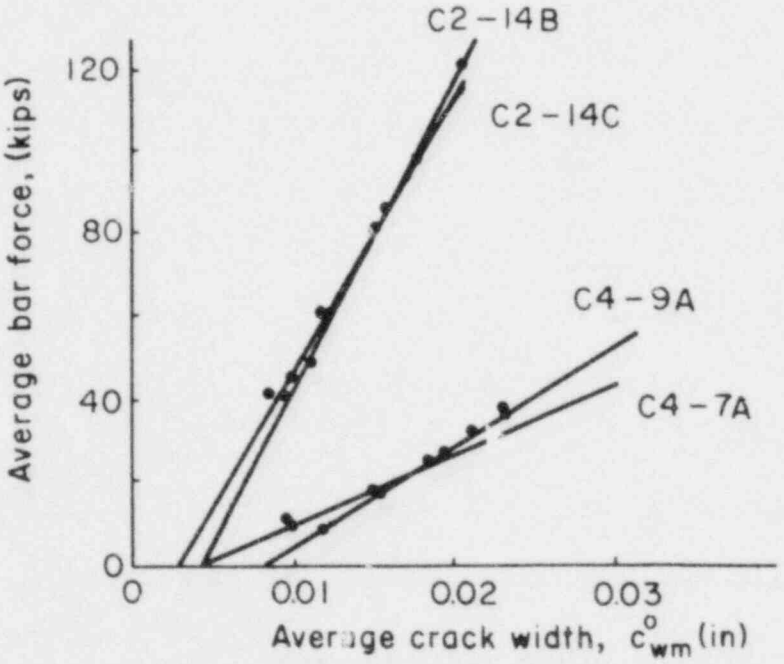

Fig. 3.6. Axial restraint stiffness for test Series C (Ref. 61).

$$K_N = \frac{\pi d^2}{8}\sqrt{\frac{E_s}{(1+n\rho)d}}\sqrt{a_1 + \frac{a_2 c_w}{3} + \frac{a_3 c_w^2}{8}} \quad (k/in) \qquad (3.3)$$

where $n = E_s/E_c$ is the ratio of moduli of steel and concrete, ρ the reinforcement ratio, d the bar diameter in inches and a_1, a_2 and a_3 are empirical constants determined from analysis of the Cornell University test data:

$a_1 = 16.7\sqrt{f_c'}$ ksi/in $(4540\sqrt{f_c'}$ MN/m$^3)$

$a_2 = -8260\sqrt{f_c'}$ ksi/in^2 $(8.82 \times 10^7\sqrt{f_c'}$ MN/m$^4)$

$a_3 = 1.12 \times 10^6\sqrt{f_c'}$ ksi/in^3 $(4.7 \times 10^{11}\sqrt{f_c'}$ MN/m$^5)$

(f_c' is in psi)

This expression (Eqn. 3.3) was based on the analysis proposed by Watstein and Bresler (Ref. 121) for the estimation of bond slip at the steel-concrete interface. According to Ref. 35, comparison of the above expression for K_N (Eqn. 3.3) with direct measurements in Refs. 61 and 127 did not give satisfactory results. The variation of K_N according to Eqn. 3.3 as a function of the crack width c_w is shown in Fig. 3.7. The extensional stiffness K_N tends to decrease with increasing crack width. This is valid only for crack widths less or equal to 0.010 in., because for higher values K_N increases. According to Eqn. 3.3, the axial stiffness values of a single bar range between

$$4.1\ K_0 \le K_N \le 1.8\ K_0 \quad (0 \le c_w \le 0.010\text{in.}) \qquad (3.4a)$$

where

$$K_0 = \frac{\pi d^2}{8}\sqrt{\frac{E_s}{(1+n\rho)d}}\ \sqrt[4]{f_c'} \quad (k/in) \qquad (3.4b)$$

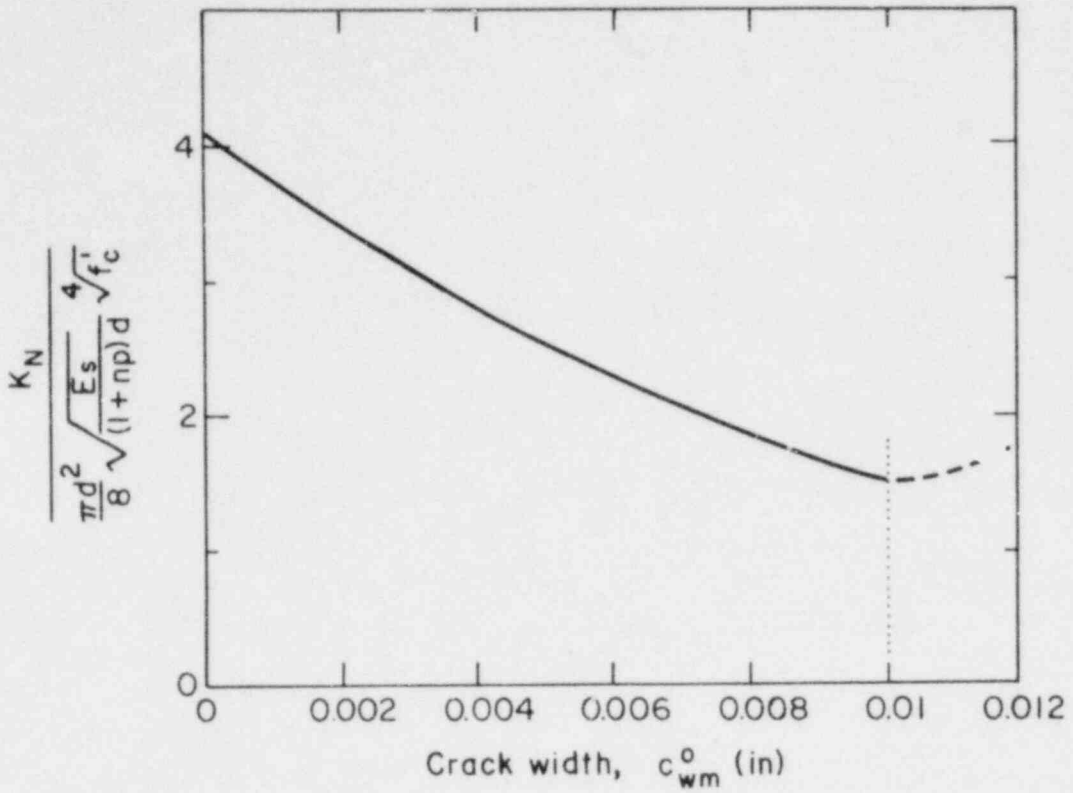

Fig. 3.7. Extensional stiffness of a single bar (Fardis and Buyukozturk).

It is pointed out that one basic difference between the relations 3.2 and 3.3 is that the latter is a function of the crack width induced by tensioning the reinforcing bar. The former equation results in a constant axial stiffness at least up to a maximum crack width value of 0.020 in. Both, however, depend heavily on the bar diameter rather than the reinforcement ratio ρ. Therefore, if the steel ratio in a concrete prism with a single bar of diameter d is increased by decreasing the concrete cross-sectional area A_c, the extensional stiffness should decrease accordingly approaching the axial stiffness of the unbonded bar $A_s E_s/\ell_{cm}$, where A_s is the cross-sectional area of the bar and ℓ_{cm} is the average crack spacing. For comparison, the axial stiffness for a single No.4, No.8 and No.9 rebar

and two steel ratios of 0.0122 and 0.0244 are calculated using both expressions (see Table 3.D). Expression 3.3 gives results similar to those

Table 3.D. Axial stiffness K_N calculated according to Eqns. 3.2 and 3.3.

K_N (k/in) per bar	ρ = 0.0122 (A_c = 36 in^2)			ρ = 0.0244 (A_c = 18 in^2)			
	No.4	No.6	No.9	No.4	No.6	No.9	c_w(in)
Eqn. 3.2	520	1160	2600	520	1160	2600	$0<c_w<0.02$
Eqn. 3.3	310	570	1050	300	540	1000	0.010
	460	850	1530	440	810	1480	0.005
	590	1090	2000	570	1040	1920	0.002

predicted by Eqn. 3.2 for a crack width not larger than 0.002 in.; K_N then decreases down to about half of that value at a crack width of 0.010 in. It also appears that for the same size bar the estimated value of the axial stiffness for ρ equal to 0.0122 and 0.0244 is identical using Eqn. 3.2 and slightly smaller using Eqn. 3.3 for the higher ρ value of 0.0244.

3.2.2 Crack spacing and steel strain formulae

Due to the contribution of concrete in tension, the overall axial stiffness of a reinforced concrete prism of length ℓ_{cm} (average crack spacing) can be considerably higher than the axial stiffness of an unbonded bar of the same length. Thus, the average tensile strain in the bar ε_{sm} between two primary tension cracks will be lower than the steel strain at the cracks. An effective average steel strain ε_{sm} is assumed uniformly distributed along the rebar within the uncracked block of concrete.

Consider a simple case of a single bar of diameter d embedded in a concrete prism of a length larger than the average crack spacing ℓ_{cm}. A tensile stress f_s is applied to both ends of the rebar as shown in Fig. 3.8a.

According to the assumption of equal crack spacings and crack widths, the average crack width c^o_{wm} can be estimated using the following expression

$$c^o_{wm} = (\varepsilon_{sm} - \varepsilon_{cm})\, \ell_{cm} \tag{3.5}$$

where ε_{sm} is the average effective strain in the bonded rebar shown in Fig. 3.8b and ε_{cm} is the average residual strain in the concrete shown in Fig. 3.8c.

The longitudinal strain in the concrete ε_{cm} in most cases remains relatively small compared with steel strain ε_{sm} (see Refs. 78 and 123) although the total elongation of the prism could significantly increase due to the internal cracking. The crack opening at the concrete surface is normally several times larger than the extension of the concrete adjacent to the rebar.

Ignoring the strain term ε_{cm}, Eqn. 3.5 becomes

$$c^o_{wm} = \varepsilon_{sm}\, \ell_{cm} \tag{3.6}$$

Many expressions have been developed in the literature regarding the prediction of crack widths, which depend on the existing crack spacing and the average steel strain. A thorough discussion comparing various proposed

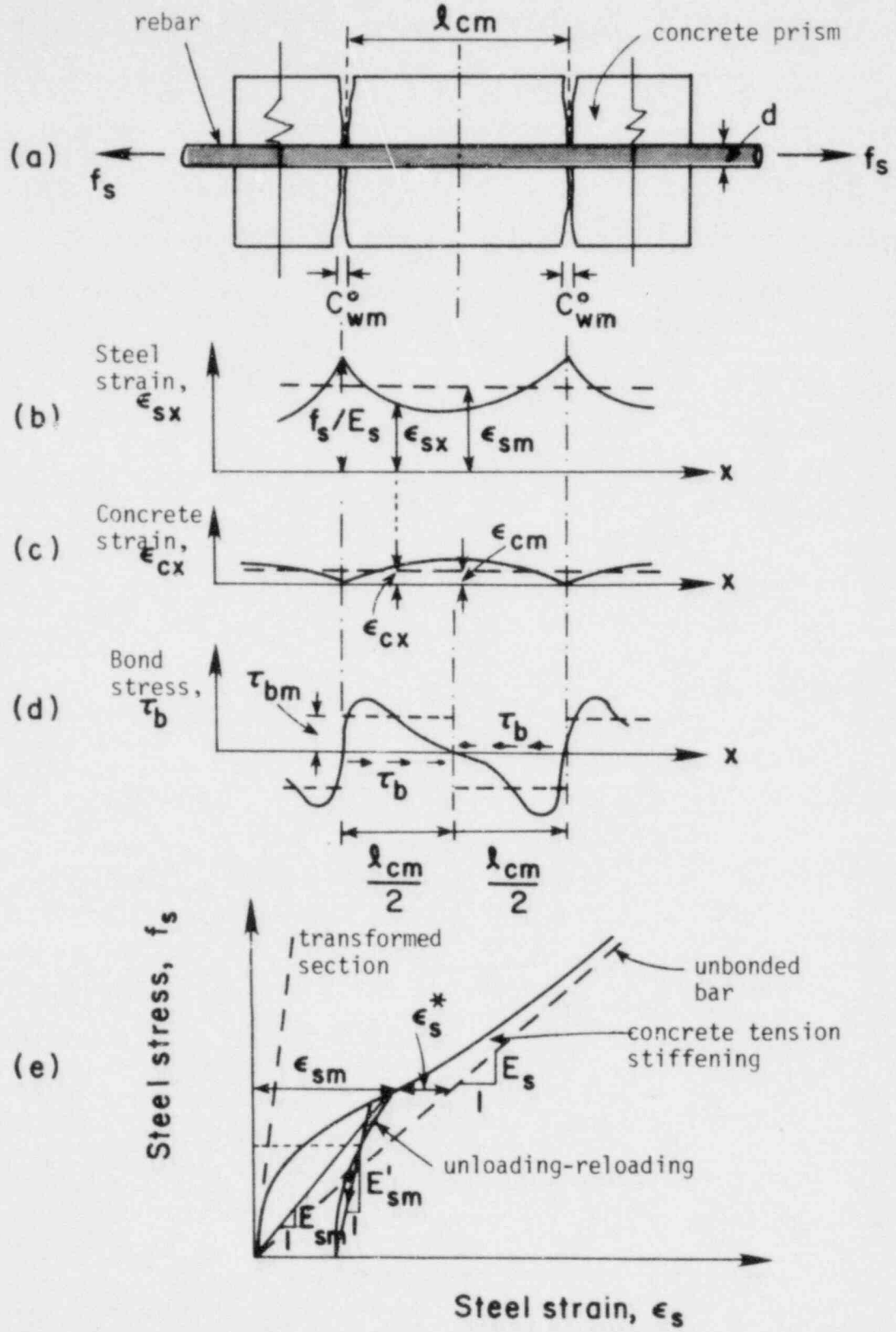

Fig. 3.8. Strain distribution in a rebar embedded in a concrete prism subjected to a tensile stress f_s.

formulae for crack spacing is given in Ref. 19. Since this is outside the scope of the present work only selected expressions for calculating the average crack spacing and the average steel strain are given below. The main parameters influencing the crack spacing are the concrete cover, the bond characteristics of the reinforcement, the steel ratio and the bar size. On the other hand, the average steel strain mainly depends on the steel ratio, the level of the applied steel stress, the concrete tensile strength and the load history.

a) Crack spacing:

Holmberg and Lindgren (beams, slabs, 1970)(Ref. 56):

$$\text{maximum average } \ell_{c,max} = 6 + k_1 \sqrt{\frac{c_b B}{\Sigma d}} \text{ (cm)} \tag{3.7a}$$

Holmberg and Lindgren (walls, 1972)(Ref. 57):

$$\text{minimum average } \ell_{c,min} = 0.055 + 0.144 \frac{d_1 A_t}{\Sigma d^2} \text{ (m)} \tag{3.7b}$$

Gergely and Lutz (1968)(Ref. 45):

$$\text{maximum average } \ell_{c,max} = 2.2 \sqrt[3]{A_t c_s} \tag{3.7c}$$

Broms (1965)(Refs. 15, 16):

$$\text{average } \ell_{cm} = 2 c_s \tag{3.7d}$$

Houde (1973)(Ref. 58):

$$\text{average } \ell_{cm} = 3c_m \tag{3.7e}$$

CEB (1978)(Refs. 21, 71):

$$\text{average } \ell_{cm} = 2(c_m + \frac{s}{10}) + k_2 k_3 \frac{d}{\rho} \tag{3.7f}$$

where

c_m = minimum concrete cover

c_s = minimum cover to bar centroid

$B_o = A_t$ = effective tension area of concrete

d = bar diameter

d_1 = diameter of that bar with the smallest concrete cover

R = gradient effect (pure tension $R = 1$)

s = spacing of bars ($s \leq 15\ \phi$)

ρ = steel ratio

k_1 = coefficient depending on reinforcement type ($k_1 = 0.8$ for deformed bars)

k_2 = 0.4 for deformed bars

k_3 = 0.25 for pure tension.

b) Steel strain:

Geistefeldt (1976)(Ref. 43):

$$\varepsilon_{sm} = \varepsilon_s(1 - A^m) \tag{3.8a}$$

where

$$A = \frac{1}{[1 + (\frac{f_s \rho}{0.9 f_t'} - 1) \frac{\rho}{0.005}]^2}$$

Morita (1965)(Ref. 50):

$$\varepsilon_{sm} = \frac{1}{E_s} (f_s - k_1 k_2 \frac{f_t'}{\rho}) \tag{3.8b}$$

where

$$k_1 k_2 = \frac{1}{4.5 \times 10^3 \varepsilon_s + 0.84} + 0.02 > 0.01$$

CEB (1978)(Refs. 21,71):

$$\varepsilon_{sm} = \varepsilon_s [1 - k_3 k_4 (\frac{f_{sr}}{f_s})^2] \geq 0.4 \varepsilon_{cm} \frac{f_s}{E_s} \tag{3.8c}$$

where

$\varepsilon_s = \frac{f_s}{E_s}$ = steel strain at the crack

m = coefficient indicating the level of concrete stiffening effect (m = 1 for full contribution of concrete; m = 100 for no contribution)

f_s = applied steel stress

ρ = steel ratio = A_s/A_c

f_t' = tensile strength of concrete

f_{sr} = steel stress at first cracking

k_1, k_3 = coefficients taking into account the effect of bond (= 1 for high bond bar; =0.5 for plain bar)

k_4 = coefficient taking into account the effect of the type of load (= 1 for static load; =0.5 for repeated load)

k_2 = ratio of average tensile stress in the midway between two primary cracks to the tensile strength of concrete ft'.

The crack spacing values ℓ_{cm} (in inches) predicted by Eqns. 3.7a to 3.7f for the biaxial specimens employed in this work are summarized in Table 3.E. According to the geometry in the single and the double layer

Table 3.E. Predicted crack spacing values ℓ_{cm} according to Eqns. 3.7a to 3.7f (cracks normal to the steel shown in col. 1).

Steel Rebars at 6 in. Spacing	Average $\ell_{c,min}$ (in) Eqn. 3.7b	Average $\ell_{c,max}$ (in) Eqn 3	Average $\ell_{c,max}$ (in) Eqn. 3.7c	Average ℓ_{cm} (in) Eqn. 3.7d	Average ℓ_{cm} (in) Eqn. 3.7e	Average ℓ_{cm} (in) Eqn. 3.7f
1-No.6 (single layer)	9.1	11.3	10.5	6.0	7.9	12.6
2-No.6 (double layer)	6.2	8.8	9.5	4.5	5.6	9.3

direction of the No.6 bars the following parameters are given,

Single layer: $c_m = 2.62$ in.; $c_s = 3$ in.; $B_o = A_t = 36$ in.^{2}; $d = d_1 = 0.75$ in.; $R = 1$; $s = 6$ in.; $\rho_x = 0.0122$; $k_1 = 0.8$, $k_2 = 0.4$ and $k_3 = 0.25$.

Double layer: $c_m = 1.88$ in.; $c_s = 2.26$ in.; $B_o = A_t = 36$ in.^{2}; $d_{eff} = 1.06$ in. (equivalent bar diameter for two No.6 bars); $R = 1$; $s = 6$ in.; $\rho_y = 0.0244$; $k_1 = 0.8$; $k_2 = 0.4$ and $k_3 = 0.25$.

The above expressions for the effective steel strain ε_{sm} can be written in the following general form

$$\varepsilon_{sm} = \varepsilon_s - \varepsilon_s^* \tag{3.9}$$

where ε_s is the steel strain at the crack (unbonded bar) and ε_s^* is the

effective contribution in tension of the concrete surrounding the bar through the developed average bond stresses τ_{bm} at the concrete-steel interface, and assumed uniformly distributed along each half of the crack spacing (see Fig. 3.8d).

The strain term ε_s^*, at least for deformed bars, can be assumed to be independent of bond characteristics since it is proportional to the ratio

$$\tau_{bm}\, \ell_{cm}/d$$

In the above ratio the numerator does not vary significantly because the bond stresses increase with decreasing crack spacing. Therefore the strain term ε_s^* depends mainly on the bar diameter d.

Several methods and approaches have been proposed to account for the tension stiffening effect of concrete. One approach is to assume a stress-strain curve for the concrete in tension with a specific unloading path. A stepwise (by Scanlon (Ref. 104)), gradual (by Lin and Scordelis (Ref. 75)) or discontinuous piecewise linear path (by Gilbert and Warner (Ref. 48)) have been used in the analysis of slabs and beams (see Figs. 3.9(a,b,c)). An alternative indirect method, employed in Ref. 48, is to assume a modified stress-strain diagram for the steel (see Fig. 3.9d), where the equivalent tensile stress carried by the concrete has been added to the steel stress at the level of the reinforcement. This allows for a decrease in stiffness as the steel stress increases and cracking propagates.

According to the latter approach an effective secant steel modulus E_{sm} for the initial loading describing the overall axial stiffness of the prism can be defined as follows

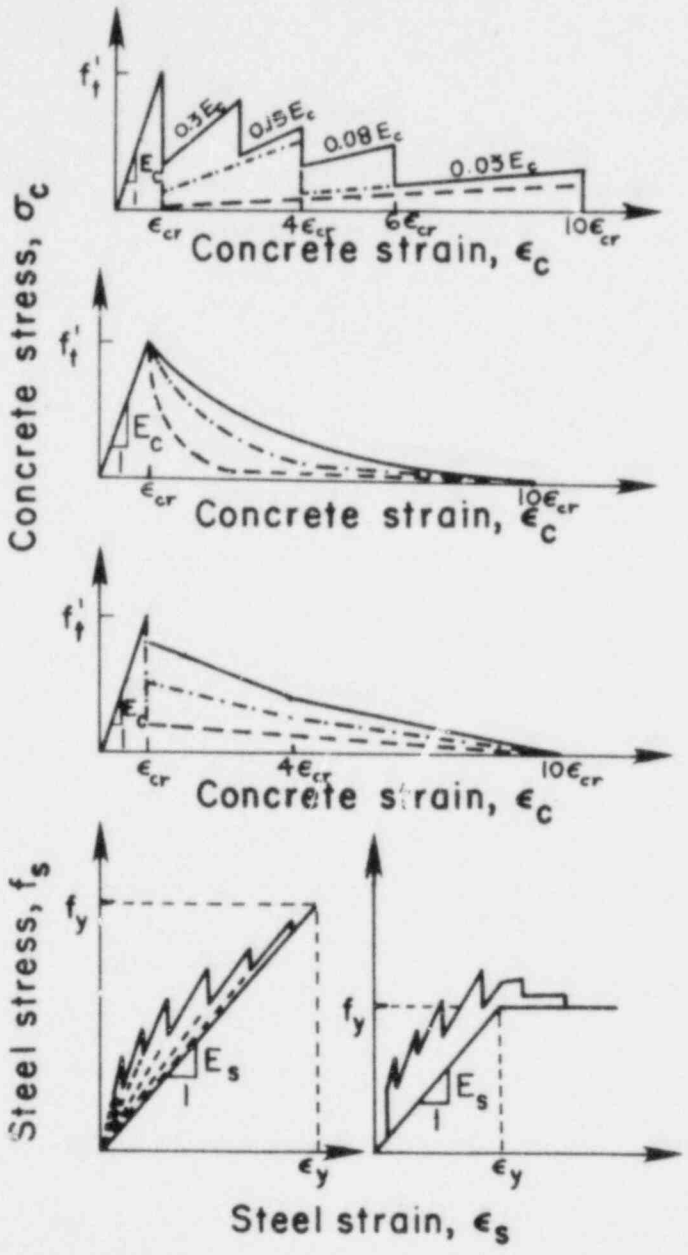

a)Stepped response after cracking
b)Gradually unloading response after cracking
c)Discontinuous unloading response after cracking
d)Modified steel stress-strain diagram

Fig. 3.9. Different methods to account for the tension stiffening effect of concrete.

$$E_{sm} = f_s/\varepsilon_{sm} = f_s/(\varepsilon_s - \varepsilon_s^*) \tag{3.10}$$

As ε_s^* decreases with the degradation of concrete due to cracking, E_{sm} approaches the Young's modulus of the unbonded bar

$$E_s = f_s/\varepsilon_s \tag{3.11}$$

Eqn. 3.10 can be also written as

$$E_{sm} = \psi E_s \tag{3.12}$$

where ψ (a function of ρ and concrete cover) is a magnification factor ($\psi \geq 1$)(Murashev (Ref. 91)) indicating the contribution of concrete.

According to Watstein and Mathey (Ref. 122) the relationship between the ratio E_{sm}/E_s and the applied tensile stress f_s is given in Fig. 3.10 for No.4, No.5, No.6 and No.7 deformed bars (f_y = 102 ksi). For static loading the factor ψ varied between 1.45 ($f_s = 0.3f_y$) and 1.07 ($f_s = 0.9f_y$) for No.6 bars.

The above secant effective moludus E_{sm}, which decreases with increasing values of steel ratio ρ at the same applied steel stress after first cracking, has to be distinguished from the tangent unloading-reloading effective modulus E_{sm}' shown in Fig. 3.8e. Since in the specimens of the present study the tension in the bars is released after an orthogonal cracking pattern has been achieved at a steel stress of 36 ksi, the aforementioned tangent modulus E_{sm}' is really the modulus that affects the axial stiffness of the specimen, instead of the secant E_{sm}. This tangent modulus

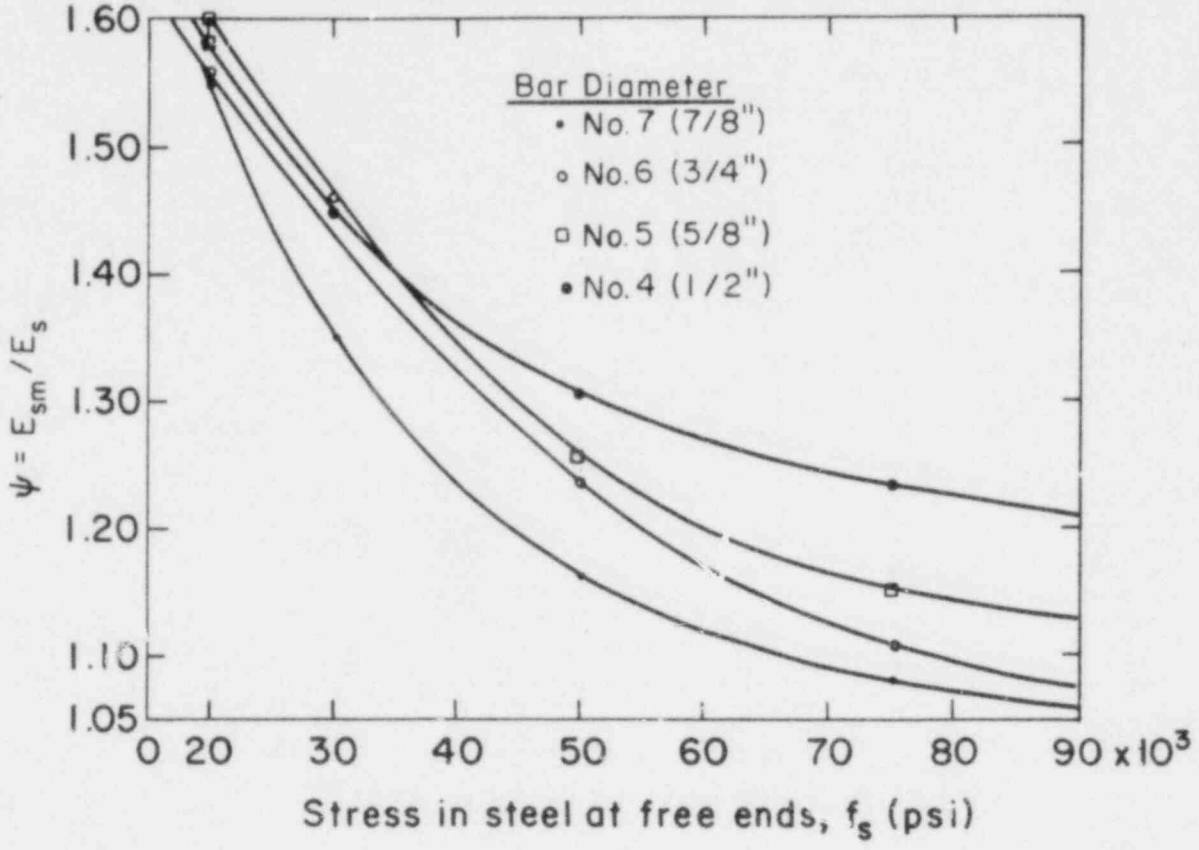

Fig. 3.10. Relationship between the effective modulus of elasticity E_{sm} of an embedded bar and the stress at its end (E_s is the modulus of an unbonded bar)(Watstein and Mathey[5],Ref. 122).

E_{sm}', which will determine the initial extensional stiffness of the already cracked specimens in each direction of the reinforcement, will be described in Section 3.5.

3.3 External Elongation Measurements

To determine an estimate of the extensional stiffness K_N during unloading and reloading, after the initial cracking in the specimens, three tension tests described below were conducted. The total external elongation due to biaxial tension in the steel was measured in both orthogonal directions of the reinforcement in the following three specimens: two reinforced with No.4 (A4-2 and B4-2) and one with No.6 (C6-2) Grade 60 bars. One axial test was also completed on a similar specimen with a single layer of No.6 (C6-1) bars in one direction only. The cracking patterns of all four tensioned specimens after the crack propagation had stabilized and no more new cracks appeared are given in Figs. 3.11a to 3.11d. Unfortunately other priorities in the testing program and a congestion of the measuring devices at the central region of the specimen did not allow these measurements to be performed in more specimens.

To measure the total axial deformation at the exterior surface of the concrete during cracking, special brackets with dial gages were attached on the top of the specimen parallel to the orthogonal reinforcement in both x and y directions. Two dial gages measured the total external longitudinal elongation in the central 2 ft. square region, and two additional gages measured the total elongations over the entire 4 ft. gage length of the specimen. The position of the dial gages, which had a least reading

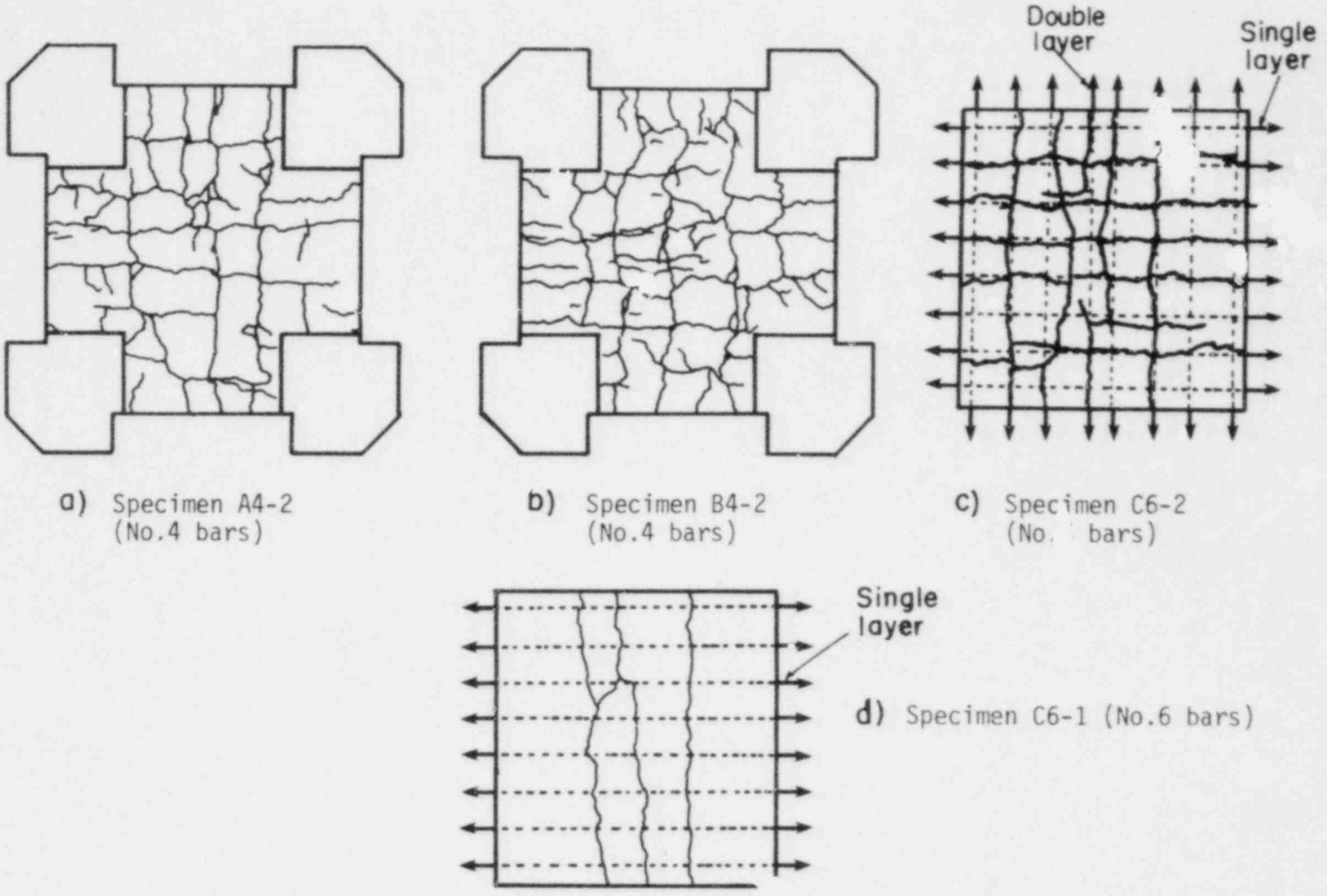

Fig. 3.11. Representative cracking of biaxially (specimens A4-2,B4-2 and C6-2) and uniaxially (specimen C6-1) tensioned flat specimens with No.4 and No.6 embedded bars.

0.0001 inches (0.0025 mm), is shown in Fig. 3.12. The measured total axial deformations on the concrete surface over a 2 and 4 ft. gage length in both orthogonal x and y directions are given in Table 3.F. Also the measured total elongations (over a gage length of 24 in. or 48 in.) in the aforementioned three specimens A4-2, B4-2, and C6-2 are plotted in Figs. 3.13a, 3.13b and 3.13c, respectively, as a function of the applied tensile stress in each bar (No.4 or No.6) for the single and the double steel layers. For comparison the line indicating an unbonded bar is also included in the above figures.

As described earlier, the 1st cycle of tension was applied separately in each direction (uniaxial tension) up to a maximum of $0.6f_y$ in each bar, at which level stabilization of cracking had occurred. Since the direction parallel to the double layer offered higher stiffness than the direction with the single bars, the Poisson's effect was higher in the latter direction. However, at least in the 1st cycle of tensioning, this Poisson's effect was insignificant compared with the overall elongations of up to 0.070 in. (1.8 mm). In addition, progressive cracking due to increasing number of load cycles under tension is expected to diminish it furthermore.

The first tension crack usually formed approximately at the midwidth of the specimen and perpendicular to the double layer of reinforcement at a tensile stress smaller or equal to the stress that caused the first crack normal to the single layer. The tensile stress at cracking was in the range of 0.25 to 0.45 times the yield stress in the bar, with the lower values corresponding to the steel stress in the double layer at cracking. As the tension was increased to the $0.6f_y$ level, additional

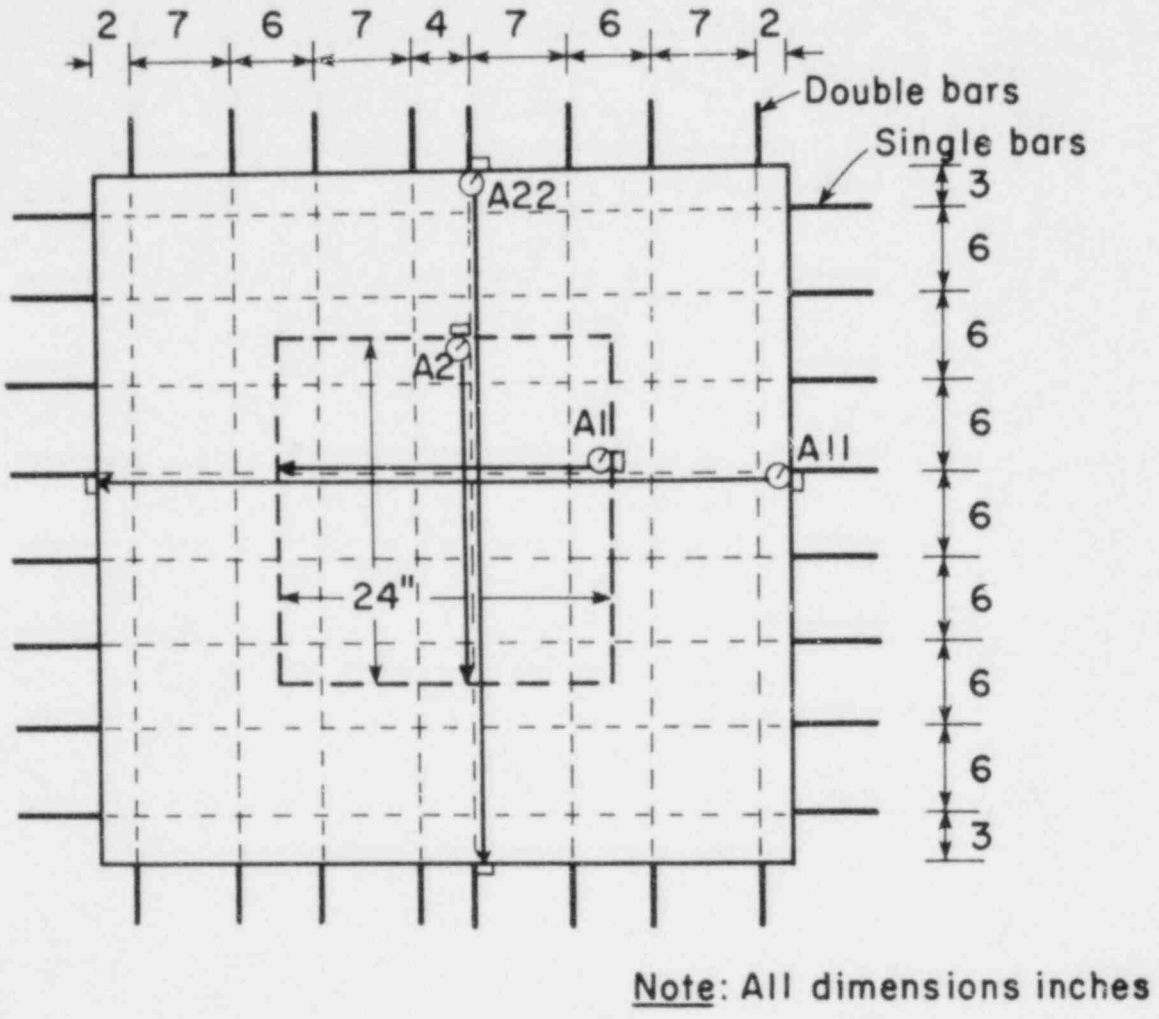

Fig. 3.12. Sketch of the instrumentation setup (dial gages) for measuring the total axial elongation of the concrete in both reinforcing directions (A1 and A2 dial gages measured the total elongation in the 24"x24" central square region of the specimen).

Table 3.F. Summary of tension test results--total surface elongations and average crack widths (measurements presented here are after tension of $0.6f_y$ has been reached in cycle 2).

Specimen No. (1)	Reinforcing Steel (2)	Gage Length, L(in) (3)	No. of Cracks, N_c (4)	f_s/f_y (5)	ΔL (in) (6)	c^o_{wm} (in) (7)
A4-2	S(2)↓	24	3	0	0.025	0.0083
	D(2)↓	24	4		0.009	0.0022
	S(2)↓	24	3	0.3	0.048	0.016
	S(3)↑	24	3		0.042	0.014
	D(2)↓	24	4		0.015	0.0038
	D(3)↑	24	4		0.013	0.0032
	S(2)↑	24	3	0.6	0.062	0.0207
	S(3)↑	24	3		0.069	0.023
	D(2)↑	24	4		0.022	0.0055
	D(3)↑	24	4		0.022	0.0055
	S(3)↑	24	3	0.9	0.109	0.0363
	D(3)↑	24	4		0.040	0.010
B4-2	S(2)↓	24	3	0	0.028	0.0093
	S(2)↓	48	5		0.034	0.0068
	D(2)↓	24	4		0.015	0.0038
	D(2)↓	48	6		0.019	0.0032
	S(2)↓	24	3	0.3	0.060	0.020
	S(3)↑	24	3		0.054	0.018
	S(2)↓	48	5		0.074	0.0148
	S(3)↑	48	5		0.067	0.0134
	D(2)↓	24	4		0.038	0.0095
	D(3)↑	24	4		0.035	0.0083
	D(2)↓	48	6		0.046	0.0077
	D(3)↑	48	6		0.043	0.0072
	S(2)↑	24	3	0.6	0.076	0.0253
	S(3)↑	24	3		0.077	0.0257
	S(2)↑	48	5		0.092	0.0184
	S(3)↑	48	5		0.097	0.0194
	D(2)↑	24	4		0.054	0.0135
	D(3)↑	24	4		0.053	0.0132
	D(2)↑	48	6		0.067	0.0112
	D(3)↑	48	6		0.066	0.011
C6-2	S(2)↓	24	3	0	0.006	0.002
	D(2)↓	24	4		0.004	0.001
	S(2)↓	48	5		0.022	0.0044
	D(2)↓	48	6		0.007	0.0012

(Continued)

Table 3.F. (Continued)

Specimen No. (1)	Reinforcing Steel (2)	Gage Length, L(in) (3)	No. of Cracks, N_c (4)	f_s/f_y (5)	ΔL (in) (6)	c^o_{wm} (in) (7)
C6-2 (cont'd)	S(2)↓	24	3	0.3	0.036	0.012
	S(3)↑	24	3		0.022	0.0073
	S(2)↓	48	5		0.057	0.0114
	S(3)↓	48	5		0.040	0.008
	D(2)↓	24	4		0.016	0.004
	D(3)↑	24	4		0.015	0.0038
	D(2)↓	48	6		0.026	0.0043
	D(3)↑	48	6		0.025	0.0042
	S(2)↑	24	3	0.6	0.054	0.018
	S(3)↑	24	3		0.039	0.013
	S(2)↑	48	5		0.085	0.017
	S(3)↑	48	5		0.065	0.013
	D(2)↑	24	4		0.026	0.0065
	D(3)↑	24	4		0.025	0.0062
	D(2)↑	48	6		0.042	0.007
	D(3)↑	48	6		0.043	0.0072
	S(3)↑	24	3	0.9	0.050	0.0167
	S(3)↑	48	5		0.082	0.0164
	D(3)↑	24	4		0.033	0.0082
	D(3)↑	48	6		0.046	0.0077
C6-1	S(2)↓	24	3	0	0.027	0.009
	S(2)↓	24	3	0.3	0.056	0.0187
	S(3)↑	24	3		0.054	0.018
	S(2)↑	24	3	0.6	0.083	0.027
	S(3)↑	24	3		0.086	0.0287
	S(3)↑	24	3	0.9	0.099	0.033

Notes:

(1) A4-2 (two-way reinforcement of No.4 bars)
B4-2 (duplicate specimen of A4-2)
C6-2 (two-way reinforcement of No.6 bars)
C6-1 (one-way/single layer of No.6 bars)

(2) S = single layer; D = double layer
() = cycle No.
↑ = loading; ↓ = unloading

(4) N_c = No. of primary cracks at $f_s/f_y = 0.6$ (Cycle 1)

(7) $c^o_{wm} = \Delta L/N_c$

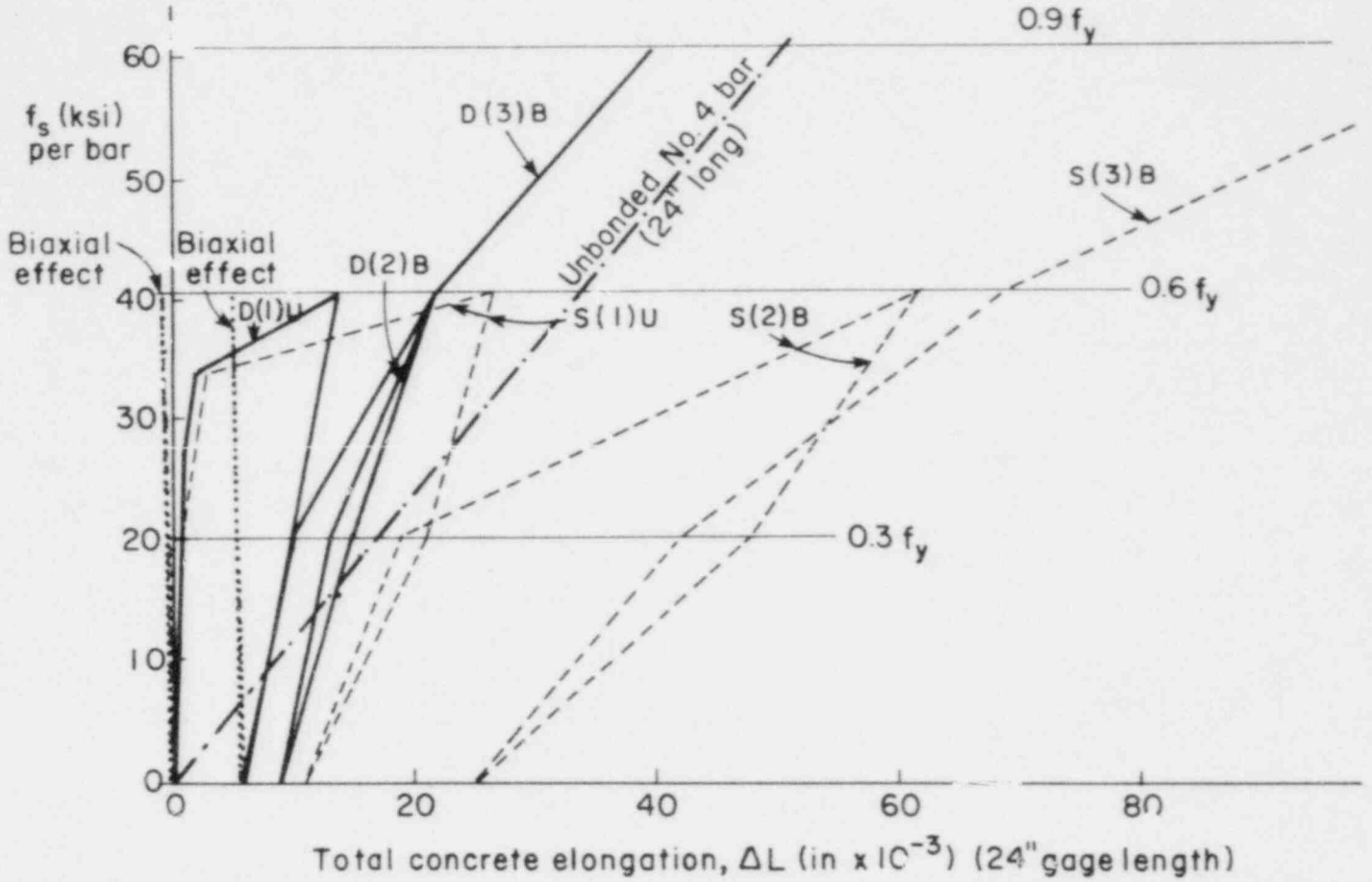

a) Specimen A4-2

Fig. 3.13. Measured total concrete elongation versus the applied bar stress.

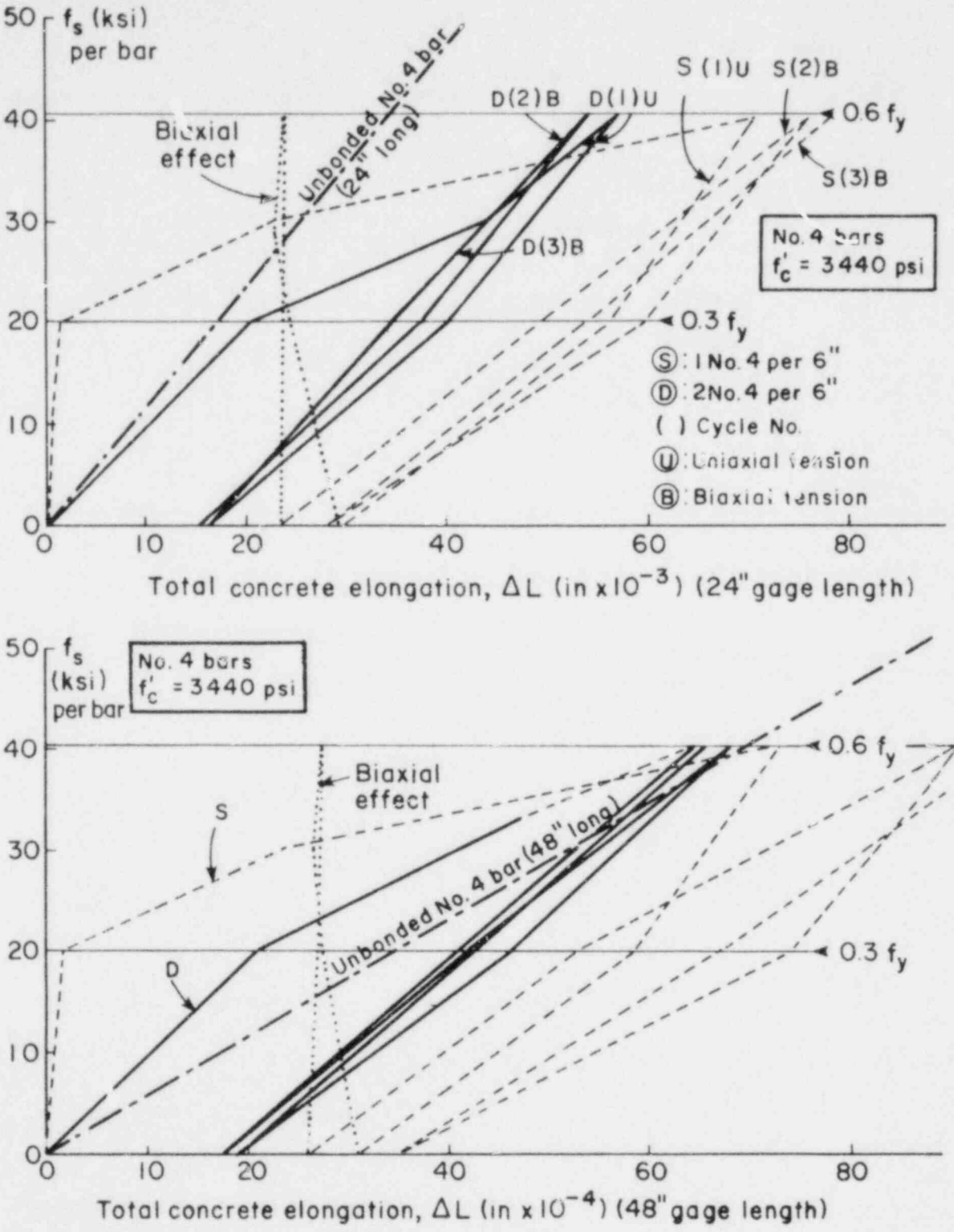

b) Specimen B4-2

Fig. 3.13. (Continued)

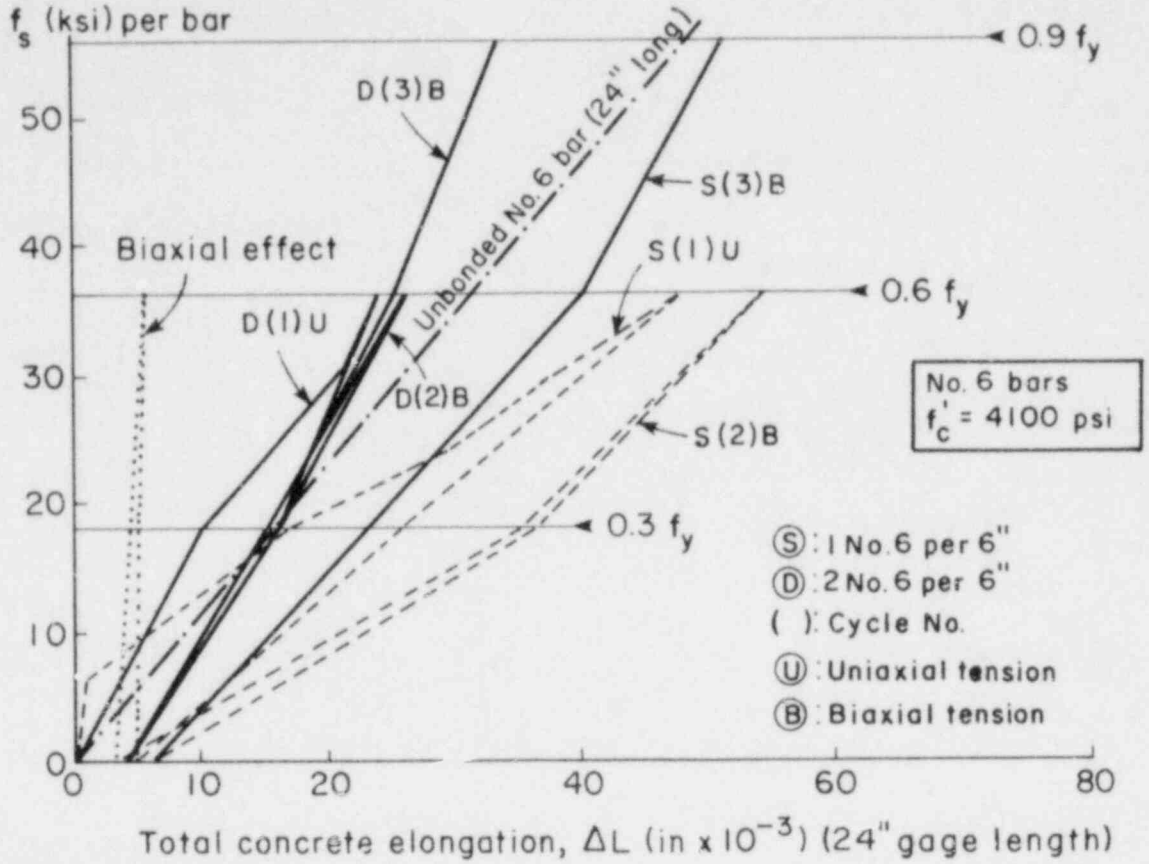

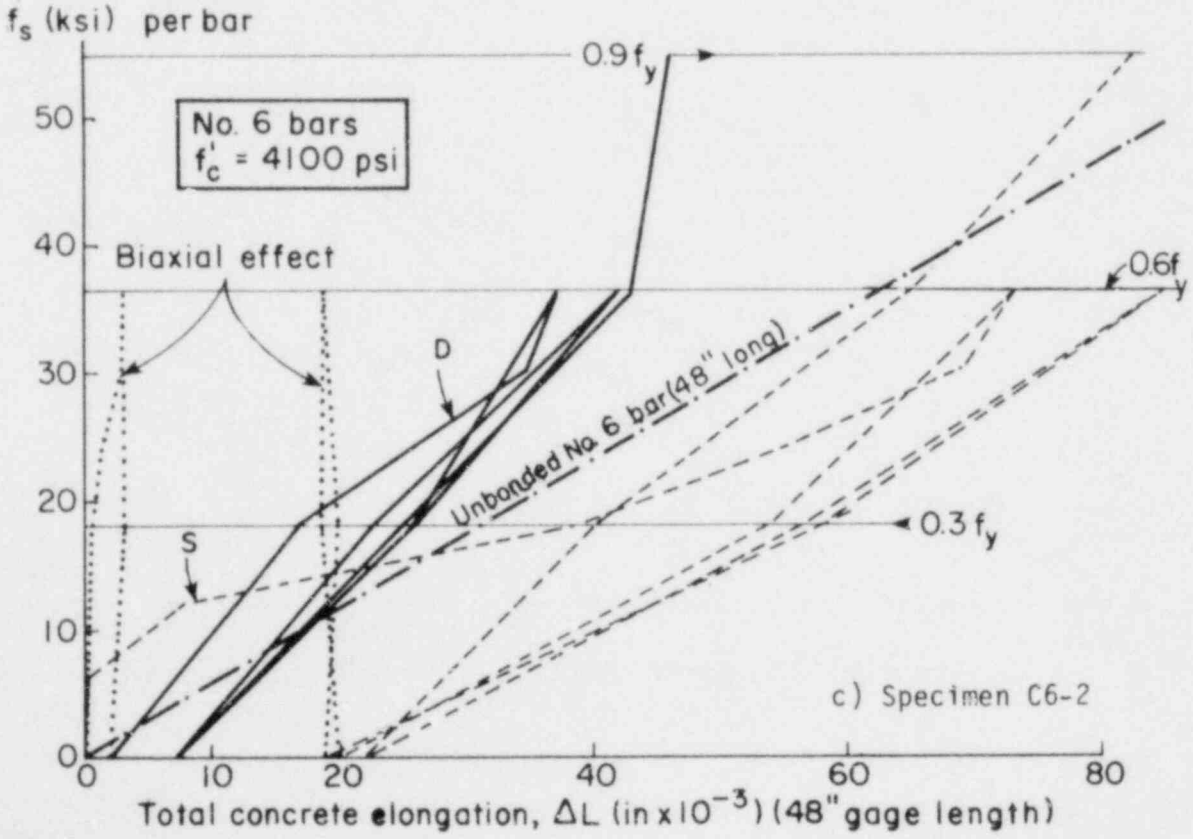

Fig. 3.13. (Continued)

orthogonal cracks formed over the entire width of the specimen. About 4 to 5 and 6 to 7 cracks formed normal to the single and the double layers of bars, respectively.

After the initial loading and unloading (1st cycle) was completed in each direction and the specimen was subjected to biaxial tension for two additional cycles, significant deterioration in the bond mechanism was observed. During unloading appreciable irrecoverable crack openings were recorded in both directions. Values of up to 0.030 and 0.015 in. residual total crack deformations, in a gage length of 24 in., were measured parallel to the single and the double layer direction, respectively. These values correspond to average individual crack widths of about 0.006 in. and 0.002 in. for the cracks normal to the single and the double layer directions, respectively. Therefore, some residual tensile stresses were expected in the steel crossing the cracks even after the release of the tensile load in the bars. This was also observed by Bresler and Bertero (Ref. 13)(see Fig. 3.14) and Mirza and Houde (Ref. 89). One explanation of the above hysteretic behavior is believed to be the wedging action of the uncracked concrete teeth inclined to the bars along the steel-concrete interface (see Fig. 3.15), which did not permit full recovery of the local deformations.

Due to the fact that the critical tension level of $0.6f_y$ was reached and surpassed and the orthogonal cracking stabilized, no significant further degradation was expected at subsequent cycles. Thus, the axial deformations recorded during the unloading-reloading stage (cycles 2 and 3) can provide a realistic estimate of the extensional stiffness, at least for the initial cycles of shear loading. An approximately linear response was

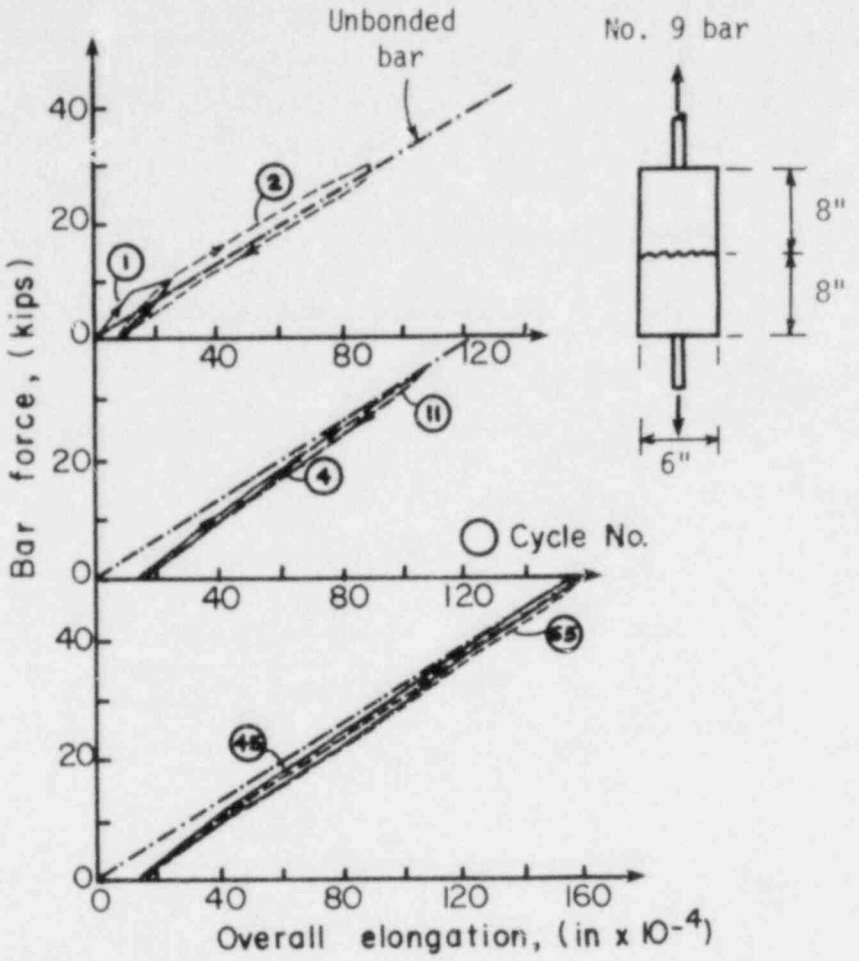

Fig. 3.14. Exterior over-all elongation (Bresler and Bertero, Ref. 13)

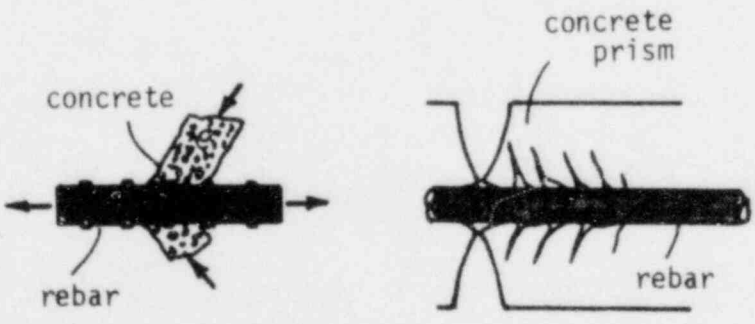

Fig. 3.15. Wedging action and internal cracking of an axially tensioned concrete prism reinforced with a single bar.

observed in the load-deformation curves during the 3rd cycle of tensioning, which confirmed in a way the above argument of stable response. Similar behavior was observed by Bresler and Bertero (Ref. 13)(see Fig. 3.14) and Edwards and Yannopoulos (Ref. 21)(see Fig. 3.16).

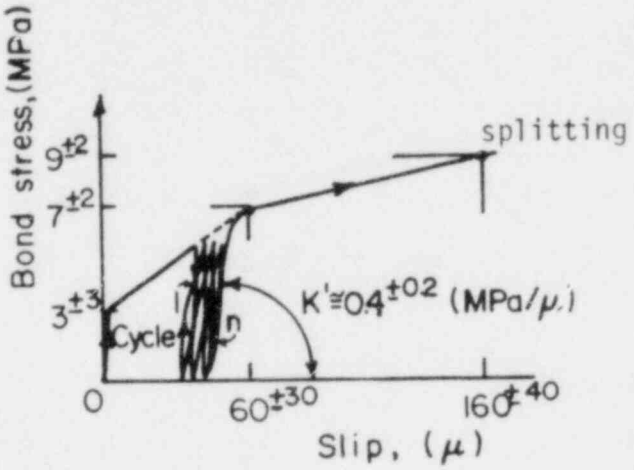

Fig. 3.16. Repeated local bond-slip. An experimental example together with scatter limits (based on Edwards and Yannopoulos, Ref. 21).

There was an apparent shift of the load-deformation curve to the right for the single layer, resulting in crack openings larger (by a factor of about 2) than the corresponding deformations for the double layer. The double layer of bars had a minimum concrete cover, which was about 2/3 of the available minimum concrete cover in the single layer. Thus, since the surface crack width is known to be a function of the concrete cover, smaller crack widths at smaller crack spacings would result normal to the double layer. In addition, since there was less concrete to carry the tensile stresses transferred by the double layer steel, it is reasonable to

assume that most of the internal cracking would have occurred at the $0.6f_y$ tension level before releasing the load in that direction. Therefore the unloading and reloading stiffness is likely to be higher in the double layer than in the single layer (see Figs. 3.13a to 3.13c). On the other hand, larger crack openings were present at the tension cracks perpendicular to the single layer causing larger residual crack widths at the tension cracks after the tension in the bars was released.

3.4 Crack Spacing Measurements

The crack spacing of the two sets of orthogonal tension cracks formed at a biaxial tension level of $0.6f_y$ were measured in a total of eighteen specimens (the sixteen specimens for the shear tests plus two of the axial test specimens). Above the $0.6f_y$ stress level no additional cracks appeared on the surface of the specimens.

All crack spacing measurements were performed directly above the reinforcement under tension in order to be consistent, since in between the bars the crack spacings could be different. Recording the crack spacings of the cracks induced by the eight single and double bars within the 48 in. wide central flat region of the biaxially reinforced specimens, a total statistical sample of 654 and 714 measurements was accumulated for the cracks perpendicular to the single and double bars, respectively. As shown in Table 3.G, the average spacing of the cracks normal to the single layer was found to be 6.85 in. (17 mm) and normal to the double layer 6.37 in. (16 mm) with a standard deviation of 2.48 in. (6.3 cm) and 2.08 in. (5.3 cm), respectively. Therefore, the scatter of the sampling data was about ±36% to ±33% in the direction of the single and the double bars, respectively. As stated by Mirza

and Houde (Ref. 89) and others, the average crack spacing will be approximately 1.5 times the minimum crack spacing and thus a minimum value of 33% scatter was anticipated. Having in mind that the formation of cracks is influenced by variables with their own statistical scatter, such as the tensile strength of concrete and shrinkage cracking, the scatter in the measured values of crack spacing could very well reach the 50% level.

It is shown in Table 3.G that if the crack spacing measurements in the four 1 ft. wide outer regions in each direction were included in the sampling

Table 3.G. Statistical measure of crack spacing ℓ_{cm} in eighteen flat specimens for the cracks normal to the reinforcing steel, shown in col. 1 (No.6 bars).

Reinforcing Steel (1)	Region Sampled (2)	No. of Crack Spacing Measurements (3)	Average Crack Spacing, ℓ_{cm}(in) (4)	Standard Deviation (in) (5)	Average Max. Crack Spacing, $\ell_{c,max}$(in) (6)	Average Min. Crack Spacing, $\ell_{c,min}$(in) (7)
Single layer	24" wide	458	7.23	2.55	11.33	3.44
	48" wide	654	6.85	2.48	11.50	3.11
Double layer	24" wide	507	6.56	2.16	10.72	3.33
	48" wide	714	6.37	2.08	11.00	3.22

Notes:

(1) All eighteen specimens were reinforced with No.6 bars; This reinforcing steel caused the cracks with an average spacing shown in col. 4.

(2) The 24 inch wide region corresponds to the middle 2 ft. wide flat section of the specimen.

data, the calculated average crack spacing would drop by about 5% and 3% in the single and the double layer, respectively. This is probably due to the

effect of the four thickened corners in lowering the average crack spacing value expected otherwise in the 6 in. thick flat specimens. Thus, the measurements in the 2 ft. square central region were more representative of the real cracking pattern.

Although the experimental data from the results of one specimen reinforced with a single layer of No.6 bars in one direction only (C6-1) was not sufficient for definite conclusions, a general trend could be identified. In specimen C6-1, definitely larger external elongations were recorded at the concrete surface as compared to its companion specimen C6-2 reinforced with a two-way reinforcement. Tensioning of the former specimen resulted in larger crack spacings with a minimum spacing larger than the average minimum spacing in the biaxial specimens. Possible reasons for the smaller extensional stiffness experienced by specimen C6-1 were the nonexistence of transverse steel that could cause larger number of cracks parallel to it and the larger concrete cover present. Also only three primary cracks formed on the surface of the specimen, as shown in Fig. 3.11d. Thus, since these three cracks happened to form within the 2 ft. gage length with no cracks at the outer 1 ft. regions the measurements at the central 2 ft. gage length could lead to false conclusions as far as the effective extensional stiffness of the entire 4 ft. wide specimen was concerned.

In general, the tension cracks tended to form over the transverse reinforcement, where the net concrete area to resist tension was minimum (see the cracking pattern in Fig. 3.11c). This showed that the crack spacing ℓ_{cmi} (i = x, y) in the biaxially tensioned reinforced concrete panels depended not only on the concrete cover, bar spacing, bar diameter and

reinforcement ratio as suggested by Broms (Refs. 15 and 16), Goto (Ref. 49), CEB Bulletin (Ref. 21), Gergely and Lutz (Ref. 45), Holmberg and Lindgren (Refs. 56 and 57), Rao (Ref. 101) and others, but also on the spacing of the transverse steel in the orthogonal direction (tests on two-way slabs by Nawy and Blair (Ref. 92)). The influence of transverse reinforcing was also mentioned by Beeby (Ref. 10) in his attempt to develop a more general cracking theory of hardened concrete. He stated that, the transverse bars in walls and slabs under membrane tension ". . . can act as crack formers. . . ." Additional experimental evidence supporting the latter was provided by Lenschow and Sozen (Ref. 71), where the crack spacing in their orthogonally reinforced specimens B4 and B10 averaged the spacing of the transverse reinforcement in each direction.

The above observation appeared to be more consistent for the cracks parallel to the single bar layer (produced by tensioning the bars in the double layer), since the single layer bars were uniformly distributed over the width of the specimen at 6 inches spacing. The bars in the double layer, however, were spaced in pairs at varying distances center to center (5 to 7 inches), due to spacing constraints of the tensioning reaction frame. Thus, it is clear that in some cases of orthogonally reinforced flat concrete structural elements the spacing of transverse reinforcement could be the controlling factor in the crack formation, if it is not much smaller or larger than the minimum crack spacing expected in the case with no transverse steel present. The scatter of the data was slightly smaller in the case of cracking normal to the double layer, which meant that a more uniform crack spacing existed in that direction. Thus, the crack spacing perpendicular to the heavier reinforced section was bound to be closer to

the uniform 6 in. spacing of the single bars than the more variable crack spacing in the orthogonal direction. The chances that the transverse bar spacing controlled the tension cracking were much higher in the former case.

Since the primary parallel cracks would be a major cause of internal secondary longitudinal cracks at the transverse reinforcement, a higher level of bond deterioration was expected for the biaxially tensioned specimens compared with specimens under uniaxial tension, especially for tension levels higher than $0.6f_y$ and under fully reversing shear loads.

It should be also pointed out that smaller crack spacings were recorded for the cracks normal to the double layer. This verifies the well established fact that crack spacing is proportional to the ratio of the bar diameter to the reinforcement ratio d/ρ (Beeby (Ref. 10)).

Comparing the measured crack spacing values given in Table 3.G with the predicted values according to Eqns. 3.7a to 3.7f (see Table 3.E, page), it appears that, although the above formulae do not include the effect of transverse steel, most of them give reasonable values. Regarding the average crack spacing ℓ_{cm}, Eqn. 3.7f (CEB) seems to overestimate it in both reinforcing directions while Eqns. 3.7d (Broms) and 3.7e (Houde) predict acceptable values, especially for the spacing of the cracks normal to the single layer (the orthogonal direction is more affected by the transverse steel). Satisfactory predictions for the maximum average crack spacing $\ell_{c,max}$ (col. 6 in Table 3.G) are given by Eqns. 3.7a (Holmberg and Lindgren) and 3.7c (Gergely and Lutz).

For a general cracking theory to be developed a more extensive experimental study on biaxial tension tests is definitely needed. Important

parameters such as biaxial tension, ratio of the biaxial tensile stresses, reinforcement ratio in each direction, and spacing of the transverse bars and their effect on the effective axial stiffness must be investigated in more detail.

3.5 Extensional Stiffness Expression

An expression for the estimation of the unloading-reloading extensional stiffness $K_{Ni}(i = x, y)$ in orthogonally precracked membrane two-way reinforced concrete elements is developed in this section assuming uniformly distributed parallel cracks at an average crack spacing $\ell_{cmi}(i = x, y)$ in the x and y reinforcing directions (see Fig. 3.17).

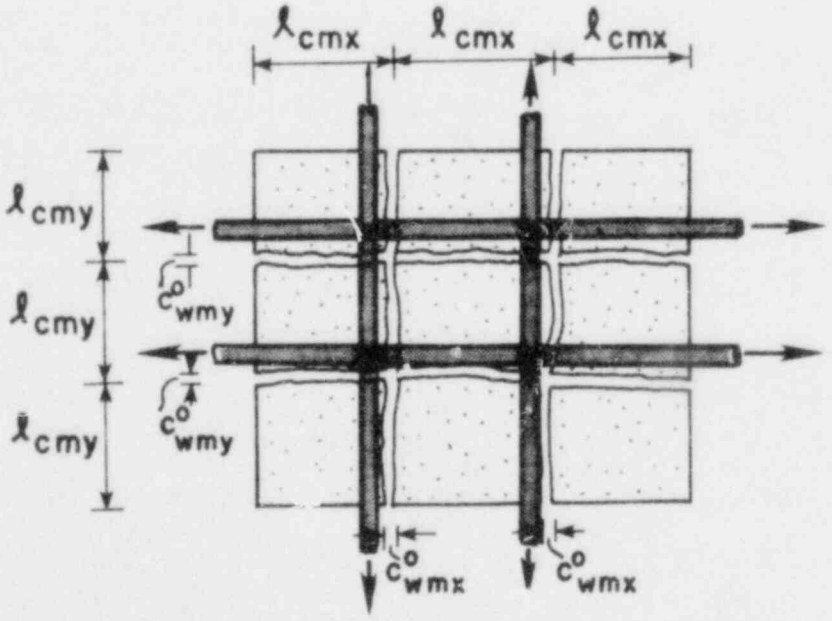

Fig. 3.17. Idealized orthogonally cracked reinforced concrete element.

It is assumed that the axial stiffness K_{Ni} of a reinforced concrete prism is proportional to the amount of steel and inversely proportional to a length L_i taken as the basis of the axial measurements in both directions, that is,

$$K_{Ni} = A_{si}E'_{smi}/L_i \tag{3.13}$$

where

E'_{smi} = tangent effective modulus of steek (ksi) in the i = x, y direction,

A_{si} = steel cross-sectional area in the i(x, y) direction, and

L_i = base length in the i(x, y) direction.

There were no internal measurements of the steel strains conducted in the specimens tensioned. Instead, the external elongations recorded on the concrete surface will be used to determine an estimate of the average steel strain ε_{smi} as a function of the applied steel stress f_{si}(i = x, y). This average steel strain is calculated from the following relation

$$\varepsilon_{smi} = \Delta L_i/L_i \tag{3.14}$$

where ΔL_i is the total elongation measured within a given gage length (in.), and L_i is the gage length (14 or 48 in.). After the steel strain is determined, an estimate of the tangent effective modulus E'_{smi} can be calculated.

How accurately Eqn. 3.14 predicts the internal average steel strains depends on the actual position of the dial gages shown in Fig. 3.18. If for the central gage length of 24 in. the targets were ideally at A and B, that is at the midway between the orthogonal cracks, the steel strains $\Delta L/L$ measured should be equal to the actual strains ε_{sm} because of symmetry. However, if the targets happen to be closer to the points A' and B' at the crack tips, the measurements will result in higher calculated values of ε_{sm} than actually exist. On the other hand, if the gage length happens to be the distance A"B" the steel strains will be underestimated. The targets for the 48 in. gage length were placed at the edges of the specimen

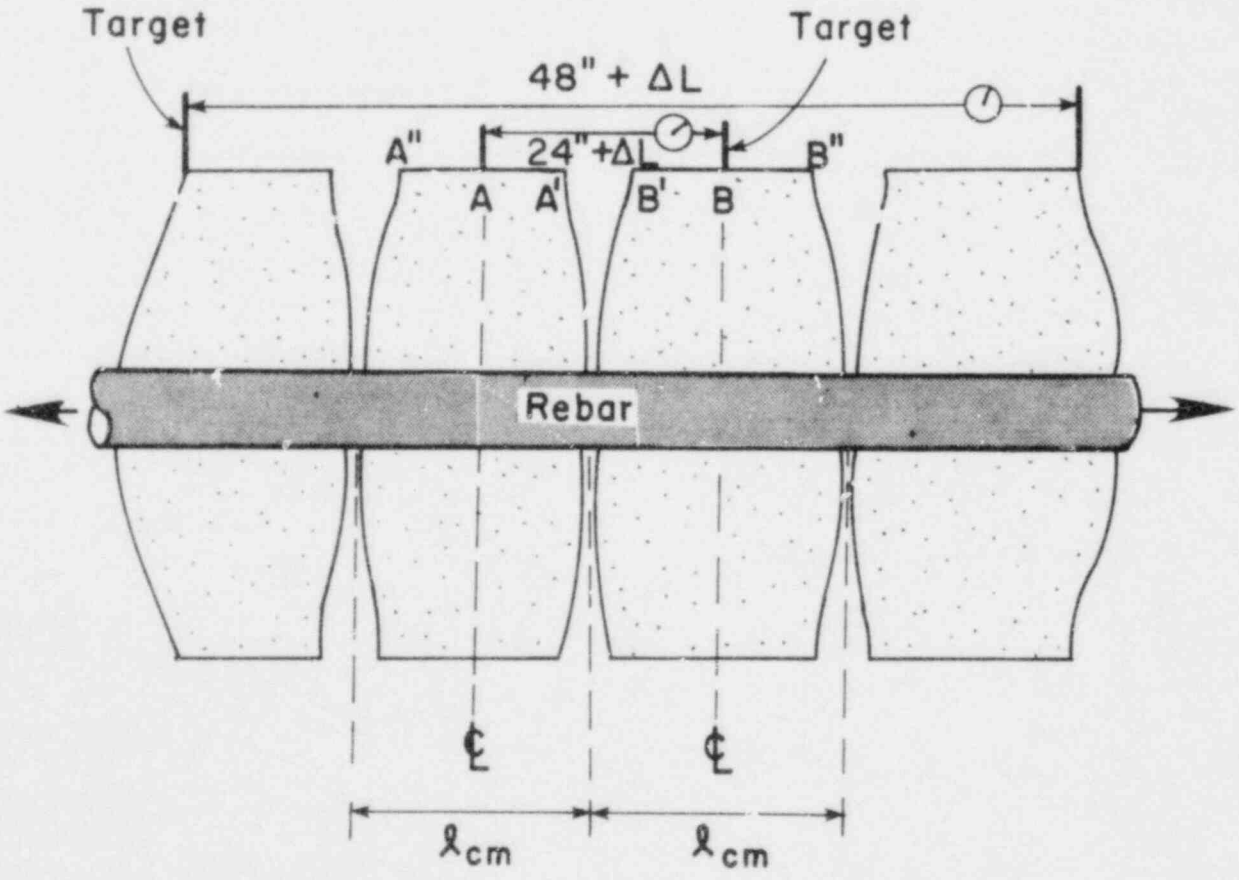

Fig. 3.18. Positioning of the gage-targets on the concrete surface.

and therefore the elongations measured will result in lower steel strains since they are not taking into account the expansion of the concrete at the level of the reinforcement (see Fig. 3.18). It is believed that by utilizing the data based on both gage lengths, the accuracy of Eqn. 3.14 will be improved.

As shown in Figs. 3.13a to 3.13c, in the post-cracking unloading-reloading stage (after the specimen has been cracked at $0.6f_y$ tension level) the axial elongation $\Delta L_i (i = x, y)$ varies approximately linearly versus the applied axial tension in terms of the dimensionless stress ratio $a_{si} = f_{si}/f_y$ $(i = x, y)$ in each direction.

Thus, the assumed axial stiffness equation for the composite concrete-steel element at the level of the bar during reloading is of the following form,

$$\epsilon_{smi} = c_1 + c_2 a_{si} \tag{3.15}$$

where c_1 and c_2 are determined from the available experimental data. The constant c_1 is the residual steel strain present after the full release of the tensile load in the bars.

The trend of the data shows that for a given steel stress the average steel strain is proportional to the steel ratio ρ. Thus, ϵ_{smi} will be proportional to the ratio

$$f(\rho_i) = \rho_i E_s \tag{3.16}$$

To determine the relative effect of the reinforcement ratio ρ_i on the steel strain in the three biaxial tests conducted a dimensionless factor $\lambda_{\rho i}$ is introduced,

$$\lambda_{\rho i} = f(\rho_i)/f^*(\rho_i) \tag{3.17}$$

where $f(\rho_i)$ is a function of ρ_i and E_s, given for any specimen by the relation 3.16, and $f^*(\rho_i)$ is the arithmetic value of $f(\rho_i)$ in Eqn. 3.16 for a specific case taken as the basis of the comparative study.

Choosing specimen C6-2(No.6 bars) as the specimen to which the other two specimens A4-2 and B4-2 are to be compared, the following values for $f^*(\rho_i)$ are calculated in each direction,

$$\begin{aligned} &\underline{i = x \text{ (single layer)}}: \quad f^*(\rho_x) = 0.0122 \times 28000 = 5.6 \text{ (ksi)} \\ &\underline{i = y \text{ (double layer)}}: \quad f^*(\rho_y) = 2\, f^*(\rho_x) = 11.2 \text{ (ksi)} \end{aligned} \tag{3.18}$$

Thus, from Eqns. 3.16, 3.17 and 3.18 we get

$$\begin{aligned} &\underline{i = x}: \quad \lambda_{\rho x} = 0.18\, \rho_x E_s \\ &\underline{i = y}: \quad \lambda_{\rho y} = 0.09\, \rho_y E_s \end{aligned} \tag{3.19}$$

The normalized average steel strains

$$\varepsilon_{smi}^* = \lambda_{\rho i}\, \varepsilon_{smi} \tag{3.20}$$

are plotted versus the applied biaxial tensile stress ratio a_{si} in Fig. 3.19 for all three axial tests.

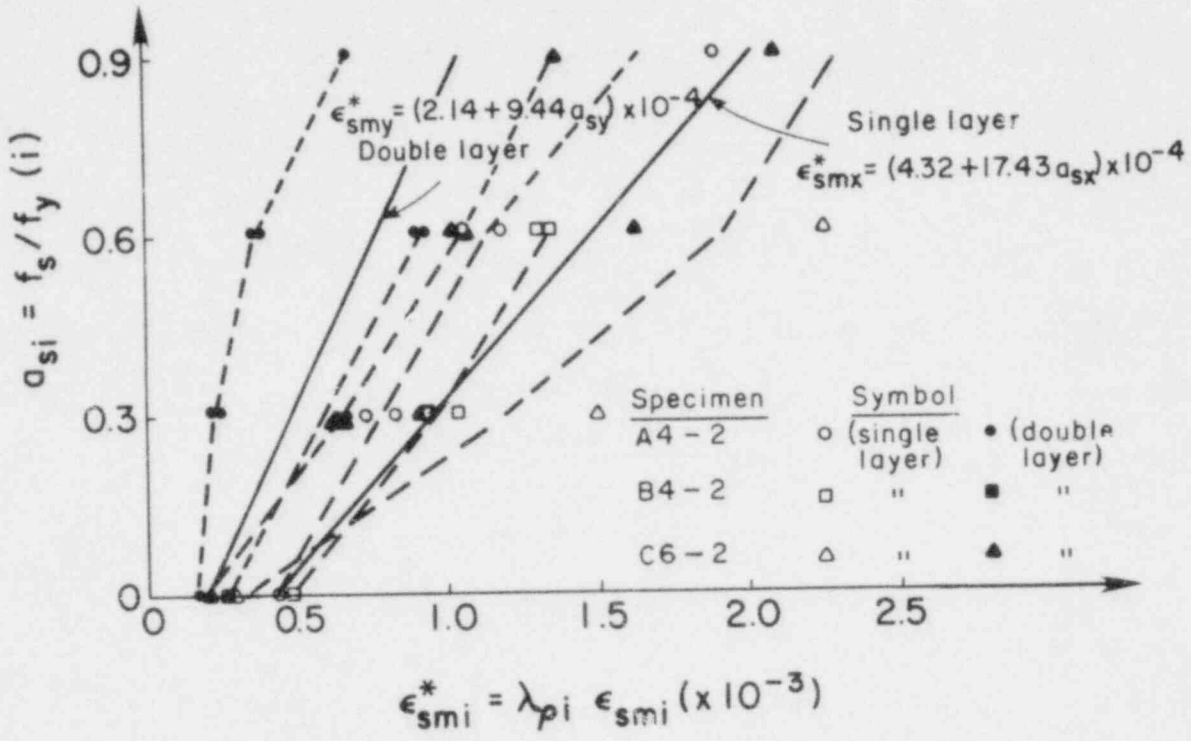

Fig. 3.19. Normalized steel strain values ϵ_{smi}^* versus the applied bar stress to yield strength ratio.

A linear regression analysis of the data with a correlation factor of 0.82 and 0.78 in the x and y direction, respectively, results in the following straight lines:

$$\underline{i = x}: \quad \epsilon_{smx}^* = (4.32 + 17.4\ f_{sx}/f_y) \times 10^{-4}$$

$$\underline{i = y}: \quad \epsilon_{smy}^* = (2.14 + 9.4\ f_{sy}/f_y) \times 10^{-4} \quad (\approx \epsilon_{smx}^*/2, \text{ for } f_{sx} = f_{sy}) \tag{3.21}$$

Although the scatter of the data points in Fig. 3.19 is considerable, the correlation factors of 0.82 and 0.78 are satisfactory since they depend on variables with high experimental uncertainty.

Substituting ε_{smi}* from Eqn. 3.20 in terms of the calculated average steel strain ε_{smi} in each test, Eqn. 3.21 gives,

$$\varepsilon_{smi} = [(2.4 + 10.3\ a_{si})\ \frac{f_y}{\rho_i E_s}]\ x\ 10^{-3} \qquad (3.22)$$

From the above Eqn. 3.22 the tangent effective modulus E'_{smi} of the specimens tensioned in the orthogonal x and y directions is given by the following expression,

$$E'_{smi} \simeq 100\ \rho_i E_s \qquad (3.23)$$

In Table 3.H the computed values of E'_{smi} using relation 3.23 are tabulated in col. 3 for the limited extensional tests conducted here. Also the effective modulus E'_{smi} calculated from a regression analysis of the data of each test specimen separately are displayed in col. 4 for comparison. The results for steel ratios between 0.010 and 0.025 (the steel ratios usually present in actual containments) appear reasonable. Surprisingly, for ρ equal to 0.0055, values for E'_{smi} as low as 60% of the Young's modulus of an unbonded bar E_s are computed. A possible explanation for this may be that the smaller number of cracks present normal to the No.4 bars cause larger surface crack openings that would tend to produce unreliable estimates for the steel strains. The longitudinal steel

Table 3.H. Comparison between the predicted and experimental effective steel modulus E'_{smi} (i = x, y) values.

Specimen No. (1)	ρ_i (2)	E'_{smi} (Eqn. 3.23) (3)	E'_{smi} (Exper.) (4)
A4-2 (No.4)	0.0055 (x)	0.6 E_s	0.6 E_s
	0.0110 (y)	1.1 E_s	1.7 E_s
B4-2 (No.4)	0.0055 (x)	0.6 E_s	1.0 E_s
	0.0110 (y)	1.1 E_s	1.2 E_s
C6-2 (No.6)	0.0122 (x)	1.2 E_s	1.3 E_s
	0.0244 (y)	2.4 E_s	2.0 E_s

Note:

(4) The experimental measurements based on both 24 and 48 inch gage lengths are used to compute E'_{smi}.

strains for each specimens based only on the 24 in. gage length are plotted together with the unbonded bar for comparison in Fig. 3.20.

More extensive tests have to be performed with a wider variety of steel ratios and bar sizes so that more accurate relations between the effective tangent modulus E_{sm}' and the steel ratio and bar diameter can be obtained. Such an expression could be of the following power form

$$E_{sm}' = \frac{g_1 \rho^{g_2} E_s}{d} \tag{3.24}$$

with g_2 less than 1.0.

Based on Eqn. 3.23 for the effective initial tangent modulus of pre-cracked biaxially tensioned specimens, an expression for the initial extensional stiffness K_{Ni} can be formulated as follows according to Eqn. 3.13,

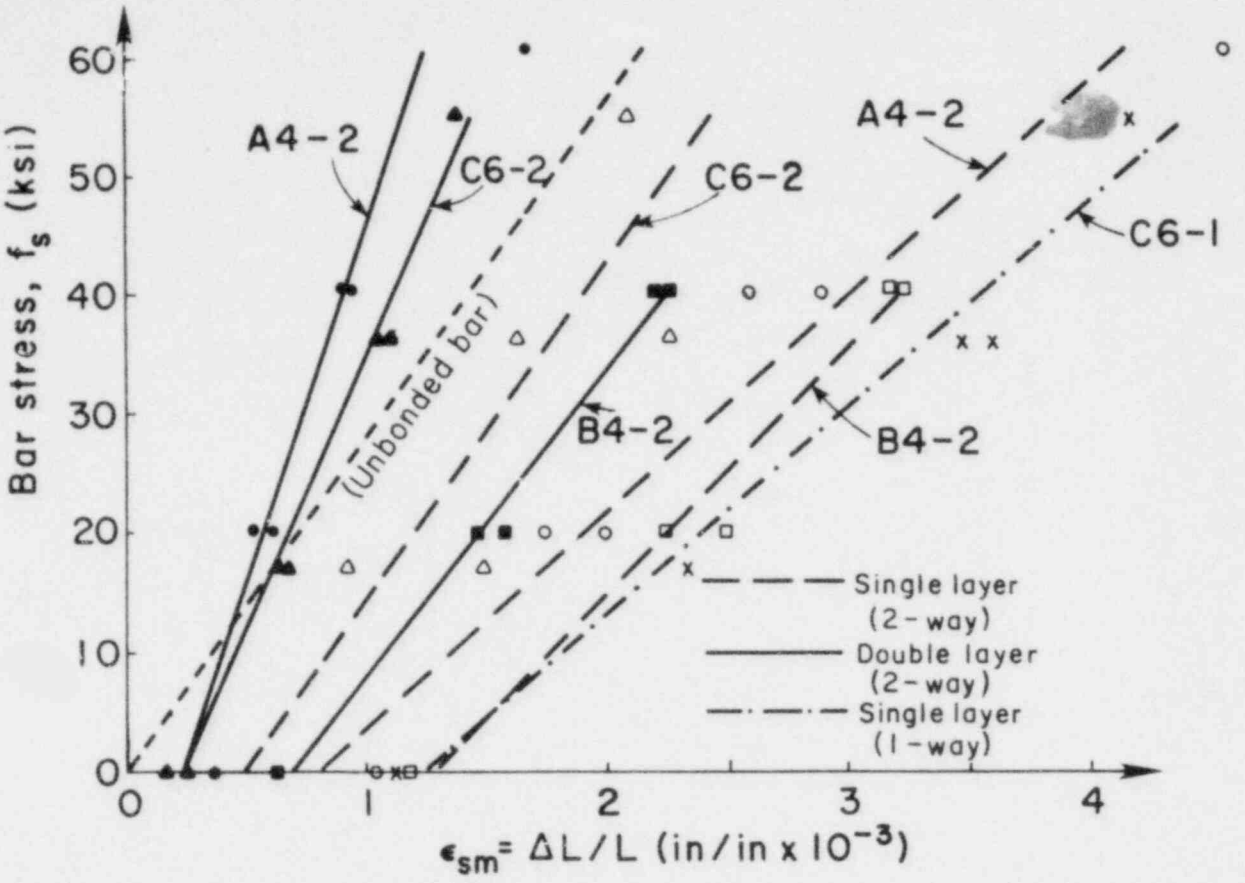

Fig. 3.20. Predicted longitudinal steel strain versus the applied bar stress (gage length L = 24 in.).

$$K_{Ni}{}_{(i=x,y)} = \frac{100\ \rho_i E_s}{\ell_{cmi}} \left(\frac{\pi d_i^{\,2}}{4}\right)_{(i=x,y)} \quad (k/in) \tag{3.25}$$

if base length L_i is taken the average crack spacing ℓ_{cmi}.

The variation of the average initial crack width c^o_{wmi} for the No.6 bars (Specimen C6-2) is also plotted in Fig. 3.21 versus the applied rebar tension f_s in both x and y directions assuming that

$$c^o_{wmi} = (\Delta L/N_c)_i \tag{3.26}$$

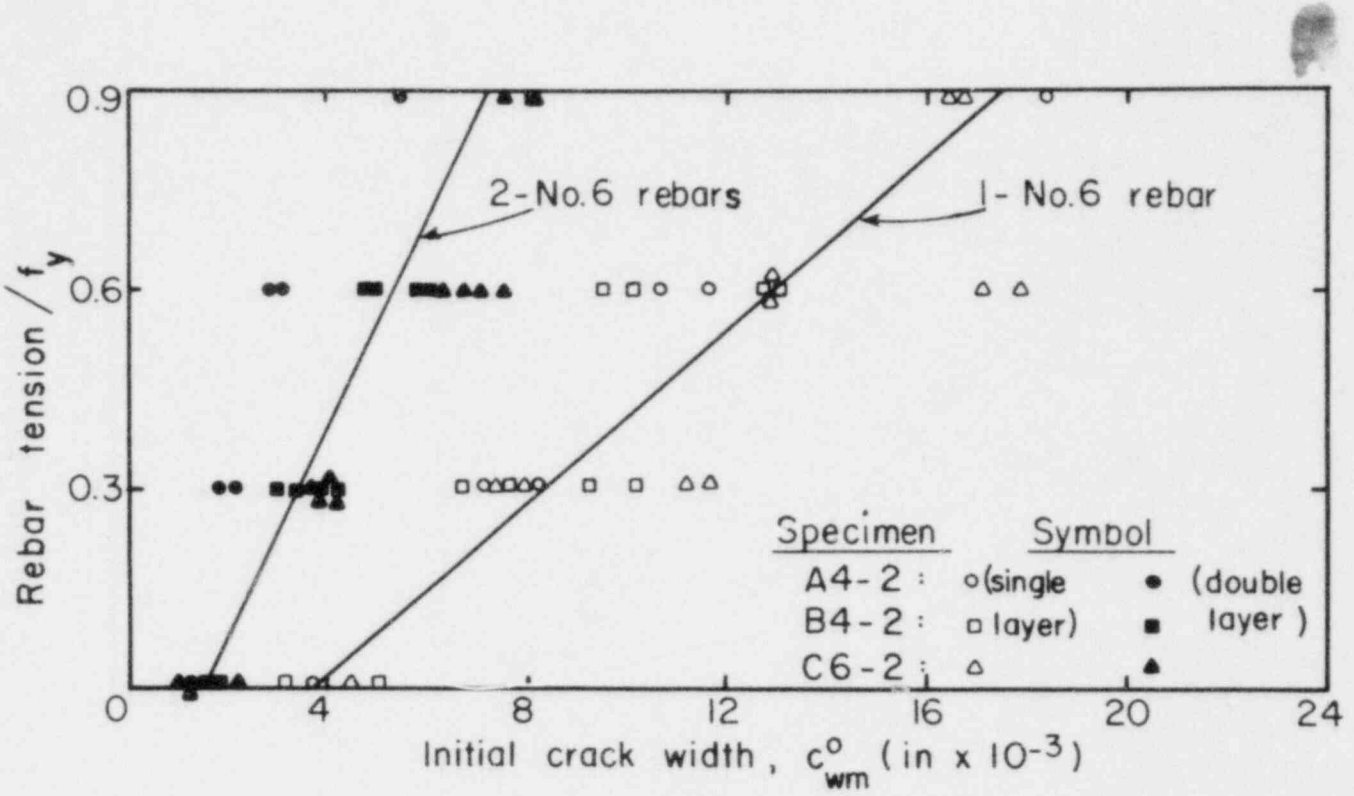

Fig. 3.21. Estimated average initial crack width versus the applied bar tension in both the single (1-No.6 bar) and the double layer of bars (2-No.6 bars).

with

ΔL_i = total elongation measured on the concrete surface in the i(x,y) direction (see col. 6 in Table 3.F).

N_{ci} = the number of primary orthogonal cracks normal to the i(x,y) direction and within the corresponding gage length of 24 or 48 in.

The values of c^o_{wm} are given in col. 7 in Table 3.F. These results are valid for ρ_x/ρ_y equal to 0.5, an average compressive cylinder strength of concrete of about 3800 psi (26 MPa) and for the case of reinforced concrete panels precracked at a biaxial tensile stress of $0.6f_y$ in the reinforcing bars. For a steel ratio of 0.0122 in the x direction the average initial crack width varies from 0.0035 to 0.0175 in. (0.09 to 0.44 mm) corresponding to a range of biaxial tension between 0 and $0.9f_y$. In the y direction (steel ratio equal to 0.0244) the c^o_{wmy} varies from 0.0015 to 0.007 in. (0.04 to 0.18 mm).

The calculated extensional stiffness values using the expression in Eqn. 3.25 are shown in Table 3.I, for a single No.6 and No.4 reinforcing bar in both x and y directions. Uniaxial extensional stiffness values according to Eqn. 3.2 are also included in Table 3.I.

Axial tests were also performed on larger scale orthogonally reinforced flat specimens at Portland Cement Association Laboratories (Refs. 73 and 96). These 2 inch thick specimens were reinforced with No.14 and No.18 bars at 12 inch spacing, as shown in Fig. 3.22. The increase in the crack width was measured for specimens MB1 and MB3 versus the applied bar force as shown in Fig. 3.23. Values of extensional stiffness equal to 3000 k/in (MB1) and 4800 k/in (MB3) were calculated for the No.14 bars

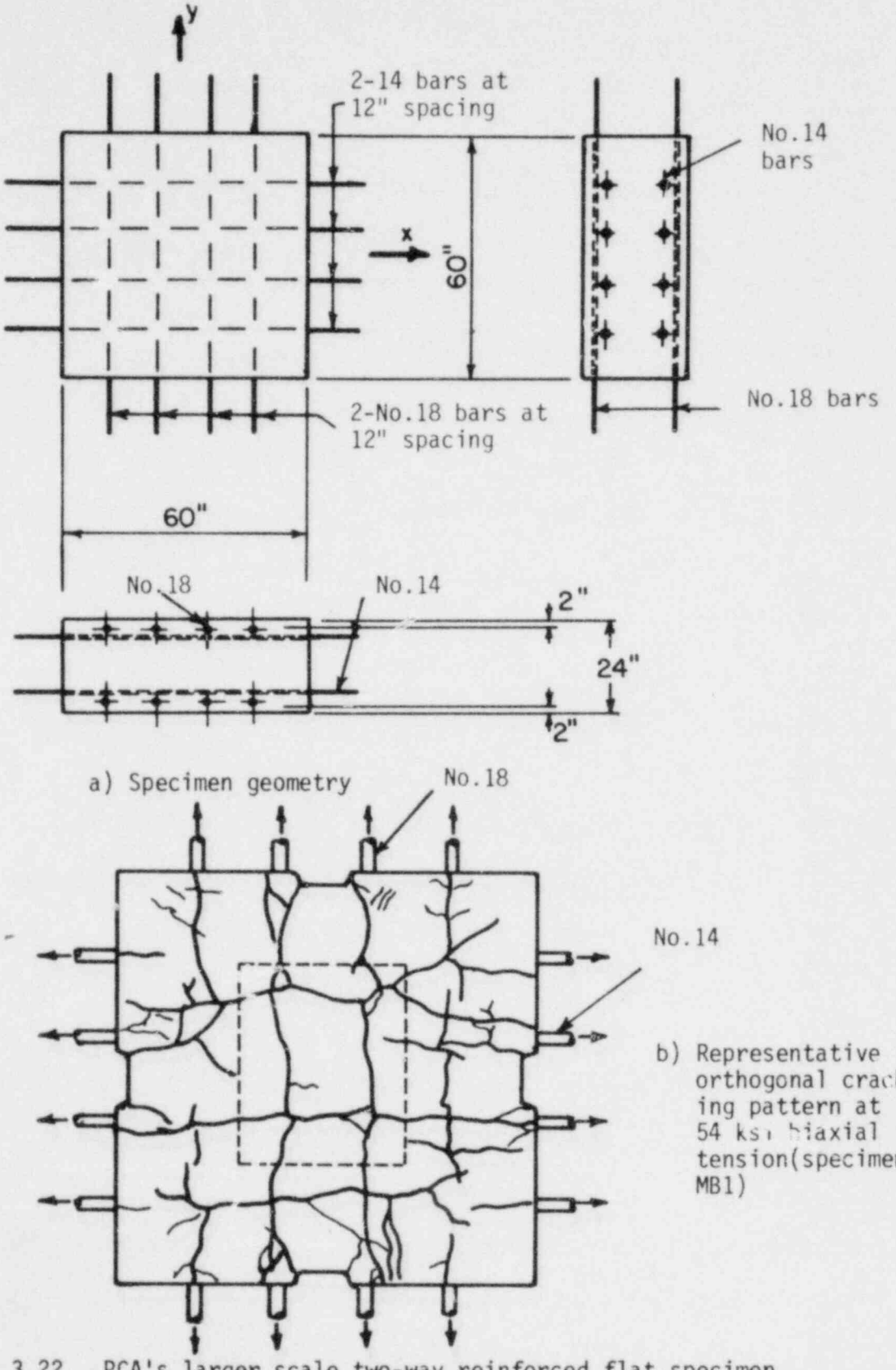

Fig. 3.22. PCA's larger scale two-way reinforced flat specimen.

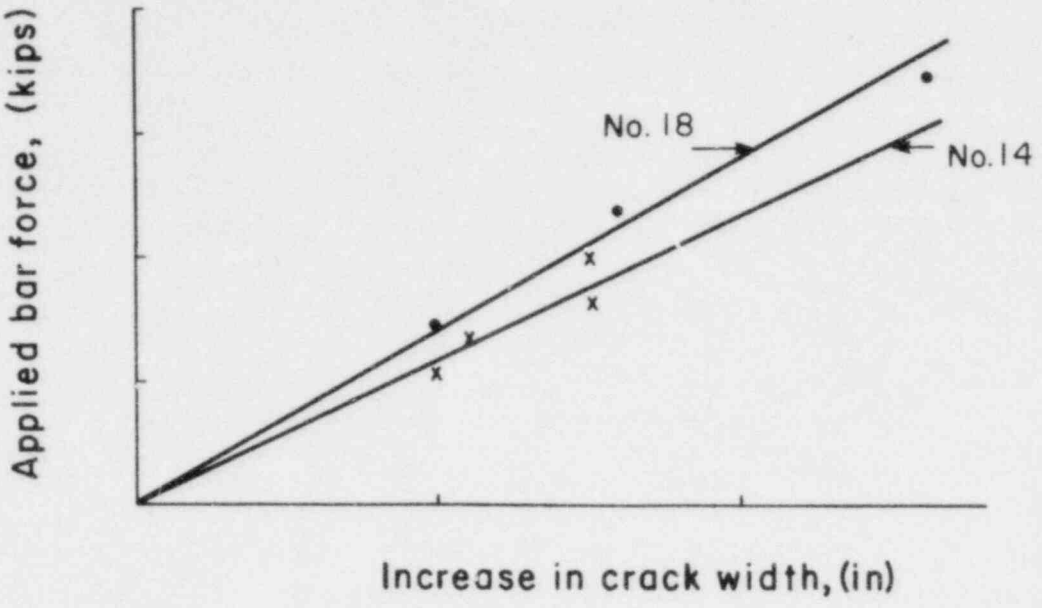

a) specimen MB 3

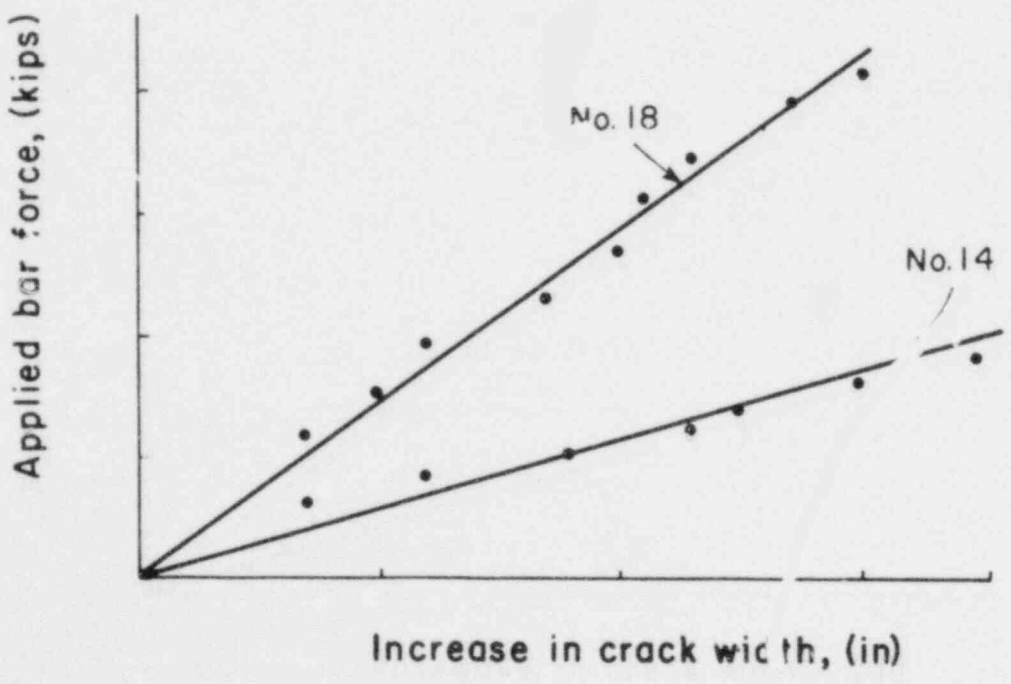

b) specimen MB 1

Fig. 3.23. Estimate of the extensional stiffness K_N in the PCA biaxial specimens.

Table 3.I. Calculated biaxial and uniaxial extensional stiffness values for a single No.4 or No.6 reinforcing bar and a ratio of biaxial applied stresses $f_{sx}/f_{sy} = 0.5$.

Reinf. Direction (1)	Steel (2)	Bar Diameter d(in) (3)	Reinf. Ratio, ρ_i (4)	Average Crack Spacing ℓ_{cmi}(in) (5)	Biaxial K_N(k/in) (Eqn. 3.26) (6)	Uniaxial K_N(k/in) (Eqn. 3.2) (7)
x (single layer)	1-No.4	0.5	0.0055	7.15	465	515
	1-No.6	0.75	0.0122	7.23	2300	1160
y (double layer)	1-No.4	0.5	0.0110	5.65	1030	515
	1-No.6	0.75	0.0244	6.56	4420	1160

Notes:

(5) As the average crack spacing ℓ_{cm} was chosen the value measured in the middle 24 inch wide region.

(6) The extensional stiffness calculated per rebar corresponds to 36 in.^{2} concrete area for the single layer and 18 in.^{2} for the double layer.

(ρ_x = 0.013) and 5900 k/in (MB3) and 7400 k/in (MB1) for the No.18 bars (ρ_y = 0.022). The average crack spacings in the direction of the No.14 (x) and No.18 (y) bars were estimated as equal to 12 and 18 in. for specimen MB1 and 12 and 8 in. for specimen MB3 in the x and y direction, respectively. Using expression 3.25, developed from the tests on the present smaller scale specimens with smaller size bars, the extensional stiffness values predicted for a single No.14 and No.18 rebar are presented in col. 6 of Table 3.K. The measured values of K_N are also included in col. 8. In col. 7 the predicted values according to Eqn. 3.2 for uniaxial specimens (Jimenez et al. (Ref. 61)) are also included.

Table 3.K. Comparison of predicted and experimental values of the extensional stiffness for a single No.14 and No.18 reinforcing bar (PCA biaxial specimens).

Specimen No. (1)	Steel (2)	Bar Diameter d(in) (3)	ρ (4)	ℓ_{cm} (in) (5)	Predicted Biaxial K_N(k/in) (Eqn. 3.25) (6)	Predicted Uniaxial K_N(k/in) (Eqn. 3.2) (7)	Measured K_N (k/in) (8)	Free Bar AE/ℓ_{cm} (k/in) (9)
MB1	No.14	1.75	0.013	12	7000	6300	3000	5600
	No.18	2.25	0.022	18	13000	10400	7400	6200
MB3	No.14	1.75	0.013	12	7000	6300	4800	5600
	No.18	2.25	0.022	8	29400	10400	5900	14000

In the above Table 3.K it appears that the expression developed from the smaller scale specimens overestimates the measured values of extensional stiffness for No.14 and No.18 bars, predicting values at least twice as large as measured, especially for the No.18 bars. This shows that the expression 3.25 is likely to be not valid for larger size bars, since the splitting effects and the extent of internal cracking can be significantly higher in the latter case resulting in lower values of extensional stiffness. Also, almost all the measured values of K_N in col. 8 are smaller than the estimated axial stiffness of the same size unbonded bar of length equal to the average crack spacing ℓ_{cm}. This perhaps indicates that the measured K_N values are smaller than they actually are, since they are computed based on individual crack width measurements on the surface of the concrete. Thus, these measurements would definitely underestimate the axial stiffness of the composite concrete-steel element at the level of the reinforcement. The predicted K_N values based on uniaxial test results

(col. 7) approach the predicted values based on the biaxial test results (col. 6) particularly in the case of No.14 bars (largest bar used in the uniaxial tests). Since Eqn. 3.2 depends only on the bar size (diameter d) and does not account for different crack spacings, it gives the same value for K_N in the case of the No.18 bars in specimens MB1 and MB3. It is a fact that the predictions for K_N based on the uniaxial results are closer to the measured values of K_N than those based on the biaxial tests.

In conclusion, it should be pointed out that the derived expression for the extensional stiffness or orthogonally reinforced concrete panels with No.6 bars (Eqn. 3.25) does not include the degrading effect of cyclically applied shear. More experimental work on different size bars is needed to study this effect as the number of shear loading cycles increases.

CHAPTER 4

ENGINEERING MODEL OF SHEAR TRANSFER

4.1 Introduction

The accuracy of any method used to analyze a reinforced concrete structure is dependent upon how realistic the assumptions for the material properties are. These assumptions have a direct influence on the calculated structural stiffness values, such as the effective shear stiffness of a cracked reinforced concrete panel subjected to membrane biaxial tension and shear. This stiffness controls the deformational behavior of the structure over a considerable range of the shear loading, and is nonlinear because of cracking, crack propagation, bond deterioration, and other effects. Cyclic loading effects must be also incorporated for reversing loads such as seismic shear forces.

Consider a flat reinforced concrete cracked membrane element idealized from a wall of a cylindrical containment initially subjected to normal tensile stresses σ_{N_x} and σ_{N_y}, as shown in Fig. 4.1. An orthogonal reinforcement net is assumed with parallel tensile cracks already formed perpendicular to the reinforcement bars in the x and y directions. These orthogonal cracks are spaced at equal distances $\ell_{cmi}(i = x, y)$ with an average initial crack width c^{o}_{wmi} $(i = x, y)$ present at each crack, the value of which depends on the applied tension $f_{si}(i = x, y)$ in the bars and to a lesser extent, the bar diameter. At a certain level of a superimposed uniformly applied shear stress v, diagonal cracking forms along

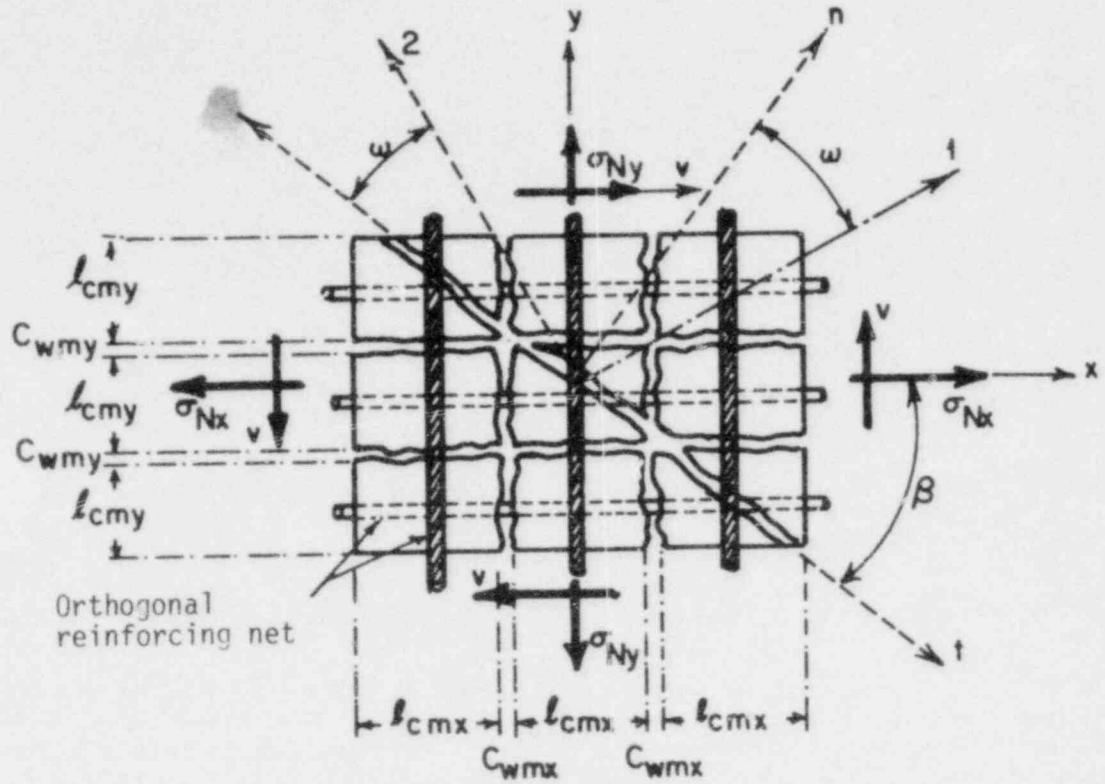

Fig. 4.1. Idealized flat reinforced concrete membrane element cracked orthogonally and diagonally.

the direction (t) at an angle β with the x axis and perpendicular to the maximum principal tensile strain (1) (direction (1) is normal to direction (t) at cracking initiation). Subsequently, as the shear stress is increased, additional inclined cracking and redistribution of internal stresses cause a rotation of the principal strain directions (1) and (2) (in general not coinciding with the directions of principal stresses) through an angle ω relative to the normal (n) and tangential (t) local coordinates of the original diagonal cracks, respectively.

The stiffness equations relating the stresses $\bar{\sigma}$ and strains $\bar{\varepsilon}$ in the above concrete-steel composite element, in any reference coordinate system, can be written in condensed form as follows,

$$\{\bar{\sigma}\} = [\bar{K}]\ \{\bar{\varepsilon}\} \tag{4.1}$$

where $[\bar{K}]$ is the global stiffness matrix that includes the stiffness due to both concrete and steel. At the cracked stage the global stiffness $[\bar{K}]$ is the sum of the stiffness of the concrete between the major cracks, the contribution to stiffness due to interface shear transfer of concrete along each individual crack (cracked concrete), the stiffness of the reinforcing net in the x and y directions, and the dowel action of the bars at the cracks.

Let us assume that the directions of orthotropy due to cracking coincide with the local coordinate system (n,t) of the inclined cracking and remain fixed, independent of the possible rotation of the principal strain directions (1) and (2) as cracks propagate. In a biaxial state of plane stress the composite orthotropic stiffness equations in the (n,t) coordinate system can be formulated as,

$$\begin{Bmatrix} \sigma_{N_n} \\ \sigma_{N_t} \\ v \end{Bmatrix} = [K_{nt}] \begin{Bmatrix} \varepsilon_{N_n} \\ \varepsilon_{N_t} \\ \gamma \end{Bmatrix} \tag{4.2a}$$

with

$$[K_{nt}] = \frac{1}{(1 - \nu_{nt}\nu_{tn})} \begin{bmatrix} E_{nn} & \nu_{nt}E_{nn} & 0 \\ \nu_{tn}E_{tt} & E_{tt} & 0 \\ 0 & 0 & G_{cr}(1 - \nu_{nt}\nu_{tn}) \end{bmatrix} \tag{4.2b}$$

where E_{nn}, E_{tt} are the composite moduli in the orthotropic directions, ν_{ij} are the Poisson's ratios governing the strain in the i-direction (i = n, t) due to a direct strain in the j-direction (j = n, t), and G_{cr} is an effective shear modulus of the cracked element that includes the effects of interface shear transfer and dowel action. To assure symmetry of the global stiffness matrix $[K_{nt}]$ in Eqn. 4.2b the following relation must be true

$$\nu_{tn}/\nu_{nt} = E_{nn}/E_{tt} \tag{4.2c}$$

with the composite moduli E_{nn} and E_{tt} being related to the extensional stiffness K_{Ni} (i = x, y) of the reinforced concrete element, subjected to biaxial tension in both x and y directions of the reinforcing steel.

The main objective of this chapter is to derive a formulation for the shear modulus term G_{cr}, based on the present experimental data of biaxially tensioned specimens and additional data obtained from uniaxial tests. Under the applied shear stress v, the gross shear distortion γ due to crack opening and slip at each crack in the reinforced concrete element has been measured (see Section 2.6). These experimental values for the effective shear rigidity will be compared with the values predicted by the expression to be formulated. The composite element shown in Fig. 4.1 has dimensions that include a sufficient number of cracks and

reinforcing bars such that an equivalent uniform distribution of internal stresses and strains can be assumed.

A literature review of the stiffness and strength of the shear transfer mechanisms is given in Section 4.2 of this chapter. This is followed by a formulation of the effective shear modulus G_{cr} based on a simple engineering model of the shear stress-shear slip relation for an individual crack in a uniaxial case. The latter relation is generalized for two orthogonal sets of parallel cracks as a function of the initial crack width in both axial directions, the normal restraining stiffness, and the dowel stiffness of the bars. The experimental results of the present research, reflecting the effects of biaxial cracking, applied bar tension and shear stress as well as cycling, are utilized to help arrive at the expression for the degrading shear rigidity of a cracked reinforced concrete panel. Finally, in Section 4.4 the type of failure mode is identified and free body equilibrium analyses for all specimens at failure conditions are performed. Also, the level of bar tensions and dowel forces and the possibility of kinking in the bars along the failure crack are discussed.

4.2 Literature Review

An extensive literature exists on the shear transfer mechanism in cracked concrete. Considerable experimental research has been conducted involving shear on a single crack plane (uniaxial tests) at various universities and research laboratories, including the University of Washington, Cornell University, University of California at Berkeley, University

of Canterbury, University of Sheffield, Cement and Concrete Association, Universities of Darmstadt, Braunschweig, and Stuttgart in W. Germany, University of Toronto, McGill University, Technical University of Milan, University of Technology at Delft and others. Monotonic, repeated and fully reversing cyclic shear loading has been studied. Only recently, experimental work has been conducted on specimens subjected to combined biaxial tension and shear loads (Cornell University, Portland Cement Association, and the University of Toronto).

The literature survey is divided into four sections. The first two sections (4.2.1 and 4.2.2) deal with the two main mechanisms of shear transfer along the interface of a single crack: the interface shear transfer (IST) and the dowel action (DA), respectively. The expressions for the shear stress-shear displacement relationships and the resulting shear stiffness obtained by various investigators for the above two mechanisms in uniaxially reinforced concrete blocks are presented and critically discussed. Also some expressions for the dowel ultimate capacity of the reinforcing bars, crossing the shear crack under consideration, are given. The third section (4.2.3), which is more pertinent to the present work, contains a description of the analytical methods used to predict deformations and stresses in cracked reinforced concrete flat elements under in-plane normal tensile and shear stresses and the different ways researchers have modeled the shear modulus of cracked concrete for analysis purposes. Furthermore, the parallel experimental work at the Portland Cement Association (PCA) Laboratories on the response of larger scale flat reinforced concrete elements subjected to combined biaxial tension and in-plane shear. Finally, in the fourth section (4.2.4), the experimental

work on the ultimate strength of precracked reinforced concrete specimens with a single shear interface plane is reviewed.

4.2.1 Interface shear transfer stiffness (single crack)

The stiffness K_{IST} due to interface shear transfer at the crack under consideration is defined as the shear stress transmitted through the irregularities of the concrete shearing surfaces as a result of a unit shear displacement (slip) along the crack. The units for K_{IST} are ksi/in (MPa/mm).

Although experimental evidence from pavement and beam tests (Refs. 1, 24, 37, 64, 65, 95, 107, 114, 118 and 124) has provided valuable information about the contribution of the various mechanisms of shear transfer, that research did not produce any shear stress-shear slip relationships, and therefore it is not discussed here. A discussion of the above studies was presented in Ref. 61. The researchers cited below conducted direct shear tests on precracked concrete specimens, where they isolated the interface shear transfer mechanism (also called aggregate interlock) and studied the effect of the initial crack width, aggregate size and shape, compressive strength of concrete, normal restraining stiffness, and shear stress level on the value of shear slip. The initial crack width present in these experimental studies ranges between 0.002 and 0.030 in. (0.05 to 0.76 mm). The major test results discussed in this section regarding the interface shear transfer stiffness are summarized in Table 4.A.

Table 4.A. Summary of shear stress-shear slip proposed relationships for the IST mechanism (units are in psi and inches unless stated otherwise).

Reference	Type of Research	c^o_{wm} in (mm)	Load History	Shear Stress (v_{IST}) vs. Shear Slip (Δ_s) Relationship Proposed (IST Mechanism)
37, 38	E(1)	0.0025(0.064) to 0.015(0.38)	M	$v_{IST} = (\frac{467}{c^o_{wm}} - 8410)(0.0225\sqrt{\sigma_{co}} - 0.409)(\Delta_s - 0.0436\, c^o_{wm})$
76, 97	E(1)	0.005(0.127) to 0.02(0.51)	M	Bilinear: $v_{IST}^{(1)} = (\frac{485}{c^o_{wm}} - 8300)[\Delta_s + 2(\sqrt{r^2 + c^{o\,2}_{wm}} - r)]$ $v_{IST}^{(2)} = (1190/c^o_{wm} - 8200)\,\Delta_s - 156.38$
			C	Upper portion: $\Delta_s = 0.01\, c^o_{wm}\,[(2n + 86) + 5.72 \times 10^{-2}\, v_{IST}]$
58, 88	E(1)	0.002(0.05) to 0.02(0.51)	M	$c^o_{wm} \geq 0.002$ in.: $v_{IST} = 57(\frac{1}{c^o_{wm}})^{3/2}\sqrt{\frac{f_c'}{5000}}\,\Delta_s$ $c^o_{wm} < 0.002$ in.: $v_{IST} = [G_o - (G_o^3/[\lambda(\frac{1}{c^o_{wm}})^2 + G_o^2])]\,\Delta_s$
116, 117	E(2)	-	M	---
126	E(3)	0.02(0.51) to 0.03(0.762)	C(R)	d = 1.375 in.: $v_{IST} = \Delta_s/2 \times 10^{-4}$ d = 1.0 in.: $v_{IST} = \Delta_s/3.2 \times 10^{-4}$ (after 25 cycles)
70	E(3)	0.01(0.254) to 0.03(0.762)	C(R)	---

(Continued)

Table 4.A. (Continued)

Reference	Type of Research	c_{wm}^{o} in (mm)	Load History	Shear Stress (v_{IST}) vs. Shear Slip (Δ_s) Relationship Proposed (IST Mechanism)
61	E(3)	0.01(0.254) to 0.02(0.51)	M	$v_{IST} = \Delta_s / f_a$; $f_a = 3.9\,(c_{wm}^{o} - 0.002) + 0.0367 - 1.09 \times 10^{-7} \frac{K_N}{c_{wm}^{o}}$
			C(R)	$\Delta_s^{(n)} = v_{IST}\, f_a\, n^{(5.2\, c_{wm}^{o} + 0.12)}$
4	A	(see Refs. 37, 38)	M	$v_{IST} = C(\Delta_s^2 + c_w^2)^m$; $C = A_o c_{wm}^{o-2m}$; $m = \log_e[\frac{v_u}{A_o \Delta_{su}} - \frac{(\Delta_{su}^2 + c_w^2)}{c_{wm}^{o\,2}}]$ $v_u = (262 - 702\, f_c')(0.3 - 10.42\, c_w)$; $\Delta_{su} = 7.517 \times 10^{-4} + 0.638\, c_w$
35	A	(see Refs. 61, 62, 70, 126)	M,C(R)	$v_{IST} = c_1(f_s + K_N\, c_{wm}^{o}) + c_2 K_N \Delta_s$
9	A	(see Ref. 97)	M	$v_{IST} = v_u r(\frac{\alpha_3 + \alpha_4 \lvert r \rvert^3}{1 + \alpha_4 r^4})$ (MPa); $r = \Delta_s / c_w$; $v_u = v_o \frac{\alpha_o}{\alpha_o + c_w^2}$; $\alpha_o = 0.01\, D_a^2$; $\alpha_3 = \frac{2.45}{v_o}$(N/mm^2); $\alpha_4 = 2.44(1 - \frac{4}{v_o}$ N/mm^2); $v_o = 0.245\, f_c'$

Notes: E = experimental work ((1) for constant c_w; (2) for constant c_w/Δ_s; (3) for constant K_N)

A = analytical work

M = monotonic shear

C = cyclic shear (not reversing)

C(R) = reversing cyclic shear

a) Monotonic shear

Fenwick and Paulay (Ref. 38), Paulay and Loeber (Refs. 76, 97) and Houde and Mirza (Refs. 58, 88) conducted experiments on similar specimens (see Figs. 4.2a, 4.3a and 4.4a, respectively). The initial width at the crack with a shearing area of 12.25 in^2 (79 cm^2) (Fenwick), 33.5 in^2 (216 cm^2) (Loeber) and 12.25 in^2 (79 cm^2) (Houde) was held constant during the test by providing the required normal forces. Each of the investigators concluded that interface shear stiffness K_{IST} was inversely proportional to the initial crack width and proportional to the concrete compressive strength (the rate of influence of the latter was greater for smaller crack openings). The effect of aggregate size and shape was not significant and it depended on the quality of the aggregate used; that is, the degree of irregularity in the shape of the crack interface.

The empirical relationships for the interface shear transfer stiffness K_{IST} (ksi/in) proposed by Fenwick and Houde (see Figs. 4.2b and 4.4b) are (see also Table 4.A):

Fenwick: $$K_{IST} = \left(\frac{0.467}{c^o_{wm}} - 8.41\right)\left(0.0225\sqrt{\sigma_{co}} - 0.409\right) \quad \text{(ksi/in)} \tag{4.3}$$

with

$$2700 \leq \sigma_{co} \leq 8100 \text{ psi}$$

Houde: $$K_{IST} = 0.057 \left(\frac{1}{c^o_{wm}}\right)^{3/2} \sqrt{\frac{f_c'}{5000}} \quad \text{(ksi/in)} \tag{4.4}$$

with

$$2370 \leq f_c' \leq 7340 \text{ psi}$$

where σ_{co}, f_c' are the cube and cylinder compressive strength of concrete,

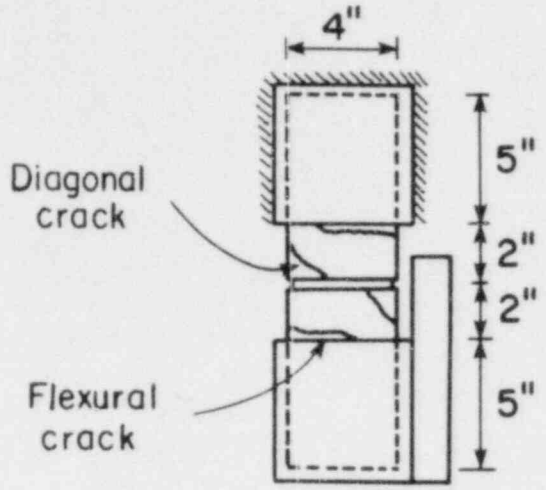

a) Direct test specimen used by Fenwick

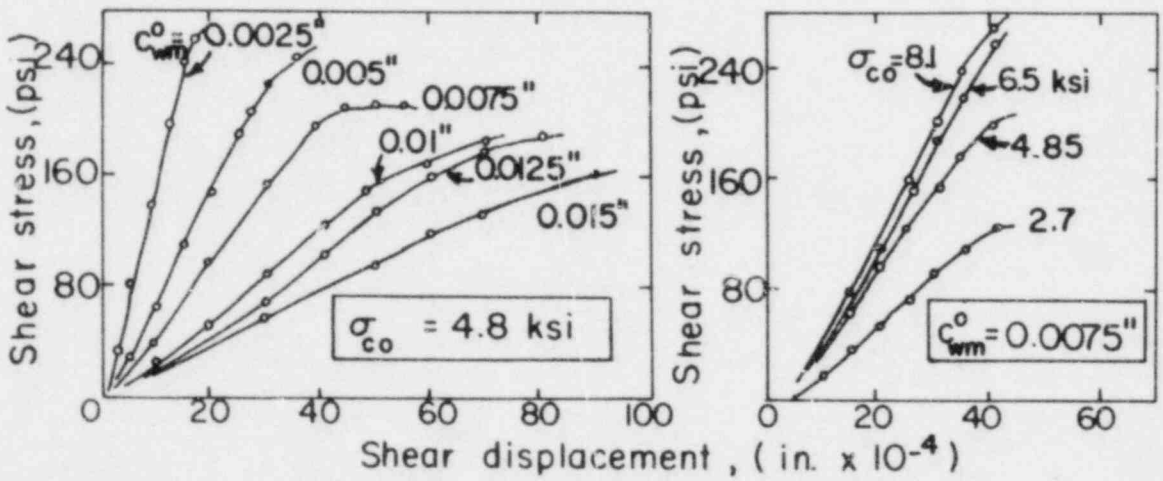

b) Effect of the initial crack width and the compressive concrete strength on the shear stiffness

Fig. 4.2. Typical results from Fenwick's investigation (Ref. 38).

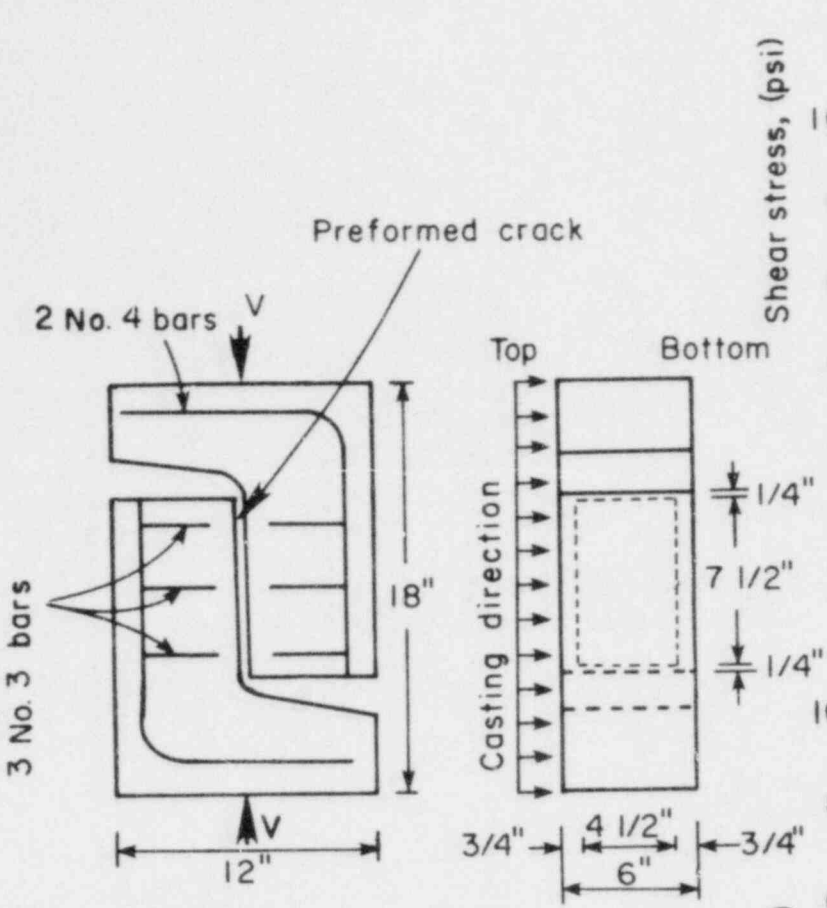

a) Specimen geometry

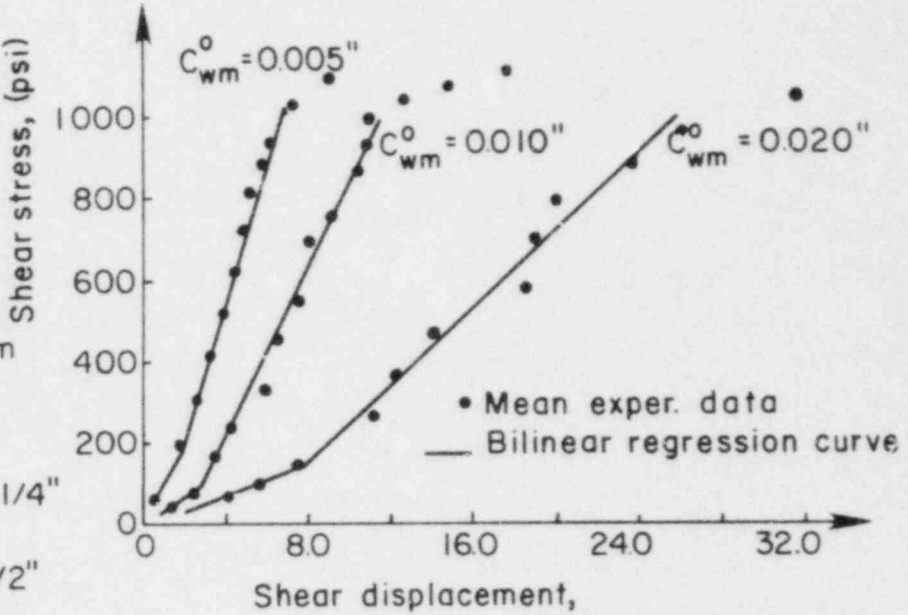

b) Typical shear stress-shear displacement relationships for different crack widths (monotonic shear)

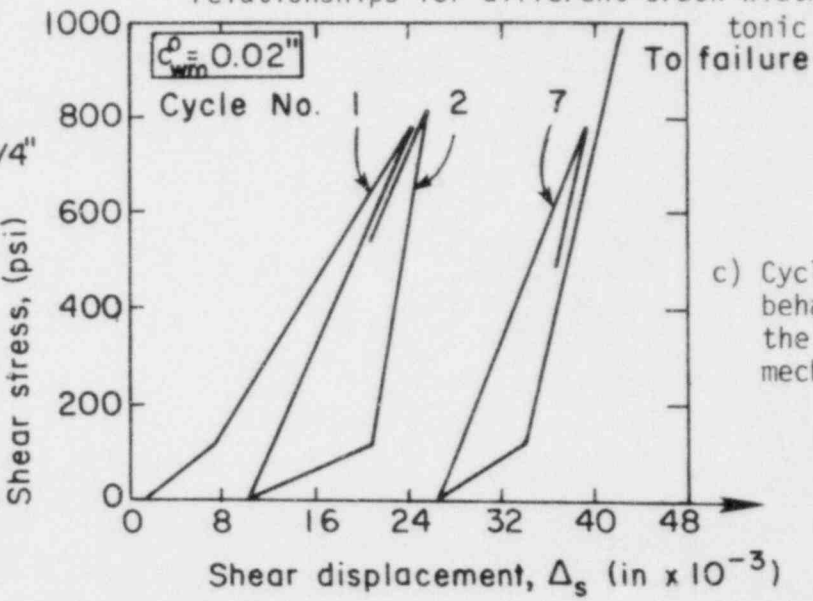

c) Cyclic behavior of the IST mechanism

Fig. 4.3. Experimental results from Paulay and Loeber's study of the interface shear transfer mechanism.

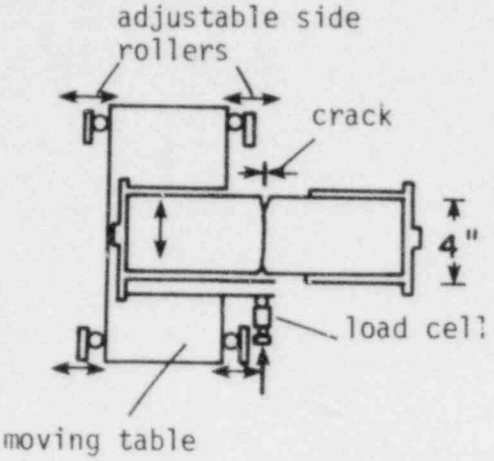

a) Specimen geometry

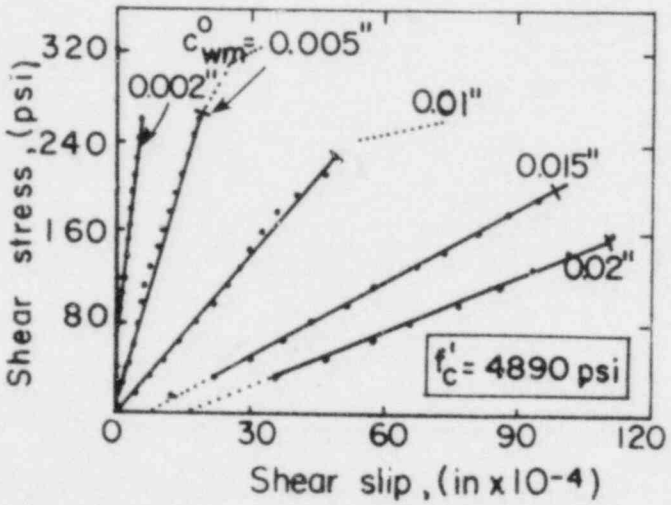

b) Shear stiffness of the IST mechanism under monotonic shear loading

Fig. 4.4. Experimental study of the IST mechanism by Houde and Mirza (Refs. 58 and 88).

respectively (both in psi), and c^o_{wm} is the initial crack width in inches.

Loeber presented a bilinear shear stress-shear slip relation that was mainly affected by the initial crack width (see Fig. 4.3b). He proposed the following expressions for the shear stiffness:

$$K_{IST} = \frac{0.485}{c^o_{wm}} - 8.3 \text{ (ksi/in), for } v_{IST} \leq 100 \text{ psi} \quad (4.5a)$$

$$K_{IST} = \frac{1.19}{c^o_{wm}} - 8.2 \text{ (ksi/in), for } v_{IST} > 100 \text{ psi} \quad (4.5b)$$

where v_{IST} is the shear transferred at the crack plane (for $f_c' = 5000$ psi). In Figs. 4.5 and 4.6 the shear stress v_{IST} versus the shear displacement Δ_s, and the shear stiffness K_{IST} versus the initial crack width c^o_{wm} at low shear stresses (up to 100 psi or 0.7 MPa), respectively, are plotted for comparison of the results by Fenwick, Loeber and Houde. Fenwick's and Loeber's expressions give almost identical response at any value of initial crack width. The interface shear transfer stiffness K_{IST} increases with decreasing initial crack width. The rate of increase in K_{IST} becomes higher as the initial crack width decreases, particularly for values of c^o_{wm} less than 0.010 in. Houde's expression for the shear stiffness results in higher values at initial crack widths less than 0.010 in. (0.25 mm). For c^o_{wm} values larger than 0.020 in. (0.5 mm) all expressions result in an approximately constant shear stiffness of about 10 ksi/in. (2.72 MPa/mm). At shear stresses larger than 100 psi Loeber's experimental data shows a drastic increase in shear stiffness especially for small initial crack width values. This large increase in shear

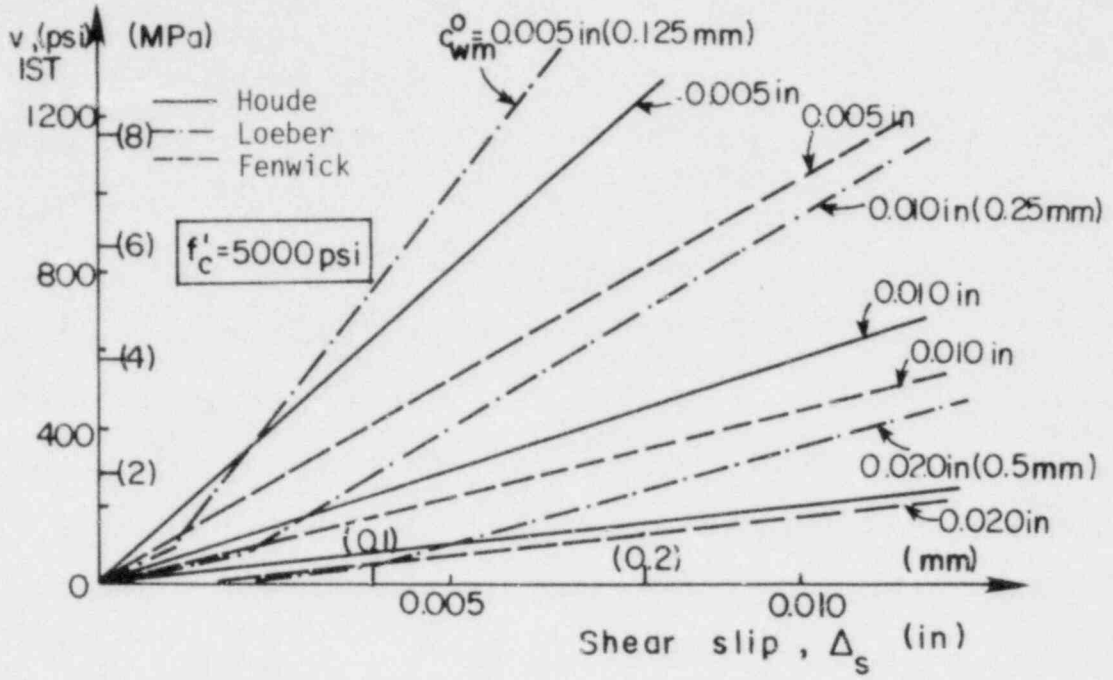

Fig. 4.5. Shear stress-shear slip relationships for the IST mechanism (Ref. 43).

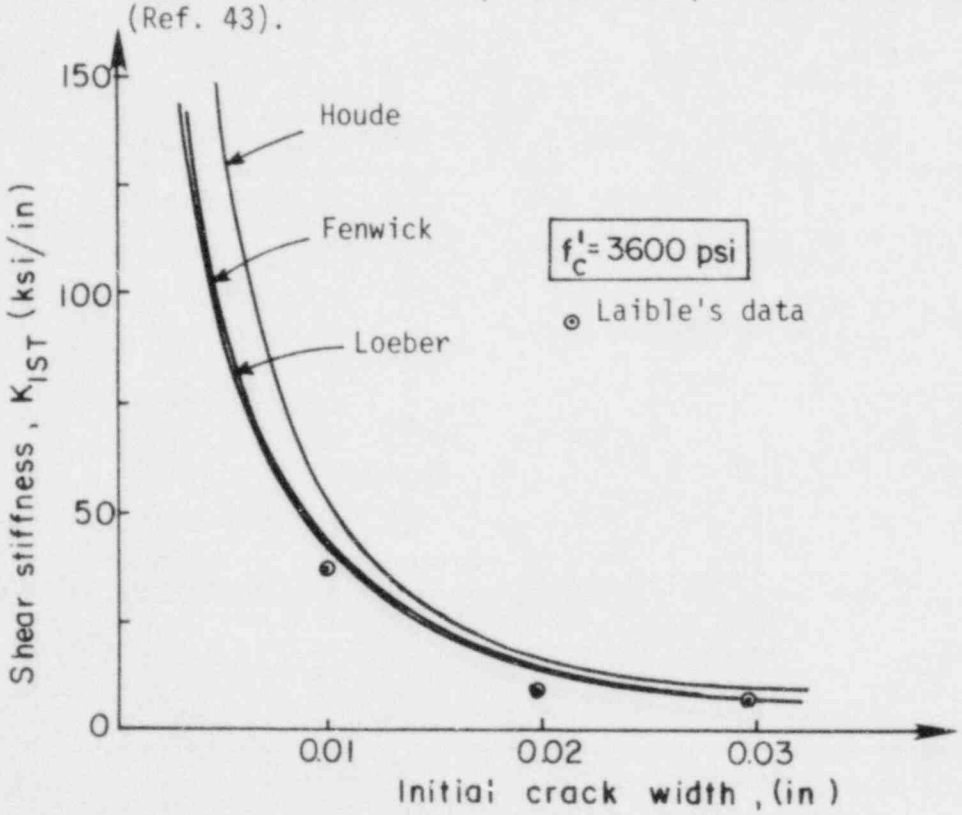

Fig. 4.6. IST stiffness versus initial crack width under monotonic shear (Ref. 61).

stiffness appears to be less severe as the initial crack width increases.

White and Holley (Ref. 126) and Laible et al. (Ref. 70) used similar precracked concrete block specimens with a shear transfer cross-sectional area of 240 or 280 in^2 (1550 or 1806 cm^2) and 300 in^2 (1935 cm^2), respectively (see Figs. 4.7 and 4.8a). They let the crack width change for preselected values of the initial crack width, maintaining a constant extensional stiffness through four external rods. These clamping rods were fastened with nuts to heavy steel cross beams bolted to the top and bottom of the specimen before the formation of the crack at the shear plane. The shear load was applied to the precracked specimen by hydraulic rams acting against a prestressed concrete test frame, as shown in Fig. 4.7. For the positive portion of the first shear loading cycle they found that for a given shear stress the corresponding shear displacement was inversely proportional to the normal stiffness K_N provided by the clamping rods. The effect of reversing cyclic shear applied to the same specimens (see Figs. 4.8b and 4.8c) is discussed in Section 4.2.1b. Laible's data points for the shear stiffness are included in Fig. 4.6 for comparison. It appears that they form a lower bound for the K_{IST} values computed by Eqns. 4.3 to 4.5.

Jimenez et al. (Ref. 61) proposed an interface shear stiffness relation for both constant and changing crack width. The normal stiffness in their uniaxially tensioned specimens (see Fig. 4.9) was provided by Grade 60 embedded reinforcing bars ranging in size between No.7 and No.14 and crossing a shearing area of 225 in^2 (0.145 m^2). By regression analysis of the experimental results of Fenwick and Houde (for constant crack width) and

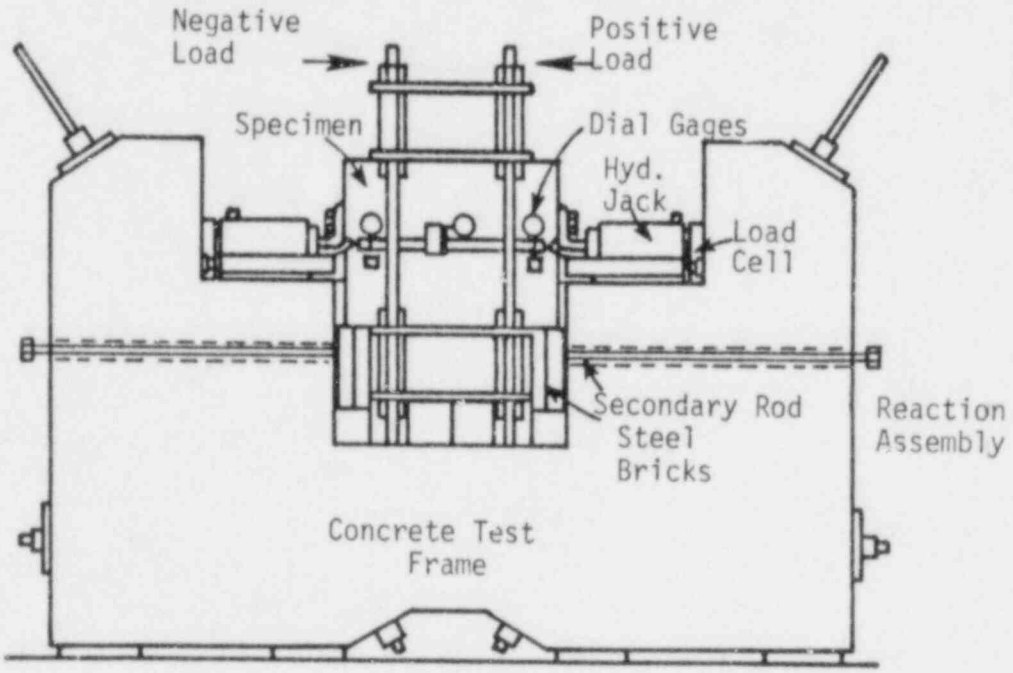

Fig. 4.7. Test setup used by White and Holley (Ref. 126) and Laible (Ref. 70).

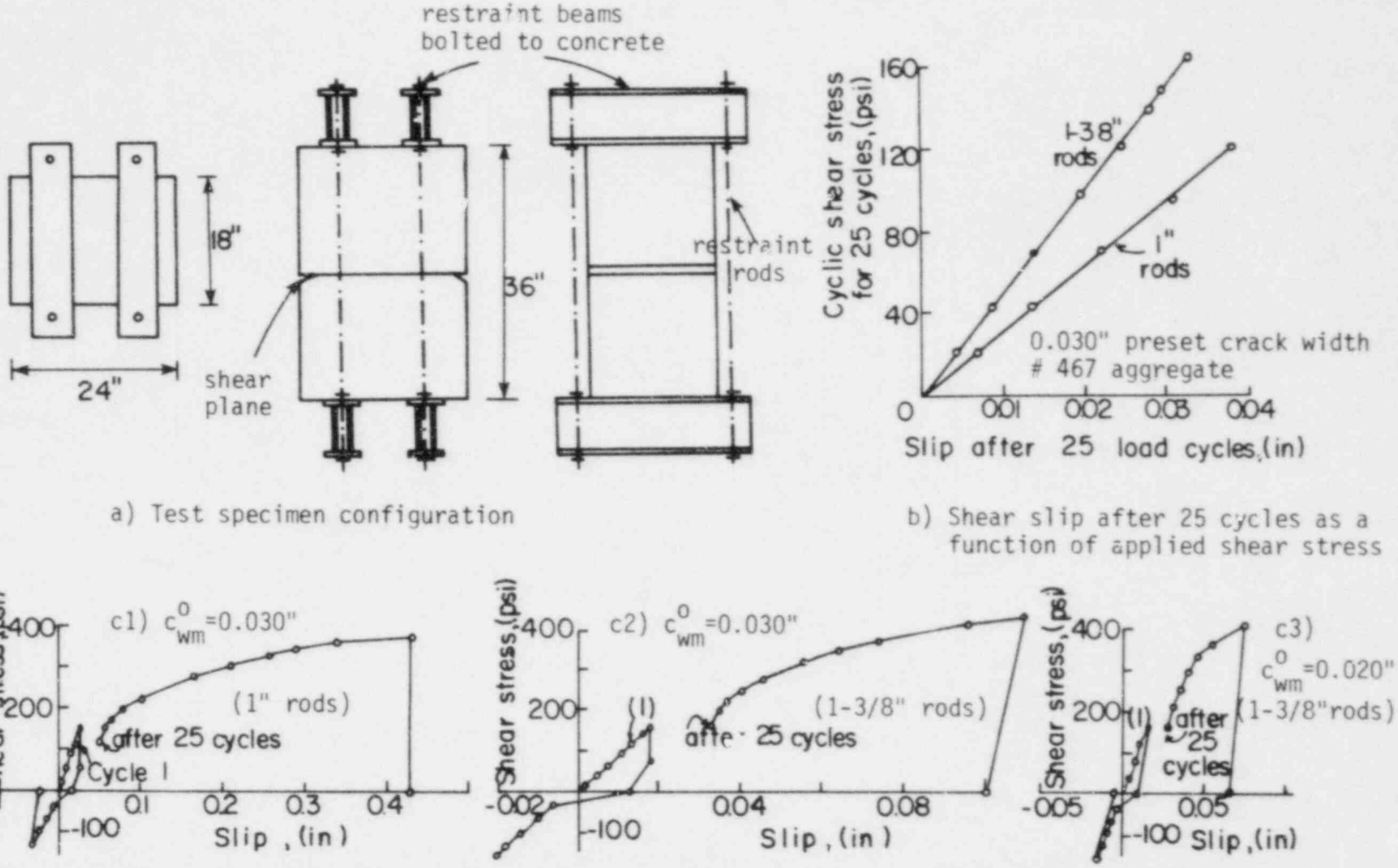

a) Test specimen configuration

b) Shear slip after 25 cycles as a function of applied shear stress

c) Shear stress-shear slip response under fully reversing cyclic shear

Fig. 4.8. Experimental investigation on IST at a single crack by White and Holley (Ref. 126).

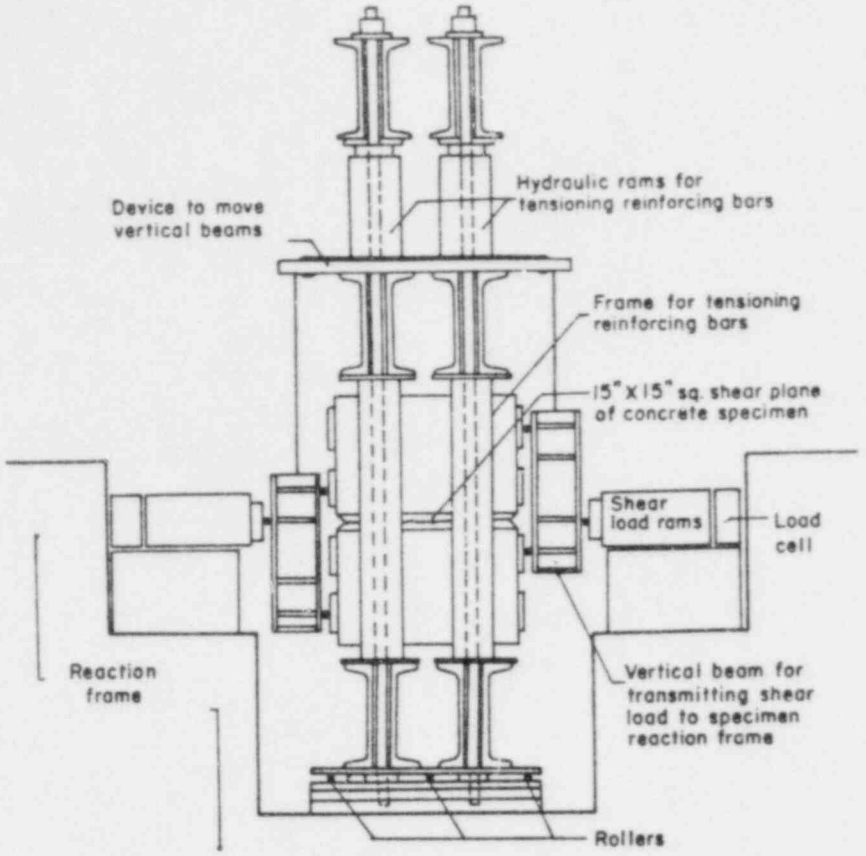

a) Test setup

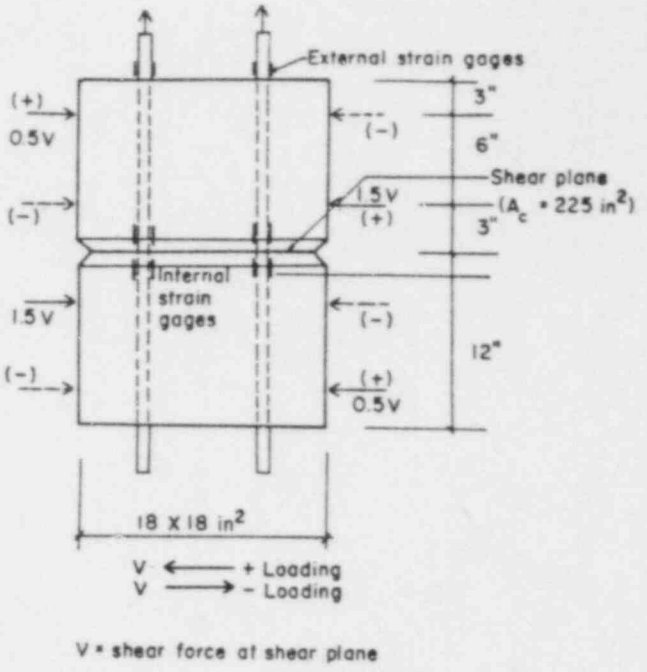

b) Specimen geometry

Fig. 4.9. Test setup and specimen used by Jimenez et al. (Ref. 61).

Loeber (for varying crack width) they obtained the following equation for the interface shear transfer stiffness K_{IST} at the 1st cycle of shear loading (maximum shear stress of 300 psi or 2.07 MPa) and initial crack width values between 0.005 and 0.030 in. (0.13 and 0.76 mm),

$$K_{IST} = [3.9(c^o_{wm} - 0.002) - 1.09 \times 10^{-7} \frac{K_N}{c^o_{wm}} + 0.0367]^{-1} \quad \text{(ksi/in)} \tag{4.6}$$

where K_N is the extensional stiffness in kips/in.

Jimenez et al. also analyzed Laible's results and proposed an alternative interface shear transfer stiffness relation as follows

$$K_{IST} = \frac{5.4 \times 10^{-3} \, K_N^{0.45}}{c^o_{wm}} \quad \text{(ksi/in)} \tag{4.7}$$

where c^o_{wm} was in the range of 0.010 and 0.030 in. and the applied shear stress was less or equal to 180 psi (1.24 MPa).

In Fig. 4.10, taken from Ref. 61, the shear stiffness determined by Eqns. 4.6 and 4.7 is plotted versus the initial crack width for two values of the extensional stiffness K_N equal to 3420 and 7840 k/in (599 and 1373 kN/mm). Both equations give similar shear stiffness values for any value of c^o_{wm} at K_N equal to 7840 k/in, and for c^o_{wm} larger than or equal to 0.020 in. at K_N equal to the lower value of 3420 k/in. In general, the interface shear transfer stiffness for a given initial crack width increases with increasing normal extensional stiffness.

Al-Mahaidi (Ref. 4), assuming a toothlike idealization for the crack interface and using experimental data by Fenwick, proposed the following nonlinear formula for the shear stiffness K_{IST} as a function of the current

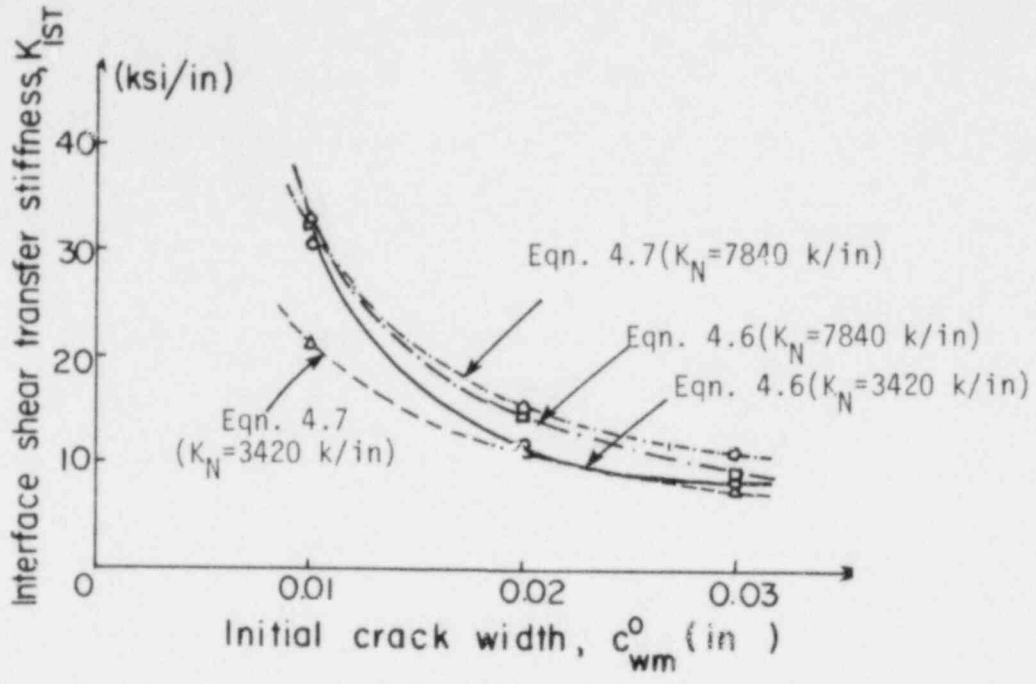

Fig. 4.10. IST stiffness versus initial crack width according to Eqns. 4.6 and 4.7.

crack width c_w and crack slip Δ_s, the initial crack width c^o_{wm}, the crack slip Δ_{su} and shear stress v_u at failure, and the cylinder compressive strength of concrete f_c',

$$K_{IST} = C(\Delta_s^2 + c_w^2)^m,$$

where

$$C = A_o c^{o\,-2m}_{wm} \qquad (4.8)$$

$$m = \log_e \left[\frac{v_u}{A_o \Delta_{su}} - \frac{(\Delta_{su}^2 + c_w^2)}{c^{o\,2}_{wm}}\right]$$

$$v_u = (262 + 702\, f_c')(0.3 - 10.42\, c_w)$$

$$\Delta_{su} = 7.517 \times 10^{-4} + 0.638\, c_w$$

This expression gives results that are in good agreement with Houde's and Fenwick's experimental data for initial crack widths larger than 0.005 in. (0.13 mm). For initial crack width values less than 0.005 in., however, the above expression results in significantly different values of interface shear stiffness.

Fardis and Buyukozturk (Ref. 35) performed a statistical analysis on data from experiments done at Cornell University (Refs. 61, 62, 70, 126, 127) in order to predict the shear transfer stiffness of precracked reinforced concrete. They formulated two- and three-dimensional mathematical models and implemented them in a finite element analysis program. The major factors that influence the shear stiffness K_s (including both interface shear transfer and dowel action contributions) in their expression are the normal restraining stiffness K_N, the initial crack width c^o_{wm}, and the additional force applied perpendicular to the crack plane. Assuming a linear monotonic response for the 1st load cycle they proposed the following shear stiffness relationships for the combined effect of interface shear transfer and dowel action

$$K_s = K_{DA}, \text{ for } v \leq K_{DA}\ (b_1 c^o_{wm}) \tag{4.9a}$$

and

$$K_s = \frac{K_N}{b_2} + K_{DA}, \text{ for } v \geq K_{DA}\ (b_1 c^o_{wm}) \tag{4.9b}$$

where K_{DA} is the dowel stiffness to be determined and $b_1 = 0.29$, $b_2 = 1.12$ are crack surface parameters evaluated from the experimental behavior. Parameter b_1 denotes the amount of the "free slip" taking place at the crack interface at the initiation of shear loading and parameter b_2

represents the contribution of the interface shear transfer mechanism to shear resistance. The above expressions with b_1 and b_2 constant indicated that the interface shear transfer stiffness

$$K_{IST} = \frac{K_N}{b_2} \tag{4.10}$$

is only a function of the extensional stiffness K_N, which as they pointed out is inconsistent with the experimental evidence showing a strong influence of the initial crack width c^o_{wm} on K_N.

Leombruni et al (Ref. 73) improved the above equation by evaluating the coefficient b_2 as a function of the initial crack width c^o_{wm} for the 1st cycle average slip by regression analysis of experimental data from direct shear tests performed at Cornell University (Refs. 61, 70, 126 and 127) as follows

$$\underline{\text{linear form}}: \quad b_2 = 62.4\ c^o_{wm} \tag{4.11a}$$

$$\underline{\text{power form}}: \quad b_2 = 642.7\ c^{o\ 1.637}_{wm} \tag{4.11b}$$

Initial crack width values in the range of $0 < c^o_{wm} \leq 0.03$ in. were considered. The above two functions for b_2 are plotted together with the experimental data in Fig. 4.11. The data for large initial crack widths of about 0.03 in. strongly influences the form of the function describing the parameter b_2. Since there is considerable scatter in the data and both proposed expressions for b_2 do not show satisfactory correlation with the

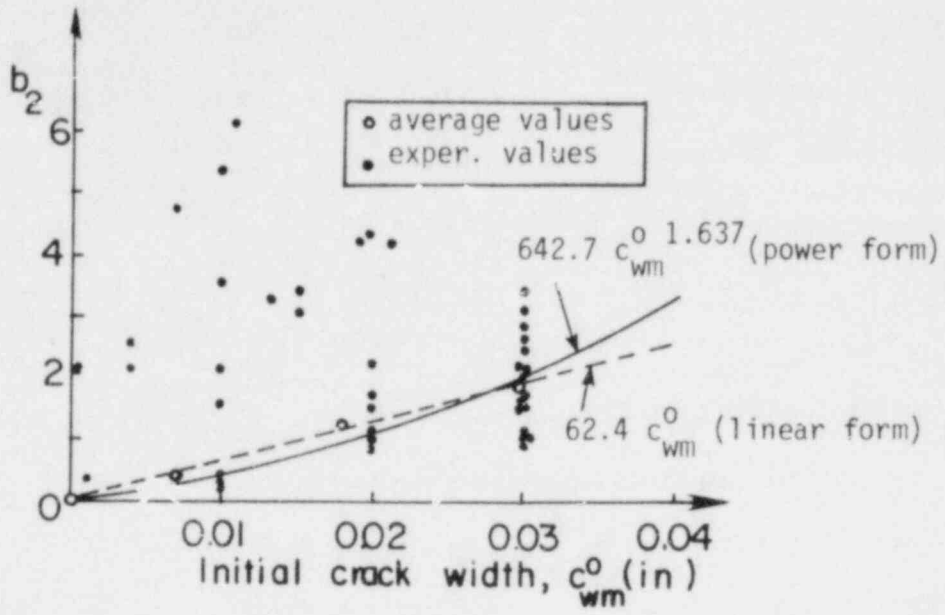

Fig. 4.11. Influence of the initial crack width c^o_{wm} on b_2 from shear slip data (Ref. 35).

experimental values, especially for low values of the initial crack width, use of the more complex power form appears to be unjustified.

Bazant and Gambarova (Ref. 9) recently proposed a basic approach to predict the shear transfer and confinement across a rough crack. They fitted a nonlinear stress-strain relation to the exper mental data by Loeber and Paulay (Ref. 97), and neglecting the dowel stiffness, concluded that the shear stiffness due to interface shear transfer primarily depended on the ratio of the crack slip to crack width, $r = \Delta_s/c_w$, according to the following expression (see Fig. 4.12)

$$v_{IST} = v_u r \left(\frac{\alpha_3 + \alpha_4 |r|^3}{1 + \alpha_4 r^4}\right) \quad \text{(MPa)}, \tag{4.12}$$

with

$$v_u = v_o \left(\frac{\alpha_o}{\alpha_o + c_w^2}\right)$$

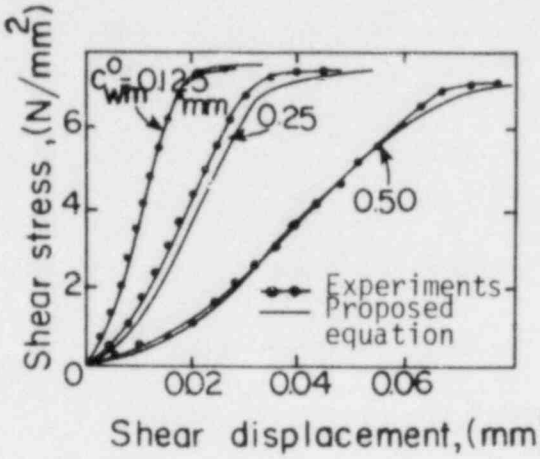

a) Comparison with Paulay and Loeber's results

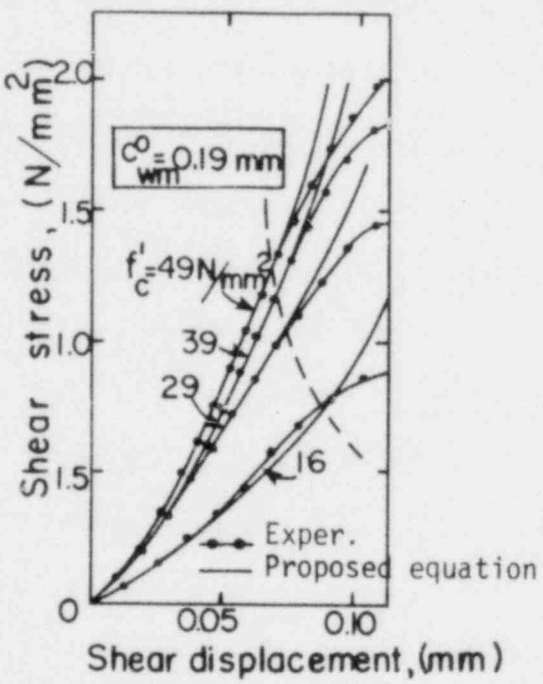

b) Comparison with Fenwick's results

Fig. 4.12. Proposed shear stress-shear slip equations by Bazant and Gambarova (Ref. 9).

$$\alpha_3 = \frac{2.45}{v_o} \quad \text{(MPa)}$$

$$\alpha_4 = 2.44 \left(1 - \frac{4}{v_o} \text{ MPa}\right)$$

$$v_o = 0.245 f_c' \quad \text{(MPa), and}$$

$$\alpha_o = 0.01 D_a^2$$

where v_o is the limiting value of the maximum shear stress v_u (in MPa) when c_w approached zero, and D_a is the average aggregate size in mm.

In spite of the extensive experimental data and analytical studies available, the use of empirical expressions with their limitations and simplifications of the actual response are still unavoidable. A fully rational approach to the problem appears impossible due to the scatter of the data regarding the initial crack width measurements in addition to the random shape of the interface at the crack. However, the accumulated knowledge from each research program has contributed to a better understanding of the factors and their influence on the behavior of the interface shear transfer. It is well established that the shear resistance provided by the interface shear transfer mechanism at a preformed crack in a reinforced concrete member is an efficient means to transmit shear loads.

A linear or a bilinear shear load-shear slip relationship has been found to describe very well the measured response during tests with monotonically applied shear stress of up to 300 psi (2.07 MPa). The major parameters that affect the interface shear transfer stiffness K_{IST} are

the initial crack width (inversely proportional and highly nonlinear variation) and the extensional stiffness in the direction normal to the crack plane (proportional variation). The compressive strength of concrete (for typical values between 3000 and 4000 psi or 21 and 28 MPa), the reinforcing pattern at the crack and the externally applied normal tension have a relatively minor effect. The influence of the loading history (cyclic loading and shear stress level) is discussed in the next section.

b) Cyclic shear

The effect of cyclic shear loading has been investigated on the same direct shear tests described in the previous Section 4.2.1a, by White and Holley (Ref. 126), Paulay and Loeber (Ref. 97), Laible et al. (Ref. 70), and Jimenez et al. (Refs. 61, 62).

White and Holley studied the effect of fully reversed shear to simulate seismic loads in pressurized nuclear containment vessels. Each concrete block specimen was subjected to reversing shear stresses between 120 psi and 160 psi (0.83 MPa and 1.1 MPa) for a maximum of 55 load cycles. Representative shear stress-shear slip hysteresis loops are shown in Fig. 4.8c for preset crack widths of 0.030 in. and 0.020 in. (0.76 mm and 0.51 mm). The measured interface shear stiffness at any peak shear stress after 25 cycles of loading at a preset initial crack width of 0.030 in. and normal restraining stiffness provided by four steel rods of diameter d was nearly constant and equal to

$$K_{IST} = 5 \text{ (ksi/in)}, \text{ for } d = 1.375 \text{ in.} \quad (4.13a)$$

and

$$K_{IST} = 3.1 \text{ (ksi/in)}, \text{ for } d = 1.0 \text{ in.} \quad (4.13b)$$

This implies that the total slip after 25 load cycles is a linear function of the applied shear stress (see Fig. 4.8b). The unsupported length ℓ of these external rods with a cross-sectional area equal to A_s provided an equivalent extensional stiffness $A_s E_s/\ell$ that could be easily changed to a certain extent by varying the length of the rods. The height of the specimen ℓ, which was equal to 36 in. (91.4 mm), was chosen to provide a very conservative representation of the clamping flexibility for the vertical reinforcing bars in secondary nuclear containment vessels. The above shear stiffness values (Eqns. 4.13a and 4.13b) showed a 60% increase in shear stiffness for a 90% increase in the normal restraining stiffness present at the crack plane.

This research program was extended and additional tests were conducted in similar specimens by Laible. Fully reversing shear of about 180 psi (1.24 MPa) was applied to the majority of the specimens for 25 cycles. Laible proposed that when the interface shear transfer was the predominant mechanism, the applied shear stresses were resisted by two major modes: the bearing mode, in which shear was transferred through contact of the concrete asperities of the crack surfaces and not much overriding occurred; and the frictional mode, in which the normal restraining stiffness provided the required friction along the interface for the shear transfer. This meant small changes in crack widths and crack slips during the 1st loading cycle (especially for small crack openings) when the bearing mode predominated, and large crack slips and crack widths in subsequent cycles (or at large initial crack openings), when the latter mode was controlling behavior. Thus the normal extensional stiffness in the reinforcement crossing the crack was a significant factor only in the

frictional mode. Laible found that for the 1st cycle and especially for small initial crack widths of less than 0.010 in. (0.25 mm), the bearing mode of shear transfer along the irregular asperities prevailed at the crack plane. At subsequent cycles or at earlier cycles and initial crack widths larger than 0.010 in. the frictional mode of interface shear transfer controlled. Cyclic loading resulted in a nonlinear hardening type response with increasing stiffness after the initial "free slip" took place (see Fig. 4.13). This was attributed to the grinding action of the frictional mode at the crack interface, which increased the effective contact area of the crack surfaces due to crushing of the protruding particles. As a result, an increase in shear stiffness took place at high shear stresses. The relatively low shear stiffness observed at small shear stresses during reloading was also due to the above degradation of concrete at the crack plane.

Paulay and Loeber studied the effect of repetitive (but not reversed) shear loads producing very high shear stresses of 800 to 830 psi (5.52 to 5.73 MPa) for 33 cycles, while the crack width was kept constant. A bilinear representation of the shear stress-shear slip relation was adopted for a given value of initial crack width (see Fig. 4.3c). The following expression for the shear slip of the upper portion of the load-displacement curve as a function of the applied shear stress level v_{IST}, the initial crack width c_{wm}^{o} (inches), and the number of cycles n was determined from the experimental data

$$\Delta_s = 0.01\, c_{wm}^{o}\, [(2n + 86) + 5.72 \times 10^{-2}\, v_{IST}] \qquad \text{(in.)} \qquad (4.14)$$

where V_{IST} is in psi.

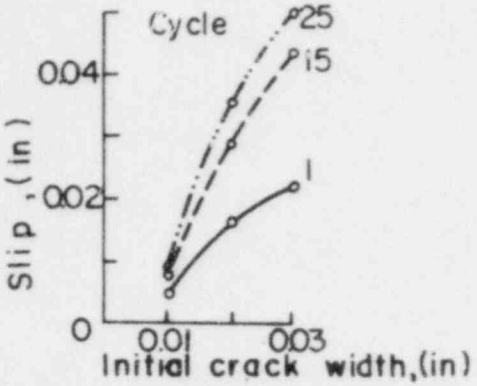

a1) Variation of slip with initial crack width

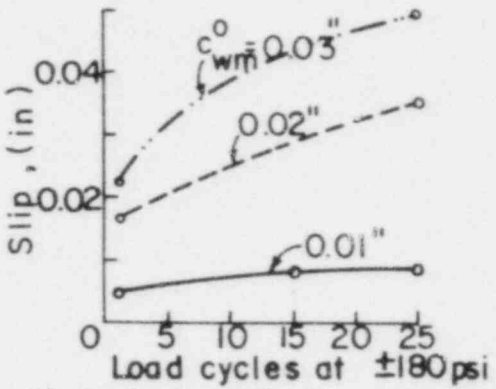

a2) Variation of slip with load cycles

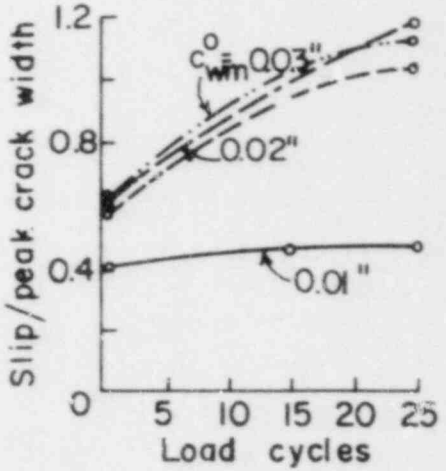

a3) Variation of slip-to-peak crack width with load cycles

a) Slip as a function of crack width and cycling (restraint stiffness K = 3420 kip/in.).

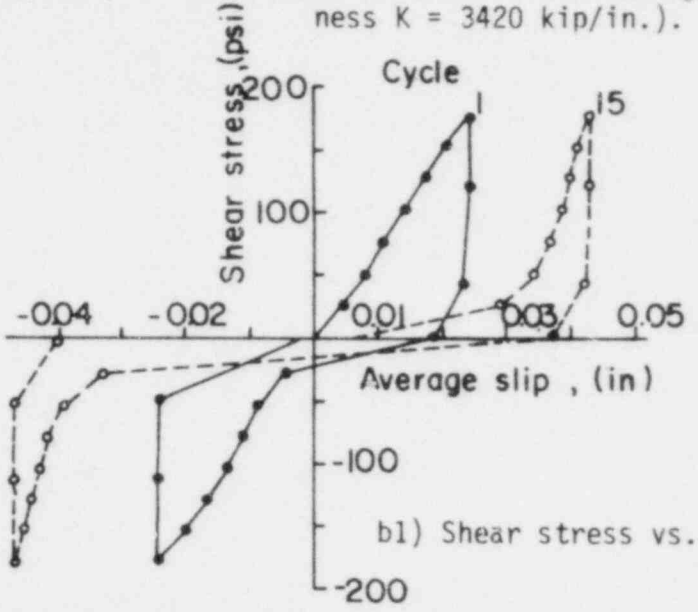

b1) Shear stress vs. slip

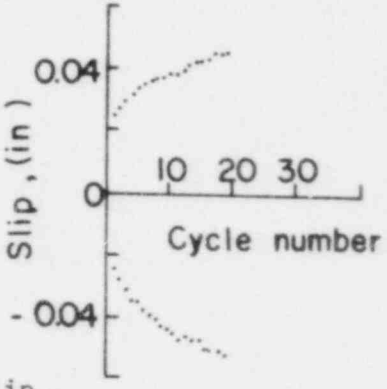

b2) Slip vs. cycle number

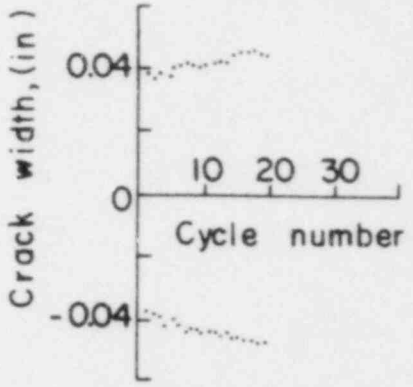

b3) Crack width vs. cycle number

b) Typical test results: Specimen A1, initial crack width = 0.030 in. and restraint stiffness = 3420 kip/in.

Fig. 4.13. Typical test results from Laible et al. (Ref. 70).

In the above equation the residual slip at zero shear

$$\Delta_{s(r)} = 0.01\ c^{o}_{wm}\ (2n + 86) \tag{4.15}$$

increases with increasing number of cycles and initial crack width.

The upper portion of the loading curve (high shear stresses) exhibited a nearly constant tangent interface shear transfer stiffness according to the relation

$$K_{IST} = 1.75/c^{o}_{wm} \qquad \text{(ksi/in)} \tag{4.16}$$

Again, the shear stiffness K_{IST} showed a nonlinear dependence on the initial crack width, and increased with decreasing c^{o}_{wm} . Although the secant shear stiffness at each shear stress level decreased with cycling, the tangent shear stiffness of the steeper portion of the curve remained approximately unchanged for a given value of the initial crack width.

Jimenez et al. performed additional experiments on large block specimens with larger size embedded bars and found results similar to those of Laible. From a regression analysis of Laible's experimental data, they obtained an expression for the ratio of the shear displacement $\Delta_s^{(n)}$ at the nth cycle to the shear displacement $\Delta_s^{(1)}$ at the 1st cycle as a function of the number of cycles n and the initial crack width c^{o}_{wm} as follows,

$$\phi^{(n)}_{IST} = n^{(5.2\ c^{o}_{wm} + 0.12)} \tag{4.17}$$

This expression (Fig. 4.14) is valid for initial crack widths from 0.010

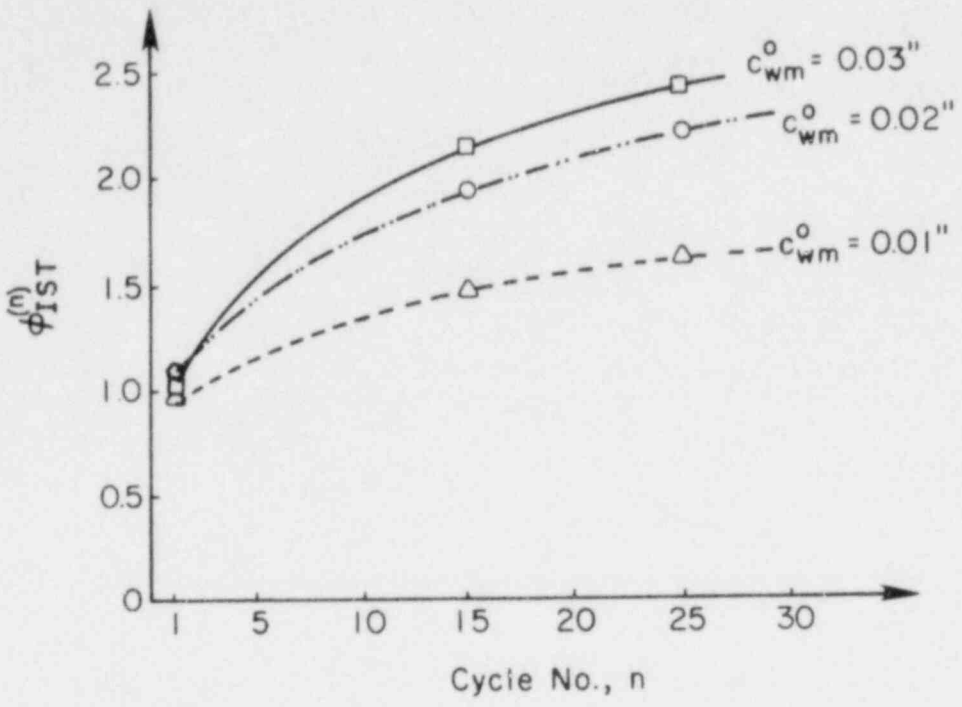

Fig. 4.14. Increase in maximum shear displacement with cycling (Ref. 61).

to 0.030 in. (0.25 to 0.76 mm) and steel ratios between 0.0107 and 0.0214. Thus, the maximum displacement at cycle n is given by the expression

$$\Delta_s(n) = \Delta_s(1)\ \phi_{IST}^{(n)} \tag{4.18}$$

where

$$\Delta_s(1) = K_{IST}^{-1}\ v_{IST}$$

is calculated from Eqn. 4.6 for monotonic shear loading.

Jimenez et al. also modeled the experimental shear stress-shear slip hysteresis loops with linear segments for the loading and unloading portion (see Fig. 4.15) and developed a computer program to predict the shear displacements at a certain shear stress level and load cycle number.

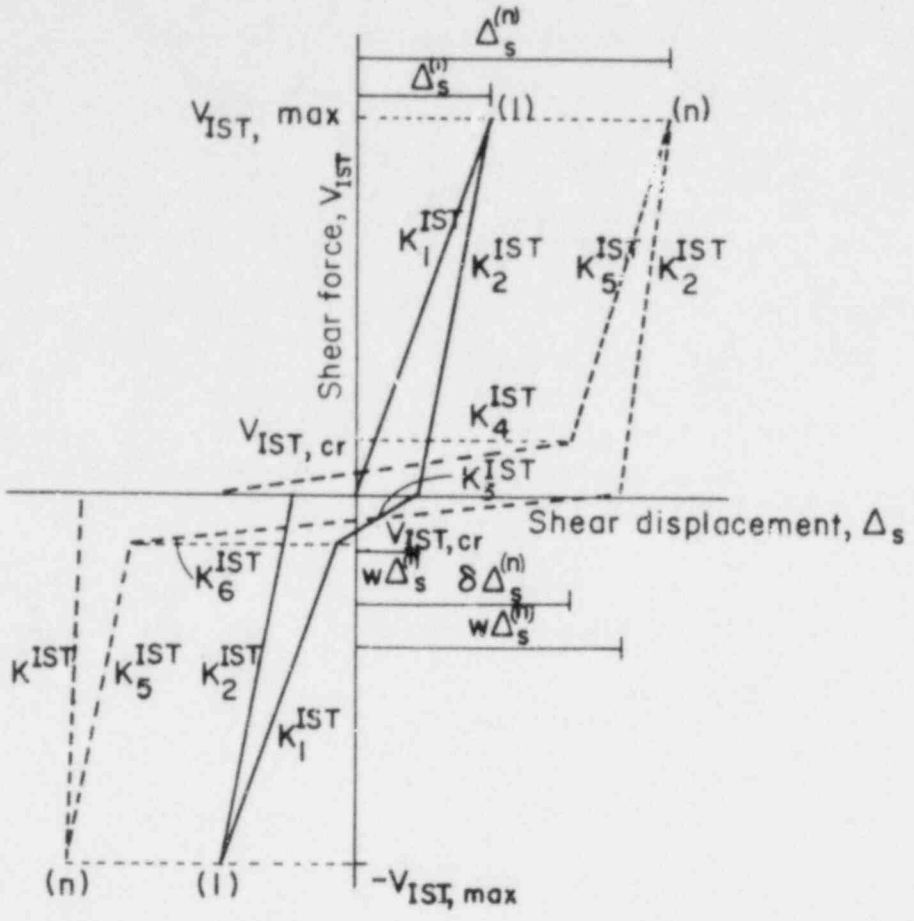

Fig. 4.15. Idealization of the IST experimental hysteresis loops (Ref. 61).

According to the experimental evidence reviewed in this section, it is evident that fully reversing cyclic shear loading greatly affects the response of the interface shear transfer mechanism and its shear stiffness, particularly at large initial crack widths (larger than 0.020 in.). The influence of cyclic shear depends on both the peak shear stress and the magnitude of the initial crack width. For small initial crack widths (less than 0.010 in.) an increase in the peak shear stress results in an irreversible damage of the shearing surfaces. The resulting gains in crack width and slip are more severe than those which would have been

caused by cycling at the same peak shear stress level. At a fixed shear stress level the shear displacements increase with cycling, the rate of increase being higher in the initial load cycles, as shown in Fig. 4.14. A stable condition is reached unless the applied shear approaches the ultimate shear capacity. Aggregate size becomes relatively more effective in resisting slip as the number of load cycles increases. Peak shear slips increase with decreasing aggregate size.

After several load cycles at each peak shear stress, little additional crushing and smoothening of the concrete takes place at the shear plane. As the two opposite faces of the crack slide they also move apart from each other due to the introduced dilatancy, and the local roughness becomes less important as a viable means to transfer shear. Therefore, the same amount of shear requires larger slips to occur, causing a faster decrease in shear stiffness. Similar loss in shear stiffness occurred at the beginning of cycling but for larger values of initial crack width.

The main characteristics of the observed nonlinear stiffening response of the interface shear transfer mechanism are:

a) Significant reduction in the initial shear stiffness at low shear stresses (less than 50 psi or 0.34 MPa) due to the finite size of the crack and the loose material at the crack.

b) Distinct increase in the tangent shear stiffness for shear stresses larger than 50 psi due to increase in shear resistance after the open crack closes and the crushed concrete is compacted. The mechanism in this hardening region is very efficient in transferring shear stresses with relatively small increases in shear displacements.

c) Tangent shear stiffness during unloading is either equal to or larger than that observed during loading, resulting in an increasing value of residual slip and hysteretic behavior. Very rarely were the measured slips at zero shear as small as 50% of the slips at peak shear. Usually they were as large as 80 to 90% of the peak values (see Fig. 4.8c). This was probably the main reason for the soft response at low shear stresses during subsequent reloading in the opposite direction.

d) The area enclosed by the shear stress-shear slip hysteresis loops (see Fig. 4.13b(1)) which is a measure of the hysteretic damping coefficient of the structure, decreased with cycling. In other words, the ability of the cracked region to absorb energy by direct bearing or by friction at the rough interface decreased with increasing number of shear load cycles.

4.2.2 Dowel stiffness and strength (single crack)

Different types of tests have been performed to study the dowel stiffness K_{DA} (k/in), that is, the relation between the shear dowel force and the corresponding shear displacement of an embedded bar crossing a single crack. There are three main modes of deformation for a rebar subjected to a shear load; bending, shearing, and kinking, shown in Fig. 4.16 (Ref. 98) together with the shear capacity corresponding to each mode.

Experiments have been conducted on pavement joint, divided beam, beam-end, and direct dowel specimens. Dowel stiffness and dowel splitting load expressions proposed by each investigator are given in Table 4.B.

Table 4.B. Summary of dowel force-dowel slip relationships for DA mechanism.

Reference	Type of Test	Load History	Dowel Force (V_{DA}), Dowel Slip (Δ_{sd}) Relationship	Dowel Splitting Load (V_{do})
42	Analysis of "BOEF"	M	$V_{DA} = \frac{3E_s I_s \beta^3 \Delta_{sd}}{3+6\beta\ell+6(\beta\ell)^2+2(\beta\ell)^3}$; $\beta = \sqrt[4]{\frac{k_f d}{4E_s I_s}}$; $k_f = 21.5\ f_c'$ (MPa/mm)	---
68	Divided beams	M	$V_{DA} = c_1\sqrt{f_c'}\ (dI_t b^3)^{1/4}$	---
37,38	Direct shear (long and short dowel)	M	$V_{DA} = 445\ V_{do}\Delta_{do}$ (before cracking); $\Delta_{do} \leq 0.0023$ in. for bottom cast dowels	$V_{do} = 0.174 s_r b_n f_{st}$ (s_r<5.875") $V_{do} = 1.02 b_n f_{st}$ (s_r>5.875")
115	Divided beams	M	---	$V_{do} = 2.04+0.1 b_n^2 f_t'$
7	Divided beams	M	$V_{DA} = 317\ V_{do}\Delta_{do}$ (before cracking); $\Delta_{sd} = \gamma_o V_{DA}^2$ (after cracking); $\gamma_o = 0.45 \frac{x_s^2}{I_t}$	$V_{do} = 0.045\ b_n d\sqrt[3]{f_c'}$
63	Analysis of "BOEF" With Stirrups	M	--- ($k_f = \frac{E_c b_n}{h_{ef}}$)	---
30	Direct Shear (Inclined Bars)	M	$\Delta_{sd} = \frac{3V_{DA}}{10^6 d}\sqrt{\frac{1}{\sigma_{co}}\tan(\frac{V_{DA}}{V_{du}}\frac{\pi}{2})}$	$V_{do} = 0.2d^2 f_y \sin\delta[\sqrt{1+\frac{\sigma_{co}}{0.03 f_y \sin^2\delta}}-1]$

(Continued)

Table 4.B. (Continued)

Reference	Type of Test	Load History	Dowel Force (V_{DA}), Dowel Slip (Δ_{sd}) Relationship	Dowel Splitting Load (V_{do})
58	Beam-End Specimens	M	$V_{DA} = 2000\, V_{do}\Delta_{do}$ (before cracking); $\Delta_{do} \leq 0.005$ in.	$V_{do} = 0.040\, b_n \sqrt[3]{f_c'}$
33	Direct Shear	M,C(R)	$V_{DA} = k_f^{3/4}\, d/0.23$; $k_f = 1000$ (ksi/in)	---
109	Direct Shear	M,C(R)	$V_{DA} = \frac{d}{8}\sqrt[4]{\pi E_s k_f^3}\,(\frac{f_c'}{4000})^{3/2}$ (before cracking)	---
4	Analysis	M	$V_{DA} = c_1 + c_2(m+1)\,\Delta_d^m$; $c_1 = D_{so}$; $c_2 = \frac{D_{sf}-D_{so}}{\Delta_{do}^m}$; $m = \frac{1}{(\frac{D_{so}}{D_{sf}}) - 1}$	(see Ref. 30)
61	Direct Shear ("BOEF")	M,C(R)	(M): $V_{DA} = (\frac{n_b d^{1.75}}{3.2\times10^{-3}})\Delta_{sd}^{(1)}$; $k_f = 750$(ksi/in), at 1st cycle with $V_{DA} \leq 5$ ksi/bar; (C): $\Delta_{sd}^{(n)} = \phi_{DA}^{(n)}\Delta_{sd}^{(1)}$; $\phi_{DA}^{(n)} = 0.029n + 0.97$	$V_{do} = \frac{db_n}{n_b}[0.47 + \frac{0.54\, c_m}{\frac{b_n}{n_b^2} + d}]$ (no transverse steel); $+ (7n_b c_m - 8.5)\rho_t f_{yt}$ (with transverse steel)

Notes: M = monotonic shear.

C(R) = cyclic reversing shear.

"BOEF" = beam on elastic foundation.

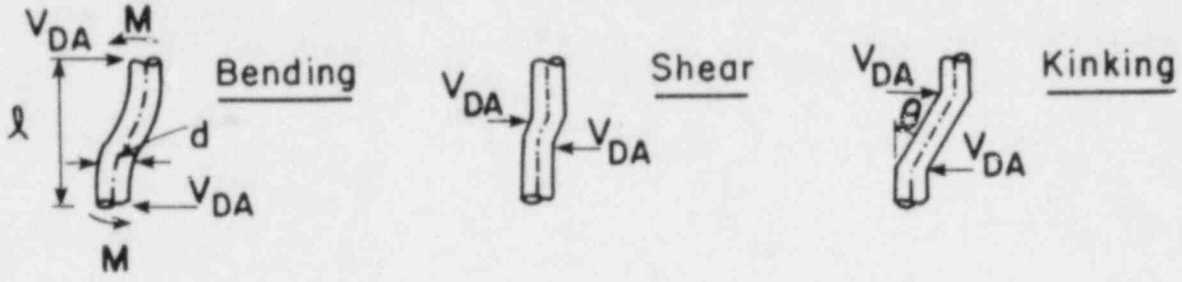

$$V_{du} = \frac{2M_u}{\ell} = \frac{4dA_s f_y}{3\pi} \qquad V_{du} = \frac{A_s f_y}{\sqrt{3}} \qquad V_{du} = A_s f_y \sin\theta$$

Fig. 4.16. Dowel action mechanisms of shear transfer at a crack.

a) Monotonic shear

The majority of the beam-end specimens by Gergely (Ref. 46), Houde (Ref. 58) and Kemp et al. (Ref. 67), shown in Fig. 4.17, and the divided beam specimens by Krefeld and Thurston (Ref. 68), Taylor (Ref. 115) and Baumann (Ref. 7), shown in Fig. 4.18, failed by horizontal concrete splitting along the reinforcement, where the concrete cover was minimum. The major variables influencing the dowel stiffness in a beam subjected to monotonic shear were found to be the minimum concrete cover c_m, the net width of concrete b_n, the bar diameter d, the compressive concrete strength f_c', and the distance of the crack to the first stirrup. The influence of the inclination angle of the rebar to the crack plane on dowel stiffness was not studied in the beam tests mentioned above.

As far as the dowel strength is concerned, it was determined that in the beam-end tests the bar diameter did not have a significant influence on bond splitting when no transverse steel was present. Transverse

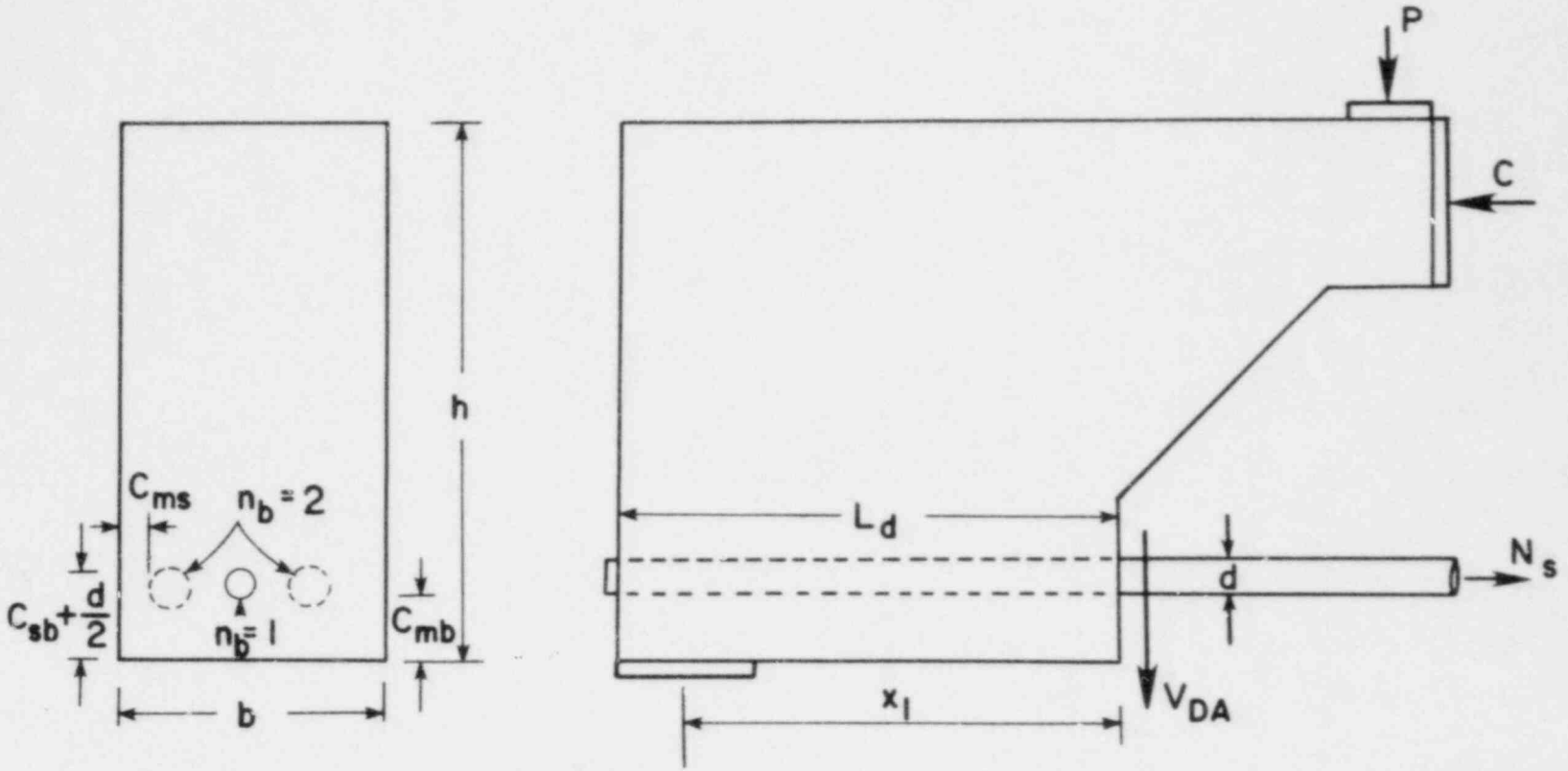

Fig. 4.17. Beam-end specimen.

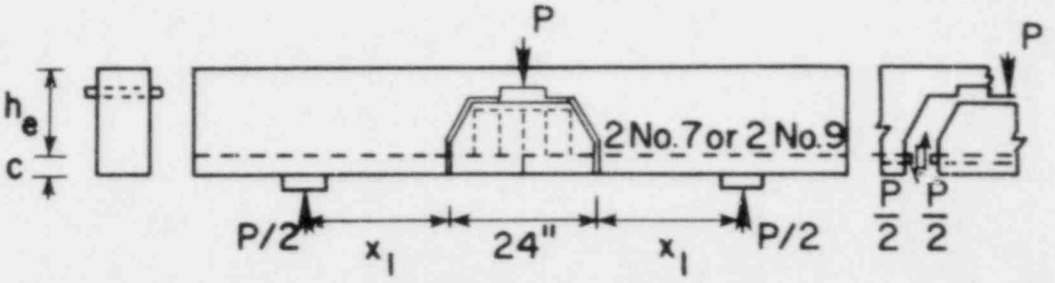

Fig. 4.18. Divided beam specimen.

reinforcement placed at less than 1 in. (25 mm) distance from the crack could improve the behavior by preventing dowel splitting and confining the surrounding concrete. This was also observed by Sharma (Ref. 107) in his experiments on the splitting strength of concrete.

The effect of a simultaneous axial tension in the bar on the dowel stiffness was studied by several researchers in the above beam tests (Refs. 58, 67 and 107). It was found that the axial stress had to be at least 70 to 80% of the yield strength of the bar to have a significant effect in reducing the dowel stiffness by partially plastifying the bar.

Since the response of the dowel mechanism in planar structures (such as in the flat specimen in the present experimental investigation) is much different than that in the beam tests, a detailed description is undertaken below only of the experimental and analytical studies performed on direct dowel specimens. The interested reader can find additional information on the beam-type tests in Ref. 61. In planar structural elements, due to the existence of a larger concrete depth under each bar, the support provided by the concrete to each bar is far better than in a beam. Redistribution of stresses and higher dowel stiffnesses are possible in the former case, while in the latter splitting along the bar usually controls. A sketch of the different dowel stiffness response in the cases of a beam and a planar element is given in Fig. 4.19 (see Ref. 120).

In the direct dowel tests under monotonic shear, specimens tested by Eleiott (Ref. 33)(see Fig. 4.20), Stanton (Ref. 109)(see Fig. 4.21), and Jimenez et al. (Ref. 61)(see Fig. 4.9b) failed by splitting in the concrete, while those by Dulacska (Ref. 30)(see Fig. 4.22a), and Paulay et al. (Ref. 98)(see Fig. 4.23a) by yielding of the reinforcement. The latter failure

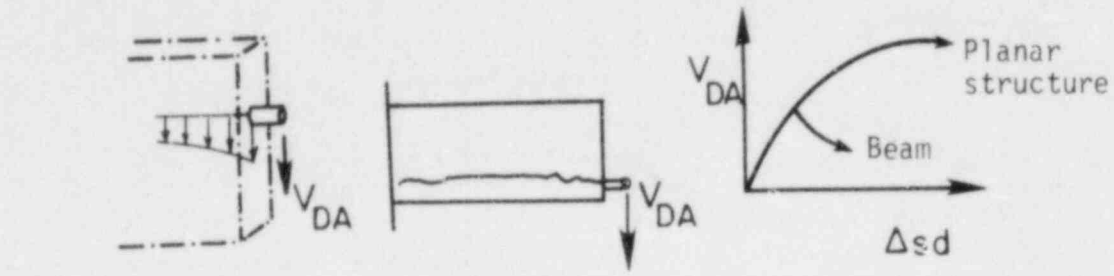

a) Planar structure b) Beam c) Load deflection curves

Fig. 4.19. Dowel cracking.

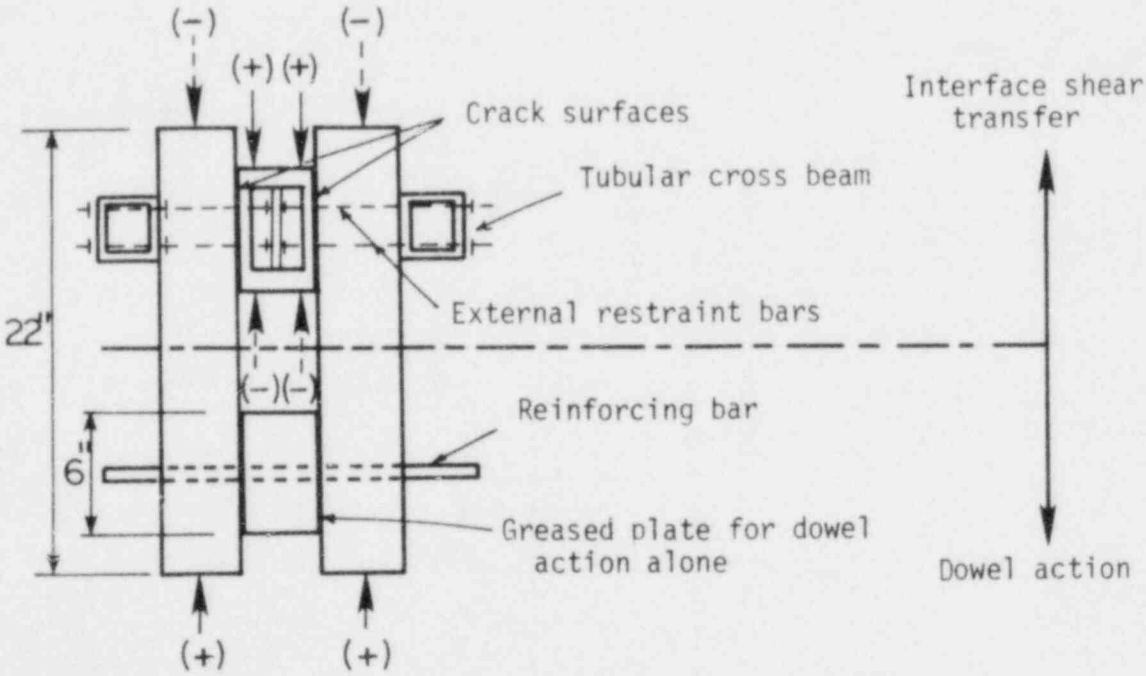

Fig. 4.20. Eleiott's test specimen.

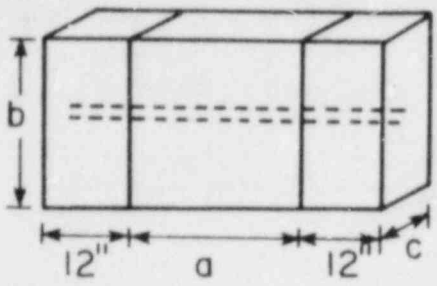

a) Specimen design

Note: 12" < a < 24"
20" < b < 24"
7.5" < c < 8"

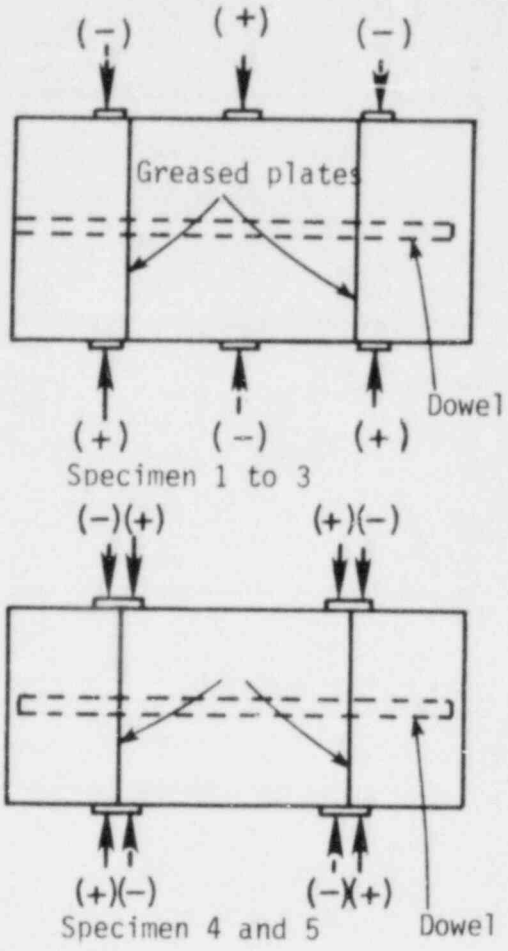

b) Loading patterns

Fig. 4.21. Stanton's test specimen.

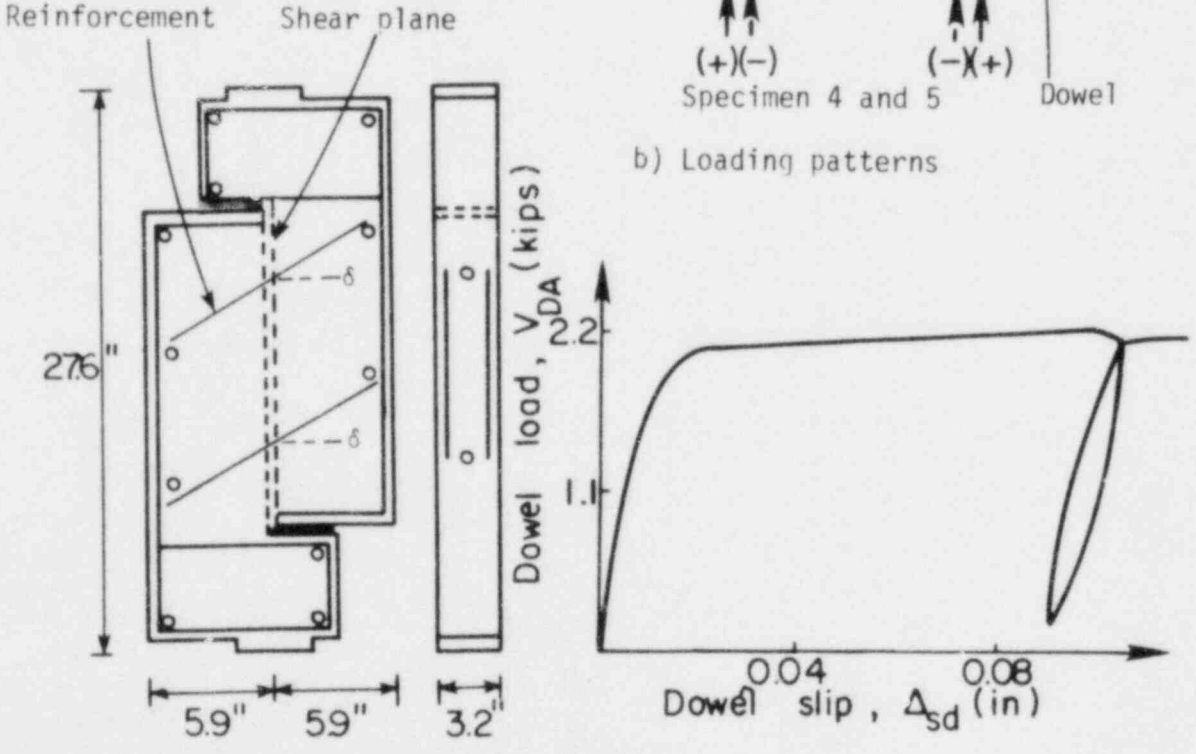

a) Test specimen

b) Typical dowel load - displacement curve

Fig. 4.22. Study of dowel action by Dulacska (Ref. 30).

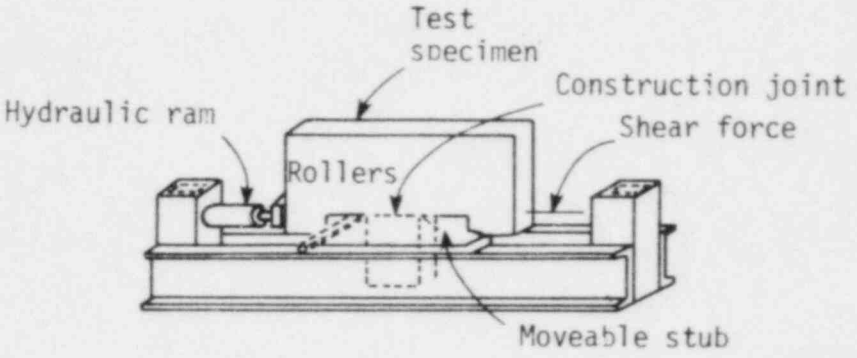

a) Test specimen.

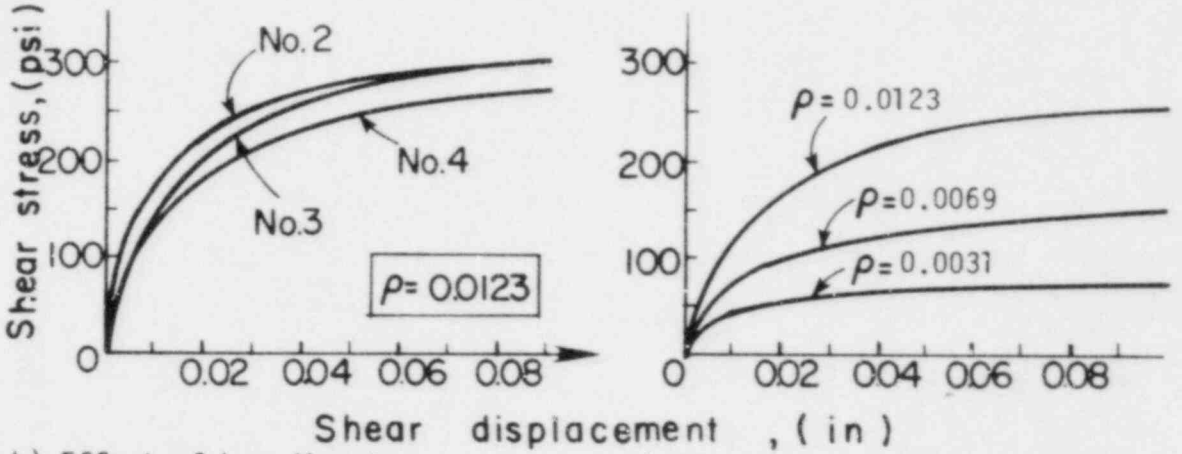

b) Effect of bar diameter

c) Effect of reinforcement ratio

Fig. 4.23. Test specimen and dowel load-displacement response from Paulay et al. (Ref. 98).

mechanism was mainly due to the presence of better confinement provided by the transverse steel.

Dulacska performed direct dowel tests with bars inclined to the shear crack at preselected angles δ (10, 20, 30 and 40 degrees) to study also the effect of the inclination angle on the dowel stiffness and strength. The specimen, shown in Fig. 4.22a, consisted of two concrete blocks separated by two 0.0078 in. (0.20 mm) thick layers of brass to ensure that the relative slip of the two blocks would be resisted only by the dowel forces in the reinforcement crossing the artificial crack provided. Reinforcement in the form of closed stirrups with a diameter of 0.39 in. (10 mm), 0.254 in. (6.5 mm) and 0.546 in. (14 mm) was used.

The empirical dowel force-displacement relation determined from the experiments was similar to that of an ideally elastoplastic behavior (see Fig. 4.22b) and was of the following form

$$\Delta_{sd} = \frac{3\ V_{DA}}{d \times 10^3} \sqrt{\frac{1}{\sigma_{co}} \tan\left(\frac{V_{DA}}{V_{du}} \frac{\pi}{2}\right)} \qquad \text{(in.)} \qquad (4.19)$$

where Δ_{sd} is the dowel slip (in.), V_{DA} the dowel force (kips), V_{du} the ultimate dowel force (kips), d the diameter of the reinforcement (in.), and σ_{co} the cube compressive strength of concrete (ksi). Compressive strengths of concrete in the range from 1420 psi (9.8 MPa) to 4540 psi (31.3 MPa) were measured. The effect of the bar inclination δ was found to be insignificant compared with the effect of the bar diameter and the compressive strength of concrete.

The main parameters that influenced the ultimate dowel force V_{du} were the bar diameter d and the concrete cube compressive strength σ_{co} according to the relationships given below,

$$V_{du} = 0.2\ d^2\ f_y\ \sin\delta\ \left[\sqrt{1 + \frac{\sigma_{co}}{0.03 f_y\ \sin^2\delta}} - 1\right],\ \text{for}\ \delta > 0\ \text{deg.} \quad (4.20a)$$

and

$$V_{du} = 1.16\ d^2\ \sqrt{f_y\ \sigma_{co}}\ ,\quad \text{for}\ \delta = 0\ \text{deg.} \quad (4.20b)$$

where f_y is the yield strength of the steel and δ is the inclination angle (degrees). For a given value of f_y and σ_{co} the maximum dowel force is directly proportional to the square of the bar diameter.

Paulay et al. (see Fig. 4.23) concluded that the dowel shear stiffness was proportional to the reinforcement ratio available at the shear crack and independent of the bar size. According to them, among the three possible dowel mechanisms (see Fig. 4.16), the major ones were direct shear and kinking of the bar, the latter mechanism being more important for larger crack width values. The dowel load-dowel slip curves given in Fig. 4.23(b,c) showed a nonlinear response similar to Dulacska's relation (Eqn. 4.19).

Eleiott's smaller scale specimens (described in the previous section) were used to study the behavior of the dowel action mechanism for embedded No.4 and No.6 reinforcing bars crossing a 15 in^2 shearing area with greased steel plates. Although the shear loading was cyclic, the response during the 1st cycle under monotonically increasing shear will be presented here. Eleiott modeled the reinforcement as a beam on an elastic foundation and proposed the following dowel stiffness relation for the 1st load cycle,

$$K_{DA} = k_f^{3/4} d / 0.23 \qquad \text{(k/in)} \qquad (4.21)$$

where k_f is the effective foundation modulus assumed to be equal to 1000 ksi/in for the narrow range of bar sizes studied, and d is the bar diameter (inches). The above relation indicated that dowel stiffness was proportional to the bar diameter, while Dulacska found that it was proportional to the square of the bar diameter.

Substituting the value of 1000 ksi/in for k_f in the above Eqn. 4.21 a value for the dowel stiffness K_{DA} under monotonic shear equal to

$$K_{DA} = 773.2\ d \qquad \text{(k/in)} \qquad (4.22)$$

is obtained as a function of the bar diameter only.

Several analytical studies were based on the above mentioned model developed by Friberg (Ref. 42), considering the embedded bar as a beam on an elastic foundation ("BOEF"). Various tests were performed on contraction pavement joints aiming for an estimate of the foundation modulus of concrete k_f, a very important parameter of dowel stiffness. In Friberg's model the concrete around the bar and in the opposite direction of the dowel displacement was ignored and the bar was assumed to be supported by the concrete under the bar, acting as an elastic foundation with a modulus k_f. According to "BOEF" model, the dowel stiffness depended on the "free length" of the bar 2ℓ, which is the total unbonded length of the bar due to the relative slip of the bar and crushing of the concrete at the crack (see Fig. 4.24), the bar diameter d, and especially on the concrete foundation modulus k_f.

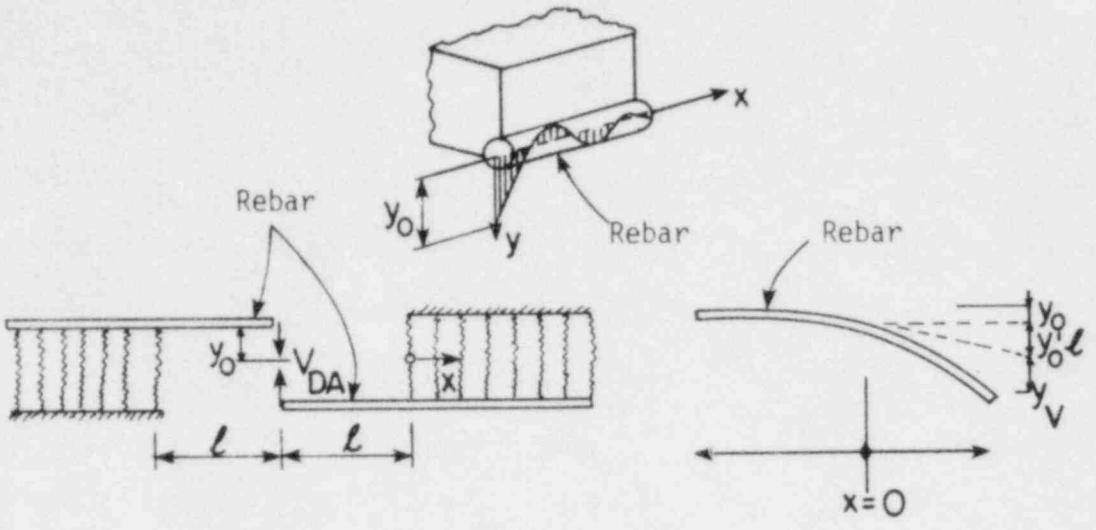

Model and partial displacements

Fig. 4.24. Reinforcing bar as a beam on elastic foundation (Friberg, Ref. 42).

If the reinforcing bars are inclined to the crack, for example in the case of an orthogonally reinforced planar concrete element with diagonal cracking, the "free length" of the bar is influenced also by the inclination angle δ between the bar axis and the direction normal to the crack. According to Schaefer (Ref. 105), the "free length" of the bar 2ℓ was proportional to the inclination angle δ. Also, according to Leonhardt (Ref. 74), kinking of the bar and wedging action was enhanced in the case of bars inclined to the crack.

The determination of the foundation modulus k_f is a very difficult task, due to the fact that it is affected by the axial stress in the bar, the level of concrete confinement, the concrete cover and load cycling. In a review by Finney (Ref. 39) the values of k_f varied from about 700 to 8800 ksi/in (190 to 2400 MPa/mm) with average values from 900 to 2600

ksi/in (250 to 700 MPa/mm). The expressions for k_f given by various researchers are shown in Table 4.B.

Johnston (Ref. 63) presented an analytical model for beams that combined the idea of "BOEF" with the inclusion of stirrups as elastic supports in resisting the applied dowel forces after the concrete cover cracked horizontally. Depending on the value of critical dowel deflection that caused the longitudinal cracking, the dowel stiffness decreased generally with increasing axial tensile stress. It was found that for ratios of axial stress to yield strength higher than 0.8, the presence of axial stress in the rebar had a more severe influence on dowel stiffness. The critical deflection of the bar causing horizontal cracking on the cover, the modulus k_f and the stirrup elastic spring constant were not determined in his study, but reasonable assumptions were made for their values.

Stanton, using Friberg's expression for the dowel stiffness, calculated the effect of the "free length" for several values of the foundation parameter β_f equal to

$$\beta_f = \sqrt[4]{k_f/4\ E_s I_s} \qquad (\text{in.}^{-1}) \qquad (4.23)$$

where $E_s I_s$ is the bending stiffness of the rebar. Reinforcing bars with a diameter of 1.375 in. or 35 mm (No.11) and 2.25 in. or 57 mm (No.18) were employed in his specimens, shown in Fig. 4.21. In a plane stress elasticity analysis of a bar bearing on one half of its perimeter against the concrete (see Fig. 4.25b), he found that k_f depended only slightly upon the bar size and that horizontal splitting would tend to form before the vertical splitting. He proposed the following dowel stiffness relation

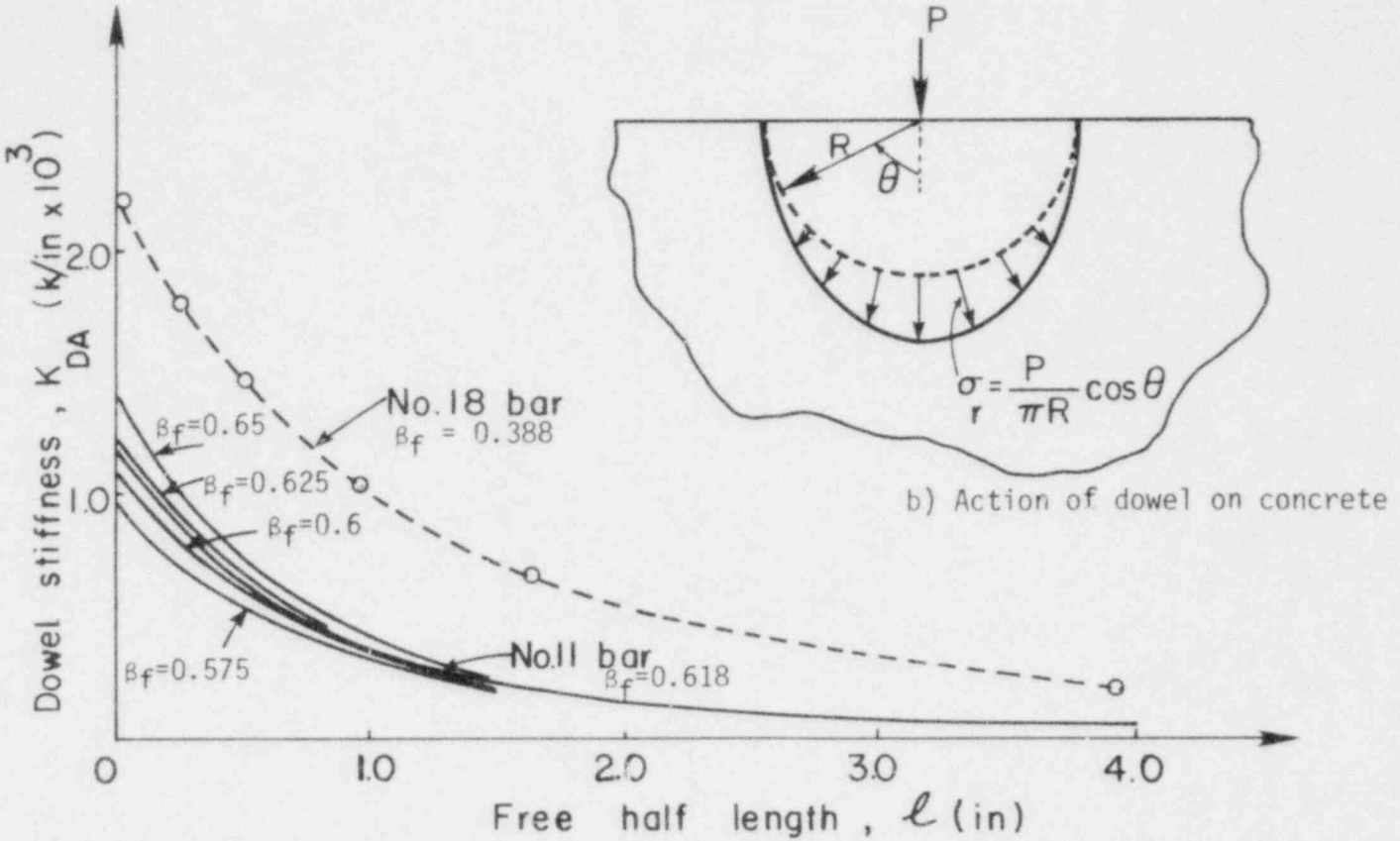

b) Action of dowel on concrete

a) Dowel stiffness as a function of free half-length

Fig. 4.25. Dowel stiffness according to Stanton (Ref. 109).

for the 1st load cycle of his experimental results, assuming that no local concrete crushing took place under the applied dowel force ("free length" equal to zero) and neglecting the effect of shear strains in the rebars,

$$K_{DA} = E_s I_s \beta_f^3 \left(\frac{f_c'}{4000}\right)^{3/2} = \frac{d}{8}\sqrt[4]{\pi E_s k_f^3}\left(\frac{f_c'}{4000}\right)^{3/2} \qquad \text{(k/in)} \qquad (4.24)$$

where f_c' is given in psi. For a nonzero "free length" the expression for dowel stiffness was given as follows

$$K_{DA} = 3\, E_s I_s \beta_f^3/(3 + 6t + 6t^2 + 2t^3) \qquad \text{(k/in)} \qquad (4.25)$$

where $t = \beta_f \ell$ with β_f determined from Eqn. 4.23 and ℓ being the half "free length" (in.). The dowel stiffness for a single No.11 and No.18 bar is plotted versus the half "free length" for various values of the parameter β_f in Fig. 4.25a.

Jimenez et al. investigated the dowel behavior for No.9 and No.14 bars (test series D) in the same specimens as in test series (C) but with greased steel plates placed at the crack plane to eliminate the interface shear transfer action. They also used the "BOEF" model to evaluate the foundation modulus k_f from the test series (D) specimens, assuming that the effect of the half "free length" of the bar ℓ was of the same order as the initial crack width and therefore could be neglected. An average value of 750 ksi/in (200 MPa/mm) was obtained for k_f. The dowel stiffness expression proposed for the 1st cycle and for dowel shear stresses less than or equal to 5 ksi (34.5 MPa) had the following form,

$$K_{DA} = 312\, n_b d^{1.75} \qquad \text{(k/in)} \qquad (4.26)$$

where n_b is the number of bars per layer and d the bar diameter (in.).

Regarding the dowel capacity of the rebars, Jimenez et al. developed a dowel splitting load expression from a regression analysis of divided beam and beam-end specimen tests (Refs. 7, 58, 67, 68, 115) with or without transverse reinforcement. The dowel load (in kips) required to produce a concrete splitting failure was

$$V_{do} = \frac{db_n}{n_b} \quad 0.47 + \frac{0.54\ c_m}{\left(\frac{b_n}{n_b^2} + d\right)} \qquad \text{(kips)} \qquad (4.27)$$

where c_m is the minimum concrete cover, d the bar diameter, b_n the net width at a layer of bars (perpendicular to the shear force), and n_b the number of bars in a layer, with all dimensions in inches.

Al-Mahaidi (Ref. 4) in his analysis of reinforced concrete deep members proposed a nonlinear dowel force-dowel displacement relation in terms of the slip Δ_{sd} (in.) in a determinate form represented by a polynomial based on Dulacska's experimental results as follows,

$$V_{DA} = (667 - 1208\Delta_{sd}^{0.198})\ \Delta_{sd} \qquad \text{(kips)} \qquad (4.28)$$

assuming an initial tangent dowel stiffness of 667 k/in (117 kN/mm), a value estimated from the test results. This form of force-displacement resulted in the following nonlinear dowel stiffness as a function of Δ_{sd},

$$K_{DA} = 667 - 1447\ \Delta_{sd}^{0.198} \qquad \text{(k/in)} \qquad (4.29)$$

In Table 4.C the dowel stiffness values K_{DA} at the 1st load cycle (monotonic shear) for a single No.6 and No.14 reinforcing bar predicted by Eqn. 4.24 (Stanton, Ref. 109), Eqn. 4.21 (Eleiott, Ref. 33), Eqn. 4.26 (Jimenez et al., Ref. 61), Eqn. 4.19 (Dulacska, Ref. 30) and Eqn. 4.29 (Al-Mahaidi, Ref. 4) are compared. Foundation modulus values of concrete k_f from 750 to 3000 ksi/in have been assumed for Eqns. 4.24 and 4.21 that include k_f as a parameter. Eqn. 4.15, developed assuming k_f = 750 ksi/in for No.9 and No.14 bars, gives the lowest dowel stiffness value of 190 k/in for a No. 6 bar, for which a higher foundation modulus than 750 ksi/in is likely to be true. Since Eqns. 4.21, 4.19 and 4.29 were based on test results with relatively small size bars (0.39 to 0.75 in. bar diameter), they give more similar K_{DA} values for the No.6 rebar than for the No.14 rebar. For the No.14 rebar Eqn. 4.21 (Eleiott) predicts approximately twice as large K_{DA} values than Eqn. 4.24 (Stanton), which is probably more appropriate for large size bars (No.14 and No.18).

Summarizing, the "BOEF" model seems to be a good assumption for the case of membrane elements with in-plane shear forces, at least for low and intermediate shear stress levels. The dowel response at that load stage can be approximated as linear. On the contrary, for higher shear stresses a nonlinear behavior was observed. Another important point derived from the experimental work is that the chances of a splitting failure before the full shear capacity of the bar is reached are increased with increasing bar size.

b) Cyclic shear

The major objective in the direct dowel tests performed by Eleiott (Ref. 33), Stanton (Ref. 109), and Jimenez et al. (Ref. 61), described in

Table 4.C. Comparison of predictive expressions on dowel stiffness K_{DA} of a single No.6 or No.14 reinforcing bar at the 1st load cycle (E_s = 28000 ksi, f_c' = 3800 psi).

Reference		K_{DA} (k/in) for one No.6 bar					K_{DA} (k/in) for one No.14 bar				
		k_f = 750 (ksi/in)	1000	1500	2000	3000	k_f = 750 (ksi/in)	1000	1500	2000	3000
109 (Eqn. 4.24)		214	265	360	447	606	500	620	841	1043	1414
33 (Eqn. 4.21)		467	580	786	975	1322	1090	1353	1834	2275	3084
61 (Eqn. 4.26)		190	-	-	-	-	830	-	-	-	-
	(a)	V_{DA}/V_{du} = 0.25:									
30 (Eqns. 4.19 and 4.20)		894	894	894	894	894	2087	2087	2087	2087	2087
	(b)	V_{DA}/V_{du} = 0.5:									
		576	576	576	576	576	1343	1343	1343	1343	1343
4 (Eqn. 4.29)		667	667	667	667	667	667	667	667	667	667

Notes: For Ref. 30 (Dulacska) the dowel stiffness K_{DA} is calculated at two force levels V_{DA}/V_{du} equal to 0.25 and 0.5 since the relation in Eqn. 4.19 is nonlinear (V_{du} ≈ 12 kips for a No.6 bar and 64 kips for a No.14 bar assuming f_c' = 3800 psi, δ = 0 deg., and f_y = 61 ksi).

the previous section, was to study the effect of cyclic shear on the dowel stiffness and strength. The influence of the applied shear stress level and axial stress in the reinforcing bars was also investigated in the experiments by Eleiott, and Jimenez et al.

Eleiott studied the effect of 15 to 20 load reversing cycles at a steel shear stress level equal to either 5.1 ksi (35.2 MPa) per No.6 bar or 13.5 ksi (93.2 MPa) per No.4 bar. Both No.4 and No.6 reinforcing bars were used. For zero axial stress in the bars the load-slip hysteresis loops and the slip versus the number of load cycles are given in Fig. 4.26a.

For the same shear stress level the rate of increase in the slip decreased with increasing number of cycles (see stable behavior after 10 cycles at a steel shear stress of 11.2 ksi (77.3 MPa) per No.4 bar in Fig. 4.26a. After increasing the shear stress level, the rate of increase of slip increased again, but the response was not influenced strongly by the initial 15 load cycles at 11.2 ksi. The hysteretic behavior was similar to that of the interface shear transfer mode with the only major difference of much smaller residual slips at zero stress. Eleiott was not able to quantify the effect of the bar size on the dowel stiffness because of the inconsistency and unreliability of some of the test results.

Eleiott also found that after a number of cycles the concrete did not show signs of additional crushing. An increase in the dowel stiffness was evident after the free slip took place at low shear stresses. The bar could eventually come into full contact with the compacted concrete as the shear stresses increased. As a result, the shear stiffness of the bar increased.

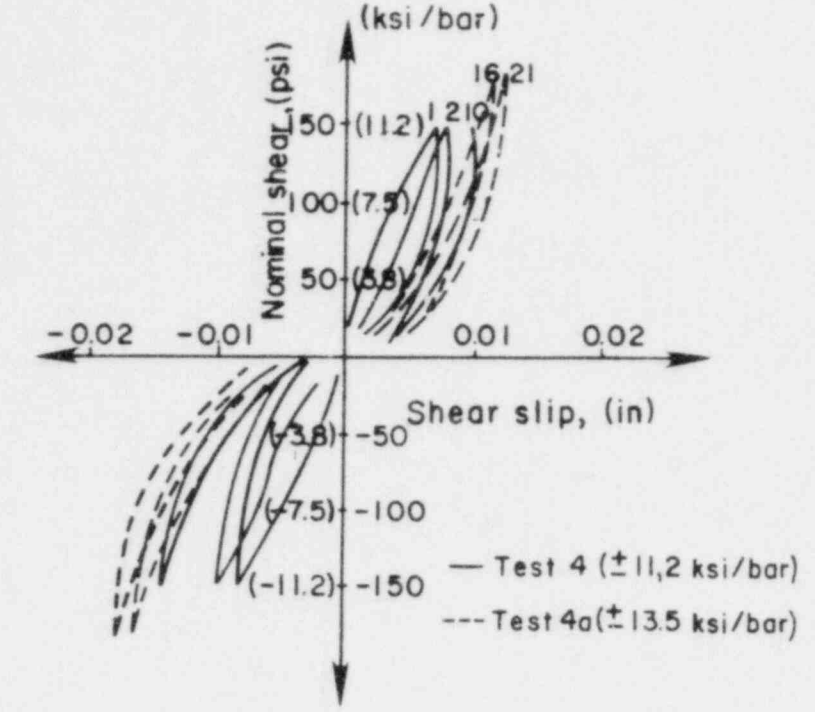

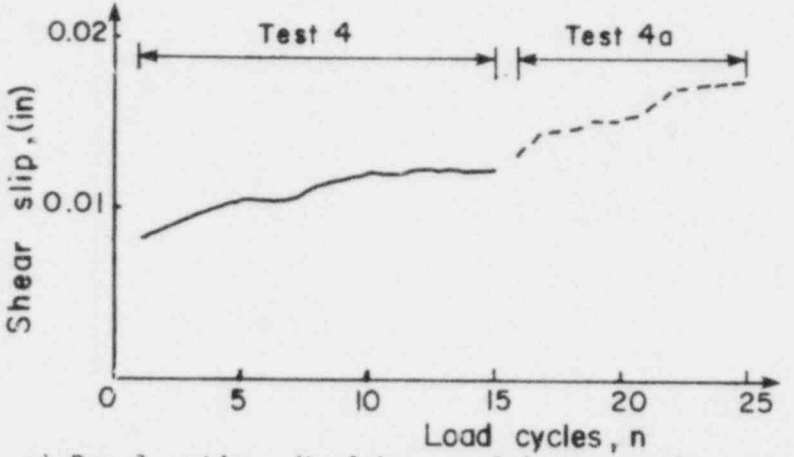

a) Dowel action, No.4 bar, axial stress $f_t = 0$

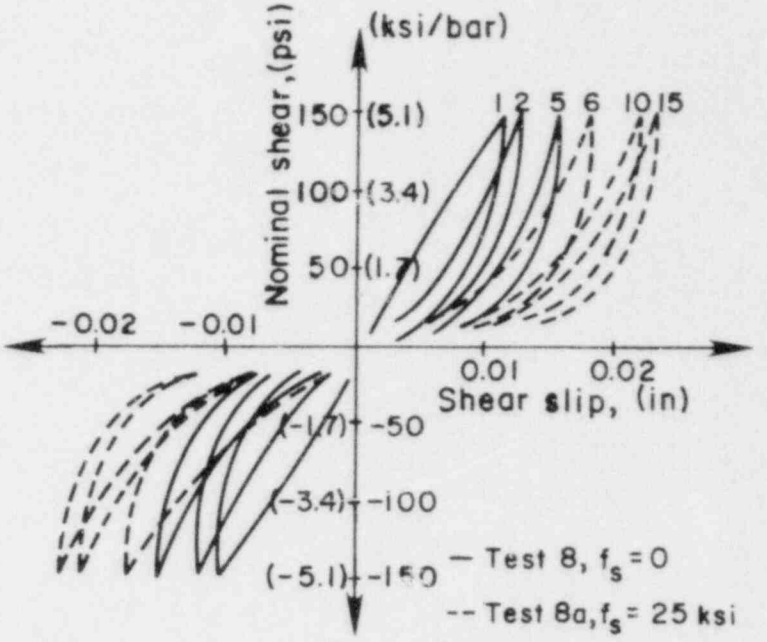

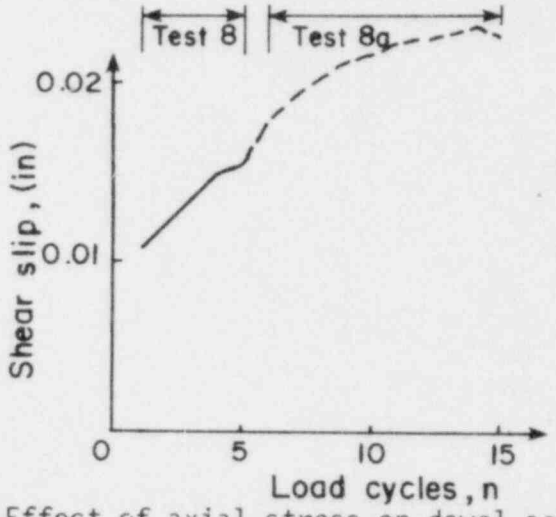

b) Effect of axial stress on dowel action, No.6 bar.

Fig. 4.26. Cyclic test results on dowel action by Eleiott (Ref. 33).

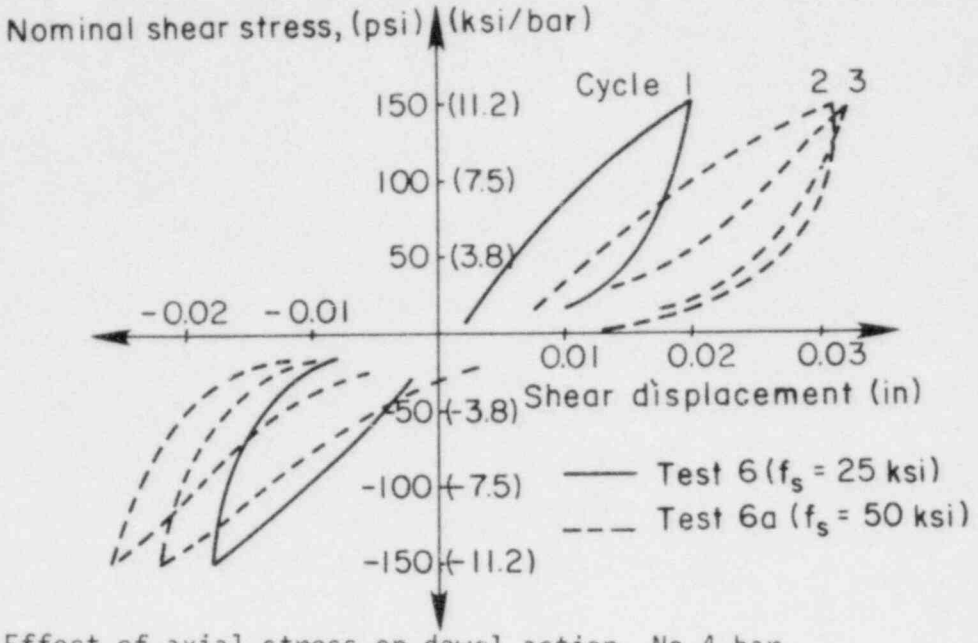

c) Effect of axial stress on dowel action, No.4 bar.

Fig. 4.26. (Continued).

Regarding the effect of the axial stresses in the bar, an applied axial tension of 25 ksi (172.5 MPa) caused deterioration of the bond transfer doubling the average crack width after 15 cycles with most of the increase happening during the 1st cycle (see Fig. 4.26b). The above tension level also caused approximately a 50% increase in the slip, thus lowering the corresponding dowel stiffness. Further increase of the axial stress to 50 ksi (345 MPa) resulted in severe damage of the concrete and caused dowel-induced cracking and subsequent splitting failure. The detrimental effect of the axial tensile stress on the dowel stiffness is shown in Fig. 4.26c.

Stanton, in his linear relation for dowel stiffness given in the previous section for monotonic shear, did not take into account the hardening response of the load-displacement curves (see Fig. 4.27). The effect of axial tension on the dowel behavior and the determination of the dowel

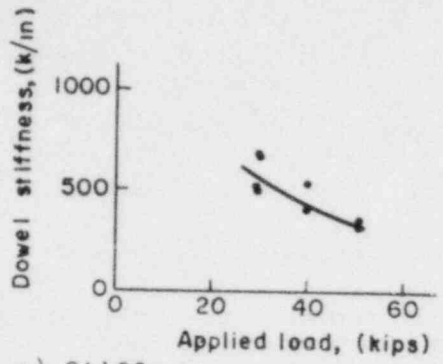

a) Stiffness versus applied load

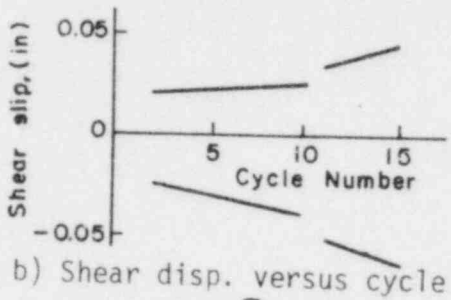

b) Shear disp. versus cycle number

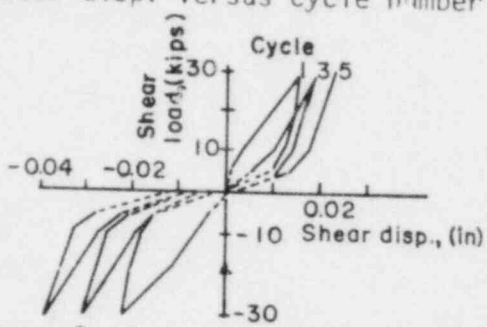

c) Shear load versus displacement

Fig. 4.27. Typical results from Stanton's investigation on dowel action (Ref. 109).

splitting load were not included in his model. In all specimens tested under cyclic shear a splitting failure was initiated at the shear plane, causing premature loss of the shear resistance and probably not allowing the full dowel capacity of the bars to be developed.

Jimenez et al. arrived at conclusions similar to those of Eleiott and Stanton insofar as far as the influence of the cyclic loading was concerned. As in Stanton's tests, the use of relatively large bars by Jimenez et al. (No.14) as dowels resulted in splitting of the concrete. The effect

of fully reversing shear up to ±200 psi (1.38 MPa)(corresponding to a steel shear stress of ±11.25 ksi or 77.3 MPa for a No.9 bar and ±10 ksi or 69 MPa for a No.14 bar) was taken into account in the dowel stiffness model proposed through a correction factor $\phi_{DA}^{(n)}$, the ratio of the peak dowel displacement $\Delta_{sd}^{(n)}$ after n number of cycles to the peak dowel displacement $\Delta_{sd}^{(1)}$ at the 1st cycle, as follows

$$\phi_{DA}^{(n)} = \Delta_{sd}^{(n)} / \Delta_{sd}^{(1)} = 0.029\ n + 0.97 \tag{4.30}$$

Thus, the peak dowel displacement at cycle n under a dowel force V_{DA} (kips) was given according to the following relation

$$\Delta_{sd}^{(n)} = \phi_{DA}^{(n)}\ \Delta_{sd}^{(1)}, \tag{4.31a}$$

with

$$\Delta_{sd}^{(1)} = K_{DA}^{-1}\ V_{DA} \tag{4.31b}$$

where K_{DA}^{-1} was the dowel flexibility given by Eqn. 4.26 for monotonic shear. Employing the above expressions and assuming a bilinear relationship for dowel response after the 1st cycle of loading, the actual dowel stress-dowel slip loops, shown in Fig. 4.28a, were idealized by linear segments, as shown in Fig. 4.28b. Since the degrading influence of increasing bar tension is not included in Eqn. 4.30, it is expected to predict much smaller losses in shear stiffness with increasing bar tension.

It is well established by the direct dowel tests reported in the literature that reversed cycling, in cases where the applied shear is resisted only by dowel action at a preset crack, caused severe crushing of concrete,

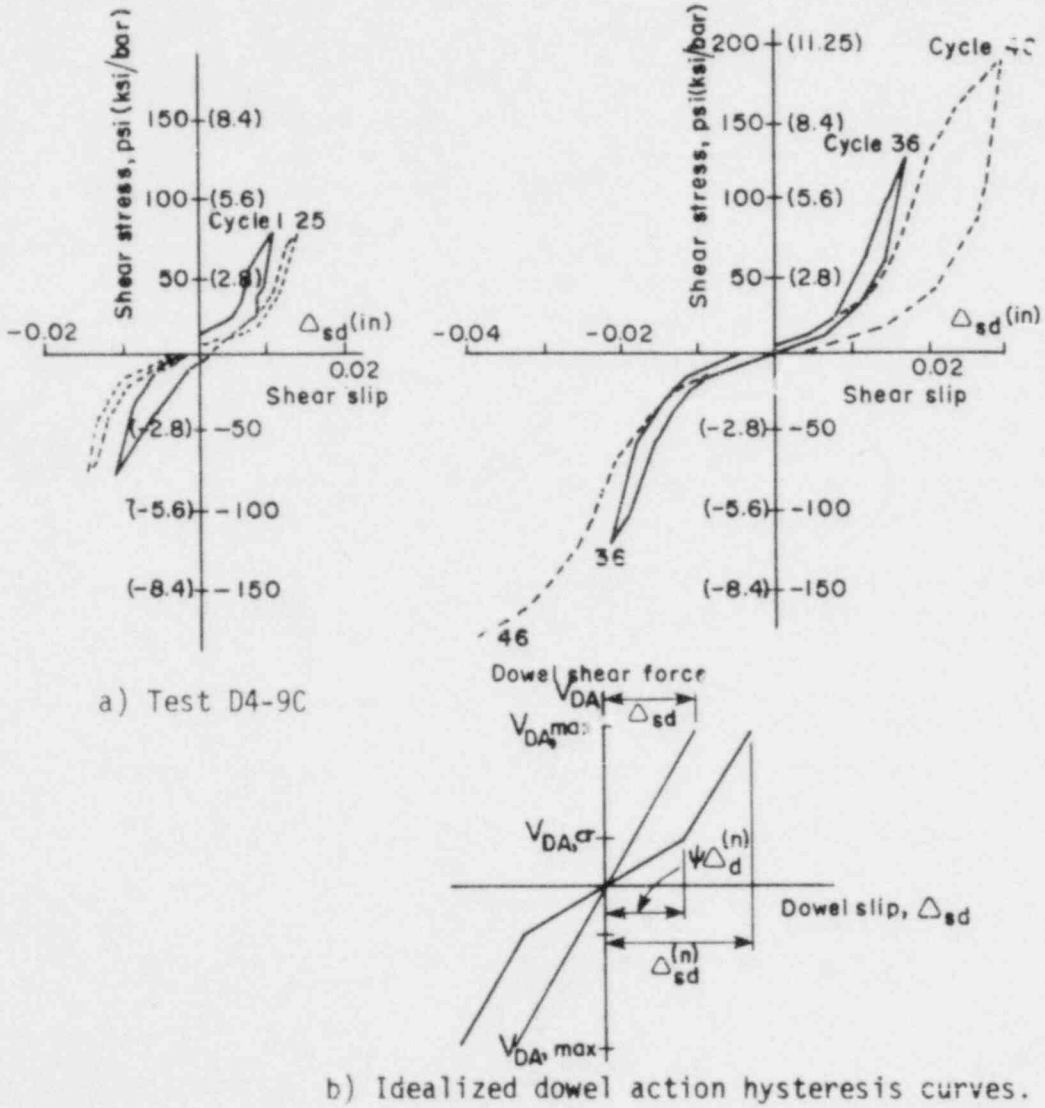

a) Test D4-9C

b) Idealized dowel action hysteresis curves.

Fig. 4.28. Dowel tests under cyclic shear by Jimenez et al. (Ref. 61).

mainly in the initial cycles. As the concrete was compacted the dowel stiffness increased and the response became more stable with no appreciable increases in dowel displacements, unless failure was approached. Also, in contradiction to the interface shear transfer behavior, negligible amounts of residual dowel slips were measured. In addition, the area enclosed by the hysteresis loops was smaller compared with that of the interface shear transfer loops, showing smaller energy absorbing ability for the dowel action mode.

The tests with varying axial tensile stress confirmed the fact that increasing tensile stresses in the bars caused reduction in the dowel stiffness. As the bond stresses increased, microcracks formed inclined to the bars (see Refs. 14, 49, 77, 94 and 112) and resulted in softening of the surrounding concrete close to the crack by increasing the unbonded free length of the bar. Negligible amounts of residual dowel slips were measured.

In general, according to studies on dowel action, the dowel mechanism could contribute a significant amount to the overall shear stiffness, ranging from about 10 to 40%. The dowel action contribution increased with increasing crack opening. The ability of the reinforcement bars to transfer shear depended on the specimen configuration and the size of the bars.

4.2.3 Shear stiffness in reinforced concrete panels

Reinforced concrete walls or panels subjected to in-plane biaxial and shear loads have been studied by various investigators. The different points of view and assumptions for the analysis of the above membrane elements by each researcher are given in Section 4.3.2.1.

4.2.3.1 Analytical and experimental models for membrane elements

Flügge (Ref. 40) in his analysis of shells under membrane tensile normal forces N_x, N_y and shear loads V assumed that cracking in the concrete was normal to the reinforcement. The normal forces (both tensile and compressive) were sustained by the steel and the shear forces by the concrete by means of friction along the existing cracks. No tension was sustained by the concrete. Flügge did not attempt to satisfy compatibility between the tensile strains of steel and the compressive strains in concrete. Although his analysis included in an approximate fashion the influence of interface shear transfer mechanism through friction, other mechanisms such as dowel action were excluded. Also, if the cracks are not normal to the reinforcement, as he assumed, axial forces in the rebars can resist some of the applied shear loads.

Falconer (Ref. 34) presented a theoretical analysis of the two-dimensional stress state induced in a two-way reinforced concrete element. He assumed that the existing compression in the concrete was inclined to the vertical normal applied stress at an unknown angle β (see Fig. 4.29). He developed the three equilibrium relations for the applied and resisting forces in the element and realized that having 4 unknowns (the direct stresses in the reinforcement σ_1, σ_2, the concrete stress σ_c and the inclination angle β) and three available equations, the problem of determining the internal stress distribution had one degree of indeterminacy. His theory did not provide that additional relation needed to determine the fourth unknown, the angle β.

Peter (Ref. 100) tested and analyzed a number of square concrete plates with orthogonal reinforcement inclined to the direction of principal

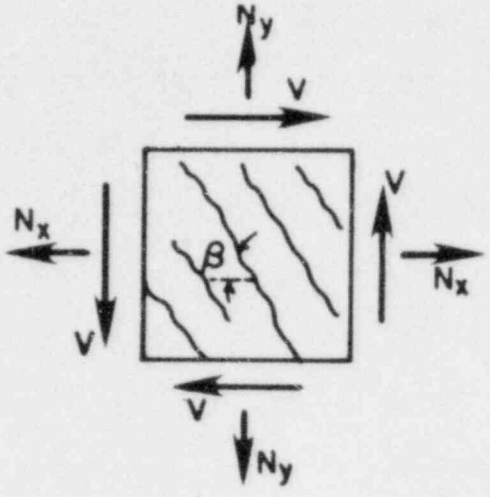

Fig. 4.29. Reinforced concrete shell element subjected to membrane forces (Ref. 34).

stress at a varying angle of 0 to 45 degrees. A uniform plane stress state in an arbitrary direction was considered. In addition to the equilibrium relations he considered the displacement compatibility relations assuming a simplified cracking pattern, with the cracks forming normal to the uniaxial load or to the direction of the maximum principal tensile stress. He also took into account the shear stress transferred at the crack surface.

Baumann (Ref. 8) presented two different approaches to this problem. The first was an application of the principle of limit design in determining the angle as the orientation of the cracks or as the angle β that created a failure mechanism. No strain requirements had to be satisfied, as the tensile strain in concrete could assume any value and continuity between strain in concrete and steel was satisfied automatically. When the yield stage was reached in the steel and the steel stress did not change

while the reinforcement deformed, the compressive strains contributed in attaining a geometrically possible state of plastic strain. An additional relation was obtained by minimizing the required amount of reinforcement. From this relation an optimum angle β_{opt} was determined.

In his alternative approach, he considered in addition to the equilibrium equations the compatibility relation of the displacements at a crack. He minimized the complementary stress energy Q_c of the internal stresses in the system, which were the tensile stresses in the reinforcement, the compressive stress in the concrete and the shear stress, v, at the crack interface. From the above relation ($\partial Q_c / \partial v = 0$) he calculated the shear force along the crack, obtaining in that manner an additional relation in terms of the statically indeterminate angle β, which made possible its calculation. Thus, Baumann employed energy principles to obtain another equation (equivalent to the compatibility equation) to determine the angle β.

Gupta (Ref. 50) discussed the proposed code requirements by ACI Committee 349 (Ref. 2). Making the assumption that the reinforcement was provided in two orthogonal directions, he applied the optimum limit design approach or the so-called principle of maximum resistance. The latter states that in a safe design the component of the resisting forces, N_i^* ($i = x, y$) and V^*, should be greater or equal to the component of the applied forces, N_i and V ($N_i^* \geq N_i$ and $V^* \geq V$).

He concluded that the ACI recommendation in Section 19.3.3 to provide reinforcement "in two or more directions . . . to resist the component of the principal membrane tensile stresses in each direction" gave insufficient reinforcement in the case of combined membrane biaxial tensile stresses and shear stresses, and that the ACI approach did not take into

account properly the applied shear force. Therefore, in the case of a two-way orthogonal reinforcement the steel provided would not be fully stressed under the normal tensile forces. For example, in the case of a high pressurization condition in a nuclear containment vessel, the only way to transfer superimposed high membrane shear forces would be by means other than axial shear forces in the rebars, such as dowel action or interface shear transfer. As a result of the above argument, ACI Committee 349 revised its code requirements to state that reinforcement should be provided "in two or more directions and shall be proportioned such that its resistance in any direction exceeds the component of applied forces in that direction." Brondum-Nielsen (Ref. 17) obtained expressions similar to those of Gupta using graphic means to solve the equilibrium equations in the limit state.

Also, in Ref. 51 Gupta considered the case of two- or three-way membrane reinforcement in shells and concluded that for an orthogonal pattern (and when crack size was not a significant design consideration) the minimum total principal tensile strain in concrete would be in the order of 2.5 times the yield strain of steel for a critical value of angle β equal to 45 degrees. Larger tensile strains in the concrete could be obtained for other values of the angle β. This analysis, which was based on both equilibrium and compatibility considerations, showed that the magnitude of deformation in the concrete in the post-cracking condition could be very large, resulting in undesirable crack width values for the above two-way reinforcing pattern.

Duchon (Ref. 29) presented an analysis of a reinforced concrete wall section of a nuclear containment structure with a four-way reinforcement

in directions independent of the principal directions. The membrane element was subject to combined biaxial tensile stresses and shear stresses. Smeared fine diagonal cracks were assumed to form throughout the concrete block element (see Fig. 4.30) perpendicular to the direction of the maximum principal tensile strain and inclined at an angle β to the horizontal.

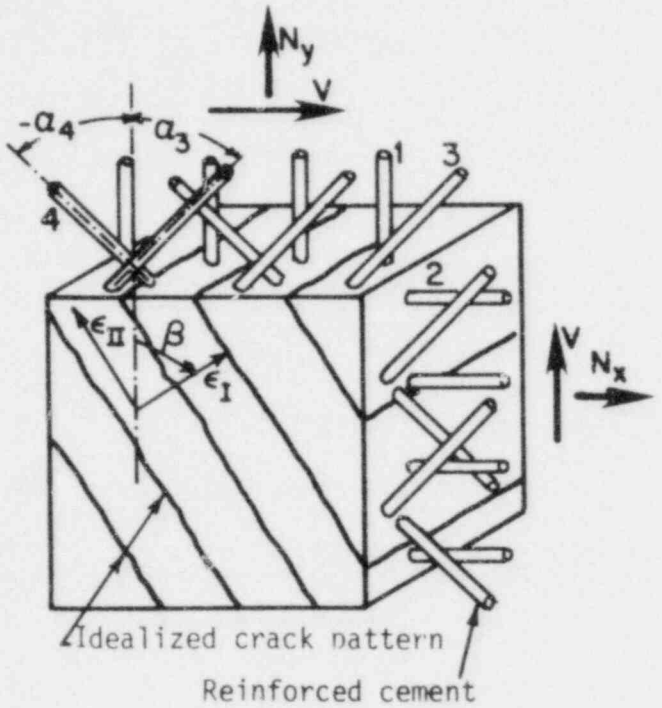

Fig. 4.30. Typical cracked reinforced concrete wall element (Ref. 29).

Using both equilibrium and compatibility conditions, he solved for the three unknowns, that is, the principal concrete strains ε_I, ε_{II} and the inclination angle β (see Appendix B). The concrete was assumed to act in compression only and the reinforcement steel in tension and compression. The value of the angle β was determined by an iterative process until the

assumed value of β and the calculated values of ε_I and ε_{II} satisfied the constraint equations of equilibrium and compatibility.

Collins (Ref. 25) proposed a diagonal compression field theory for a more rational design of reinforced concrete members under shear. He focused on the fact that the angle of inclination of the concrete compression struts was not usually 45 degrees, as it is assumed to be in most current building codes for the design of shear reinforcement. The provision for the contribution of concrete to shear resistance is, of course, an improvement on the ACI code after realizing that the 45 degree truss analogy gave conservative results. Assuming the inclination angle β (see Fig. 4.31) as a variable would definitely improve the understanding of the response and behavior of reinforced concrete under shear.

To determine the value of the angle β, Collins employed both the equilibrium and compatibility relations, including also the effect of prestressing in the longitudinal steel of a reinforced concrete beam. He derived the following quadratic equation in terms of the angle β and for a given value of the transverse strain ε_t,

$$\frac{(1 + \frac{1}{n\rho_t})}{(1 + \frac{1}{n\rho_\ell})} \tan^4\beta + \frac{\frac{\varepsilon^*}{\varepsilon_t}}{(1 + n\rho_\ell)n\,\rho_t} \tan^2\beta - 1 = 0 \qquad (4.32)$$

where ρ_ℓ, ρ_t were the longitudinal and transverse steel ratios, respectively, $n = E_s/E_c$ was the moduli ratio and ε^* a strain parameter indicating the intensity of prestress and axial load. Actually, Duchon's analysis would result in exactly the same equation, if the longitudinal and

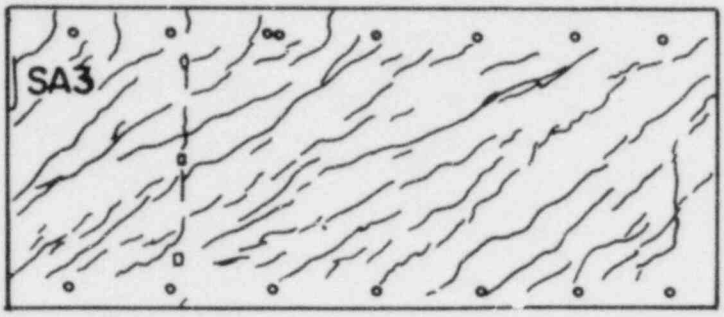

a) Symmetrical reinforced concrete box-beam loaded in shear.

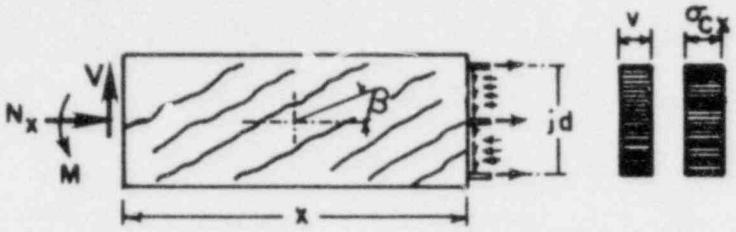

b) Free body diagram of beam section.

Fig. 4.31. Diagonal cracking in a reinforced concrete beam (Ref. 25).

transverse steel were thought of as a two-way orthogonal reinforcement in the uncracked concrete element assumed by Duchon.

Collins predicted that after the transverse steel had yielded, the applied shear could be resisted only by increasing the transverse steel strain until the longitudinal steel also eventually yielded, or when the concrete compressive strain reached its limiting value.

Bazant and Gambarova (Ref. 9) developed a so-called "rough crack" model for a cracked reinforced concrete plate element subject to in-plane forces (see Fig. 4.32). Neglecting extensional stiffness, dowel action, and kinking of the steel reinforcement along the cracks, they determined the overall tangent stiffness matrix $[\tilde{R}]$ for reinforced concrete by adding the contribution of the steel net (average strains in steel were assumed equal to those of the cracked concrete as a whole) to that of the cracked

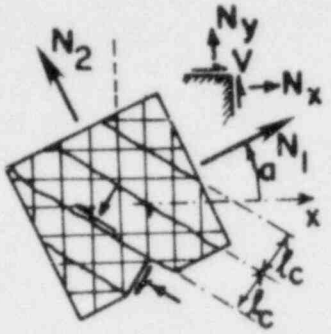

Fig. 4.32. Diagonally cracked reinforced concrete element subjected to in-plane forces (Ref. 9).

and uncracked concrete. Interface shear transfer at the crack was taken into account and only monotonic loading was considered.

A parallel experimental program was conducted at the Portland Cement Association (PCA) Laboratories by Oesterle and Russell (Ref. 96) to study the shear transfer in larger scale flat concrete specimens orthogonally reinforced with No.14 and No.18 bars, as shown in Fig. 3.22a in Section 3.5. The latter specimens with steel ratios of 0.013 and 0.022 in the direction of No.14 and No. 18 bars, respectively, were 60 inch square and 24 inch thick concrete slabs. They were subjected to combined biaxial tension (specimen MB3 at $0.6f_y$ tension and specimen MB1 at $0.9f_y$ tension) and membrane monotonic shear. The shear stress-shear strain response for the PCA specimens MB1 and MB3 is shown in Fig. 4.33 along with the curves of the companion specimens .6(M) and .9(M) of the present study (see Chapter 2). The tangent shear stiffness measured for shear stresses higher than 100 psi is essentially the same in both the present and the PCA specimens. There is, however, a significant shift of the data for specimens .6(M) and .9(M) to higher total shear distortions at low shear stresses. A possible reason may be the effect of more shrinkage cracking in the smaller specimens before the shear was applied. Apparently curing conditions for the latter

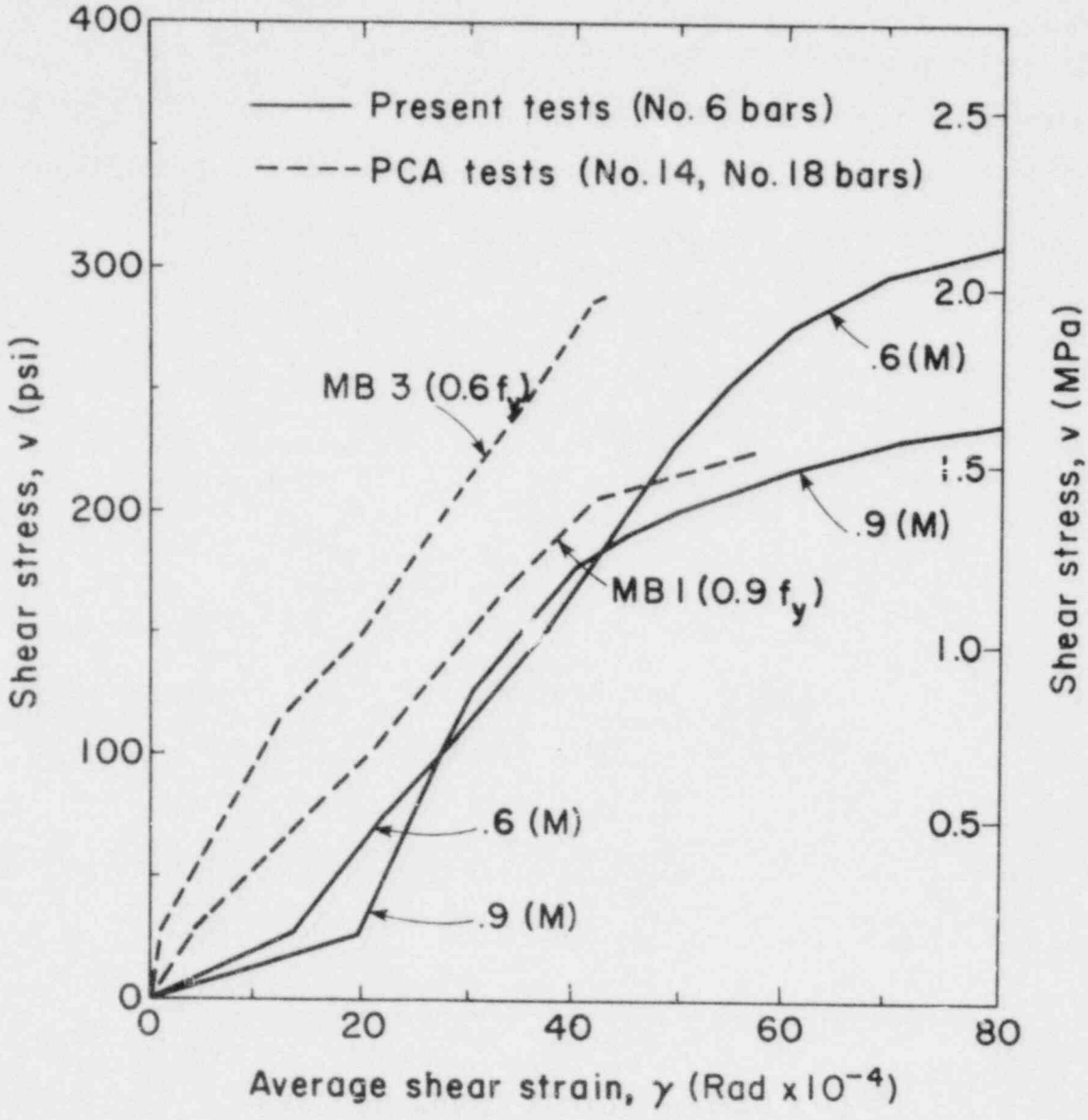

Fig. 4.33. Comparison of shear stress-shear strain curves for present tests (.6(M), .9(M)), and PCA tests (MB3, MB1) under monotonic shear.

specimens seem to have a great influence on the shear stiffness at low shear stresses. The failure crack in the specimens with No.6 bars formed inside the gage length for measuring the diagonal deformations at the central region, whereas it was outside the instrumented grid in the PCA's larger specimens. Thus, inelastic deformations near failure were recorded only in the smaller specimens.

4.2.3.2 Effective shear modulus

The most common representation of the effective shear modulus G_{cr} in the cracked stage is to assume one of the following three cases:

a) $G_{cr} = G_o$ (full shear transfer capability, same as in the uncracked stage)

b) $G_{cr} = 0$ (interface shear transfer and dowel action ignored)

c) $G_{cr} = \alpha G_o$, with $\alpha < 1$ (reduced shear transfer capability)

Full shear transfer capability was assumed by Zienkiewicz et al. (Ref. 129), Swoboda (Ref. 111), Nielsen and Braestrup (Ref. 93), Thuerlimann (Ref. 119) and CEB-Model Code (Ref. 20) in their analysis of reinforced concrete beams subjected to shear. Cervenka (Ref. 23), on the other hand, assumed zero shear transferability after cracking; that is, the contribution of interface shear transfer and dowel action was neglected. Thus, the cracked concrete was assumed to be capable of carrying tensile or compressive loads parallel to the crack only. In the above studies only monotonic shear was considered.

An alternative approach to retain some shear stiffness after cracking is to employ a shear transfer factor α ($\alpha < 1$) that results in a reduced shear modulus of

$$G_{cr} = \alpha G_o, \tag{4.33a}$$

where

$$G_o = E_c/2(1 + \nu) \tag{4.33b}$$

is the shear modulus for the uncracked concrete. If a constant value for G_{cr} is assumed in the post-cracking range the mechanisms of interface shear transfer and dowel action are not properly modeled, since a decrease of G_{cr} is expected as the cracks increase in number and size.

This type of formulation for the shear modulus under monotonic loading conditions was employed by Hand et al. (Ref. 52)(α = 0.4), Suidan and Schnobrich (Ref. 110)(α = 0.5), Krishnamoorthy and Panneerselvam (Ref. 69) and Salem and Mohraz (Ref. 103). The latter found no effect of the value of α (as long as it was not zero) on the ultimate load of shallow beams. For deep beams, where failure was more likely to be in shear rather than flexure, they suggested that a critical value of α existed, below which premature failure was predicted.

Yuzugullu and Schnobrich (Ref. 128), in their finite element analysis of shear wall frame systems, compared load-displacement curves resulting from use of various values for α (1.0, 0.25, 0.125 and 0). The influence of the factor α for one particular structure (specimen A-1) can be seen in Fig. 4.34. Up to about 75% of the monotonically applied failure load the different assumed values of α resulted in similar response, with α = 0.125 showing the closest agreement with the test data. Above this load level, all values of α gave displacements that were too small.

Agrawal et al. (Ref. 3) based their proposed analytical model on the elasto-plastic idealization of the stress-strain curve of concrete. They

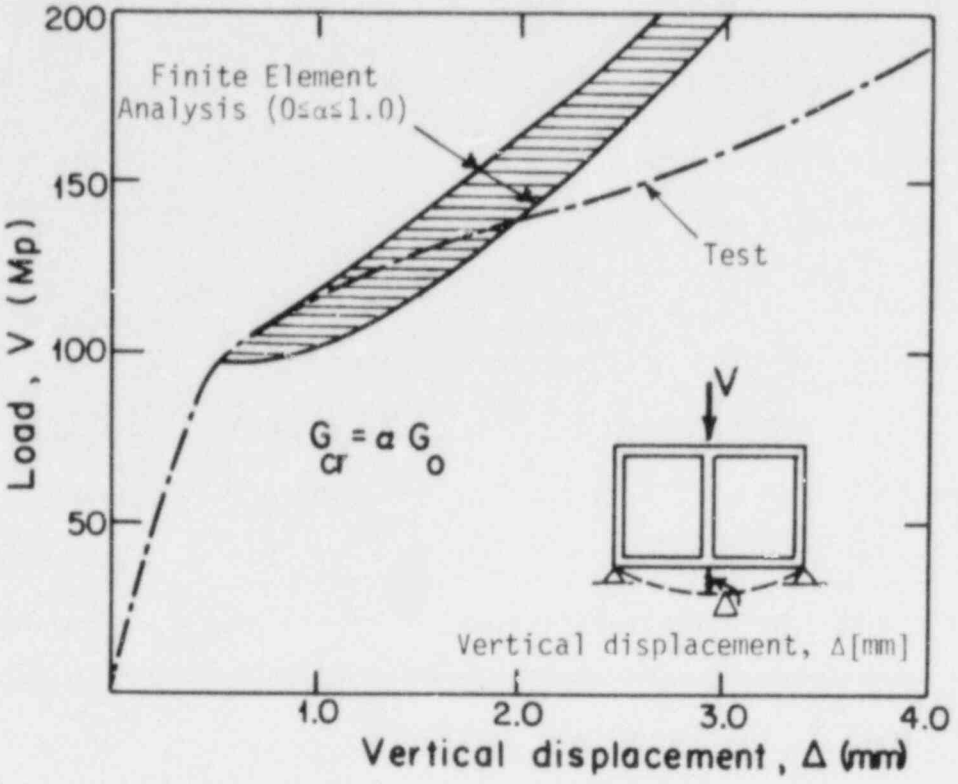

Fig. 4.34. Influence of the shear reduction factor α on the load-displacement curves of a shear-wall-frame system (Ref. 128).

predicted the behavior of a shear panel, using a shear reduction factor $\alpha = 0.5$ for one set of parallel diagonal open cracks and $\alpha = 0.25$ for two sets of open cracks (each set orthogonal to each other). The latter case was supposed to model the effect of reversing cyclic shear in a simplified fashion, assuming a constant 50% reduction in the effective shear modulus for any number of cycles. They concluded that neglecting the effect of shear transfer altogether would lead to numerical instability of the system, when for example, all the elements around a specific node have two sets of open cracks.

Isenberg and Adham (Ref. 59) derived a mathematical model of stress-strain relations for reinforced concrete from the properties of the

reinforcing steel, the concrete, and the bond-slip behavior, assuming orthotropic behavior during cracking. The following expression for the effective shear modulus of reinforced concrete membranes, subjected to monotonic shear and normal stresses in the plane of the membrane cracked in the orthogonal (x) and (y) directions, was presented

$$G_{cr} = \frac{1}{2}\{[(1 - \alpha_{bx})\frac{E_{cx}}{2(1 + \nu_{yx})} + \frac{E_s}{2(1 + \nu_s)}\rho_x]$$

$$+ [(1 - \alpha_{by})\frac{E_{cy}}{2(1 + \nu_{xy})} + \frac{E_s}{2(1 + \nu_s)}\rho_y]\} \qquad (4.34)$$

where subscripts x, y denote the orthotropic directions (perpendicular to the orthogonal tension cracks) and $\alpha_{bi}(i = x, y)$ is a variable bond slip modulus given by the formula

$$\alpha_{bi} = c_{wmi}/(c_{wmi} + \ell_{cmi}), \qquad (4.35)$$

where c_{wmi} and ℓ_{cmi} were the average crack width and crack spacing in the (i) direction, respectively. Eqn. 4.35 was used to estimate the reduced stiffness of the section at various stages of loading. In the above expression for G_{cr} (Eqn. 4.34), E_{ci} $(i = x, y)$, E_s and ν_{xy}, ν_{yx}, ν_s were the concrete initial modulus in tension, the modulus of steel and the Poisson's ratios, respectively. Although this formula took into account (in an average fashion) the effects of cracking, progressive degradation of bond, inelasticity in compression and confining stress in the stress-strain relations, it was not based on any experimental evidence. In several

calculations, for typical examples, G_{cr} varied from 0.75 to 1.0 times the shear modulus for uncracked concrete.

Holland and Runkeby (Ref. 55) discussed the above research by Isenberg and Adham and proposed that a reasonable approximation after cracking was to assume that G_{cr} was equal to zero, although there was some contribution to stiffness between the cracks in the direction normal to the crack due to the embedded reinforcement. Using experimental data from tests by Peter (Ref. 100), who tested a number of reinforced concrete plates with orthogonal reinforcement deviating at an angle of 0 to 45 degrees from the principal stress direction, they computed the crack directions assuming zero tensile and shear stiffness in the concrete and elastic steel with axial stiffness that included the contribution of concrete in tension.

Since no experimental shear-strain relationship for cracked concrete was available, Franklin (Ref. 41) and Darwin and Pecknold (Ref. 28) related G_{cr} to the orthotropic stiffnesses E_1 and E_2 parallel to the principal directions (1) and (2), according to the relations,

$$G_{cr} = \frac{E_1(1 - \nu_2) + E_2(1 - \nu_1)}{4(1 - \nu_1\nu_2)} \quad \text{(Ref. 41)} \tag{4.36a}$$

$$G_{cr} = \frac{E_1 + E_2 - 2\nu\sqrt{E_1E_2}}{4(1 - \nu^2)} \quad \text{(Ref. 28)} \tag{4.36b}$$

where ν_1, ν_2 were the Poisson's ratios in directions (1) and (2), respectively. Poisson's ratio ν used by Darwin was a simplified equivalent Poisson's ratio equal to $\sqrt{\nu_1\nu_2}$ to insure that neither direction was favored. The above expressions (Eqns. 4.36) for $E_1 = E_2 = E_c$ and $\nu_1 = \nu_2$ reduce to the shear modulus of uncracked concrete G_o.

For one set of cracks (monotonic shear) perpendicular to the direction of principal tension (1), that is for $E_1 = 0$ and $\nu_1 = 0$, Eqns. 4.36a and 4.36b result in the following expression for the shear modulus,

$$G_{cr} = 0.25\ E_c \tag{4.37}$$

For $\nu = 0.16$, Eqn. 4.36 takes on the value

$$G_{cr} = 0.58\ G_o \tag{4.38}$$

From the great variability in methods for determining G_{cr}, it is clear that the formulation of the shear modulus should result from a more refined model for shear transfer which reflects the variation of the shear rigidity as a function of the crack width, shear slip, the level of the applied shear stress, and the type of loading. Recently, several analytical expressions have been presented for the lateral shear rigidity of shear walls and cylindrical containment structures (such as nuclear containment vessels). For the special case of a pressurized containment, horizontal and vertical cracks would be present and the ability of the shear transfer mechanisms to transmit the required shear forces is very important, especially for fully reversing shear loading due to seismic forces.

Castellani and Fontana (Ref. 18) gave a simplified formula for G based on the experimental findings of Paulay and Loeber (Ref. 97) for monotonic shear as follows,

$$G_{cr} = \left[\frac{1}{G_o} + \frac{1}{\ell_{cm}}\left(\frac{\Delta_s}{v}\right)\right]^{-1} = \left[\frac{1}{G_o} + \frac{1}{K_s}\right]^{-1} \tag{4.39}$$

where ℓ_{cm} = average crack spacing

Δ_s = crack slip

v = shear stress

K_s = shear stiffness along the cracks

It is not clear how this expression (Eqn. 4.39) accounted for both interface shear transfer and dowel action. It seemed that the effective shear modulus G_{cr} was practically independent of changes in crack spacing ℓ_{cm}, since when ℓ_{cm} increased the crack width and the shear flexibility $1/K_s$ were proportionally increasing, also.

Cedolin and Dei Poli (Ref. 22) suggested a linear relation for G_{cr} as a function of the principal tensile strain normal to the crack ε_I, assuming smeared representation of cracking, as follows

$$G_{cr} = G_o, \text{ for } \varepsilon_I < \varepsilon_{to} \tag{4.40a}$$

$$G_{cr} = F(1 - \frac{\varepsilon_I}{\varepsilon_c}), \text{ for } \varepsilon_I \geq \varepsilon_{to}, \tag{4.40b}$$

where ε_c was equal to a value of 0.004 to 0.005 that corresponded to a tensile strain in concrete resulting from a crack width of about 0.75 mm (0.03 in.)(interpolation from Ref. 97), and ε_{to} the cracking tensile strain of concrete (= 0.0002). The above value of ε_c corresponded to a negligible ability to transfer shear along the cracks. The constant F was a function of the shear modulus for uncracked concrete G_o, that is, a function of the Young's modulus of concrete E_c. Values such as $0.2E_c$, $0.1E_c$ and $0.01E_c$ were input for F to study the influence of the shear constant. The best results for a shallow beam tested by Bresler and

Scordelis (Ref. 12) were found using $\varepsilon_c = 0.004$ and $F = 0.1E_c = 0.24G_o$. G_{cr} reduced to zero at a principal strain of 0.004, which was about 20 times the cracking tensile strain ε_{to}. However, in experiments on shear panels, the maximum tensile strain at failure was found to be about 5 times the ε_{to}. Thus, the reduction of G_{cr} to a very small value appeared to take place at strains close to $5\varepsilon_{to}$ rather than $20\varepsilon_{to}$.

Al-Mahaidi (Ref. 4), in postulating an analogy between the (G_{cr}, ε_I) relation and the shear stiffness at a single crack, suggested the following expression for G_{cr},

$$G_{cr} = G_o, \text{ for } \varepsilon_I < \varepsilon_{to} \tag{4.41a}$$

$$G_{cr} = 0.4\, G_o/(\varepsilon_I/\varepsilon_{to}), \text{ for } \varepsilon_I \geq \varepsilon_{to} \tag{4.41b}$$

These expressions assumed that at the inception of cracking ($\varepsilon_I = \varepsilon_{to}$) G_{cr} reduced to 40% of G_o. At failure of the shear panels ($\varepsilon_I = 5\varepsilon_{to}$) the shear rigidity became $0.08G_o$, a value that was considered small enough to reflect the severe degradation of cracked concrete with large crack openings. In Fig. 4.35 a comparison of suggested expressions for G_{cr}/G_o is given for shear panels and deep beams.

Geistefeldt (Ref. 44), in his refined nonlinear three-dimensional mechanical model for reinforced concrete, included the contribution of concrete between cracks to the tension stiffness normal to the cracks and the reduction of shear modulus G_{cr} with crack opening. For the uniaxial case he modeled the relation of shear stress v and shear strain γ by introducing a "shear spring" k_s of length ℓ as follows

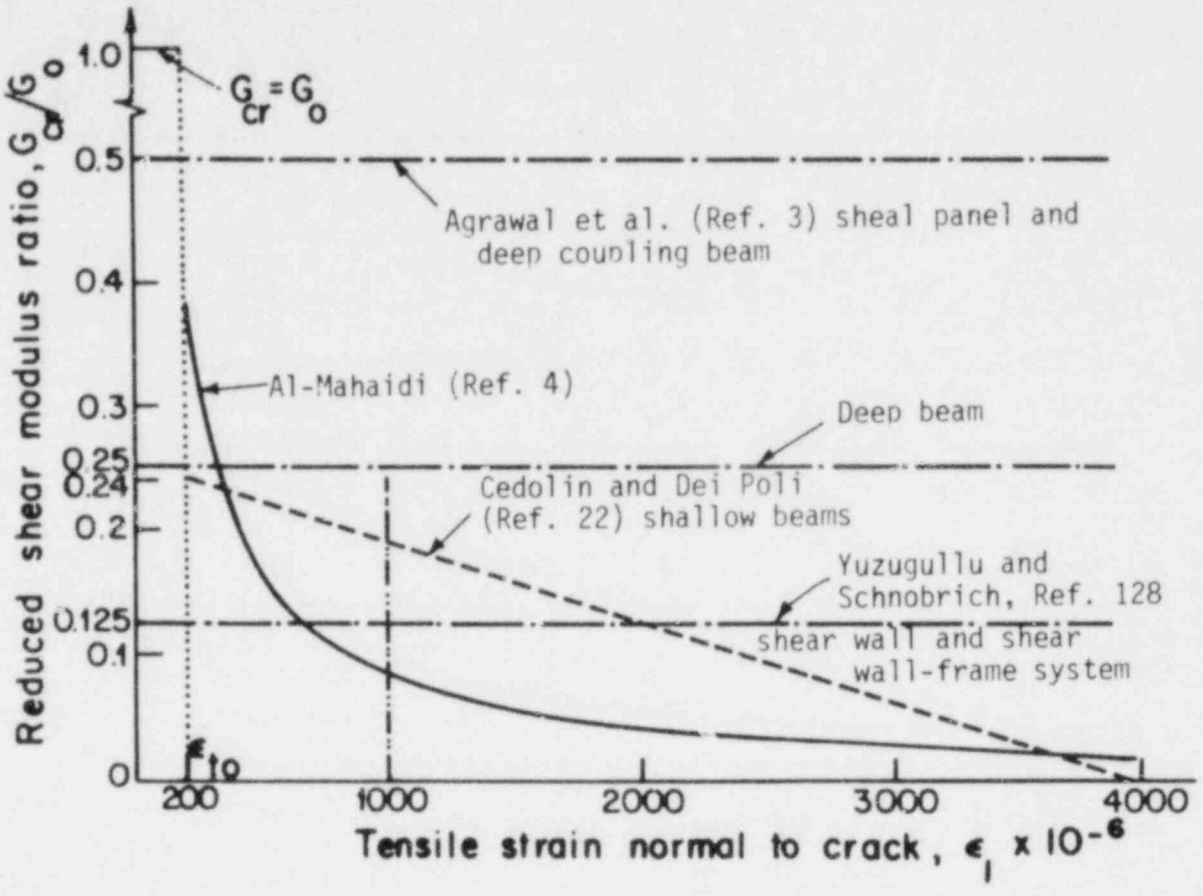

Fig. 4.35. Proposed expressions for the shear modulus ratio G_{cr}/G_o (Ref. 4).

$$\gamma = v(\ell/k_s) \tag{4.42}$$

The overall shear strain γ was the sum of three components: uncracked reinforced concrete with perfect bond (u), reinforcement free in surrounding concrete (r), and a "crack part" which included the shear strains due to shear transfer along the cracks and proportional to the ratio of crack slip to crack width (c). The above three components were treated as three "shear springs" in series, in which the shear stress in each one was equal to the applied shear stress and the shear strains were proportioned according to fictitious spring lengths $\alpha_1\ell$, $\beta_1\ell$ and $\gamma_1\ell$, as follows (for $\ell = 1$)

$$\gamma = \left(\frac{1}{k_s}_u + \frac{1}{k_s}_r + \frac{1}{k_s}_c\right) v \qquad (4.43a)$$

with

$$G_{cr} = \left[\frac{\alpha_1}{k_s}_u + \frac{\beta_1}{k_s}_r + \frac{\gamma_1}{k_s}_c\right]^{-1}, \text{ and } \alpha_1 + \beta_1 + \gamma_1 = 1 \qquad (4.43b)$$

For the case of two sets of parallel cracks in two different directions, under a biaxial stress state, the previous relation (Eqn. 4.43) was generalized by introducing new component factors to account for the effect of the cracking in one direction on the properties in the other direction (see Fig. 4.36).

Collins (Ref. 25) studied the behavior of symmetrical reinforced concrete beams monotonically loaded in shear, considering both equilibrium and compatibility conditions that existed between average stresses and strains in various directions, respectively. Predicting the response of

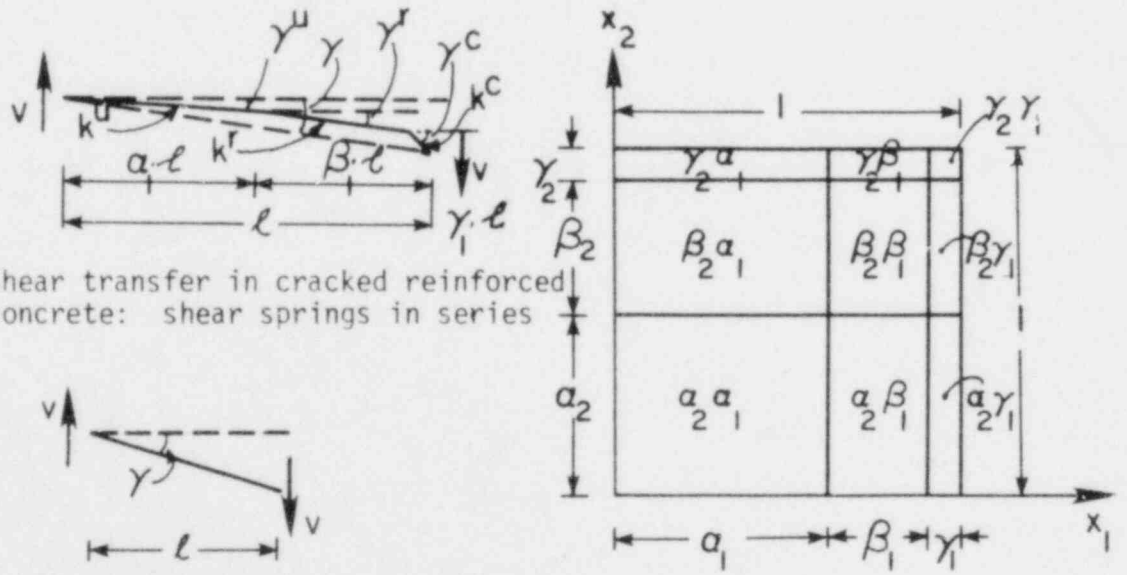

b) Shear transfer in cracked reinforced concrete: shear springs in series

a) 1-dimensional "shear spring"

c) Biaxial model

Fig. 4.36. Shear transfer model in cracked reinforced concrete according to Geistefeldt (Ref. 44).

two reinforced beams prior to yielding (tested by Arbesman in the University of Toronto (Ref. 5)), he arrived at the following linear expression between the applied shear stress v and the resulting shear strain γ,

$$\gamma = \frac{2v}{E_c}\left[1 + \sqrt{(1 + \frac{1}{n\rho_t})(1 + \frac{1}{n\rho_\ell})}\right] \tag{4.44}$$

defining an effective shear modulus G_{cr} for diagonally cracked reinforced concrete as

$$G_{cr} = \frac{0.5E_c}{1 + \sqrt{(1 + \frac{1}{n\rho_t})(1 + \frac{1}{n\rho_\ell})}} \tag{4.45}$$

where E_c was the modulus of elasticity of concrete, n the modular ratio E_s/E_c, ρ_ℓ the reinforcement ratio of the longitudinal passive steel and ρ_t the reinforcement ratio of the transverse steel. For values of E_c = 3500 ksi, n = 8, ρ_ℓ = 0.0122 and ρ_t = 0.0244, Eqn. 4.45 results in a value of G_{cr} equal to

$$G_{cr} = 0.125\ G_o \tag{4.46}$$

for G_o = 1500 ksi. The above values for E_c, n, ρ_ℓ, ρ_t, and G_o correspond to the properties of the biaxial test specimens in the present study for a zero axial tension in both orthogonal directions of the reinforcement.

Fardis and Buyukozturk (Ref. 35) used a simple mathematical model based on statistical analysis of available experimental data of tests performed at Cornell University (Ref. 61, 62, 70, 126 and 127) to estimate the shear slip during shear transfer across the cracks in reinforced concrete. Assuming uniformity of strains and stresses in a cracked block having equally spaced cracks in both directions i and j, they developed the following effective shear rigidity relationship between the shear

stress v_{ij} and shear strain γ_{ij} (see Fig. 4.37),

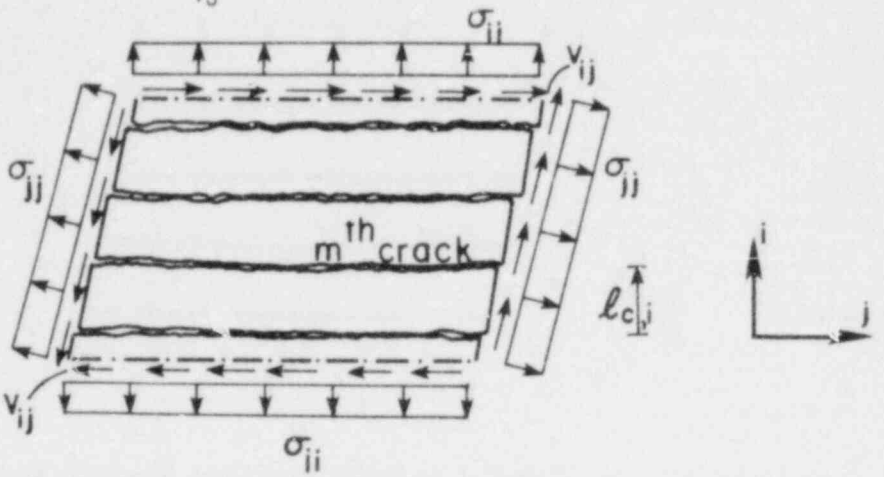

Fig. 4.37. Idealized cracked concrete element (Fardis and Buyukozturk, Ref. 35).

$$v_{ij} = \frac{1}{\left(\frac{1}{G_o} + \frac{1}{\alpha_i} + \frac{1}{\alpha_j}\right)} \left(\gamma_{ij} \frac{c_1}{(1 + \beta_i)} \varepsilon_{ii} - \frac{c_1}{(1 + \beta_j)} \varepsilon_{jj}\right), \qquad (4.47)$$

where G_o = shear modulus of uncracked concrete,

$\alpha_m = \left(\bar{K}_{N,i} + c_2 \bar{K}_{DA,i}\right) \ell_{c,m}/c_2 \quad (m = i, j)$,

$\beta_m = c_2 \bar{K}_{DA,i}/\bar{K}_{N,i} \quad (m = i, j)$,

ε_{ii}, ε_{jj} = an effective uniform normal strain by summing the increments in crack widths over all the cracks along the i and j directions, respectively, if the concrete tensile stresses were neglected,

c_1, c_2 = 0.23, 1.16 = constants based on statistical analysis of the test data,

$\bar{K}_{N,m}$ = extensional stiffness in the m(= i, j) direction per unit area,

$\bar{K}_{DA,m}$ = dowel stiffness in the m(= i, j) direction per unit area, and

$\ell_{c,m}$ = crack spacing in the m(= i, j) direction.

They reported effective shear rigidity values of the order of 10% of the uncracked concrete shear modulus.

Assuming for simplicity that the shear rigidity relation did not involve normal strains, the effective shear modulus was given by the following expression

$$G_{cr} = \frac{v_{ij}}{\gamma_{ij}} = \left[\frac{1}{G_o} + \frac{b}{\ell_{c,i}(\bar{K}_{N,i} + b\bar{K}_{DA,i})} + \frac{b}{\ell_{c,j}(\bar{K}_{N,j} + \bar{K}_{DA,j})}\right]^{-1} \quad (4.48)$$

where b = 1.72. They pointed out that the above functional model, developed to predict the shear modulus under monotonic shear, could also incorporate cyclic behavior by including the effect of cycling through the coefficients b in Eqn. 4.48 and c_1, c_2 in Eqn. 4.47. These coefficients were a function of the internal friction angle and the friction due to the local roughness. The degrading influence of cyclic shear on these friction coefficients could be expressed in terms of the number of cycles n. They agreed, however, that the reported information was not enough to support a predictive model taking into account fully cyclic response.

4.2.4 Ultimate strength

During the last decade the ultimate shear capacity of precracked reinforced concrete connections with or without tension in the reinforcement crossing the shear plane has been studied by several investigators. Both monotonic and cyclic reversing shear loading have been considered in these investigations. In the work reviewed below the shear load was always applied along a single crack. The empirical design relations and the

mechanical models proposed were developed to predict the maximum shear stress transferred at a predefined single crack by means of the combined mechanisms of the interface shear transfer and dowel action in the reinforcement normal to the crack plane. Of course, in the case of the reinforcement being inclined to the crack plane, axial forces in the reinforcing bars would also resist a portion of the applied shear load. The latter has to be taken into account in the present work since diagonal cracks inclined to the orthogonal reinforcement formed during the application of shear.

Seeking a simple method to design connections in precast reinforced concrete, composite beams and corbels Birkeland and Birkeland (Ref. 11) and Mast (Ref. 80) introduced the concept of shear-friction. According to this concept, the applied shear stresses at the crack interface are resisted by the friction along the rough shear plane. These frictional stresses in the concrete are induced by the normal component of the stresses in the reinforcement crossing the crack. The separation of the crack surfaces as slip takes place under the shear load produces tensile forces N_s in the steel and equal normal compressive forces N_c in the concrete at the crack interface. Thus, the ultimate shear force V_u transmitted at the crack at yield of the reinforcing bars is proportional to the compressive force N_c. A proportionality factor μ was defined as the coefficient of friction or in other words the tangent of the angle of internal friction ϕ assuming a certain condition at the interface. A schematic representation of the shear-friction model is shown in Fig. 4.38.

According to the above figure, vertical equilibrium results in the following expression for the ultimate shear capacity.

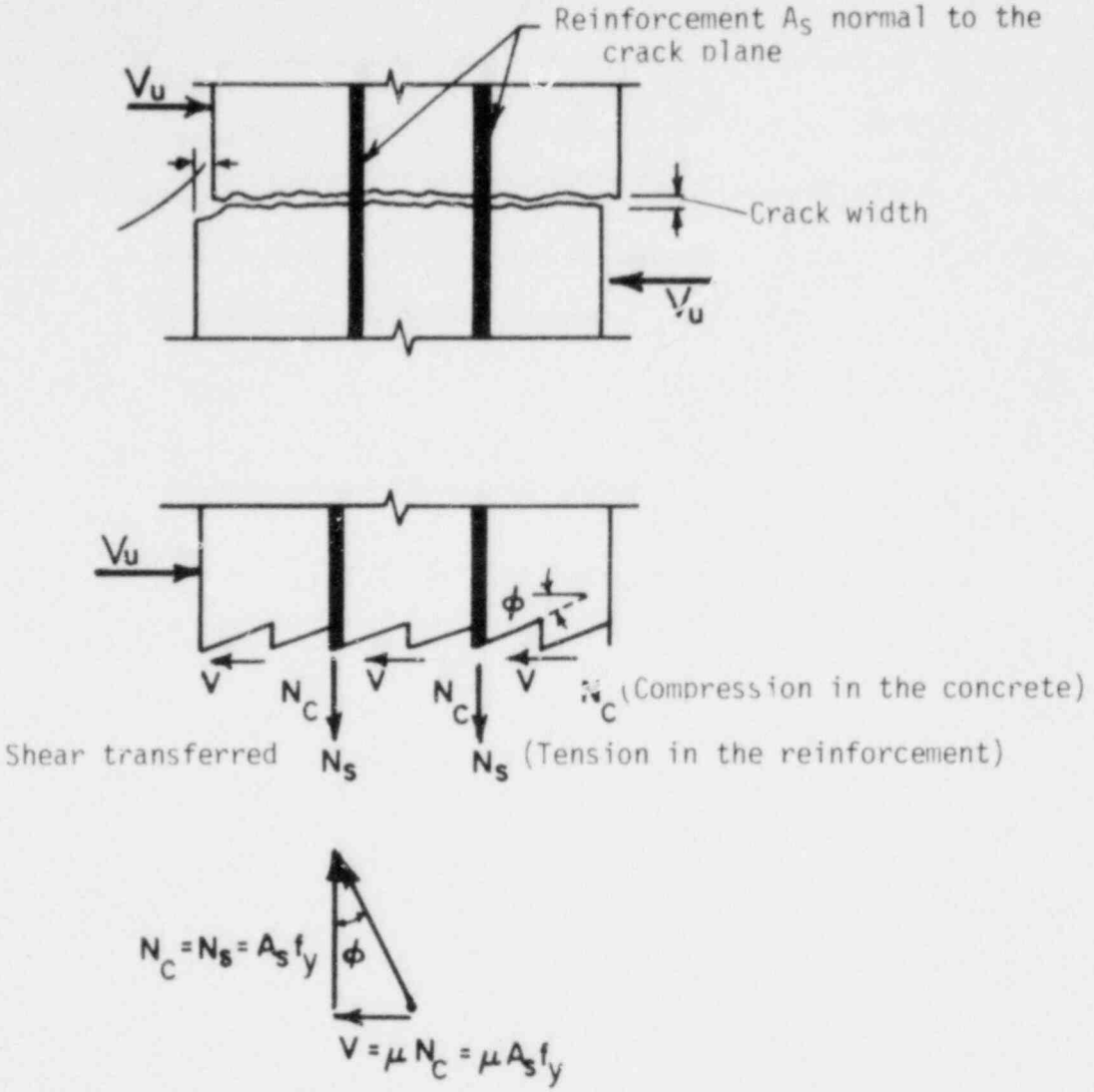

Fig. 4.38. Schematic diagram of the shear-friction concept.

$$V_u = A_s f_y \tan\phi \quad \text{forces)} \tag{4.49}$$

$$v_u = \rho f_y \tan\phi \quad \text{(stresses)} \tag{4.50}$$

where ρ is the steel ratio at the crack. In the above equations dowel action was assumed insignificant and it is neglected. Since shear

is transferred by tension in the reinforcement, the reinforcing bars should be well anchored on both sides of the failure crack in order to be able to develop their yield strength. In addition, the concrete in the vicinity of the crack should be well confined so that premature splitting does not occur. Also, if external tension was present in the steel, additional reinforcement should be provided over that required by the shear-friction theory, since the applied tension would decrease the effective clamping force across the shear plane.

The coefficient of friction $\mu = \tan \phi$ for various interface conditions was determined experimentally. Recommended values of $\tan \phi$ to be used in design are given in Table 4.D (see Ref. 11). These values for the

Table 4.D. Recommended values for μ according to Ref. 11.

Crack Interface Condition	Recommended $\mu = \tan \phi$
Concrete to concrete (rough interface)	1.4
Concrete to concrete (smooth interface)	0.7
Concrete to steel (composite beams)	1.0
Concrete to steel (field-welded inserts)	0.7

coefficient of friction are valid for monotonic shear loading and for normal weight concrete only. If cyclic shear is applied reduced values should be used.

Fattah Shaikh (Ref. 36, in his suggested revisions to the shear-friction provisions contained in Section 2.2 of the PCI Manual on Design of

Connections for Precast Prestressed Concrete (Ref. 99), proposed to account for all friction mechanisms by means of an effective coefficient of friction μ_e determined by the following relation presented by Raths (Ref. 102),

$$v_u = c_R \mu_e \rho f_y \tag{4.51}$$

where v_u is the nominal ultimate shear stress along the interface and c_R is a capacity reduction factor (equal to 0.85).

This effective coefficient of friction μ_e is calculated from the relation

$$\mu_e = 1000 c_d^2 \mu / v_u \tag{4.52}$$

where c_d is a constant denoting the density of the concrete (c_d = 1.0 for normal weight concrete, c_d = 0.85 for sand-light weight concrete and c_d = 0.75 for all-light weight concrete) and $\mu = \tan \phi$ the coefficient of static friction. The constant of 1000 used in Eqn. 4.52 provided a reasonable value for a safe lower bound in the case of uncracked direct shear tests, according to Fattah Shaikh.

Based on the experimental results by Birkeland and Raths, the previously defined effective friction coefficient μ_e could be expressed as follows

Birkeland and Birkeland:

$$\mu_e = 1122/v_u = 33.5/\sqrt{\rho f_y} \quad (\mu = 1.4) \tag{4.53a}$$

with

$v_u = 33.5\sqrt{\rho f_y}$ (psi), and

Raths:

$$\mu_e = 1400/v_u = 37.4/\sqrt{\rho f_y} \quad (\mu = 1.4) \tag{4.53b}$$

with

$$v_u = 37.4\sqrt{\rho f_y} \quad \text{(psi)}$$

Mattock (Ref. 81 to 86) performed an extensive experimental study on various types of precracked and uncracked specimens subjected to pure shear (see Fig. 4.39). He suggested that a cohesional shear strength at the interface was apparent at low values of steel ratios ρ. He also concluded that an external normal stress σ_N (negative when tensile) at the crack plane, acting simultaneously with the shear stresses, had a similar effect on the shear transfer strength as the change in the stress parameter (ρf_y). Thus, the use of the combined expression ($\rho f_y + \sigma_N$) instead of (ρf_y) was appropriate.

By fitting the available data for initially cracked specimens a friction coefficient of $\mu = 0.8$ with a mean cohesional strength of 400 psi (2.76 MPa) was determined. He proposed the following predictive equations for the mean and the lower bound value of the ultimate strength v_u under monotonic shear

mean value:

$$v_u = 400 + 0.8\,(\rho f_y + \sigma_N) \quad \text{(psi)}$$

or

$$v_u = 2.76 + 0.8\,(\rho f_y + \sigma_N) \quad \text{(MPa)} \tag{4.54a}$$

lower bound value:

$$v_u = 200 + 0.8\,(\rho f_y + \sigma_N) \quad \text{(psi)}$$

or

$$v_u = 1.38 + 0.8\,(\rho f_y + \sigma_N) \quad \text{(MPa)} \tag{4.54b}$$

with v_u less or equal to $0.3f_c'$.

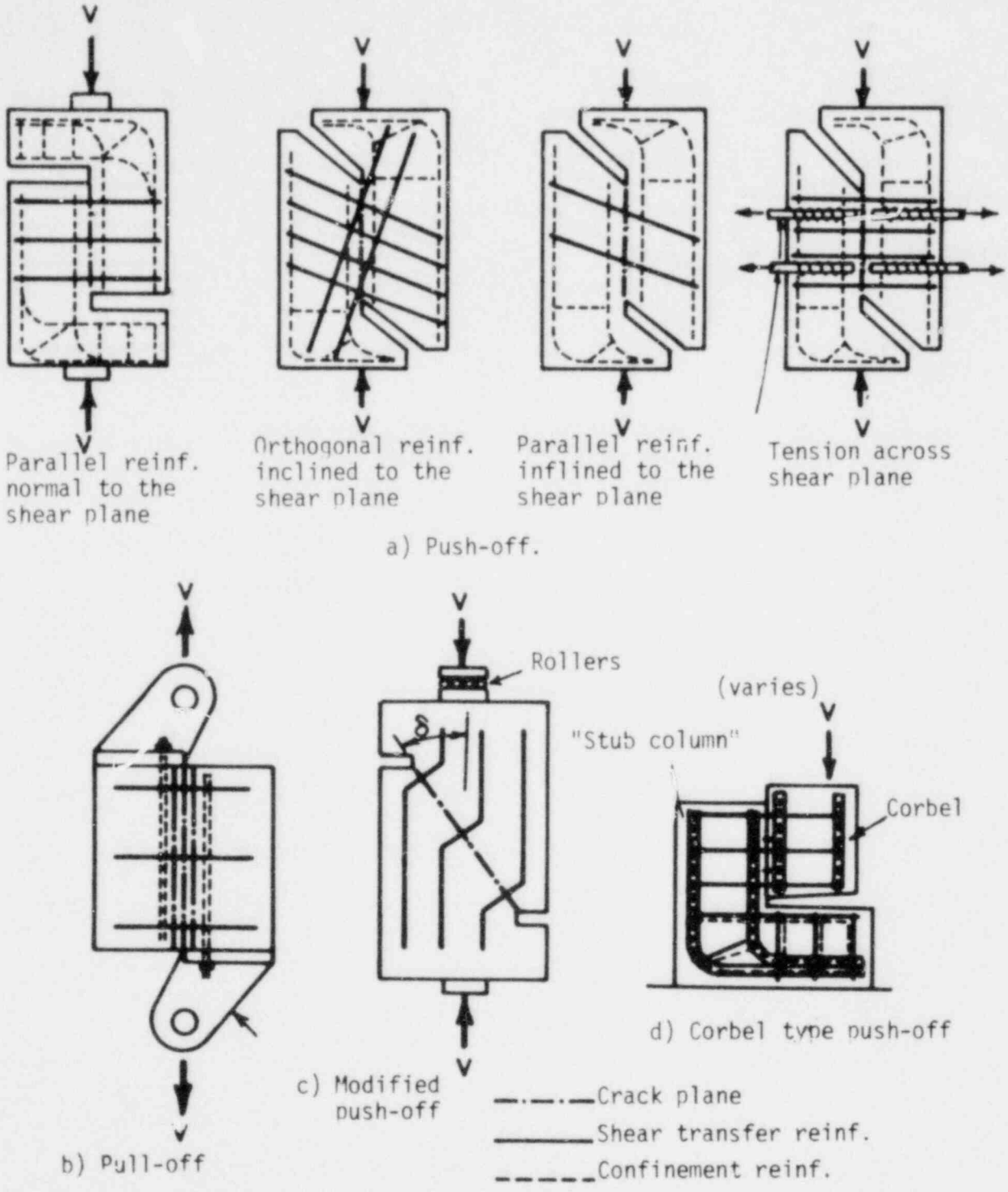

Fig. 4.39. Different shear transfer test specimens used by Mattock.

Mattock's expressions suggested the following effective friction coefficient, according to the revised expression

$$\mu_e = v_u/(\rho f_y + \sigma_N), \tag{4.55}$$

mean value: $$\mu_e = \frac{0.8\ v_u}{(v_u - 400)} = \frac{400}{(\rho f_y + \sigma_N)} + 0.8 \tag{4.56a}$$

lower bound value: $$\mu_e = \frac{0.8\ v_u}{v_u - 200} = \frac{200}{\rho f_y + \sigma_N} + 0.8 \tag{4.56b}$$

For comparison the ultimate strength v_u and the effective friction coefficient μ_e were plotted versus the axial stress parameter normal to the crack $(\rho f_y + \sigma_N)$ according to various investigations in Figs. 4.40a and 4.40b (see Ref. 36), respectively, for normal weight concrete and monotonic shear. Data derived only from tests on precracked specimens with or without applied tension across the shear plane was considered. Very small differences exist in the values of the ultimate strength v_u predicted by the various proposed expressions except for the shear-friction theory ($\mu = 1.4$). The latter gave conservative results for $(\rho f_y + \sigma_N)$ less than 500 psi (3.45 MPa). This was due to the fact that the shear-friction theory with $\mu = 1.4$ underestimated the effective coefficient of friction μ_e for small values of $(\rho f_y + \sigma_N)$ despite the fact that values of μ_e greater than 3.0 could be reached in that region. Mattock's linear expressions (Eqns. 4.54a and 4.54b) appears to be the simplest of all and adequately describing the available experimental data.

Hermansen and Cowan (Ref. 53) and Cowan and Cruden (Ref. 27) questioned, as did Mattock, the original form of the cohesionless shear-

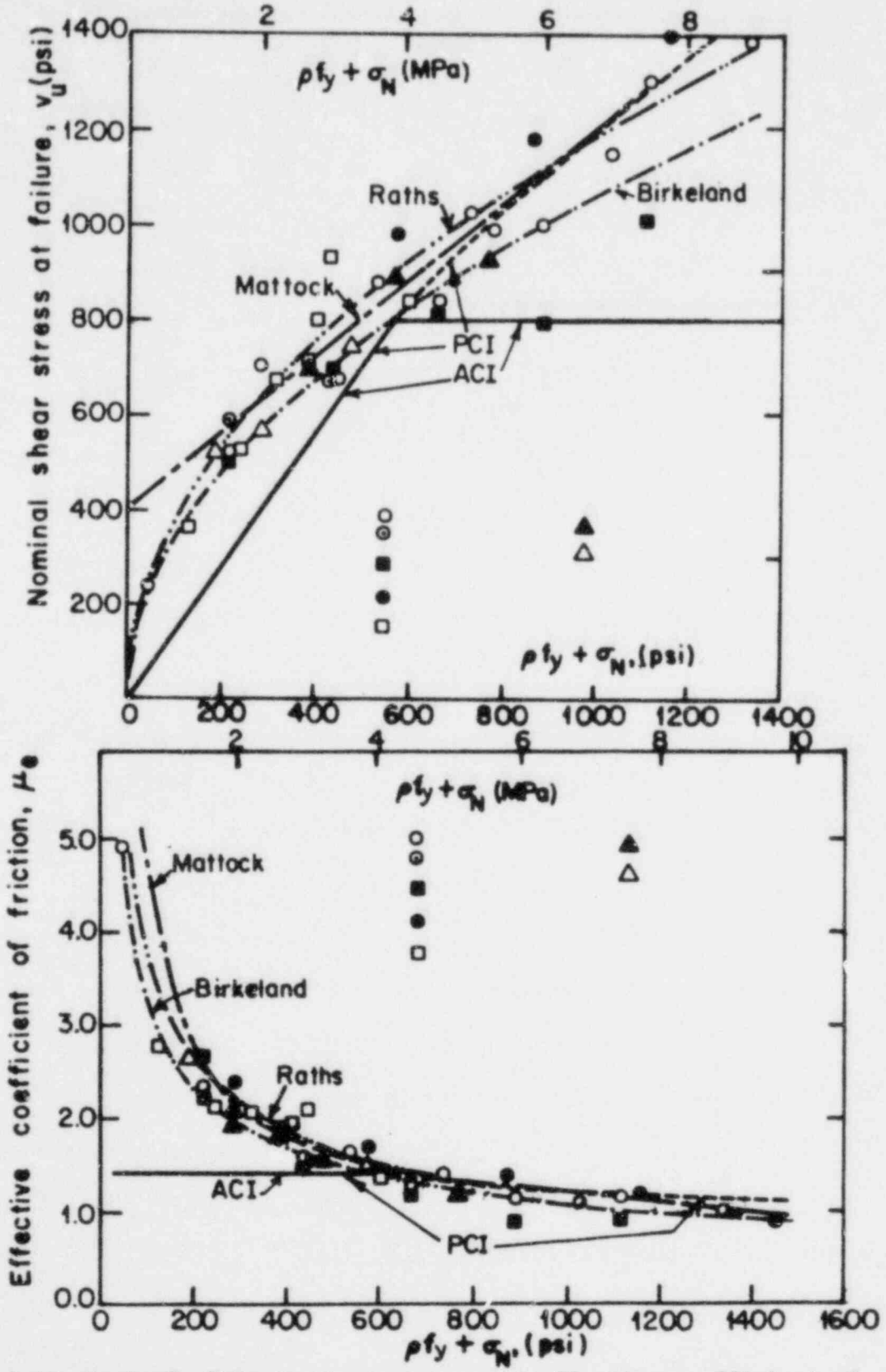

Fig. 4.40. Nominal ultimate shear stress and effective coefficient of friction versus ($\rho f_y + \sigma_N$) for normal weight concrete.

friction formulation. They concluded, from tests on reinforced concrete brackets, that including an apparent cohesive stress would provide more realistic ultimate strength values for small steel ratios.

Cowan pointed out that the shear-friction concept should not be used if a rotational rather than a sliding failure mechanism was indicated by a free-body analysis. He suggested that the former failure mode, although rare, could control in the case of reinforced concrete brackets with a shear load eccentricity to bracket depth (from the top to the bottom steel) ratio a/b_d larger than 0.65 (long brackets). In that case, equilibrium of moments about the compression center should be applied instead:

$$Va = A_s f_y z \tag{4.57}$$

where z was the lever arm between the centers of tension and compression. This indicated that for a non-sliding failure with a number of reinforcing bars crossing the primary crack the effective lever z would depend on how many bars could reach their yield strength.

A possible diagonal tension opening mode of failure in reinforced concrete panels subjected to combined biaxial tension and shear is related to the above described behavior in that depending on the effective axial stiffness of reinforcing across the crack, a rotation of the separated concrete blocks is possible if yielding occurs only in a limited number of bars with the rest remaining understressed. This failure mechanism will undoubtedly result in a lower ultimate shear transfer capacity as compared with a mechanism that would cause yielding in all bars at failure.

Of course, dowel forces have to be taken into account since they can be significant, as will be shown later in this chapter.

Regarding the effect of repeated cyclic shear, Mattock (Ref. 84) concluded that typical cyclic loading histories resulted in a decrease of about 20% in the ultimate strength as compared with the monotonically loaded specimens.

The experimental work reviewed to this point was related to specimens with small size bars that were confined with heavy transverse reinforcement at the shear plane, which guaranteed reinforcement yielding and excluded other premature modes of failure such as splitting in the concrete. Jimenez et al. (Ref. 61) conducted shear transfer tests on block specimens with No.7, No.9 and No.14 bars under combined uniaxial tension and monotonic or cyclic shear, and found that as the bar size increased a concrete splitting failure occurred. No transverse confinement steel was present at the shear plane in these tests. Specimens C4-7A with four No.7 and C4-9A with four No.9 rebars failed at 850 and 900 psi (5.86 and 6.21 MPa) shear stress, respectively, from yielding in the reinforcement. However, specimens C2-14A to C2-14D with two No.14 rebars failed at a much lower shear stress of about 260 psi (1.79 MPa) due to the formation of splitting cracks along the reinforcement. This demonstrated the detrimental effect of the larger size bars on the integrity of the surrounding concrete as the dowel forces increased with increasing bar size.

The following predictive expression was proposed by Jimenez et al. for the ultimate strength v_u attained by means of the combined mechanisms of the interface shear transfer and dowel action

$$v_u = \frac{V_u}{A_c} = \frac{4 b_n d}{A_c} \left[0.47 + \frac{0.54 c_m}{\frac{b_n}{n_b^2} + d}\right] \sqrt{1 - \frac{N_s^2}{N_{so}^2}} \qquad \text{(psi)}, \tag{4.58}$$

where b_n was the net width of the concrete (in), d the bar diameter (in), A_c the shearing area at the crack plane (in^2), c_m the minimum concrete cover (in), n_b the number of rebars, N_s the externally applied tensile force in the reinforcement and N_{so} the splitting axial force given by the relation

$$N_{so} = \frac{d\, L_d\, c_m \sqrt{f_c'}}{(35.4d + 0.573\, L_d)} \qquad \text{(kips)}, \tag{4.59}$$

where L_d was the development length of the rebar (in).

The above Eqn. 4.58 is plotted in Fig. 4.41 for different values of L_d/d expected in actual secondary containment vessels with No.18 bars, together with Mattock's lower bound expression (Eqn. 4.54b). By considering the reduction in the bar development length to diameter ratio due to cracking in the vessel and assuming a value of L_d/d equal to 5.33 both equations showed similar results for N_s/N_{sy} ratios larger than about 0.6 (N_{sy} is the yield strength of the bar under pure axial load). For axial stress levels smaller than 60% of the yield strength in the steel Mattock's expression predicted much higher ultimate strengths (above the $8\sqrt{f_c'}$ level) as the ratio N_s/N_{sy} decreased. This difference in the ultimate strength at low values of applied uniaxial tension was due to the already mentioned heavy transverse confinement provided in Mattock's specimens and probably due to the smaller size bars employed in his tests.

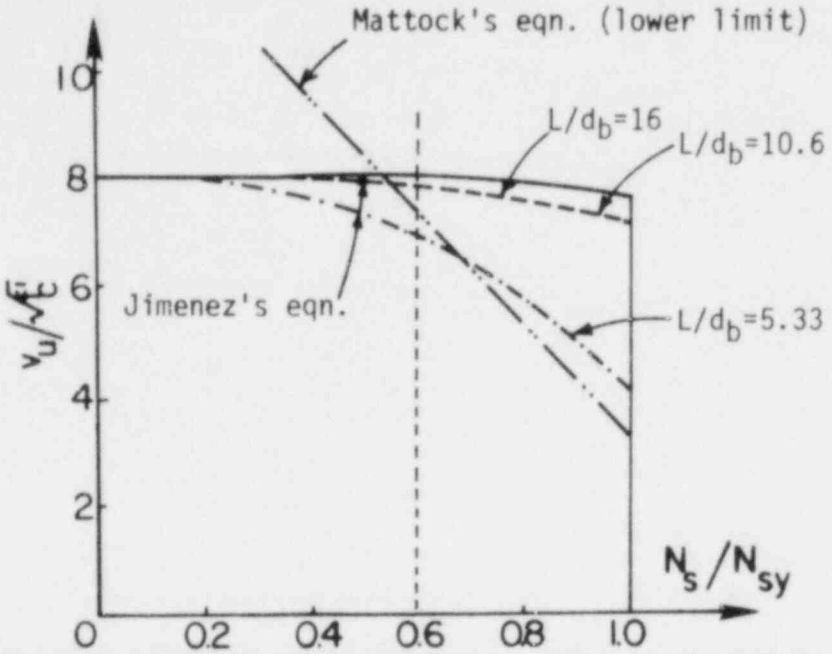

Fig. 4.41. Ultimate strength under monotonic shear predicted by Jimenez et al. (Ref. 61) and Mattock et al. (Ref. 85).

The same results on ultimate strength under cyclic shear and uniaxial tension from the experiments conducted by Jimenez et al. (Ref. 61) along with the results obtained on the biaxially tensioned flat specimens described in Chapter 2, are also plotted in Fig. 4.42 in terms of the shear stress parameter $v_u/\sqrt{f'_c}$ versus the normal stress parameter $(\rho f_y - \sigma_N)$. The straight line from the shear-friction theory with a friction coefficient of 1.4 together with Mattock's results are also included in the above figure.

An approximately 50% variation in strength is observed in the present results with applied biaxial tension ranging from 0 to $0.9f_y$. For low values of $(\rho f_y - \sigma_N)$, less than about 200 psi (1.38 MPa), the results from the present experiments on biaxial specimens correlate well with Mattock's results, while the shear-friction theory is on the conservative side. As the applied tension decreases or the reinforcement ratio increases, the strength of the biaxially tensioned specimens are substantially lower than those predicted by Mattock's expressions. For the latter case, where the rebar tension is smaller than $0.6f_y$, the shear-friction theory gives

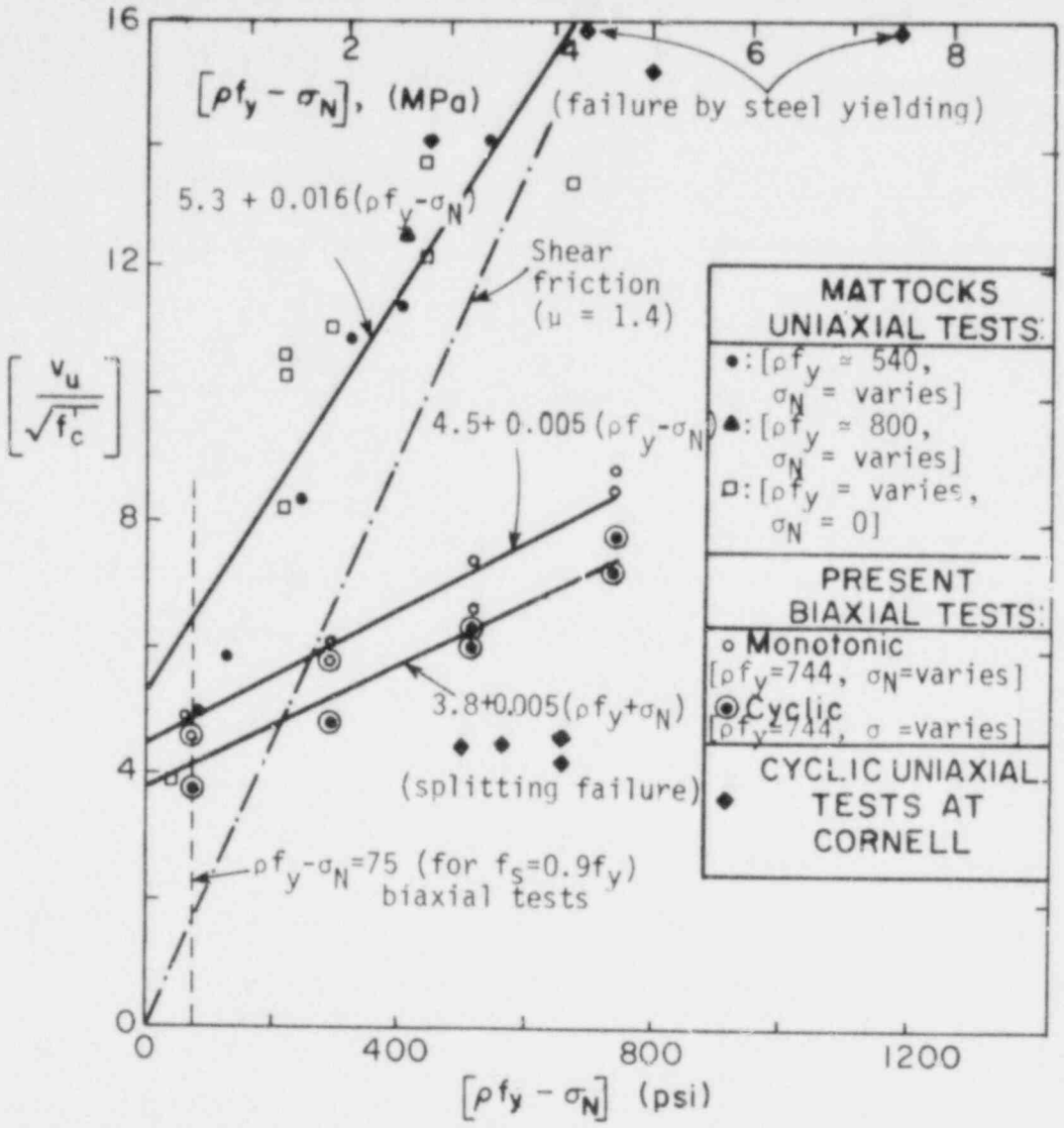

Fig. 4.42. Comparison of the ultimate strength results by Mattock, Jiminez and shear-friction theory.

unconservative results. The effects of bidirectional cracking, biaxial tension, and the absence of any effective concrete confinement (no stirrups were used) combine to produce these somewhat lower strength values. The ultimate strength values found by Jimenez et al. in the univaxial specimens that failed due to steel yielding are at least twice as large as those measured in the present biaxial specimens. On the contrary, if the uniaxial specimens failed due to splitting in the concrete, they showed lower ultimate strength compared with the biaxial specimens.

Concluding, it appears that in both the uniaxially and the biaxially tensioned reinforced concrete specimens the ultimate strength v_u increased with increasing reinforcement ratio and decreasing applied tension in the rebars. However, the level of the maximum shear stress transferred depended also upon the mode of failure (yielding of the reinforcement or splitting in the concrete) and the type of the failure mechanism (sliding, opening or rotational). Cycling was found to cause a decrease in the shear capacity under monotonic shear of about 15 to 20%. The influence of the biaxially applied bar tension and the bidirectional cracking on the mode of failure and the ultimate strength will be discussed in Section 4.4.

4.3 Shear Transfer Engineering Model

Duchon's compression-tension truss model (Ref. 29) predicts a conservative upper limit estimate for stresses and strains in a reinforced concrete containment wall, since concrete tensile strength is neglected. Duchon assumed no shear transfer taking place along the already formed orthogonal cracks produced by internal pressurization in the containment vessel. Thus, he neglected the interface shear transfer and dowel action at low membrane shear stress levels before the formation of the diagonal cracks. As a result, his model becomes unrealistic at shear stresses less than 100 psi (0.70 MPa). Also, as the combination of diagonal tension and compressive concrete struts becomes the major shear resistance mode after the formation of additional diagonal cracks, the dowel action in the rebars along these diagonal cracks was not accounted for.

However, a shear force could exist at the diagonal cracks that would be equilibrated by the axial forces in the reinforcing bars inclined to the cracks, the dowel forces, and the possible shear forces in the steel due to kinking of these bars at large crack openings. Therefore, in addition to the separation of the crack surfaces, a slip is possible along the diagonal cracks. As a result, the orientation of the principal stresses could be different from that of the principal strains parallel and normal to the plane of the diagonal cracks.

In Fig. 4.43 the calculated average shear strain in the present tests for monotonic shear (1st positive cycle) and different levels of bar tension are compared with the predicted response given by Duchon's model described in Appendix B (see Fig. B.1).

Since shear transfer due to slip at the orthogonal cracks is neglected, in this model, large total shear distortions are calculated at low shear stresses. The tangent shear stiffness values predicted can be realistic only for shear stresses higher than about 100 psi, at which level the diagonal cracks start forming. A constant tangent shear modulus value G_{cr} of about $0.13G_o$ (linear response) is predicted by Duchon, independent of the biaxial tension level, compared with the $0.05G_o$ to $0.07G_o$ values measured in the biaxial tests.

Duchon's mathematical model for two-way orthogonal reinforcement (see Appendix B) is modified in this section to include shear transfer by the combined mechanisms of interface shear transfer and dowel action through sliding along the preexisting orthogonal cracks at shear stresses lower than about 100 psi. This will cause an increase in the secant shear modulus predicted by Duchon at shear stresses less than 100 psi. In other

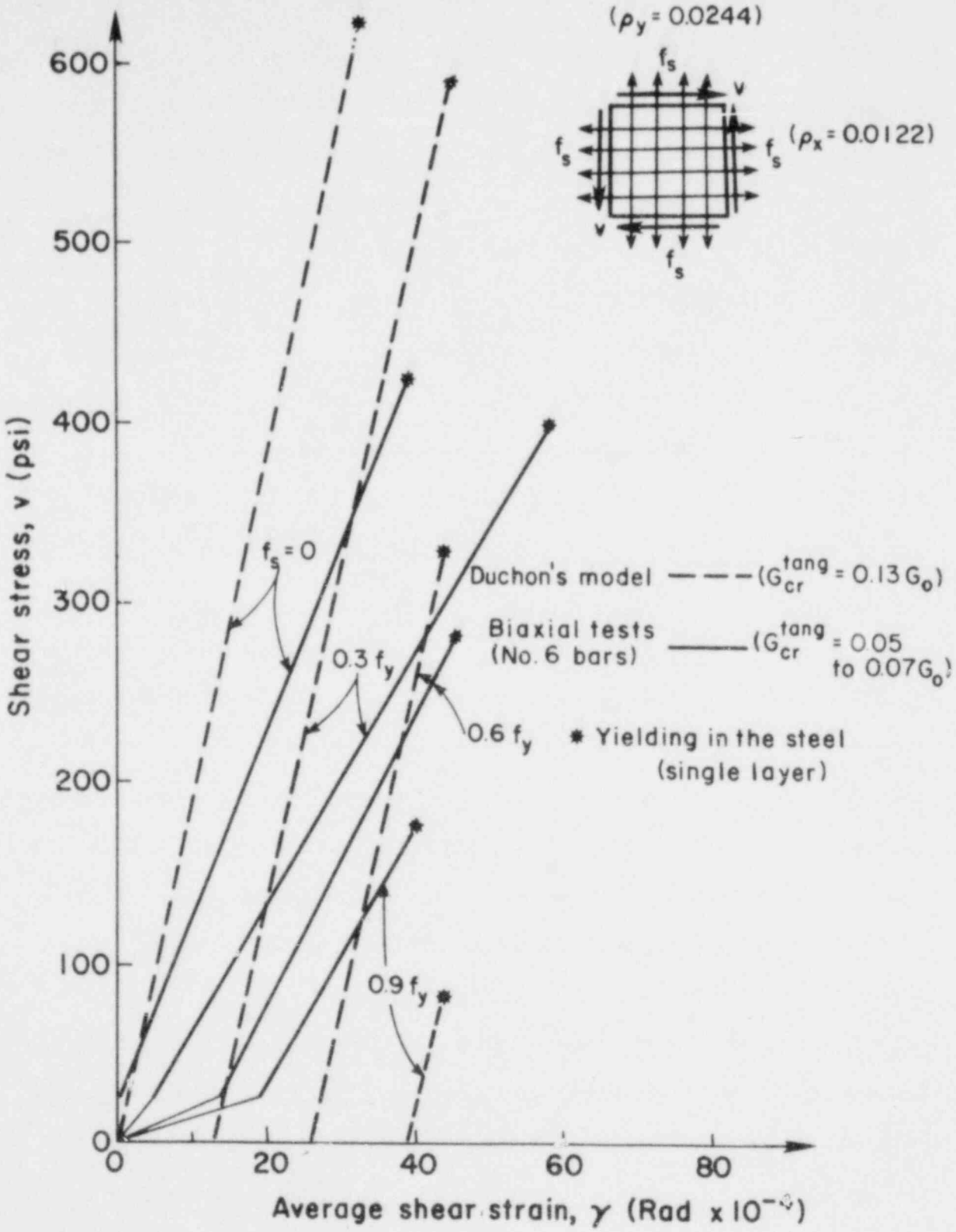

Fig. 4.43. Comparison between the experimental results of biaxial specimens and the predicted results by Duchon's model.

words, there will be a shift of Duchon's shear stress-shear strain (v, γ) plot to the left for low shear stresses.

Duchon assumed that the concrete was a continuum with an infinite number of fine diagonal cracks perpendicular to the direction of the maximum principal tensile strain. Thus, no bond transfer and consequently no concrete tension stiffening effect was accounted for in determining the average steel stresses σ_v and σ_h in the vertical and horizontal reinforcement (see constitutive Eqns. B.3 in Appendix B). However, in reality the rebars, especially at the central portion of the specimen, were partially bonded with the uncracked concrete contributing to the effective axial tension stiffness. An estimate of the effective axial stiffness is employed in this work based on experimental results from the axial tests described in Chapter 3. It is true that as the applied shear stresses approach the failure level the contribution of concrete in tension decreases and becomes insignificant for high shear stress levels. Therefore, it may be neglected in that case, and Duchon's model should predict quite well the effective total shear distortion of a cracked reinforced concrete panel under in-plane shear forces approaching failure.

4.3.1 Shear transfer sliding mode

At low shear stresses and before the formation of the diagonal cracks the applied shear force is carried by the combined mechanisms of interface shear transfer (IST) and dowel action (DA) along the existing orthogonal tension cracks. The embedded reinforcing bars are normal to the orthogonal cracks.

a) Single crack

First, the possible shear transfer mechanisms existing along an idealized saw-tooth type single crack, as shown in Fig. 4.44, will be identified. A total tensile load N is applied through a uniformly distributed reinforcing bars crossing the crack at right angles (see Fig. 4.44a). This causes an average initial crack width c^o_{wm} (Stage I), with its magnitude depending on the extensional stiffness K_N in the direction parallel to the reinforcing bars. The upper and lower parts of the concrete block are then subjected to a uniform shear force V parallel to the crack. To transfer this force across the crack a relative slip of the crack interfaces is required. The amount of that slip at a given applied shear force defines the shear stiffness K_s at that crack.

Initially, the applied shear is resisted by the dowel forces in the bars (Stage II, Fig. 4.44b) until the asperities of the rough surfaces at the crack interface come into firm contact. Then, the shear resistance is increased, since the IST mechanism is mobilized (Stage III, Fig. 4.44c). Additional shear forces are transferred across the crack contact surface areas by the normal (bearing) σ_n and tangential (frictional) stresses σ_t in the concrete. An additional shear slip is induced, as the crack surfaces try to override each other. This shear slip results in increasing the initial crack width and consequently the steel tensile forces in the embedded bars at the vicinity of the crack.

During the shear transfer Stage III (see Fig. 4.45) equilibrium between the applied forces N, V and the resisting forces in the concrete and steel results in the following equations in the directions parallel and normal to the crack direction.

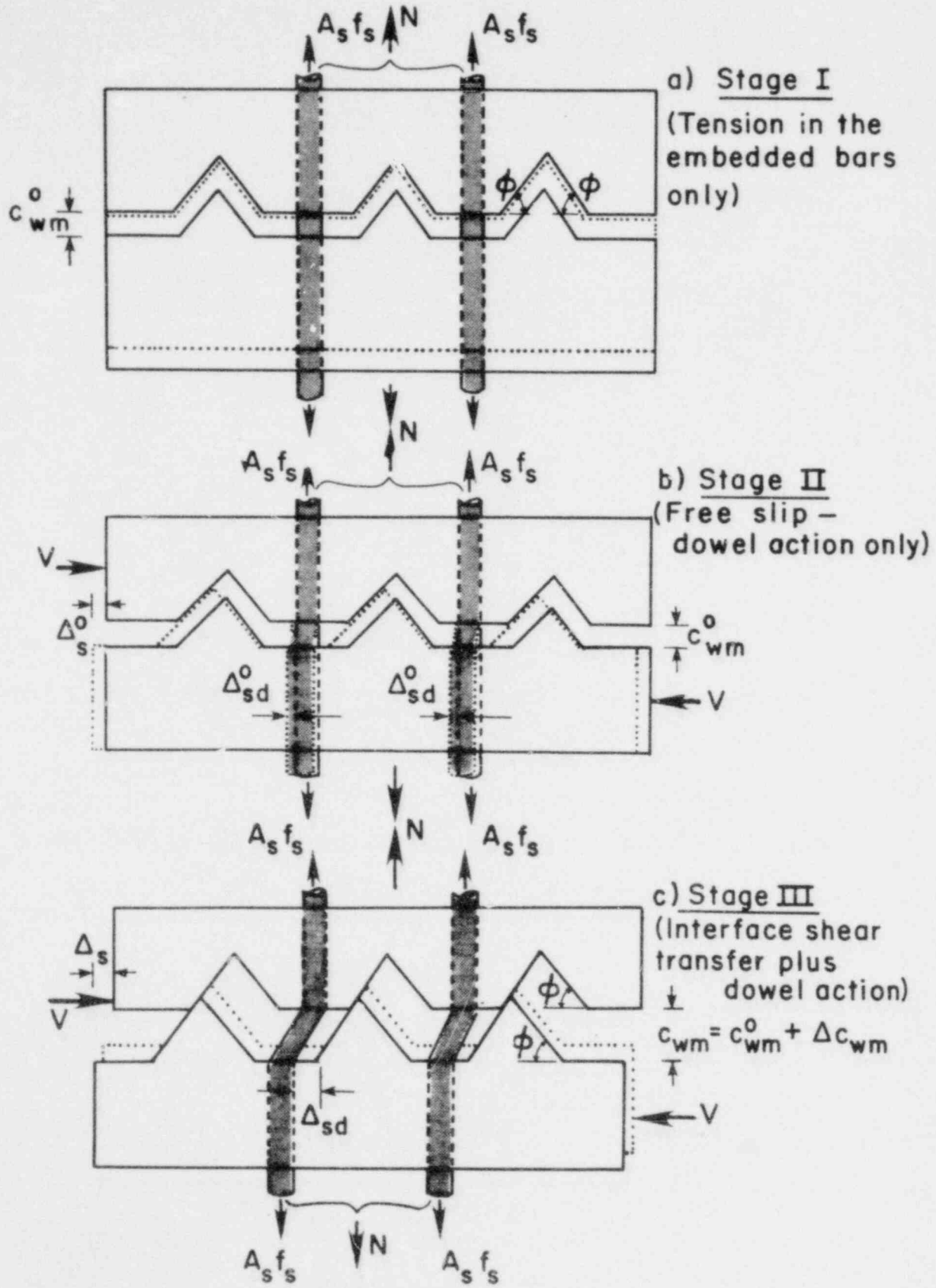

Fig. 4.44. Saw-tooth type idealization of a single crack.

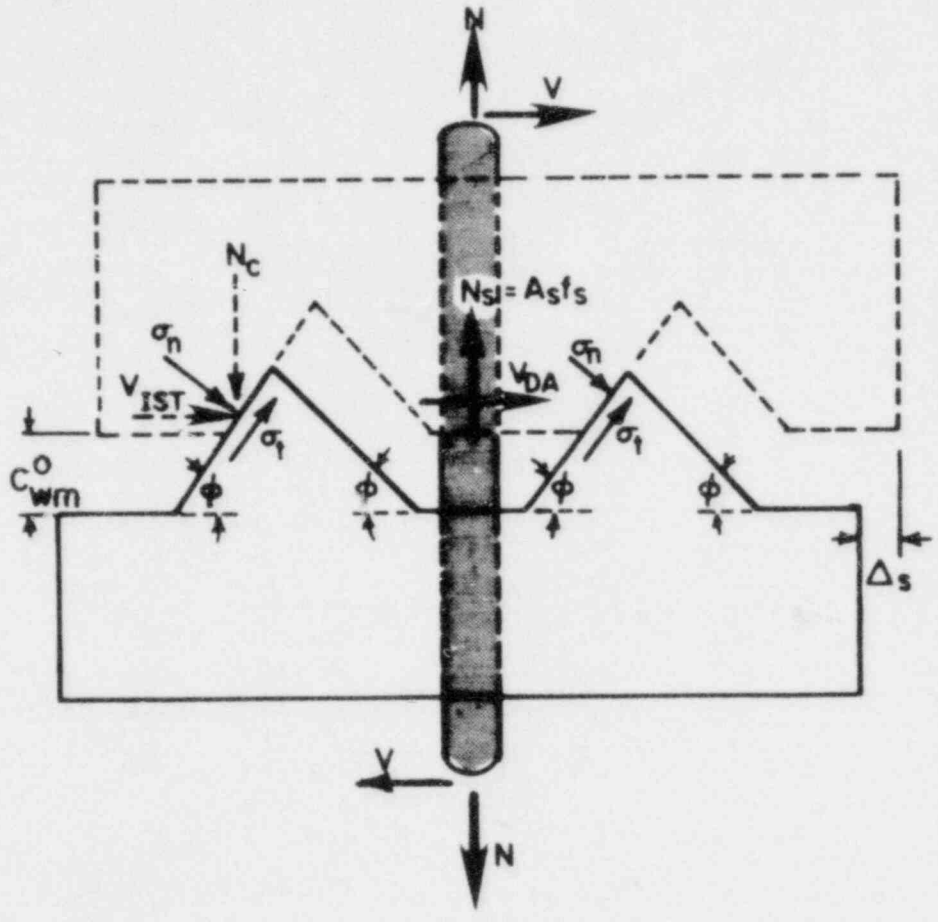

Fig. 4.45. Equilibrium of applied and resisting forces at a single crack.

Parallel to the crack ($\Sigma X = 0$):

$$V = V_{IST} + V_{DA} = (\sigma_n \sin\phi + \sigma_t \cos\phi)\, A_{cc} + n_b A_b v_s \qquad (4.60a)$$

Normal to the crack ($\Sigma Y = 0$):

$$N = N_c + N_s = (\sigma_t \sin\phi - \sigma_n \cos\phi)\, A_{cc} + n_b A_s \sigma_s \qquad (4.60b)$$

where

σ_t = concrete frictional stress tangential to the contact surface

σ_n = concrete bearing stress normal to the contact surface

A_{cc} = total contact area

σ_s = bar tensile stress at the crack

v_s = dowel shear stress per bar at the crack (including kinking)

A_s = bar cross-sectional area

n_b = number of reinforcing bars crossing the crack

V_{DA} = total dowel shear force resisted by the bars (including kinking)

V_{IST} = total shear force resisted by the IST mechanism in the concrete

N_c = total normal compressive force at the concrete interface

N_s = total normal force resisted by the bars

ϕ = inclination angle of the concrete teeth

The above idealized angle ϕ depends on the aggregate size and orientation of the shear plane and the friction coefficient of the rough interface.

According to Eqn. 4.60b, the increase in bar tension (N_s - N) due to the increase of the crack widt' (dilatancy) is equilibrated by an equal normal compressive force in the concrete interface N_c.

Solving for σ_N from Eqn. 4.60b,

$$\sigma_n = \sigma_t \tan - \frac{N - N_s}{A_{cc} \cos\phi} \tag{4.61}$$

Substituting σ_n from Eqn. 4.61 in Eqn. 4.60a, the total shear force V transferred across the crack is given by the following relation

$$V = \frac{\sigma_t A_{cc}}{\cos\phi} - (N - N_s) \tan\phi + V_{DA} \tag{4.62}$$

Dividing by the shearing area A_c at the crack, Eqn. 4.62 can be written in terms of stresses as follows

$$\frac{V}{A_c} = v = v_{IST}^t + (\rho\sigma_s - \sigma_N)\tan\phi + v_{DA} = v_{IST}^t + v_{IST}^n + v_{DA} \qquad (4.63)$$

with

$$v_{IST}^t = \frac{\sigma_t A_{cc}}{\cos\phi\, A_c}$$

$$v_{IST}^n = (\rho\sigma_s - \sigma_N)\tan\phi$$

$$\sigma_N = \frac{N}{A_c}$$

and (4.64)

$$v_{DA} = \rho v_s$$

where v_{IST}^t is the frictional shear stress carried solely by the concrete, v_{DA} is the total shear stress transferred by dowel action and kinking (at large crack openings or shear slips), ρ is the steel ratio in the direction normal to the crack and σ_N the applied normal tensile stress in the same direction, calculated relative to the projected crack area.

The tensile force N is applied by tensioning the embedded bars. Thus, the total applied normal stress σ_N is equal to

$$\sigma_N = n_b A_s f_s / A_c = \rho f_s \qquad (4.65)$$

Substituting σ_N from Eqn. 4.65 in Eqn. 4.63, the total shear stress transferred at the crack is equal to

$$v = v^t_{IST} + \rho(\sigma_s - f_s)\tan\phi + v_{DA} \tag{4.66}$$

The second part of the right hand side in Eqn. 4.66 denotes the shear stress

$$v^n_{IST} = (\rho\Delta\sigma_s)\tan\phi \tag{4.67}$$

transmitted across the crack by means of friction due to the compressive stresses

$$\sigma_c = \rho(\sigma_s - f_s) = \rho\Delta\sigma_s \tag{4.68}$$

in the concrete caused by the increase in bar tension at the crack. The effective shear friction coefficient $\mu = \tan\phi$ can be determined only experimentally. The above restraining stress σ_c depends on the extensional stiffness K_N.

The shear stress transferred by means of the IST and the DA mechanisms is given by the following equations

$$v_{IST} = v^t_{IST} + v^n_{IST} = v^t_{IST} + \mu[\rho(\sigma_s - f_s)] \tag{4.69a}$$

and

$$v_{DA} = \rho v_s \tag{4.69b}$$

To satisfy compatibility of displacements, the shear displacement required to mobilize the IST and DA mechanisms at the crack plane is equal to the measured relative slip, Δ_s, of the crack interfaces. Therefore,

$$v_{IST} = K_{IST}\Delta_s$$

$$v_{DA} = K_{DA}\Delta_s \tag{4.70}$$

where K_{IST} and K_{DA} are the shear stiffnesses at the single crack corresponding to interface shear transfer and dowel action (possible kinking is included at large shear slips), respectively.

During the initial free slip Δ_s^o, which is a function of the initial crack width c_{wm}^o, before the crack surfaces come into contact, dowel action is the major shear transfer mechanism. Therefore, the plot of shear stresses v versus the corresponding slips Δ_s will exhibit a hardening response for slip values larger than Δ_s^o, as shown in Fig. 4.46. For shear slips Δ_s larger than v_o/K_{DA} the IST mechanism is also mobilized and both shear stiffnesses (K_{IST} and K_{DA}) contribute to shear transfer. Thus, the slip predicted for a given applied shear stress v_x is given by the following expressions (assuming constant stiffnesses K_{DA}, K_{IST} up to a shear stress v_x)

$$\Delta_s = \frac{v_x}{K_{DA}}, \text{ for } v_x \leq v_o \; (= K_{DA}\Delta_s^o), \tag{4.71a}$$

and

$$\Delta_s = \Delta_s^o + \frac{v_x - v_o}{K_{IST} + K_{DA}} = \frac{\Delta_s^o K_{IST}}{K_{IST} + K_{DA}} + \frac{v_x}{K_{IST} + K_{DA}}, \text{ for } v_x > v_o \tag{4.71b}$$

with

$$\Delta_s^o = \frac{c_{wm}^o}{\tan\phi} = \delta_1(\phi)\, c_{wm}^o \tag{4.72a}$$

and

$$c_{wm}^o = \delta_2 + \delta_3 f_s = \varepsilon_{sm}\ell_{cm} \tag{4.72b}$$

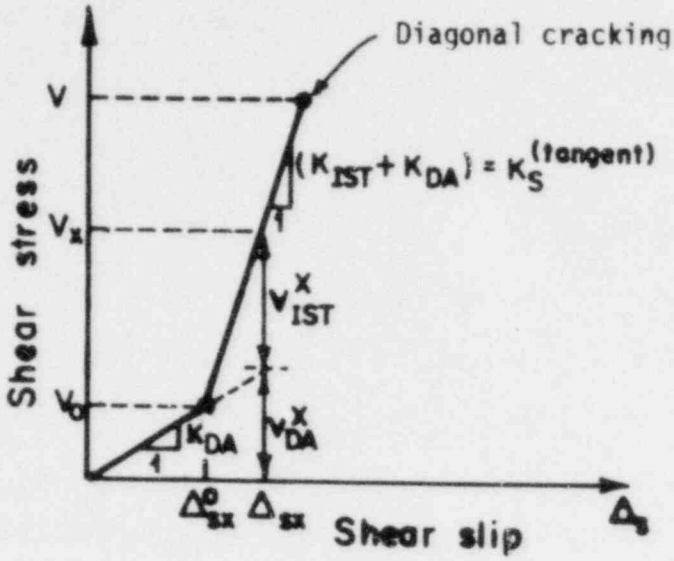

Fig. 4.46. Bilinear idealization of the shear stress-slip relationship along an orthogonal crack parallel to the x direction.

where coefficient δ_1 is a function of the slope ϕ, which models the crack roughness, and coefficients δ_2, δ_3 are a function of the steel ratio ρ and the average crack spacing ℓ_{cm} as described in Chapter 3.

From Eqn. 4.71b it is true that the tangent shear stiffness of the (v, Δ_s) relationship for combined (IST + DA) is equal to

$$K_s \text{ (tangent)} = K_{IST} + K_{DA} \tag{4.73}$$

The shear stiffness due to IST only, according to Eqn. 4.69a, is a function of both the extensional stiffness K_N and the initial crack width c_{wm}^o, that is the initially applied and constantly maintained steel stress. Also, K_{DA} is not actually constant, particularly as v increases.

For the evaluation of an effective shear stiffness at a single crack, expressions for the individual stiffnesses K_{IST}, K_{DA} and K_N are required.

In the work reported here (see Chapter 2) measurements of slips and crack width changes during the application of shear were conducted for selected orthogonal cracks. These results, although they provided information on the shear stiffness at one small region of the crack (where the gages were mounted), cannot really be utilized to determine a good estimate for the average stiffness along the entire length of the crack under shear loading. They may be used only for qualitative conclusions.

Regarding the stiffness components K_{IST} and K_{DA}, expressions have been developed from experimental studies on uniaxial specimens with a single preexisting crack performed at Cornell, McGill, and the University of Canterbury. Jimenez et al. (Ref. 61) proposed the following expression for the K_{IST} stiffness

$$K_{IST} = [3.9(c^o_{cm} - 0.002) + 0.0367 - 1.09 \times 10^{-7} \frac{K_N}{c^o_{wm}}]^{-1} \quad \text{(ksi/in)} \tag{4.74}$$

for initial crack widths between 0.005 and 0.030 in., applied shear stresses less than 300 psi and concrete compressive strengths between 3000 and 4000 psi. In the above expression (Eqn. 4.74), K_{IST} increases with decreasing applied tension (or initial crack width) and increasing normal restraint stiffness provided by the reinforcement. The initial crack width c^o_{wm} in Eqn. 4.74 can be expressed in terms of the applied tension f_s, steel ratio ρ in the direction normal to the crack, the average crack spacing ℓ_{cm} for a set of parallel cracks, and the extensional stiffness K_N according to the following relation derived from the present biaxial tests described in Chapter 3 (see Eqn. 3.22)

$$c^{o}_{wm} = \ell_{cm}\varepsilon_{sm} = (2.4 + 10.3\,\frac{f_s}{f_y})(\frac{\ell_{cm} f_y}{\rho E_s}) \times 10^{-3}$$

$$= 0.0024\,\frac{\ell_{cm} f_y}{\rho E_s} + f_s K_N^{-1} \quad \text{(in)} \tag{4.75}$$

The shear stiffness K_{IST}, given by Eqn. 4.74, is valid only for monotonically applied shear. For reversing cyclic shear, a reduction factor should be used based on experimental data, as follows

$$K_{IST}\ \text{(cyclic)} = q\ K_{IST}\ \text{(monotonic)}, \tag{4.76}$$

where q is less than 1.0 and depends on the applied tension f_s, the number of cycles, the maximum shear stress level, and the steel ratio ρ.

The major difficulty in determining the dowel stiffness K_{DA} for monotonic shear is the estimation of the effective foundation modulus of concrete k_f, which influences significantly the stiffness provided by the dowel. As pointed out in the literature review in this chapter, a large scatter exists for the measured values of k_f. In Ref. 73 an approximate linear relation between k_f and the applied tensior f_s, based on experimental data from uniaxial dowel tests (Refs. 61 and 127), has the following form

$$k_f = 2961 - 29\ f_s \qquad (k/in^3) \tag{4.77}$$

Computing k_f from Eqn. 4.77, the dowel stiffness per bar may be calculated from the relation

$$K_{DA} = \frac{d}{8}\sqrt[4]{\pi E_s k_f^3}\sqrt{\left(\frac{f_c'}{4000}\right)^3} \qquad (k/in) \qquad (4.78)$$

given in Ref. 109 for bar sizes up to No.14. The effect of crack width on the dowel stiffness given by Eqn. 4.78 is built in the parameter of the effective foundation modulus of concrete k_f.

Assuming an average foundation modulus of 750 k/in^3 (Ref. 61) the expression for the dowel stiffness of a single bar of diameter d is given by

$$K_{DA} = 312\ d^{1.75} \qquad (k/in) \qquad (4.79)$$

b) Two-way orthogonal cracking

In precracked reinforced concrete panels with two sets of orthogonal cracks assumed equally spaced and subjected to uniformly distributed total normal tensile forces N_x, N_y and pure shear V, the shear slips and crack widths in the x and y directions will result in an average shear distortion γ of the panel (see Fig. 4.47).

An effective tangent shear modulus G_{cr} can be evaluated in a similar way described in Ref. 73 by adding the average distortions of the uncracked concrete blocks between the orthogonal cracks ($\gamma^{(u)}$) and the distortions caused by the relative slips along the cracks ($\gamma^{(cr)}$), that is

$$\gamma = \gamma^{(u)} + \gamma^{(cr)} \qquad (4.80)$$

with

$$\gamma^{(u)} = (V/A_c)\ G_o^{-1}, \qquad (4.81a)$$

and

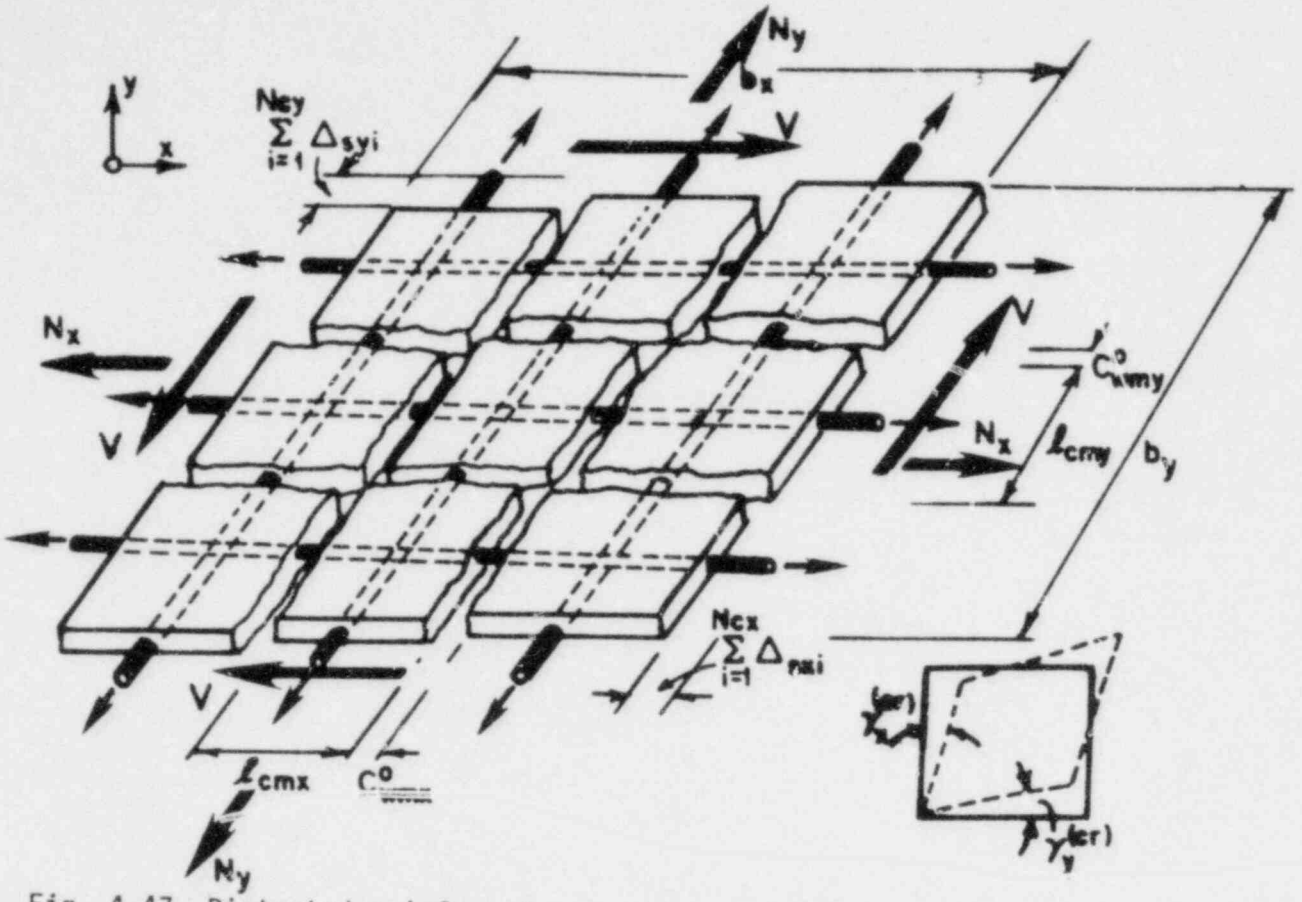

Fig. 4.47. Distorted reinforced concrete panel subjected to combined biaxial tension and membrane shear (sliding along the orthogonal cracks).

$$\gamma^{(cr)} = \gamma_x^{(cr)} + \gamma_y^{(cr)} = \frac{\sum_{i=1}^{N_{cx}} \Delta_{sxi}}{b_y} + \frac{\sum_{i=1}^{N_{cy}} \Delta_{syi}}{b_x} \simeq \frac{\Delta_{sx}}{\ell_{cmy}} + \frac{\Delta_{sy}}{\ell_{cmx}} \qquad (4.81b)$$

where G_o is the shear modulus for uncracked concrete, Δ_{sxi} and Δ_{syi} are the crack slips at the ith crack in the x and y directions, b_x ($\simeq N_{cx}\ell_{cmy}$) and b_y ($\simeq N_{cy}\ell_{cmx}$) are the panel dimensions, N_{cx} and N_{cy} are the number of orthogonal cracks parallel to the x and y directions and Δ_{sx}, Δ_{sy} are the total average estimated slips in the x and y directions.

Substituting Δ_{sx} and Δ_{sy} from Eqn. 4.71 in Eqn. 4.81b,

$$\gamma^{(cr)} = \left(\frac{1}{K^x_{DA}\ell_{cmy}} + \frac{1}{K^y_{DA}\ell_{cmy}}\right)v, \text{ for } v \leq v_o \tag{4.82a}$$

and

$$\gamma^{(cr)} = \frac{\Delta^o_{sx}}{\ell_{cmy}}\left(\frac{K^x_{IST}}{K^x_{IST} + K^x_{DA}}\right) + \frac{\Delta^o_{sy}}{\ell_{cmx}}\left(\frac{K^y_{IST}}{K^y_{IST} + K^y_{DA}}\right)$$

$$+ \left[\frac{1}{(K^x_{IST} + K^x_{DA})\ell_{cmy}} + \frac{1}{(K^y_{IST} + K^y_{DA})\ell_{cmx}}\right]v, \text{ for } v > v_o \tag{4.82b}$$

where v_o is taken as equal to 50 psi, at which level an increase in shear stiffness was observed in the present biaxial tests.

From Eqns. 4.80, 4.81a and 4.82 the following expressions are derived for the effective tangent shear modulus for the cracked concrete panel G^t_{cr} (see Fig. 4.48)

$$G^t_{cr} = \left[\frac{1}{K^x_{DA}\ell_{cmy}} + \frac{1}{K^y_{DA}\ell_{cmx}} + \frac{1}{G_o}\right]^{-1}, \text{ for } \gamma \leq \gamma_o \tag{4.83a}$$

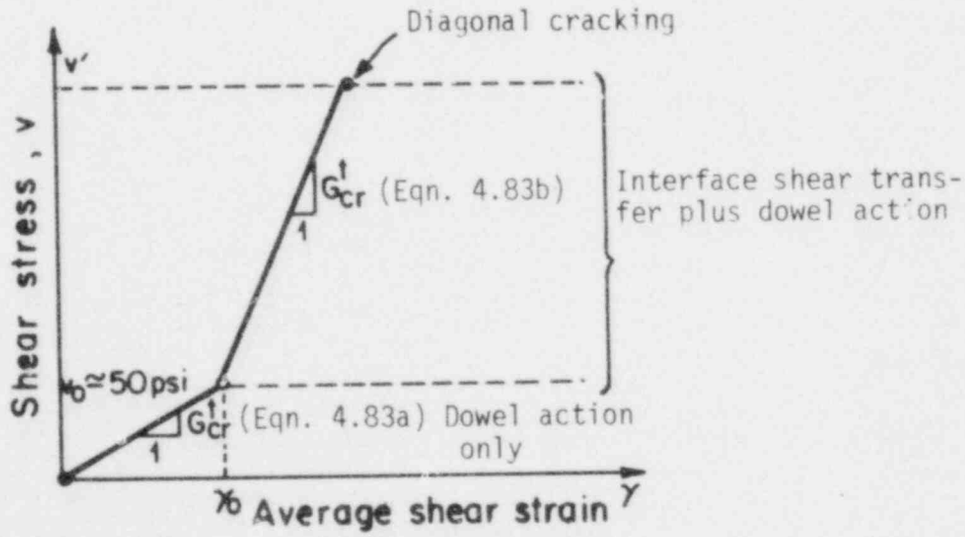

Fig. 4.48. Idealized shear stress-strain bilinear curve when orthogonal cracking is present.

and

$$G^{t}_{cr} = \left[\frac{1}{(K^{x}_{IST} + K^{x}_{DA})\ell_{cmy}} + \frac{1}{(K^{y}_{IST} + K^{y}_{DA})\ell_{cmx}} + \frac{1}{G_o}\right]^{-1}, \text{ for } \gamma > \gamma_o \quad (4.83b)$$

where γ_o is the shear strain at a shear stress v_o equal to about 50 psi.

4.3.2 Shear transfer diagonal tension mode

With the occurrence of the first diagonal cracks at a shear stress of about 100 psi the diagonal cracks tend to close (see Figs. 2.26 from the present results and 4.49 from the PCA biaxial tests) and the major shear transfer mode gradually changes from that of sliding to a diagonal tension-compression strut system. An expression for the shear rigidity will be derived for shear stresses above the 100 psi level transferred by means of the latter mode. Before formulating the governing equations of the shear transfer, the fact that diagonal cracks were initiated at relatively low shear stresses will be discussed in the following section.

a) Diagonal cracking

After all bars were tensioned up to 36 ksi and all primary orthogonal cracking had taken place there would be a certain bond stress distribution between two adjacent cracks at the steel-concrete interface. As shown in Fig. 4.50a, the orthogonal cracks tend to form along the transverse reinforcing bars in both directions.

It appears reasonable to assume that in addition to the shear stresses v due to the applied shear forces, there will be additional localized shear stresses τ_b due to bond on the edges of the uncracked concrete block ABCD in Fig. 4.50a. For the applied shear and tension shown in this

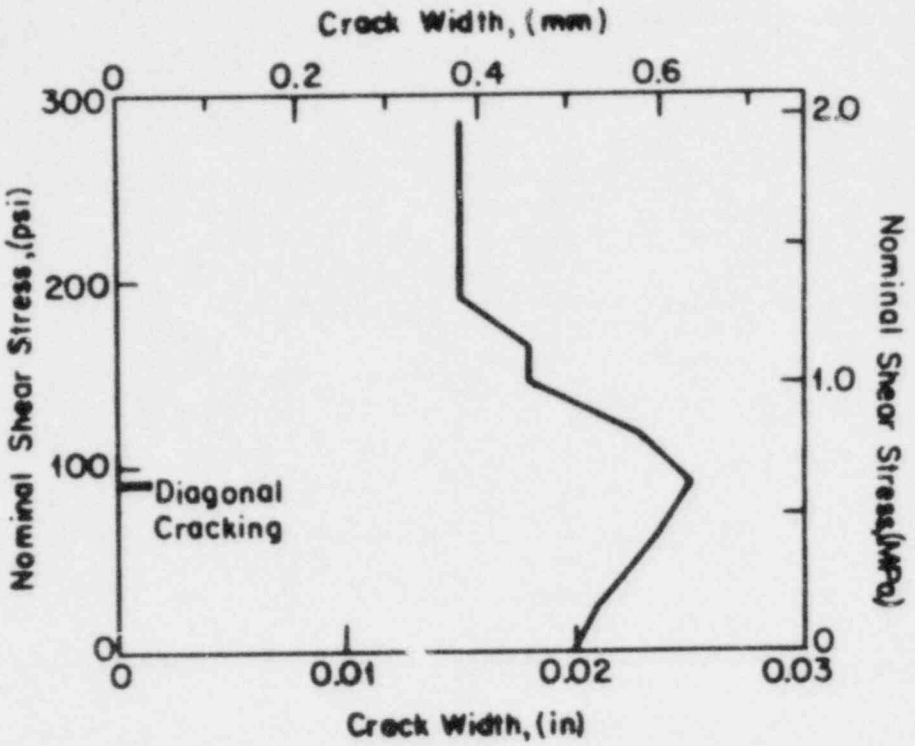

Fig. 4.49. Crack width change versus applied shear stress in PCA's specimen MB3 (Ref. 96).

figure, the bond stresses at the upper left and lower right corners of the concrete block will result in a higher total shear stress. This can cause diagonal cracking at a lower applied shear stress level than expected in the case of pure shear without biaxial tension.

The average value of bond stress that will contribute to the formation of diagonal cracking depends on the critical bond stress that causes first internal cracking during the initial tensioning. As the tension in the bar increases, high diagonal principal tensile stresses σ_I present at the interface can cause internal inclined cracking at an angle of 45 to 60 degrees to the bar axis, as shown in Fig. 4.50a. This has been confirmed experimentally by Broms and Lutz (Ref. 16), Goto (Ref. 49)(see

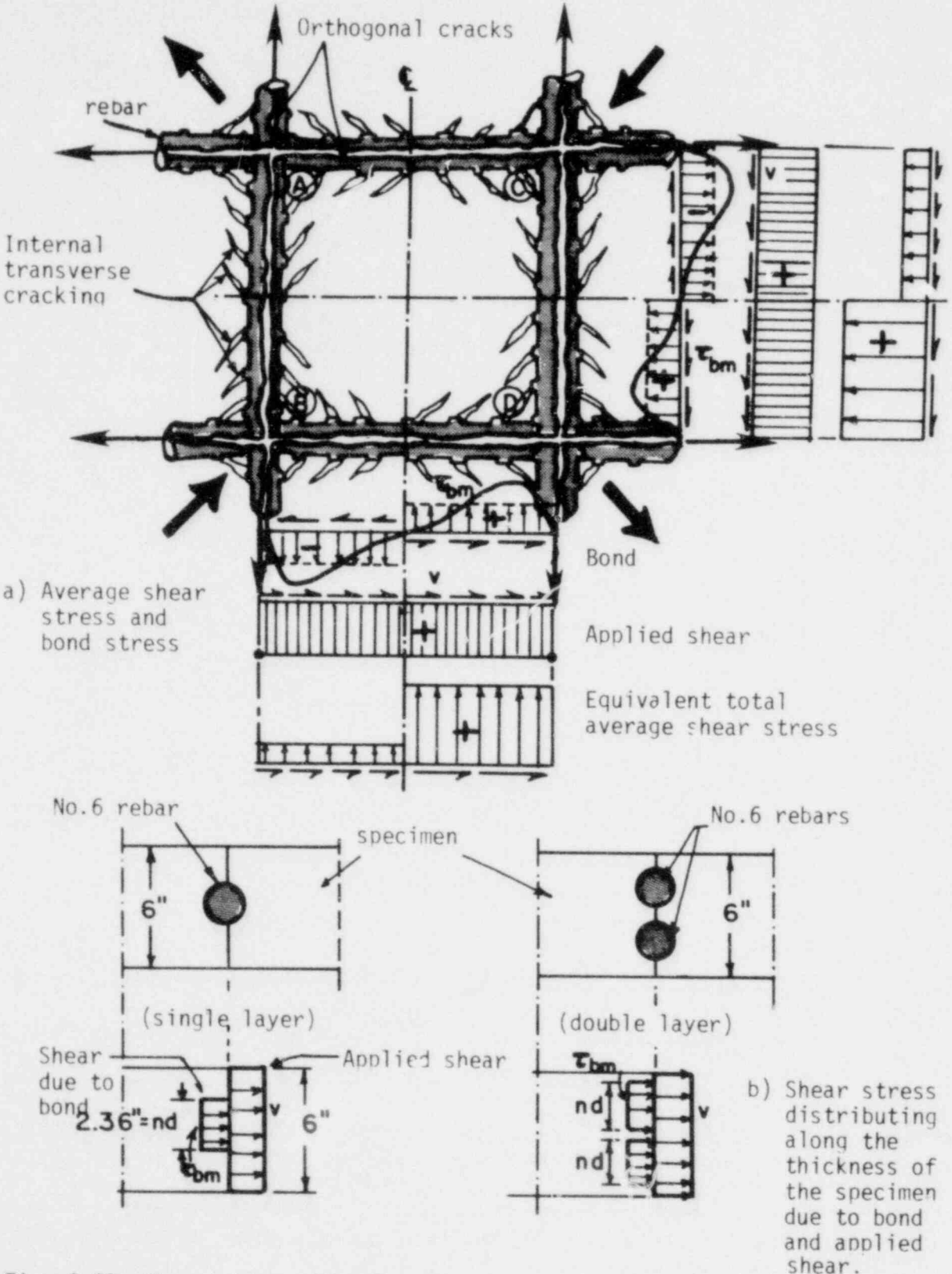

Fig. 4.50. Shear stress distribution at the edges of the uncracked concrete block ABCD.

Fig. 4.51) and analytically by Bresler and Bertero (Ref. 13). The latter performed a three-dimensional axisymmetric finite element analysis of a reinforced concrete cylindrical prism with an embedded bar, and calculated principal tensile stresses σ_I high enough to cause internal transversal cracking. As the tensile load increases new internal inclined cracks form farther from the primary cracks. This results in progressive degradation of the tension stiffening effect in concrete. The severity of this internal inclined cracking at the bars can be seen in the present experimental results from the fact that even at zero tension (after bars had been tensioned at $0.6f_y$) diagonal cracks appeared at the low shear stress level of about 100 psi.

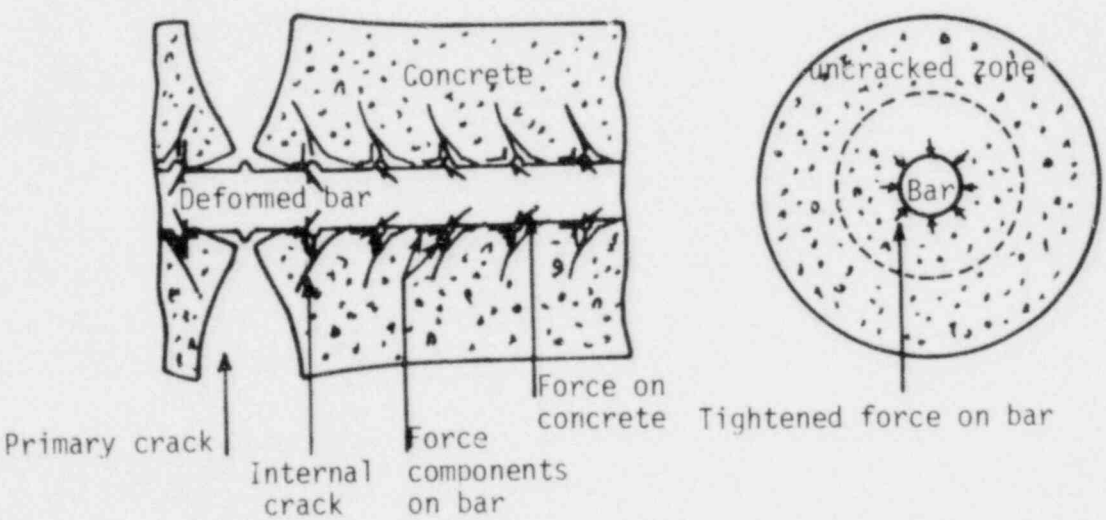

a) Longitudinal action of axially loaded specimen

b) Cross section

Fig. 4.51. Deformation of concrete around reinforcing steel after formation of internal cracks according to Goto (Ref. 49).

The critical bond stress to initiate internal transverse cracking depends mainly on the tensile strength of concrete f_t', the concrete

cover, and the type of loading (Tassios, Ref. 113). For moderate confinement (radial concrete stress $|\sigma_{cy}| < f_t'$), as shown in Fig. 4.52 taken from Ref. 113, and tensile longitudinal concrete stresses $0 < \sigma_{cx} < f_t'$ the critical bond stress $\tau_{b,cr}$ could reach a value equal to f_t' ($\simeq$ 400 psi for an average concrete compressive strength of f_c' = 3800 psi, assuming $f_t' = 6.5\sqrt{f_c'}$). Radial compression (σ_{cy}) due to shrinkage or other confining effects could increase $\tau_{b,cr}$ to values higher than f_t' (see Fig. 4.52).

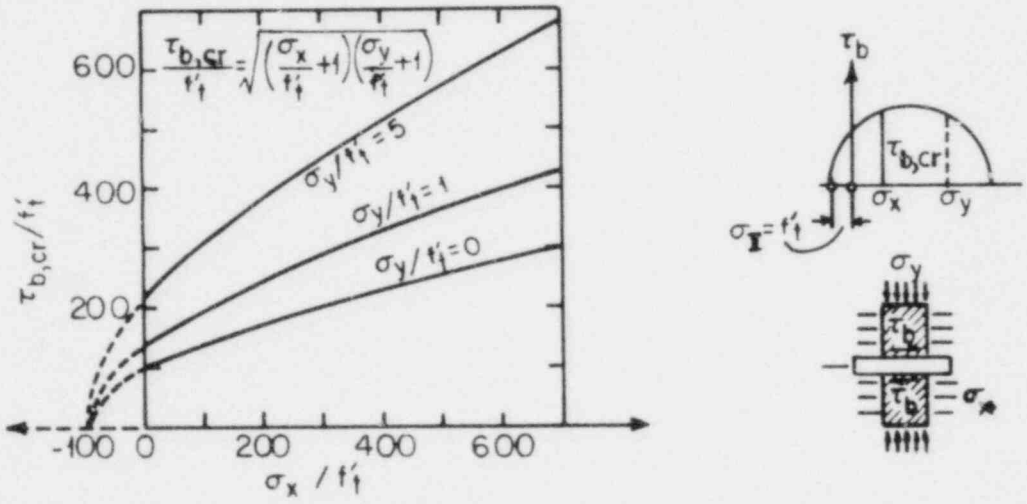

Fig. 4.52. Effect of longitudinal (σ_x) and radial (σ_y) stresses on the critical bond stress $\tau_{b,cr}$ (transverse cracking) according to Tassios (Ref. 113).

Bresler and Bertero (Ref. 13) computed in their analysis maximum principal tensile stresses in the concrete at the steel-concrete interface that were approximately equal to twice the maximum bond stress ($\sigma_I \simeq 2\ \tau_{b,max}$), as shown in Fig. 4.53. This means that at first transverse cracking the maximum bond stress will be equal to

$$\tau_{b,max} \simeq 0.5\ f_t' \qquad (4.84)$$

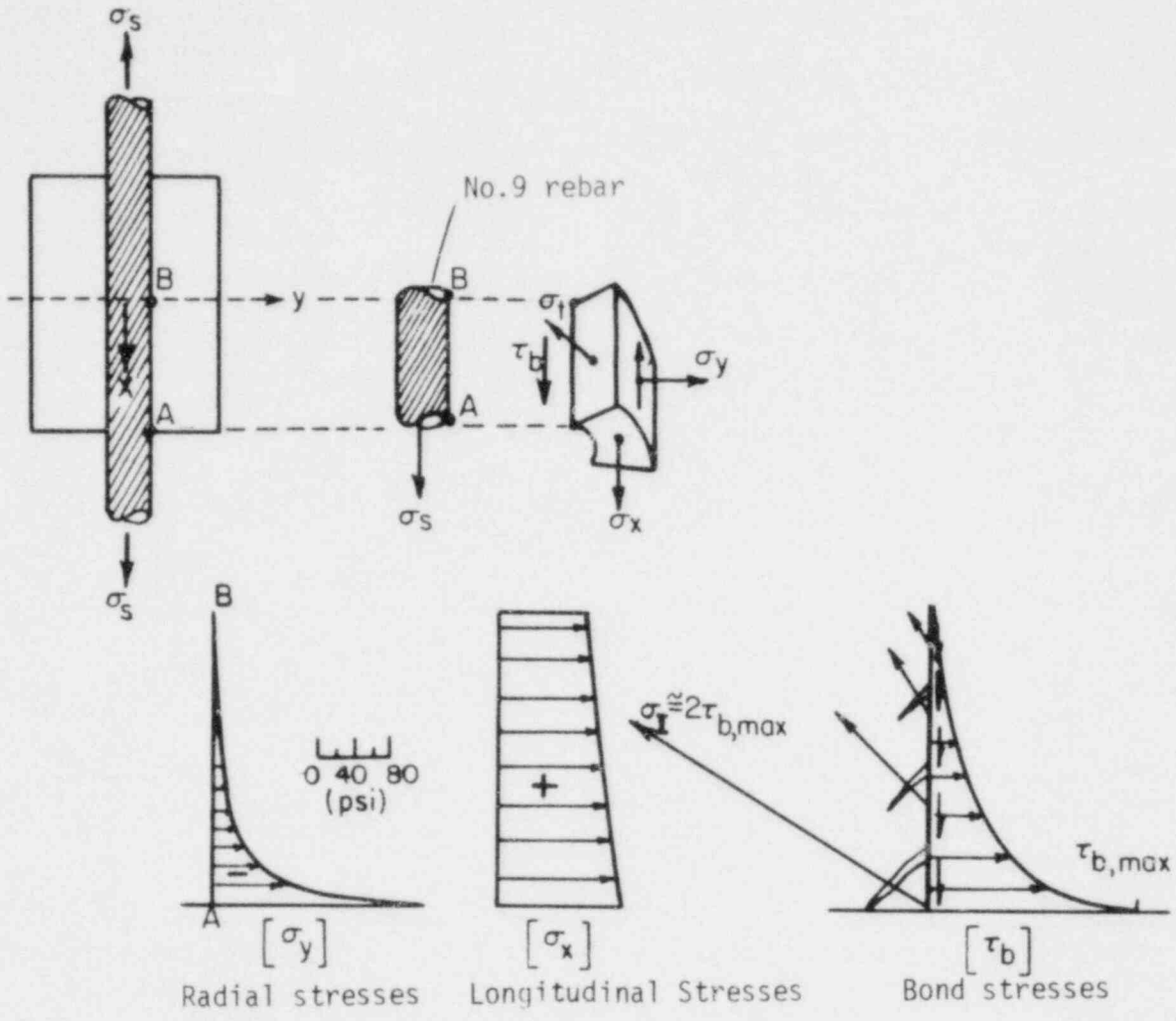

Fig. 4.53. Concrete stresses at the steel-concrete interface according to Bresler and Bertero (Ref. 13).

Ismail and Jirsa (Ref. 60) also calculated average bond stresses of about 240 to 450 psi for applied tensile stresses between 10 and 40 ksi (f_y = 48 ksi) in a No.9 rebar (Specimens T20 and T40). The corresponding relative percentage contribution of concrete to carry tensile strains was estimated as 30 to 5% for the above steel stress levels.

To get a rough estimate of the average bond stresses τ_{bm} along a No. 6 reinforcing bar (diameter d = 0.75 in.) tensioned at a relatively low stress σ_s of 19 ksi ($\cong 0.3f_y$) the following simplified expression is used

$$\tau_{bm} = \frac{2(\sigma_s - \sigma_i)A_s}{\pi d \ell_{cm}} = \frac{2\Delta\sigma_s A_s}{\pi d \ell_{cm}} \tag{4.85}$$

A linear distribution of steel stresses is assumed along each average half distance $\ell_{cm}/2(\cong 3$ in.) of two primary cracks, as shown in Fig. 4.54.

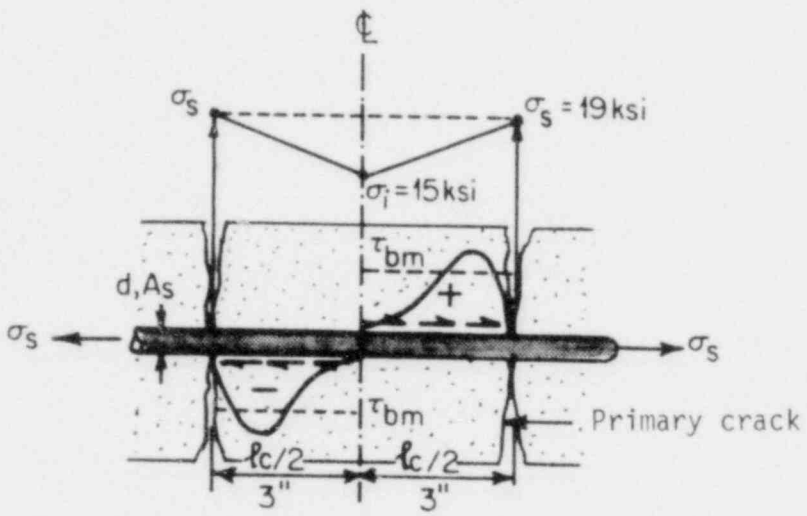

Fig. 4.54. Simplified steel stress distribution for estimating the average bond stresses τ_{bm}.

The relative contribution of concrete ξ_c is given by the relation

$$\xi_c \cong \frac{\sigma_s - \sigma_i}{2\sigma_s} = \frac{\Delta\sigma_s}{2\sigma_s} \tag{4.86}$$

Assuming a reasonable value for ξ_c equal to 10%,

$$\Delta\sigma_s = 2 \times 0.1 \times 19 = 3.8 \text{ ksi} \tag{4.87}$$

and

$$\tau_{bm} = \frac{2 \times 3.8 \times 0.44}{\pi \times 0.75 \times 6} = 236 \text{ psi} \tag{4.88}$$

The bond stress of 236 psi is indeed within the $0.5 f'_t < \tau_{bm} < f'_t$ range that other researchers have cited. It appears that even a relatively low tensile stress of $0.3f_y$ in the present specimens could initiate internal inclined cracking. Since the above value of 236 psi is an average value, the maximum value $\tau_{b,max}$ close to the cracks could be about twice as much.

Consequently, in addition to the applied shear stress v at the level of the reinforcement, there will be a localized shear stress distribution due to bond τ_{bm}, as shown in Fig. 4.50b. The shear stresses due to bond acting within an equivalent height equal to πd and $2\pi d$ in the single and the double layer direction, respectively, could substantially increase the total actual shear stress transferred along the edges of the corners A and C in Fig. 4.50a. These arguments confirm, at least qualitatively, the experimental results which indicated that diagonal cracking started forming on the concrete surface at an applied shear stress of about 100 psi. It should also be pointed out that the existing internal transverse cracks near the intersection region of the orthogonal bars could propagate under the applied diagonal tension and furthermore instigate the occurrence of the surface diagonal cracks at an earlier stage. The fact that the diagonal cracks initiated next to bar intersections was confirmed in the present experiments.

b) Shear rigidity of diagonally cracked concrete (v > 100 psi)

At initiation of diagonal cracking at about 100 psi the applied shear is mainly resisted by compressive stresses σ_{cd} in the concrete struts between the diagonal cracks and tensile stresses in the orthogonal steel (see Fig. 4.55). There will still be some slipping at the orthogonal cracks as the diagonal compression stress increases with increasing shear. With most of the orthogonal cracks closing (especially at the central region of the specimen) and with additional diagonal cracks forming, the major shear transfer mode is that of diagonal tension (resisted by the steel) and diagonal compression (resisted by the concrete). The shear rigidity of the cracked panel then depends mainly on the extensibility of the panel normal to the diagonal cracks and the compressibility of the concrete struts parallel to the diagonal cracks. It is obvious that this compression-tension type of load transfer will eventually result in predominantly diagonal crack opening.

Assuming that the first diagonal cracks formed at an angle β to the horizontal axis x, the diagonal strut compressive stress σ_{cd} will result in compressive stresses σ_{cx}, σ_{cy} and shear stresses v along a horizontal and a vertical cross section (see Fig. 4.56). From equilibrium of stresses, the required compressive stresses in the concrete are

$$\sigma_{cx} = \frac{v}{\tan\beta}$$

$$\sigma_{cy} = v\tan\beta \qquad (4.89)$$

where v is the applied shear stress.

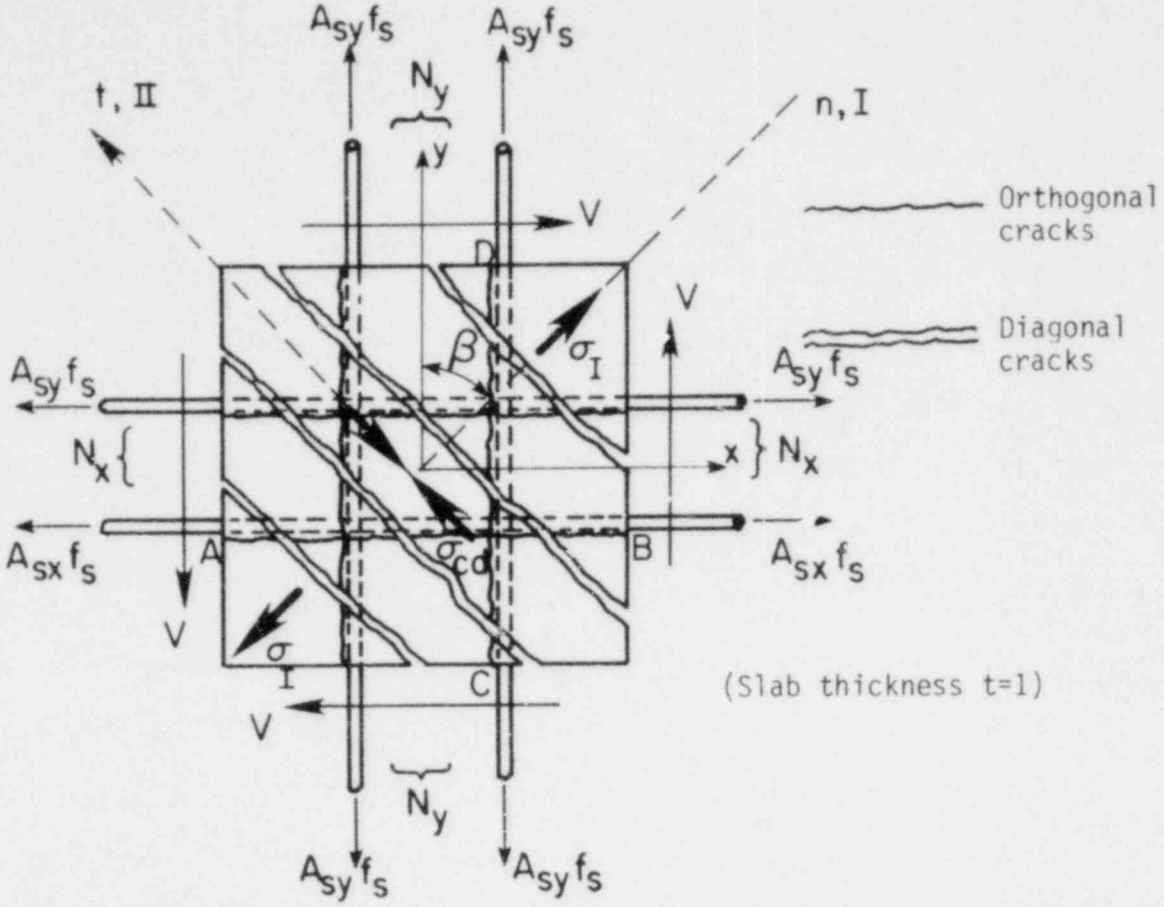

Fig. 4.55. Diagonal tension-compression strut mode.

If we neglect the tensile stresses in the concrete (principal diagonal tension $\sigma_I = 0$), the Mohr circle for average concrete stresses and strains is shown in Fig. 4.57a and 4.57b, respectively. The average diagonal compression σ_{cd} is equal to the principal compressive stress σ_{II} in the direction tangential to the diagonal cracking and is equal to

$$\sigma_{cd} = \frac{v}{\tan\beta} + v\tan\beta = v(\tan\beta + \frac{1}{\tan\beta}) = \frac{v}{\sin\beta\cos\beta} \qquad (4.90)$$

This relation is identical to the third equilibrium equation (B.1c') (see Appendix B) in Duchon's model. Since there were no tensile stresses allowed in the concrete, no shear stresses are transferred parallel to

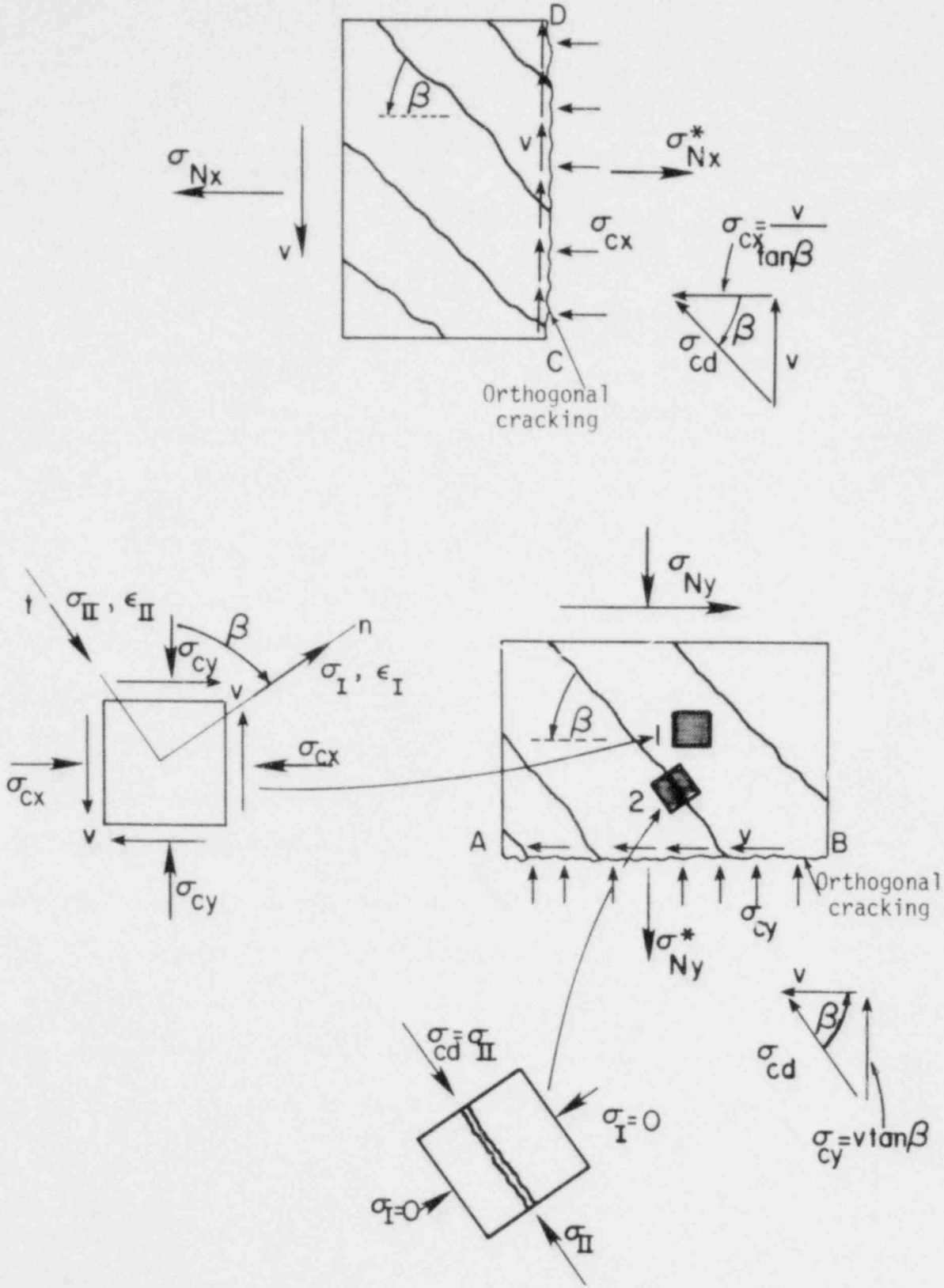

Fig. 4.56. Equilibrium of concrete stresses at initial diagonal cracking.

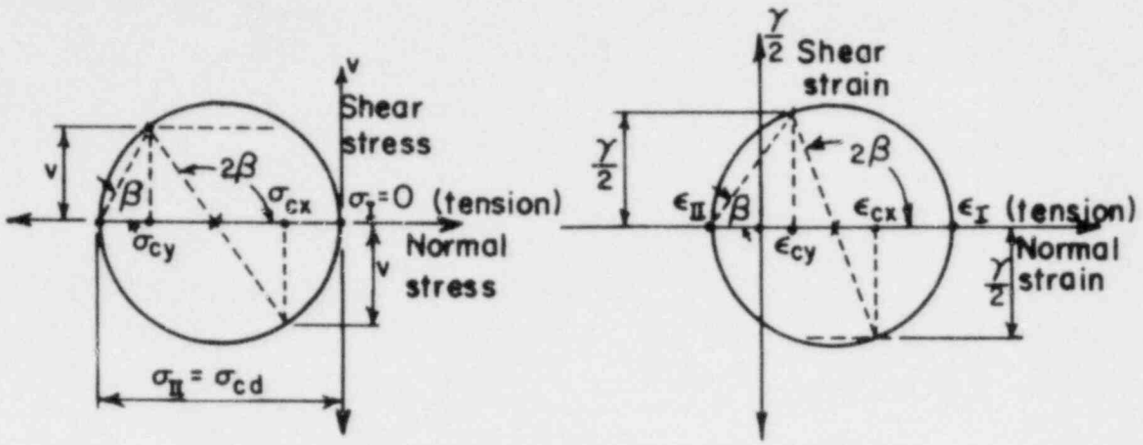

a) Concrete stresses b) Concrete strains

Fig. 4.57. Mohr's circle for stress and strain (concrete tensile stresses are neglected).

the diagonal crack, as shown in element 2 of Fig. 4.56. This means that no shear transfer (IST and DA) is taking place along the diagonal cracks.

A more realistic picture is given in Fig. 4.58 (see Baumann, Ref. 8). The stress state in element 2 along the diagonal crack that formed at an applied shear stress v is given in this figure as the shear stress increased to v'. In general, the directions of principal stresses (σ_I,σ_{II}) will change, rotating at an angle ω relative to the previous directions normal and parallel to the initial diagonal cracks (inclined at an angle β to the horizontal). If the concrete strut can carry tensile stresses (σ_I less than the concrete tensile strength f'_t), a shear stress τ will be present at the existing diagonal crack interface and normal to the strut. The corresponding Mohr circle for the stresses in concrete in the latter case is shown in Fig. 4.58. Since there are tensile stresses carried by the concrete, the compressive stress σ_{cd} will be given by the following relation

$$\sigma_{cd} = v'(\tan\beta + \frac{1}{\tan\beta}) - \sigma_I \qquad (4.91)$$

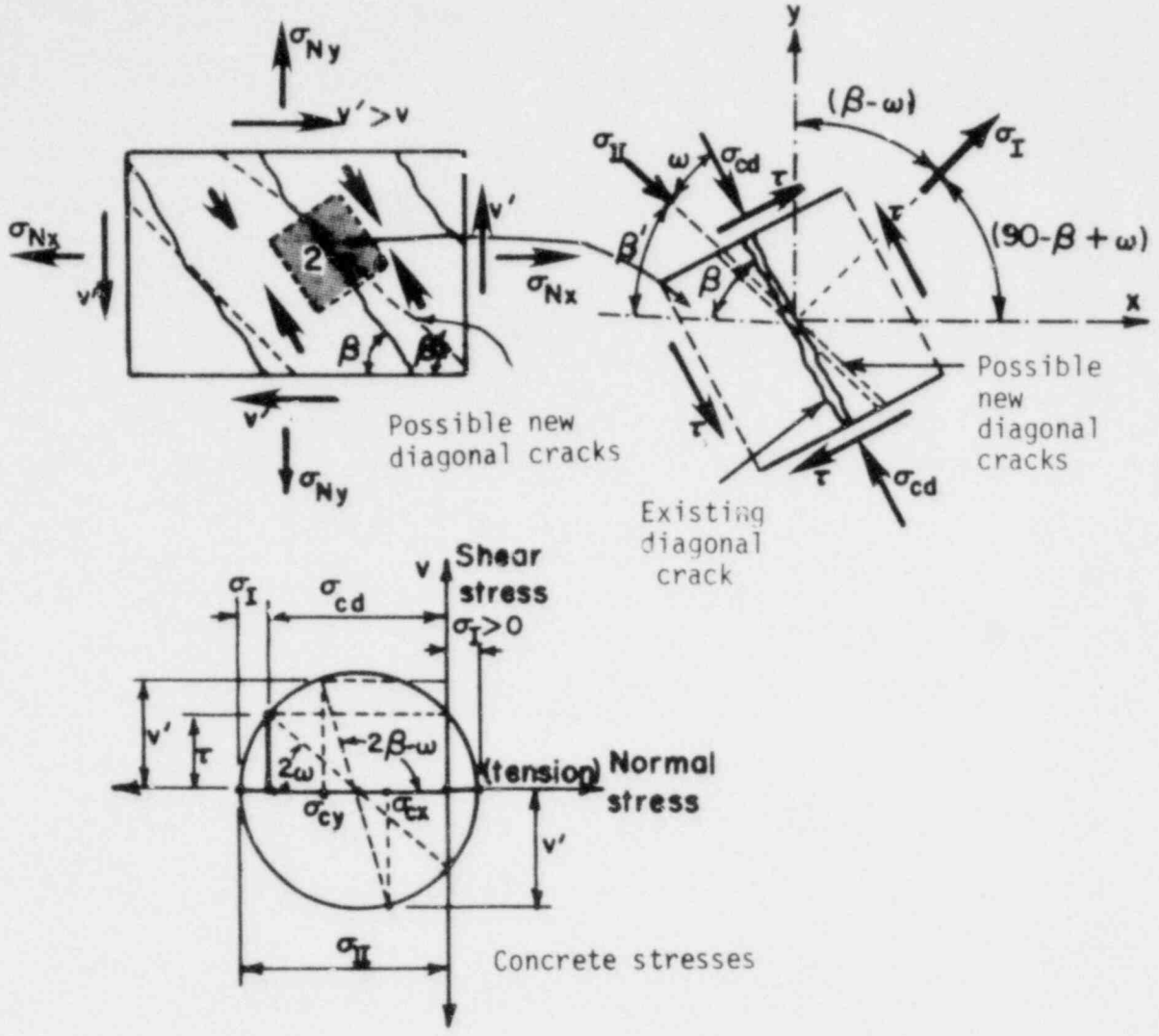

Fig. 4.58. Shear transfer along the existing diagonal cracks.

The value of σ_{cd} computed using the above Eqn. 4.91 will be smaller than that resulting from Eqn. 4.90, where no shear transfer was assumed. As the applied shear stress v is increasing, new diagonal cracks may form perpendicular to the direction of the maximum principal tension when σ_I reaches the value of the concrete tensile strength f'_t. The additional cracking will lower the tensile stresses in concrete and eventually the Mohr circle,shown in Fig. 4.58,will shrink, becoming identical to the

case shown in Fig. 4.57. The new diagonal cracking inclined at an angle $\beta' = \beta - \omega$ to the horizontal is shown in Fig. 4.58 with dashed line.

With the maximum principal tensile strain ε_I (see Fig. 4.57) increasing, the shear strain γ will also increase, further decreasing the effective shear rigidity of the panel. The stress condition described in the previous paragraph may exist again until either the reinforcing bars crossing the new diagonal crack yield or the concrete struts fail under the compressive stress σ_{cd}. In the present experimental work it was found that the former failure mode controlled the shear capacity of the reinforced concrete panels subjected to biaxial tension and shear.

To be sure that the panel's shear rigidity is not overestimated, at least for shear stresses higher than 100 psi, and since not enough experimental evidence exists on the amount of shear carried by the concrete struts, Eqn. 4.90 is adopted here.

The governing equations developed by Duchon (Eqn. B.4' in Appendix B), resulting from the consideration of both equilibrium and compatibility, are repeated here with consistent notation

$$\begin{Bmatrix} \sigma_{Nx} \\ \sigma_{Ny} \\ v \end{Bmatrix} = E_s \begin{bmatrix} \rho_x \sin^2\beta & \left(\rho_x \cos^2\beta + \frac{\cos^2\beta}{n}\right) \\ \rho_y \cos^2\beta & \left(\rho_y \sin^2\beta + \frac{\sin^2\beta}{n}\right) \\ 0 & \frac{-\sin\beta\cos\beta}{n} \end{bmatrix} \begin{Bmatrix} \varepsilon_I \\ \varepsilon_{II} \end{Bmatrix}, \tag{4.92}$$

where n is the ratio of the Young's modulus of steel E_s to an effective Young's modulus of concrete E_{ce}, σ_{Nx} and σ_{Ny} the applied normal stresses and ρ_x, ρ_y the steel ratios in the x and y direction, respectively.

The equivalent concrete modulus in compression E_{ce}, described by the constitutive relationship

$$E_{ce} = \sigma_{cd}/\varepsilon_{cd} \quad , \tag{4.93}$$

where ε_{cd} is the compressive concrete strain in the diagonal strut, will definitely depend on the actual stress conditions shown in Fig. 4.59. It appears that the compressive axial stiffness of the concrete struts will be negatively affected by the transverse expansion due to crack opening at the diagonal cracks, which depends on the stiffness of the shear transfer mechanisms and the tensile stresses in the reinforcing bars crossing the cracks.

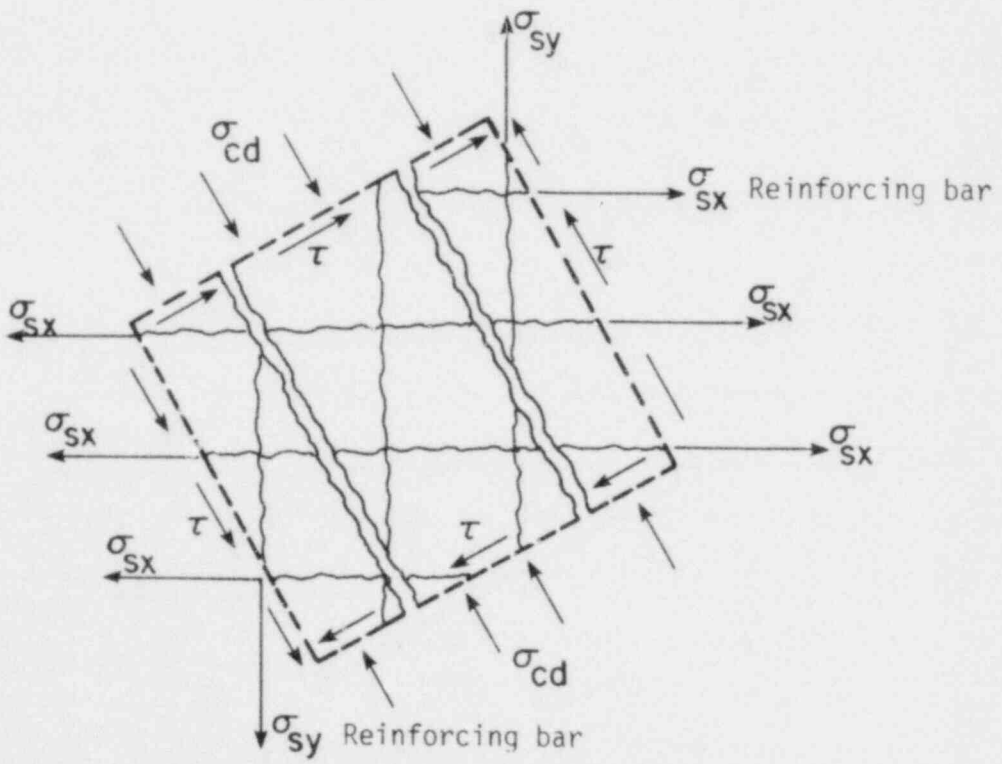

Fig. 4.59. Stress condition for a diagonal concrete strut.

According to the experimental evidence reported by Collins (Ref. 25) on shear tests of beams, where the average principal compressive stress σ_{cd} and compressive strain ε_{cd} were computed from the applied shear and the inclination angle β, the relationship between σ_{cd} and ε_{cd} depends on the strain ratio $\gamma_{max}/\varepsilon_{II}$. That is, for given value of ε_{II}, the value of σ_{cd} decreases with increasing $\gamma_{max}/\varepsilon_{II}$, or ,in other words, with increasing strain normal to the diagonal cracks (less confinement for the struts). Thus, a decrease in the compressive modulus in the concrete struts, as shown in Fig. 4.60, is expected compared with the stress-strain relationship of a cylinder test. Due to the scatter of the above experimental results and the lack of more extensive data the effective compressive modulus E_{ce} is taken as equal to the ultimate secant modulus E_{cu} measured in the cylinder tests. As shown in Fig. 2.2 in Chapter 2, the average value of the secant modulus at ultimate is equal to about 1900 ksi (initial modulus E_{co} = 3500 ksi). Therefore, the moduli ratio n in Eqns. 4.92 is computed from

$$n = E_s/E_{cu} \tag{4.94}$$

It is evident that the use of E_{cu}, instead of E_{co}, for the compressive modulus in concrete will result in lower values for the tangent shear modulus G_{cr} of cracked concrete in the relationship

$$v = \gamma G_{cr} \tag{4.95}$$

To determine the expression for the effective shear modulus G_{cr}, the shear strain as a function of the applied shear stress v, the normal

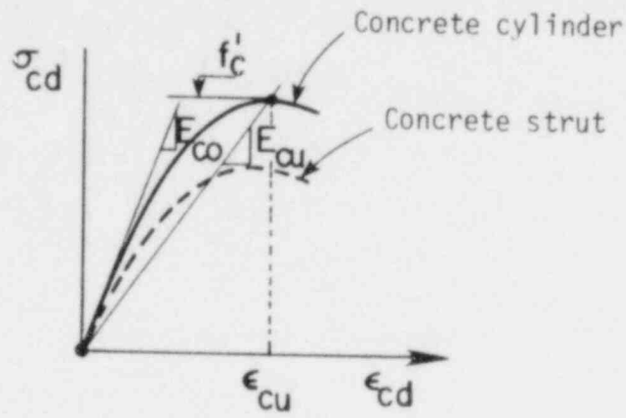

Fig. 4.60. Compressive stress-strain relationship for the diagonal concrete strut.

stresses σ_{Nx} and σ_{Ny} and the inclination angle β of the compressive struts is first determined. From Eqn. B.8 in Appendix B the average shear strain of the panel (see also Fig. 4.57) is given by

$$\gamma = (\epsilon_{cx} + \epsilon_{cy} - 2\epsilon_{II}) \sin 2\beta \ , \tag{4.96}$$

where ϵ_{cx} and ϵ_{cy} are the average tensile strains in the concrete carried entirely by the steel.

From the equilibrium equations in the x and y direction the above tensile strains can be obtained from the following relations

$$\begin{aligned} \sigma_{Nx} &= \epsilon_{cx} E_s \rho_x + \sigma_{cd} \sin^2\beta \\ \sigma_{Ny} &= \epsilon_{cy} E_s \rho_y + \sigma_{cd} \cos^2\beta \end{aligned} \tag{4.97}$$

with

$$\sigma_{cd} = \epsilon_{II} E_{cu} = -\nu \left(\tan\beta + \frac{1}{\tan\beta}\right) = -\frac{\nu}{\sin\beta\cos\beta} \tag{4.98}$$

Thus,

$$\varepsilon_{sx} = \frac{\sigma_{Nx}}{\rho_x E_s} + \frac{v\tan\beta}{\rho_x E_s} = \varepsilon_{cx} \quad , \tag{4.99a}$$

and

$$\varepsilon_{sy} = \frac{\sigma_{Ny}}{\rho_y E_s} + \frac{v}{\rho_y E_s \tan\beta} = \varepsilon_{cy} \tag{4.99b}$$

Also,

$$\varepsilon_{II} = - \frac{v}{E_{cu} \sin\beta\cos\beta} \tag{4.100}$$

Thus, Eqn. 4.96 reduces to

$$\gamma = [\frac{v\tan\beta}{\rho_x E_s} + \frac{v}{\rho_y E_s \tan\beta} + \frac{2v}{E_{cu} \sin\beta\cos\beta}]\sin2\beta + [\frac{\sigma_{Nx}}{\rho_x E_s} + \frac{\sigma_{Ny}}{\rho_y E_s}]\sin2\beta =$$

$$= \frac{2}{E_{cu}}[1 + (1 + \frac{1}{n\rho_x})\sin^2\beta + (1 + \frac{1}{n\rho_y})\cos^2\beta] + [\frac{\sigma_{Nx}}{\rho_x E_s} + \frac{\sigma_{Ny}}{\rho_y E_s}]\sin2\beta \tag{4.101}$$

The second part of the right hand side of Eqn. 4.101 depends on the applied normal stresses and the inclination angle β and denotes the effect of normal stresses σ_{Nx} and σ_{Ny} on the shear rigidity of a reinforced concrete panel (see Fig. 4.61).

The tangent shear modulus given by

$$G_{cr}^{t} = \frac{E_{cu}}{2[1 + (1 + \frac{1}{n\rho_x})\sin^2\beta + (1 + \frac{1}{n\rho_y})\cos^2\beta]} \tag{4.102}$$

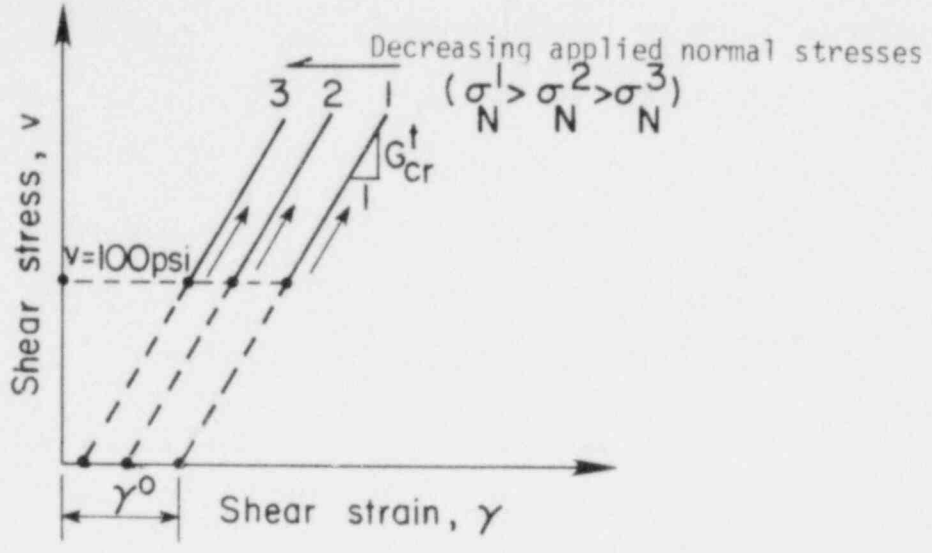

Fig. 4.61. Shear stress-strain diagram according to Eqn. 4.101.

depends also on the inclination angle β, mainly a function of the applied shear stress v, and certain properties of the panel such as the moduli ratio $n = E_s/E_{cu}$ and the steel ratios ρ_x, ρ_y in the direction of the reinforcing bars. For standard values of β between 30 and 60 degrees, the diagonal compressive stress σ_{cd} is approximately linear with the applied shear stress v, since it varies as $(\tan\beta + \frac{1}{\tan\beta})$. The latter expression remains approximately constant, especially for small variations of the angle β. Thus, since γ is basically proportional to σ_{cd} (see Eqns. 4.97 and 4.98), the tangent shear modulus given by Eqn. 4.102 and shown in Fig. 4.61 is expected to be nearly constant.

It should be pointed out here that, according to Eqn. 4.101, the tangent shear modulus G_{cr}^t, given by Eqn. 4.102, is nearly independent of the level of the applied normal stresses. There is only an insignificant influence of the value of σ_{Nx} and σ_{Ny} on G_{cr}^t since the inclination angle β will be related somewhat differently to the shear stress v for various

levels of applied normal stresses.

The shear stress-strain relationship obtained above will be adopted here for values of shear stress v higher than 100 psi, at which diagonal cracking formed. The equation that relates the applied normal and shear stresses with the corresponding inclination angle β of the principal tensile strain to the y axis may be obtained by equating the expressions for ε_{II} given by the second and third equations of Eqn. 4.92.

Thus,

$$v = -\frac{\sin\beta\cos\beta}{Dn}\left(-\rho_x \sin^2\beta\ \sigma_{Ny} + \rho_y \cos^2\beta\ \sigma_{Nx}\right), \tag{4.103}$$

where D is the determinant of the system of equations in Eqn. 4.92 and is given by Eqn. B.6 in Appendix B.

Dividing both sides of Eqn. 4.103 by $\cos^4\beta$ and rearranging terms, we get the following quadratic transcendental equation

$$\tan^4\beta + \frac{\tan^3\beta}{(1+n\rho_y)}\left(\frac{\sigma_{Ny}}{v}\right) - \frac{\rho_y \tan\beta}{\rho_x(1+n\rho_y)}\left(\frac{\sigma_{Nx}}{v}\right) - \frac{\rho_y(1+n\rho_x)}{\rho_x(1+n\rho_y)} = 0 \tag{4.104}$$

According to Eqn. 4.104, there will be certain limitations on the range of the angle β for the model to be valid for given values of n, ρ_x, ρ_y, σ_{Nx} and σ_{Ny}. If the Mohr circle for stresses in the concrete (see Fig. 4.57) properly described the stress state, it would be expected that for β equal to 45 degrees the shear stress v would approach infinity. It is clear, however, that for v approaching infinity the angle β approaches a value β_1^* which atisfies the relation

$$\tan^4\beta_1^* = \frac{\rho_y(1+n\rho_x)}{\rho_x(1+n\rho_y)} \tag{4.105}$$

This value of β_1^* is different from 45 degrees for the general case with unequal steel ratios ρ_x and ρ_y. Actually, for β equal to β_1^* the system becomes unstable and the system of Eqns. 4.92 are no longer valid. They are valid only for β less than β_1^* when $\sigma_{Ny} > \sigma_{Nx}$ and β larger than β_1^* when $\sigma_{Ny} < \sigma_{Nx}$. Incidentally, the above value β_1^* is the angle for pure shear (no biaxial tension), in which case the effective shear modulus given by Eqn. 4.102 is independent of the angle β and is equal to

$$G_{cr}^t = \frac{E_{cu}}{2[1 + \sqrt{(1 + \frac{1}{n\rho_x})(1 + \frac{1}{n\rho_y})}]} \tag{4.106}$$

This is identical to the expression for G_{cr} in diagonally cracked reinforced concrete beams developed by Collins (Ref. 25).

The other critical value of β is at shear stress v equal to zero. According to Eqn. 4.104, this occurs when β is equal to β_2^* given by

$$\tan^2\beta_2^* = \sigma_{Nx}\rho_y/\sigma_{Ny}\rho_x \tag{4.107}$$

If the normal stresses σ_{Nx} and σ_{Ny} are applied by tensioning the reinforcing bars in the x and y direction, respectively, as it is the case here, they are equal to

$$\sigma_{Nx} = \rho_x f_s$$

$$\sigma_{Ny} = \rho_y f_s \quad , \tag{4.108}$$

where f_s is the applied tensile stress in each bar.

Thus, Eqn. 4.107 becomes

$$\tan^2\beta_2^* = 1 \ , \tag{4.109}$$

which results in

$$\beta_2^* = 45 \text{ deg.} \tag{4.110}$$

Indeed, the initial diagonal cracks in the specimens tested were inclined at an angle to the axis very close to 45 degrees.

Concluding, the value of the angle β should be within the following limits

$$\beta_2^* < \beta < \beta_1^* \ , \text{ for } \quad \sigma_{Ny} > \sigma_{Nx} \tag{4.111a}$$

and

$$\beta_2^* > \beta > \beta_1^* \ , \text{ for } \quad \sigma_{Ny} < \sigma_{Nx} \tag{4.111b}$$

Substituting ρ_x=0.0122, ρ_y=0.0244 and n=14.7 (E_s=28000 ksi and E_{cu}= 1900 ksi) in Eqn. 4.105, β_1^* becomes equal to about 49 degrees, independent of the applied bar tension in the x and y direction. According to Eqn. 4.111a, since $\rho_y > \rho_x$ or $\sigma_{Ny} > \sigma_{Nx}$, the present model gives sensible results only for $45 \leq \beta \leq 49$ degrees in the case of the biaxial specimens with No.6 bars described in Chapter 2.

The predicted values for the effective shear modulus according to the

shear transfer model presented in this section and Section 4.3.1 are compared with the experimental results from both the present research program and a parallel research at the Portland Cement Association in Section 4.3.3.

4.3.3 Theoretical predictions versus experimental results (shear stress-shear strain curves)

First, the predicted values for the effective shear rigidity based on the 3-stage stiffness model, described in Sections 4.3.1 and 4.3.2, are compared with the experimental results of the present biaxial tests with No. 6 reinforcing bars. Four selected biaxial tension levels of 0, $0.3f_y$, $0.6f_y$, and $0.9f_y$ plus monotonically applied shear are considered in this section.

Then, the predicted response of biaxially tensioned specimens with larger size bars (No. 14 and No. 18) is compared with the measured data from the experiments at PCA (Ref. 96). The orthogonal reinforcing bars in these specimens (see Fig. 3.22a) are tensioned to a stress of $0.6f_y$ (MB3) and $0.9f_y$ (MB1) and the shear stress (applied through special fixtures at three positions along each side of the specimen) is increased monotonically until failure is reached by yielding in the steel.

a) Present tests (small size bars)

The following variables are either measured or given:

d = diameter of the No. 6 bars in x and y directions = 0.75 in.

ρ_x = steel ratio in x direction (single layer) = 0.0122

ρ_y = steel ratio in y direction (double layer) = 0.0244

E_{cu} = secant Young's modulus in compression of concrete at ultimate = 1900 ksi.

E_s = elastic Young's modulus of steel = 28000 ksi

n = moduli ratio = E_s/E_{cu} = 14.7

G_o = initial shear modulus of uncracked concrete = 1500 ksi

ℓ_{cmx} = average spacing of the orthogonal cracks normal to the x direction = 7.2 in.

ℓ_{cmy} = average spacing of the orthogonal cracks normal to the y direction = 6.6 in.

c^o_{wmx} = average initial crack width estimate for the cracks normal to the x direction (according to Eqn. 4.75) at selected biaxial tension levels = 0.004 in. (zero tension).
= 0.008 in. ($0.3f_y$ tension).
= 0.013 in. ($0.6f_y$ tension).
= 0.018 in. ($0.9f_y$ tension).

c^o_{wmy} = average initial crack width estimate for the cracks normal to the y direction (according to Eqn. 4.75) at selected biaxial tension levels = 0.002 in. (zero tension)
= 0.004 in. ($0.3f_y$ tension)
= 0.006 in. ($0.6f_y$ tension)
= 0.007 in. ($0.9f_y$ tension)

β = inclination angle of the diagonal cracks to the x direction = 45 deg.

The predicted shear stress-shear strain relationship is represented by three tangent shear stiffness expressions (shear modulus G^t_{cr}) within certain shear stress levels, as follows:

Segment 1 (for $v \leq 50$ psi;only DA at the orthogonal cracks):

$$G_{cr}^{t1} = \left[\frac{1}{K_{DA}^{x}\,\ell_{cmy}} + \frac{1}{K_{DA}^{y}\,\ell_{cmx}} + \frac{1}{G_o}\right]^{-1} \quad \text{(ksi)} \qquad (4.112a)$$

Segment 2 (for $50 < v \leq 100$ psi;combined (IST+DA) at the orthogonal cracks):

$$G_{cr}^{t2} = \left[\frac{1}{(K_{IST}^{x}+K_{DA}^{x})\ell_{cmy}} + \frac{1}{(K_{IST}^{y}+K_{DA}^{y})\ell_{cmx}} + \frac{1}{G_o}\right]^{-1} \quad \text{(ksi)} \qquad (4.112b)$$

Segment 3 (for $v > 100$ psi;diagonal tension-compression strut mode):

$$G_{cr}^{t3} = \frac{E_{cu}}{2\left[1 + (1+\frac{1}{n\rho_x})\sin^2\beta + (1+\frac{1}{n\rho_y})\cos^2\beta\right]} \quad \text{(ksi)} \qquad (4.112c)$$

The shear stiffness values for dowel action , K_{DA}, and interface shear transfer mechanism, K_{IST}, are calculated from Eqns. 4.78 and 4.74 (Section 4.3.1a), respectively. These values for the four biaxial tension levels studied are shown in Table 4.E.

Since the measured total extensional stiffnesses in the direction of the reinforcing bars,

$$K_{Nx} = 2300 \times 8 = 18400 \text{ (k/in)}$$
$$K_{Ny} = 4400 \times 16 = 70400 \text{ (k/in)} , \qquad (4.113)$$

are higher than the suggested limit value of

$$K_{Ni}^{o} = 3.4 \times 10^{5}\ c_{wmi}^{o} \quad (i=x,y)\ , \tag{4.114}$$

given in Ref. 61, the shear stiffness of IST is calculated using the following expression

$$K_{IST}^{i} = [3.9\ (\ c_{wmi}^{o} - 0.002)]^{-1} \qquad \text{(ksi/in)} \tag{4.115}$$

This is the case of infinite axial stiffness, at which the normal axial stiffness does not affect the interface shear transfer stiffness K_{IST}.

The computed values for the tangent effective shear modulus G_{cr}^{t} and the corresponding ratio G_{cr}^{t}/G_{o} for each of the three segments of the

Table 4.E. Shear stiffness values assumed for present tests.

Specimen No.	.0(M)	.3(M)	.6(M)	.9(M)
f_s(ksi)	0	18.3	36.6	54.9
(1) k_f(k/in^3)	2960	2430	1900	1370
f'_c(psi)	3320	3940	3500	3600
(2) K_{DA}^{x}(ksi/in)	14	15	11	9
(3) K_{DA}^{y}(ksi/in)	27	30	21	17
K_{IST}^{x}(ksi/in)	128	43	23	16
(4) K_{IST}^{y}(ksi/in)	1000	128	64	51

Notes:

(1) Foundation modulus k_f is calculated from Eqn. 4.77 (Section 4.3.1a).

(2),(3) The total normalized DA stiffness = $\dfrac{(K_{DA} \text{ per bar}) \times (\text{number of bars})}{\text{effective shearing area}(=288\ \text{in}^2)}$.

(4) K_{IST}^{y} = 1000 ksi/in is an arbitrarily chosen large number since c_{wmy}^{o} happens to be equal to 0.002 in (see Eqn. 4.115).

shear stress-shear strain curve are given in Table 4.F.

The predicted response according to the above values is compared with the experimental results at each tension level in Fig. 4.62a (measured average data points for the 1st load cycle are shown as full dots in Fig. 4.62a). As shown in this figure, the predicted shear stress-shear strain

Table 4.F. Predicted values for the tangent effective shear moduli during the 1st cycle of shear loading.

	Biaxial Tension	0	$0.3f_y$	$0.6f_y$	$0.9f_y$
($v \leq 50$ psi)	$G_{cr}^{t1}, (G_{cr}^{t1}/G_o)$ (ksi)	59(0.039)	66(0.044)	46(0.031)	38(0.025)
($50 < v \leq 100$)	$G_{cr}^{t2}, (G_{cr}^{t2}/G_o)$ (ksi)	532(0.35)	240(0.16)	146(0.10)	112(0.07)
($v > 100$ psi)	$G_{cr}^{t3}, (G_{cr}^{t3}/G_o)$ (ksi)	154(0.10)	154(0.10)	154(0.10)	154(0.10)

curves are shifted to the left relative to the experimental findings, as expected. Significant shrinkage cracking present prior to the application of the shear load could be the major cause of the low shear stiffness values measured at shear stresses less than 50 psi. For shear stresses higher than 50 psi (see Table 4.G), the proposed expressions predict at least twice as large tangent shear modulus values as the measured average values. These high values could be explained from the fact that in the simplified model the DA and the IST stiffnesses are assumed constant and independent of the applied shear stress v. However, with increasing shear

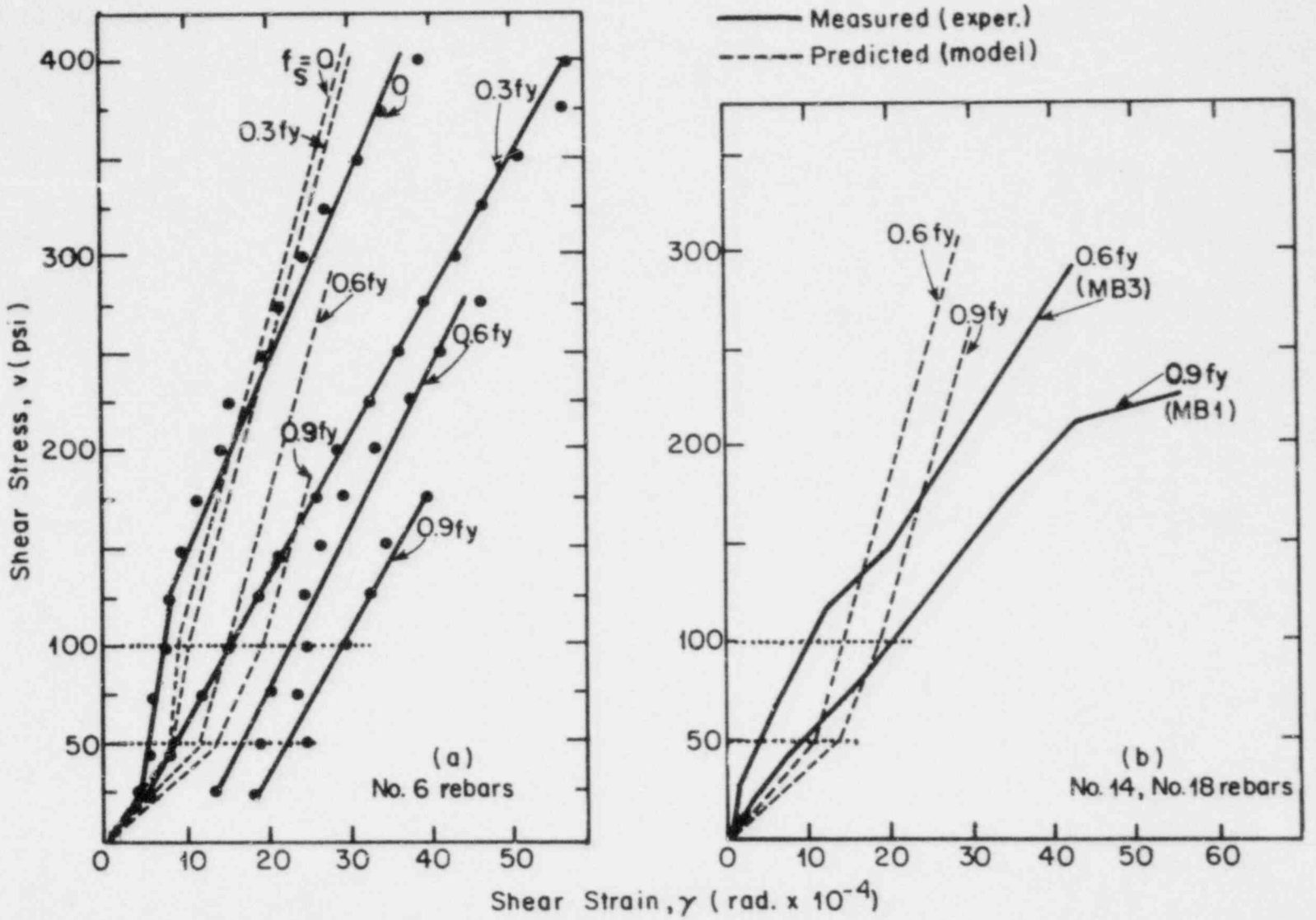

Fig. 4.62. Comparison of measured and predicted shear stress-shear strain response.

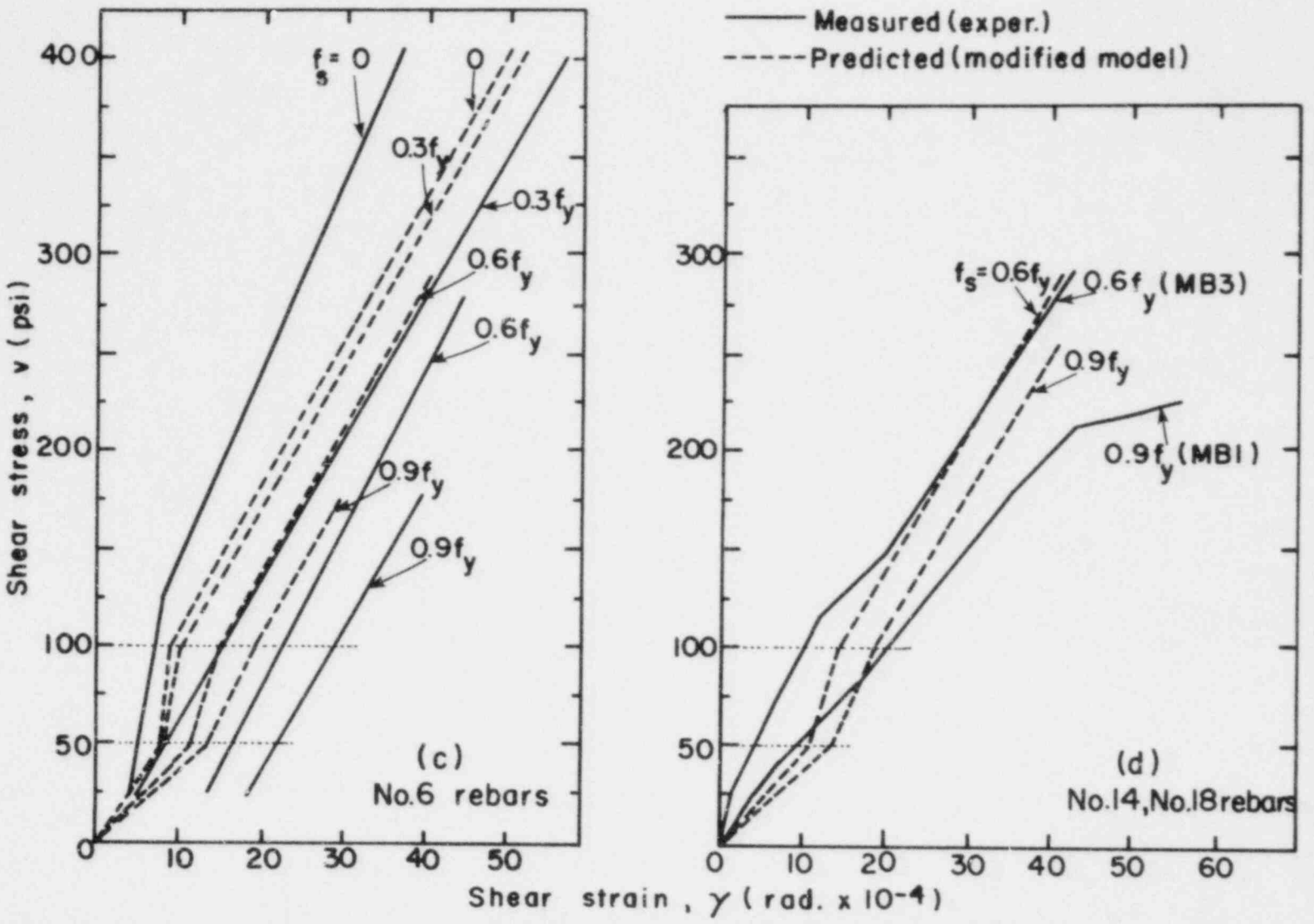

Fig. 4.62. (Continued).

Table 4.G. Comparison of the predicted and measured shear modulus values for cracked reinforced concrete.

Biaxial Tension	0		$0.3f_y$		$0.6f_y$		$0.9f_y$	
G^t_{cr}/G_c	Exp.	Pred.	Exp.	Pred.	Exp.	Pred.	Exp.	Pred.
$50 < v \leq 100$ psi	0.17	0.35	0.05	0.16	0.06	0.10	0.05	0.07
$v > 100$ psi	0.06	0.10	0.05	0.10	0.06	0.10	0.05	0.10

stress both shear transfer mechanisms become less effective in resisting shear forces (nonlinear effect). Therefore, the effects of DA and IST are not additive. As the tensile stresses in the steel increase due to shear slip or opening of the cracks, the DA shear transfer mechanism becomes less effective permitting larger shear distortions. Also, as the diagonal cracks open due to increasing diagonal deformations at shear stresses higher than 100 psi, the IST mechanism offers less resistance causing further increase in the average tensile stresses in the reinforcement. The value of the foundation modulus of concrete, k_f, decreases with the progressive crushing of the concrete adjacent to the bars at the primary cracks,as the tension in the steel increases and kinking of the bars becomes more significant. All the above factors could interact to substantially lower the predicted effective shear rigidity of the reinforced concrete panels. The level of biaxial tension does not appear to affect appreciably the effective tangent shear modulus for cracked concrete,

especially after the diagonal cracks have formed. Of course, increasing biaxial tension results in increasing total shear deformations and consequently causes a decrease in the secant shear stiffness.

Because the proposed shear stiffness model does not account for all the flexibility resulting from the extensive diagonal cracking, particularly for shear stresses above 100 psi, a modified version is shown in Fig. 4.62c. The experimental curves compare well with the predictions of the less stiff model, in which the effective tangent shear modulus G^t_{cr} for shear stresses above 100 psi is taken as half the value given by Eqn. 4.112c. It should be mentioned again here that the predicted shear stiffness response partly depends on the assumed value of the effective compressive modulus for the cracked concrete, taken in the case of Fig. 4.62a as equal to E_{cu} (= 1900 ksi).

b) PCA tests (large size bars)

For the two specimens (MB1, MB3) considered in this comparison the following are given:

d_x = diameter of No. 14 bars parallel to the x direction
= 1.75 in.

d_y = diameter of No. 18 bars parallel to the y direction
= 2.25 in.

ρ_x = eight No. 14 bars in a (60x24) in^2 shearing area of concrete
= 0.013

ρ_y = eight No. 18 bars in a (60x24) in^2 shearing area of concrete
= 0.022

E_{co} = initial compressive Young's modulus of concrete = 3380 ksi

$E_{cu} \cong E_{co}/2$ = 1690 ksi

E_s = 27500 ksi (specimen MB3)

= 29000 ksi (specimen MB1)

n = 16.3 (specimen MB3)

= 17.2 (specimen MB1)

G_o = 1450 ksi

$\ell_{cmx} = \ell_{cmy}$ = 15 in. for both specimens (a representative orthogonal cracking pattern is shown in Fig. 3.22b)

$c^o_{wmx} = c^o_{wmy}$ = 0.02 in. (specimen MB3 ; f_s = 36 ksi)

= 0.03 in. (specimen MB1 ; f_s = 54 ksi)

β = 45 deg.

Since the measured axial stiffnesses in both specimens (given in Ref. 73) in the x and y directions,

K_{Nx} = 4800 (k/in) x 8 = 38400 (k/in)

K_{Ny} = 5900 (k/in) x 8 = 47200 (k/in) [specimen MB3]

and

K_{Nx} = 3000 (k/in) x 8 = 24000 (k/in)

K_{Ny} = 7400 (k/in) x 8 = 59200 (k/in) [specimen MB1]

are higher than the upper limit K^o_{Ni}, given by Eqn. 4.114, Eqn. 4.115 is again used to compute the interface shear transfer stiffness K_{IST}.

The calculated values for K_{DA}, K_{IST}, and G^t_{cr} are summarized in Table 4.H. The experimental (v,γ) curves are drawn together with the predicted curves in Fig. 4.62b for comparison. The predicted shear

Table 4.H. Predicted results for PCA's larger scale tests.

	Specimen No.	MB3 (f_s=36 ksi)	MB1 (f_s=54 ksi)
	k_f(k/in^3)	1920	1400
	(1) K^x_{DA}(ksi/in)	5	4
	(2) K^y_{DA}(ksi/in)	10	8
	K^x_{IST}(ksi/in)	14	9
	K^y_{IST}(ksi/in)	14	9
($v \leq 50$ psi)	G^{t1}_{cr}(G^{t1}_{cr}/G_o) (ksi)	45(0.03)	36(0.025)
($50 < v \leq 100$)	G^{t2}_{cr}(G^{t2}_{cr}/G_o) (ksi)	141(0.10)	102(0.07)
($v > 100$)	G^{t3}_{cr}(G^{t3}_{cr}/G_o)	147(0.10)	152(0.10)

Notes: (1),(2) To find the DA stiffness per in^2 of effective concrete shearing area the total dowel stiffness of all bars (k/in) is divided by a tributary concrete shearing area, rather than the total cross-sectional area of (60 x 24)in^2.

stiffness for shear stresses less than 50 psi and biaxial tension of $0.6f_y$ appears to be approximately three times as large as the experimental data (predicted effective shear modulus equal to $0.11G_o$ versus the measured value of $0.03G_o$). This means that either the No. 14 and No. 18 bars offer higher dowel resistance than estimated from Eqn. 4.78 (Section 4.3.1a) or that appreciable amount of shear is also carried by the IST mechanism. Due to the relatively large thickness (24 in.) in the PCA specimens compared with the smaller scale specimens

(6 in. thick) more orthogonal cracks exist that do not penetrate the full thickness in the former specimens. Thus, the IST mechanism is likely to be mobilized faster in the larger scale specimens, increasing the overall shear rigidity at very low shear stresses ($v < 50$ psi). For shear stresses above 50 psi, the engineering model predicts an effective tangent shear modulus of approximately $0.10G_o$ compared with a value of about $0.05G_o$ measured in the PCA tests. As mentioned for the smaller scale specimens, this could be explained from the fact that the degradation due to bidirectional cracking and nonlinear behavior of the shear transfer mechanisms (especially at shear stresses higher than 100 psi) are not fully accounted for in the proposed shear stiffness model.

The results of the more flexible modified predictive model with half as much shear stiffness for shear stresses higher than 100 psi are plotted together with the PCA test results in Fig. 4.62d. As in the case of the smaller scale specimens, the latter model predicts a response much closer to the experimental findings.

4.4 Equilibrium Model at Failure

As the failure load was approached, a major diagonal crack formed near a corner of the specimen, where the tensile component of the shear load was applied (see cracking patterns in Fig. 2.15 of Chapter 2). The inclination angle β of this failure crack to the horizontal (single layer of bars) was approximately 45 degrees for the $0.9f_y$ tension and increased to about 60 degrees as the tension decreased to zero. Thus, at low biaxial tension levels the failure crack crossed more bars in

the direction of the single layer and less bars in the orthogonal direction as compared to specimens with high applied bar tension.

It appears that behavior characterized by diagonal tension opening at the cracks resulted in yielding of the steel, causing further increase in shear deformations and eventually an inability to transfer additional shear. To investigate the above failure mechanism, the equilibrium of applied and resisting forces of a free body at the corner where failure occurred is considered, as shown in Fig. 4.63. Since average crack openings larger than 0.050 in were observed at the failure diagonal crack at ultimate load, no shearing forces in the concrete along the crack (IST) are assumed.

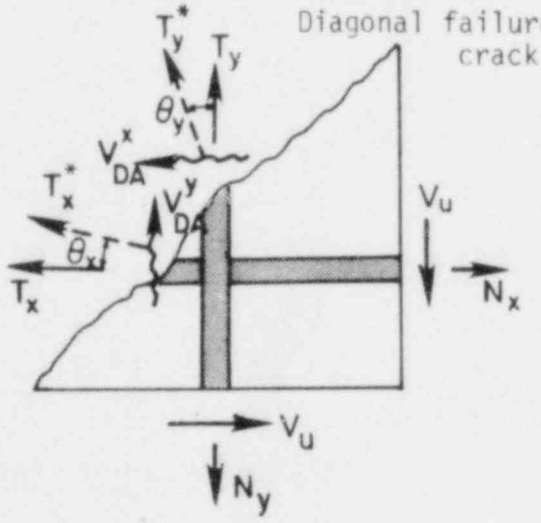

Fig. 4.63. Applied and possible resisting forces.

The external forces are the applied corner nominal shear force at failure (half of the total ultimate shear force Vu) and the tensile loads in the bars N_x, N_y determined from load cells and electrical wire gages, respectively. The resisting forces are the axial tensile forces T_x, T_y and the dowel shear forces V_{DA}^y, V_{DA}^x in the bars crossing the primary

diagonal crack at failure in the x (single layer of bars) and y direction (double layer), respectively. The resisting forces T_x and T_y, shown in Fig. 4.63, correspond to the axial forces in the bars if kinking is taken into account. This would cause a reorientation of the bars at the crack of an angle θ_x and θ_y relative to the original x and y directions, respectively (see Fig. 4.64). The latter phenomenon of kinking, which would result in additional resisting shear forces in the bars, will be discussed later in this section.

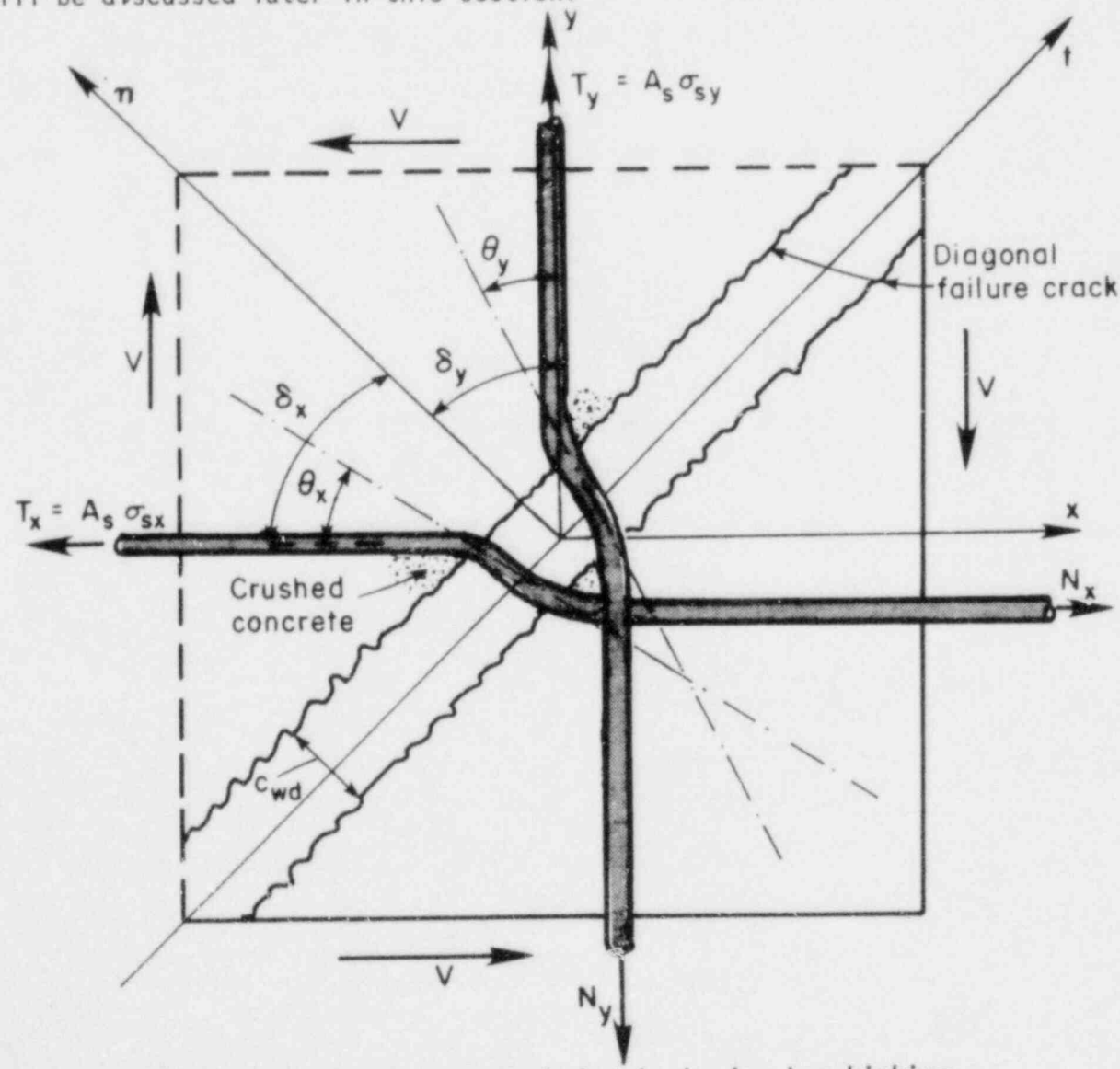

Fig. 4.64. Exaggerated sketch showing bar kinking.

Assuming only dowel action in the bars and simultaneous yielding in the reinforcement, equilibrium of forces in the i(= x,y) direction results in the following equation

$$\frac{V_u}{2} = A_{si} f_y + V_{DA}^i - N_i \qquad (4.117)$$

where

V_u = total applied nominal ultimate shear force

A_{si} = cross-sectional area of bars in the i(x,y) direction

V_{DA}^i = dowel force in the bars perpendicular to the i(x,y) direction

N_i = normal force applied in the i(x,y) direction

Substituting the applied forces into Eqn. 4.117, the dowel forces per bar, V_{DA}^i, are calculated for all specimens and are shown in columns 6 and 7 of Table 4.1. Included in this table are the number of bars active in resisting shear (columns 4 and 5) and the net resisting axial forces in the steel ($A_{si} f_y - N_i$) (columns 8 and 9). The free body equilibrium diagrams at failure for selected specimens at biaxial tension levels of 0, $0.3f_y$, $0.6f_y$ and $0.9f_y$ are given in Fig. 4.65. The dowel forces in the innermost horizontal and vertical bars are neglected because these bars have relatively short development lengths and the concrete will probably split at low shear loads, thus permitting axial forces at the crack not larger than the applied bar force.

For monotonic shear and biaxial tension of $0.9f_y$ (specimen .9(M)) dowel forces of 5.9 kips and 9.2 kips are calculated per bar in the

Table 4.1. Dowel forces calculated at full or partial yielding in the active reinforcing steel.

Specimen No. (1)	Type of Shear Loading (2)	Ultimate Shear At Corner (kips) (3)	Active Steel At Failure Crack: Single Layer (x) (4)	Active Steel At Failure Crack: Double Layer (y) (5)	Dowel Forces Per Bar For Full Yielding of Active Steel (kips): Single Layer (x) (6)	Dowel Forces Per Bar For Full Yielding of Active Steel (kips): Double Layer (y) (7)	Net Resisting Axial Force In Steel (Full Yielding)(kips): (x) (8)	Net Resisting Axial Force In Steel (Full Yielding)(kips): (y) (9)	Dowel Forces Per Bar For Partial Yielding (kips): Single Layer (x) (10)	Dowel Forces Per Bar For Partial Yielding (kips): Double Layer (y) (11)	Net Resisting Axial Force In Steel (Partial Yielding) (kips): (x) (12)	Net Resisting Axial Force In Steel (Partial Yielding) (kips): (y) (13)
.0(M)	Monotonic	70.6	3-No.6	4-No.6	(-12.2)	(-2.5)	80.4	107.2	(-3.3)	4.2	53.6	80.4
.3(M)		64.8	3-No.6	6-No.6	(-16.0)	1.4	56.4	112.8	(-3.5)	4.5	37.6	75.2
.6(M)		54.0	4-No.6	6-No.6	(-2.6)	3.6	32.1	64.2	2.8	5.4	21.4	42.8
.9(M)		43.2	3-No.6	6-No.6	9.2	5.9	7.8	15.6	10.9	6.3	5.2	10.4
.0(A)	Cyclic	61.2	3-No.6	4-No.6	(-15.3)	(-4.8)	80.4	107.2	(-6.4)	1.9	53.6	80.4
.0(B)		61.2	3-No.6	4-No.6	(-15.3)	(-4.8)	80.4	107.2	(-6.4)	1.9	53.6	80.4
.0(C)		68.4	3-No.6	4-No.6	(-12.9)	(-3.0)	80.4	107.2	(-4.0)	3.7	53.6	80.4
.3(A)		54.0	3-No.6	4-No.6	(-7.1)	(-0.6)	56.4	75.2	(-0.8)	4.1	37.6	56.4
.3(B)		54.0	3-No.6	4-No.6	(-7.1)	(-0.6)	56.4	75.2	(-0.8)	4.1	37.6	56.4
.3(C)		57.6	3-No.6	4-No.6	(-5.9)	0.3	56.4	75.2	0.4	5.0	37.6	56.4
.6(A)		46.8	3-No.6	6-No.6	(-5.8)	2.5	32.1	64.2	1.3	4.2	21.4	42.8
.6(B)		39.6	4-No.6	6-No.6	(-6.2)	(-1.1)	42.8	64.2	(-0.8)	2.2	26.7	42.8
.6(C)		43.2	3-No.6	6-No.6	(-7.0)	1.8	32.1	64.2	0.1	3.6	21.4	42.8
.9(A)		32.4	3-No.6	6-No.6	5.6	4.1	7.8	15.6	7.3	4.5	5.2	10.4
.9(B)		39.6	4-No.6	6-No.6	6.0	4.8	10.4	15.6	7.3	5.5	6.5	10.4
.9(C)		36.0	3-No.6	6-No.6	6.8	4.7	7.8	15.6	8.5	5.1	5.2	10.4

Notes: Cols. (6), (7), (10), (11): Negative sign means that the bar forces in the orthogonal direction are overestimated.

Cols. (8), (9), (12), (13): Net axial bar forces are the difference between resisting and applied bar forces.

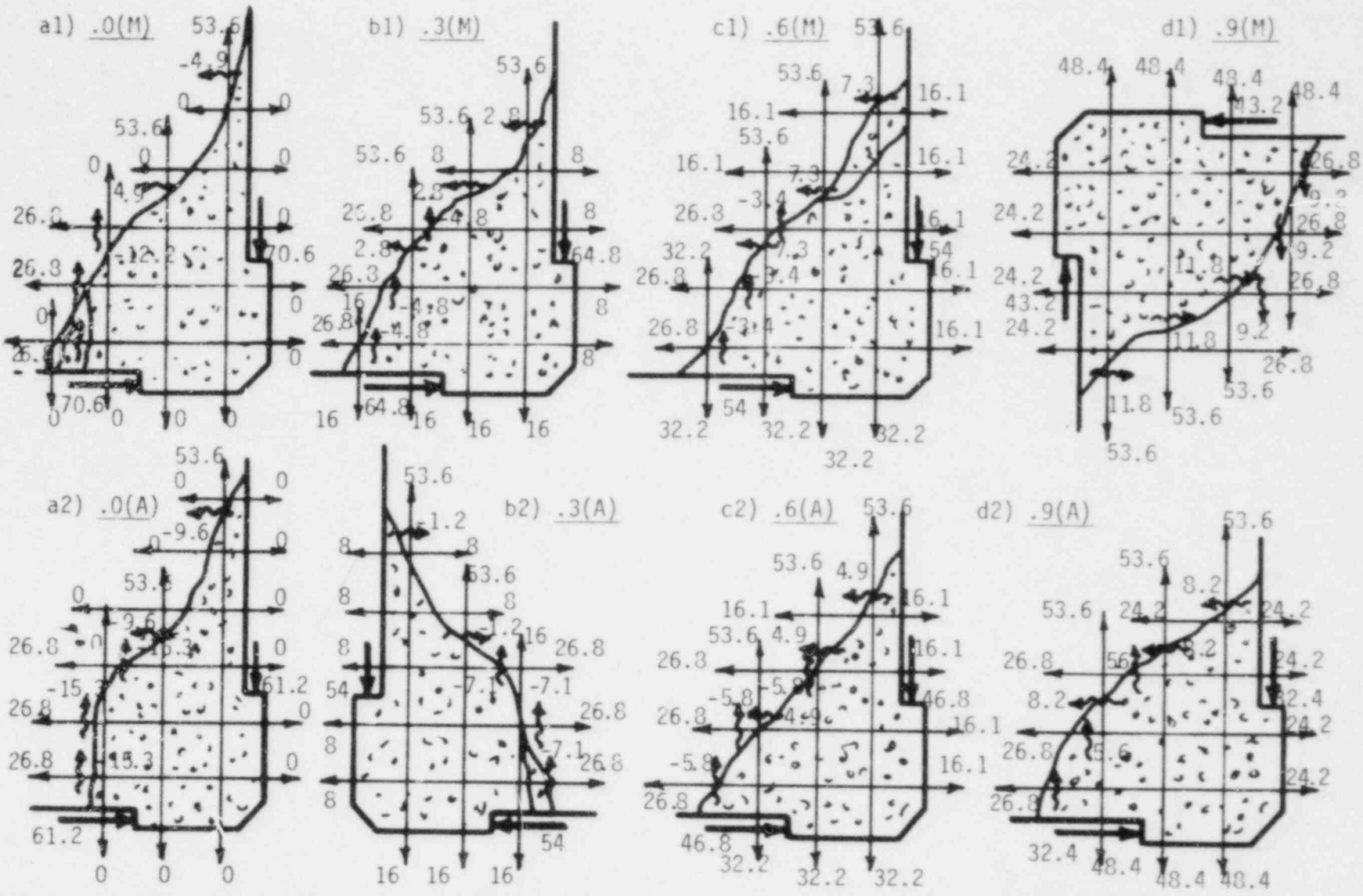

Fig. 4.65. Free body equilibrium diagrams at failure for selected specimens (full yielding of active steel). All forces shown are in kips.

double and the single layer, respectively (see Fig. 4.65 (d1)). Under cyclic shear and $0.9f_y$ tension (specimen .9(A)), however, lower dowel bar forces of about 4.1 and 5.6 kips exist at the diagonal crack in the double and the single layer, respectively (see Fig. 4.65 (d2)), because cycling weakens the DA mechanism. Negative dowel forces found for lower biaxial tensions (positive direction of dowel forces is shown in Fig. 4.63) indicate that in that reinforcing direction the assumed resisting forces are larger than the applied forces. This means that either not all the bars are yielding (in the weak reinforcing direction of the single layer) or no yielding at all takes place (particularly in the strong reinforcing direction of the double layer of bars).

As shown in Fig. 4.65, the development lengths of the bars crossing the inclined crack are shorter for those bars further away from the sides of the specimen. Thus, it is more likely (especially at low biaxial tension levels) that an assumption of partial yielding would be more realistic than that of full yielding. A linear distribution of the axial bar forces is postulated assuming yielding only in the bar (single layer) or pair of bars (double layer) with the largest development length. The corresponding free body equilibrium diagrams for selected specimens and the applied and resisting forces assuming partial yielding in the steel are shown in Fig. 4.66. The dowel forces calculated are given also in columns 10 and 11 of Table 4.I. As expected, larger dowel forces are needed in this case since the net axial forces in the bars resisting the applied shear load (columns 12 and 13) are smaller than those in the case of simultaneous yielding in all bars. For biaxial tension of $0.9f_y$ similar results are found in both cases because the bar forces are only

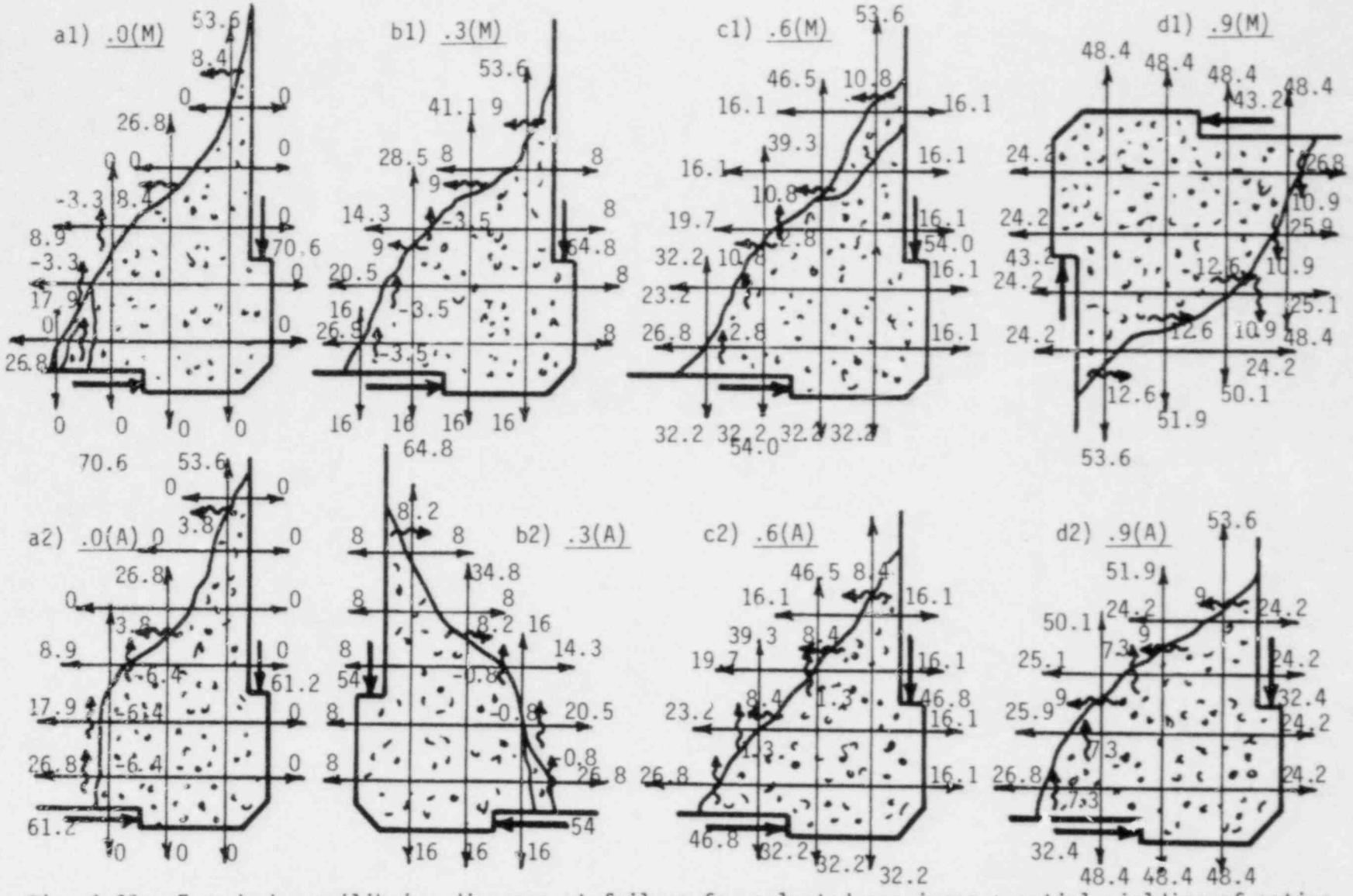

Fig. 4.66. Free body equilibrium diagrams at failure for selected specimens (partial yielding of active steel;linear distribution of axial bar forces). All forces shown are in kips.

within 10% of the yield strength and simultaneous yielding in both directions is very possible. This was also confirmed experimentally. The crack opening was practically uniform along the diagonal failure crack in the case of the $0.9f_y$ tension. As the biaxial tension decreased, the crack opening became more uneven, being largest at the level of the outermost bar in the single layer. This indicates that yielding was probably initiated in that bar.

The shear forces of 9.2 and 10.9 kips per bar in the single layer of specimen .9(M) calculated for full and partial yielding, respectively, seem relatively high. Similar high dowel forces exist in specimens .9(A), .9(B) and .9(C). A peak dowel force (parallel to the crack direction) of about 8.1 kips is calculated using Dulacska's Eqn. 4.20 for a No. 6 bar inclined 45 degrees to the crack with no tension (12 kips for a No. 6 bar normal to the crack). Therefore, considering the degrading effect of the extremely high tension of $0.9f_y$ and the fact that the shear force in the bar at zero tension would be smaller than the above estimated value of 8.1 kips (about 8.1 cos45° = 5.7 kips), it does not seem possible that DA alone could resist those high shear forces at yielding. Other mechanisms must be present. Interface shear transfer in the concrete, although possibly present at low biaxial tension when the failure diagonal crack widths are much smaller, is not likely to be mobilized at $0.9f_y$ bar tension with crack openings larger than 0.10 in. near failure. The only possible mechanism that could be present in addition to DA is kinking of the No. 6 bars due to the above large crack openings (see Fig. 4.63).

Assume the reinforcing bar is inclined to the crack direction (see Fig. 4.64). As the crack width increases under the application of shear, the bar adjacent to the crack would tend to remain perpendicular to the separating crack surfaces. The same could happen to a rebar normal to the crack direction due to a shear slip parallel to the crack. In both cases, the so-called "kinking effect" causes a reorientation θ_i of the bar axis at the crack, resulting in additional shear forces $T_i^* \sin\theta_i$ (see Fig. 4.64), where the bar force at the crack T_i^* is roughly equal to the assumed axial bar force T_i ($T_i = T_i^* \cos\theta_i \cong T_i^*$). This angle θ_i due to kinking, assumed to be constant at the crack opening, is expected to increase with increasing crack opening, inclination angle δ_i of the bar axis to the direction normal to the crack, and compressive strength of concrete (progressive crushing and compacting of concrete under the bar results in straightening of the bar) or with decreasing bar diameter.

In Ref. 71, Lenschow and Sozen discussed the effectiveness of reinforcing bars inclined to principal stress axes as they investigated the possibility of reorientation of the bars due to kinking. In their analysis they assumed a second order shape for the bent portion of the bar and an increase of shear force due to kinking uniformly distributed over an equivalent length ℓ_e (see Fig. 4.67), and proposed the following expression for θ

$$\tan\theta = c_{wd} \sin\delta/\ell_e \cong \theta \quad \text{(rad.)} \tag{4.118}$$

where c_{wd} is the average crack opening of the diagonal crack.

Assuming also an equivalent uniform stress distribution of the reaction forces (beam on an elastic foundation) to the applied dowel

shear force V_{DA} (see Fig. 4.67) and considering only the stress block of length ℓ_e, the following expression can be derived for ℓ_e (see Refs. 4 and 30)

$$\ell_e = 0.5\ V_{df}/d\ \sigma_{co} \qquad \text{(in)} \tag{4.119}$$

where V_{df} is the total dowel force at failure in kips, d is the bar diameter in inches and σ_{co} is the cube compressive strength of concrete in ksi ($\sigma_{co} \cong 1.4\ f'_c$).

From Eqns. 4.118 and 4.119 we get

$$\theta = 2c_{wd}d\ \sigma_{co}\ \sin\delta/V_{df} \qquad \text{(rad.)} \tag{4.120}$$

In the above Eqn. 4.120, the dowel force at failure is proportional to d and the yield strength of steel f_y. Thus, kinking is expected to decrease with increasing bar size.

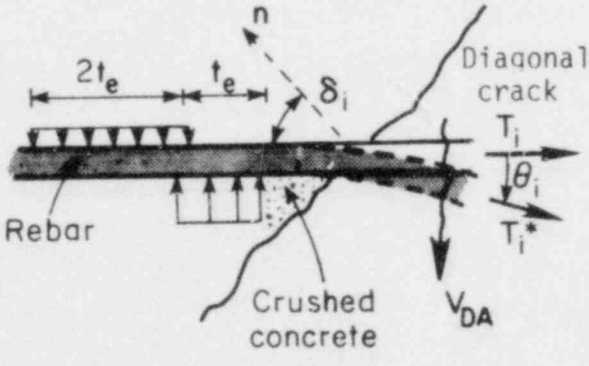

Fig. 4.67. Single bar subjected to dowel force.

For a No. 6 reinforcing bar, assuming a dowel force at failure of 5 kips, inclination angle δ = 45 degrees and σ_{co} = 5.3 ksi (f'_c = 3.8 ksi), the kinking angle θ is estimated for different crack openings c_{wd}. These θ values together with the calculated shear forces due to kinking, V_{dk} = T sinθ, for a bar force T equal to 53.6 kips ($0.9f_y$) are shown in Table 4.J.

It can be seen that for a crack opening of 0.10 in. kinking of about 7 degrees is estimated. This would result in about 6.5 kips additional shear. Thus, the values of dowel shear forces calculated at a bar tension of $0.9f_y$, shown in Table 4.I, are justifiable if kinking in the bars is taken into account.

Table 4.J. Estimated values of kinking angle θ and kinking shear forces V_{dk} for a single No. 6 bar (f_y = 61 ksi, δ = 45 degrees, f'_c = 3800 psi, V_{df} = 5 kips).

c_{wd} (in)	0.010	0.020	0.040	0.080	0.10
θ (degrees)	1	1	3	5	7
V_{dk} (kips)	0.9	0.9	2.8	4.7	6.5

Concluding, the second term of the right-hand side in the ultimate strength Eqns. 2.7a and 2.7b (Chapter 2), $0.005(\rho f_y - \sigma_N)\sqrt{f'_c}$ or $0.3(\rho f_y - \sigma_N)$ (for an average compressive strength of concrete

f'_c = 3800 psi), suggests that only about 1/3 of the total number of bars in the weak reinforcing direction (single layer) is really effective in resisting the applied shear near failure at all biaxial tension levels. This confirms the fact (shown in Table 4.I, column 4), that the active No. 6 bars in the single layer crossing the failure diagonal crack are only three out of a total of eight bars. The above finding also shows that the ultimate strength values predicted by Eqns. 2.7a and 2.7b are conservative. Because of the way the pure shear stress state was simulated by pushing and pulling on the corners of the specimens, half of the total nominal shear applied on the corner (based on the total cross-sectional area of the specimen) is resisted only by about 1/3 of the total amount of reinforcement.

CHAPTER 5

DESIGN CONSIDERATIONS FOR NUCLEAR SECONDARY CONTAINMENT VESSELS

Based on the experimental results of this work on the shear stiffness and strength of precracked orthogonally reinforced concrete panels under combined biaxial tension and membrane shear, implications in the design of nuclear containment vessels are discussed in this chapter. First, the code criteria for the loading case of combined internal pressurization (p) and membrane shear (V) according to the current code provisions are presented in Section 5.1. Typical reinforcing patterns and membrane stresses in the wall of a containment vessel are included in Section 5.2. Finally, tentative recommendations on the design of reinforced concrete containment vessels with two-way orthogonal steel are given in Section 5.3.

5.1 Code Design Criteria for Combined Internal Pressurization and Membrane Shear

One criteria load combination in the design of reinforced concrete secondary nuclear containment vessels is the combined accidental internal pressurization (p) plus shear forces generated by an earthquake (E). According to the current ASME-ACI 359-77 code provisions for the design of concrete reactor vessels and containments (Ref. 6), the following factored load combinations are considered:

a) $1.25P_a + 1.25E_o$ (Abnormal/Severe Environment loads)

b) $1.0P_a + 1.0E_{ss}$ (Abnormal/Extreme Environmental loads)

where P_a is the design internal pressure load (45 to 65 psi or 0.31 to 0.45 MPa) and E_O, E_{SS} are the shear loads generated by the operating basis earthquake and the safe shutdown earthquake, respectively. In computing the seismic response forces due to either the E_O or E_{SS} earthquake, only the dead load and existing live loads need be considered.

For the containment to be accepted as a safe structure, according to Article CC-6200 of ASME Code on structural acceptance requirements, it is subjected to an internal pressurization acceptance test. The internal pressure is increased from atmospheric pressure to at least 1.15 times the design pressure P_a and the structure is checked to assure that

a) No yielding develops in the conventional reinforcement as deduced from crack width measurements and strain gage and deflection gage data.

b) No visible signs of permanent damage have occurred to either the concrete wall or the steel liner.

c) The deflection recovery at maximum expected deflection points within 24 hours after depressurization is not less than 70% in reinforced concrete containment vessels (not less than 80% for prestressed concrete containment vessels).

Due to the internal pressure p the concrete wall will first crack in the vertical direction since the principal tensile hoop stress is twice the meridional principal tensile stress. Horizontal cracks will also form separating the wall in a large number of concrete blocks held together by the reinforcement and the internal steel liner. Under the above biaxial membrane stress state the reinforcement crossing the orthogonal cracks will be subjected to tensile stresses.

According to the currently proposed revisions in the ASME-ACI 359-77 Code (paragraph CC-3421.5.1) by the ACI Joint Committee JC-6-87, the allowable shear stresses for the factored load combinations of the Abnormal/Severe Environmental and Abnormal/Extreme Environmental categories (see page 345) carried by the interface shear transfer (IST) mechanism in the concrete, v_c, should not exceed 60 psi (0.41 MPa) provided that

a) The specified design compressive strength of concrete is not less than 3000 psi (20.7 MPa).

b) The maximum loss by weight of the coarse aggregate is not higher than 40% when tested according to ASTM C 131 requirements.

Otherwise v_c should not be higher than 40 psi (0.28 MPa).

When the peak membrane shear stress due to the seismic forces v_u is larger than the above allowable shear stress v_c in the concrete, diagonal steel must be added to resist the remainder of the shear ($v_u - v_c$). A meridional and hoop reinforcing system may be used for the Severe Environmental and Extreme Environmental loading categories (no biaxial tension) provided that the peak membrane shear stress v_u is not higher than $8.5\sqrt{f_c'}$ (470 to 540 psi or 3.24 to 3.73 MPa, for $3000 \leq f_c' \leq 4000$ psi or $20.7 \leq f_c' \leq 27.6$ MPa). If v_u exceeds this limit, diagonal steel is required and v_c should not be higher than 160 psi (1.1 MPa).

Regarding the shear capacity of reinforced concrete containments, the membrane tangential shear, v_c, allowed by the ASME Code is based on experimental results of isolated cracks with the shear resistance being provided by the IST mechanism alone. The allowable shear stress values guarantee negligibly small slip displacements rather than preclude failure in steel (yielding) or the concrete (crushing). Also, the shear resistance

provided by the dowel action (DA) was not considered in determining the limiting values for shear stresses. Thus, these recommended shear stress values are expected to be very conservative.

The influence of biaxial tension and cyclic shear on the shear stiffness of a containment is not dealt with in the code provisions.

5.2 Typical Reinforcing Schemes and Stresses in Containments

Typical dimensions for a secondary reinforced concrete containment are shown in Fig. 5.1. A 1/4 to 1/2 inch thick steel liner plate is

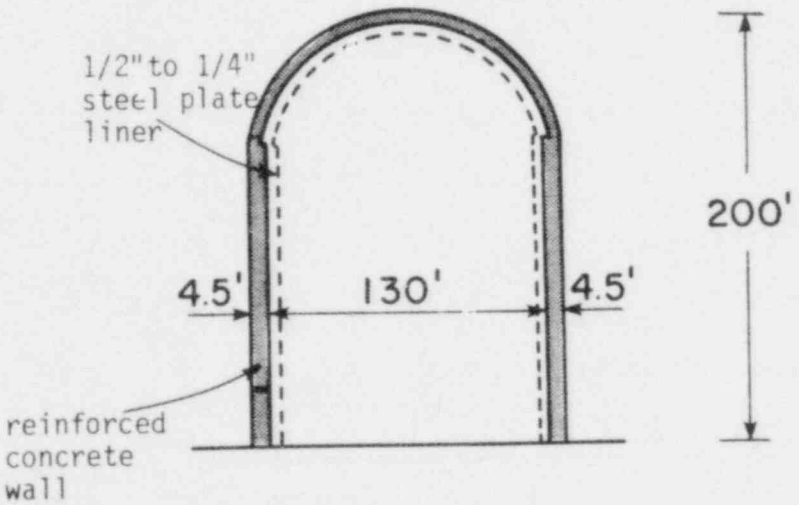

Fig. 5.1. Dimensions of a reinforced concrete containment vessel.

anchored to the 4.5 ft. thick concrete wall to assure leak tight integrity during the service life of the containment. The steel liner is not, however, counted on to provide additional strength. Reinforcement ratios between 0.015 and 0.025 are provided in the vertical and horizontal directions (the reinforcement ratio in the vertical direction is smaller than

that in the horizontal direction). A representative orthogonal reinforcing pattern in a containment wall consists of three and four layers of No.18 bars spaced at about 16 in. in the vertical and the horizontal direction, respectively.

In the case of two-way orthogonal reinforcement (horizontal and vertical) and neglecting bending effects in the wall away from the base of the cylindrical vessel, the following principal tensile stresses in the hoop direction, σ_h, and meridional direction, σ_m, can be calculated for an internal pressure p equal to 50 psi (0.34 MPa), as shown in Fig. 5.2,

$$\sigma_h = pR/t = 722 \text{ psi } (4.98 \text{ MPa})$$
$$\sigma_m = pR/2t = 361 \text{ psi } (2.49 \text{ MPa}) \quad (5.1)$$

where R is the radius of the cylindrical vessel and t is the wall thickness.

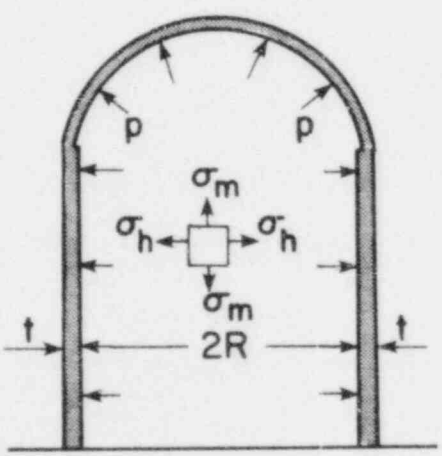

Fig. 5.2. Principal tensile stresses in the cylindrical wall of a containment due to internal pressure p.

To be conservative, the dead load effect of the reinforced concrete containment wall on the meridional principal stress σ_m (Eqn. 5.1) is not taken into account.

Assuming that the steel ratios in the horizontal and vertical directions are equal to $\rho_h = 0.0244$ and $\rho_m = \rho_h/2 = 0.0122$, respectively, as chosen in the experimental program described in this report, the reinforcing bars will be tensioned to a stress equal to approximately 30 ksi. This is about 50% of the yield strength of the steel.

The membrane tangential shear stresses resulting from an earthquake loading must be transferred across the existing orthogonal cracks by means of the IST and DA shear transfer mechanisms causing shear slips at the cracks and shear distortion in the wall. As diagonal cracks start forming at shear stresses as low as 75 psi (0.52 MPa), the diagonal tension mode becomes the major means to resist the applied shear. This is basically accomplished through the axial tensile forces in the reinforcement crossing the cracks and the compressive forces resisted by the inclined struts of concrete.

Normally a four-way reinforcing arrangement is used in the design of reinforced concrete containments. Diagonal steel (No.18 bars) is placed at ±45 degrees to the orthogonal steel (hoop and meridional) to carry the remainder ($v_u - v_c$) of the shear stresses in the wall. This inclined steel requires continuously curved reinforcing bars which are expensive to fabricate as well as creating congestion problems. Therefore, the elimination or at least the reduction of the additional diagonal steel is highly desirable. Experimental results regarding the study of the effect of diagonal steel on the cracking distribution and the shear stiffness

and strength of biaxially tensioned reinforced concrete panels by Conley, White, and Gergely will be soon reported in Ref. 26.

5.3 Tentative Design Recommendations (Two-way Orthogonal Steel)

A major problem in the design of reinforced concrete containment vessels is to determine the level of shear stress that can be safely transferred in the cracked cylindrical wall without yielding in the reinforcement. This was the failure mode in the biaxial tests conducted with either No.6 (Cornell) or No.14 and No.18 bars (PCA). Another important design aspect is to establish whether the use of a two-way orthogonal reinforcing pattern (without diagonal bars) is a more efficient way to transmit shear forces in precracked reinforced concrete vessels.

The experimental data on the shear capacity of precracked reinforced concrete panels reinforced with No.6 bars and subjected to monotonic or cyclic shear plus biaxial tension can contribute to improve the recommended design values of peak membrane shear. The ultimate strength results from the biaxial tests with No.6 bars are shown in Figs. 5.3a and 5.3b as a function of the stress parameter $\rho f_y (1 - f_s/f_y)$. In the above expression, ρ is the steel ratio in the weak direction (yielding in the steel will first occur in that direction) and f_s/f_y is the ratio of the applied tensile stress to the yield strength of the steel (biaxial tension level). The stress parameter $\rho f_y(1 - f_s/f_y)$ denotes the maximum axial resisting force that the reinforcing bars could provide normal to the orthogonal cracks before reaching their yield strength, as the applied shear stress increases. Fig. 5.3b includes the effect of the compressive strength of

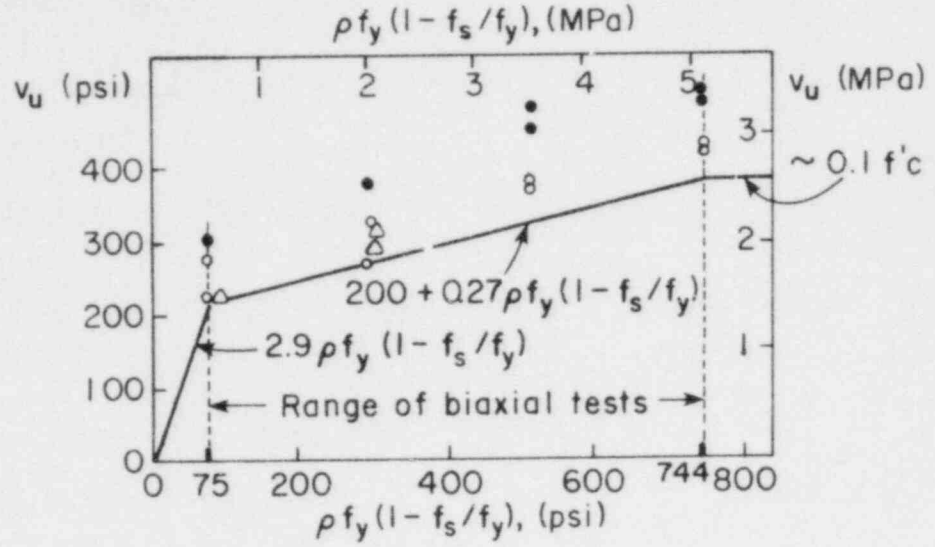

a) v_u versus $\rho f_y(1-f_s/f_y)$

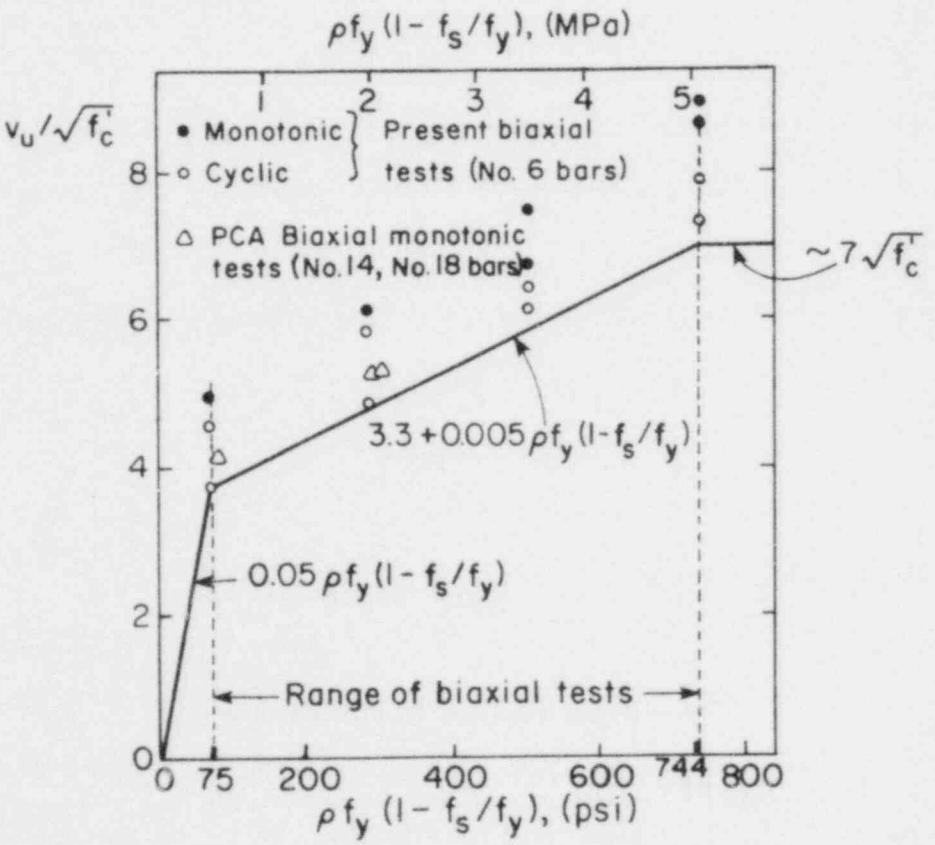

b) $v_u/\ f'_c$ versus $\rho f_y(1-f_s/f_y)$

Fig. 5.3. Lower bound values of ultimate strength as a function of the stress parameter $\rho f_y(1-f_s/f_y)$ in the biaxial specimens.

concrete f_c' on the ultimate strength v_u in terms of the shear stress expression $v_u/\sqrt{f_c'}$. The biaxial tests by PCA (specimens MB1, MB3 and MB4 with No.14 and No.18 bars) under monotonic shear (Ref. 96) are also plotted in the above two figures. Since the experimental data demonstrated that the ultimate strength increases with increasing reinforcement ratio ρ or decreasing biaxial tension level f_s/f_y, the tentative recommended values for the ultimate shear v_u will be given as a function of the aforementioned parameter $\rho f_y(1 - f_s/f_y)$.

Until additional data for critical reinforcement ratios larger than 0.0122 and results from the cyclic tests at PCA with larger size bars are available, the lower bound straight lines, shown in Figs. 5.3a and 5.3b, can conservatively provide the recommended design values for shear strength in the presence of biaxial tension between 0 and 0.9 f_y. The range of the parameter $\rho f_y(1 - f_s/f_y)$ is between 75 psi (0.52 MPa) and 744 psi (5.13 MPa) for specimens with No.6 bars. For values of the above parameter of less than 75 psi, it is assumed that the ultimate strength v_u decreases linearly, becoming zero for $\rho = 0$ or $f_s = f_y$. For $\rho f_y(1 - f_s/f_y)$ larger than 744 psi, the allowable shear stress is set constant at $7\sqrt{f_c'}$ or 400 psi (2.76 MPa), since no data exists to justify higher values. At these high shear stress levels, which will correspond to either large values of ρ or low biaxial tension levels, the compressive strength of concrete f_c' could control instead of the yield strength of the steel.

According to Figs. 5.3a and 5.3b, the following values of ultimate strength v_u are tentatively recommended:

$$v_u = 0.05\, \rho f_y(1 - f_s/f_y)\, \sqrt{f_c'} \text{ (psi)} \qquad (5.2a)$$

or

$$v_u = 2.9\ \rho f_y(1 - f_s/f_y)\ (\text{psi}),\ \text{for}\ \rho f_y(1 - f_s/f_y) \leq 75\ \text{psi} \qquad (5.2a)$$

$$v_u = [3.3 + 0.005\ \rho f_y(1 - f_s/f_y)]\ \sqrt{f_c'}\ (\text{psi})$$

or

$$v_u = 200 + 0.27\ \rho f_y(1 - f_s/f_y)\ (\text{psi}),$$
$$\text{for}\ 75 < \rho f_y(1 - f_s/f_y) \leq 744\ \text{psi} \qquad (5.2b)$$

and

$$v_u = 7\sqrt{f_c'}\ (\text{psi})$$

or

$$v_u = 400\ (\text{psi}),\ \text{for}\ \rho f_y(1 - f_s/f_y) > 744\ \text{psi} \qquad (5.2c)$$

The above recommended values of v_u for biaxially tensioned orthogonally reinforced concrete panels are valid for initial crack widths at the orthogonal cracks smaller than 0.020 in., compressive strength of concrete in the range $3000 \leq f_c' \leq 4000$ psi (typical of containment structures) and Grade 60 steel. These allowable membrane shear stresses, although higher than those given by the current code, are still considered to be conservative. The diagonal tension failure mode observed near a corner in the biaxially cracked specimens causing yielding of the reinforcing bars is not as likely to occur in the wall of a containment. The uncracked concrete blocks in the wall are restrained from moving far apart, since the containment is a continuous cylindrical structure. Furthermore, the stress values plotted in Fig. 5.3 are calculated on the entire cross section of the specimen (288 in ^{2}), while failure occurred in a corner of the specimen. Also, the reinforcing bars in the hoop and meridional directions are not tensioned at the same stress as it is the case in the experiments. In

addition, due to the fact that the distribution of membrane shear stresses in a cylindrical shell is sinusoidal the shear stress will be zero at some regions in the wall. Thus, the diagonal cracks forming in the wall cannot propagate all the way around the periphery of the shell. Also, the nonlinear response of the cracked wall and the overturning effect which would close the cracks in one half of the shell and open them further in the other half will result in redistribution of the shear stresses. As a result, the inclined (diagonal) cracks will tend to be discontinuous making it very difficult for a diagonal opening type mode to occur at failure. Nonlinear finite element analysis including the effects of both horizontal and vertical cracking has to be used to predict the actual shear distribution in the cracked containment wall (see Ref. 108). Also, tests on models of containments are needed to study the combined effects of seismic shear and internal pressurization and correlate these findings with the results on isolated flat specimens reported in this report.

Values of the shear modulus G_{cr} for the cracked vessel usually used in design range between $0.4G_o$ to $0.6G_o$, where G_o is the shear modulus of uncracked concrete. In the concrete panels reinforced with orthogonal steel only (No.6 bars) the effective tangent shear modulus in the cracked stage and prior to the yielding of the steel was found to be about $0.05G_o$ to $0.07G_o$, for biaxial tension larger than $0.3f_y$ and shear stresses higher than 125 psi. For low values of fully reversing cyclic shear (less than 50 psi), extremely low values for the shear modulus equal to $0.01G_o$ to $0.02G_o$ were measured. At least for intermediate shear stresses during the 1st load cycle, no appreciable influence of the level of biaxial tension on the tangent shear modulus was evidenced. The secant

shear modulus, on the other hand, decreased with increasing applied tension in the reinforcing bars due to larger total shear deformations occurring at larger crack openings.

The rate of degradation increased with shear cycling and increasing shear stress level. All this indicates the severity of the cracking in the concrete mainly due to the simultaneous action of biaxial tension and shear that produced diagonal cracks in addition to the already existing orthogonal cracks. Therefore, the response of structural elements such as the steel liner and the anchors supporting it on the concrete wall should be carefully studied and the possible implications in controlling the large shear deformations should be reconsidered. The low shear stiffness of the concrete will result in a substantial transfer of shear forces into the liner. Thus, the composite behavior of the wall and the liner under reversing shear and biaxial tensile loads has to be investigated. Of course, the actual distribution of shear stresses around the circumference of the vessel and the frequency content of the seismic excitation will have a major influence on the effect of shear deformations on the stresses and strains in the steel liner.

Cycling at the same peak shear stress decreased the area contained under the experimental shear stress-shear strain hysteresis loops, particularly at the initial cycles. Thus, the effective hysteretic damping decreased initially with a tendency to stabilize after 10 load cycles at the same peak shear stress. The above factors plus the highly nonlinear hysteretic response can have significant implications in a dynamic analysis of a containment structure (see Refs. 47 and 108).

Concluding, it should be pointed out that the upper shear stress limit of $v_u = 8.5\sqrt{f_c'}$, recommended in the ASME-ACI 359-77 Code for no biaxial tension, appears relatively high unless steel ratios above 0.025 are used. Furthermore, at this stress level the resulting shear deformations would be very high. For zero biaxial tension and reversing shear (assuming f_y = 60 ksi), Eqns. 5.2b become as follows

$$v_u = (3.3 + 300\rho)\sqrt{f_c'} \quad \text{(psi)}$$

or (5.3)

$$v_u = 200 + 16200\rho \quad \text{(psi)}$$

For a typical steel ratio of ρ = 0.015, Eqns. 5.3 result in ultimate strength values of about $7.8\sqrt{f_c'}$ or 440 psi (3.04 MPa). However, a more realistic case of loading would be that of combined biaxial tension of $0.6f_y$ and reversing shear, as described in Section 5.2. In this case and for f_y = 60 ksi and ρ = 0.015, Eqns. 5.2b result in much lower ultimate strength values of about $v_u = 5\sqrt{f_c'}$ or 300 psi (2.07 MPa). Before more final recommendations can be suggested regarding the upper limit of the membrane tangential shear stress in reinforced concrete containments, additional information is needed from parallel research programs on shear transfer.

The results of the research program at PCA on cyclically loaded specimens with No.14 and No.18 bars are necessary to avoid unconservative predictions by extrapolating design values from experiments with relatively small size bars, such as No.6 bars. Also, tentative recommendations on four-way reinforcing patterns will be contained in a companion NRC report

on additiona¹ NRC-sponsored experiments (Ref. 26). Based on the above studies, provisions on the limitation of shear deformations in containment walls depending on the biaxial tension level have to be incorporated in the ASME Code.

CHAPTER 6

CONCLUSIONS AND COMMENTS ON FUTURE RESEARCH NEEDS

6.1 Conclusions

The major accomplishments of this research work are summarized here:

a) The effective shear stiffness of precracked concrete panels orthogonally reinforced with No.6 bars and subjected to simultaneous biaxial tension and shear (monotonic or fully reversing cyclic) was determined. This evaluation of the effective shear modulus of cracked concrete will contribute to an improvement in the static and dynamic analysis of similar structural elements loaded in membrane shear.

b) Ultimate strength interaction curves were established for monotonic and cyclic shear with simultaneous biaxial tension. The ultimate strength was expressed as a function of the applied bar tension, which was held constant in both orthogonal reinforcing directions during the application of shear. The effect of cycling on the ultimate strength was also determined.

c) An engineering model was formulated to predict the shear stress-shear strain relationship of the cracked reinforced concrete panels with orthogonal steel. Shear resistance is provided by the interface shear transfer and dowel action mechanisms, when only orthogonal cracking is present, and by axial forces in the reinforcing bars and compressive strut action in the concrete after diagonal cracking becomes the predominant mode of deformation.

d) The observed failure mechanism under combined shear and biaxial tension is described and the relative amounts of tensile stress, dowel force, and kinking effect in the reinforcement are estimated performing free body equilibrium analyses under failure load conditions for all specimens.

e) The initial extensional stiffness in the two reinforcing directions is given, based on a series of axial tests with No.4 and No.6 embedded bars. Thus, the average initial crack widths corresponding to the preselected biaxial tension levels of 0, $0.3f_y$, $0.6f_y$ and $0.9f_y$ can be indirectly estimated also.

Based on the experimental study of biaxially tensioned orthogonally reinforced concrete panels with No.6 bars subjected to simulated seismic membrane shear, the following main conclusions are drawn:

Strength:

1) The major failure mode is diagonal opening along an inclined crack forming near the corner that is loaded in tension from the equivalent shear loading, and not that of sliding along an orthogonal crack. The shear capacity appears to be governed by yielding in the reinforcement of the single layer (weak direction with $\rho = 0.0122$) at least for values of $\rho f_y(1 - f_s/f_y)$ up to 744 psi. No data is available for values of this stress parameter higher than 744 psi; at some higher transition level, concrete compressive strength could control. Until additional experimental evidence becomes available, the peak shear stress v_u under cyclic loading should not exceed $0.1\ f_c'$ to assure yielding of the steel prior to splitting or crushing in the concrete.

2) For ρf_y equal to 744 psi (5.13 MPa) in one direction (single layer) and twice as much in the orthogonal direction (double layer) the peak monotonic shear v_u decreases approximately linearly with increasing biaxial tension in the orthogonal steel. The mean values of v_u are given by the following straight line relations:

$$v_u \text{ (monotonic)} = (8.5 - 4.0\, f_s/f_y)\ \sqrt{f_c'}$$

or

$$v_u \text{ (monotonic)} = 510 - 220\, f_s/f_y \quad \text{(psi)} \tag{6.1}$$

This corresponds to a peak shear of 8.5 $\sqrt{f_c'}$ or 510 psi (3.52 MPa) at zero tension (after specimens were precracked) decreasing to a value of about 5 $\sqrt{f_c'}$ or 310 psi (2.14 MPa) at $0.9f_y$ applied tension in the rebars during the application of shear.

3) A reduction of about 15 to 20% in shear capacity (relative to the monotonically loaded specimens) is caused by a fully reversing cyclic shear. Ten fully reversing load cycles were applied at each prespecified peak shear stress level, beginning at a shear stress of ±125 psi (0.86 MPa) and increasing to higher levels in increments of 50 psi (0.34 MPa). The mean ultimate strength values v_u under cyclic shear also decrease linearly with increasing tension and are given by the following relations:

$$v_u \text{ (cyclic)} = (7.4 - 3.7\, f_s/f_y)\ \sqrt{f_c'}$$

or

$$v_u \text{ (cyclic)} = 428 - 200\, f_s/f_y \quad \text{(psi)} \tag{6.2}$$

A maximum shear of 7.4 $\sqrt{f_c'}$ or 430 psi (2.97 MPa) at zero tension decreases to about 4 $\sqrt{f_c'}$ or 250 psi (1.72 MPa) at $0.9f_y$. The difference between the ultimate strength for monotonic and cyclic shear is approximately 75 psi (0.52 MPa).

4) A lower bound expression for design ultimate strength, given in terms of ρf_y, $\sqrt{f_c'}$, and the ratio f_s/f_y, is shown in Fig. 5.3.

5) Free body equilibrium analyses were performed for all specimens at the ultimate shear load assuming simultaneous yielding in the reinforcement in both orthogonal directions and no interface shear transfer in the concrete along the failure diagonal crack, where crack openings larger than 0.05 in. were evidenced. To satisfy equilibrium, dowel forces of about 6 kips per bar in the double layer and 9 kips per bar in the single layer were calculated for specimen .9(M). With decreasing applied bar tension, as shown in Section 4.4, the net resisting axial forces in the bars increase, and as a result smaller dowel forces are needed to transfer the applied shear. The better bond transfer at low applied tensions, due to less deterioration of the concrete near the bars, can indeed enhance the ability to transfer shear by means of axial forces in the bars inclined to the diagonal cracks. It is experimentally confirmed that the number of active bars resisting the applied shear in the weak single layer direction increases with decreasing biaxial tension. That is, the inclination angle of the failure crack to the horizontal (single layer direction) increases from about 45 degrees to about 60 degrees with decreasing bar tension from $0.9f_y$ to 0, respectively.

6) At biaxial tension higher than $0.6f_y$, kinking of the bars is possible for diagonal crack openings larger than 0.05 in. For a diagonal

crack inclined at 45 degrees to the horizontal and with an average crack opening of about 0.10 in., kinking of about 7 degrees is estimated for a No.6 bar. This corresponds to a shear force provided by the bar at the crack of about 3 kips with the bar tensioned to $0.9f_y$, an appreciable force compared with the dowel force values given in the previous paragraph.

7) The ultimate shear stresses v_u measured in the present tests are conservative because they are based on the total cross-sectional area of the specimen and failure occurred along a diagonal crack. Since the pure shear stress condition is approximated by pushing and pulling on the corners, half of the total shear applied at each corner is resisted in each direction by the axial and shear forces in the bars crossing the failure crack. However, according to the equilibrium checks, the number of reinforcing bars resisting 50% of the total shear corresponds to about 25 to 30% of the total amount of steel in the same direction.

Cracking and stiffness behavior:

1) Orthogonal cracks that formed during the application of biaxial tension follow very closely the reinforcing pattern of the specimen. This shows that the spacing of the transverse reinforcing bars in orthogonally reinforced concrete panels plays a significant role in the formation of the cracks produced by tension in the bars.

2) Diagonal cracking occurs at relatively low shear stress levels of about 100 psi (0.69 MPa), and sometimes as low as 75 psi (0.52 MPa), and causes further degradation of the shear stiffness as the shear distortion increases with the opening of the diagonal cracks. This is a major reason for the irreversible loss in shear stiffness and strength. The diagonal

tension-compression strut system gradually becomes the prevailing shear transfer mode that finally results in a diagonal tension opening failure near a corner of the specimen.

3) Tangent extensional stiffness in the direction of the double layer is about twice that provided by the single layer, after the specimens were initially cracked at a bar tension of $0.6f_y$ in both directions. Smaller average crack widths are calculated at the tension cracks normal to the double layer than those normal to the single layer. As a result, more cracks (smaller crack spacing) are observed in the direction normal to the double layer of No.6 bars. Residual crack widths of about 0.002 and 0.004 in. are estimated for zero tension in the orthogonal cracks normal to the double and the single layer of bars, respectively.

4) Measured effective shear modulus values in the cracked panels under monotonic shear are less than 10% of that for uncracked concrete (G_o). The biaxial tension level does not seem to affect the tangent shear modulus, which remains approximately constant at about $0.05G_o$ to $0.07G_o$ for intermediate shear stress levels. For shear stresses less than 50 psi (0.34 MPa), dowel action is the major shear transfer mechanism until the interface shear transfer mechanism is mobilized as the two crack surfaces come closer to each other.

5) Reversing cyclic shear and an increase in the peak shear stress level results in progressive degradation of the shear stiffness due to increased diagonal cracking, especially for lower biaxial tension levels. Cumulative gains in shear deformations of about 10 to 20% were measured at selected peak shear stress levels after 10 full cycles of reversing shear. At high tensions the increase in deformations is approximately

constant, becoming higher near failure. An approximately constant 5% increase was recorded at the end of the 2nd cycle at a peak shear stress level lower than 0.8 times the shear capacity. Changes in the peak shear stress are more critical in lowering the shear stiffness at biaxial tension levels higher than $0.6f_y$.

6) For cyclic shear stresses less than 50 psi, extremely low shear rigidity values of about $0.01G_o$ to $0.02G_o$ are measured with dowel action resisting most of the shear forces. As the shear stress increases, slipping at the orthogonal cracks results in the mobilization of the combined mechanisms of (IST + DA). Thus, the effective tangent shear rigidity shows a significant increase for shear stresses larger than 50 psi. At zero bar tension, a large decrease in the tangent shear stiffness from about $0.45G_o$ down to $0.08G_o$ results after some 80 load cycles at selected shear stress levels. With $0.9f_y$ tension in the bars, the shear stiffness remains practically constant at $0.04G_o$, showing an insignificant influence of cycling at these high tension levels. For shear stress ratios v/v_u less than 0.9, it is possible to have as much as 250% increase in average peak shear deformations relative to the peak deformation at 125 psi shear stress. For shear stresses higher than 125 psi the unloading portion of the shear stress-shear deformation curves is almost vertical, exhibiting large residual deformations at zero load.

General:

1) The area under the hysteresis loops for shear stress reversals decreases initially with an increasing number of cycles and seems to remain essentially constant after at least two load cycles have been completed.

Thus, cycling leads to a reduction in the ability to absorb energy during cracking, which in other words means a decrease in the effective hysteretic damping of the structure. This is very important for the dynamic analysis of the cracked containment wall under a simulated seismic loading.

2) The effect of diagonal steel will be determined after additional tests at Cornell University are completed. Also, the results from the experimental work at PCA on larger scale specimens subjected to cyclic shear are needed to determine any potential splitting effects of large size bars.

6.2 Comments on Future Research Needs

The following suggestions for further research related to the shear transfer phenomenon are outlined here:

1) The results from the experimental study currently underway at Cornell on the effect of smaller size bars (No.4) as orthogonal steel, as well as the influence of additional diagonal bars on the shear stiffness and strength of similar specimens, will be reported soon (see Ref. 26). The results from PCA's larger scale tests under cyclic shear are also considered to be essential in formulating final design guidelines.

2) The effect of lower peak shear stress levels after an application of relatively high shear stresses should be studied more extensively, particularly for determining the shear rigidity of the specimen. A similar type of loading may occur during an earthquake.

3) The composite action of the concrete containment wall and the steel liner under combined biaxial tension and cyclic shear has to be given further attention. The low shear stiffness values observed in the present

tests raise the question of structural integrity for the steel liner which is forced to undergo the same shear distortions as the concrete wall. In addition to theoretical studies, experiments can be conducted on flat concrete specimens with a steel plate anchored on one side. That way the actual response of a cracked containment would be more accurately modeled.

4) More strain measurements on the reinforcing bars are needed at locations near expected cracking to measure the actual bar tension increases during the application of shear. Since the exact position of the orthogonal cracks is not known, probably the best approach would be to mount the strain gages on the rebars at distances equal to the spacing of the transverse bars. By instrumenting two bars in each direction a good estimate of the average tensile stresses in the steel at the cracks can be achieved.

5) A study of the possible shrinkage effects on the residual strains and stresses in the concrete prior to the application of shear is very important. The influence of the specimen size, casting method and curing conditions on shrinkage cracking should be probably taken into consideration. This may help explain the soft response evidenced at the initiation of shear loading.

6) Experiments conducted on specimens with two-way reinforcement but with tension applied to the bars in only one direction will provide data to help determine the effect of initial cracking on shear stiffness and strength. The effect of initial compression can also be studied on prestressed flat specimens, so that the degrading influence of diagonal cracking alone (no orthogonal cracks) on the shear rigidity of the structure can be investigated.

7) The experiments performed at Cornell and elsewhere to study the effect of reversing cyclic shear are performed under static shear loads. A true dynamic loading, such as a simulated earthquake excitation of specific frequency, would provide important information on the actual response of a containment. This type of loading might further reduce the shear stiffness, since the frictional component of the IST mechanism is expected to become less effective. The observed dynamic behavior from these tests should be compared to the results of a dynamic analysis utilizing the experimental shear rigidity values in the biaxial tests. Additional simulated dynamic tests on containment models would definitely complement the above suggested work, helping also to identify the primary failure mode in the containment wall under combined internal pressurization and simulated seismic loading.

8) After additional data on the effects of parameters, such as reinforcement ratio, bar size, true dynamic loading, frequency level of the excitation, and diagonal steel are available more rational design guidelines for containments or other similar heavy-walled concrete structures can be established.

REFERENCES

1. Acharya, D.M., and Kemp, K.O., "Significance of Dowel Forces on the Shear Failure of Rectangular Reinforced Concrete Beams without Web Reinforcement", ACI Journal, Proceedings Vol. 62, October 1965, pp. 1265-1278.

2. ACI Committee 349, "Code Requirements for Nuclear Safety Related Concrete Structures", ACI Journal, Proceedings Vol. 73, No. 1, January 1976.

3. Agrawal, A.B., Jaeger, L.G., and Mufti, A.A., "Crack Propagation and Plasticity of Reinforced Concrete Shear-Walls under Monotonic and Cyclic Loading", Proceedings of the International Conference on Finite Element Methods in Engineering, The University of Adelaide, Adelaide, Australia, December 1976.

4. Al-Mahaidi, R.S., "Non-Linear Finite Element Analysis of Reinforced Concrete Deep Members", Ph.D. Thesis, Cornell University, May 1978 (also Report No. 79-1, Department of Structural Engineering, January 1979).

5. Arbesman, B., "The Effects of Stirrup Cover and Amount of Reinforcement on Shear Capacity of Reinforced Concrete Beams", M. Eng. Thesis, University of Toronto, Canada, 1975.

6. ASME Boiler and Pressure Vessel Code, Section III, Division 2, "Code for Concrete Reactor Vessels and Containments", The American Society of Mechanical Engineers, New York, July 1977.

7. Baumann, T., "Versuche zum Studium der Verdubelungswirkung der Biegezugbewehrung eines Stahlbetonbalken", Materialprüfungsamt für das Bauwesen der Technischen Hochschule, München, Bericht No. 77, 1968.

8. Baumann, T., "Zur Frage der Netzbewehrung von Flächentragwerken", Der Bauingenieur, Vol. 47, Heft 10, 1972, pp. 367-372.

9. Bazant, Z.P., and Gambarova, P., "Rough Cracks in Reinforced Concrete", Reprint No. 3579, National Convention of ASCE, Boston, April 1979.

10. Beeby, A.W., "The Prediction of Crack Widths in Hardened Concrete", The Structural Engineer, Vol. 57A, No. 1, January 1979.

11. Birkeland, P.W., and Birkeland, H.W., "Connections in Precast Concrete Construction", ACI Journal, Proceedings Vol. 63, No. 3 March 1966, pp. 345-367.

12. Bresler, B., and Scordelis, A.C., "Shear Strength of Reinforced Concrete Beams", ACI Journal, Proceedings Vol. 60, No. 1, January 1963, pp. 51-72.

13. Bresler, B., and Bertero, V., "Behavior of Reinforced Concrete Under Repeated Load", Journal of the Structural Division, ASCE, Vol. 94, No. ST6, June 1968, pp. 1567-1590.

14. Broms, B.B., "Stress Distribution, Crack Patterns, and Failure Mechanisms of Reinforced Concrete Members", ACI Journal, Proc. Vol. 61, No. 12, December 1964, pp. 1535-1556.

15. Broms, B.B., "Crack Width and Crack Spacing in Reinforced Concrete Members", with supplement, ACI Journal, Proceedings Vol. 62, October 1965, pp. 1237-1255.

16. Broms, B.B., and Lutz, L.A., "Effects of Arrangement of Reinforcement on Crack Width and Spacing of Reinforced Concrete Members", with supplement, ACI Journal, Proceedings Vol. 62, No. 11, November 1965, pp. 1395-1409.

17. Brondum-Nielsen, T., "Optimum Design of Reinforced Concrete Shells and Slabs", Report No. 1-44, Structural Research Laboratory, Univ. of Denmark, Copenhagen, 1974, pp. 190-200.

18. Castellani, A., and Fontana, A., "Effects of Thermal Cracking on the Dynamic Behavior of Reinforced Concrete Containment Structures", IV SMiRT, Structural Mechanics in Reactor Technology, Paper J4/5, San Francisco, 1977.

19. CEB Bulletin d'Information, "Fissuration", No. 89, March 1973.

20. CEB Bulletin d'Information, No. 117, Vol. 2, "Model Code for Concrete Construction", December 1976.

21. CEB Bulletin, "Model Code for Concrete Structures", Granada, September 1977.

22. Cedolin, L., and Dei Poli, S., "Finite Element Non-Linear Plane Stress Analysis of Reinforced Concrete", Studi e Rendiconti, Construzioni in Cemento Armato, Vol. 13, Politecnico di Milano, 1976, pp. 3-33.

23. Cervenka, V., "Inelastic Finite Element Analysis of Reinforced Concrete Panels Under In-Plane Loads", Ph.D. Thesis, University of Colorado, Boulder, 1970.

24. Colley, B.E., and Humphrey, H.A., "Aggregate Interlock at Joints in Concrete Pavements", PCA Research and Development Laboratories, Bulletin D124, 1967 (also Highway Research Record, No. 189, 1967, pp. 1-18).

25. Collins, M.P., "Towards a Rational Theory for Reinforced Concrete Members in Shear", Journal of the Structural Division, ASCE, Vol. 104, No. ST4, April 1978, pp. 649-666.

26. Conley, C.H., White, R.N., and Gergely, P., "The Effects of Reinforcement Ratio and Orientation on the Strength and Stiffness of Reinforced Concrete Panels Subjected to Combined Biaxial Tension and Shear", M.S. Thesis, Department of Structural Engineering, Cornell University, Ithaca, N.Y., May 1980 (to be published as an NRC report, NUREG/CR-1650, 1980).

27. Cowan, J., and Cruden, A.F., "Second Thoughts on Shear Friction", Concrete Magazine, August 1975, pp. 31-32.

28. Darwin, D., and Pecknold, D.A., "Analysis of Reinforced Concrete Shear Panels Under Cyclic Loading", Journal of the Structural Division, ASCE, Vol. 102, No. ST2, Proc. Paper 11896, February 1976, pp. 355-369.

29. Duchon, N.B., "Analysis of Reinforced Concrete Membrane Subject to Tension and Shear", ACI Journal, Proc. Vol. 69, No. 9, September 1972, pp. 578-583.

30. Dulacska, H., "Dowel Action of Reinforcement Crossing Cracks in Concrete", ACI Journal, Proc. Vol. 69, No. 12, December 1972, pp. 754-757 (with supplement).

31. Ebbinghaus, P., "Herleitung eines Verfahrens zur Berechnung von Stahlbetonscheiben unter Berucksichtigung der Rissenwicklung", Dissertation, RWTH, Aachen, 1975.

32. Edwards, A.D., and Yannopoulos, P.J., "Local Bond Stress-Slip Relationships Under Repeated Loading", Magazine of Concrete Research, Vol. 30, No. 103, June 1978, pp. 62-72.

33. Eleiott, A.F., "An Experimental Investigation of Shear Transfer Across Cracks in Reinforced Concrete", M.S. Thesis, Cornell University, Ithaca, N.Y., June 1974.

34. Falconer, B.H., "Theory of Stresses Induced in Reinforced Concret by Applied 2-Dimensional Stress", ACI Journal, Proc. Vol. 53, No. 3, September 1956, pp. 277-293.

35. Fardis, M.N., and Buyukozturk, O., "Shear Transfer Model for Reinforced Concrete", Journal of the Engineering Mechanics Division, ASCE, Vol. 105, No. EM2, April 1979, pp. 255-275.

36. Fattah Shaikh, A., "Proposed Revisions to Shear-Friction Provisions", PCI Journal, March/April 1978, pp. 12-21.

37. Fenwick, R.C., "The Shear Strength of Reinforced Concrete Beams", Ph.D. Thesis, University of Canterbury, Christchurch, New Zealand, 1966.

38. Fenwick, R.C., and Paulay, T., "Mechanisms of Shear Resistance of Concrete Beams", Journal of Structural Division, ASCE Vol. 94, No. ST10, Proc. Paper 2325, October 1968, pp. 2325-2350.

39. Finney, E.A., "Structural Design Considerations for Pavement Joints", ACI Journal, Proc. Vol. 53, No. 1, July 1956, pp. 1-28.

40. Flügge, W., "Static und Dynamik der Schalen", 3rd ed., Berlin, Springer-Verlag, 1962.

41. Franklin, H.A., "Non-Linear Analysis of Reinforced Concrete Frames and Panels", Ph.D. Thesis, University of California, Berkeley, 1970 (also as a Report No. SESM-70-5).

42. Friberg, B.F., "Design of Dowels in Transverse Joints of Concrete Pavements", Transactions, ASCE, Vol. 105, 1940, pp. 1076-1116.

43. Geistefeldt, H., "Stahlbetonscheiben im Gerissenen Zustand -Berechnung mit Berücksichtigung der rissabhängigen Schubsteifigkeit im Materialgesetz", Bericht No. 76-19, Institut für Static der Technischen Universität Braunschweig, Braunschweig, 1976.

44. Geistefeldt, H., "Constitutive Equations for Cracked Reinforced Concrete Based on a Refined Model", IV SMiRT, Structural Mechanics in Reactor Technology, Paper H5/2, San Francisco, 1977.

45. Gergely, P., and Lutz, L.A., "Maximum Crack Width in Reinforced Concrete Flexural Members", ACI Special Publication SP 20, 1968.

46. Gergely, P., "Splitting Cracks Along the Main Reinforcement in Concrete Members", Department of Structural Engineering, Report to Bureau of Public Roads U.S. Department of Transportation, Contract CPR-11-3627, Cornell University, Ithaca, N.Y., April 1969.

47. Gergely, P., and Smith, J.K., "Seismic Response of Cracked Cylindrical Concrete Structures", Proceedings of the U.S. National Conference on Earthquake Engineering, Stanford University, Stanford, California, August 1979, pp. 185-192.

48. Gilbert, R.I., and Warner, R.F., "Tension Stiffening in Reinforced Concrete Slabs", Journal of Structural Division, ASCE, Vol. 104, No. ST12, December 1978, pp. 1885-1900.

49. Goto, Y., "Cracks Formed in Concrete Around Deformed Tension Bars", ACI Journal, Proceedings Vol. 68, No. 4, April 1971, pp. 244-251.

50. Gupta, A.K., Discussion of "Proposed Addition to Proposed ACI Standard: Code Requirements for Nuclear Safety Related Concrete Structures", by ACI Committee 349, ACI Journal, Proceedings Vol. 73, No. 7, July 1976, pp. 431-432.

51. Gupta, A.K., "Membrane Reinforcement in Shells", IIT Research Institute Report 78J061, Eng. Division, Chicago, Illinois, July 1978.

52. Hand, F.R., Pecknold, D.A., and Schnobrich, W.C., "Non-Linear Layered Analysis of Reinforced Concrete Plates and Shells", Journal of the Structural Division, ASCE, Vol. 99, No. ST7, Proc. Paper 9860, July 1973.

53. Hermansen, B.R., and Cowan, J., "Modified Shear-Friction Theory for Bracket Design", ACI Journal, Proceedings Vol. 71, No. 2, February 1974, pp. 55-60.

54. Hofbeck, J.A., Ibrahim, I.O., and Mattock, A.H., "Shear Transfer in Reinforced Concrete", ACI Journal, Proc. Vol. 66, No. 2, February 1969, pp. 119-128.

55. Holland, I., and Munkeby, E., Discussion of the paper by Isenberg and Adham, "Analysis of Orthotropic Reinforced Concrete Structures", Journal of the Structural Division, ASCE, Vol. 97, No. ST10, October 1971, pp. 2607-2610.

56. Holmberg, A., and Lindgren, S., "Crack Spacing and Crack Widths due to Normal Force or Bending Moment", National Swedish Building Research, Document D2, 1970.

57. Holmberg, A., and Lindgren, S., "Cracks in Concrete Walls", National Swedish Building Research, Document D7, 1972.

58. Houde, J., "Study of Force-Displacement Relationship for the Finite Element Analysis of Reinforced Concrete", Structural Concrete Series, No. 73-2, McGill University, Montreal, December 1973.

59. Isenberg, J., and Adham, S., "Analysis of Orthotropic Reinforced Concrete Structures", Journal of the Structural Division, ASCE, Vol. 96, No. ST12, Proc. Paper 7782, December 1970, pp. 2607-2623.

60. Ismail, M.A.F., and Jirsa, J.O., "Bond Deterioration in Reinforced Concrete Subject to Low Cycle Loads", ACI Journal, Proceedings Vol. 69, No. 6, June 1972, pp. 334-343.

61. Jimenez, R., Gergely, P., and White, R.N., "Shear Transfer Across Cracks in Reinforced Concrete", Report 78-4, Department of Structural Engineering, Cornell University, Ithaca, N.Y., August 1978.

62. Jimenez, R., Perdikaris, P.C., Gergely, P., and White, R.N., "Interface Shear Transfer and Dowel Action in Cracked Reinforced Concrete Subject to Cyclic Shear", Proceedings of the Specialty Conference on "Methods of Structural Analysis", ASCE, Vol. 1, University of Wisconsin, Madison, August 1976, pp. 457-475.

63. Johnston, D.W., and Zia, P., "Analysis of Dowel Action", Journal of the Structural Division, ASCE, Vol. 97, No. ST5, May 1971, pp. 1611-1630.

64. Jones, R., "The Ultimate Strength of Reinforced Concrete Beams in Shear", Magazine of Concrete Research, Vol. 8, August 1956.

65. Kani, G.N.J., "The Riddle of Shear Failure and Its Solution", ACI Journal, Proceedings Vol. 61, No. 4, April 1964.

66. Kemp, E.L., Brezny, F.S., and Unterspan, J.A., "Effect of Rust and Scale on the Bond Characteristics of Deformed Reinforcing Bars", ACI Journal, Proceedings Vol. 65, No. 9, September 1968, pp. 743-756.

67. Kemp, E.L., Wilhelm, W.J., and Chen, N.J., "An Investigation of the Parameter Influencing Bond Behavior with a View towards Establishing Design Criteria", Final Report No. FHWA-WV-77-6, Department of Civil Engineering, West Virginia University, Morgantown, West Virginia, November 1977.

68. Krefeld, W.J., and Thurston, C.W., "Contribution of Longitudinal Steel to Shear Resistance of Reinforced Concrete Beams", ACI Journal, Proceedings Vol. 63, No. 3, March 1966, pp. 325-344.

69. Krishnamoorthy, C.S., and Panneerselvam, A., "A Finite Element Model for Non-Linear Analysis of Reinforced Concrete Framed Structures", The Structural Engineer, No. 8, Vol. 55, August 1977, pp. 331-338.

70. Laible, J.P., White, R.N., and Gergely, P., "An Experimental Investigation of Seismic Shear Transfer Across Cracks in Concrete Nuclear Containment Vessels", ACI Special Publication SP 53-9, "Reinforced Concrete Structures in Seismic Zones", Detroit, Michigan, 1977, pp. 203-226.

71. Lenschow, R.J., and Sozen, M.A., "A Yield Criterion for Reinforced Concrete under Biaxial Moments and Forces", Civil Engineering Studies, Structural Research Series No. 311, University of Illinois, Urbana, Illinois, July 1966.

72. Lenschow, R.J., and Sozen, M.A., "A Yield Criterion for Reinforced Concrete Slabs", ACI Journal, Proceedings Vol. 64, No. 5, May 1967, pp. 266-273.

73. Leombruni, P., Buyukozturk, O., and Connor, J.J., "Analysis of Shear Transfer in Reinforced Concrete with Application to Containment Wall Specimens", Report R79-26, Department of Civil Engineering, Massachusetts Institute of Technology, June 1979.

74. Leonhardt, F., "Vorlesungen über Massivbau, Vierter Teil, Nachweis der Gebrauchsfahigkeit", Springer-Verlag, 1976.

75. Lin, C.S., and Scordelis, A.C., "Nonlinear Analysis of Reinforced Concrete Shells of General Form", Journal of Structural Division, ASCE, Vol. 101, No. ST3, March 1975, pp. 523-538.

76. Loeber, P.J., "Shear Transfer by Aggregate Interlock", M.E. Thesis, University of Canterbury, Christchurch, New Zealand, 1970.

77. Lutz, L.A., "Information on the Bond of Deformed Bars from Special Pullout Tests", ACI Journal, Proceedings Vol. 67, No. 11, November 1970, pp. 885-887.

78. Lutz, L.A., and Gergely, P., "Mechanics of Bond and Slip of Deformed Bars in Concrete", ACI Journal, Proceedings Vol. 64, November 1967, pp. 711-721.

79. Marcus, H., "Load Carrying Capacity of Dowels at Transverse Pavement Joints", ACI Journal, Proc. Vol. 48, No. 2, October 1951.

80. Mast, R.F., "Auxiliary Reinforcement in Concrete Connections", Journal of the Structural Division, ASCE, Vol. 94, No. ST6, June 1968, pp. 1485-1504.

81. Mattock, A.H., and Hawkins, N.M., "Shear Transfer in Reinforced Concrete-Recent Research", PCI Journal, Vol. 17, March/April 1972, pp. 55-75.

82. Mattock, A.H., "Effect of Aggregate Type on Single Direction Shear Transfer Strength in Monolithic Concrete", Report SM 74-2, Department of Civil Engineering, University of Washington, Seattle, Washington, August 1974.

83. Mattock, A.H., Discussion of the paper, "Modified Shear-Friction Theory for Bracket Design", by B.R. Hermansen and J. Cowan, ACI Journal, Proceedings Vol. 71, No. 8, August 1974, pp. 421-423.

84. Mattock, A.H., "The Shear Transfer Behavior of Cracked Monolithic Concrete Subject to Cyclically Reversing Shear", Report SM 74-4, Department of Civil Engineering, University of Washington, Seattle, Washington, November 1974.

85. Mattock, A.H., Johal, L., and Chow, H.C., "Shear Transfer in Reinforced Concrete with Moment or Tension Acting across the Shear Plane", PCI Journal, Vol. 20, July/August 1975, pp. 76-93.

86. Mattock, A.H., "Shear Transfer under Monotonic Loading across an Interface between Concretes Cast at Different Times", Report SM 76-3, Department of Civil Engineering, University of Washington, Seattle, Washington, September 1976.

87. Mills, G.M., "A Partial Kinking Yield Criterion for Reinforced Concrete Slabs", Magazine of Concrete Research, Vol. 27, No. 90, March 1975, pp. 13-22.

88. Mirza, M.S., and Houde, J., "A Finite Element Analysis of Shear Strength of Reinforced Concrete Beams", ACI Special Publication SP 42-5, Vol. 1, "Shear in Reinforced Concrete", Detroit, Michigan, 1974, pp. 103-128.

89. Mirza, S.M., and Houde, J., "Study of Bond Stress-Slip Relationships in Reinforced Concrete", ACI Journal, Proceedings Vol. 76, No. 1, January 1979, pp. 19-46.

90. Morita, S., Discussion of the paper "Effects of Arrangements of Reinforcement on Crack Width and Spacing of Reinforced Concrete Members" by B.B. Broms and L.A. Lutz, ACI Journal, Proceedings Vol. 62, No. 6, June 1966, pp. 1807-1812.

91. Murashev, V.I., "Calculation of Crack Width and Flexural Rigidity of Reinforced Concrete Members Subjected to Bending", Symposium on Bond and Crack Formation in Reinforced Concrete, Stockholm, 1957.

92. Nawy, E.G., and Blair, K., "Further Studies on Flexural Crack Control in Structural Slab Systems", ACI Special Publication SP30-1, "Cracking, Deflection, and Ultimate Load of Concrete Systems", Detroit, Michigan, 1971, pp. 1-41.

93. Nielsen, M.P., and Braestrup, M.W., "Plastic Shear Strength of Reinforced Concrete Beams", Report No. R73, Structural Research Laboratory, Technical University of Denmark, 1976.

94. Nilson, A.H., "Bond Stress-Slip Relations in Reinforced Concrete", Report No. 345, Department of Structural Engineering, Cornell University, Ithaca, N.Y., December 1971.

95. Nowlen, W.J., "Influence of Aggregate Properties on Effectiveness of Interlock Joints in Concrete Pavements", PCA Research of Development Laboratories, Bulletin D139, 1968.

96. Oesterle, R.G, and Russell, H.G., "Tangential Shear Tests of Reinforced Concrete Containment Elements", presented at the 5th SMiRT Conference, Berlin, August 1979 (also to be published in "Nuclear Engineering and Design").

97. Paulay, T., and Loeber, P.J., "Shear Transfer by Aggregate Interlock", ACI Special Publication SP 42-1, "Shear Transfer in Reinforced Concrete", Vol. 1 , Detroit, Michigan, 1974, pp. 1-15.

98. Paulay, T., Park, R., and Phillips, M.H., "Horizontal Construction Joints in Cast-in-Place Reinforced Concrete", ACI Special Publication SP-42-27, "Shear in Reinforced Concrete", Vol. 2, Detroit, Michigan, 1974, pp. 599-616.

99. PCI Committee on Connection Details, PCI Manual on Design of Connections for Precast Prestressed Concrete, Prestressed Concrete Institute, Chicago, 1973, pp. 22.

100. Peter, J., "Zur Bewehrung von Scheiben und Schalen für Hauptspannungen Schiefwinklig zur Bewehrungsrichtung", Dissertation TH Stuttgart, 1964 (also in Die Bautechnik, Vol. 43, No. 5, May 1966, pp. 149-154, and Vol. 43, No. 7, July 1966, pp. 240-248).

101. Rao, P.S., "Unlagerung der Schnittkräfte in Stahlbetonkonstruktionen", Deutscher Ausschuss für Stahlbeton, Heft 177, Berlin, 1966.

102. Raths, C.H., Discussion of the paper, "Design Proposals for Reinforced Concrete Corbels", by A.H. Mattock, PCI Journal, Vol. 22, No. 2, March/April 1977, pp. 93-98.

103. Salem, M.H., and Mohraz, B., "Nonlinear Analysis of Planar Reinforced Concrete Structures", Civil Engineering Studies, Structural Engineering Series No. 410, University of Illinois, Urbana, Illinois, July 1974.

104. Scanlon, A., "Time Dependent Deflections of Reinforced Concrete Slabs", Ph.D. Thesis presented at the University of Alberta, Edmonton, Alberta, Canada, 1971.

105. Schaefer, H., "Zur Berechnung von Stahlbetonplatten", Dissertation, T.H. Darmstadt, 1976.

106. Scordelis, A.C., Ngo, D., and Franklin, H.A., "Finite Element Study of Reinforced Concrete Beams with Diagonal Tension Cracks", UC SESM Report No. 70-19, University of California, Berkeley, December 1970.

107. Sharma, N.K., "Splitting Failures in Reinforced Concrete Members", Ph.D. Thesis, Department of Structural Engineering, Cornell University, Ithaca, N.Y., 1969.

108. Smith, J.K., Gergely, P., and White, R.N., "The Effects of Cracks on the Seismic Analysis of Reinforced Concrete Nuclear Containment Vessels", Research Report No. 368, Department of Structural Engineering, Cornell University, Ithaca, N.Y., April 1977 (also published as a Ph.D. Thesis in the Department of Structural Engineering, Cornell University , May 1977).

109. Stanton, J., "The Dowel Action of Reinforcement and the Nonlinear Dynamic Analysis of Concrete Nuclear Containment Vessels", M.S. Thesis, Cornell University, Ithaca, N.Y., August 1976.

110. Suidan, M., and Schnobrich, W.C., "Finite Element Analysis of Reinforced Concrete", Journal of the Structural Division, ASCE, Vol. 99, No. ST10, October 1973, pp. 2109-2122.

111. Swoboda, G., "Rissuntersuchungen in Stahlbetonbalken und Scheiben mit Hilfe des L.S.T.-Element", Der Bauingenieur, Vol. 50, No. 12, 1975, pp. 465-468.

112. Tanner, J.A., "An Experimental Investigation of Bond Slip in Reinforced Concrete", M.S. Thesis, Department of Structural Engineering, Cornell University, Ithaca, N.Y., December 1971.

113. Tassios, T.P., "Properties of Bond between Concrete and Steel under Load Cycles Idealizing Seismic Actions", State of the Art Report presented at the AICAP-CEB Symposium of Structural Concrete under Seismic Action, May 1979, Rome.

114. Taylor, H.P.J., "Shear Stresses in Reinforced Concrete Beams in Shear", Magazine of Concrete Research, Vol. 8, August 1956, pp. 69-84.

115. Taylor, H.P.J., "Investigation of the Dowel Shear Forces Carried by the Tensile Steel in Reinforced Concrete Beams", Cement and Concrete Association, TRA-431, November 1969.

116. Taylor, H.P.J., "Investigation of the Forces Carried across Cracks in Reinforced Concrete Beams in Shear by Interlock of the Aggregate", Cement and Concrete Association, Report No. 42.447, London, November 1970.

117. Taylor, H.P.J., "The Fundamental Behavior of Reinforced Concrete Beams in Bending and Shear", ACI Special Publication SP 42-3, "Shear in Reinforced Concrete", Vol. 1, Detroit, Michigan, 1974, pp. 43-77.

118. Taylor, R., "A Note of the Mechanism of Diagonal Cracking in Reinforcement", Magazine of Concrete Research, Vol. 11, No. 31, March 1959, pp. 151-158.

119. Thuerlimann, B., "Shear Strength of Reinforced and Prestressed Concrete Beams- CEB Approach", and "Torsional Strength of Reinforced and Prestressed Concrete -CEB Approach", Lecture, ACI Symposium at Philadelphia, 1976.

120. Walraven, J.C., "Mechanisms of Shear Transfer in Cracks in Concrete", A Survey of Literature, Stevin Laboratory, Report 5-78-12, University of Technology, Delft, Holland, December 1978.

121. Watstein, D., and Bresler, B., "Bond and Cracking in Reinforced Concrete", Ch. 4, "Reinforced Concrete Engineering", Vol. 1, edited by B. Bresler, John Wiley & Sons, New York, N.Y., 1974, pp. 151-193.

122. Watstein, D., and Mathey, R.G., "Evaluation of Width of Cracks in Concrete at the Surface of Reinforcing Steel by means of Tensile Bond Specimens", Symposium on Bond and Crack Formation in Reinforced Concrete, Stockholm, 1957.

123. Watstein, D., and Mathey, R.G., "Width of Cracks in Concrete at the Surface of Reinforcing Steel Evaluated by means of Tensile Bond Specimens", ACI Journal, Proceedings Vol. 56, No. 1, July 1959, pp. 47-56.

124. Watstein, D., and Mathey, R.G., "Strains in Beams Having Diagonal Cracks", ACI Journal, Proceedings Vol. 55, No. 4, December 1958.

125. Wegner, R., "Tragverhalten von Stahlbetonplatten mit Nichtlinearen Materialgesetzen im Gerissenen Zustand-Finite-Element-Methode", Bericht Nr. 74-11, Institut für Static, TU Braunschweig, Braunschweig, 1974.

126. White, R.N., and Holley, M.J., "Experimental Studies of Membrane Shear Transfer", Journal of the Structural Division, ASCE, Vol. 98, No. ST8, Proc. Paper 9145, August 1972, pp. 1835-1852.

127. White, R.N., and Gergely, P., "Shear Transfer in Thick-Walled Reinforced Concrete Structures under Seismic Loading", Report No. 75-10, Department of Structural Engineering, Cornell University, Ithaca, N.Y., 1975.

128. Yuzugullu, O., and Schnobrich, W.C., "A Numerical Procedure for the Determination of the Behavior of a Shear Wall Frame System", ACI Journal, Proceedings Vol. 70 , July 1973, pp. 474-479.

129. Zienkiewicz, O.C., Phillip's, D.V., and Owen, P.R.J., "Finite Element Analysis of Some Concrete Non-Linearities - Theory and Examples", Proceedings of the Seminar "Concrete Structures Subjected to Triaxial Stresses", Bergamo, Italy, May 1974.

APPENDIX A

Table A.1. Test results at peak shear stress levels for all specimens under combined biaxial tension and shear, reinforced with No.6 reinforcing bars (all units are in (in x 10^{-3})).

Notes: †Questionable data, *Failure.

	MONOTONICALLY LOADED SPECIMENS																			
Shear Stress	.0(M)					.3(M)					.6(M)					.9(M)				
v(psi)	C1	S1	C2	S2	Δd	C1	S1	C2	S2	Δd	C1	S1	C2	S2	Δd	C1	S1	C2	S2	Δd
0	0	0	0	0	0	0	0	0	0	0	0	0	0	0	0	0	0	0	0	0
25	-	-	-	-	-		-0.8	2.3	-3.1	12.8	2	3	2	4	26	1	-11	0	5	83
50	3.3	-0.1	2.0	0.9	5.8	-	-1.2	1.2	-3.1	19.0	3	5	6	8	40	1	-13	-1	5	88
75	2.8	-0.6	1.8	1.5	10.3	-	-1.6	1.0	-3.6	23.5	7	6	11	9	54	1	-13	-2	5	90
100	2.2	-1.3	1.7	2.3	15.3	-	-1.8	-0.3	-3.9	28.7	8	6	15	10	64	1	-15	-2	5	96
125	1.5	-1.9	1.6	3.0	20.0	-	-1.9	-2.4	-4.3	36.2	9	6	18	10	72	1	-16	-3	5	101
150	1.0	-2.6	1.6	3.9	25.0	-	-2.0	-2.8	-4.5	39.2	10	6	20	10	80	1	-17	-4	5	109
175	0.6	-3.7	1.4	4.4	30.2	-	-2.0	-3.7	-4.8	44.6	11	6	21	11	89	1	-18	-5	6	118
200	1.0	-6.1	0.7	4.2	37.4	-	-1.9	-5.0	-5.0	51.9	11	6	23	11	96	2	-19	-5	6	136
225	1.2	-7.9	0.1	3.9	42.2	-	-1.7	-6.0	-5.2	59.9	12	6	23	12	104	2	-20	-6	7	170
250	2.1	-10.2	-0.3	4.4	48.6	-	-1.5	-6.8	-5.6	67.1	12	7	24	12	112	2	-20	-6	7	242
275	2.1	-11.5	-0.4	2.6	52.4	-	-1.3	-6.8	-6.4	71.8	12	7	25	12	123	2	-20	-6	7	318
300	1.6	-13.5	-0.7	-1.0	59.0	-	-1.0	-6.6	-9.4	77.4	13	7	25	12	141	3*	-18†	-3†	7	441*
325	1.6	-14.9	-0.7	-2.6	63.9	-	-0.8	-6.7	-11.1	81.0	13	7	25	12	182	-	-	-	-	-
350	1.6	-17.4	-0.9	-3.9	71.8	-	-0.7	-6.8	-13.4	86.9	13	7	26	13	265	-	-	-	-	-
375	1.6	-18.4	-1.9	-4.7	77.6	-	-0.6	-6.8	-14.3	91.1	13*	7	27	13	401*	-	-	-	-	-
400	1.4	-18.6	-3.5	-5.5	87.2	-	-1.0	-3.4	-14.1	98.2	-	-	-	-	-	-	-	-	-	-
425	1.4	-19.4	-4.4	-6.3	95.4	-	-1.0	-2.6	-14.3	103.4	-	-	-	-	-	-	-	-	-	-
450	1.8	-26.6	-5.7	-6.3	111.4	-	-0.7	0.3	-14.8	120.7	-	-	-	-	-	-	-	-	-	-
475	1.9†	-31.1†	-6.5†	-5.2†	145.0†	-	-1.0*	1.3	-15.2	156.2*	-	-	-	-	-	-	-	-	-	-
480	*	-	-	*	200.0†	-	-	-	-	-	-	-	-	-	-	-	-	-	-	-

Table A.1. (Continued)

Spec. No.	Peak Shear Stress v(psi)	CYCLICALLY LOADED SPECIMENS														
		Cycle 1					Cycle 2					Cycle 10				
		C1	S1	C2	S2	Δd	C1	S1	C2	S2	Δd	C1	S1	C2	S2	Δd
	+25	3.5	-1.0	9.5	3.0	15.0	9.5	-4.0	13.0	6.5	30.0	16.0	-3.5	15.5	6.5	32.0
	-25	7.5	1.0	10.0	4.0	17.0	11.5	0.5	15.0	5.0	18.0	15.5	1.0	17.0	0.5	15.0
	+50	20.0	-5.0	19.5	7.0	34.0	22.5	-5.0	20.5	6.0	34.0	26.5	-5.0	21.0	5.5	33.0
	-50	17.5	1.0	17.5	0.5	19.0	20.0	1.5	18.0	-0.5	22.0	21.0	2.0	18.5	-2.5	27.0
	+75	27.0	-5.5	22.0	5.5	36.0	27.0	-6.0	22.5	5.5	38.0	31.0	-9.0	26.0	2.5	44.0
	-75	21.5	2.0	18.5	-3.0	31.0	20.5	2.0	18.5	-2.5	31.0	25.0	2.5	21.0	-4.0	35.0
	+100	33.5	-9.5	27.0	3.5	49.0	34.5	-9.5	27.0	3.0	47.0	37.0	-11.5	30.0	1.0	42.0
	-100	24.0	2.5	20.0	-5.0	41.0	26.0	3.0	21.0	-5.0	47.0	24.5	3.5	21.0	-7.5	60.0
	+125	37.0	-12.0	30.0	0.5	42.0	37.0	-12.5	30.5	-0.5	45.0	38.0	-15.0	32.0	-5.5	42.0
.9(A)	-125	26.0	3.5	22.0	-7.0	62.0	25.5	4.0	22.0	-8.0	66.0	21.5	3.5	23.5	-10.5	80.0
	+150	38.5	-15.5	32.5	-7.0	46.0	39.0	-17.0	33.0	-9.5	44.0	41.5	-23.0	35.0	-20.0	46.0
	-150	21.5	3.5	23.0	-11.0	82.0	23.0	4.0	24.5	-12.0	88.0	21.0	4.0	27.0	-14.5	108.0
	+175	42.0	-23.5	35.5	-23.5	46.0	42.0	-24.5	36.5	-26.5	63.0	45.5	-28.5	36.5	-28.0	111.0
	-175	20.5	5.0	27.5	-19.5	106.0	21.0	4.5	27.5	-20.5	107.0	17.5	3.0	26.5	-29.0	100.0
	+200	50.0	-34.0	37.5	-30.0	140.0	54.0	-38.5	39.0	-31.0	155.0	54.0	-45.5	33.0	-31.5	187.0
	-200	16.5	-1.5	29.5	-38.0	98.0	12.5	-1.5	26.5	-43.5	104.0	1.5	1.5	24.5	-61.0	-
	+225	51.5	-48.0	35.5	-32.5	190.0	52.0†	-49.0†	34.5†	-34.0†	203.0†	-	-	-	-	-
	-225	-6.5	1.0	26.0	-65.0	200.0	-7.5†	1.0†	24.5†	-67.0†	198.0†	-	-	-	-	-
		(the loading for Cycle 2 was not incremental)														
	+125	5.5	-19.5	5.5	4.0	77.0	2.0	-21.0	7.0	2.5	78.0	3.0	-27.5	11.0	-4.0	83.0
	-125	6.5	14.0	13.5	-12.0	63.0	5.0	14.5	15.0	-14.5	68.0	10.0	10.5	19.5	-23.0	85.0
	+175	0.5	-32.5	10.5	-4.0	92.0	-1.0	-34.0	11.5	-8.5	81.0	-7.0	-45.0	13.0	-9.0	82.0
.9(B)	-175	9.5	7.5	20.0	-25.5	94.0	9.5	8.5	21.5	-30.5	116.0	7.0	-1.0	24.0	-35.5	142.0
	+225	-17.5	-51.5	14.0	-9.5	97.0	-33.0	-65.5	5.5	-8.5	136.0	-	-	-15.5	11.0	338.0
	-225	4.5	1.0	26.0	-42.5	172.0	-7.5	-2.5	24.0	-36.0	216.0	-	-	21.5	-25.0	352.0
	+275	-	-	-20.0	15.5	390.0	-	-	-	-	-	-	-	-	-	-
	-275	-	-	20.5	1.0†	692.0	-	-	-	-	-	-	-	-	-	-

Table A.1 (Continued)

Spec. No.	Peak Shear Stress v(psi)	CYCLICALLY LOADED SPECIMENS														
		Cycle 1					Cycle 2					Cycle 10				
		C1	S1	C2	S2	Δd	C1	S1	C2	S2	Δd	C1	S1	C2	S2	Δd
	+125	-4.0	-20.5	-	12.0	62.0	-2.0	-20.0	-	12.0	58.0	-1.0	-22.7	-	10.5	50.0
	-125	-2.0	7.0	-	-5.5	40.0	-2.0	7.4	-	-6.0	42.0	-3.0	5.0	-	-4.7	50.0
	+175	-2.0	-33.5	-	14.5	76.0	-1.5	-34.0	-	14.5	77.0	-0.5	-32.3	-	12.3	70.0
	-175	-3.0	3.5	-	-5.5	59.0	-3.2	4.0	-	-5.5	61.0	-3.6	8.5	-	-10.3	84.0
.6(A)	+225	-1.5	-33.2	-	10.8	71.0	-1.5	-33.7	-	10.8	72.0	-1.7	-33.3	-	8.3	74.0
	-225	-5.0	11.0	-	-12.9	100.0	-5.1	11.3	-	-13.2	103.0	-9.5	15.1	-	-18.7	125.0
	+275	-2.4	-33.9	-	8.8	84.0	-3.6	-35.8	-	8.7	93.0	-3.0	-40.3	-	9.5	131.0
	-275	-10.5	15.7	-	-19.3	134.0	-11.9	15.5	-	-20.5	142.0	-14.0	15.7	-	-24.5	175.0
	+325	-5.5	-47.8	-	9.0	-*	-	-	-	-	-	-	-	-	-	-
	-325	-16.8	18.9	-	-22.5	-*	-	-	-	-	-	-	-	-	-	-
	+125	13.0	-3.0	-3.0	1.0	27.0	13.0	-2.5	-5.0	-2.5	31.0	14.5	-3.0	-9.0	-9.5	40.0
	-125	-7.5	4.5	1.0	-15.5	50.0	-6.5	4.5	3.0	-16.5	56.0	-7.0	2.5	3.5	-24.0	67.0
	+175	15.0	-3.5	-9.5	-11.0	46.0	14.0	-4.0	-9.5	-12.0	49.0	-10.0	-6.0	-5.5	-19.5	51.0
.6(B)	-175	-8.0	2.5	4.0	-26.5	72.0	-8.0	2.5	4.0	-27.0	76.0	-27.0	1.0	7.0	-32.0	93.0
	+225	-12.0	-7.0	-5.5	-21.0	57.0	-12.0	-7.0	-5.0	-21.5	58.0	-20.5	-8.0	-4.0	-26.0	70.0
	-225	-28.0	1.0	8.5	-33.5	101.0	-28.0	1.0	8.0	-32.5	102.0	-29.0	0.0	9.0	-35.5	117.0
	+275	-24.5	-10.0	-4.5	-27.5	80.0	-27.0	-10.0	-5.0	-28.0	81.0	-13.0	-4.0	-4.0	-24.0	-*
	-275	-30.0	0.0	9.0	-35.5	129.0	-30.0	0.0	9.5	-35.0	150.0	-5.5†	-4.0†	3.0†	-31.5†	-*

Table A.1. (Continued)

Spec. No.	Peak Shear Stress v(psi)	CYCLICALLY LOADED SPECIMENS													
		Cycle 1					Cycle 2					Cycle 10			
		C1	S1	C2	S2	Δd	C1	S1	C2	S2	Δd	C1	S1	C2	S2	Δd
.3(A)	+125	-1.0	-4.0	-1.0	3.0	30.0	-1.0	-3.0	0.0	3.0	34.0	-1.0	-1.0	0.0	4.0	39.0
	-125	0.0	3.0	7.0	2.0	13.0	-1.0	3.0	7.0	2.0	12.0	-1.0	3.0	7.0	2.0	11.0
	+175	0.0	-1.0	-1.0	5.0	48.0	0.0	0.0	-1.0	5.0	51.0	0.0	1.0	-1.0	6.0	53.0
	-175	0.0	4.0	8.0	2.0	9.0	0.0	4.0	7.0	1.0	11.0	0.0	4.0	8.0	2.0	17.0
	+225	0.0	2.0	-1.0	6.0	56.0	1.0	3.0	0.0	6.0	57.0	2.0	3.0	0.0	7.0	59.0
	-225	0.0	4.0	8.0	1.0	23.0	1.0	4.0	9.0	1.0	26.0	1.0	5.0	9.0	1.0	32.0
	+275	2.0	3.0	1.0	7.0	63.0	2.0	3.0	1.0	7.0	64.0	2.0	2.0	1.0	8.0	72.0
	-275	1.0	5.0	9.0	0.0	39.0	1.0	5.0	8.0	0.0	41.0	1.0	6.0	8.0	2.0	45.0
	+325	2.0	2.0	1.0	8.0	76.0	2.0	1.0	1.0	8.0	77.0	1.0	1.0	2.0	9.0	78.0
	-325	-1.0	6.0	8.0	2.0	53.0	-2.0	6.0	8.0	2.0	57.0	-5.0	6.0	8.0	3.0	62.0
	+375	1.0	1.0	2.0	9.0	80.0	0.0	2.0	2.0	9.0	80.0	-	-	-	-	-
	-375	-7.0	6.0	8.0	2.0	72.0	-7.0	6.0	8.0	2.0	78.0	-	-	-	-	-
.3(B)	+125	2.0	0.1	4.8	-4.2	29.0	2.0	0.5	5.9	-3.9	30.0	2.0	0.4	6.0	-4.4	37.0
	-125	0.0	0.0	5.8	1.3	10.0	0.0	0.5	6.9	1.4	10.0	0.0	0.2	7.6	2.4	14.0
	+175	2.0	0.4	5.9	-4.8	44.0	2.5	0.4	6.3	-2.6	44.0	3.0	0.1	6.1	-0.6	45.0
	-175	0.5	-0.4	7.4	3.6	20.0	0.5	-0.8	7.4	4.3	22.0	0.5	-1.5	7.1	5.6	27.0
	+225	3.0	0.0	6.1	-1.0	50.0	3.5	0.2	6.3	-0.8	50.0	4.0	0.5	7.4	-0.8	41.0
	-225	1.0	-1.7	7.1	6.3	32.0	1.0	-1.7	7.0	6.4	35.0	0.5	-1.6	4.0	7.5	43.0
	+275	4.0	0.6	7.2	-1.4	45.0	4.0	0.9	6.9	-2.0	46.0	4.0	1.0	7.0	-2.4	44.0
	-275	0.0	-1.6	1.6	8.3	48.0	0.0	-1.5	1.7	8.0	47.0	0.0	-2.3	1.7	8.9	45.0
	+325	4.0	1.2	7.0	-3.2	47.0	4.0	1.1	6.7	-3.7	48.0	6.0	0.3	7.4	-3.7	44.0
	-325	0.0	-3.1	0.0	9.3	53.0	-0.5	-3.7	-0.3	9.5	55.0	2.0	-11.5	0.6	9.1	68.0
	+375	7.5	0.4	7.5	-4.4	49.0	8.0	0.7	5.5	-5.6	54.0	-	-	-	-	-
	-375	3.0	-10.7	-0.8	10.0	82.0	2.5	-11.3	-0.5	9.1	92.0	-	-	-	-	-

Table A.1. (Continued)

Spec. No.	Peak Shear Stress v(psi)	CYCLICALLY LOADED SPECIMENS														
		Cycle 1					Cycle 2					Cycle 10				
		C1	S1	C2	S2	Δd	C1	S1	C2	S2	Δd	C1	S1	C2	S2	Δd
	+125	0.7	0.3	-2.6	-3.1	2.6	0.2	0.5	-2.2	-3.5	4.6	-1.2	0.2	0.3	-5.3	5.2
	-125	0.5	-0.5	5.9	6.2	18.6	-0.7	-0.6	6.6	7.0	19.6	-2.4	-0.6	7.7	7.8	19.6
	+175	-2.0	0.1	-0.2	-7.7	8.4	-2.8	-0.2	0.4	-8.5	9.4	-2.8	-0.3	4.3	-11.4	15.9
	-175	-5.1	-0.4	8.8	8.5	19.4	-6.4	-0.4	8.7	8.0	17.8	-7.5	0.2	9.2	6.8	18.3
	+225	-3.2	-0.2	4.7	-13.8	20.8	-3.0	-0.2	5.2	-14.3	21.6	-3.0	-0.5	6.3	-14.0	22.3
	-225	-9.7	0.4	9.6	7.7	20.0	-10.3	0.3	9.6	8.0	21.7	-10.3	-0.2	9.9	8.5	25.2
.0(A)	+275	-3.6	-0.7	6.0	-17.1	27.8	-3.6	-0.8	5.8	-17.3	29.2	-3.4	-0.7	6.3	-15.2	29.5
	-275	-11.5	-0.7	10.3	8.0	31.0	-10.5	-2.1	10.4	6.9	33.6	-8.5	-3.6	11.0	7.7	35.1
	+325	-3.7	-0.7	5.2	-18.4	36.1	-3.7	-0.7	5.0	-18.1	38.0	-2.5	0.1	4.5	-19.6	42.3
	-325	-9.3	-4.5	11.4	7.1	41.8	-8.9	-4.9	11.4	6.8	43.4	-7.6	-4.5	11.2	5.9	41.7
	+375	-3.1	0.8	7.1	-17.1	46.1	-2.8	1.3	5.7	-21.8	51.5	-2.2	3.1	2.5	-48.7	73.6
	-375	-9.3	-5.3	12.4	4.3	55.2	-9.6	-5.4	12.4	3.7	57.1	-8.4	-5.3	12.4	-0.6	62.9
	+425	-3.4	3.5	2.8	-206.5†	175.4*	-	-	-	-	-	-	-	-	-	-
	-425	-	-	-	-	-	-	-	-	-	-	-	-	-	-	-
	+125	2.6	2.6	11.9	4.1	24.2	2.6	2.4	12.7	4.1	26.2	2.3	2.4	13.2	4.6	25.2
	-125	1.1	0.4	2.0	-0.3	15.7	1.2	0.3	2.2	-0.4	17.0	1.4	0.3	2.6	-0.6	18.0
	+175	2.3	2.5	13.7	4.9	28.4	2.2	2.4	13.9	5.1	29.5	-0.8†	2.3	13.6	5.3	34.2
	-175	1.5	0.2	2.2	-1.2	18.1	1.9	0.0	2.8	-1.5	18.0	1.7	-0.2	4.5	-1.4	18.6
.0(B)	+225	-2.0†	2.1	13.7	5.7	38.2	-2.6†	1.8	13.4	6.2	39.0	-2.7†	1.3	13.6	6.6	42.3
	-225	1.9	-0.7	4.2	-1.5	17.9	2.1	-0.9	4.1	-1.1	16.8	2.2	-1.5	5.3	-0.3	16.8
	+275	-3.8†	0.7	13.6	6.9	46.6	-3.1†	0.1	13.6	7.4	45.6	-3.3†	-0.2	13.1	7.5	48.2
	-275	2.3	-3.1	4.6	-0.2	19.5	1.6	-3.9	4.7	0.3	20.4	1.7	-2.9	5.3	-0.4	20.2
	+325	-3.7†	-0.2	13.0	6.2	53.3	-3.8†	0.1	12.9	6.3	55.2	-3.7†	-0.1	12.4	6.0	55.8
	-325	0.4	-2.3	4.0	-0.3	24.4	0.7	-1.6	3.5	-0.1	26.5	0.4	-0.3	2.7	1.3	27.4
	+375	-5.1†	0.7	12.2	6.3	68.3	-4.9†	0.9	12.1	6.5	63.4	-8.4†	-1.0	11.0	5.6	69.7

Table A.1. (Continued)

Spec. No.	Peak Shear Stress v(psi)	CYCLICALLY LOADED SPECIMENS														
		Cycle 1					Cycle 2					Cycle 10				
		C1	S1	C2	S2	Δd	C1	S1	C2	S2	Δd	C1	S1	C2	S2	Δd
	-375	0.2	0.8	1.8	1.9	29.6	0.0	1.6	1.0	2.9	26.2	-	(No Reading)			-
.0(B)	+425	-9.5†	-1.4	11.6	5.9	104.6	-8.8†	-1.6	13.3	6.2	153.6					
Cont.	-425	-	(No Reading)			-	-	(No Reading)			-	(Failed at 3rd Cycle)				
	0	-	-	-	-	0										
	+125	-	-	-	-	32.0										
	+150	-	-	-	-	35.0										
	+175	-	-	-	-	45.0										
.9(C)	+200	-	-	-	-	53.0										
	+225	-	-	-	-	67.0										
	+250	-	-	-	-	111.0										
	+250	-	-	-	-	172.0	-	-	-	-	301.0					
	-250	-	-	-	-	136.0	-	-	-	-	402.0					
	0	0.0	0.0	0.0	0.0	0.0										
	+125	-2.2	5.1	-2.3	-6.4	23.9										
	+150	-1.8	6.3	-1.8	-6.9	28.8										
	+175	-1.8	7.2	-1.7	-6.9	31.8										
	+200	-1.7	9.1	-1.5	-6.4	37.8										
	+225	-0.1	10.3	-1.5	-6.5	43.4										
.6(C)	+250	0.9	11.6	-1.5	-7.1	52.6										
	+275	1.3	12.1	-1.4	-7.4	58.2										
	+300	2.5	13.6	-1.3	-8.0	82.8										
	+300	3.3	15.2	-0.8	-7.1	129.4	1.8	17.2	-1.3	-2.1	188.7					
	-300	-22.6	9.3	-9.3	-7.6	127.4	-22.6	14.2	-12.4	-7.0	194.2	(Failed at 7th Cycle)				

Table A.1. (Continued)

Spec. No.	Peak Shear Stress v(psi)	CYCLICALLY LOADED SPECIMENS														
		Cycle 1					Cycle 2					Cycle 10				
		C1	S1	C2	S2	Δd	C1	S1	C2	S2	Δd	C1	S1	C2	S2	Δd
.3(C)	0	0.0	0.0	0.0	0.0	0.0										
	+125	2.4	-0.2	8.3	7.0	35.0										
	+150	3.4	-1.2	9.1	7.0	38.0										
	+175	3.9	-1.2	9.2	7.0	42.0										
	+200	4.4	-1.2	9.9	7.5	47.5										
	+225	4.7	-1.2	10.1	8.0	52.0										
	+250	5.2	-1.2	10.7	8.0	59.2										
	+275	5.4	-1.2	10.9	8.0	65.2										
	+300	6.4	-1.1	11.9	8.5	73.0										
	+325	6.7	-1.0	12.1	9.0	77.5										
	+350	7.5	-0.6	12.6	9.0	87.2										
	+375	7.8	1.1	12.9	9.0	95.5										
	+375	9.3	-0.8	14.2	9.0	109.5	10.3	-4.6	16.5	8.5	116.5	11.8	-	17.6	7.0	240.0
	-375	2.4	-3.6	-0.5	-7.5	60.0	-2.3	-12.6	-0.7	-8.0	76.0	-5.0	-	-8.0	-7.0	230.0
	+400	11.6	-	17.3	7.0	302.0										
	-400	*	*	*	*	*										
.0(C)	0	0.0	0.0	0.0	0.0	0.0										
	+25	0.1	0.2	-1.1	0.0	1.0										
	+50	0.1	0.2	-1.8	-0.3	2.6										
	+75	0.1	0.0	-2.5	-0.8	4.1										
	+100	0.1	-0.3	-2.9	-1.1	4.7										
	+125	-0.1	-0.6	-3.3	-2.2	5.3										
	+150	0.1	-1.1	-3.8	-2.8	6.4										
	+175	-0.4	-1.6	-4.2	-3.5	7.8										

Table A.1. (Continued)

Spec. No.	Peak Shear Stress v(psi)	CYCLICALLY LOADED SPECIMENS														
		Cycle 1					Cycle 2					Cycle 10				
		C1	S1	C2	S2	Δd	C1	S1	C2	S2	Δd	C1	S1	C2	S2	Δd
	+200	-0.6	-1.9	-4.5	-4.2	8.3										
	+225	-1.4	-2.4	-4.6	-5.1	10.0										
	+250	-1.8	-2.8	-4.6	-5.7	13.4										
	+275	-2.2	-3.1	-4.6	-6.4	16.6										
.0(C)	+300	-2.6	-2.9	-3.9	-7.1	21.7										
Cont.	+325	-2.7	-2.7	-3.4	-7.2	26.2										
	+350	-3.1	-[illegible].6	-3.0	-7.8	31.8										
	+375	-3.1	-[illegible].4	-2.8	-7.8	36.5										
	+400	-3.0	-[illegible].2†	-2.3	-8.1	43.4										
	+425	-3.0	-[illegible].2†	-1.9	-8.5	48.9										
	+425	-1.2	-0.8	1.9	-9.2	57.2	0.7	2.2	-4.7	-8.0	60.0	3.5	4.8	-12.8	-10.9	68.4
	-425	3.5	1.8	-11.0	2.4	48.3	4.6	6.3	-21.0	3.7	52.5	8.7	9.0	-29.6	3.5	66.8
	+450	4.1	4.9	-17.3	-12.8	74.4	4.6	3.6	-21.7	-13.4	76.1	6.5	[illegible].0	-35.8	-14.0	84.2
	-450	10.2	9.0	-33.7	3.5	72.6	10.8	8.9	-36.6	3.5	74.6	9.7	7.6	-65.0	-53.4	69.1
	+475	9.6	3.6	-74.7	-92.0	132.4										

APPENDIX B

MATHEMATICAL MODEL BY DUCHON (Ref. 29)

The governing equilibrium, compatibility and constitutive equations for a typical wall element (see Fig. B.1) subjected to combined biaxial tension (N_y, N_x) and shear (V) are given as follows:

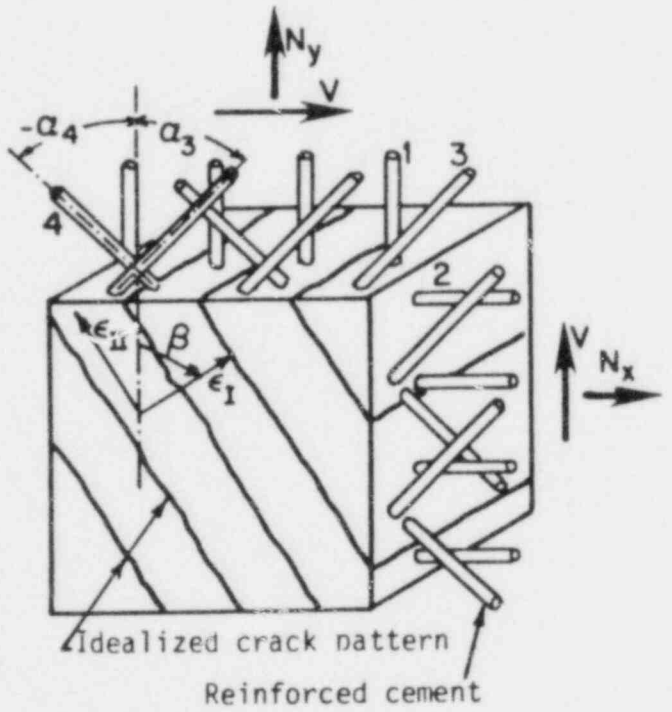

Fig. B.1. Typical reinforced concrete wall element.

a) Equilibrium equations:

$$N_y/A_c = \rho_1\sigma_1 + \rho_3\sigma_3 \cos^2 a_3 + \rho_4\sigma_4 \cos^2 a_4 + \sigma_{II} \sin^2\beta \quad \text{(B.1a)}$$

$$N_x/A_c = \rho_2\sigma_2 + \rho_3\sigma_3 \sin^2 a_3 + \rho_4\sigma_4 \sin^2 a_4 + \sigma_{II} \cos^2\beta \quad \text{(B.1b)}$$

$$V/A_c = \rho_3\sigma_3 \sin a_3 \cos a_3 + \rho_4\sigma_4 \sin a_4 \cos a_4 - \sigma_{II} \sin\beta \cos\beta \quad \text{(B.1c)}$$

where ρ_i, σ_i are the steel percentage ratios and the steel stresses in the i = 1 to 4 directions, respectively, and A_c is the concrete shearing area.

b) Compatibility equations:

$$\varepsilon_1 = \varepsilon_I \cos^2\beta + \varepsilon_{II} \sin^2\beta \qquad \text{(B.2a)}$$

$$\varepsilon_2 = \varepsilon_I \sin^2\beta + \varepsilon_{II} \cos^2\beta \qquad \text{(B.2b)}$$

$$\varepsilon_3 = \varepsilon_I \cos^2(\beta-a_3) + \varepsilon_{II} \sin^2(\beta-a_3) \qquad \text{(B.2c)}$$

$$\varepsilon_4 = \varepsilon_I \cos^2(\beta-a_4) + \varepsilon_{II} \sin^2(\beta-a_4) \qquad \text{(B.2d)}$$

where ε_i are the strain components in the i = 1 to 4 for the steel and in the i = I and II for the concrete (principal strains).

c) Constitutive equations:

Steel:

$$\sigma_i = \varepsilon_i E_s \ (i = 1 \text{ to } 4) \qquad \text{(B.3a)}$$

Concrete:

$$\sigma_I = 0 \qquad \text{(tension)} \qquad \text{(B.3b)}$$

$$\sigma_{II} = \varepsilon_{II} E_c \qquad \text{(compression)} \qquad \text{(B.3c)}$$

where E_s and E_c are the Young's moduli for steel and concrete, respectively.

For a given value of the inclination angle β of the diagonal cracks, the unknown concrete strains ε_I and ε_{II} can be calculated from any two equations (B.1), that represent a nonhomogeneous system. By an iterative

process the correct value of β can be determined so that the third equation is also satisfied.

In the case of an orthogonal reinforcing net (steel bars in the 1, 2 directions), which is pertinent to the present work, the above Eqns. B.1 to B.3 take the following form (see Fig. B.2).

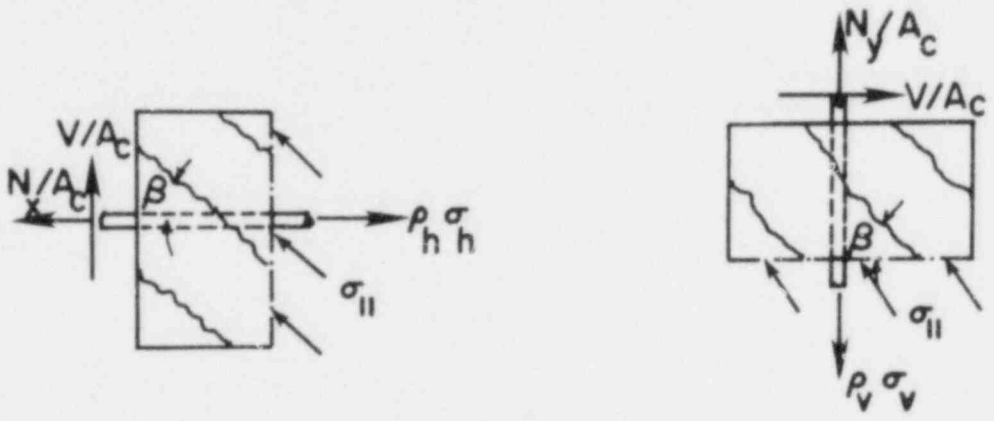

Fig. B.2. Equilibrium of applied and resisting stresses (orthogonal steel).

a) Equilibrium:

$$N_y/A_c = \sigma_v\rho_v + \sigma_{II} \sin^2\beta \qquad \text{(B.1a)'}$$

$$N_x/A_c = \sigma_h\rho_h + \sigma_{II} \cos^2\beta \qquad \text{(B.1b)'}$$

$$V/A_c = -\sigma_{II} \sin\beta \cos\beta \qquad \text{(B.1c)'}$$

b) Compatibility:

$$\varepsilon_v = \varepsilon_I \cos^2\beta + \varepsilon_{II} \sin^2\beta \qquad \text{(B.2a)'}$$

$$\varepsilon_h = \varepsilon_I \sin^2\beta + \varepsilon_{II} \cos^2\beta \qquad \text{(B.2b)'}$$

c) Constitutive:

$$\sigma_v = \varepsilon_v E_s$$

$$\sigma_h = \varepsilon_h E_s \qquad \text{(B.3a)'}$$

$$\sigma_I = 0 \qquad \text{(B.3b)'}$$

$$\sigma_{II} = \varepsilon_{II} E_c \qquad \text{(B.3c)'}$$

where directions 1 and 2 have been substituted with v and h, respectively.

Substituting the relations (B.3)' in the equilibrium Eqns. (B.1)' and utilizing the compatibility Eqns. (B.2)' we get the following set of equations

$$\begin{Bmatrix} N_y \\ N_x \\ V \end{Bmatrix} = A_s E_s \begin{bmatrix} \rho_v \cos^2\beta & (\rho_v \sin^2\beta + \frac{\sin^2\beta}{n}) \\ \rho_h \sin^2\beta & (\rho_h \cos^2\beta + \frac{\cos^2\beta}{n}) \\ 0 & \frac{-\sin\beta \cos\beta}{n} \end{bmatrix} \begin{Bmatrix} \varepsilon_I \\ \varepsilon_{II} \end{Bmatrix} \qquad \text{(B.4)'}$$

where $n = E_s/E_c$.

Solving for I and II from the set of the first two equations in (B.4)' we find

$$\begin{Bmatrix} \varepsilon_I \\ \varepsilon_{II} \end{Bmatrix} = \frac{1}{D} \begin{bmatrix} (\rho_h \cos^2\beta + \frac{\cos^2\beta}{n}) & (-\rho_v \sin^2\beta - \frac{\sin^2\beta}{n}) \\ -\rho_h \sin 2\beta & \rho_v \cos^2\beta \end{bmatrix} \begin{Bmatrix} \frac{N_y}{A_c E_s} \\ \frac{N_x}{A_c E_s} \end{Bmatrix} \qquad \text{(B.5)}$$

with a determinant D equal to

$$D = \rho_v\rho_h (\cos^2\beta - \sin^2\beta) + \rho_v \frac{\cos^4\beta}{n} - \rho_h \frac{\sin^4\beta}{n} \tag{B.6}$$

The principal concrete strains ε_I and ε_{II} for given applied external loads N_y, N_x (normal), and V (shear) are computed using Eqns. (B.5) so that the third equation of (B.4)'

$$\varepsilon_{II} = - \frac{1}{\sin\beta \cos\beta} \frac{nV}{A_s E_s} \tag{B.7}$$

is also satisfied for a certain value of the angle β.

Knowing ε_I and ε_{II} the shear strain γ_{vh} is calculated from the relation

$$\gamma_{vh} = (\varepsilon_I - \varepsilon_{II}) \sin 2\beta \tag{B.8}$$

NRC FORM 335 (7-77)

U.S. NUCLEAR REGULATORY COMMISSION

BIBLIOGRAPHIC DATA SHEET

1. REPORT NUMBER (Assigned by DDC)
NUREG/CR-1602

4. TITLE AND SUBTITLE (Add Volume No., if appropriate)
Strength and Stiffness of Tensioned Reinforced Concrete Panels Subjected to Membrane Shear, Two-Way Reinforcing

2. (Leave blank)

3. RECIPIENT'S ACCESSION NO.

7. AUTHOR(S)
P. C. Perdikaris, R. N. White and P. Gergely

5. DATE REPORT COMPLETED
MONTH: March YEAR: 1980

9. PERFORMING ORGANIZATION NAME AND MAILING ADDRESS (Include Zip Code)
Department of Structural Engineering
Cornell University
Hollister Hall
Ithaca, NY 14853

DATE REPORT ISSUED
MONTH: July YEAR: 1980

6. (Leave blank)

8. (Leave blank)

12. SPONSORING ORGANIZATION NAME AND MAILING ADDRESS (Include Zip Code)
Division of Reactor Safety Research
Office of Nuclear Regulatory Research
U.S. Nuclear Regulatory Commission
Washington, DC 20555

10. PROJECT/TASK/WORK UNIT NO.

11. CONTRACT NO.
FIN No. B5688

13. TYPE OF REPORT
Technical Report

PERIOD COVERED (Inclusive dates)

15. SUPPLEMENTARY NOTES

14. (Leave blank)

16. ABSTRACT (200 words or less)

This report presents results of an experimental program to investigate seismic shear transfer in a cracked reinforced concrete containment vessel without diagonal reinforcement. The test specimen was designed and constructed to represent the stress conditions in the wall of a pressurized containment subjected to tangential shear stresses such as those induced by an earthquake. Four monotonic and twelve reversing shear load tests were done on 4 ft square by 6 in. thick flat specimens reinforced with steel bars in two orthogonal directions.

Test parameters included the level of biaxial tension applied to the bars (from 0 to $0.9f_y$) and the loading history. Results are given for strength, stiffness, development of cracking, and degradation effects produced by cyclic shear. Engineering models for predicting strength and stiffness are given, along with preliminary design implications. A comprehensive review of pertinent literature is also included.

17. KEY WORDS AND DOCUMENT ANALYSIS

17a. DESCRIPTORS
Containment structures, shear tests, seismic design, biaxial tension, shear strength, shear stiffness, cyclic loads, dowel forces

17b. IDENTIFIERS/OPEN-ENDED TERMS
Structural walls, concrete (reinforced)

18. AVAILABILITY STATEMENT
Unlimited

19. SECURITY CLASS (This report)
Unclassified

21. NO. OF PAGES

20. SECURITY CLASS (This page)

22. PRICE
$